

Complexity

Foundations and Applications of Process-based Modeling of Complex Systems

Lead Guest Editor: Francis Heylighen

Guest Editors: Peter Dittrich and Tomas Veloz





Foundations and Applications of Process-based Modeling of Complex Systems

Complexity

Foundations and Applications of Process-based Modeling of Complex Systems

Lead Guest Editor: Francis Heylighen


Guest Editors: Peter Dittrich and Tomas Veloz



Copyright © 2022 Hindawi Limited. All rights reserved.

This is a special issue published in "Complexity." All articles are open access articles distributed under the Creative Commons Attribution License, which permits unrestricted use, distribution, and reproduction in any medium, provided the original work is properly cited.

Chief Editor

Hiroki Sayama , USA

Associate Editors

Albert Diaz-Guilera , Spain
Carlos Gershenson , Mexico
Sergio Gómez , Spain
Sing Kiong Nguang , New Zealand
Yongping Pan , Singapore
Dimitrios Stamovlasis , Greece
Christos Volos , Greece
Yong Xu , China
Xinggang Yan , United Kingdom




Academic Editors

Andrew Adamatzky, United Kingdom
Marcus Aguiar , Brazil
Tarek Ahmed-Ali, France
Maia Angelova , Australia
David Arroyo, Spain
Tomaso Aste , United Kingdom
Shonak Bansal , India
George Bassel, United Kingdom
Mohamed Boutayeb, France
Dirk Brockmann, Germany
Seth Bullock, United Kingdom
Diyi Chen , China
Alan Dorin , Australia
Guilherme Ferraz de Arruda , Italy
Harish Garg , India
Sarangapani Jagannathan , USA
Mahdi Jalili, Australia
Jeffrey H. Johnson, United Kingdom
Jurgen Kurths, Germany
C. H. Lai , Singapore
Fredrik Liljeros, Sweden
Naoki Masuda, USA
Jose F. Mendes , Portugal
Christopher P. Monterola, Philippines
Marcin Mrugalski , Poland
Vincenzo Nicosia, United Kingdom
Nicola Perra , United Kingdom
Andrea Rapisarda, Italy
Céline Rozenblat, Switzerland
M. San Miguel, Spain
Enzo Pasquale Scilingo , Italy
Ana Teixeira de Melo, Portugal

Shahadat Uddin , Australia
Jose C. Valverde , Spain
Massimiliano Zanin , Spain

Contents

Towards an Analytic Framework for System Resilience Based on Reaction Networks

Tomas Veloz , Pedro Maldonado, Evo Bussensiers, Alejandro Bassi, Shima Beigi , Marta Lenartowicz, and Francis Heylighen 



Research Article (29 pages), Article ID 9944562, Volume 2022 (2022)

Reaction Network Modeling of Complex Ecological Interactions: Endosymbiosis and Multilevel Regulation

Tomas Veloz  and Daniela Flores 


Research Article (12 pages), Article ID 8760937, Volume 2021 (2021)

Investigating Transformational Complexity: Counting Functions a Region Induces on Another in Elementary Cellular Automata

Martin Biehl  and Olaf Witkowski 


Research Article (8 pages), Article ID 7501405, Volume 2021 (2021)

Role of Recovery in Evolving Protection against Systemic Risk: A Mechanical Perspective in Network-Agent Dynamics

Chulwook Park 

Research Article (23 pages), Article ID 4805404, Volume 2021 (2021)

Complex Service Process Optimization Based on Service Touchpoint Association and the Design Structure Matrix

Zhonghang Bai, Chang Liu, Huihui Sun, and Man Ding 


Research Article (19 pages), Article ID 7431369, Volume 2021 (2021)

Understanding Ecosystem Complexity via Application of a Process-Based State Space rather than a Potential Surface

C. Gaucherel , F. Pommereau, and C. Hély

Research Article (14 pages), Article ID 7163920, Volume 2020 (2020)

Simulation of Nonradiative Energy Transfer in Photosynthetic Systems Using a Quantum Computer

José Diogo Guimarães, Carlos Tavares , Luís Soares Barbosa, and Mikhail I. Vasilevskiy



Research Article (12 pages), Article ID 3510676, Volume 2020 (2020)

Study of the Complexity Game of Supply Chain Green Innovation Introduction under EPR Policy and Government Subsidies

Xueli Zhan , Yi Tian , Chengjin Liu , Aili Hou , and Junhai Ma 



Research Article (18 pages), Article ID 5342606, Volume 2020 (2020)

Predicting Excavation-Induced Tunnel Response by Process-Based Modelling

Linlong Mu , Jianhong Lin, Zhenhao Shi , and Xingyu Kang


Research Article (11 pages), Article ID 9048191, Volume 2020 (2020)

Depth Penetration and Scope Extension of Failures in the Cascading of Multilayer Networks

Wen-Jun Jiang, Run-Ran Liu , and Chun-Xiao Jia 


Research Article (11 pages), Article ID 3578736, Volume 2020 (2020)

Set-Based Differential Evolution Algorithm Based on Guided Local Exploration for Automated Process Discovery

Si-Yuan Jing 



Research Article (19 pages), Article ID 4240584, Volume 2020 (2020)

Freight Time and Cost Optimization in Complex Logistics Networks

Egemen Sert, Leila Hedayatifar , Rachel A. Rigg, Amir Akhavan, Olha Buchel, Dominic Elias Saadi, Aabir Abubaker Kar, Alfredo J. Morales, and Yaneer Bar-Yam

Research Article (11 pages), Article ID 2189275, Volume 2020 (2020)




Impact of Cell Size Effect on Nutrient-Phytoplankton Dynamics

Tiancai Liao, Hengguo Yu , Chuanjun Dai, and Min Zhao 

Research Article (23 pages), Article ID 8205696, Volume 2019 (2019)

Research Article

Towards an Analytic Framework for System Resilience Based on Reaction Networks

Tomas Veloz ^{1,2,3} **Pedro Maldonado**^{1,2} **Evo Busseni**¹ **Alejandro Bassi**^{1,2}
Shima Beigi ¹ **Marta Lenartowicz**¹ and **Francis Heylighen** ¹

¹Centre Leo Apostel, Vrije Universiteit Brussel, Rue de la Strategie 33, Brussels 1060, Belgium

²Fundación para el Desarrollo Interdisciplinario de la Ciencia, la Tecnología y las Artes, Santiago, Chile

³Universidad Andres Bello, Departamento Ciencias Biológicas, Facultad Ciencias de la Vida, Santiago 8370146, Chile

Correspondence should be addressed to Tomas Veloz; tveloz@gmail.com

Received 3 April 2021; Revised 8 December 2021; Accepted 24 December 2021; Published 31 January 2022

Academic Editor: Alejandro F. Villaverde

Copyright © 2022 Tomas Veloz et al. This is an open access article distributed under the Creative Commons Attribution License, which permits unrestricted use, distribution, and reproduction in any medium, provided the original work is properly cited.

Reaction network is a promising framework for representing complex systems of diverse and even interdisciplinary types. In this approach, complex systems appear as self-maintaining structures emerging from a multitude of interactions, similar to proposed scenarios for the origin of life out of autocatalytic networks. The formalism of chemical organization theory (COT) mathematically specifies under which conditions a reaction network is stable enough to be observed as a whole complex system. Such conditions specify the notion of organization, crucial in COT. In this paper, we show that the structure and operation of organizations can be advanced towards a formal framework of resilience in complex systems. That is, we show that there exist three fundamental types of change (state, process, and structural) defined for reaction networks, and that these perturbations not only provide a general representation of perturbations in the context of resilience but also pave the ground to formalize different forms of resilient responses. In particular, we show that decomposing the network's operational structure into dynamically decoupled modules allows to formalize what is the impact of a perturbation and to what extent any potential compensation to that perturbation will be successful. We illustrate our approach with a toy model of a farm that operates in a sustainable way producing milk, eggs, and/or grains from other resources. With the help of simulations, we analyze the different types of perturbations and responses that the farm can undergo and how that affects its sustainable operation.

1. Introduction

An important challenge of our century is to understand the structural conditions under which systems become sustainable and resilient. Complex system literature seeks for conditions that can provide an answer independent of the nature of the system in question. Sustainable systems are conceived as being capable of sustaining indefinitely, making efficient use of critical resources and recycling whatever is possible. When a system not only self-maintains but also grows in a mutually constructive relationship with its milieu, it fulfills the ideal of sustainable development [1, 2]. Eco-systems normally develop in a sustainable way with an approximately constant level of resource income [3]. Economic systems, on the other hand, although they self-

maintain and grow, are often unsustainable: they consume more of certain resources than they produce. Therefore, they are likely to collapse when the resource reserve is eventually exhausted. For example, the Middle East and North Africa's (MENA) economy is largely relying for its energy on oil and other fossil fuels that are in limited supply and cannot be renewed [4]. On the other hand, when an unsustainable economic system persists and is deemed too big to fail irrespective of the imbalance it brings about, it becomes destructive. Creating a sustainable economy means shifting to resources that are renewable, either through a dependable external input (e.g., wind energy) or through recycling within the network (e.g., biofuel derived from plants grown and harvested by the system) [5]. While it is best known for physical resources, the challenge of sustainability applies to

all systems, including social and informational. Each human organization, large or small, in instituting a boundary between itself and its respective milieu engages with this very question: can it develop in a simultaneously self-constructive and non-exploitative manner?

Complex systems should not just be able to maintain themselves in ideal circumstances; they should also be able to return to self-maintenance when pushed away from this desired state by external challenges. Such capacity for a system to recover efficiently from stressful circumstances is called resilience [6–8]. Resilient systems should be able to return to their preferred configuration even when confronted with serious perturbations that destroy or change some of their components, thus making them deviate from this configuration. Thus, dependably resilient systems can be seen as goal-directed in the cybernetic sense, with maintenance of their essential organization as the implicit goal that they will defend against internal and external perturbations [9, 10]. That is necessary to make them impervious to dangers such as the error catastrophe and the lack of critical resources that threaten the survival of autocatalytic networks in common scenarios for the origin of life. As the range of circumstances with which the system has to deal expands, its strategies will need to become more complex. Thus, as it evolves and learns to cope with increasingly diverse and complex perturbations, its behavior will appear increasingly intelligent [11] and directed at increasingly more difficult to reach goals. To understand how such resilient systems could have evolved out of non-directed causal processes, we need to analyze, first, the precise features that determine resilience and, then, the steps by which these features could have been acquired.

The sustainability and resilience of a complex system should be seen as two sides of the same coin, since both are necessary for the system to thrive. However, conceptual and mathematical modeling of both aspects simultaneously remains difficult because of lack of integration between various theoretical constructs and available formalisms. Reaction networks (RNs) have been proposed as a general language for modeling complex systems [12–15]. In particular, by applying an analytical framework for reaction networks called chemical organization theory (COT), it is possible to compute the set of possible observable systems within a reaction network universe, i.e., systems that persist sufficiently long so that they can be identified and observed. These sufficiently stable systems are called organizations. They correspond to structurally closed and self-maintaining sub-networks of the reaction network [16, 17]. Such operational closures maintained by the otherwise interconnected and interdependent systems are captured by the concept of *autopoiesis*. Autopoiesis (“self-production”) refers to self-maintaining dynamics that can be observed in systems as diverse as individual organisms, populations, ecosystems, economies, cities, cultures, institutions, legal frameworks, information systems, and so on. Since the sustainability of a complex system depends on the interplay between such formations operating at different levels or scales, a formal language capable of modeling sustainability must be applicable to each of their respective heterogeneous dynamics, as well as their mutual dependencies.

While the COT formalism elegantly describes what makes a reaction network sustainable, it does not yet explain what would make it resilient, i.e., able to cope with perturbations. In this paper, we first elaborate on a deeper view of what a perturbation means by reviewing the different kinds of perturbations that exist, next we review structural results on COT which allow to link the different kinds of perturbations to the structure and stability of the reaction network, and then we elaborate a qualitative dynamical analysis based on computational simulations of the perturbations and the dynamical responses of a toy-model reaction network. Namely, we show that the resilience of a reaction network do not only depends on its structure but also on how it is operated. This operation is described by the processes applied to the reaction network, and that certain non-intuitive behaviors can happen. This last aspect opens important questions towards the development of a formal framework for resilience in complex systems. Regarding the deeper understanding of perturbations, we show that reaction networks can be subjected to three fundamentally different types of environmental perturbations: change of state, meaning variation in the values of the defining variables (quantity of the different “species”); change of process, meaning variation in the way the network operates; and change of structure, meaning addition or elimination of reactions and species. Regarding the review of structural results, we review the decomposition theorem for reaction networks and explain how it helps to identify the impact of, and the potential responses to, perturbations of the different kinds. Regarding the qualitative analysis, we develop a toy-example reaction network that models the productive processes of a farm involving use of resources such as grass and water, production of goods such as milk and eggs, and operative actions such as selling goods or investing in infrastructure that can sustainably operate in different ways, for example, either seeking for optimizing profit or optimizing sustainable growth. We then study the effects of the different kinds of perturbations on the farm depending on the way it operates. This leads us to a formal framework for developing and assessing the success of potential mitigation strategies, represented as state, process, or structural counter-perturbations.

2. Resilience: A Brief Review of the Literature

Resilience is a highly elusive concept with over 150 definitions ranging from ecology, engineering, economics, organizations, and psychology and adjacent terminologies such as vulnerability, coping capacity, adaptive capacity and robustness, and so on which can be found in the literature [7].

The term resilience stems from a Latin root, *resilire*, to leap back or to rebound. An important definition was given by Holling inspired by ecological systems [18]. Resilience according to Holling “indicates the persistence of relationships within a system and is a measure of the ability of these systems to absorb changes of state variables, driving variables, and parameters, and still persist. In this definition resilience is the property of the system and persistence or probability of extinction is the result. Resilience is the ability of a system to absorb external stresses.”

In Holling's approach, resilience is intricately linked to "external shocks" that provoke changes within the "internal ecosystem" of the system of interest. The latter reflects an important characteristic about the nature and complexity of homeostatic processes in an ecosystem. In this version of resilience, homeostatic processes are considered to be an umbrella term for Holling's "changes of state variables, driving variables, and parameters."

Resilience according to Holling has two distinct end points: (a) persistence as a function of "ability to absorb changes of state variables, driving variables, and parameters," and (b) probability of extinction (i.e., which opens space for alternative methods that have "persistence intention" or "transformative intentions" at heart). One important feature to reach these resilient conditions is anticipating a system's recovery response by sole measurement of its ability to throw off the impact of shocks on its growth path or by its potential to throw it off its growth [19].

In [6], resilience is defined as "the capacity of a system to absorb shocks and reorganise while undergoing change so as to still retain essentially the same function, structure, identity, and feedback." In this classic paper, resilience as a collective variable is characterized by four different dimensions, namely, latitude, resistance, precariousness, and cross-scale dynamics. These aspects have been modeled from the perspective of dynamical systems by elaborating on the notion of attractor and its surrounding basin of attraction [20]. Latitude measures the room that perturbations have to push the system away from its present attractor but without leaving the basin. As long as it stays within the basin, the dynamics will anyway bring the system back to the attractor, thus automatically absorbing the perturbation. For example, the presence of high biodiversity in an ecosystem makes it possible for the replacement of lost species if and when perturbations occur, providing more latitude for manoeuvring in the overall system.

Resistance represents the effort needed or difficulty for a perturbation to change the state of the system. In contrast to latitude, resistance is mostly related to the kinds of negative feedback mechanisms that a system has developed in the course of its history in order to suppress perturbation. Precariousness refers to the closeness of the current system's state to a limit or threshold (typically the boundary separating the present basin from one leading to a different attractor) beyond which it would no longer be able to operate. For example, the human body is precarious in the sense that if its internal temperature would be increased with just a few degrees, it would not be able to survive. Yet, it is a highly resistant system because it has evolved a very effective mechanism of temperature regulation to suppress such temperature changes. Finally, cross-scale dynamics refer to a system's dependence at a particular focal scale on the influences of states at scales above and below. Cross-scale relations also refer to the ways latitude, resistance, and precariousness are influenced by the states and dynamics of the (sub) systems at scales above and below the scale of interest [6].

Resilience has also been measured and defined as a measure of complementary stress [21], as the pull strength of

a basin of attraction in behavioral development literature [22], and as the width of a basin of attraction [23]. Scheffer in [23] elaborates on the latter form as follows: "the width of the basin of attractor indicates resilience of a system and is the magnitude of change that can be accommodated before the system undergoes a quantitative change marked by a critical transition to a different and undesirable state."

To avoid a presumably common mistake of equating resilience with robustness/resistance and to encourage adaptive management of resources versus common command and control methods, a further distinction is made between ecological resilience and engineering resilience.

Engineering resilience is focused on the near-equilibrium steady states, where "resistance to disturbance" and "speed of return" to the equilibrium are measures of resilience. While the engineering resilience definition is highly focused on constancy and structural robustness of the system, ecological resilience is focused on the magnitude of disturbances that can be absorbed before the system changes its structure by changing the variables and processes that control its behavior [24, 25].

While most literature makes a sharp distinction between these two forms of resilience, one can see that both definitions are concerned with the system's continuity in a time of change. Studying a four-case scenario, including high-risk/low-resilience, high-risk/high-resilience, low-risk/low-resilience, and low-risk/high-resilience profiles, it has been shown that there is a significant difference between risk management and resilience management: "risk management helps the system prepare and plan for adverse events, whereas resilience management goes further by integrating the temporal capacity of a system to absorb and recover from adverse events and then adapt" [26].

Further, attempts to create an offshoot of the resilience concept such as "adaptive resilience," "static resilience," "specific resilience," and "general resilience," have been proposed [8].

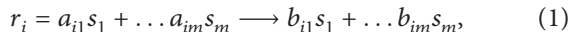
As discussed by Scheffer in [23], attention to the memory of a system shifts the discourse of resilience towards *adaptability*, which is the capacity of people in a social-ecological system to manage resilience through collective action, *transformability*, which refers to a fundamental alteration of the nature of a system once the current ecological, social, or economic condition becomes untenable or undesirable [6], and probability of extinction [18]. Transformability means the ability to create and define a new attractor that directs the development of the system by introducing new components and ways of making a living, thereby changing the state variables and often the scales of key cycles that define the system.

In conclusion, the literature on resilience proposes a wide range of notions that can help us to better understand what resilience is and how it can be formalized but does not as yet propose an integrated theory. Our work intends to advance towards such a theory by providing novel formalizations of the state, process and structure of self-sustaining systems, the corresponding types of perturbations, the effect of these perturbations on the system's self-maintenance, and the potential responses to safeguard that self-maintenance.

3. Chemical Organization Theory

Chemical organization theory (COT) was developed in the mid-2000s in order to model complex dynamical production systems (such as chemical systems) where new components, so called “species,” can appear and disappear [16]. The central element of COT is a structure called “organization,” which is defined as a closed and self-maintaining sub-network of reactions that consume and produce species. COT leverages from the fact that there are three increasingly precise, but complex, ways to represent a reaction network. In the simplest *relational* description of a reaction network, reactions only describe which species are transformed by which reactions. This level focuses on the connectivity properties of the reaction network using set-theoretical structures, while ignoring the quantitative aspects. In the *stoichiometric* description of a reaction network, the quantity of each species consumed and produced by a reaction is included. At this level, properties about the dynamical operation of the reaction network within a fixed time span, described by linear-algebraic structures, are of interest. However, there is no information about general time evolution. In the *kinetic* description of a reaction network, the state of the reaction network is specified by the concentration of each species and is subject to rules to update both the state of the reaction network and the occurrence of reactions over time. This allows determining the time evolution of the system. However, this requires solving a potentially large system of differential or difference equations, implying heavy numerical computation. Therefore, COT aims to derive the most important dynamic properties of a reaction network, such as stationary states, attractors, and responses to perturbations, from the description at the stoichiometric and relational levels, where properties can be computed in terms of simpler mathematical structures at a much lower computational cost than in the kinetic level where the actual dynamics occur. For a comprehensive introduction to COT, we refer the readers to [14, 16].

3.1. Reaction Networks. Let $M = \{s_1, \dots, s_m\}$ be a finite set of m species reacting with each other according to a finite set $R = \{r_1, \dots, r_n\}$ of n reactions. The set of species and reactions is called the *reaction network* (M, R) . A reaction r_i is represented by



with $a_{ij}, b_{ij} \in \mathbb{N}_0$, for $i = 1, \dots, n$.

Reactions describe which collections of species transform into which new collections. For a given reaction $r_i \in R$, the species s_j to be transformed, i.e., such that $a_{ij} > 0$, are called *reactants* of r , and the species to be created, such that $b_{ij} > 0$, are called *products*.

In COT, we focus on the properties of subsets of species $X \subseteq M$. Note that for all X , there is a unique maximal set of reactions $R_X \subseteq R$ defined as the set of all reactions whose reactants are in X . Thus, each set X induces a *sub-network* (X, R_X) .

As an example of how reaction networks can be used to model non-biochemical systems, consider a farm where farmers have different productive processes based on the available resources, which can be obtained from the environment (water) or grown within the farm (cows and grass) or obtained as a result of the functioning of the farm (milk and dung) and infrastructure (infrstr), and that the farm acquires money by selling products of such functional processes (milk) to grow more infrastructure. Therefore, we might model the latter narrative as a reaction network with the set of species $\{\text{water, grass, cows, infrstr, farmer, milk, dung}\}$ and the following reactions (see Table 1).

3.2. Closure, Connectivity, and Semi-Self-Maintenance. In order to trace the formation, persistence, and dissolution of a sustainable reaction network, we first need a formal indication of what is the extent at which it can operate. We introduce the notion of closed set of species to encode the reaction sub-networks (X, R_X) that do not produce species outside X .

Definition 1. X is closed iff the products of every reaction in R_X are in X [14].

Another interesting property for reaction networks is connectivity. Connected species in X can be seen as *potentially co-dependent* species in the reaction network because the consumption of one of them might affect the production of all the species connected to it. In general, X can be decomposed into connected modules whose reactions are *independent*.

Definition 2. Two species $s_j, s_k \in X$ are directly connected in X if and only if there exists a reaction $r_i \in R_X$ such that both species are active in the reaction, i.e., s_j and s_k are reactants or products of r_i . We say s_j and s_k are connected in X if and only if there exists a sequence of species $s_0, \dots, s_p \in X$ such that $s_0 = s_j$, $s_p = s_k$ and for all $l = 0, \dots, p - 1$, we have that s_l and s_{l+1} are directly connected in X .

It is worth to notice that a closed set might be composed by various disconnected smaller closed sets. In that case, the dynamic operation of the complete reaction network can be understood as the dynamics of independent smaller systems. For example, consider $X = \{a, b, c, d\}$ and the reactions $\{a \longrightarrow b, b \longrightarrow a, c \longrightarrow d, d \longrightarrow c\}$. The connected components of X are $\{a, b\}$ and $\{c, d\}$. Indeed, identifying independent behavioral modules of a reaction network is useful from both computational and mathematical perspectives because it provides resources for an algorithmic *divide-and-conquer* strategy and also can deepen the understanding of the structure of the reaction network.

While the notion of closure in Definition 1 corresponds to the notion of a *closed system* in general system theory, there is another form of *operational closure*, meaning that the system can self-maintain while also accepting environmental inputs and releasing outputs. Such operational

TABLE 1: Examples of reactions and their meaning according to the simple narrative of how a milk-based farm works.

| Reaction | Meaning |
|---|------------------|
| $\emptyset \longrightarrow \text{water}$ | Access to water |
| $\text{grass} + \text{cows} + \text{infrstr} + \text{water} \longrightarrow \text{milk} + \text{cows} + \text{dung} + \text{infrstr}$ | Producing milk |
| $\text{milk} + \text{farmer} \longrightarrow \text{money} + \text{farmer}$ | Selling milk |
| $\text{infrstr} \longrightarrow \emptyset$ | Infrstr degrades |
| $\text{money} + \text{farmer} + \text{infrstr} \longrightarrow \text{farmer} + 2\text{infrstr}$ | Reinvesting |

closure, native to the autopoietic system literature [27], can be represented as semi-self-maintenance.

Definition 3. X is semi-self-maintaining if and only if for each reactant $s \in X$ of a reaction $r \in R_X$, there is a reaction $\bar{r} \in R_X$ such that s is a product of \bar{r} .

A set of species that is semi-self-maintaining can produce all the species consumed by its associated set of reactions. However, such recreation might not be quantitatively balanced. As an example, consider the reactions $\{a \longrightarrow b, 2b \longrightarrow a\}$. In the example, the set $\{a, b\}$ is semi-self-maintaining but cannot self-maintain quantitatively because every time b is produced from a , $2b$ are required to compensate such production. In order to clarify how balanced production can occur in a reaction network, we need to formalize how it operates.

3.3. Operational Processes. The dynamics of the reaction network in a given time interval are determined by how much each reaction occurs in the time frame. Indeed, the more a reaction happens, the more their reactants and products will be consumed and produced, respectively. Thus, the relative frequencies among reactions determine the productive features of the reaction network. A particular specification of the occurrence of reactions within a time interval is called *operational process*, or simply *process*, and we denote it by \mathbf{v} . In traditional reaction network modeling, \mathbf{v} is directly determined by the state of the system and known as flux vector [12]. The notion of process is more general than that of flux vector. Since reactions in our framework are not only of chemical nature, the processes determining the state changes of the reaction network could be not only determined by the state of the system but also driven by decisions of agents or by other external influences such as control systems. Moreover, the time unit at which the process occurs is not necessarily fixed as in traditional reaction network modeling. Thus, a process corresponds to a non-negative vector $\mathbf{v} = (\mathbf{v}[1], \dots, \mathbf{v}[n])$, where $\mathbf{v}[i]$ specifies the extent at which reaction r_i is happening in the time interval in consideration, $i = 1, \dots, n$.

We say a process \mathbf{v} can be applied to X if all the reactions in the process can be triggered by the species in the set X . Hence, \mathbf{v} can be applied to X only if $\mathbf{v}[i] > 0$ implies $r_i \in R_X$, for $i = 1, \dots, n$.

In order to represent how species are globally transformed in the reaction network by the application of a process, let us represent the state of a reaction network by a vector \mathbf{x} of non-negative coordinates such that $\mathbf{x}[j]$ corresponds to the number (or concentration) of species of type s_j

in the reaction network, $j = 1, \dots, m$. In addition, note that the numbers a_{ij} and b_{ij} in (1) can be used to encode the way in which species are consumed and produced by the reactions. Thus, we can build a *stoichiometric matrix* $\mathbf{S} \in \mathbb{N}^{m \times n}$ such that $\mathbf{S}[j, i] = b_{ij} - a_{ij}$.

From here, we can compute the new state $\mathbf{x}_\mathbf{v}$ of the reaction network associated to a state \mathbf{x} and a process \mathbf{v} by the following equation:

$$\mathbf{x}_\mathbf{v} = \mathbf{x} + \mathbf{S}\mathbf{v}. \quad (2)$$

In the case of discrete dynamics, $\mathbf{S}\mathbf{v}$ represents the variation in amount of species over the time interval at which the process occurred. For continuous dynamics, $\mathbf{S}\mathbf{v}$ represents the derivative of \mathbf{x} with respect to time.

3.4. Process Space and Self-Maintenance. Note that when a process \mathbf{v} assigns a non-negative rate to reactions contained in R_X only, it can be applied to X . However, \mathbf{v} might not be feasible for the dynamical constraints that rule the reaction network. For example, it might be that the current state \mathbf{x} does not have enough species to trigger the particular amount of times that a certain reaction is required by the process (lack of reactants) or that some dynamical constraints lead some processes unfeasible [28].

As a simple example, suppose we have a system with two reactions that require the same reactant and produce different products: $r_1 = \text{money} \longrightarrow \text{food}$ and $r_2 = \text{money} \longrightarrow \text{clothes}$, that the state of the system is only one unit of the species money, thus $\mathbf{x} = (1, 0, 0)$, and that reactions can only occur in discrete numbers. Thus, the process $(1, 1)$ is unfeasible. Indeed, the only feasible processes under the constraints that rule the dynamics of this situation are $\mathbf{v} = (1, 0)$ and $(0, 1)$.

In order to formalize what processes can be successfully applied to the reaction network, we introduce a set of feasible processes $\Pi(R_X)$ that can be applied to X and call it the *process space*. Notably, the process space in most chemical systems is determined by the mass-action kinetic law, which states that the rate $\lambda(r_i)$ of reaction r_i is given by

$$\lambda(r_i, \mathbf{x}) = k_i \prod_{j=1}^n \mathbf{x}[j] (t)^{a_{ij}}, \quad (3)$$

where k_i is the intrinsic reaction rate of r_i , $\mathbf{x}[j](t)$ is the concentration of species s_j at time t , and a_{ij} is the amount of reactants of type s_j required to trigger r_i (as defined in (1)). To illustrate this concept, consider the reaction $r = 2s_1 + s_2 \longrightarrow s_3$. The rate of this reaction is given by $\lambda(r, \mathbf{x}) = k\mathbf{x}[1](t)^2\mathbf{x}[2](t)$, where k is the intrinsic rate of r .

Note that for the case of mass-action kinetics, the process space is a function of \mathbf{x} and defined by

$$\Pi(R_X, \mathbf{x}) = \text{vs.tv}[i] = \lambda(r_i, \mathbf{x}), \quad (4)$$

with $\lambda(r_i, \mathbf{x})$ as in (3).

Thus, the notion of process space generalizes the notion of kinetic law because $\Pi(R_X)$ allows for specifications of what processes are feasible that might or might not depend on the state of the system, time, control systems, external agents, etc.

This formulation of the process space can be used to formalize the notion of operational closure, in the sense of autopoietic systems [27], leading to the concept of *self-maintaining processes* for reaction networks.

Definition 4. X is self-maintaining if and only if there exists $\mathbf{v} \in \Pi(R_X)$ such that $r_i \in R_X$ implies $\mathbf{v}[i] > 0$ and $\mathbf{x}_{\mathbf{v}}[j] \geq \mathbf{x}[j]$, for $j = 1, \dots, m$.

A set of species that is self-maintaining encounters processes in its process space such that all the reactions of a reaction network into consideration have a positive rate and, when applied, all the consumed species of the set are produced in equal or larger amount. This implies that a self-maintaining set of species is able to operate activating all the reactions in R_X without decreasing and possibly increasing their concentration.

3.5. Organizations and Autopoietic Systems. With both the structural and processual dimensions of sustainability represented in the formalism by closure and self-maintenance, respectively, we can see how the language of the COT allows us to identify complex systems at different stages of their formation with variable degrees of closure towards the status of a full *organization*.

Definition 5. Let $X \subseteq M$, and X is an organization if and only if X is structurally closed and self-maintaining.

Because organizations are closed, meaning they do not generate novel species, and self-maintaining, meaning they can fully operate without decreasing the species concentration, they represent an abstraction of the persistent dynamical behaviors such as fixed points, periodic orbits, and limit cycles of a reaction network [16, 17].

Therefore, the ability to unambiguously identify stable systems as organizations is one of the core features of this framework. Indeed, an organization can be attributed an identity and associated to an emergent behavioral unit because it is stable enough in time to be observed as such, and this stability is the consequence of a self-maintaining process available in its process space repertoire (also known as cognitive domain as introduced by Varela [29]). The latter idea establishes a formal equivalency between the organizations understood as stable unities and autopoietic systems [30, 31]. The representability of the persistence of identity in time makes the reaction network formalism suitable as a language for modeling systems, as the set of organizations of a reaction network can be said to capture all systems observable in the reaction network universe [14].

Most interestingly, the reaction network formalism allows us not only to identify all complete organizations that co-exist at the particular moment in time but also to asynchronously trace their emergence at all stages of development towards self-maintenance and structural closure, as well as their subsequent decomposition into functional units. Therefore, systems modeling in the reaction network framework does not require that we begin with a pre-existing, pre-defined system. Instead, we begin from a collection of reactions playing the role of fundamental processes, whose reactants and products can be of any nature (chemical, biological, cognitive, semiotic, and so on). Hence, a reaction network can represent a universe whose evolution is driven by the ways in which combinations of entities transform into other combinations. Notably, (i) systems are thought to be stable enough in time so they can be observed and (ii) systems hold certain properties that define their qualitative identity. Thus, in the reaction network framework, we define a system as a sub-network (X, R_X) of (M, R) such that X is an organization. The latter entails a dynamic notion of qualitative identity: a system is continuously changing its inner components and sub-processes, but the identity and unity persist as long as the reaction network is structurally closed and its processes are self-maintaining. Therefore, the reaction network (M, R) plays the role of the universe of interactions, while the organizations play the role of potentially observable systems in this universe.

This feature of the COT modeling language is crucial for the simultaneous study of resilience and sustainability. By modeling systems as temporary, perishable formations within a much wider “primordial” universe, we can, first, simulate and test the durability of our pre-existing systems of interest in their response to various configurations of stressors and, second, gauge the environmental impact of our systems’ functioning. This includes the formative processes that will be mobilized in the environment as a result.

It is important to mention that the approach to autopoiesis and stability in reaction networks given by COT provides a complementary framework to several other approaches that aim at linking the structure and dynamics of reaction networks. For example, deficiency theory [32, 33] incorporates the idea of complex dynamics as collections of reacting species and derives structural conditions for the existence of equilibrium states. The relation between COT and deficiency theory has been discussed in [34]. Similarly, the relation between COT and MR systems and RAF sets has been discussed in [35]. The relation between COT and Petri net analysis [36, 37] has been discussed in [38]. Therefore, COT can be integrated with these other formal analysis methods in biochemistry [39] in order to formalize the more intuitive notions of resilience existing in the literature.

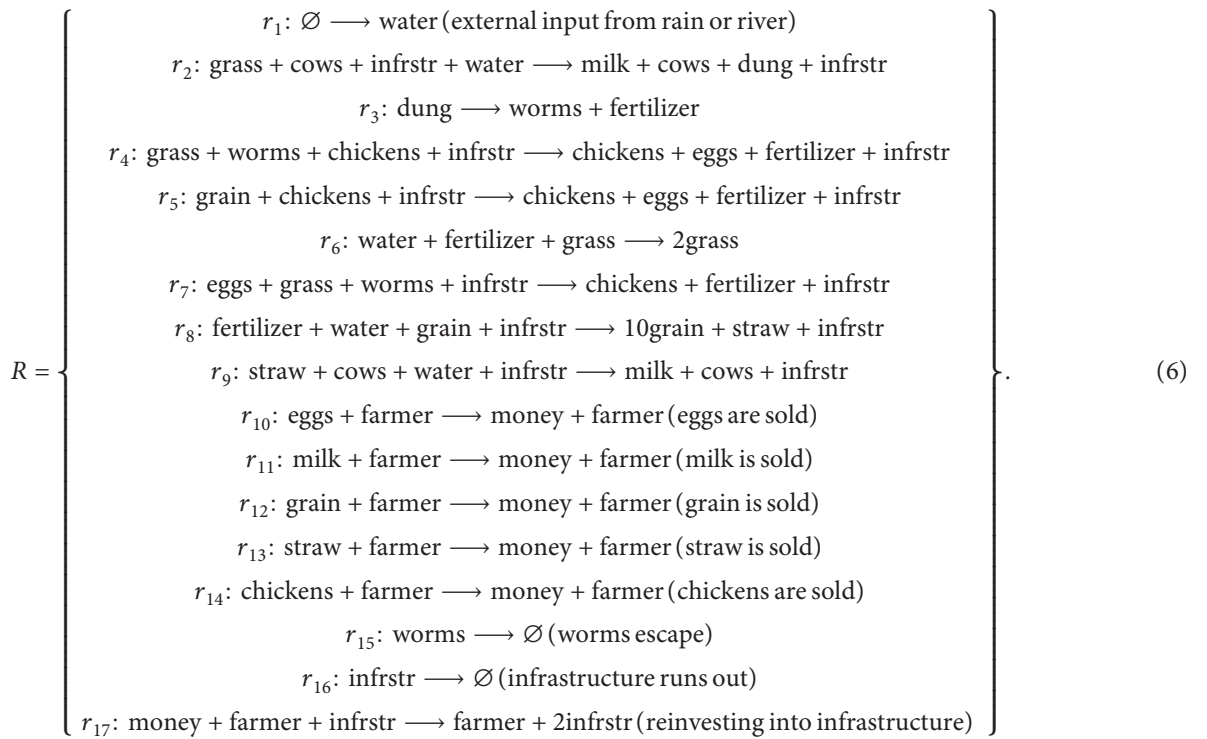
3.6. Reaction Network Toy Example: A Farm. We now illustrate the application of COT to a concrete situation. Consider a farm that operates applying a number of processes (reactions). The basic goal of the farm is to survive, i.e., not running out of resources so that it goes bankrupt, and the secondary goal is to grow, i.e., increasing the amount of

resources that it produces, most concretely food and money. The set of species we consider to model the farm is the following:

$$\mathcal{M} = \{\text{water, grass, cows, infrstr, milk, dung, worms, fertilizer, chickens, eggs, grain, straw, money, farmer}\}. \quad (5)$$

Infrastructure here is everything needed to let the farm run: buildings, milking machines, tractors, laborers, land, etc. The farmer is the manager of the farm, who invests money from the farm proceeds to keep the infrastructure running and developing.

We now introduce the set of reactions R describing the different basic processes that can possibly happen in our model:



Note that every subset of species of M can be interpreted as a possible situation of the farm. For example, if we consider the reactants of the reaction r_2 only, i.e., the set $\{\text{grass, cows, infrstr, water}\}$, we refer to a situation such as the farmer is operating the farm with cows and infrastructure only, and, for example, no chickens are available. Note that for such set of starting species, the reactions r_1, r_2 , and r_{16} are active. Since the operation of starting a farm will produce milk and dung (products of r_2), reactions r_3 and r_{11} will activate. In turn, the products of r_3 will activate reactions r_{15} and r_6 and the products of r_{11} will activate reaction r_{17} . At that stage, nothing else can be activated, and thus the operation of the farm starting from the set $\{\text{grass, cows, infrstr, water}\}$ reaches a closed set representing a grainless and chickenless farm $\text{GCL} = \{\text{grass, cows, milk, dung, fertilizer, worms, water, infrastructure, farmer, money}\}$.

Interestingly, GCL is self-maintaining for a process \mathbf{v} holding the following conditions:

- $\mathbf{v}[1]$ at a larger or equal rate than $\mathbf{v}[2] + \mathbf{v}[6]$ (water is not depleted).
- $\mathbf{v}[2]$ occurs at a larger or equal rate than $\mathbf{v}[3]$ (dung is not depleted).
- $\mathbf{v}[3]$ occurs at a larger or equal rate than $\mathbf{v}[6]$ (fertilizer is not depleted).
- $\mathbf{v}[6]$ occurs at a larger or equal rate than $\mathbf{v}[2]$ (grass is not depleted).
- $\mathbf{v}[2]$ occurs at a larger or equal rate than $\mathbf{v}[11]$ (milk is not depleted).
- $\mathbf{v}[11]$ occurs at a larger or equal rate than $\mathbf{v}[17]$ (money is not depleted).

- (g) $\mathbf{v}[17]$ occurs at a larger or equal rate than $\mathbf{v}[16]$ (infrastructure is not depleted).

For example, suppose that \mathbf{v} reflects the monthly operation of the farm, and that the units of all species are adapted accordingly. Note that the process where $\mathbf{v}[1] = 2, \mathbf{v}[2] = 1, \mathbf{v}[3] = 1, \mathbf{v}[6] = 1, \mathbf{v}[11] = 1, \mathbf{v}[16] = 1, \mathbf{v}[17] = 1$ holds the above conditions and thus proves the self-maintenance of GCL. However, that very same process with $\mathbf{v}[3] = 2$ is not self-maintaining because dung is consumed more than what is produced. Thus, GCL requires for being an organization that some processes in $\Pi(R_{\text{GCL}})$ hold the above conditions (a)–(g).

Additionally, note that certain closed sets cannot be self-maintaining for any process. For example, {water, infrastructure, worms, dung, fertilizer} cannot be self-maintaining because infrastructure and dung cannot be produced by any of the reactions that can be activated by such set. Interestingly, this set is compatible with a situation where the farmer left the farm and took his animals and productive resources, leaving the infrastructure with no productive capacity. In COT, we say the set {water, infrastructure, worms, dung, fertilizer} is not semi-self-maintaining (see Definition 3). Therefore, closed sets $X \subseteq M$ that are not semi-self-maintaining cannot be self-maintaining, independent on how $\Pi(R_X)$ is defined, because semi-self-maintenance is a necessary condition for self-maintenance [16].

By using a software to compute organizations [40], we obtain that the organizations of this reaction network are the following:

- (i) {water} (no farm).
- (ii) GCL (grainless and chickenless farm) = $M - \{\text{chickens, eggs, grain, straw}\} = \{\text{grass, cows, milk, dung, fertilizer, worms, water, infrastructure, farmer, money}\}$
- (iii) CL (chickenless farm) = $M - \{\text{chickens, eggs}\} = \{\text{grass, cows, milk, dung, fertilizer, worms, grain, straw, water, infrastructure, farmer, money}\}$.
- (iv) GL (grainless farm) = $M - \{\text{grain, straw}\} = \{\text{grass, cows, milk, dung, fertilizer, worms, chickens, eggs, water, infrastructure, farmer, money}\}$.
- (v) M (fully functional farm).

These organizations form a partial ordered set as it can be seen in Figure 1.

The latter analysis shows that COT is useful to comprehend what are the crucial sets of species in our model that can operate in a closed and self-maintaining way, i.e., as organizations. Moreover, it allows us to identify the kinds of processes that will operate the farm in a sustainable way. The latter is a much more efficient analytical strategy than simulating the reaction network under a variety of circumstances, especially for large reaction networks. Indeed, the number of sub-networks at which a reaction network could converge is exponential with the number of species, while the number of organizations of several reaction networks analyzed in previous research has been shown to grow

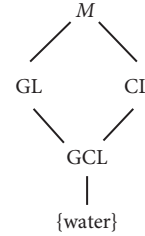


FIGURE 1: Organization ordering.

at a much smaller rate (nearly linear) with respect to the number of species [41, 42].

From here, it is important to understand what are the potential impacts in the organization's operation for a given unexpected perturbation.

4. A Systemic Framework for Perturbations and Responses

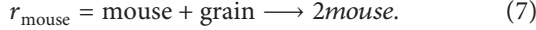
4.1. Perturbations and Structural Changes. In traditional dynamical systems, perturbations correspond to either a change in the (initial) state of the system or a change in the parameters that rule its evolution. The former case is applied, for example, to perform stability analysis, while the latter is applied to bifurcation and other parametric analyses [20].

When a system is represented by a reaction network, the first type of change corresponds to a change in the state \mathbf{x} , exactly in the same way as in traditional dynamical systems. The second type of change corresponds to a change in the process space $\Pi(R_X)$, i.e., a modification of what reaction rates are allowed for the processes that can be applied to the reaction network. In addition to these two types of change, for complex systems, there is a third type of change which is highly relevant but can hardly be represented using traditional dynamical systems. This change corresponds to adding or removing entities or interactions. In dynamical systems, this will modify the structure of the dynamical equations before and after perturbation, so measuring change for such types of changes is far from simple. For complex systems represented by means of graphs or agent-based models, this is represented by the addition of a vertex or edge and agent or rule, respectively, but there is no clear way to link the dynamics of the new network to this structural change [43]. For a system represented by a reaction network, the structural change is similar to the one obtained for a graph. Thus, a structural perturbation corresponds to the addition of a new reaction, which might or might not include new species. However, different to the network and agent-based model approach, the structural change can be tackled by COT.

That is, the addition of a reaction by a structural perturbation changes the process vectors available and eventually the species set as well, implying the emergence of a new organizational structure. Indeed, an added, or eliminated, reaction will add a new dimension to, or set to zero the value of, the process vector, respectively. Therefore, structural perturbations of eliminating nature might be equivalent to process perturbations (when a reaction is

eliminated) or to a state perturbation (when a species is eliminated). However, structural perturbations of constructive nature do not have a counterpart as state or process perturbations because they increase the dimension of the state or process vector (respectively).

As an example of the latter concepts, consider the farm model in equation (6) and the entire farm M as our organization. An example of state perturbation is the accidental death of one or more cows. This perturbation will reduce the number of cows, which in turn could reduce the capacity of the farm to produce milk by reactions r_2 and r_9 . If that occurs, some processes where $\mathbf{v}[2]$, $\mathbf{v}[9]$, or both are too large will not be feasible anymore. Thus, the state perturbation might be able in some cases to modify the process space $\Pi(R)$. Indeed, if the perturbation is too large (too many cows die), this could modify the process space so that M can no longer operate in a self-maintaining manner. For an example of a process perturbation, consider climate change affecting the input of water by r_1 represented by the value $\mathbf{v}[1]$, so that it remains smaller than a certain critical value w_{\max} reflecting the scarcity of water available to run the farm. Under such perturbation, processes that require too much water would not be possible any longer, so the potential ways of operating the farm are modified, again threatening the possibility of M to operate in a self-maintaining way. An example of a structural perturbation is the arrival of mice that eat the grains produced by reaction r_8 in equation (6). Such perturbation would appear as a reaction



This structural perturbation induces a process space perturbation, as the number of reactions is increased and thus the dimension of the process vector. It is likely that under the new processes, we will observe a reduction of the amount of grain produced by the normal operation of the farm, threatening of course its self-maintenance.

In Table 2, we summarize the types of perturbations that a reaction network can be subjected to.

We now turn to a more detailed description of the inner structure of the operation of a reaction network, which will help us to better understand how perturbations threaten the self-maintenance of organizations.

4.2. Catalysts, Overproducible, and Fragile Components. The study of reaction networks has developed several structural notions that help to link structure and dynamics [32, 39]. In this section, we will introduce some elements that advance our understanding on the impact that the different kinds of perturbations explained in the previous section might have on an organization [44].

Definition 6. A species $s_j \in X$ is a catalyst w.r.t X if and only if $r_i \in R_X$ implies $a_{ij} = b_{ij}$, for $i = 1, \dots, n$.

Note that the catalysts of a set X are not affected by the choice of the process $\mathbf{v} \in \Pi(R_X)$ because they are equally consumed and produced by every reaction. This implies that a state perturbation will only have effect on the concentration

of a catalyst if the perturbation is on the catalyst itself. Additionally, we can infer that a process space perturbation will not have an effect on the catalyst concentration. Interestingly, a structural perturbation which eliminates reactions will not modify the defining feature of catalysts, and they will still be produced and consumed at equal amount by all available reactions. However, the addition of new reactions might change the status of catalysts in case one of the new reactions consumes a catalyst in a different amount to what produces it. The maximal set of catalysts w.r.t X is always unique, will be called the *catalyst component* of X , and will be denoted by E_X . For example, in the farm model given by equation (6), we have that $E_M = \{\text{farmer, cows}\}$.

Definition 7. A species $s_j \in X$ is overproducible w.r.t X if and only if there exists a process $\mathbf{v} \in \Pi(R_X)$ such that for \mathbf{x}_v in equation (2), we have $\mathbf{x}_v[j] > \mathbf{x}[j]$ and $\mathbf{x}_v \geq \mathbf{x}$.

An overproducible species is such that specific processes are able to produce it without decreasing the amount of any of the species. For this reason, overproducible species can grow indefinitely in principle. This, on the one hand, is useful to the system as overproducible species can be considered as infinite resources, but it could also be problematic to the system when their growth negatively affects other productive processes, and there is no way to control such indefinite growth. Let us consider, for example, the organization GCL, and let us assume that the process space is such that $\mathbf{v}[i]$ can take any non-negative value for $r_i \in R_{\text{GCL}}$, and zero else.

An example of an overproducible species in the farm model is water. This is trivially shown by a process vector where the only non-zero value is $\mathbf{v}[1]$. Since $\mathbf{v}[1]$ can take any positive value, for any choice of the values of $\mathbf{v}[i]$ where $r_i \in R_{\text{GCL}}$, we can increase $\mathbf{v}[1]$ to be large enough so there is more water than what is required to trigger the other reactions specified by \mathbf{v} . This in turn can be applied to overproduce other species as the following examples show:

- (i) Overproducing milk: \mathbf{v}_1 such that $\mathbf{v}_1[1] = 2, \mathbf{v}_1[2] = 1, \mathbf{v}_1[3] = 1, \mathbf{v}_1[5] = 1, \mathbf{v}_1[15] = 1$.
- (ii) Overproducing money: \mathbf{v}_2 such that $\mathbf{v}_2[1] = 2, \mathbf{v}_2[2] = 1, \mathbf{v}_2[3] = 1, \mathbf{v}_2[5] = 1, \mathbf{v}_2[15] = 1, \mathbf{v}_2[11] = 1$.
- (iii) Overproducing milk and money: \mathbf{v}_3 such that $\mathbf{v} = \mathbf{v}_1 + \mathbf{v}_2$.

The latter shows that a process $\mathbf{v} = \mathbf{v}_1 + \mathbf{v}_2$, where \mathbf{v}_1 overproduce a species s_1 and \mathbf{v}_2 overproduces s_2 , overproduces $\{s_1, s_2\}$. Thus, the maximal set of overproducible species w.r.t X is always unique, will be called the *overproducible component* of X , and will be denoted by F_X .

F_X is sensitive to the structure of the process space and thus to process space perturbations. That is, if the process vectors $\mathbf{v} \in \Pi(R_X)$ that can overproduce species in F_X are no longer possible after the perturbation, some species will not belong to F_X and thus F_X will become smaller. In such case, X might still be an organization, but constrained to having a maximal production zero for species that were overproduced prior the perturbation.

TABLE 2: Types of perturbations and description of how they affect the organizations of a reaction network.

| Type/feature | Perturbations | Example | Closure | Self-maintenance |
|--------------|---------------|---------------|--------------|------------------|
| State | \mathbf{x} | Cows die | No change | Might change |
| Process | $\Pi(R_X)$ | Dry year | No change | Might change |
| Structural | R_X | Mouse arrival | Might change | Might change |

Interestingly, in the absence of process space perturbations, if s is overproduced in X , then s is overproduced in every X'^X . This means that structural perturbations which add reactions or species will not alter the overproducibility of s . However, structural perturbations which eliminate species or reactions can modify the overproducibility of some species.

Note that having defined E_X and F_X , we have that $X - (E_X \cup F_X)$ entails the part of X which might be most problematic for self-maintenance.

Definition 8. Let $C_X = X - (E_X \cup F_X)$. We call C_X the fragile component of X .

Note that for a species s in C_X , we can infer that (i) its maximal overproduction is zero ($s \notin F_X$) and (ii) it cannot be equally consumed and produced in all of the reactions, and it participates in ($s \notin E_X$). Therefore, s must be consumed more than produced by at least one reaction. Hence, if s is not produced more than consumed by another reaction, then X is not semi-self-maintaining, and thus X is not self-maintaining. In Table 3, we summarize the components of the reaction network that can be affected by a perturbation of different kind.

4.3. The Inner Structure of the Fragile Component.

Analyzing the inner structure of the fragile component reveals extremely interesting features about the inner working of an organization. That is, if X is self-maintaining, it can be shown that for any two species $s_1, s_2 \in C_X$, we have that either both species are needed to produce each other, meaning they belong to the same co-dependent productive cycle, or there are two sets of reactions $\mathcal{R}_1, \mathcal{R}_2 \subseteq X$, one associated to s_1 and the other associated to s_2 , such that the reactions in $\mathcal{R}_1 \cap \mathcal{R}_2$ do not contain reactants or products in C_X , meaning that their self-maintenance depends on independent productive cycles [44].

Definition 9. Two species s and \bar{s} in X are dynamically connected in X if and only if there exists a sequence of species $s_0, \dots, s_p \in C_X$ such that $s_0 = s$, $s_p = \bar{s}$ and for all $k = 0, \dots, p-1$, we have that s_k and s_{k+1} are directly connected in X (see Definition 2).

Dynamical connection entails connection through reactions which have reactants in C_X . Note that only species in C_X can be dynamically connected, and that dynamical connectivity depends both on the reaction network and the process space (because overproduced species depend on the process space).

It is easy to show that dynamical connectivity is an equivalence relation for C_X [45]. This implies that every species in C_X is dynamically connected to itself (reflexivity), that if s_1 is directly connected to s_2 then s_2 is dynamically connected to s_1 (symmetry), and that if s_1 is connected to s_2 and s_2 is dynamically connected to s_3 , then s_1 is dynamically connected to s_3 (transitivity). The latter implies that C_X can be partitioned into equivalence classes $\{C_X^1, \dots, C_X^d\}$, i.e., $C_X^i \cap C_X^j = \emptyset$ for $i \neq j$. The number d of equivalent classes reflects how many parts C_X can be partitioned into.

The latter result has been used to develop a decomposition theorem for the fragile component. The proof of the theorem requires a number of non-trivial steps. We refer the readers to [44] for details.

Theorem 1. Let F_X and E_X be the maximal overproduced and catalyst components of X for a given process space $\Pi(R_X)$, and let $C_X = \cup_{j=1}^d C_X^j$ be the partition of the fragile component dynamically decomposed into connected sets.

Then, X is self-maintaining if and only if $C_X^j \cup F_X \cup E_X$ is self-maintaining for $j = 1, \dots, d$.

Theorem 1 shows that the self-maintenance of a reaction network can be decomposed into independent components, and such components depend on the structure of the network, which defines the catalysts and the process space, which specifies the species that can be overproduced. That is, the overproduced and catalyst components determine the way in which the fragile component C_X is maximally decomposed into d parts, and from there the self-maintenance of each part C_X^j is independent of the other parts, for $j = 1, \dots, d$. Interestingly, the self-maintenance of each fragile component part might require the support of F_X and E_X for its self-maintenance, but since the non-negative production of both F_X and E_X is ensured in $\Pi(R_X)$, they can be safely employed as resources for the non-negative production of C_X^j . Indeed, $F_X \cup E_X$ act as a border that separates various parts of the fragile component.

4.4. Decomposition of the Reaction Network: Towards Resilience Response Mechanisms.

There are important consequences that can be obtained from Theorem 1 in relation to the response mechanisms that could explain resilience in the context of reaction networks. First, it is important to remember that state perturbations affect the self-maintenance of a reaction network only when they modify the process space $\Pi(R_X)$. Thus, since our aim is to understand whether an organization X will remain so after a perturbation, this can be analyzed by looking at process perturbations.

Second, process perturbations that do not affect F_X and E_X will not modify the decomposition of the fragile

TABLE 3: Types of perturbations and description of how they affect the catalysts and overproducible components of a reaction network.

| Type of perturbation | Perturbation vs prior | E_X | F_X |
|----------------------|------------------------------|--------------|--------------|
| State | $\mathbf{x}' > \mathbf{x}$ | No change | No change |
| State | $\mathbf{x}' < \mathbf{x}$ | No change | Might change |
| Process | $\Pi'(R_X) \subset \Pi(R_X)$ | No change | Might change |
| Process | $\Pi'(R_X)^{\Pi(R_X)}$ | No change | No change |
| Structural | $R'_X \subset R_X$ | No change | Might change |
| Structural | $R'_X \supset R_X$ | Might change | No change |

Note that if the perturbation changes F_X or E_X , there is a change in C_X .

component C_X . Thus, in this case, the self-maintenance of X depends on the conservation of the processes which self-maintain the fragile components C_X^j in the new process space. The latter implies that a resilient mechanism to counteract this perturbation needs to provide the conditions for the self-maintenance of the fragile components C_X^j affected by the perturbation.

Third, suppose that a process perturbation changes F_X to $F'_X \subset F_X$; then, there will be a new fragile component and thus a new decomposition. However, the new decomposition might conserve some of the parts of the previous fragile component decomposition. Thus, if the process perturbation does not change the self-maintaining processes of the parts of the fragile component that remained after the perturbation, the effect of the perturbation, and all mitigation strategies to compensate potential problems, can be targeted specifically to the parts of the fragile component which have been modified by the perturbation. Similarly, a structural perturbation might modify F_X or E_X , which in turn might change C_X , or it might leave F_X and E_X equal, but modify C_X only. Again, by applying Theorem 1, we are able to identify the parts of the network whose self-maintenance is going to be affected by the perturbation and perform actions, either to adapt the process space or by incorporating new reactions, to compensate the potential loss of self-maintenance of the affected parts.

An additional, and perhaps the most interesting, implication of Theorem 1 is that in case the perturbation cannot be compensated, we have that the organization will evolve to a new organization, where the overproduced species, catalysts, and parts of the fragile component which are not affected by the perturbation will remain self-maintaining. In this sense, we are not only capable of knowing the required actions to sustain a perturbed organization but also able to elucidate the evolution of an organization after a perturbation that cannot be mitigated.

Notably, perturbations can, depending on the case, be counteracted either by a modification of the process space or by a structural perturbation. A counteraction by modifying the state can only work if it leads to a change in the process space where self-maintenance is feasible. For example, consider a farm which overproduces milk and money while having a water shortage due to climate change. This is a process space perturbation, but it can be compensated by modifying the operation of the farm, for example, not overproducing milk but only money or by reducing investment in infrastructure. Both choices do not perform a structural change on the farm but modify the choice of the

process defining the adapted process space. However, it is also possible to include a new reaction, which specifies a more water-efficient way to produce milk. In such case, we compensate the water shortage by a structural perturbation which might still allow the overproduction of milk, not possible for the other mitigation strategies.

It is important to analyze in more detail the interplay between structure and operation of the organization after a perturbation. We will therefore provide some examples of perturbations, effects, and possible responses to compensate the effects in our farm model.

5. Perturbation Response Analysis of the Farm Example

In this section, we will elaborate on some cases that illustrate how different ways of operating the farm lead to different decompositions of the reaction network, and each decomposition responds differently to perturbations, so some ways of operating the farm can be understood as more resilient than others.

5.1. Two Different Ways to Operate the Farm. We will consider two different ways to operate the production of the farm in a self-maintaining way and refer to them as $Op_1(M)$ and $Op_2(M)$, such that they overproduce different sets of species, thus implying different decompositions according to Theorem 1. For the case of $Op_1(M)$, the farm is operated in a way that only money is overproduced. This represents the idea of spending the least possible resources and focusing on the production of money only. For $Op_2(M)$, the farm is operated in a way that overproduces not only money but also {grass, infrastructure, dung, fertilizer, grain}, representing the idea of a farm that seeks to build up a buffer of critical resources, while desiring to increase its productive capacities. That would be an example of sustainable growth. Therefore, in operating the farm by $Op_1(M)$, represented by the process \mathbf{v}_1 in equation (8), the two fragile components are $C_{1,1} = \{\text{water, grass, milk, dung, worms, fertilizer, chickens, eggs, grain, straw}\}$ and $C_{2,1} = \{\text{infrastructure}\}$. In the second way of operating the farm, represented by \mathbf{v}_2 in equation (8), the fragile components are $C_{2,1} = \{\text{water, milk, straw}\}$ and $C_{2,2} = \{\text{worms, chicken, eggs}\}$. Hence, while $Op_1(M)$ and $Op_2(M)$ have two fragile components each, these two components are different.

The resulting decompositions for $Op_1(M)$ and $Op_2(M)$ are shown in Figure 2.

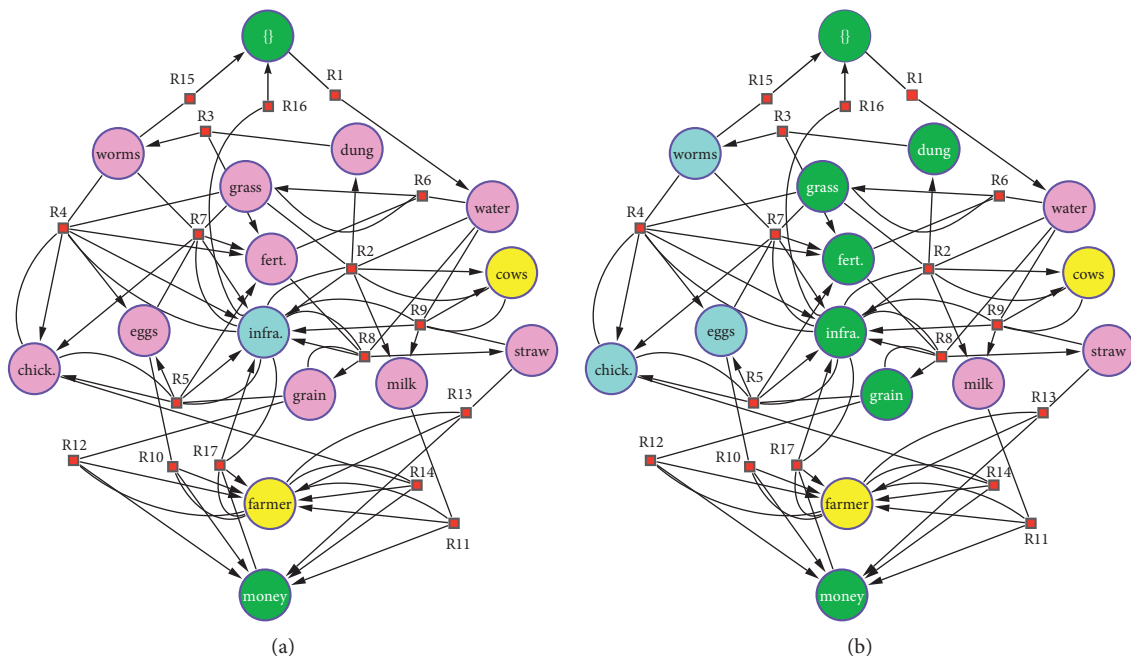


FIGURE 2: Different ways to operate the farm and their respective decompositions. Green species are overproduced, yellow species are catalysts, cyan and magenta species belong to different parts of the fragile component. Both reaction network can be decomposed in two fragile cycles, but in (a) figure the one fragile component has many more species than the (b).

In order to have a way to compare the response of two ways of operating the farm under different kinds of perturbations, the initial state of the farm, denoted by $\mathbf{x}_1(t)$ for $Op_1(M)$ and by $\mathbf{x}_2(t)$ for $Op_2(M)$ are equal. Additionally, the initial states are defined such that they have enough species to apply the processes required for the respective

operation of the farm, and such that they overproduce the same amount of money. The process vectors in each case are obtained using a software which finds a self-maintaining process which additionally overproduces a chosen set of overproduced species.

$$\begin{aligned} \mathbf{v}_1(0) &= (5.3, 1.4, 1.4, 0.5, 1.0, 2.4, 0.5, 1.0, 0.5, 1.0, 1.9, 7.7, 0.5, 0.5, 0.5, 0.5, 0.5) \\ \mathbf{v}_2(0) &= (14.0, 4.0, 3.0, 1.0, 5.0, 7.0, 1.0, 2.0, 1.0, 5.0, 5.0, 1.0, 1.0, 1.0, 1.0, 1.0, 2.0). \end{aligned} \quad (8)$$

The initial conditions, initial productions, and decomposition role of the species are shown in Table 4.

5.2. The Process Space. Note that a process vector \mathbf{v} specifies a total amount of reactants to be used by the process, which we will denote by $T(\mathbf{v})$. For a species s_j , $T(\mathbf{v})$ is calculated by $T(\mathbf{v}, j) = \sum_i \mathbf{v}[i] a_{ij}$, with a_{ij} defined in equation (1).

Thus, a given state \mathbf{x} might or might not have enough reactants for a process \mathbf{v} to be feasible. Thus, our process space $\Pi(R)(\mathbf{x})$ must be such that \mathbf{v} holds $\mathbf{x}[j] \geq T(\mathbf{v}, j)$ for all j .

Clearly, the two ways of operating the farm, specified by the processes $\mathbf{v}_1(0)$ and $\mathbf{v}_2(0)$, are feasible for $\mathbf{x}_1(0)$ and $\mathbf{x}_2(0)$, respectively. However, it is important to notice that $T(\mathbf{v}_1, j) < T(\mathbf{v}_2, j)$ for certain values of j . For example, for the species cows, with $j = 3$, we have that $T(\mathbf{v}_1(0), 3) = \mathbf{v}_1[2] + \mathbf{v}_1[9] = 1.9$, while $T(\mathbf{v}_2(0), 3) = \mathbf{v}_2[2] + \mathbf{v}_2[9] = 5$. Therefore, we need to specify how to update

the subsequent processes that are going to be applied to operate the farm.

In order to represent the evolution of the two ways of operating the farm, we define the operation of the farm at time t by the process $\mathbf{v}_i(t)$ such that it is a function of $\mathbf{x}_i(t)$, for $i = 1, 2$. Therefore, we specify the process space for operating the farm by establishing a kinetic law [32].

The process vector is built by comparing the state of the system at a given time t with the corresponding default process vector obtained using the COT software (see equation (8)). The update in the process vector attempts to find the most similar process vector to the default process, constrained to the fact that it is feasible and that positive variations in the amounts of resources imply an increase in the coordinates of the process vector. We will use this method to identify the process vector that is applied to the system when a perturbation occurs.

The specification of such process requires introducing the following function:

TABLE 4: The initial conditions, initial productions, and decomposition role of the species.

| | $\mathbf{x}(0)$ | $\mathbf{Sv}_1(0)$ | Decomp $Op_1(M)$ | $\mathbf{Sv}_2(0)$ | Decomp $Op_2(M)$ |
|------------|-----------------|--------------------|------------------|--------------------|------------------|
| Water | 14 | 0 | $C_{1,1}$ | 0 | $C_{2,1}$ |
| Grass | 13 | 0 | $C_{1,1}$ | 1 | F_2 |
| Cows | 5 | 0 | E_1 | 0 | E_2 |
| Infrastr | 17 | 0 | $C_{1,2}$ | 1 | F_2 |
| Milk | 5 | 0 | $C_{1,1}$ | 0 | $C_{2,1}$ |
| Dung | 3 | 0 | $C_{1,1}$ | 1 | F_2 |
| Worms | 3 | 0 | $C_{1,1}$ | 0 | $C_{2,2}$ |
| Fertilizer | 9 | 0 | $C_{1,1}$ | 1 | F_2 |
| Chickens | 7 | 0 | $C_{1,1}$ | 0 | $C_{2,2}$ |
| Eggs | 6 | 0 | $C_{1,1}$ | 0 | $C_{2,2}$ |
| Grain | 10 | 0 | $C_{1,1}$ | 12 | F_1 |
| Straw | 2 | 0 | $C_{1,1}$ | 0 | $C_{2,1}$ |
| Money | 2 | 11 | F_1 | 11 | F_2 |
| Farmer | 15 | 0 | E_1 | 0 | E_2 |
| Mouse | 0/10 | 0 | -/perturbation | 0 | -/perturbation |

The first column shows the initial state, and the second and fourth columns show the initial production, specified by the production vector at time zero. Positive values in the second and fourth columns represent overproduction. Zero values in the second and fourth columns represent that the species is either a catalyst or belongs to a fragile circuit. The third and fifth columns identify the specific decomposition role in each of the two ways of operating the farm, respectively. The last row represents the initial value without and with structural perturbation, as explained in Section 5.3

$$d(\mathbf{x}(t), j) = \begin{cases} \min_{i=1}^m \left(\frac{\mathbf{x}(t)[i]}{T(\mathbf{v}(0), i)} \right), & \text{for } s_i \text{ reactant of } r_j, \\ 1, & \text{if there are no reactants in } r_j, \end{cases} \quad (9)$$

where $d(\mathbf{x}(t), j)$ identifies the species at the current state $\mathbf{x}(t)$ that has decreased the most with respect to the use of resources needed for the default operation of the farm, specified by $T(\mathbf{v}(0))$, and for the case that none of the species have decreased with respect $T(\mathbf{v}(0))$, i.e., all reactants have maintained or grown with respect to the starting state, it identifies the minimal of such growth. The function $d(\mathbf{x}(t), j)$ can thus be applied to modulate the variation of the process vector in time from the starting process vector when the process is not feasible or if all the species have increased enough so the process vector, which is defined to be self-maintaining, overproduces the species.

Thus, when a species required to trigger a reaction has decreased, the process vector is going to decrease proportionally to the maximal decrease, and if all reactants have grown, the increase will be proportional to the minimum of such growth. We define the process vector at time t as follows:

$$\mathbf{v}_i[j](t) = d(\mathbf{x}(t), j)\mathbf{v}_i[j](0). \quad (10)$$

For example, consider a farm starting at state $\mathbf{x}(0)$ and the operation of the farm by a certain process vector $\mathbf{v}(0)$ such that it has increased the amount of grass in 3 units, reduced the amount of water in 2 units, and maintained equal the amount of cows and infrastructure. Since this process has only reduced water and all other resources have increased or have been maintained equal, the process to be applied at time 1, for the second coordinate $\mathbf{v}_i[2](1)$ representing r_2 , will be decreased to a factor $d(\mathbf{x}(1), 2) = (\mathbf{x}1/T(\mathbf{v}(0), 2))$,

1)) = $(\mathbf{x}[1](0) - 2/T(\mathbf{v}(0), 1))$, which represents the fact that less water is available. In Figure 3, we show that the dynamics defined in this way leave invariant the dynamic roles in $Op_1(M)$ and $Op_2(M)$. Indeed the process vector remains constant over time in both cases.

5.3. Simulating Perturbations and Measuring Role Changes.

In order to compare the impact of perturbations, we defined perturbations to the reference initial conditions specified in Table 4 as follows:

- (i) State perturbation: random change of initial state of 1%, 2%, 4%, 8%, and 16% with respect to the vector's length.
- (ii) Process perturbation: random change of initial process of 1%, 2%, 4%, 8%, and 16% with respect to the vector's length.

Additionally, we consider a structural perturbation consisting of adding the reaction specified in equation (7) to the reaction network and consider the initial value of the new last coordinate of the state vector, corresponding to the species "mouse," equal to 10 (see Table 4). For estimating the impact of state and process perturbations with and without structural perturbations, we run 1000 state and process perturbations for the two different ways of operating the farm. Each simulation runs for 3000 time steps, which is the time we observed to find dynamical convergence of the state vector.

Since the two ways to operating the farm imply different decompositions, that is, different sets of overproduced

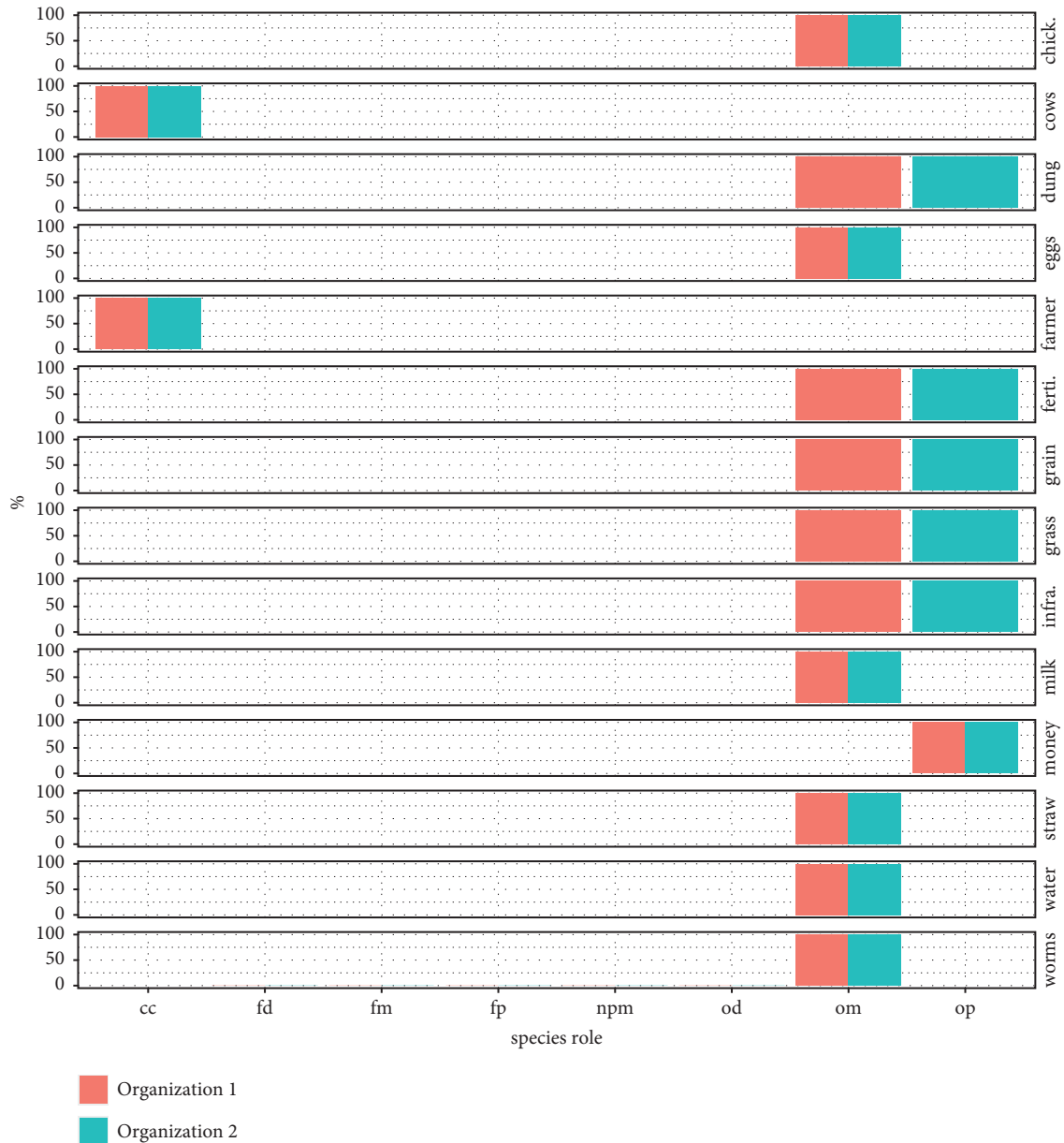


FIGURE 3: Histogram for different species roles overall time, according to Table 5, for $Op_1(M)$ and $Op_2(M)$.

species and different fragile circuits, we analyze the impact of the perturbation by measuring the changes in the decomposition roles with respect to the reference dynamics in Table 4. To do so, note first that the perturbed dynamics might reach concentration zero for some species during the simulation. Therefore, for each simulation at a given time t , the reaction network has an active part which might not be the entire reaction network, but eventually a smaller one. Therefore, at each time t , we consider first an optimal production regime for the active part of the network. This optimal production regime is identified by computing the maximal number of overproduced species and obtaining the decomposition shown in Theorem 1. Such decomposition identifies overproduced species (labelled by o), species in the fragile circuits (labelled by f), catalysts (labelled by cc), and non-

active species (labelled by np). Next, we contrast such ideal productivity regime with the actual productivity rate of each species at time t , either positive (labelled by p), zero (labelled by m), or negative (labelled by d). There is another role which is non-reactive (nr) which is reached when the species is still present, but it cannot react because the species it reacts with are in np role.

Thus, at each time t , we can identify the possible roles (see Table 5).

We will refer to the roles by pairs of ideal and actual labels. For example, a species with role om is a species which is ideally overproduced, but within the current dynamics (at time t), its production is zero. Similarly, fd is a species whose ideal role is being part of the fragile circuit, but in the current dynamics, its production is smaller than its consumption, so its concentration is decreasing.

TABLE 5: Species roles interplay between ideal and actual dynamics.

| Ideal role | Actual role | Meaning |
|------------|-------------|------------------------------------|
| o | p | Overproducible that is produced |
| o | m | Overproducible that is maintained |
| o | d | Overproducible that is consumed |
| f | p | Fragile circuit that is produced |
| f | m | Fragile circuit that is maintained |
| f | d | Fragile circuit that is consumed |
| cc | — | Catalyst (maintained by default) |
| np | m | Not present (maintained) |
| nr | m | Non-reactive (maintained) |

First column indicates the “ideal” dynamical roles that are obtained for each species from the maximal decomposition, the second column indicates the “actual” dynamical role observed in the actual dynamics, and the third column expresses the meaning of the interplay between the two roles from a dynamical perspective.

A perturbation induces a role change which might affect the ideal and/or actual roles. For example, a perturbation which reduces a certain amount of a particular kind of species might change the role of op to om , as with the current amount of species, it is not possible overproduce the species, but only maintain its value. A structural change enabling the overproduction of a species which belong to a fragile circuit before the perturbation, but where such overproduction reaction pathway is not feasible, might change fm to om .

We will focus on the dynamics of role changes to obtain a qualitative view of the dynamical changes induced by perturbations.

5.4. Average Role Changes. As a first analysis of the responses for the two ways of operating the farm under the three different types of perturbations, we measure the aggregate change of role as explained in the previous section. We simply count the proportion of species that have a role change at time t in the dynamics and average over the 1000 simulations run for each kind of perturbation.

In Figures 4 and 5, we see the change of species roles for the case of state and process perturbations. It can be noted first that the state perturbations show an impact that manifests mostly in the beginning of the simulation, while the impact of the process perturbation is incremental with a long-term asymptotic value, and that impact increases with the perturbation size for both kinds of perturbation. Moreover, we observe that the extent of the state process impact is higher on $Op_2(M)$ than in $Op_1(M)$, and that the situation reverses for process perturbations. The latter is consistent with the fact that the way the process vector is actualized in equation (10) aims at operating the farm in the most efficiently possible way, and in this case, this favours keeping the structure of $Op_1(M)$ over the structure of $Op_2(M)$. Indeed, for case of perturbations that increase species, $Op_1(M)$ can quickly return from overproduced to fragile (return from fp to fm in Table 5), while a species that becomes overproduced in $Op_2(M)$ might remain overproduced (staying in fp from fm). For perturbations that decrease species however, both $Op_1(M)$ and $Op_2(M)$ can return, for example, from fd to fm or from om to op .

For process perturbations, we observe that the perturbation changes the roles of a significant proportion of species

in the beginning of the simulation, and there is a recovery of some species roles shortly after, but later this recovery instead of driving to stabilization triggers a sustained increase of role changes with an asymptotic behavior above the role change observed at the beginning. The initial impact and the asymptotic role change are much higher in $Op_1(M)$ than in $Op_2(M)$. The explanation of this phenomena is not trivial as it involves different tendencies for changing roles depending on the role of the species and the effect of the perturbation. For this reason, in the next section, we develop a more detailed analysis of the effects and propagation of the perturbations at each of the decomposition modules.

Regarding structural perturbations, in Figures 6 and 7, we see the change of species roles for the case of state and process perturbations when the structural perturbation in equation (7) is included. Interestingly, we observe that the impact on the two ways of operating the farm qualitatively looks the same as in the case without structural perturbation, but quantitatively the impact is different for $Op_1(M)$ depending on the type of perturbation considered, while for $Op_2(M)$, the impact does not change significantly with or without structural perturbation. Indeed, for $Op_1(M)$, we observe that the state perturbation impact is amplified and the process space impact is reduced. The latter is explained by the fact that the structural perturbation implies the rapid disappearance of various species in $Op_1(M)$ (for both state and process perturbations, even for the default dynamics), which in turn derive in the convergence of the dynamics into a new and smaller organization, which is indeed stable, even in the presence of the structural perturbation. Therefore, since we compare the ideal and actual states for the existing species in the dynamics, we conclude that the structural perturbation changes the structure of the network, but within this new structure, the impact of the state and process perturbations is less strong than in the case of $Op_1(M)$ without the structural perturbation.

In order to illustrate the impact of the structural perturbation on the two ways of operating the farm, we show the most common structure that remains stable after a structural perturbation for $Op_1(M)$ and $Op_2(M)$ considering state perturbations, i.e., multiple initial conditions, in Figure 8. Note that while $Op_2(M)$ keeps the whole farm active, $Op_1(M) = GCL$, indicating that the chicken-based and grain-based productive processes are inactivated by the structural perturbation (see Figure 1).

We now turn to a more detailed analysis to observe the specific changes of roles under different types of perturbations in the specific parts of the organizations’ decomposition.

5.5. Perturbation Responses within the Decomposition.

The average role change analysis shows that the two organizations have qualitatively different responses to the state and process perturbations, and that the structural perturbation might amplify or reduce the effect of state and process perturbations. Therefore, since the way in which role changes occur is not clear from such aggregated analysis, we now observe in more detail what are the responses to

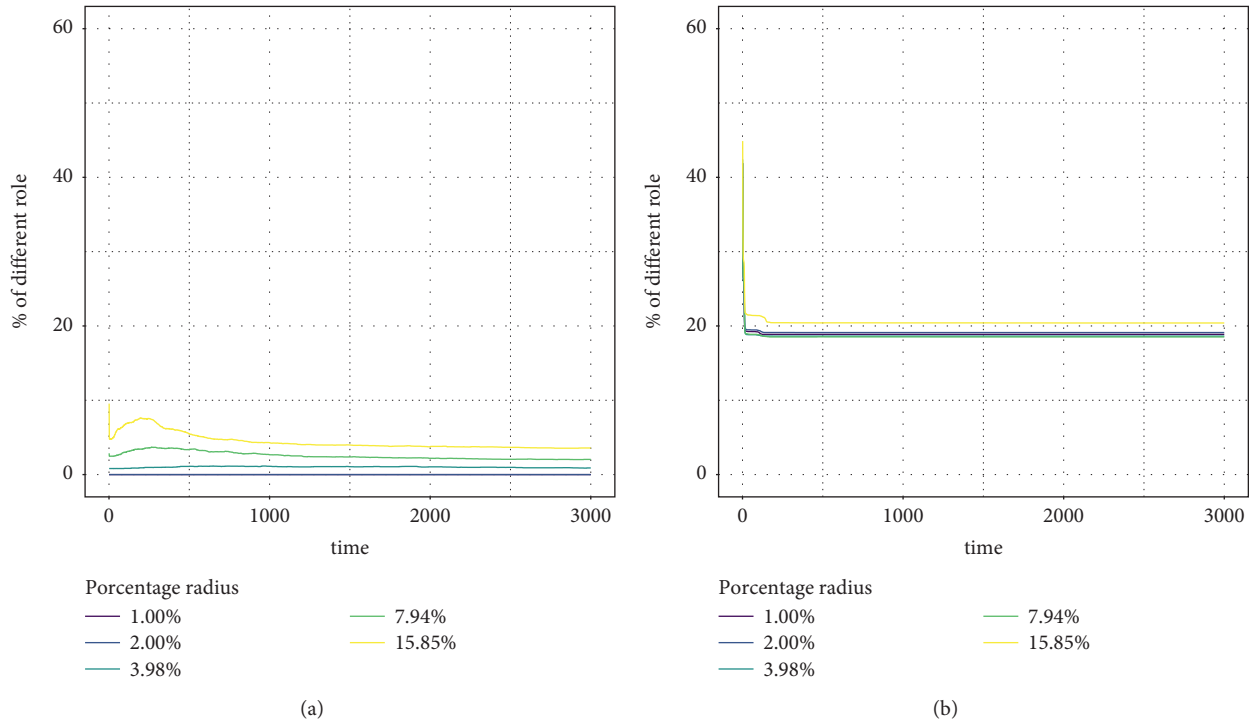


FIGURE 4: Average role change over time for state perturbations. (a) $Op_1(M)$. (b) $Op_2(M)$.

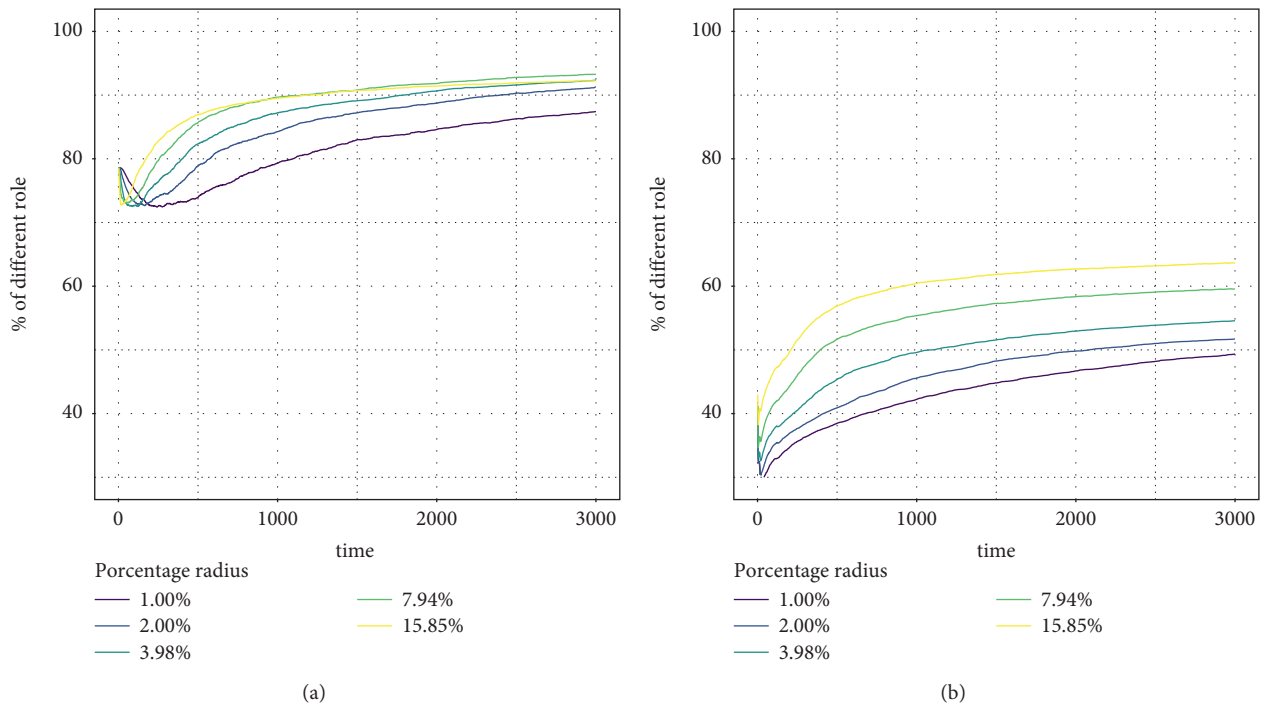


FIGURE 5: Average role change over time for process perturbations. (a) $Op_1(M)$. (b) $Op_2(M)$.

perturbations within the specific decomposition modules for different ways of operating the farm.

5.5.1. State Perturbation. In Figures 9 and 10, we observe the specific response of each species to the state

perturbations. It becomes clear that the role change is concentrated in the fragile circuits and that the change is more common for species whose ideal role is over-produced and they undergo from om to op , hence going towards their ideal role from their actual zero production role.

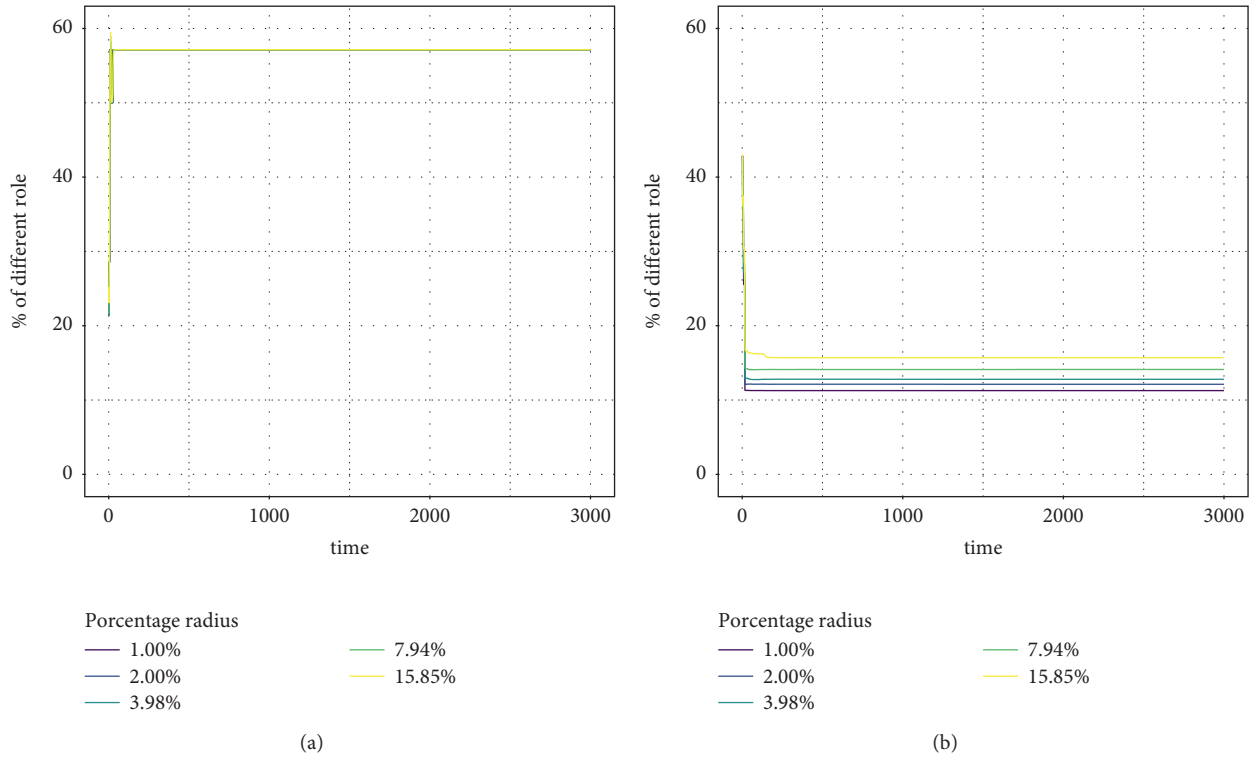


FIGURE 6: Average role change over time for state perturbation and structural perturbation. (a) $Op_1(M)$. (b) $Op_2(M)$.

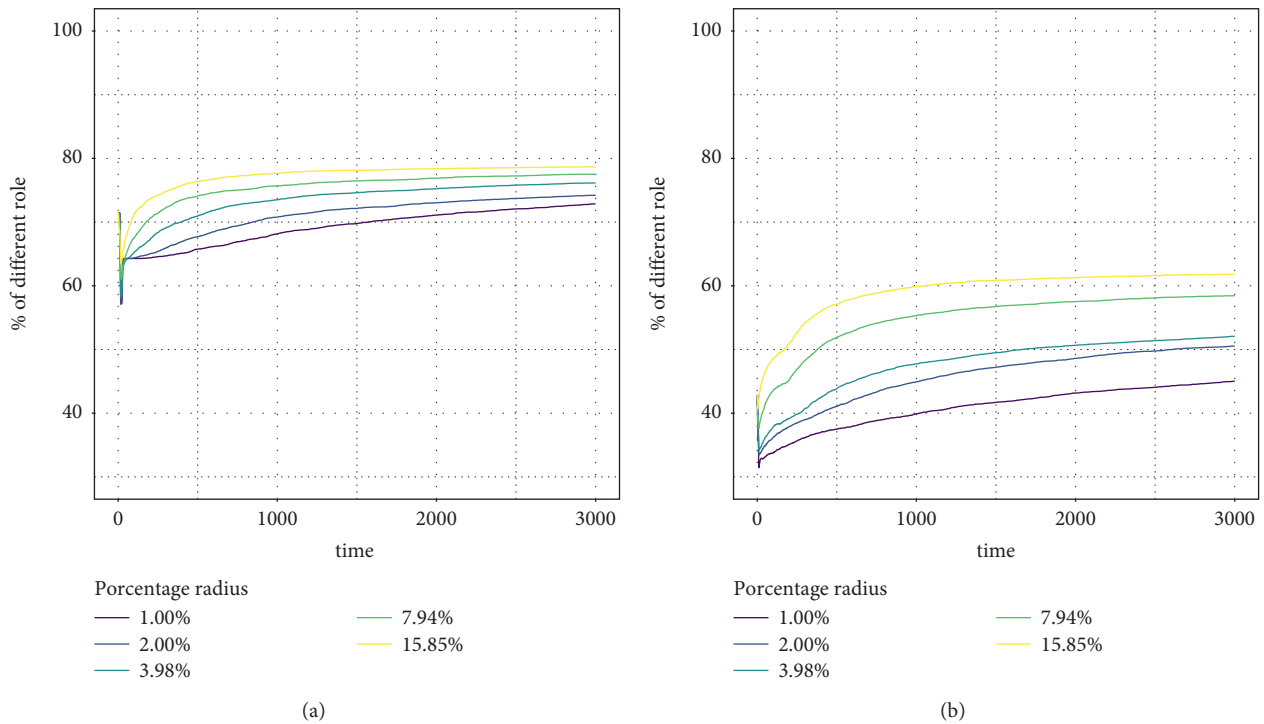


FIGURE 7: Average role change over time for process perturbation and structural perturbation. (a) $Op_1(M)$. (b) $Op_2(M)$.

Moreover, we note that the fragile circuits in $Op_2(M)$ have a higher tendency to undergo the om to op change than $Op_1(M)$ because perturbations that decrease the production of species in F (overproduced) will not harm the dynamics,

and hence there are more chances that perturbations that increase species in C (fragile circuits) become sustained as overproduction, simply because $Op_2(M)$ has more overproduced species. This can be seen, for example, in

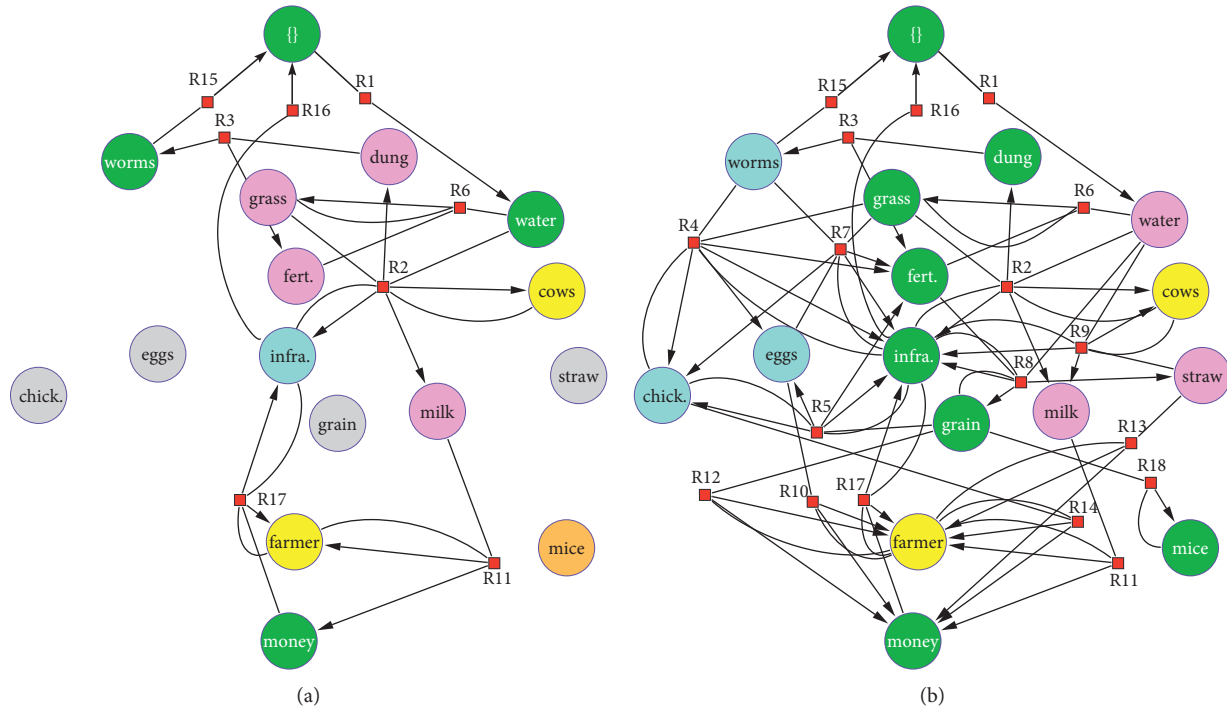


FIGURE 8: Different ways to operate the farm when the structural perturbation is added, and their most common respective decompositions obtained in the state-perturbation analysis. $Op_1(M)$ and $Op_2(M) = M$ are in the (a) and (b) figures respectively. Green species are overproduced, yellow species are catalysts, orange non-reactive species, grey non-present species, cyan and magenta species represent the two fragile circuits of the decomposition.

Figures 9(b) and 10(b) where water, milk, and straw become overproduced in a much larger proportion of cases in the latter than in the former case.

When we include the structural perturbation (Figures 11 and 12), for $Op_1(M)$, simulations show that the set $\{\text{grass, fertilizer, dung, milk}\}$ survives the perturbation in a very stable way, and that all other species in the fragile circuits become inactive. Thus, in this case, $Op_1(M) = GCL$. Within GCL , the dynamics of $Op_1(M)$ remain very stable, as no other role changes are observed in the histograms.

For $Op_2(M)$, simulations show that the effect of the structural perturbation does not inactivate the species in any of the modules as it happens for $Op_1(M)$. Indeed, it is very interesting to notice that the fragile circuit $C_{2,2} = \{\text{chicken, eggs, worms}\}$ in the absence of structural perturbation becomes generally overproduced after state perturbations, and in the presence of the structural perturbation, it remains as a fragile circuit for the majority of state perturbations. This is explained by the fact that since mouse eat grain, then there is not enough grain to overproduce the fragile circuit where chickens are part of. Note that, however, $C_{2,1} = \{\text{water, straw, milk}\}$ does not have an impact in its dynamics, as it is dynamically disconnected from the structural perturbation, due to the overproductive dynamics that separate the fragile circuits (which was not the case in $Op_1(M)$ and thus driven to a much heavier collapse).

The conclusion in this section is an example of using decomposition Theorem 1 to predict the impact of structural perturbations in the qualitative dynamics by studying changes in the ideal and actual roles of the species.

5.5.2. Process Perturbation. In Figures 13 and 14, we observe the responses to process perturbations in each of the decomposition modules for $Op_1(M)$ and $Op_2(M)$, respectively. In this case, we note that all role changes are possible, implying that the different types of process perturbations can produce different patterns of role change. Instead of analyzing the specific conditions that drive each kind of change, we keep our analysis at a qualitative level and compare the structural responses of $Op_1(M)$ and $Op_2(M)$. The most important change for $Op_1(M)$ is that the species in the bigger fragile circuit $C_{1,1}$ go to npm role, and thus $C_{1,1}$ becomes inactive in a large proportion of cases, implying that $Op_1(M)$ becomes the organization $\{\text{water, infrstr}\}$ together with the species $\{\text{money, farmer, cows, infrstr}\}$ that tend to a non-reactive (nrm) state. This implies that the farm goes bankrupt because its productive processes cease happening.

For $Op_2(M)$, we also observe that in a significant proportion of cases, fragile circuits become inactive. In those cases, as for $Op_1(M)$, we have that $Op_2(M)$ becomes the organization $\{\text{water}\}$ plus some non-reactive species. However, the fragile circuits can also become overproduced or can be maintained in a relatively similar proportion of cases. Indeed, as the perturbation size grows, the tendency of species to transit to npm role increases, indicating that for processes that start operating the farm in a far-from-sustainable way, it is less likely that the dynamics will stabilize in a fully sustainable way. Indeed, in such cases, the tendency is that fragile circuits become inactive and only overproduced species remain active. It is not clear from this analysis if the two fragile circuits become inactive for the same kind of

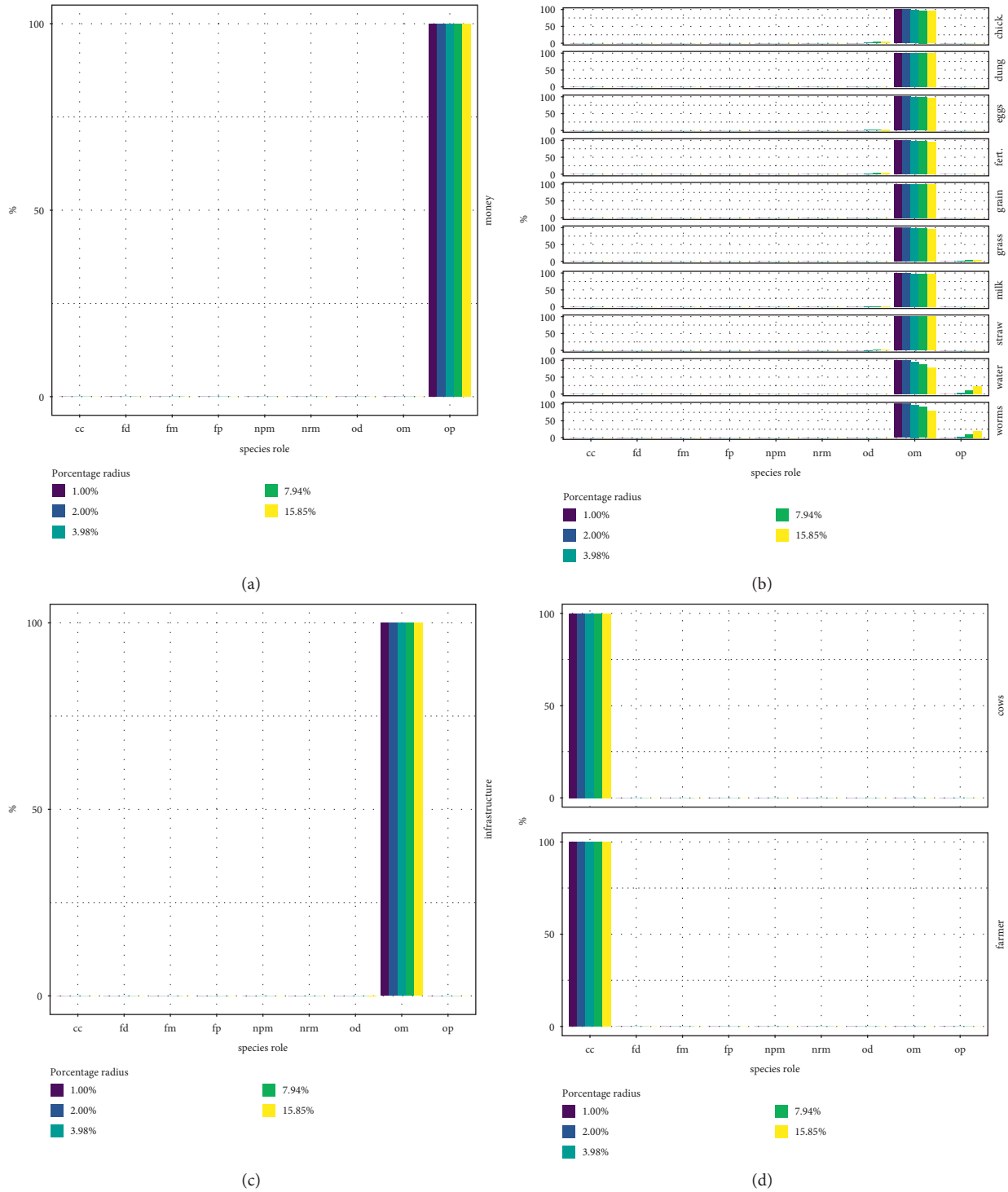


FIGURE 9: Histogram for different species roles according to Table 5 for $Op_1(M)$ for state perturbations. (a) F_1 . (b) $C_{1,1}$. (c) $C_{1,2}$. (d) E_1 .

process perturbations or in some cases one of the fragile circuits inactivates while the other remains active. We speculate that this is the case because if the fragile circuit {chickens, eggs, worms} becomes inactive, it is likely that $Op_2(M)$ becomes the organization CL , and if additionally grain changes role to npm , it might be that $Op_2(M)$ becomes the organization GCL .

When a structural perturbation is added, the effect of process perturbations changes for $Op_1(M)$ in a non-trivial way. Indeed, the process perturbation analysis in the absence of structural perturbation inactivates the entire fragile circuit $C_{1,1}$, implying that $Op_1(M)$ becomes inactive. Hence, we would expect the same in the presence of the structural perturbation, as it was shown that structural perturbations

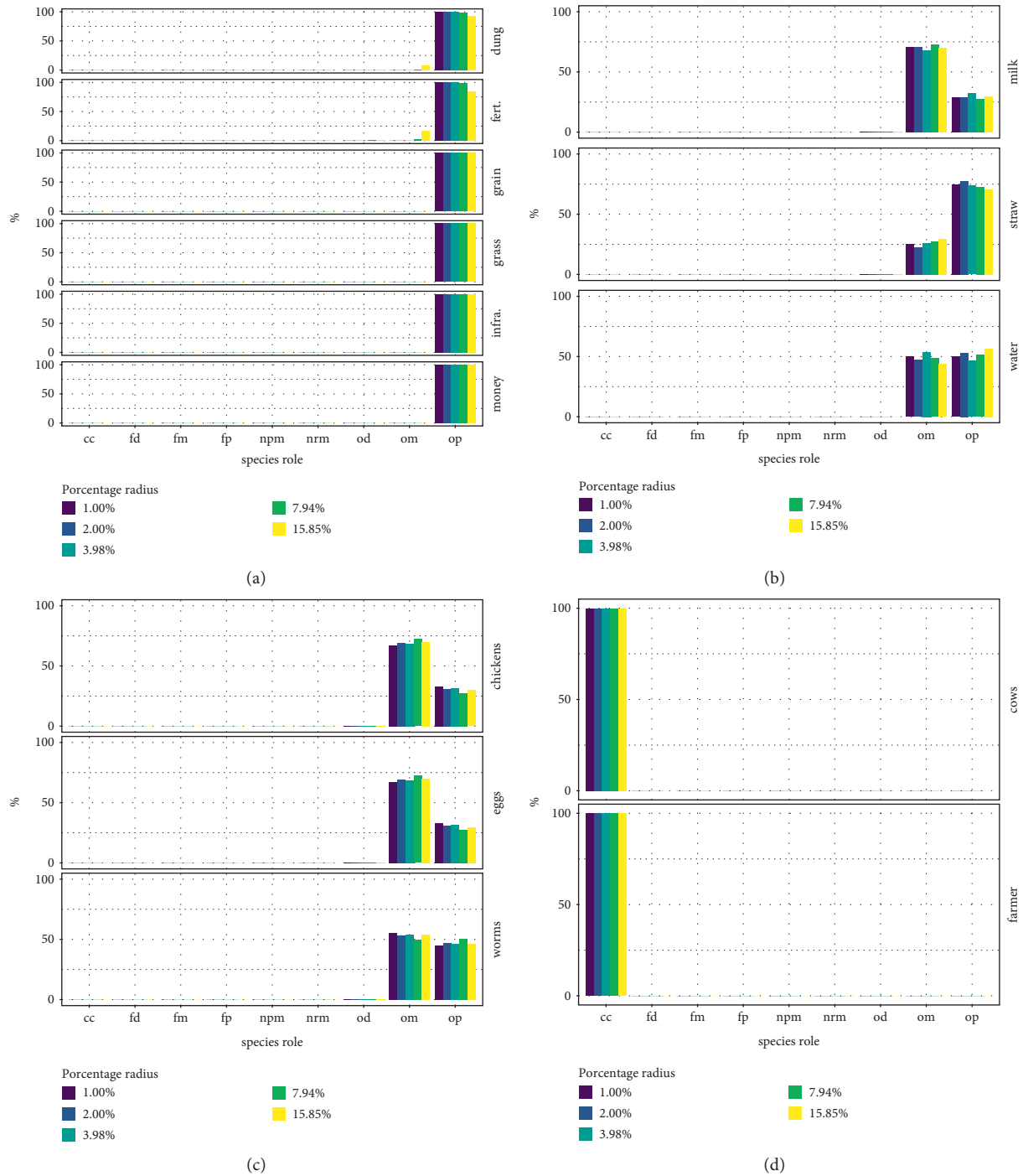
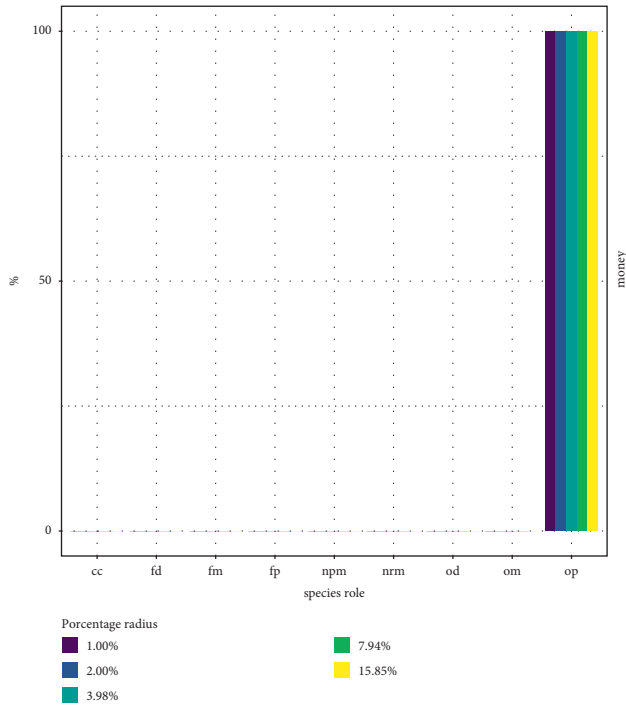


FIGURE 10: Histogram for different species roles according to Table 5 for $Op_2(M)$ for state perturbations. (a) F_2 . (b) $C_{2,1}$. (c) $C_{2,2}$. (d) E_2 .

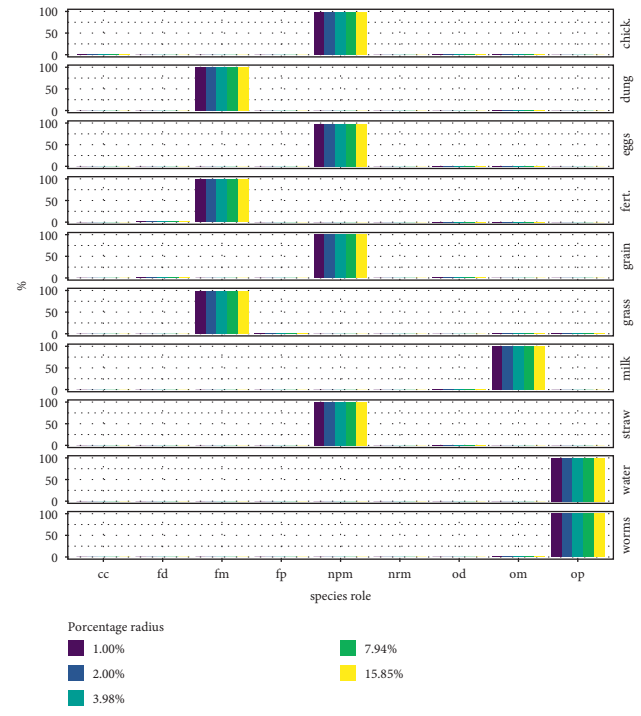
tend to inactivate species as seen in the state perturbation analysis (Figure 11). However, when structural and process perturbations combine, we observe that in a significant proportion of cases, the dynamics evolve from M towards the organization GCL (see Figure 1) and remain stable. This is a consequence that a process perturbation changes the way the farm is operated, and thus the response to the structural perturbation might be similar to the way in which $Op_2(M)$ is operated in respect to how {worms, water} becomes

overproduced, thus helping to sustain the set of species {dung, fert., grass, milk}.

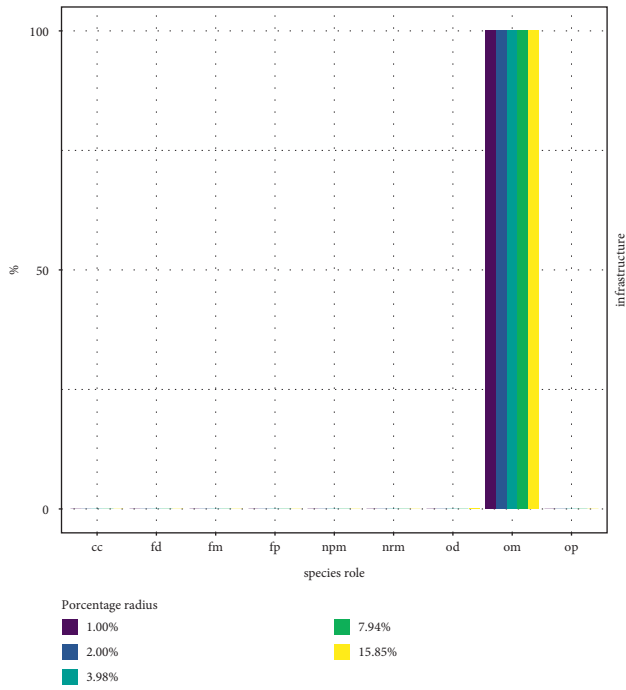
The structural and process perturbation on $Op_2(M)$ instead is able to inactivate the whole operation of the farm, especially when the perturbation is of a high value. This is different to the case when no structural perturbation was in place for $Op_2(M)$ as it was in most cases able to continue operating. This is because a process perturbation might modify the overproductive capacities



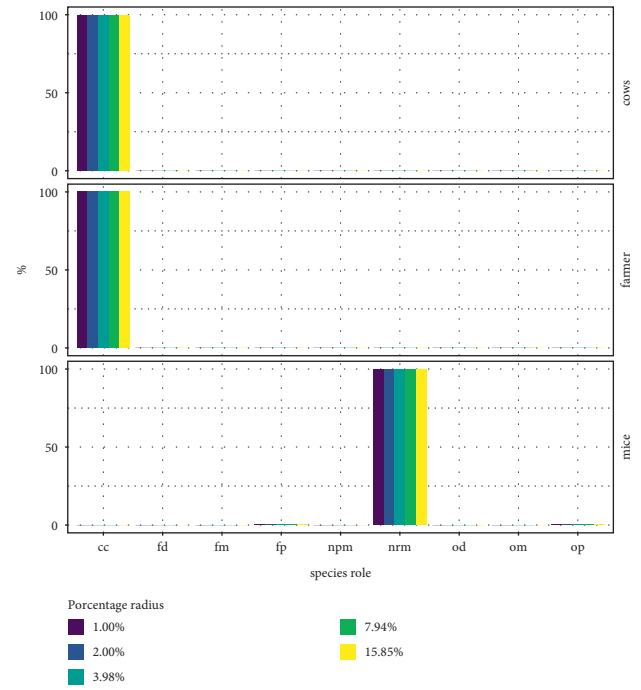
(a)



(b)



(c)



(d)

FIGURE 11: Histogram for different species roles according to Table 5 for $Op_1(M)$ for structural and state perturbations. (a) F_1 . (b) $C_{1,1}$. (c) $C_{1,2}$. (d) E_1 .

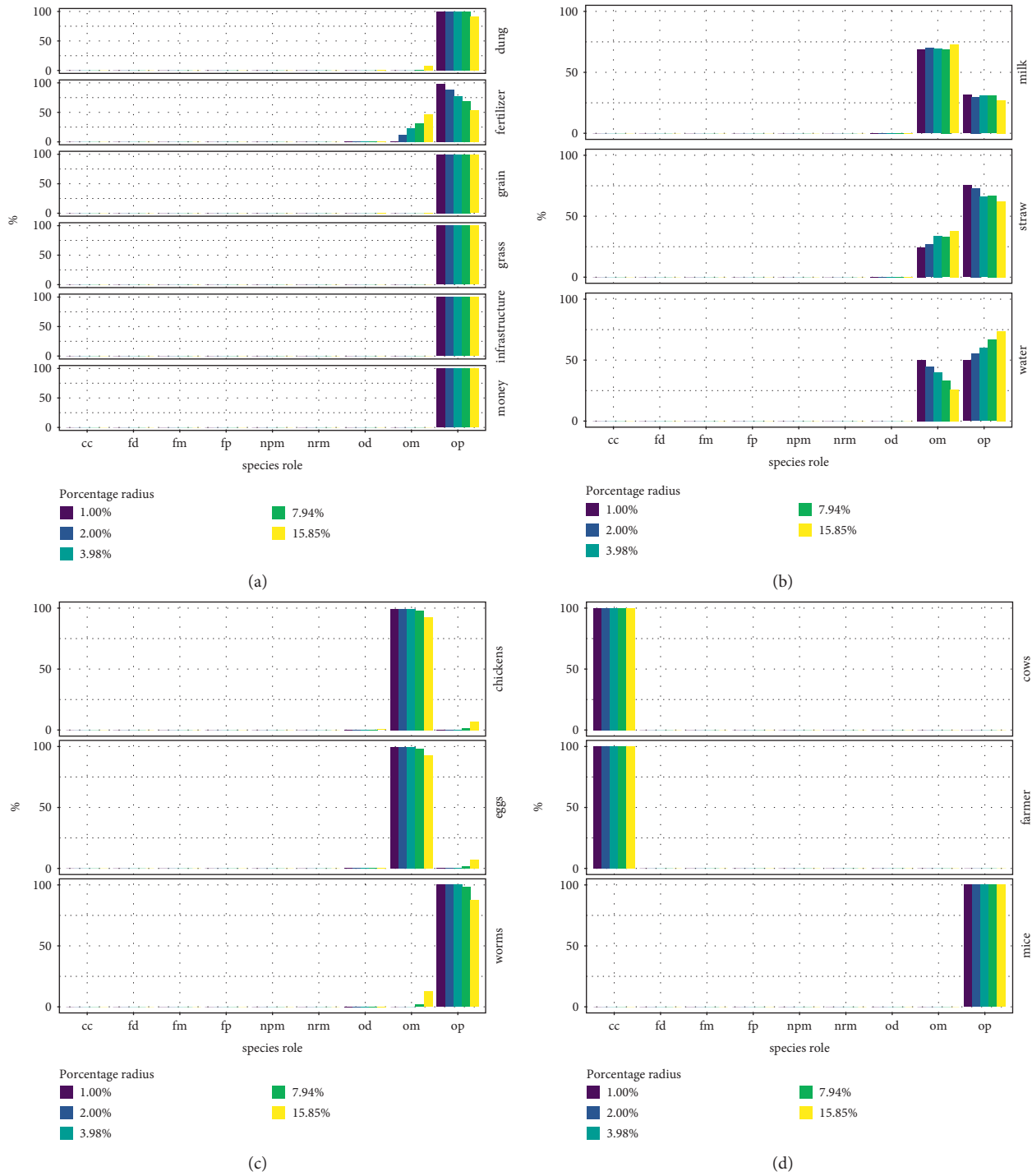
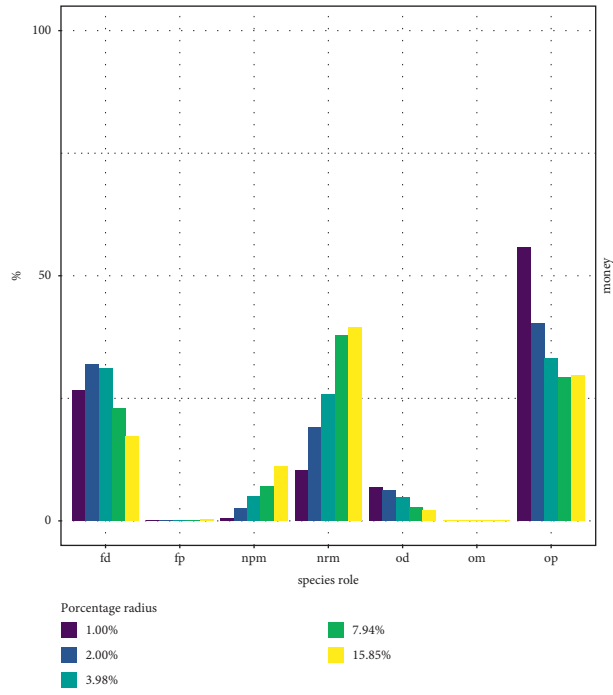


FIGURE 12: Histogram for different species roles according to Table 5 for $Op_2(M)$ for structural and state perturbations. (a) F_2 . (b) $C_{2,1}$. (c) $C_{2,2}$. (d) E_2 .

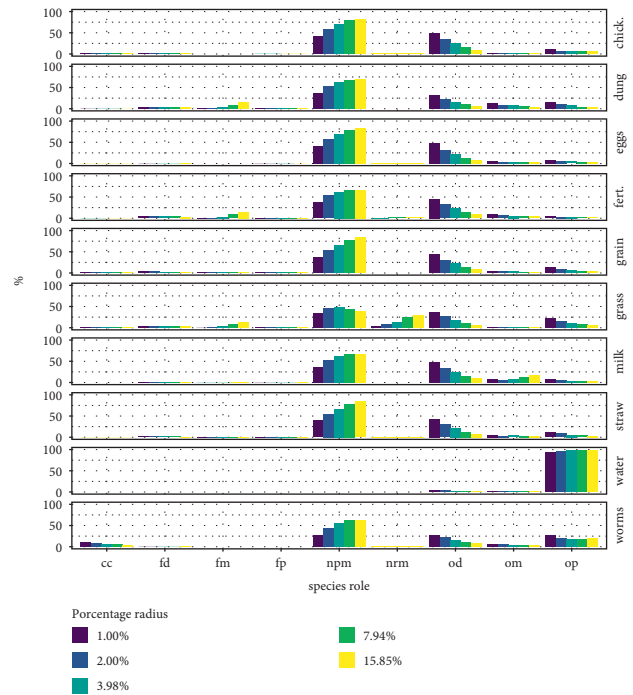
of some species, such as dung, fertilizer, or grass (see Figure 15(a)), leading them for a short time on the od state to end up in npm state. The lack of those species propagates to the fragile circuits, as seen in Figures 15(b) and 15(c), where the species go from om to od and then to npm .

Interestingly, for small-sized process perturbations, the operation of the farm in many cases might go to a different

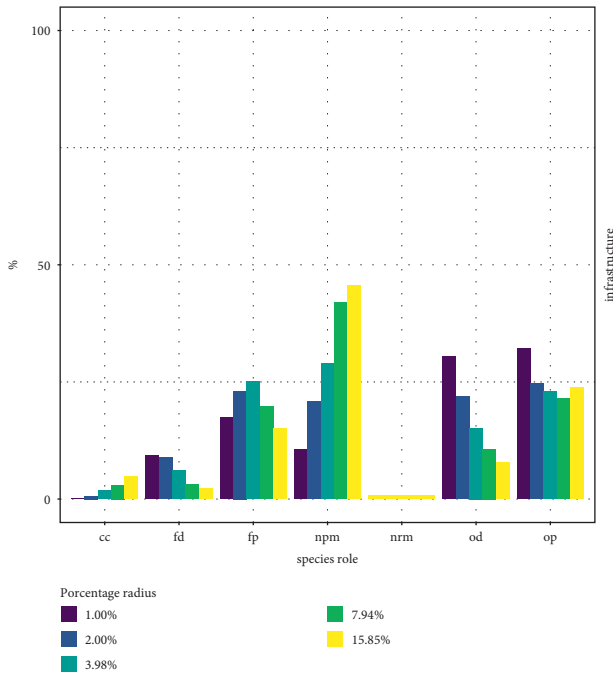
change, similar to the perturbation case without structural perturbation where the fragile circuits become overproductive (compare Figures 15 and 16 for small perturbation values). Therefore, the structural and process perturbation might drive to overproductive regimes in case of small perturbations, and when the perturbations become larger, it might become harmful, disabling the operation of the fragile circuits.



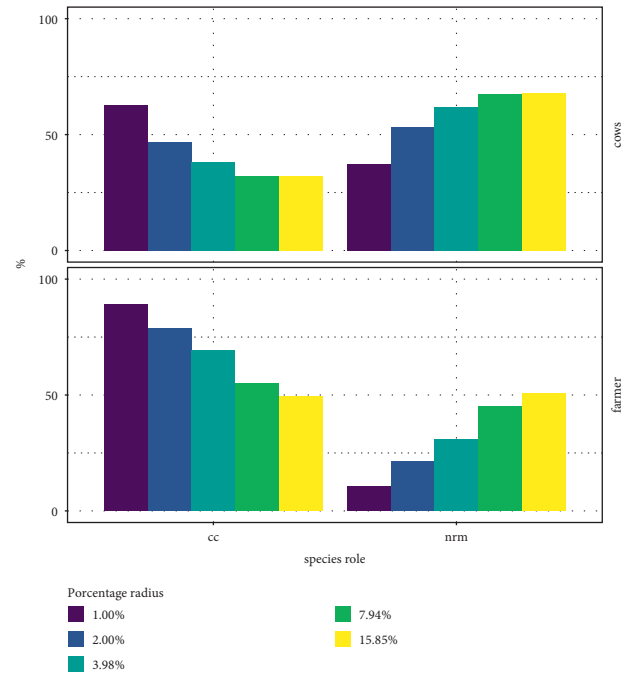
(a)



(b)



(c)



(d)

FIGURE 13: Histogram for different species roles according to Table 5 for $Op_1(M)$ for process perturbations. (a) F_1 . (b) $C_{1,1}$. (c) $C_{1,2}$. (d) E_1 .

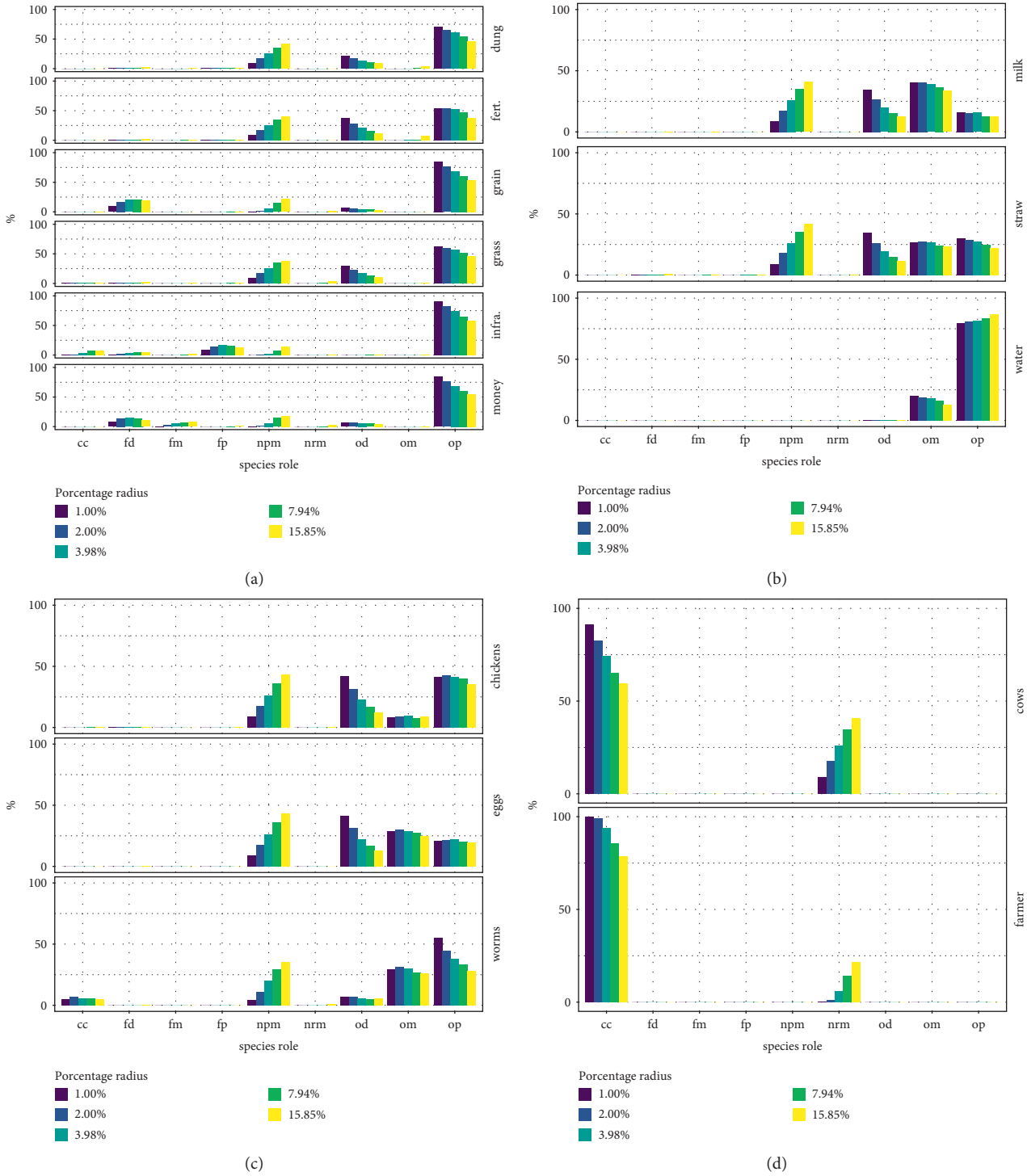


FIGURE 14: Histogram for different species roles according to Table 5 for $Op_2(M)$ for process perturbations. (a) F_2 . (b) $C_{2,1}$. (c) $C_{2,2}$. (d) E_2 .

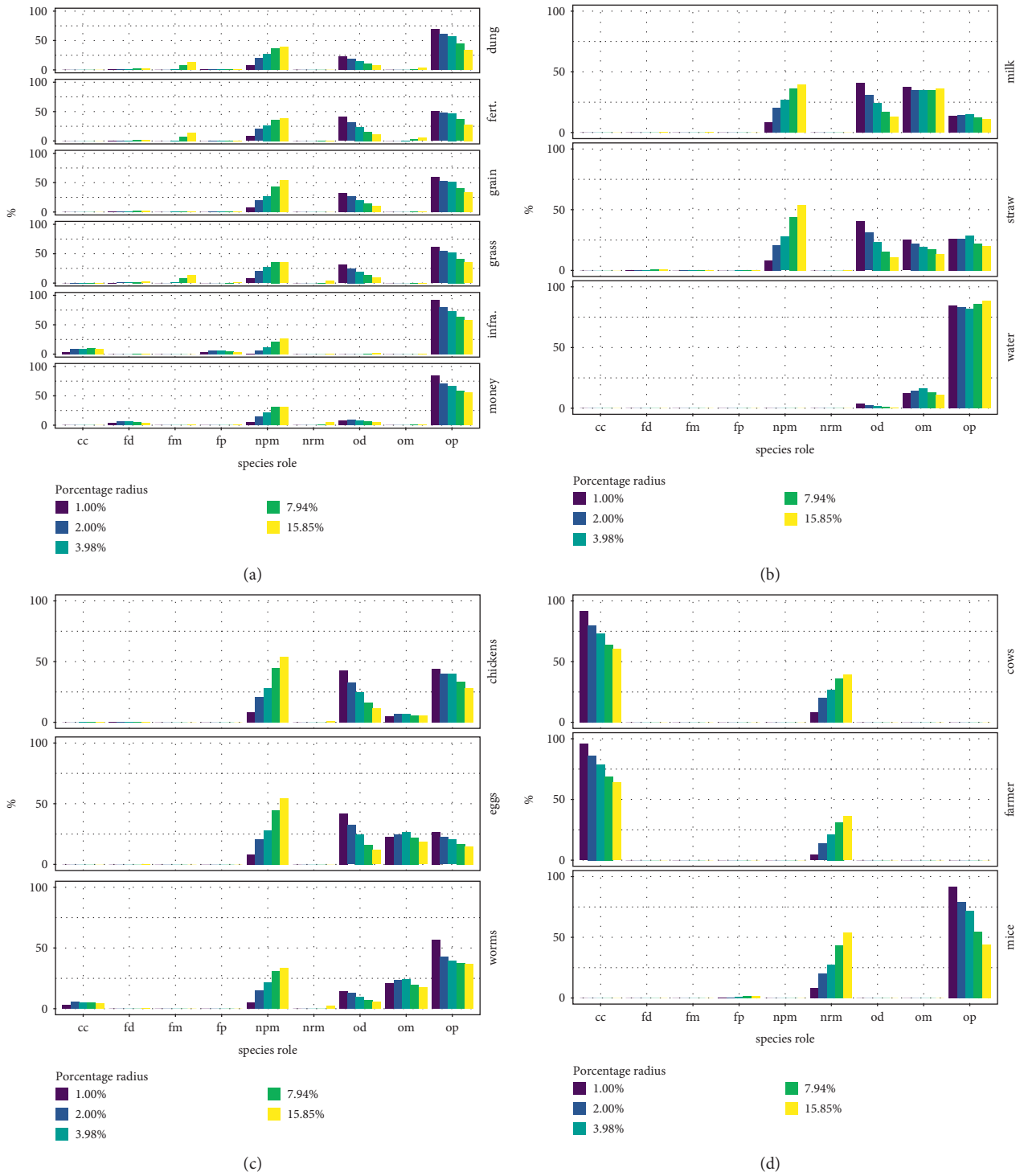


FIGURE 15: Histogram for different species roles according to Table 5 for $Op_2(M)$ for structural and process perturbations. (a) F_2 . (b) $C_{2,1}$. (c) $C_{2,2}$. (d) E_2 .

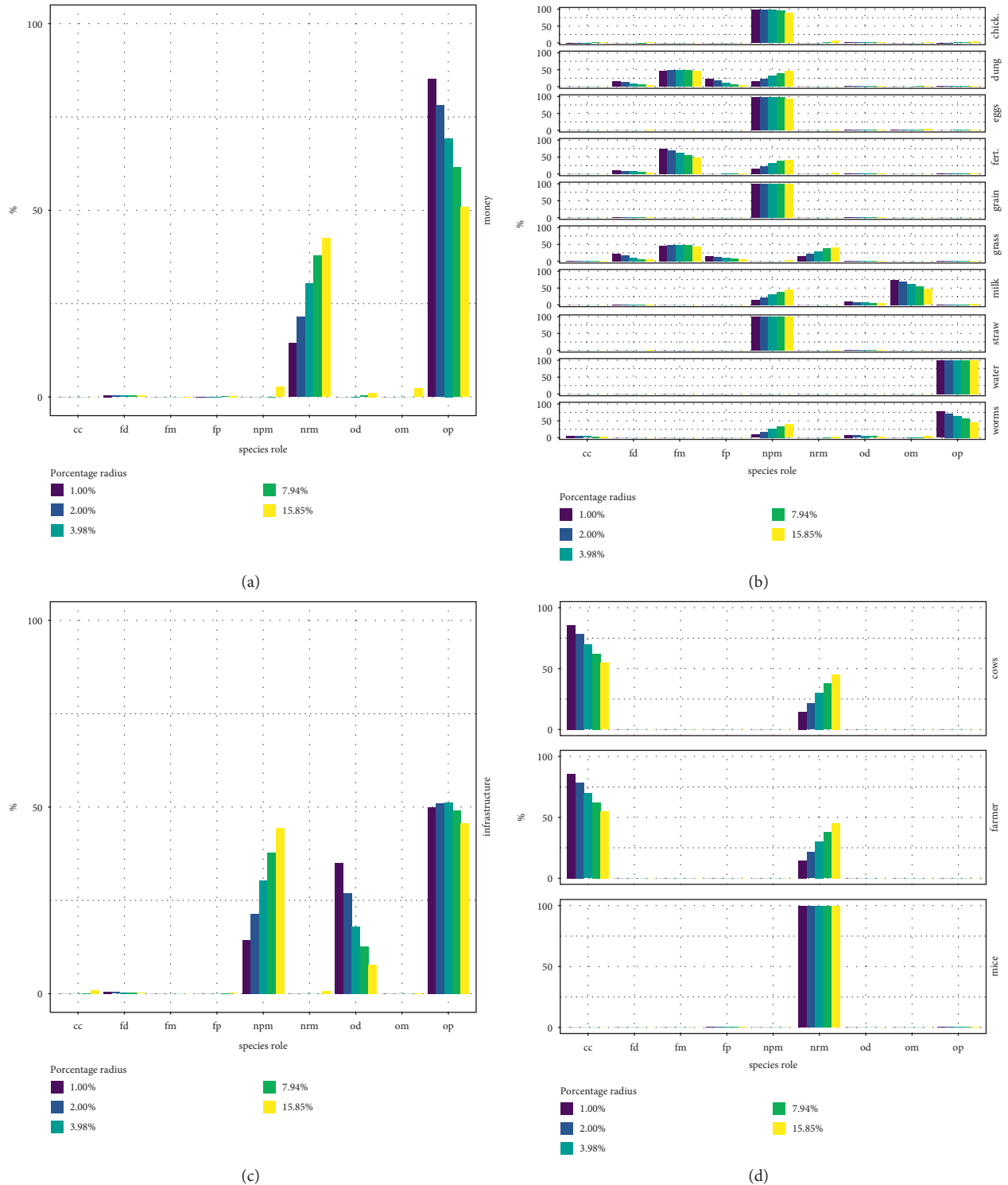


FIGURE 16: Histogram for different species roles according to Table 5 for $Op_1(M)$ for structural and process perturbations. (a) F_1 . (b) $C_{1,1}$. (c) $C_{1,2}$. (d) E_1 .

6. Conclusion

Ensuring the sustainability and resilience of complex systems such as ecosystems, organizations, and organisms is a crucial issue for the future of humanity. However, present approaches to this question lack a clear theoretical

framework, in part because of the difficulty of formalizing the complex network of interactions that determine whether a system will be able to maintain itself in the face of a wide range of perturbations.

We approached this problem by advancing on the representation of systems as reaction networks [14]. In this

approach, reactions consume combinations of species while producing new combinations of species. Chemical organization theory (COT) makes possible to identify organizations within such a network. Such organizations are by definition *self-maintaining* and therefore *sustainable* systems because every species must be produced at least as much as it is consumed by other reactions in the network.

However, COT does not specify which of these organizations would be *resilient*, i.e., able to safeguard or recover their self-maintenance when perturbed. To advance on this issue, we reviewed three fundamental types of perturbations that can occur within a reaction network [44]: (1) state perturbations change the quantity of a species as presently available in the system; (2) process perturbations change the rate of reactions that produce or consume species; (3) structural perturbations introduce or remove species or reactions in the network. This last type of qualitative perturbations, which change the state space and its dynamics, is difficult to analyze in traditional dynamic systems models, but we showed how combining structural analysis with simulations allows to represent the dynamical stability at a qualitative level.

To do so, we first explained how organizations can be decomposed into dynamical modules that have different productive roles, and that such modules are dynamically independent, and thus perturbations in many cases will not affect the whole network but only the module where the perturbation is impacting on.

To illustrate and test this analysis of reaction networks, we proposed a toy model representing the operation of a sustainable farm. This farm can produce resources such as milk, eggs, and grains from resources such as water, grass, cows, chickens, and grains. We analyzed this network with the help of the COT software we developed [40]. This allowed us first to distinguish the different self-maintaining organizations possible within the given network of reactions (see Figure 1).

We then considered two different ways of operating the farm, one which only overproduces money and uses the minimum of resources ($Op_1(M)$), and another which overproduces most of the basic resources needed for operating the farm, as an example of sustainable growth ($Op_2(M)$), and analyzed the responses of the two farm operations by analyzing how it reacts to the three types of perturbation. That is, we developed a statistical analysis considering multiple perturbations to the initial state and process, and then we introduced a structural perturbation (see equation (7)) which harms the productive capacities associated to the use of grain and repeated such analysis, so we could compare the impact of all types of perturbations on each of the ways of operating the farm.

We demonstrated that the different types of perturbations have completely different kinds of impact depending on how the organization is operating. In the absence of a structural perturbation, we find that $Op_1(M)$ is more sensitive to state and process perturbations than $Op_2(M)$, a result which is reasonable considering that $Op_2(M)$ buffers more resources than $Op_1(M)$, and thus in the absence of structural perturbations, we can conclude that sustainable

growth is more resilient than optimization of profit. This result is also obtained when structural and state perturbations are considered.

However, when structural and process perturbations are taken into consideration, we found that some not intuitive behaviors, such as stabilization of $Op_1(M)$ in the smaller organization GCL , the overproduction of $C_{2,1}$ but not overproduction of $C_{2,2}$, or the very inactivation of the whole network (leading to bankruptcy), can occur when process perturbations are considered. Therefore, we conclude that the impact of structural and process perturbations, which in common jargon mean the inclusion of new players and changing the ways the decisions are made, can be in some cases disastrous for the sustainable development of a system. We make a particular remark in this respect because, for example, major political changes regarding global warming such as creating new decision-making structures and new forms of interaction are examples of this kind of combined perturbation.

While inspiring, this particular toy model and its analysis are not yet sufficient to completely understand the notion of resilient organizations. Therefore, we conclude that in order to develop a systemic and formal notion of resilience, it is necessary to continue advancing further classifications of how different kinds of perturbations produce different kinds of responses in the operation of a system. Particularly, process and structural perturbations are linked to the productive decomposition of the reaction network, and thus the parts of the reaction network that are affected require a deeper classification of its connectivity structure, and we also consider it highly necessary to develop a taxonomy of structural responses, for example, the response of our farm model to the arrival of mice (structural perturbation in equation (7)) in our case was only resisted by the very productive capacities of the farm (enough grain is produced to sustain the productive capacities even in the presence of mice), but also other mechanisms, such as fencing the grain storage, bringing mouse predators such as cats, or installing mouse traps in the farm, are also possible ways to counteract the decrease in grain production. Since each of these solutions in turn activates other interactions (for example, cats might eat chickens or mouse traps might harm cows), it is necessary to extend our analysis to understand the mechanisms by which the different productive roles change, so *counteracting structural perturbations* can be designed.

To do so, we plan as future research applying the links between the dynamics of the reaction system, not only with the structural decomposition applied here but also with other frameworks that link structure and dynamics such as deficiency theory [32, 33], Petri net analysis [36, 37], and other frameworks in system biology [39]. We hope to integrate this kind of formal analysis with the more intuitive notions of resilience existing in the literature, with the aim of defining a general and multidimensional measure of resilience for reaction networks. We also hope to extend this analysis to examples in different fields, including metabolic, nuclear, economic, ecological, and political networks and systems [14].

We further see self-maintenance and resilience as primary characteristics of *goal-directed systems*, i.e., systems that will systematically counteract perturbations so as to reach or return to their preferred configuration. To understand this better, we will need to analyze under which conditions organizations exhibit a negative feedback that automatically suppresses deviations from their goal configuration (state or process). Overproduction seems to be a dependable way in which an organization can compensate for losses in resources (e.g., cows dying) or reductions in processes (e.g., less rain because of global warming or less production of grain because of mice eating it). On the other hand, overproduction is limited by the requirement of sustainability: not more can be produced than allowed by the overall capacity of the system. Therefore, a “judicious allocation” of overproduction over the different components of the process vector may be an effective control mechanism to keep the system on track towards its preferred mode of operation even when confronted with perturbations.

We hypothesize that the evolution of complex systems, such as living organisms, will provide them with such control mechanisms. The reason is that systems lacking such mechanism will not be sufficiently resilient to survive common perturbations and thus will be eliminated by natural selection. We hope that our simulations and further theoretical investigations will elaborate such hypotheses into a general scenario for the emergence of sustainable, resilient, and goal-directed systems.

Data Availability

Simulation data used to support the findings of this study are included within the article.

Conflicts of Interest

The authors declare that they have no conflicts of interest.

Acknowledgments

This study was supported by the John Templeton Foundation (Grant ID# 61733).

References

- [1] H. E. Daly, “Toward some operational principles of sustainable development,” *Ecological Economics*, vol. 2, no. 1, pp. 1–6, 1990.
- [2] T. P. Soubbotina, *Beyond Economic Growth: An Introduction to Sustainable Development*, The World Bank, Washington, DC, USA, 2004.
- [3] S. Ulgiati and M. T. Brown, “Monitoring patterns of sustainability in natural and man-made ecosystems,” *Ecological Modelling*, vol. 108, no. 1–3, pp. 23–36, 1998.
- [4] S. C. Bhattacharyya and A. Blake, “Analysis of oil export dependency of mena countries: drivers, trends and prospects,” *Energy Policy*, vol. 38, no. 2, pp. 1098–1107, 2010.
- [5] M. Akacem, D. D. Miller, and J. L. Faulkner, “Why the status quo is unsustainable,” in *Oil, Institutions and Sustainability in MENA*, pp. 169–173, Springer, New York, NY, USA, 2020.
- [6] B. Walker, C. S. Holling, S. R. Carpenter, and A. Kinzig, “Resilience, adaptability and transformability in social–ecological systems,” *Ecology and Society*, vol. 9, no. 2, Article ID 02028, 2004.
- [7] S. Beigi, *Mindfulness engineering: a theory of resilience for the volatile, uncertain, complex and ambiguous (VUCA) world*, PhD thesis, University of Bristol, Bristol, England, UK, 2015.
- [8] S. Beigi, “A road map for cross operationalization of resilience,” in *The Science of Hormesis in Health and Longevity*, pp. 235–242, Elsevier, Amsterdam, The Netherlands, 2019.
- [9] E. Busseniens, T. Veloz, and F. Heylighen, “Goal directedness, chemical organizations, and cybernetic mechanisms,” *Entropy*, vol. 23, no. 8, p. 1039, 2021.
- [10] T. Veloz, “Goals as emergent autopoietic processes,” *Frontiers in Bioengineering and Biotechnology*, vol. 9, p. 998, 2021.
- [11] F. Heylighen, “The growth of structural and functional complexity during evolution,” *The evolution of complexity*, vol. 8, pp. 17–44, 1999.
- [12] M. Feinberg and F. J. M. Horn, “Dynamics of open chemical systems and the algebraic structure of the underlying reaction network,” *Chemical Engineering Science*, vol. 29, no. 3, pp. 775–787, 1974.
- [13] L. Farina and S. Rinaldi, *Positive Linear Systems: Theory and Applications*, Vol. 50, John Wiley & Sons, New Jersey, NJ, USA, 2000.
- [14] T. Veloz and P. Razeto-Barry, “Reaction networks as a language for systemic modeling: fundamentals and examples,” *Systems*, vol. 5, no. 1, p. 11, 2017.
- [15] A. A. Alonso and G. Szederkényi, “Uniqueness of feasible equilibria for mass action law (mal) kinetic systems,” *Journal of Process Control*, vol. 48, pp. 41–71, 2016.
- [16] P. Dittrich and P. S. Di Fenizio, “Chemical organisation theory,” *Bulletin of Mathematical Biology*, vol. 69, no. 4, pp. 1199–1231, 2007.
- [17] S. Peter and P. Dittrich, “On the relation between organizations and limit sets in chemical reaction systems,” *Advances in Complex Systems*, vol. 14, no. 1, pp. 77–96, 2011.
- [18] C. S. Holling, “Resilience and stability of ecological systems,” *Annual Review of Ecology and Systematics*, vol. 1–23, Article ID 06566, 1973.
- [19] P. Martin-Breen and J. M. Anderies, “Resilience: a literature review,” 2011, <https://opendocs.ids.ac.uk/opendocs/handle/20.500.12413/3692>.
- [20] S. H. Strogatz, “Nonlinear dynamics and chaos,” *With Applications to Physics, Biology, Chemistry, and Engineering*, Westview press, Colorado, CO, USA, 2014.
- [21] T. Kovalenko and D. Sornette, “Dynamical Diagnosis and Solutions for Resilient Natural and Social Systems,” 2012, <https://arxiv.org/abs/1211.1949>.
- [22] M. D. Lewis, A. V. Lamey, and L. Douglas, “A new dynamic systems method for the analysis of early socioemotional development,” *Developmental Science*, vol. 2, no. 4, pp. 457–475, 1999.
- [23] M. Scheffer, *Critical Transitions in Nature and Society*, vol. 16, Princeton University Press, Princeton, NJ, USA, 2009.
- [24] B. Walker, S. Carpenter, J. Anderies et al., “Resilience management in social-ecological systems: a working hypothesis for a participatory approach,” *Conservation Ecology*, vol. 6, no. 1, 2002.
- [25] S. Carpenter, B. Walker, J. M. Anderies, and N. Abel, “From metaphor to measurement: resilience of what to what?” *Ecosystems*, vol. 4, no. 8, pp. 765–781, 2001.

- [26] I. Linkov, T. Bridges, F. Creutzig et al., “Changing the resilience paradigm,” *Nature Climate Change*, vol. 4, no. 6, pp. 407–409, 2014.
- [27] H. R. Maturana, “The organization of the living: a theory of the living organization,” *International Journal of Man-Machine Studies*, vol. 7, no. 3, pp. 313–332, 1975.
- [28] S. Peter, T. Veloz, and P. Dittrich, “Feasibility of organizations—a refinement of chemical organization theory with application to p systems,” in *Proceedings of the Eleventh International Conference on Membrane Computing (CMC11)*, Jena, Germany, August 2010.
- [29] F. Varela, “Two principles for self-organization,” in *Self-organization and Management of Social Systems*, vol. 25–32, New York, NY, USA, Springer, 1984.
- [30] H. R. Maturana and F. Varela, *Autopoiesis and Cognition: The Realization of the Living*, Springer Science & Business Media, Heidelberg, Germany, 1980.
- [31] P. Razeto-Barry, “Autopoiesis 40 years later. a review and a reformulation,” *Origins of Life and Evolution of the Biosphere*, vol. 42, no. 6, pp. 543–567, 2012.
- [32] F. Martin, *Foundations of Chemical Reaction Network Theory*, Springer, New York, NY, USA, 2019.
- [33] J. A. Papin, J. Stelling, N. D. Price, S. Klamt, S. Schuster, and B. O. Palsson, “Comparison of network-based pathway analysis methods,” *Trends in Biotechnology*, vol. 22, no. 8, pp. 400–405, 2004.
- [34] S. Rubin, T. Veloz, and P. Maldonado, “Beyond planetary-scale feedback self-regulation: gaia as an autopoietic system,” *Biosystems*, vol. 199, Article ID 104314, 2021.
- [35] D. Contreras, U. Pereira, V. C. Hernandez, B. Reynaert, and L. Juan-Carlos, *A loop conjecture for metabolic closure*, pp. 176–183, MIT PRESS, Cambridge, MA, 2011.
- [36] M. Taleb-Berrouane and F. Khan, “Dynamic resilience modelling of process systems,” *Chemical Engineering*, vol. 77, pp. 313–318, 2019.
- [37] M. Heiner, D. Gilbert, and R. Donaldson, “Petri nets for systems and synthetic biology,” in *Proceedings of the International School on Formal Methods for the Design of Computer, Communication and Software Systems*, pp. 215–264, Springer, Bertinoro, Italy, June 2008.
- [38] I. Tomás and G. Veloz, *A Computational Study of Algebraic Chemistry*, Repositorio Academico, Nuevo Leon, Mexico, 2010.
- [39] B. Palsson, *Systems Biology*, Cambridge University Press, Cambridge, UK, 2015.
- [40] Cot software analysis, “Cot software analysis,” 2021, <https://github.com/pmaldona/decom>.
- [41] F. Centler, C. Kaleta, P. S. di Fenizio, and P. Dittrich, “Computing chemical organizations in biological networks,” *Bioinformatics*, vol. 24, no. 14, pp. 1611–1618, 2008.
- [42] F. Centler, C. Kaleta, P. Speroni di Fenizio, and P. Dittrich, “A parallel algorithm to compute chemical organizations in biological networks,” *Bioinformatics*, vol. 26, no. 14, pp. 1788–1789, 2010.
- [43] L. Egli, W. Hanna, V. Radchuk, R. Seppelt, and V. Grimm, “Exploring resilience with agent-based models: state of the art, knowledge gaps and recommendations for coping with multidimensionality,” *Ecological Complexity*, vol. 40, Article ID 100718, 2019.
- [44] T. Veloz and P. Razeto-Barry, “Reaction networks as a language for systemic modeling: on the study of structural changes,” *Systems*, vol. 5, no. 2, p. 30, 2017.
- [45] B. Garrett, *Lattice Theory*, vol. 25, American Mathematical Soc, Rhode Island, USA, 1940.

Research Article

Reaction Network Modeling of Complex Ecological Interactions: Endosymbiosis and Multilevel Regulation

Tomas Veloz ^{1,2,3} and Daniela Flores ^{1,4}

¹Fundación para el Desarrollo Interdisciplinario de la Ciencia, la Tecnología y Las Artes, Arturo Prat 249, Santiago, Chile

²Universidad Andres Bello, Departamento Ciencias Biológicas, Facultad Ciencias de la Vida, Santiago 8370146, Chile

³Centre Leo Apostel, Vrije Universiteit Brussel, Rue de la Strategie 33, 1060, Brussels, Belgium

⁴Universidad de Chile, Departamento de Biología, Facultad de Ciencias, Ñuñoa, Santiago, Chile

Correspondence should be addressed to Tomas Veloz; tveloz@gmail.com

Received 10 July 2020; Accepted 29 July 2021; Published 9 August 2021

Academic Editor: Abdellatif Ben Makhlof

Copyright © 2021 Tomas Veloz and Daniela Flores. This is an open access article distributed under the Creative Commons Attribution License, which permits unrestricted use, distribution, and reproduction in any medium, provided the original work is properly cited.

Endosymbiosis is a type of symbiosis where one species of microscopic scale inhabits the cell of another species of a larger scale, such that the exchange of metabolic byproducts produces mutual benefit. These benefits can occur at different biological levels. For example, endosymbiosis promotes efficiency of the cell metabolism, cell replication, and the generation of a macroscopic layer that protects the organism from its predators. Therefore, modeling endosymbiosis requires a complex-systems and multilevel approach. We propose a model of endosymbiosis based on reaction networks, where species of the reaction network represent either ecological species, resources, or conditions for the ecological interactions to happen, and the endosymbiotic interaction mechanisms are represented by different sequences of reactions (processes) in the reaction network. As an example, we develop a toy model of the coral endosymbiotic interaction. The model considers two reaction networks, representing biochemical traffic and cellular proliferation levels, respectively. In addition, the model incorporates top-down and bottom-up regulation mechanisms that stabilizes the endosymbiotic interaction.

1. Introduction

Endosymbiosis is a particular kind of symbiosis which occurs when an organism (endosymbiont) lives within another (host) in a mutualistic relationship. This relationship is given by the coupling of the host's and endosymbiont's metabolisms through exchange of useful metabolites [1, 2]. The endosymbiotic concept was proposed by Lynn Margulis, who developed *Serial Endosymbiosis Theory* (SET) to explain the origin of plastids and mitochondria as organelles in the eukaryotic cell, promoting the emergence of eukaryotic cell complexity [3]. Endosymbiosis is recognized as a widespread mechanism in nature and is taking relevance as an evolutionary mechanism in different lineages [4]. Symbiotic interactions allow alternative ways of evolution, for example, through natural selection, in evolving complexity for a population of individuals. Endosymbiosis implies the coupling of two or more species in an intimate relationship.

Such relation leads to an increase of phenotypic complexity at the genomic, physiological, and morphological levels. Therefore, endosymbiosis enables ecological expansion into different and new niches. As Darwin said in his book *The Origin of Species*: “Natural Selection cannot possibly produce any modification in a species exclusively for the good of another species; although throughout nature one species incessantly takes advantage of, and profits by, the structures of other” [5].

One of the examples of endosymbiosis corresponds to the relationship between corals (Cnidaria, Anthozoa) and a photosynthetic algae of the genus *Symbiodinium* or *Zooxanthellae* [6], in which the latter lives within the gastrodermis coral cells. This relationship is typical when the environmental food is scarce [7, 8], and they (the *Symbiodinium* and the coral) can feed back through their metabolisms, by the nutrient acquisition via the cycling of organic compounds which supplies extra energy to both

endosymbiont and host. The latter provides an ecological advantage and thus promotes survival because the metabolic coupling between coral cells and *Symbiodinium* promotes cellular proliferation implying coral's growth. Interestingly, such growth process is regulated by the release of an inhibition factors by the endosymbiont. Namely, when certain byproducts of the energy generation process that might harm the cells surpass a threshold, inhibition factors are released, stopping the growth process [9, 10]. Thus, endosymbiosis is a multilevel and self-regulated process.

The establishment of endosymbiosis gives rise to new structural and morphological properties and thus to new evolutionary competences. However, the experimental study of endosymbiotic systems is extremely complicated, and it cannot be properly achieved by analyzing the interacting species separately [1]. For this reason, a modeling framework for the establishment of the endosymbiosis relationship is of crucial importance from an ecological perspective [11].

Such modeling framework of endosymbiosis should incorporate both the multiple levels at which the interaction takes place as well as bottom-up and top-down regulation mechanisms. Interestingly, these features are relevant not only for endosymbiosis but also for embryonic development [12], ecological trophic networks [13], and also during evolutionary processes [14, 15]. For this reason we aim at proposing a process-based and multilevel approach to the representation of endosymbiosis.

Reaction networks, and equivalent languages such as Petri Nets [16], are the main representational languages in systems biology [17, 18]. They allow for a description of the dynamical properties of complex biochemical reaction system of multilevel nature, using methods that exploit both the structure and stoichiometry of the network [19, 20]. Reaction networks can also describe processes whose entities are not only biochemical [21]. Indeed, reaction networks have been applied to model the exchange of economic goods [22], the influence of political decisions [23], the evolution of cooperation [24], and other game-theoretical settings [25]. Therefore, reaction networks can not only be applied outside biochemical settings, but also have the potential to become an intuitive language to describe and study problems of multidisciplinary nature from a systemic perspective [26, 27]. The latter can have novel and powerful applications particularly in the modeling of ecological interactions [28].

In the present study, we provide a simple mathematical model of the interaction between anthozoan corals and symbiont algae of the genus *Symbiodinium* by representing the mechanisms of their endosymbiotic interaction using reaction networks. In particular, we propose two reaction networks modeling endosymbiosis at a biochemical traffic (lower level) and cellular proliferation (upper level). We point to how endosymbiosis occurs at each level and focus on representing the multilevel regulatory mechanisms that are known to happen in this two-layer interaction process.

The paper is organized as follows. In Section 2, we review in detail the endosymbiotic mechanisms known up to date. In Section 3, we introduce the basics of ecological modeling using reaction networks. In Section 4, we propose a toy model of the endosymbiotic as well as of the multilevel

regulatory mechanisms of the *Symbiodinium*. We complement the latter with a discussion of how we could scale up to more realistic models of the interaction, and we end with a conclusion.

2. Endosymbiotic Mechanisms and Their Levels of Interaction

Corals are ancestral animals formed by only four epithelial layers: oral ectoderm, oral endoderm, aboral endoderm, and calcidodermis (Figure 1). In conditions of food limitations, corals (Cnidaria) can engulf photosynthetic dinoflagellates (algae) of the genus *Symbiodinium* from the surrounding water. *Symbiodinium* cells engulfed by the coral are hosted gastrodermis layer of the coral that surrounds the gastric cavity (oral endoderm), where they can still perform photosynthesis. Namely, the *Symbiodinium* acquires nutrients and metabolic residual compounds from the host and produces organic compounds. These organic compounds that are product of the photosynthesis not only foster the growth and respiration of endosymbionts, but also are used to produce nearly up to 95% of the host's energy demand [29].

The latter phenomenon occurs in the oral endoderm (yellow layer) within a membrane called symbiosome (white layer), produced by both the host and the *Symbiodinium* (green layer) in Figure 1.

The endosymbiotic interaction occurs in various phases: (1) initial contact; (2) engulfment; (3) sorting; (4) proliferation; (5) dynamic stability; and (6) dysfunction (Figure 2). The initial contact phase is characterized by the compatibility recognition between the host and the symbiont (Figure 2(a)). Namely, each coral lineage is compatible with one or more *Symbiodinium* lineages [31]. When compatible, the coral engulfs the algae (Figure 2(b)). After successful engulfment, the symbiosome membrane is developed promoting the stabilization and persistence of the symbiont within the cells of the coral [32]. Next, the persistence of the symbiont depends on the balance between host cell growth and proliferation of the symbiont population. The latter balance can be achieved by a series of sorting and proliferation steps, reaching the dynamic stability phase (Figure 2(c)). This last stage is characterized by the metabolic exchange and nutrient trafficking, where the products generated by dinoflagellate support coral metabolism, growth, reproduction, and survival and also promote the conservation and recycling of essential nutrients. In this phase, the typical calcium deposition of coral reef takes place. This phenomenon is strongly promoted by the endosymbiosis [33]. This calcium matrix deposition protects the coral against predators and decreases mechanical erosion of the marine environment, further promoting its persistence and growth [34] (Figure 2). The last phase of the endosymbiotic interaction is dysfunction, related to the bleaching of the calcium layer, which is explained by the *Symbiodinium* expulsion by exocytosis and coral mortality, and by host cell detachment or host cell apoptosis, generally due by the production of reactive oxygen species or cellular signaling [35]. Coral reef bleaching is increasingly

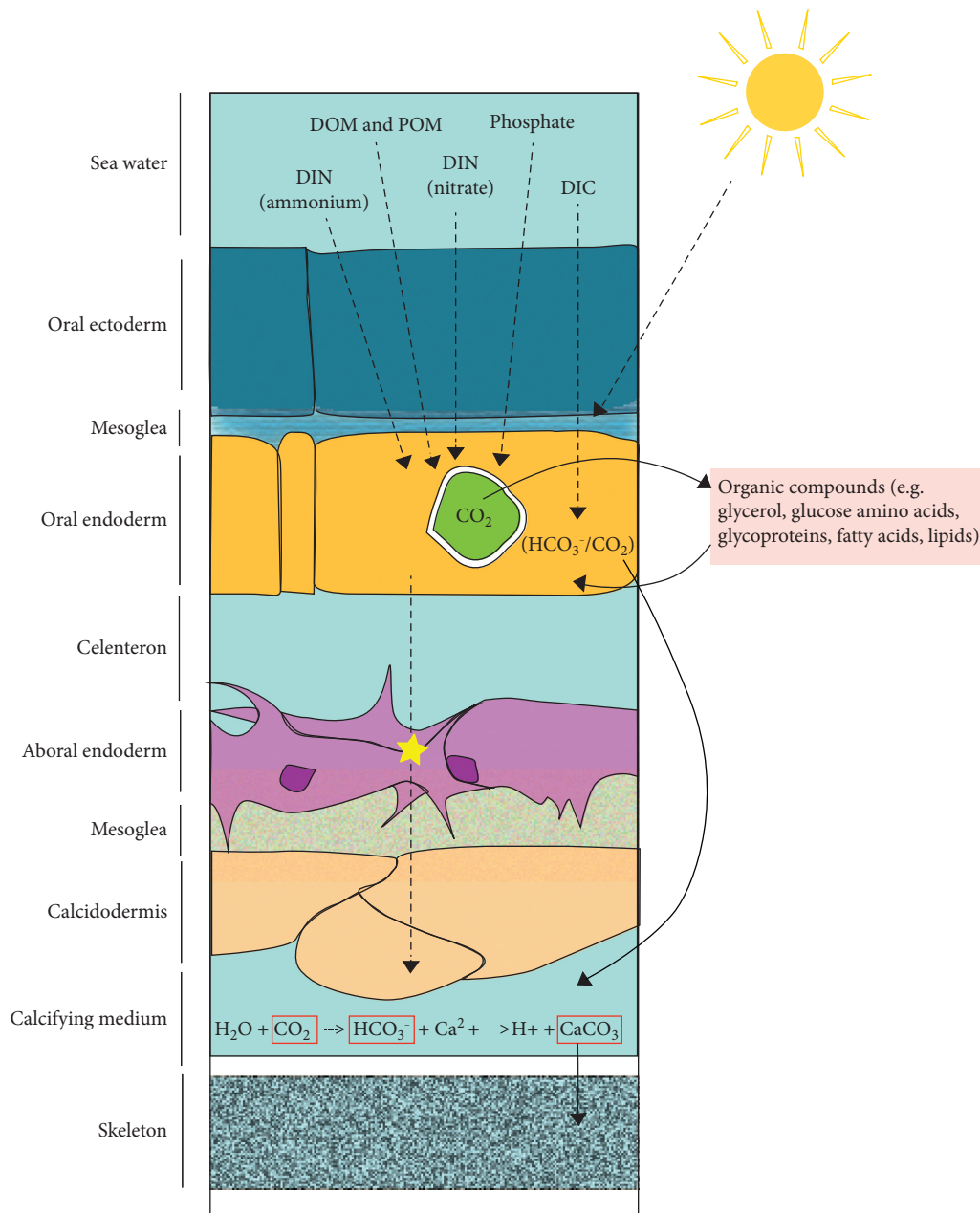


FIGURE 1: Metabolic interactions and calcification processes. DIC: dissolved inorganic carbon uptake; DOM: dissolved organic matter; POM: particulate organic matter; DIN: dissolved inorganic nitrogen.

threatened by recent changes in salinity, higher solar radiation, increased sedimentation or pollutants, elevated sea surface temperatures, and global warming [36].

In the dynamic stability phase, coral and algae metabolisms couple controlling each other's growth, promoting functional efficiency [37, 38]. Typically, coral gastrodermis regulate their density to maintain up to two *Symbiodinium* per cell [39, 40]. Such regulation incorporates various mechanisms, such as the expulsion and degradation of *Symbiodinium*, signaling factors affecting the cellular cycle such as a host release factors (HRFs) [9, 10], and other processes and biochemical factors that act as inhibitory factors (IFs) released by the host, hindering the growth of

symbionts [41–43]. The release of IFs depends on the concentration of photosynthetic byproducts in the metabolism of the endosymbiont. Thus, this factor is relevant to achieve a steady growth and nutrient traffic state.

In steady state, *Symbiodinium* is benefited by acquisition of inorganic carbon, inorganic nitrogen, and inorganic phosphate by the coral, which gives the *Symbiodinium* greater availability of these nutrients for its own growth. In turn, as a product of the photosynthesis of *Symbiodinium*, diverse compounds are generated that nourish the coral, such as glycerol, amino acids, glucose, maltose, Krebs cycle molecules, pyruvate, zooxanthellamine, and zooxanthellatoxins [44]. In this way, the coral develops mechanisms and processes that

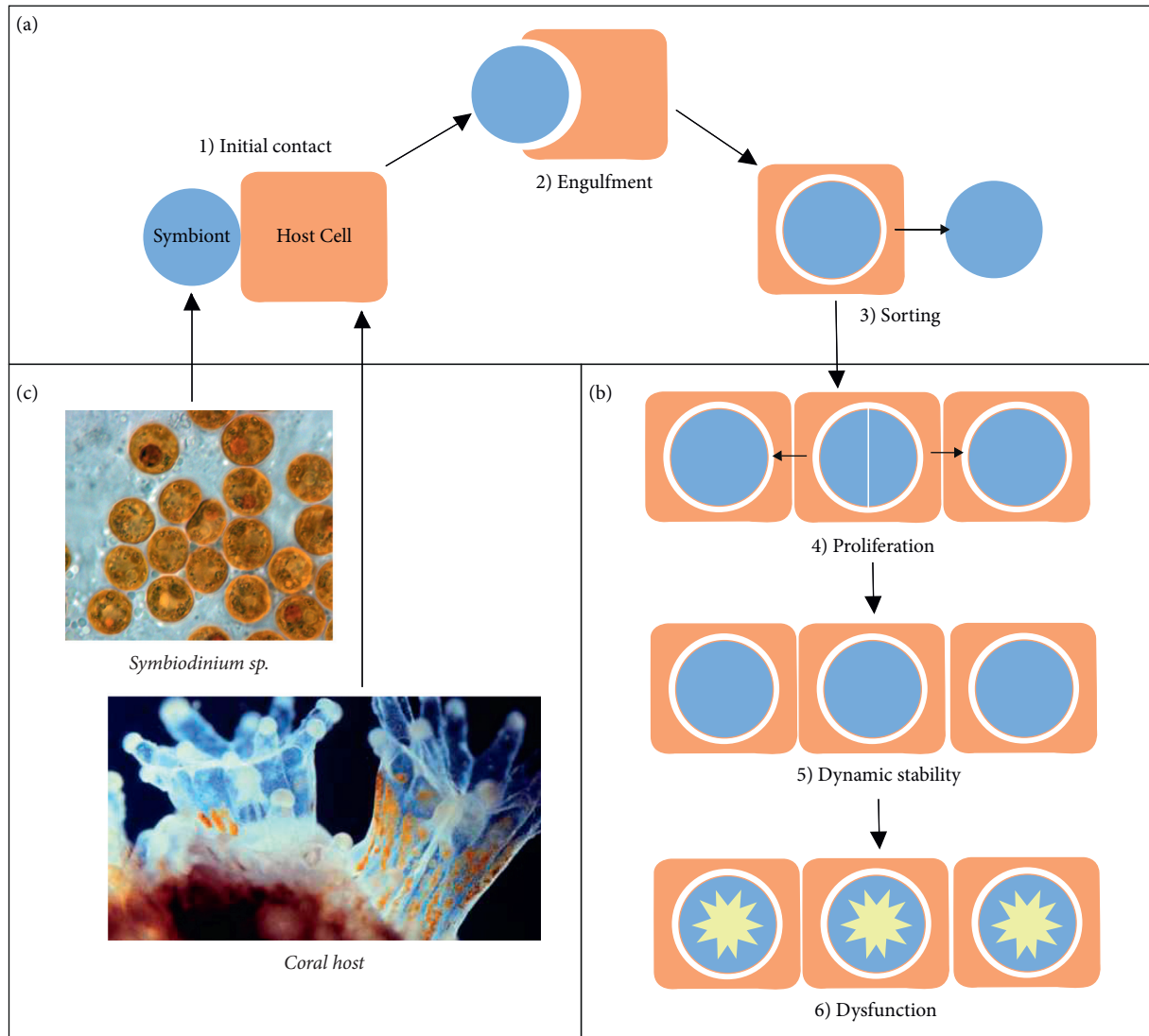


FIGURE 2: Phases of endosymbiosis establishment and persistence in cnidarian-*Symbiodinium* interaction (modified from [30]).

benefit endosymbiont and vice versa. These mechanisms can affect other processes occurring at other cellular layers of the host. For example, in the carbon metabolism, coral actively transports carbon from outside to gastrodermis cells and concentrates CO_2 near the endosymbiont from the enzyme carbonic anhydrase (CA) located around the symbiosome, fostering the algae photosynthetic process. Another example is in the nitrogen metabolism, which is necessary to the algae in the form of ammonium (NH_4^+) and nitrate (NO_3^-), to form amino acids, and which are also a resource to the coral because they are transported back to the host as a nutrient. Calcification also is promoted as a consequence of the metabolic coupling of both organisms, since dissolved inorganic carbon necessary for photosynthesis by *Symbiodinium* is also necessary to produce calcium skeleton, which is mainly composed of calcium carbonate (CaCO_3) crystallized in an organic matrix. Calcification is enhanced by light in presence of *Symbiodinium*, and this affects the balance of dissolved inorganic carbon, taking CO_2 for photosynthesis reactions, which directly promotes the precipitation of

CaCO_3 . In addition, organic products of photosynthesis are precursors of the synthesis of organic matrix, and energy and oxygen supplementation to the host increases its metabolism and promotes faster calcification [33,45]. Moreover, corals presenting *Symbiodinium* are capable of living in clear and shallow waters, where they are constantly threatened by high intensity solar radiation. Despite the fact that light levels are harmful, symbionts produce UV-absorbing sunscreen compounds, like mycosporine amino acids (MAAs), which act as light-harvesting pigments and free radical scavengers [46].

In summary, there are both metabolic coupling and regulation between *Symbiodinium* and host cells. The latter promotes their growth, reproduction, and survival at different organizational levels. We organize the levels of interaction of the endosymbiotic interaction as follows (see Table 1):

(1) Biochemical traffic level: related to the biochemical relationship and nutrient traffic inside the cells of the coral, and between the coral and *Symbiodinium* cells.

TABLE 1: Representing ecological interactions using reaction networks.

| Interaction | Positive | Neutral | Negative | Reaction |
|--------------|----------|---------|----------|---|
| Amensalism | — | x | y | $x + y \longrightarrow x$ |
| Antagonism | x | — | y | $x + y \longrightarrow 2x$ |
| Mutualism | x, y | — | — | $x + y \longrightarrow 2x + 2y$ |
| Commensalism | y | x | — | $x + y \longrightarrow x + 2y$ |
| Competition | x, y | — | x, y | $x + y \longrightarrow x$ and $x + y \longrightarrow y$ |

(2) Cellular proliferation level: related to the cellular reproduction to achieve the dynamic stability state between the cells biomass of both partners.

(3) Organismic level: related to the growth of the coral and the protection from biological and mechanical erosion due to the calcidodermis production generated in lower levels.

Therefore, when the endosymbiotic interaction is established, the above explained processes at these three levels intertwine benefiting the persistence of endosymbiosis.

3. Reaction Network Modeling of Ecological Interactions

A reaction network is defined by a pair (M, R) , where $M = \{a, b, c, \dots\}$ is a set of molecular species, and $R \subseteq \mathcal{P}_m(M) \times \mathcal{P}_m(M)$ is a set of reactions, where $\mathcal{P}_m(M)$ denotes the set of multisets of M . For example, consider

$$\begin{aligned}
 M &= \{a, b, c\}, \\
 R &= \{r_1, r_2, r_3, r_4, r_5, r_6\}, \text{ with,} \\
 r_1 &= a \longrightarrow 2a, \\
 r_2 &= a + c \longrightarrow c, \\
 r_3 &= b + c \longrightarrow b + 2c, \\
 r_4 &= a \longrightarrow \emptyset, \\
 r_5 &= c \longrightarrow \emptyset, \\
 r_6 &= b + a \longrightarrow \emptyset.
 \end{aligned} \tag{1}$$

Note that reaction $r_1 = a \longrightarrow 2a$ represents a self-reproduction process of species a , reaction $r_2 = a + c \longrightarrow c$ represents the destruction of species a out of the interaction of species a and c , and $r_3 = b + c \longrightarrow b + 2c$ represents the reproduction of species c catalyzed by b . Similarly, the destruction and disappearance of a and c are represented by r_4 and r_5 , respectively, and the mutual destruction of a and b is represented by r_6 .

The dynamics of a reaction network can be modeled using difference, stochastic, or differential equations [47], and a vast amount of literature is devoted to complement these approaches with structural analysis of the network [18–20].

Recently, reaction networks have been proposed to represent ecological interactions and ecosystems [28, 48]. In particular, contrary to traditional network approaches, which represent different ecological interactions by different types of links, reaction networks characterize types of ecological interactions by the way in which combinations of

inputs produce combinations of outputs. This opens up an exponentially wider range of interacting processes. Typical ecological interactions such as depredation, cooperation, and parasitism are easily expressed by means of reaction networks. For example, reaction $r_3 = a + c \longrightarrow c$ of the reaction network equation (1) corresponds to an amensalistic interaction, since a is destroyed in the presence of c without altering c . Likewise, $r_4 = b + c \longrightarrow b + 2c$ is a commensalistic relation, because c benefits from its interaction with b without altering b . In Table 1, we represent ecological interactions using minimal reaction networks.

Interestingly, when one is interested in representing an ecological interaction in more detail, the model of the interaction is made by a collection of reactions representing the interaction mechanism. Since the interaction mechanisms of different interaction might share some species at both resource and product levels, an ecological system is modeled by a large reaction network composed by the coupling of multiple subnetworks, each of these subnetworks representing one of the ecological interactions of the ecosystem [28].

In addition to the structural transformational relation specified by a reaction, there is usually a parameter which indicates its likelihood to happen. This value, known as kinetic parameter or kinetic rate, is indicated above the arrow which specifies the reaction. For example, in the case of competition, the reactions $r_1 = x + y \xrightarrow{k_x} x$, $r_2 = x + y \xrightarrow{k_y} y$ constrained to $k_x < k_y$, would indicate that y has a competitive advantage over x , as reaction r_2 is more likely to happen than r_1 .

Moreover, the empty set symbol \emptyset represents the environment, i.e., what is not part of the system under study. For this reason, reactions $\emptyset \xrightarrow{k} a$ and $a \xrightarrow{k} \emptyset$ indicate the *inflow* (born, entrance, spontaneous formation) of a in the system while indicates the *outflow* (death, exit, decay) of a from the system.

4. Multilevel Reaction Network Model of Endosymbiotic Interactions

In this section, we develop a reaction network model of the biochemical traffic and cellular proliferation levels of the endosymbiotic interaction depicted in Table 2. Next, we explain how to represent the regulation mechanisms occurring between these two levels. This model extends previous work [49].

4.1. Biochemical Traffic Level. At this level, endosymbiosis is characterized by the possibility to metabolize elements that coral cells alone cannot metabolize, and by the increase of

TABLE 2: Levels of interaction and processes that are enhanced by endosymbiosis at each level.

| Level of interaction | Processes driven by endosymbiosis |
|------------------------|---|
| Biochemical traffic | Biochemical interrelationship, nutrient traffic, energy flow, and calcidodermis biochemical production. |
| Cellular proliferation | Cellular reproduction and death of <i>Symbiodinium</i> and host cells. |
| Organismic | Coral growth and protection against predators and other physical threats |

calcium production, which leads to a macroscopic calcium layer that protects the macroscopic coral from predators and erosion. The following reaction network represents in a simplified way the endosymbiotic interaction at the biochemical traffic level:

Species set:

R_H : host cell resource

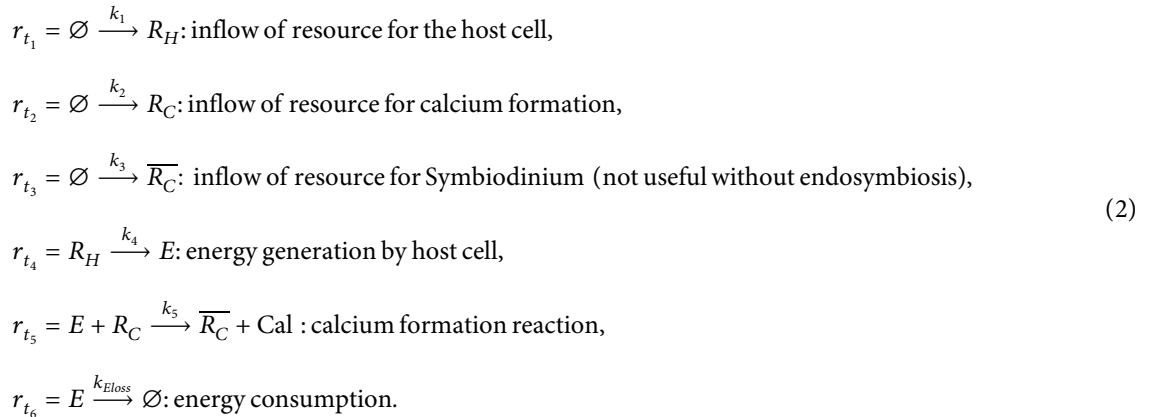
E : energy

R_C : resource to form calcium layer

\overline{R}_C : resource that is product of the calcium formation reaction

Cal_C: calcium

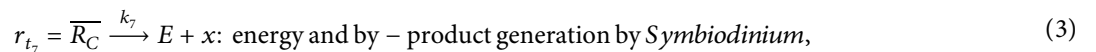
The reactions of a cell without *Symbiodinium* in it are



Note that in the model given by equation (2) there is an energy generation pathway given by the reaction sequence (r_{t_1}, r_{t_4}) , which in turns activate the calcium formation pathway (r_{t_2}, r_{t_5}) . For simplicity, the energy consumption pathway is represented by r_{t_6} . Note that if k_1 is too small, meaning that there is not enough R_H available in the

environment, the energy generation process driven by r_{t_4} might not compensate for the energy consumption represented by r_{t_6} .

When the *Symbiodinium* is present in the cell, we add the following reaction to the model:



meaning that *Symbiodinium* is capable of generating energy for the cell from the resource \overline{R}_C and creating x , which correspond to photosynthetic byproducts of algae metabolism, that can be sensed by the host. This last reaction activates a new energy generation pathway (r_{t_3}, r_{t_7}) by using

up the byproduct \overline{R}_C of r_{t_5} , and hence metabolizing \overline{R}_C to produce more Cal. The latter modifies the chemical equilibrium between R_C and \overline{R}_C by taking up more \overline{R}_C for its photosynthetic metabolism, which directly favors the precipitation of Cal by Le Chatelier's principle [33].

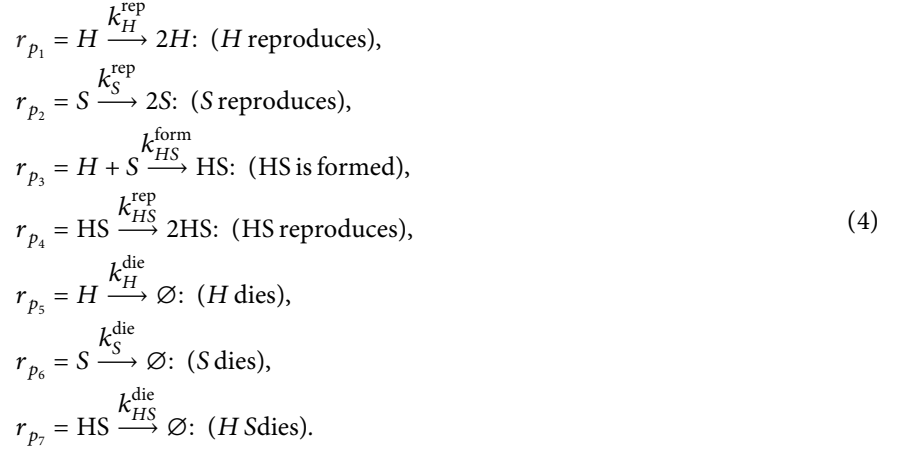
4.2. *Cellular Proliferation Level.* At the cellular proliferation level, we identify three types of cells:

H : host

S : *Symbiodinium*

HS: symbiont (host and *Symbiodinium* interacting in endosymbiosis)

Similar to the previous case, we will keep the model very simple, so we introduce reactions that account for the most basic interactions between cells, cell proliferation, and endosymbiosis. Other aspects such as the multiple manners in which the cells can die, or the environmental conditions that foster their reproduction, are not included.



Under appropriate internal cell proliferation conditions $k_{HS}^{\text{rep}} > k_S^{\text{rep}}$, and $k_{HS}^{\text{rep}} > k_H^{\text{rep}}$. This is because the *Symbiodinium* is supposed to have more energy due to its more efficient metabolic activity. Similarly, $k_{HS}^{\text{die}} < k_S^{\text{die}}$, $k_{HS}^{\text{die}} < k_H^{\text{die}}$ because HS has a larger calcium layer, which protects it best from predators, and because HS has a more diverse metabolism. On the other hand, under cell proliferation conditions that become harmful to the coral we expect $k_{HS}^{\text{rep}} < k_S^{\text{rep}}$, and $k_{HS}^{\text{rep}} < k_H^{\text{rep}}$ because the organism releases inhibitory factors that reduce its tendency to reproduce, and $k_{HS}^{\text{die}} > k_S^{\text{die}}$, and $k_{HS}^{\text{die}} > k_H^{\text{die}}$ due to *Symbiodinium* cell expulsion or degradation of HS.

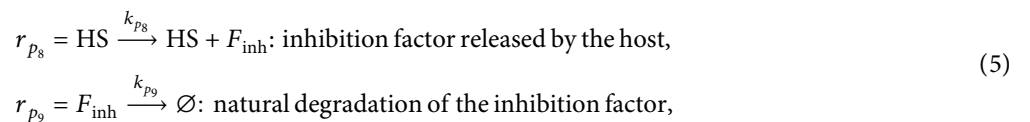
4.3. *Levels of Association and Regulation: An Example.* As seen in Section 2, it is possible to identify variables in one level that constrain or promote the activity at other levels. In this model, we consider only one top-down constraint, and one bottom-up promoter, by modifying the kinetic parameter k_{HS}^{rep} as an example of how to represent the multilevel control mechanisms.

For the bottom-up control mechanism, we have that the nutrient traffic level reactions r_{t_4} and r_{t_7} produce energy, and

that such energy is consumed by reactions r_{t_5} and r_{t_6} for metabolic survival. Therefore, when the production of energy is not enough to compensate its consumption, the cell HS will not reproduce, so r_{p_4} becomes inactive. Analogously, when the production of energy surpasses its consumption, r_{p_4} becomes active. Hence, we consider a threshold of total energy production in the lower level E^* , and when the energy in the nutrient traffic level surpasses this threshold, the kinetic parameter k_{HS}^{rep} activates.

For the top-down direction, we consider a signaling species that is known to regulate the proliferation of the *Symbiodinium* according to its sensitivity to some photosynthetic byproducts. The photosynthetic product is in this case represented by the species x at the nutrient traffic level (see r_{t_7} in equation (2)). Let the signaling species be F_{inh} , representing the factor that is released when the endosymbiont's byproducts x surpass a threshold x^* , and that is sensed by the host, deactivating the reaction r_{t_7} .

In order to provide a formal specification of the bottom-up and top-down regulatory mechanism of HS reproduction, we introduce the following reactions at the organismic level:



where $k_{p_8} = h(x - x^*)$, with $h(x - x^*)$ being the known Heaviside-step function, which is zero if $x - x^* \leq 0$ and a reference value (one for simplicity) if $x - x^* > 0$. Hence,

reaction r_{p_8} is inactive when the concentration of x is below the threshold x^* and once the concentration x surpasses the threshold x^* the inhibition factor is released,

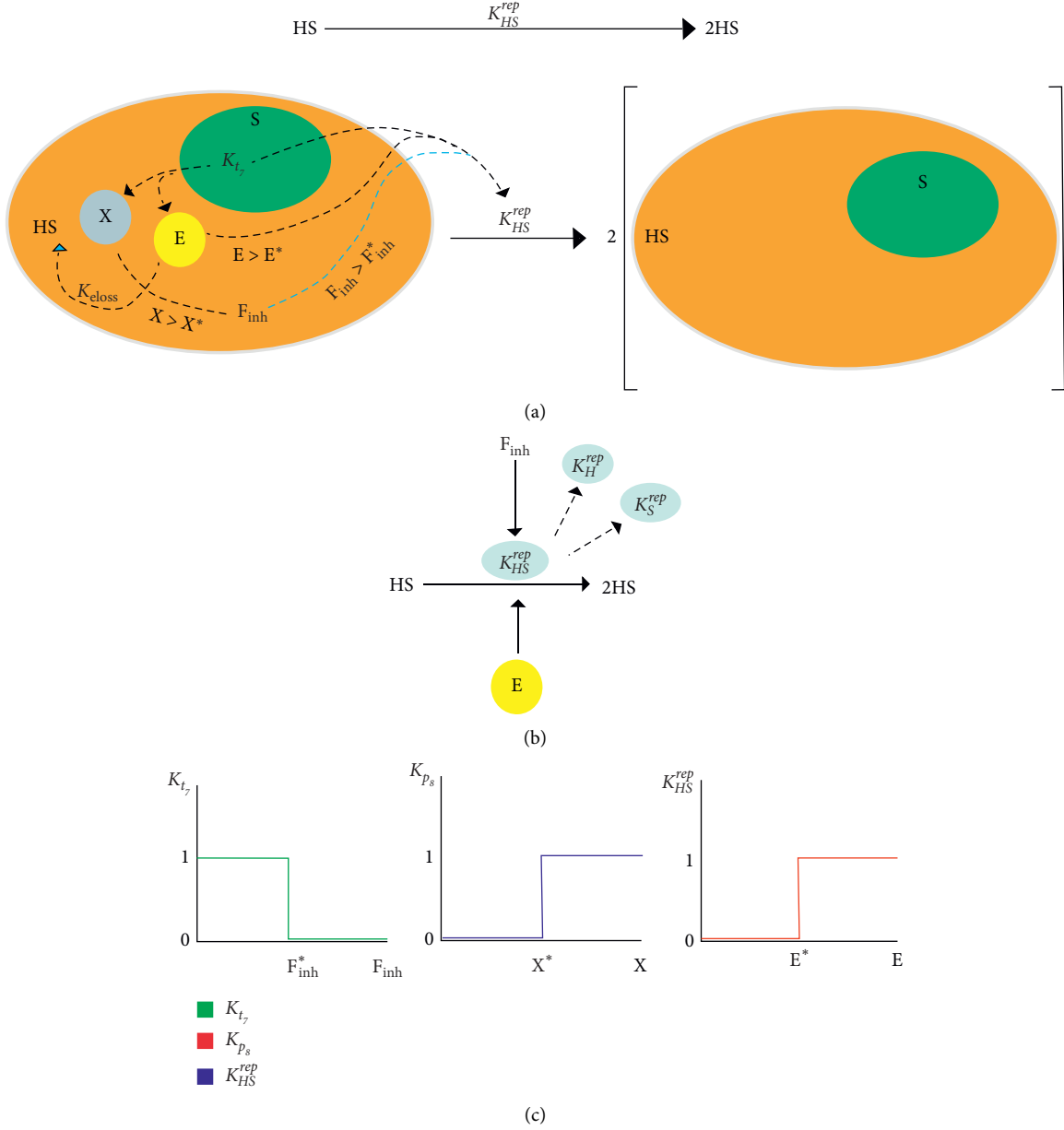


FIGURE 3: Schema of the regulation of species through two levels of interaction. (a) Representation of the interaction between the host (H in orange) and the *Symbiodinium* (S in green) in the reaction r_{p_4} , and how E , x , and F_{inh} affect the kinetic parameter k_{HS}^{rep} . Dotted lines represent ways of regulation of k_{HS}^{rep} , occurring when $E > E^*$, $x > x^*$, and $F_{inh} > F_{inh}^*$. Blue dotted line represents the release of inhibition factors by coral cells. (b) Regulation of k_{HS}^{rep} by F_{inh} and E , showing the indirect regulation of k_S^{rep} and k_H^{rep} in dotted lines. (c) Dependency of k_{t_7} , k_{p_8} , and k_{HS}^{rep} on F_{inh} , x , and E , respectively.

while k_{p_9} is a constant rate controlling the degradation of F_{inh} .

Next, the kinetic parameters k_{t_7} becomes explicitly dependent on F_{inh} to control the extra production of energy and x :

$$k_{t_7} = h(F_{inh} - F_{inh}^*), \quad (6)$$

where F_{inh}^* is the F_{inh} tolerance threshold that once surpassed the production of extra energy is inhibited.

Finally, we modify k_{HS}^{rep} , making it dependent on E as follows:

$$k_{HS}^{rep} = h(E - E^*). \quad (7)$$

Therefore, when the nutrient traffic is intensified by the presence of the *Symbiodinium*, the extra energy produced regulates in a bottom-up manner the kinetic parameter k_{HS}^{rep} of the endosymbiotic interaction at the cellular proliferation level, activating its proliferation. Conversely, when proliferation of *Symbiodinium* surpasses the amount of the byproducts required for operating its metabolism, F_{inh} is released, inhibiting in a top-down manner the kinetic parameter k_{t_7} . We represent

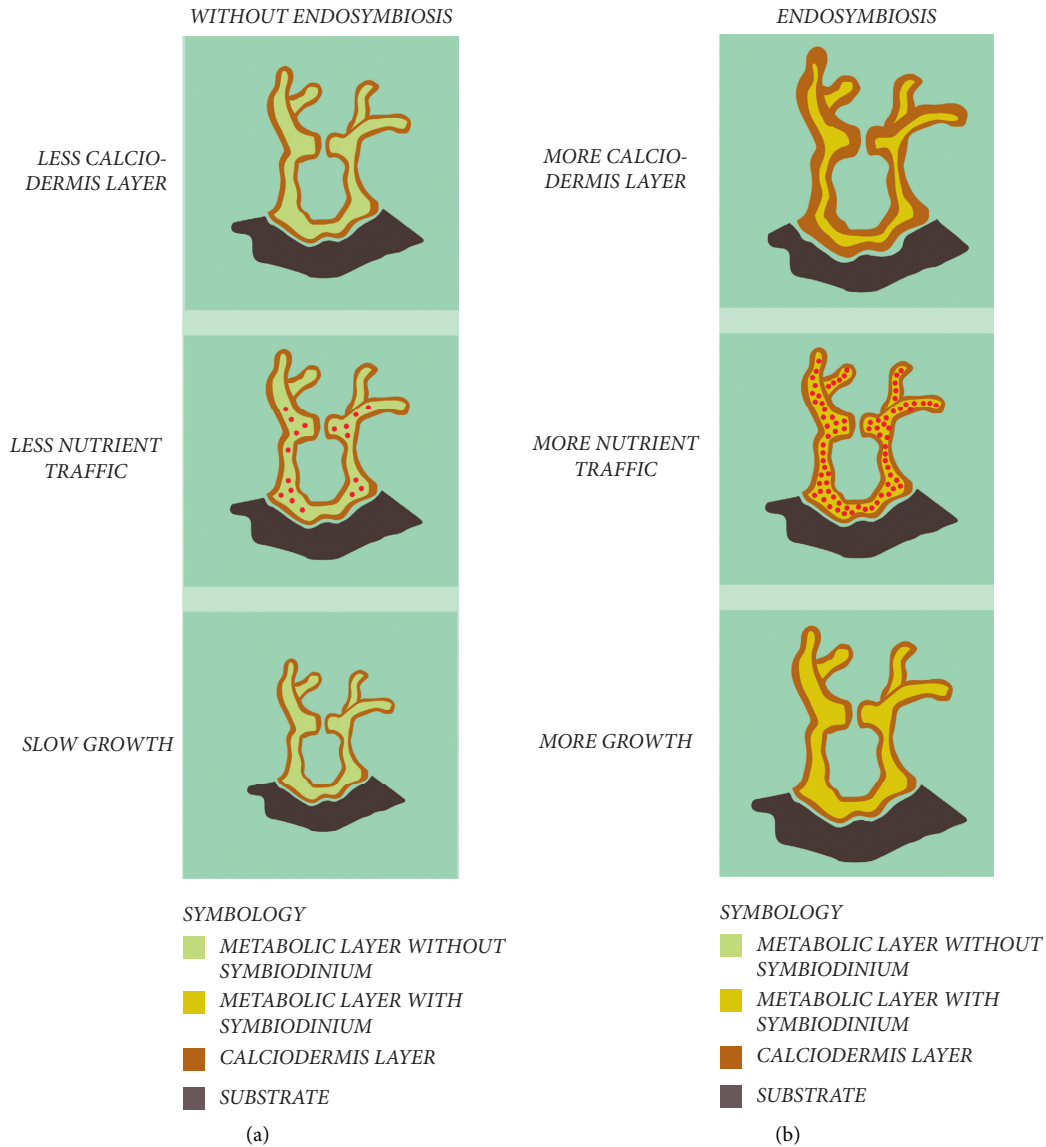


FIGURE 4: Organismal system processes, showing in a comparative scenario how different processes as calcidodermis production, nutrient traffic, and coral growth are enhanced by the endosymbiosis interaction (b) with respect to the coral without *Symbiodinium* (a).

these interrelationships in Figure 3, specifically the regulation for k_{HS}^{rep} .

5. Discussion

A key concept in biological complexity is the emergence of properties that coregulate the persistence of processes occurring at different levels, and which are needed for organisms to live and reproduce. In this sense, the representation of biological phenomena as a hierarchy of intertwined dynamical processes is an important challenge to advance our understanding of biological complexity.

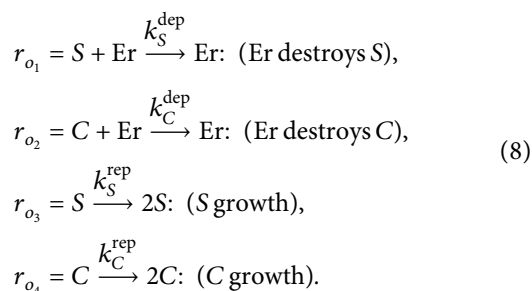
Coral endosymbiosis presents an interesting opportunity to study this issue. First, there is a concrete evidence of the microscopic interaction between the *Symbiodinium* and the coral host cell as well as evidence of the micro- and macroscopic consequences of such interaction. Secondly, levels

of interaction can be clearly delineated. Namely, in our model we considered a nutrient traffic and cellular proliferation levels, where the former is undoubtedly nested in the other. Thirdly, as explained in Section 4.3, even in our simple two-levels model, bottom-up and top-down regulatory mechanisms occur. Therefore, the coral-*Symbiodinium* endosymbiotic interaction exhibits structural features allowing a simple but explicative model of its mechanism.

Reaction network-like models of biological interactions have only recently been investigated [28, 48, 49], but seem to provide the necessary versatility to incorporate multilevel regulatory mechanisms in a sensible way. However, this approach is in its infancy and requires extensions.

We propose two ways in which our model can be extended. The first is to give a more detailed account of what occurs at each level, and the second is to incorporate more levels. For the former case, a more detailed account of the

reproduction of the symbionts within the endosymbiont could be developed. For example, we can introduce a new species HS_2 meaning that the host has two endosymbionts in it, and incorporate the reactions $HS \rightarrow HS_2$ and $HS_2 \rightarrow 2HS$ to represent the replication process of the endosymbiont. Analogously, it is possible to incorporate other necessary steps to provide a more realistic account of the phenomena such as regulation at the recognition level [50], symbiosome maturation [51], and regulation of symbiont biomass by symbiont expulsion and degradation [32, 52]. For the latter case, we can incorporate the macroscopic organismic level in our model, involving the coral's growth and survival. The simplest model of the endosymbiotic organismic activity lies at comparing the coral's ability to grow, with and without *Symbiodinium* (named S and C , respectively) under mechanical and biological erosion (Er), and its ability to reproduce. The coral's ability to grow is directly related to nutrient traffic and calcidodermis strengthening as depicted in Figure 4. For simplicity, we will provide an example focusing on the growth of C , in the presence of S , and erosion Er. Other aspects such as the reproduction of erosion factors (e.g., fish that predate the coral), or natural death of the S and C , are not incorporated.



The values k_S^{dep} , k_C^{dep} and k_S^{rep} , k_C^{rep} are the mechanical and biological erosion and growth rates of S and C , respectively.

Note that in this case the interactions that C and S have with the other species are equal. Therefore, the parameters k_S^{dep} , k_C^{dep} modulate their susceptibility to be destroyed by environmental phenomena or by predation, while k_S^{rep} , k_C^{rep} modulate their growth rate. For a more precise model of the general organismal situation, it is necessary to relate the organismal level to parameters of the lower levels such as the rate of production of the calcium layer (r_{t_5}), the free internal metabolic energy (related to the increase of the biochemical traffic), and the rate of proliferation of the cells.

On a more technical note, future models should apply reaction networks nested in compartments [53,54] instead of traditional reaction networks. Such models should be more realistic, but also grow in size and complexity. Thus, it will become necessary to apply pathway analysis methods such as flux-balance analysis [55] and chemical organization theory [19] to identify dynamical features that can be linked to the properties of the interactions, and to study how structural perturbations to the system such as the addition of new biochemical components, or new macroscopic species, affect the stability landscape of the system.

6. Conclusion

The complexity of biological processes is related to the integration of the different levels at which they occur and to the emergent properties that characterize the gaps between such levels. To address this, it is necessary to model not only the different levels at which interactions manifest, but also the interaction between these levels through multilevel regulation mechanisms. We developed a simple mechanistic model for the endosymbiotic interaction between corals and the algae (*Symbiodinium*) using reaction networks.

In our model, which complements a reaction network model of endosymbiosis between corals and dinoflagellates of the genus *Symbiodinium* [49], we incorporate biochemical species (R_H , R_C , \bar{R}_C , Cal, and x), thermodynamic species (E), cellular species (H , S , and HS), and a regulatory factor (F_{inh}). In addition, we incorporated a bilevel regulatory mechanism for the proliferation of the endosymbiotic cell HS which is fostered by the increase of its energy (occurring at the nutrient traffic level) but also regulated by the release of F_{inh} when the byproduct x of the energy production surpasses a threshold (occurring at the cellular proliferation level). This mechanism promotes the controlled organism's reproduction and is coherent with the knowledge of this interaction [11, 56].

The idea of developing multilevel interaction models for ecological interactions is relatively new in theoretical biology, as there are not many works that modulate kinetic parameters from the concentration of the system species at different levels [17]. The major innovation of this work is to consider that kinetic parameters at one level can be modulated by the presence of species (biotic or abiotic) at other levels, and thus providing a first approach to generate an integrative view of the multilevel nature of the endosymbiotic relationship.

As a final remark, we consider that this approach has the potential to describe the complexity of not only endosymbiosis, but also other complex multilevel biological interactions such as physiological approach in multiscale system biology [57, 58], cancer biology [59], and multiscale ecological approaches [60, 61].

Data Availability

Our study is theoretical. Therefore, no data were used to support this study.

Conflicts of Interest

The authors declare that they have no conflicts of interest.

Acknowledgments

The first author was funded by the John Templeton Foundation "The Origins of Goal-Directedness: A Formal Scenario Based on Chemical Organization Theory and Cybernetics" under Grant ID# 61733. The second author was funded by ANID-PFCHA/Doctorado Nacional/2019 under Grant no. 21191885.

References

- [1] U. Kutschera and K. J. Niklas, "Endosymbiosis, cell evolution, and speciation," *Theory in Biosciences*, vol. 124, no. 1, pp. 1–24, 2005.
- [2] D. M. Wilkinson, "At cross purposes," *Nature*, vol. 412, no. 6846, p. 485, 2001.
- [3] J. M. Archibald, "Endosymbiosis and eukaryotic cell evolution," *Current Biology*, vol. 25, no. 19, pp. R911–R921, 2015.
- [4] J. J. Wernegreen, "Endosymbiosis: lessons in conflict resolution," *PLoS Biology*, vol. 2, no. 3, p. e68, 2004.
- [5] C. Darwin and J. W. Burrow, "The origin of species," 1859.
- [6] R. Rowan, "Diversity and ecology of zooxanthellae on coral reefs," *Journal of Phycology*, vol. 34, no. 3, pp. 407–417, 1998.
- [7] A. C. Baker, "Symbiont diversity on coral reefs and its relationship to bleaching resistance and resilience," *Coral Health and Disease. In Coral Health and Disease*, vol. 1, pp. 177–194, 2004.
- [8] D. Yellowlees, T. A. V. Rees, and W. Leggat, "Metabolic interactions between algal symbionts and invertebrate hosts," *Plant, Cell & Environment*, vol. 31, no. 5, pp. 679–694, 2008.
- [9] P. J. McAuley, "The cell cycle of symbiotic *Chlorella*. I. the relationship between host feeding and algal cell growth and division," *Journal of Cell Science*, vol. 77, no. 1, pp. 225–239, 1985.
- [10] P. J. McAuley, "Temporal relationships of host cell and algal mitosis in the green hydra symbiosis," *Journal of Cell Science*, vol. 58, no. 1, pp. 423–431, 1982.
- [11] P. L. Antonelli, S. F. Rutz, P. W. Sammarco, and K. B. Strychar, "Evolution of symbiosis in hermatypic corals: a model of the past, present, and future," *Nonlinear Analysis: Real World Applications*, vol. 32, pp. 389–402, 2016.
- [12] P. Beldade, K. Koops, and P. M. Brakefield, "Developmental constraints versus flexibility in morphological evolution," *Nature*, vol. 416, no. 6883, pp. 844–847, 2002.
- [13] J. Sánchez-Hernández, F. Cobo, and P. A. Amundsen, "Food web topology in high mountain lakes," *PLoS One*, vol. 10, no. 11, Article ID e0143016, 2015.
- [14] S. J. Arnold, "Constraints on phenotypic evolution," *The American Naturalist*, vol. 140, pp. S85–S107, 1992.
- [15] D. T. Fraebel, H. Mickalide, D. Schnitkey, J. Merritt, T. E. Kuhlman, and S. Kuehn, "Environment determines evolutionary trajectory in a constrained phenotypic space," *Elife*, vol. 6, Article ID e24669, 2017.
- [16] V. N. Reddy, M. L. Mavrouniotis, and M. N. Liebman, "Petri net representations in metabolic pathways," *ISMB-Indian Standard Medium Weight Beam*, vol. 93, pp. 328–336, 1993.
- [17] R. Bardini, G. Politano, A. Benso, and S. Di Carlo, "Multi-level and hybrid modelling approaches for systems biology," *Computational and Structural Biotechnology Journal*, vol. 15, pp. 396–402, 2017.
- [18] D. J. Wilkinson, *Stochastic Modelling for Systems Biology*, CRC Press, Boca Raton, FL, USA, 2011.
- [19] P. Dittrich and P. S. di Fenizio, "Chemical organisation theory," *Bulletin of Mathematical Biology*, vol. 69, no. 4, pp. 1199–1231, 2007.
- [20] D. A. Fell, "Metabolic control analysis: a survey of its theoretical and experimental development," *Biochemical Journal*, vol. 286, no. 2, p. 313, 1992.
- [21] M. Feinberg and F. J. M. Horn, "Dynamics of open chemical systems and the algebraic structure of the underlying reaction network," *Chemical Engineering Science*, vol. 29, no. 3, pp. 775–787, 1974.
- [22] P. Dittrich and L. Winter, "Reaction networks as a formal mechanism to explain social phenomena," in *Proceedings of the Fourth International Workshop on Agent-Based Approaches in Economics and Social Complex Systems*, pp. 9–13, New York, NY, USA, May 2005.
- [23] P. Dittrich and L. Winter, "Chemical organizations in a toy model of the political system," *Advances in Complex Systems*, vol. 11, no. 4, pp. 609–627, 2008.
- [24] T. Veloz, P. Razeto-Barry, P. Dittrich, and A. Fajardo, "Reaction networks and evolutionary game theory," *Journal of Mathematical Biology*, vol. 68, no. 1–2, pp. 181–206, 2014.
- [25] D. Velegol, P. Suhey, J. Connolly, N. Morrissey, and L. Cook, "Chemical game theory," *Industrial & Engineering Chemistry Research*, vol. 57, no. 41, pp. 13593–13607, 2018.
- [26] T. Veloz, "Teoría de organizaciones químicas: un lenguaje formal para la autopoiesis y el medio ambiente," in *Un Concepto Vivo*, P. Razeto-Barry and R. Ramos-Jiliberto, Eds., pp. 229–245, Editorial Nueva Civilización, Santiago, Chile, 2013.
- [27] T. Veloz and P. Razeto-Barry, "Reaction networks as a language for systemic modeling: fundamentals and examples," *Systems*, vol. 5, no. 1, p. 11, 2017.
- [28] T. Veloz, "The complexity-stability debate, chemical organization theory, and the identification of non-classical structures in ecology," *Foundations of Science*, vol. 25, no. 1, pp. 259–273, 2019.
- [29] P. S. Davies, "Effect of daylight variations on the energy budgets of shallow-water corals," *Marine Biology*, vol. 108, no. 1, pp. 137–144, 1991.
- [30] S. K. Davy, D. Allemand, and V. M. Weis, "Cell biology of cnidarian-dinoflagellate symbiosis," *Microbiology and Molecular Biology Reviews*, vol. 76, no. 2, pp. 229–261, 2012.
- [31] J. E. Loram, H. G. Trapido-Rosenthal, and A. E. Douglas, "Functional significance of genetically different symbiotic algae *Symbiodinium* in a coral reef symbiosis," *Molecular Ecology*, vol. 16, no. 22, pp. 4849–4857, 2007.
- [32] W. Fitt, "Cellular growth of host and symbiont in a cnidarian-zooxanthellar symbiosis," *The Biological Bulletin*, vol. 198, no. 1, pp. 110–120, 2000.
- [33] S. Tambutté, M. Holcomb, C. Ferrier-Pagès et al., "Coral biomineralization: from the gene to the environment," *Journal of Experimental Marine Biology and Ecology*, vol. 408, no. 1–2, pp. 58–78, 2011.
- [34] J.-P. Gattuso, D. Allemand, and M. Frankignoulle, "Photosynthesis and calcification at cellular, organismal and community levels in coral reefs: a review on interactions and control by carbonate chemistry," *American Zoologist*, vol. 39, no. 1, pp. 160–183, 1999.
- [35] V. M. Weis, "Cellular mechanisms of Cnidarian bleaching: stress causes the collapse of symbiosis," *Journal of Experimental Biology*, vol. 211, no. 19, pp. 3059–3066, 2008.
- [36] T. P. Hughes, J. T. Kerry, M. Álvarez-Noriega et al., "Global warming and recurrent mass bleaching of corals," *Nature*, vol. 543, no. 7645, pp. 373–377, 2017.
- [37] N. Neckelmann and L. Muscatine, "Regulatory mechanisms maintaining the Hydra-*Chlorella* symbiosis," *Proceedings of the Royal Society of London. Series B. Biological sciences*, vol. 219, no. 1215, pp. 193–210, 1983.
- [38] C. E. Taylor, L. Muscatine, and D. R. Jefferson, "Maintenance and breakdown of the Hydra-*Chlorella* symbiosis: a computer model," *Proceedings of the Royal Society of London B Biological Sciences*, vol. 238, no. 1292, pp. 277–289, 1989.
- [39] R. D. Gates and L. Muscatine, "Three methods for isolating viable anthozoan endoderm cells with their intracellular

- symbiotic dinoflagellates,” *Coral Reefs*, vol. 11, no. 3, pp. 143–145, 1992.
- [40] L. Muscatine, C. Ferrier-Pages, A. Blackburn, R. D. Gates, G. Baghdasarian, and D. Allemand, “Cell-specific density of symbiotic dinoflagellates in tropical anthozoans,” *Coral Reefs*, vol. 17, no. 4, pp. 329–337, 1998.
- [41] A. Douglas and D. C. Smith, “The green hydra symbiosis. VIII. mechanisms in symbiont regulation,” *Proceedings of the Royal Society of London. Series B. Biological Sciences*, vol. 221, no. 1224, pp. 291–319, 1984.
- [42] P. G. Falkowski, Z. Dubinsky, L. Muscatine, and L. McCloskey, “Population control in symbiotic corals,” *BioScience*, vol. 43, no. 9, pp. 606–611, 1993.
- [43] G. J. Smith and L. Muscatine, “Cell cycle of symbiotic dinoflagellates: variation in G1 phase-duration with anemone nutritional status and macronutrient supply in the *Aiptasia pulchella*–*Symbiodinium pulchrorum* symbiosis,” *Marine Biology*, vol. 134, no. 3, pp. 405–418, 1999.
- [44] B. R. Gordon and W. Leggat, “*Symbiodinium*-Invertebrate symbioses and the role of metabolomics,” *Marine Drugs*, vol. 8, no. 10, pp. 2546–2568, 2010.
- [45] D. Allemand, É. Tambutté, D. Zoccola, and S. Tambutté, “Coral calcification, cells to reefs,” *Coral Reefs: An Ecosystem in Transition*, vol. 99, pp. 119–150, 2011.
- [46] N. N. Rosic, “Phylogenetic analysis of genes involved in mycosporine-like amino acid biosynthesis in symbiotic dinoflagellates,” *Applied Microbiology and Biotechnology*, vol. 94, no. 1, pp. 29–37, 2012.
- [47] D. Angeli, “A tutorial on chemical reaction network dynamics,” *European Journal of Control*, vol. 15, no. 3, pp. 398–406, 2009.
- [48] C. Gaucherel and F. Pommereau, “Using discrete systems to exhaustively characterize the dynamics of an integrated ecosystem,” *Methods in Ecology and Evolution*, vol. 10, no. 9, pp. 1615–1627, 2019.
- [49] T. Veloz and D. Flores, “Towards endosymbiosis modeling using reaction networks,” *Soft Computing*, vol. 25, pp. 6831–6840, 2019.
- [50] A. C. Baker, “Flexibility and specificity in coral-algal symbiosis: diversity, ecology, and biogeography of *Symbiodinium*,” *Annual Review of Ecology, Evolution, and Systematics*, vol. 34, no. 1, pp. 661–689, 2003.
- [51] M.-C. Chen, M.-C. Hong, Y.-S. Huang, M.-C. Liu, Y.-M. Cheng, and L.-S. Fang, “ApRab11, a cnidarian homologue of the recycling regulatory protein Rab11, is involved in the establishment and maintenance of the *Aiptasia*-*Symbiodinium* endosymbiosis,” *Biochemical and biophysical research communications*, vol. 338, no. 3, pp. 1607–1616, 2005.
- [52] E. A. Titlyanov, T. V. Titlyanova, V. A. Leletkin, J. Tsukahara, R. Van Woesik, and K. Yamazato, “Degradation of zooxanthellae and regulation of their density in hermatypic corals,” *Marine Ecology Progress Series*, vol. 139, pp. 167–178, 1996.
- [53] H. Fellermann and L. Cardelli, “Programming chemistry in DNA-addressable bioreactors,” *Journal of The Royal Society Interface*, vol. 11, no. 99, 2014.
- [54] S. Peter and P. Dittrich, “On the relation between organizations and limit sets in chemical reaction systems,” *Advances in Complex Systems*, vol. 14, pp. 77–96, 2011.
- [55] J. D. Orth, I. Thiele, and B. ø. Palsson, “What is flux balance analysis?” *Nature Biotechnology*, vol. 28, no. 3, pp. 245–248, 2010.
- [56] R. Cunning, E. B. Muller, R. D. Gates, and R. M. Nisbet, “A dynamic bioenergetic model for coral- *Symbiodinium* symbioses and coral bleaching as an alternate stable state,” *Journal of Theoretical Biology*, vol. 431, pp. 49–62, 2017.
- [57] J. O. Dada and P. Mendes, “Multi-scale modelling and simulation in systems biology,” *Integrative Biology*, vol. 3, no. 2, pp. 86–96, 2011.
- [58] H.-G. Holzhütter, D. Drasdo, T. Preusser, J. Lippert, and A. M. Henney, “The virtual liver: a multidisciplinary, multilevel challenge for systems biology,” *Wiley Interdisciplinary Reviews: Systems Biology and Medicine*, vol. 4, no. 3, pp. 221–235, 2012.
- [59] T. S. Deisboeck, Z. Wang, P. Macklin, and V. Cristini, “Multiscale cancer modeling,” *Annual Review of Biomedical Engineering*, vol. 13, no. 1, pp. 127–155, 2011.
- [60] N. Mayon, A. Bertrand, D. Leroy et al., “Multiscale approach of fish responses to different types of environmental contaminations: a case study,” *The Science of the Total Environment*, vol. 367, no. 2–3, pp. 715–731, 2006.
- [61] S. Rubin, T. Veloz, and P. Maldonado, “Beyond planetary-scale feedback self-regulation: gaia as an autopoietic system,” *Biosystems*, vol. 199, Article ID 104314, 2021.

Research Article

Investigating Transformational Complexity: Counting Functions a Region Induces on Another in Elementary Cellular Automata

Martin Biehl¹ and Olaf Witkowski^{2,3,4}

¹Araya Inc., Tokyo, Japan

²Cross Labs, Cross Compass Ltd., Tokyo, Japan

³Earth-Life Science Institute, Tokyo Institute of Technology, Tokyo, Japan

⁴College of Arts and Sciences, University of Tokyo, Tokyo, Japan

Correspondence should be addressed to Olaf Witkowski; olaf.witkowski@gmail.com

Received 11 July 2020; Accepted 11 June 2021; Published 29 June 2021

Academic Editor: Abdellatif Ben Makhlof

Copyright © 2021 Martin Biehl and Olaf Witkowski. This is an open access article distributed under the Creative Commons Attribution License, which permits unrestricted use, distribution, and reproduction in any medium, provided the original work is properly cited.

Over the years, the field of artificial life has attempted to capture significant properties of life in artificial systems. By measuring quantities within such complex systems, the hope is to capture the reasons for the explosion of complexity in living systems. A major effort has been in discrete dynamical systems such as cellular automata, where very few rules lead to high levels of complexity. In this paper, for every elementary cellular automaton, we count the number of ways a finite region can transform an enclosed finite region. We discuss the relation of this count to existing notions of controllability, physical universality, and constructor theory. Numerically, we find that particular sizes of surrounding regions have preferred sizes of enclosed regions on which they can induce more transformations. We also find three particularly powerful rules (90, 105, 150) from this perspective.

1. Introduction

1.1. Artificial Life. Artificial life studies “life as it could be” [1]. One approach to this is to start at the level of physics and look at artificial systems—usually dynamical systems—as artificial universes and study properties of life within them. This approach still faces fundamental problems including the lack of a formal definition of life for such systems. However, numerous metrics have been proposed in order to identify artificial universes that for one reason or another may be more suitable for life than others. Examples include measures of complexity and computational capabilities.

First restricting ourselves to discrete dynamical systems such as cellular automata, along the line of von Neumann’s work on self-reproducing automata [2], builds a ladder for tackling the intricacy of living systems (see, for example, Beer [3] and Adams et al. [4]). As pointed out by Janzing [5], it also makes the problem more accessible to the computer science community and honors the lesson learned from quantum information theory that translating physics into computer scientific language can provide a new perspective and new paradigms.

Since life—and in particular evolution—is often seen as a creative force, one relevant property might be the number of ways that things can be turned into other things within a given system. More specifically, we are interested in the number of different ways in which configurations of one region of space can alter the future consequences of another region of space. We anticipate that systems where this number is high may guarantee a combinatorial explosion of context-dependent possibilities, increasing the probability of life.

In this preliminary investigation, we look at a quantification of this notion for the set of elementary cellular automata (ECA). Next, we explain our quantification in more detail and justify design choices. We then discuss the relation of our quantification to existing ideas in the literature.

1.2. Approach: Number of Functions. We use the following notation for cellular automata. The set \mathcal{X} is the alphabet and $\mathcal{X}^{\mathbb{Z}}$ is the set of configurations, i.e., bi-infinite binary sequences. If we look at a region $R \subset \mathbb{Z}$, we write $x_R \in \mathcal{X}^R$ for its configuration.

One of the main properties of our quantification is that it looks at the local dynamics within a cellular automaton. We consider a finite region E called the environment, which can be of any shape in general, and another region V called the volume. We then want to see in how many ways the environment can influence the future of the volume. In other words, how many transforming functions on the cells in the volume V the cells in the environment E induce. The future of the volume is its future light cone in the space-time diagram of the cellular automaton. This future light cone is also influenced by cells outside the environment and volume itself. Without fixing these external cells, what will happen in the future light cone is undetermined.

Even if we were to fix the external configuration, computing the influence on the entire future light cone is intractable. We therefore pick a ball (in the appropriate way for the dimensionality of the CA) $C = E \cup V$ and only compute the configurations of all cells in the inverse light cone (IL(C)) which is the subset of the space-time diagram future cells that are completely determined by the configuration of C (see Figure 1 for an illustration of the inverse light cone for a 1D cellular automaton).

We also arbitrarily choose the environment region to be the surrounding sphere around the volume region V . Clearly, this environment and volume combination is not the only interesting one. One other possibility would be to choose the environment adjacent to but not enclosing the volume. If we see the environment as a machine that transforms the volume, then this would simplify the use of such a machine.

Each environment E then induces a function from the set of initial volume configurations to the configurations of the future light cone of the volume V that is within the inverse light cone of C . It would be possible to then count the number of different functions of this kind. However, we do not want to count two such functions as different if their difference cannot escape the inverse light cone. Intuitively, such differences only have an ephemeral effect that does not make a lasting difference. This means we only count functions as different if their effect could (at least in principle) last forever. We therefore count only the different functions from volume configurations to those cells whose effect can escape the inverse light cone. We call those cells the output cells O .

To summarize, we can say that we count the number of not provably ephemeral (i.e., possibly eternal) transformations that different environments can achieve on the volume.

There are two relevant limits of the number of functions we propose to compute. The first is the maximum number of functions that an environment E of width $|E|$ cells can induce. Since there are only $|\mathcal{X}|^{|E|}$ configurations of such an environment, there can never be more than $|\mathcal{X}|^{|E|}$ such functions (here we have $|\mathcal{X}| = 2$). As we will see there are ECAs where the number of functions that environments of various sizes can induce exhausts this limit.

The second is the number of functions from the volume to the output cells. This number is $(\mathcal{X}^O)^{\mathcal{X}^V}$. An environment that could compute all of those functions could be called

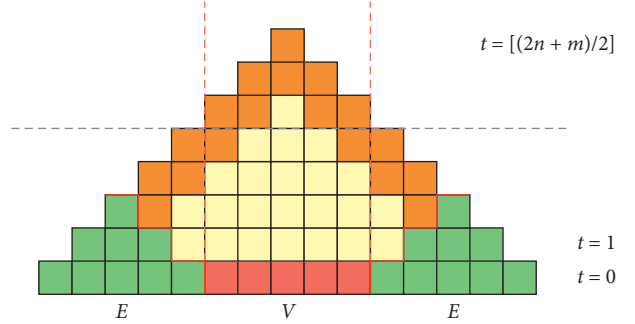


FIGURE 1: Diagram displaying an example of the inverted light cone IL(C) of the input set of cells C . The input includes volume V (in red) and environment E (in light green). The output O (in orange) contains the cells within the future light cone of C that are in the Moore neighborhood of a cell outside of IL(C). The combination of yellow and orange cells denotes the future light cone of volume V within IL(C). The red line shows the border between the environment's inverted light cone and the future lightcone of the volume. The vertical dashed lines show the future of the volume, and the horizontal dashed line shows the limit of computation considered at some time t , in Janzing's approach [5].

transformationally complete for the volume V . However, since the output cells we consider here grow with the environment sizes, this is impossible for $|V| > 1$ or $|E| > 1$. A different choice of output cells, e.g., choosing the same cells as the (initial) volume cells at a later timestep like in the theory of physical universality [5], however, could be interesting as well. In that case, there may be transformationally complete finite environments.

2. Background

2.1. Constructor Theory. Constructor theory [6] conceives of physical laws as statements that rule out the possibility of particular kinds of transformations. Our investigation here then investigates physical laws that hold not for constructors in general but for the transformations that particular kinds of finite constructors can achieve in finite time on finite substrates. The (finite) environments we are investigating are the constructors and the (also finite) volumes are the substrate. We compute all possible transformations that an environment can induce on a volume. Any transformations that we do not find are therefore impossible. This means each such impossible transformation corresponds to a resource constrained physical law in the sense of constructor theory.

2.2. Controllability. Note that we are not computing the amount of (open or closed loop) control the environment has over the future light cone of the volume.

Open-loop controllability would mean to compute how many different configurations x_O of the output cells O the different environment configurations x_E can achieve or induce. Formally, this can be expressed as the following set cardinality:

$$\left| \left\{ x_O \in \mathcal{X}^O : \exists x_E \in \mathcal{X}^E \text{ s.t. } \forall x_V \in \mathcal{X}^V, (f_{CA}(x_E, x_V))_O = x_O \right\} \right|. \quad (1)$$

Here $f_{CA}(x_E, x_V)$ is the function (induced by the particular cellular automaton rule) mapping a pair of environment configuration x_E and volume configuration x_V to their inverse light cone. $(f_{CA}(x_E, x_V))_O$ then denotes the restriction of the inverse light cone to the output cells. At most there are $2^{|O|}$ such output cell configurations. Unlike for our measure, for open-loop control, it is not important how many different functions can be induced by the environment configurations since multiple functions can be used to achieve the same output configuration. For example, take three environment configurations, where the function induced by the first maps all volume states to output state x_O , the function of the second maps all output states to y_O , and the function of the third maps some of the states to x_O and some of the states to y_O . So, the third environment configuration does not add any new achievable output configurations to those achievable by the other two environments and should not contribute positively to a measure of control. However, in our measure, since the third function is different from the other two, it does so. We count the amount of possible transformations, i.e., the *transformability*, of regions by other regions.

In closed-loop control, the environment is “allowed to know” the volume state x_V . In this case, what counts is how many different input-output pairs can be induced if the environment can be chosen for a given volume (this is not the same as the number of input-output relations that a set of environments induces since we can use a different environment for each given input to induce functions that are not induced by a single environment). Formally, this can be expressed as the following set cardinality:

$$\left| \{(x_V, x_O) \in \mathcal{X}^V \times \mathcal{X}^O : \exists x_E \in \mathcal{X}^E \text{ s.t. } (f_{CA}(x_E, x_V))_O = x_O\} \right|. \quad (2)$$

Then, any set of environment functions which contains for every input-output pair one environment pair that maps the input to the output is sufficient. So, we would need at most as many functions as there are input output pairs, i.e., in our case, $2^{|O|} * 2^{|V|}$ functions. To see this, note that for each pair, we never need more than one function to map input to output. We also always need at least one, but one function can possibly be reused for other transitions. The example we used for the open-loop case also applies for the closed-loop one. The third function can be induced by selecting either the first or second appropriately for each input so that it does not contribute positively to the closed-loop controllability either.

2.3. Physical Universality. Physical universality is defined by Janzing [5].

Definition (universal induction of bijections): A CA is said to allow for universal induction of bijections if for every finite region $V \subset C$ and every bijective map $\pi: \mathcal{X}^R \rightarrow \mathcal{X}^R$ there is a configuration $x_{C \setminus R} \in \mathcal{X}^{C \setminus R}$ of the complement of R and a time t such that $(f_{CA}^t(x_R))_R = \pi(x_R) \forall x_R \in \mathcal{X}^R$.

As noted by Janzing [7], dropping bijectivity from this definition does not lead to a stronger notion of (general)

universality since for every non-bijective function on a region R , there is a bijective function on a larger region $R \cup \bar{R}$ which induces the non-bijective function on R . However, if we are interested in a resource-constrained notion of physical universality (e.g., for a given rule do environments of finite size n exhaust their control capacities on finite volumes of size m within finite time intervals Δt), then a rule that allows the induction of all bijective functions on the finite volume will not necessarily allow the induction of all functions on this finite volume.

We therefore should consider the set of all functions for a resource-constrained version of physical universality. For a degree of universality of control of a finite environment on a finite volume within a finite time, we could then compute the fraction of all functions on the finite volume that is induced within a finite time interval.

Note that the number of functions on a finite volume V of $|V|$ cells is $(2^{|V|})^{2^{|V|}}$. If an environment E can induce all of these functions within time Δt on V , we could say that this environment is *physically universal for V within Δt* .

The number of functions on a finite volume grows faster with $|V|$ than the capacity of the environment to induce different functions within time interval Δt grows with $|E|$. The latter is $\Delta t 2^{|E|}$. To see this, note that for a fixed number $|E|$ of cells of an environment, there are $2^{|E|}$ environment states. For a fixed time t and set O_t of output cells, there is then only one function that each environment state can induce. This means that for Δt output times, we get at most $\Delta t 2^{|E|}$ functions that environments of this size can ever induce within Δt . If we find a set of cells that in fact induce this many functions on some volume V , then we say that E exhausts its control capacity on V .

2.4. Perception. We can also take the perspective of the volume rather than that of the environment. Consider the output cells as the future state of the volume. We can then see the number of functions as the number of equivalence classes on the set of environment configurations \mathcal{X}^E created by the equivalence relation:

$$\begin{aligned} x_E &\sim y_E \\ \Leftrightarrow \forall x_V \in \mathcal{X}^V : (f_{CA}^{\text{IL}}(x_E, x_V))_O &= (f_{CA}^{\text{IL}}(y_E, x_V))_O. \end{aligned} \quad (3)$$

This considers environment configurations as equivalent if they have the same influence on the transitions from volume configuration to output cell configuration. The number of such equivalence classes is identical to the number of functions we count here. This construction of equivalence classes has been used to capture perception of a stochastic process agent model in [8]. Note however that it is not clear in how far the output cells can be seen as the future state of an agent whose current state is the volume state. So, while the construction is in some sense the same, the purpose and interpretations are different. Note that the same construction of equivalence classes can also be found in [9] where it is used to coarse-grain the influence from one random variable on the transition between two others.

3. Methods

3.1. Cellular Automata. We use the reduction of the 256 ECA rules to the 88 non-equivalent ones as defined in ([10]; Table 1) and apply them to a finite and contiguous set of cells. We only consider the part of the future that is determined by the initial cells, i.e., the inverse light cone as shown in Figure 1.

We write $C = \{1, \dots, 2n + m\}$ for the index set of the initial cells where $n \in \mathbb{N}$ is called the environment thickness and $m \in \mathbb{N}$ is the volume size. For computational reasons, we only look at $0 < n, m \leq 7$. The set \mathcal{X}^C with $\mathcal{X} = \{0, 1\}$ is the set of initial configurations and an initial configuration $x_C \in \mathcal{X}^C$ is a binary vector of length $|C|$. The set $E \in C$ is the subset of cells belonging to the environment and we write $x_E \in \mathcal{X}^E$ for (initial) environment configurations. The set $V = C \setminus E$ is the set of (initial) volume cells and $x_V \in \mathcal{X}^V$ is a volume. For any set C of initial cells, we write $\text{IL}(C) \subset \mathbb{N} \times \mathbb{N}$ for the set of indices of the cells in the inverse light cone of C . An index $(t, j) \in \text{IL}(C)$ then refers to the cell $j \in C$ after t applications of the ECA dynamics. The output cells $O \subset \text{IL}(C)$ are defined as the cells within the future light cone of the volume cells C that are in the Moore neighborhood of a cell that is not in $\text{IL}(C)$. We then write $x_O \in \mathcal{X}^O$ for an output configuration (see Figure 1). Starting from an initial configuration $x_C = (x_E, x_V)$, we write $f_{CA}(x_E, x_V)$ for the configuration of the cells within the $\text{IL}(C)$ that result from the application of the ECA rule to x_C . Note that we write (x_E, x_V) for an initial configuration even though the environment cells enclose the volume cells so that (x_{E_l}, x_V, x_{E_r}) with E_l, E_r the cells on the left and right respectively would be more accurate. We also write $f_{CA}^{\text{IL}}(x_C) = f_{CA}^{\text{IL}}(x_E, x_V)$ for the spatiotemporal configuration of the entire inverse light cone (including time $t = 0$) resulting from applying f_{CA} iteratively to $x_C = (x_E, x_V)$. This lets us write $(f_{CA}^{\text{IL}}(x_E, x_V))_O$ for the configuration of the output cells when the initial configuration is (x_E, x_V) .

Our algorithm then counts for each (n, m) the number of different functions from the set \mathcal{X}^V of initial volume configurations to the set of output cell configurations \mathcal{X}^O , i.e., it computes the number of functions

$$\left| \left\{ g: \mathcal{X}^V \longrightarrow \mathcal{X}^O : \exists x_E \in \mathcal{X}^E \text{ s.t. } (f_{CA}^{\text{IL}}(x_E, x_V))_O = g(x_V) \right\} \right|. \quad (4)$$

See Algorithm 1 for how this can be computed.

4. Results

Here, we summarize the results from the runs of the method previously described.

We start by visualizing all function numbers calculated with Algorithm 1. The plot in Figure 2 displays the count for those number of functions, for each volume size and environment thickness. Each color only identifies one distinct rule and does not bear any additional meaning.

Figure 3 shows the integral of the function plotted in Figure 2, i.e., the volume under the number of functions curve. This volume corresponds, for each rule, to the total

number of functions accumulated over all computed volume and environment sizes.

We identify four distinct classes from the aspect of the curves in Figure 2, as summarized in Table 1.

4.1. Class A: “Quasi-Constant”. For 31 rules, the number of functions only increases with environment thickness and the controlled volume size does not influence the number of functions anymore if it contains more than 2 cells. Figure 4 shows a plot of the number of functions as in Figure 2, but only with the rules that satisfy the following two conditions: firstly the number of functions for a fixed environment thickness increases from volume size 1 to volume size 2, and secondly it then remains constant for the rest of the volume sizes.

4.2. Class B: “Monotonic”. 43 rules increase monotonically and are not constant, even for volume size other than 1 or 2. We note that they do not have local maxima either—this was true for Class A as well. We note that no rules at all are strictly monotonic for all environment thicknesses. There are some rules that are strictly monotonic for specific environment thicknesses, e.g., 13, 14, 28. Figure 5 plots all rules for which the number of functions induced by a fixed environment thickness increases not only from volume size 1 to 2, and never decreases when volume size increases.

4.3. Class C: “Local Maxima”. For 14 rules, we find local maxima of number of functions with respect to volume sizes. This means that for some fixed environment thickness, the number of functions drops after an increase, as volume size increases. In Figure 6, we show the high number of maxima on a plot of the number of functions over environment thicknesses and volume sizes for rule 128.

4.4. Class D: “Exceptional Rules”. For some rules among those with local maxima, we find that the maximum possible number of functions that a given environment size can induce is achieved for volume sizes larger than 2. We call these rules exceptional. In Figure 7, we show the number of functions normalized by the number of environment states for the corresponding environment thickness. A value of 1 in this graph shows that each environment configuration induces a different function. In Figure 8, we show the special case of rule 90, where we can observe a pronounced maximum for environment thickness 7 and volume size 6. In Figure 9, we show the fraction of environment configurations that induce different functions on the volumes, for variable values of environment thicknesses and volume sizes from 1 to 7.

4.4.1. Comparison with Other Classifications. We compared the classification described above with all classifications presented in Martinez [10], numbering the classification as in the paper. The results are shown in Figure 10. For each classification, we compare each of our classes with each of its

TABLE 1: Classification of the rules into four classes, corresponding to the analysis of our results.

| Type | Number | Rules |
|--|--------|---|
| Class A (monotonic and quasi-constant) | 31 | 0, 1, 2, 3, 4, 5, 8, 10, 12, 15, 19, 29, 30, 32, 34, 37, 41, 42, 50, 51, 54, 62, 76, 106, 108, 110, 132, 138, 170, 200, 204 |
| Class B (monotonic and not quasi-constant) | 43 | 7, 9, 11, 13, 14, 18, 22, 23, 24, 25, 28, 33, 35, 36, 38, 43, 44, 45, 46, 58, 60, 72, 73, 77, 78, 94, 104, 122, 126, 134, 136, 140, 142, 146, 152, 154, 156, 164, 168, 172, 178, 184, 232 |
| Class C (exhibit local maxima and not exceptional) | 14 | 6, 26, 27, 40, 56, 57, 74, 128, 130, 160, 162 |
| Class D (exceptional) | 3 | 90, 105, 150 |

Data: CA dimension d , CA alphabet $\mathcal{X} = \{0, 1\}$, finite region indices $C \subset \mathbb{N}^d$, volume cell indices $V \subset C$, environment cell indices $E \subset C$ such that $E \cap V = \emptyset, E \cup V = C$, spatiotemporal inverse light cone indices $IL(C) \subseteq \mathbb{N} \times C$, spatiotemporal output cell indices $O \subset IL(C)$, and CA induced inverse light cone function $f_{CA}^{IL}: \mathcal{X}^C \rightarrow \mathcal{X}^O$.

Result: number r of functions g induced

initialize $G \leftarrow$ empty set of maps $g: X^V \rightarrow X^O$

foreach initial environment state $x_{E_0} \in \mathcal{X}^E$ **do**

initialize $g_{x_{E_0}}: X^V \rightarrow X^O$

foreach initial volume state $x_{V_0} \in \mathcal{X}^{V_0}$ **do**

$g_{x_{E_0}}[x_{V_0}] \leftarrow f_{CA}(x_{E_0}, x_{V_0})$

end

$G \leftarrow G \cup \{g_{x_{E_0}}\}$; //only add $g_{x_{E_0}}$ to G if it is different from all previous ones

end

return $|G|$

ALGORITHM 1: Calculation of the number of functions from volume configurations to output cells.

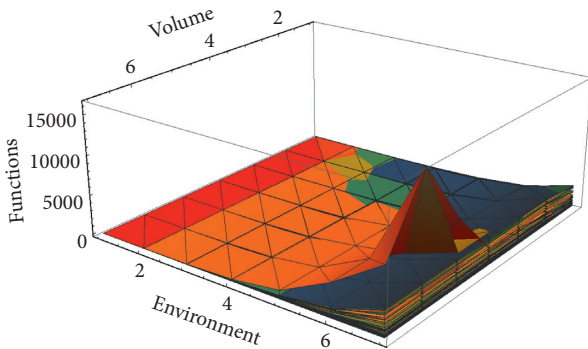
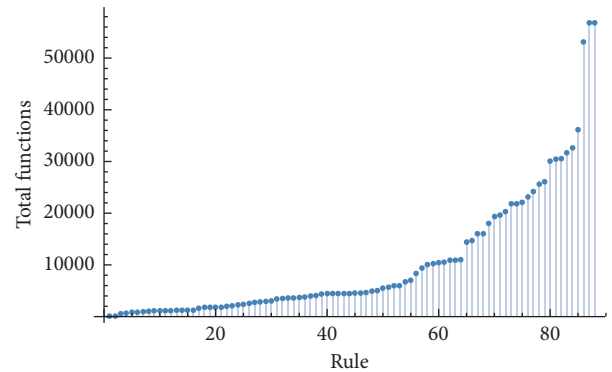


FIGURE 2: Number of functions induced by environments on enclosed volumes for environment thicknesses and volume sizes from 1 to 7. All 88 unique rules.

classes, by taking the ratio of the number of rules in intersection of the classes to the number of rules in the union of the classes. This gives a number between 0 and 1 which is represented by gray scale here where black is equal to one. A ratio of one indicates that two classes contain exactly the same rules and thus the other classification identifies exactly the same set of rules as a single class. A value of zero means that no rule is in both classes. Note that rules 11, 12, and 16 contain classes that coincide with our class of exceptional rules. Also note that classification 11b is not formally a classification.

This includes the four classes identified by Wolfram [11], as summarized in Table 2. Within Wolfram Class 4 (WC 4) rules, none has any local maximum. All four rules in Class 4 belong to our Class A: monotonic and mostly constant

FIGURE 3: Total number of functions for each of the 88 rules. The ordered list of rules in the plot is as follows: $\{0, 8, 32, 128, 4, 12, 136, 200, 2, 72, 51, 204, 34, 1, 3, 19, 76, 15, 170, 140, 160, 46, 29, 132, 36, 10, 13, 162, 5, 138, 35, 27, 40, 42, 44, 50, 7, 24, 38, 23, 77, 178, 232, 172, 108, 28, 130, 78, 33, 168, 11, 156, 57, 56, 14, 58, 152, 9, 60, 102, 184, 6, 62, 18, 25, 110, 54, 43, 142, 126, 73, 74, 104, 164, 154, 146, 134, 45, 122, 94, 37, 106, 41, 26, 30, 22, 90, 105, 150\}$.

function numbers. We note that all of the exceptional rules (Class D) are in Class 3. Interestingly, although the three rules in Class D (90, 105, 150) all have local maxima, no other Class 3 rule does.

5. Discussion

Our results indicate that the amount of functions that environments induce on volume differs strongly among the ECA rules.

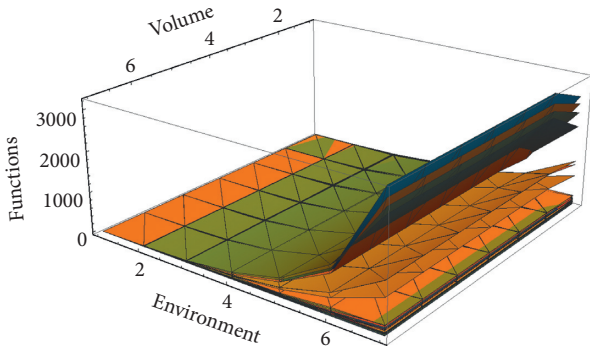


FIGURE 4: Number of functions as in Figure 2. Here we display only rules for which the number of functions for a fixed environment thickness increases from volume size 1 to volume size 2 and then remains constant for the rest of the volume sizes.

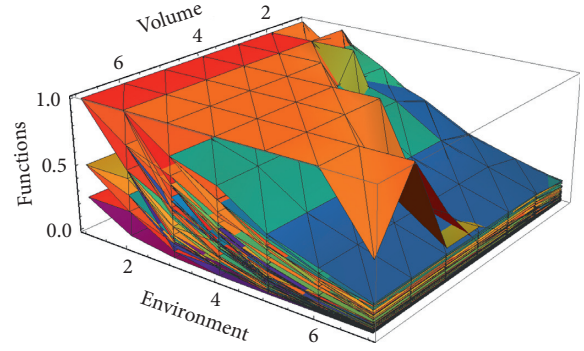


FIGURE 7: Fraction of the number of environment configurations that induce different functions on the volumes for environment thicknesses and volume sizes from 1 to 7. Note that under some rules, each environment induces a unique function for all volume sizes from 1 to 7.

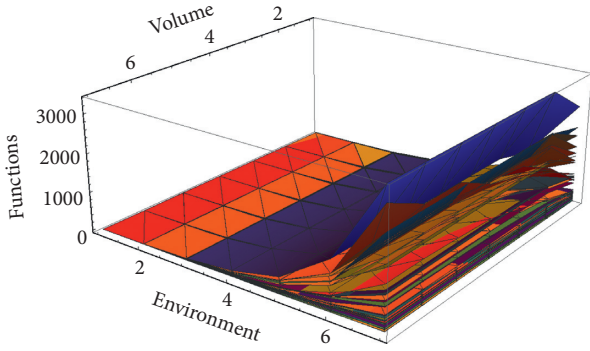


FIGURE 5: All rules for which the number of functions induced by a fixed environment thickness increases not only from volume size 1 to 2 and never decreases with increasing volume size.

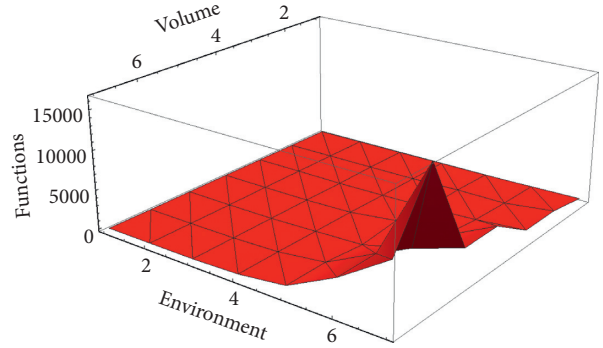


FIGURE 8: Number of functions over environment thicknesses and volume sizes for rule 90 (Class D). This is also one of the exceptional rules. Note the pronounced maximum at environment thickness 7 and volume size 6.

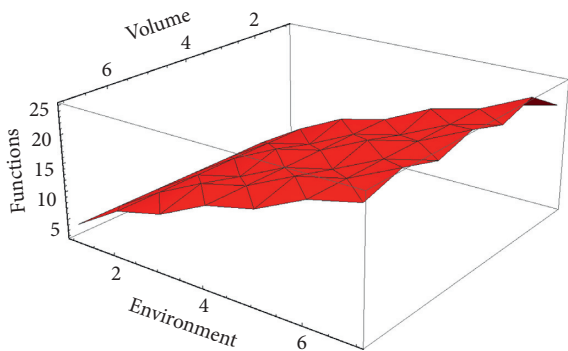


FIGURE 6: Number of functions over environment thicknesses and volume sizes for rule 128 (Class C). Note the many local maxima.

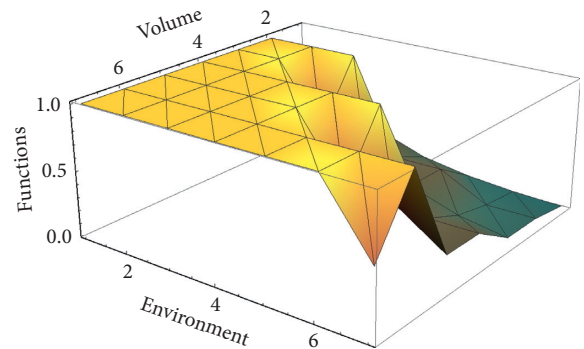


FIGURE 9: Fraction of the number of environment configurations that induce different functions as in Figure 7 for rule 90 (Class D). Note the repetitive structure.

Within the range of variables investigated, increasing the environment size appears to always increase the number of induced functions. To see that this is not trivially obvious consider the following argument. For a fixed volume size m , every environment configuration x_{E_1} at a given environment thickness n_1 will be a partial environment configuration at any larger environment thickness n_2 . This also means that

any function $f_1: \mathcal{X}^V \rightarrow \mathcal{X}^{O_1}$ induced by E_1 is still implemented by the partial environment. However, for the larger environment thickness n_2 , we count function from V to the output cells $O_2 \neq O_1$ which have moved further outward in the future light cone. This means that two

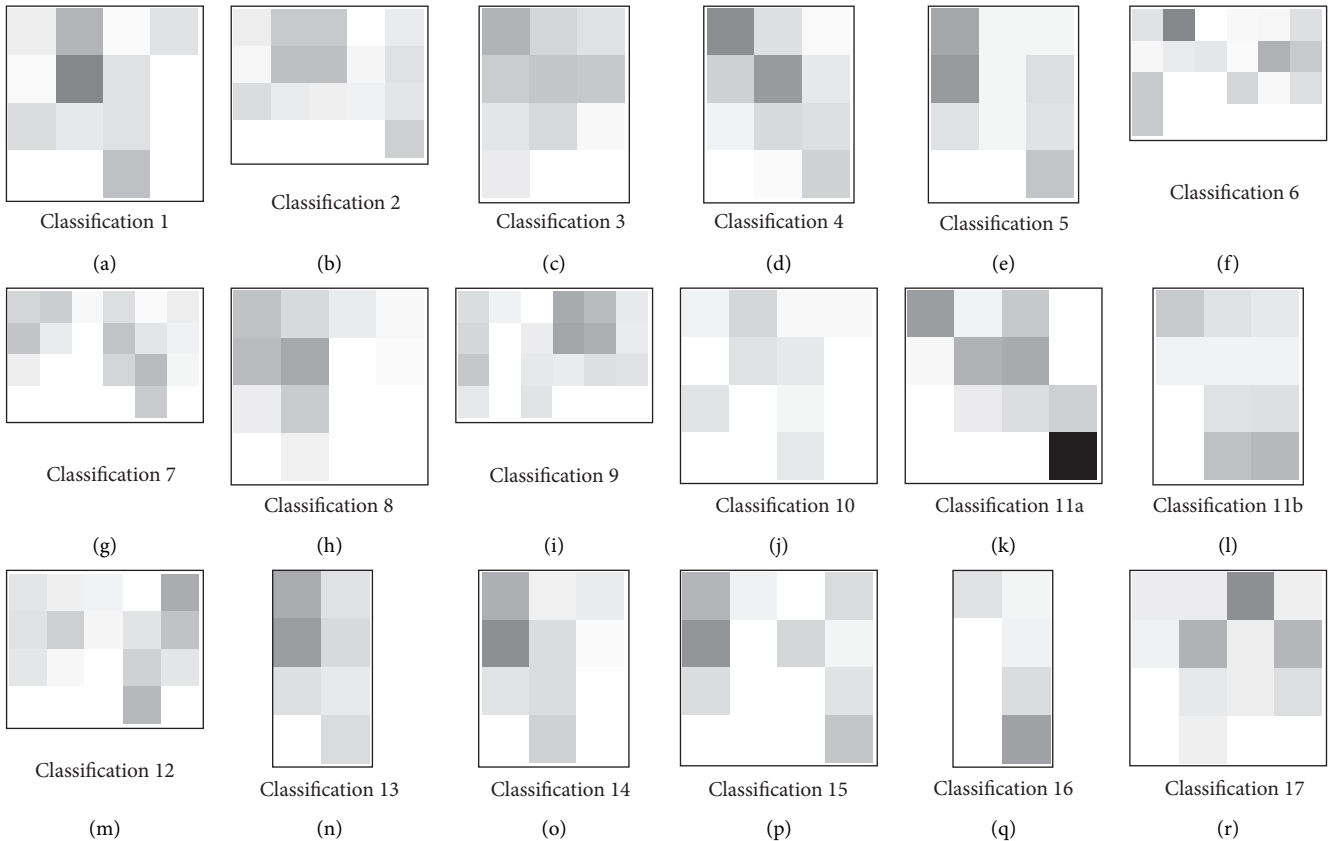


FIGURE 10: Comparison to known classifications of ECA rules. For each classification, we compare each of our four classes (rows A–D downward) with each of the classes in Martinez [10], by taking the ratio of the number of rules in intersection of the classes to the number of rules in the union of the classes. This gives a number between 0 and 1 which is represented by gray scale here where black is equal to one. A ratio of one indicates that two classes contain exactly the same rules and thus the other classification identifies exactly the same set of rules as a single class. A value of zero means that no rule is in both classes. Note that rules 11, 12, and 16 contain classes that coincide with our class of exceptional rules.

TABLE 2: Comparison of classes described above (Classes A to D, in rows) with the Wolfram classes (WC 1 to 4, in columns).

| | WC 1 | WC 2 | WC 3 | WC 4 |
|---------|--------------|--|-------------------------------|------------------|
| Class A | 0, 8, 32 | 1, 2, 3, 4, 5, 10, 12, 15, 19, 29, 34, 37, 42, 50, 51, 62, 76, 108, 132, 138, 170, 200, 204 | 30 | 41, 54, 106, 110 |
| Class B | 136, 168 | 7, 9, 11, 13, 14, 23, 24, 25, 28, 33, 35, 36, 38, 43, 44, 46, 58, 72, 73, 77, 78, 94, 104, 134, 140, 142, 152, 154, 156, 164, 172, 178, 184, 232 | 18, 22, 45, 60, 122, 126, 146 | — |
| Class C | 40, 128, 160 | 6, 26, 27, 56, 57, 74, 130, 162 | — | — |
| Class D | — | — | 90, 105, 150 | — |

different induced functions $f_1, g_1: \mathcal{X}^V \rightarrow \mathcal{X}^O$ that differ for a smaller environment thickness do not guarantee the existence of two different functions $f_2, g_2: V \rightarrow \mathcal{X}^{O_2}$ for the larger environment thickness n_2 .

The existence of local maxima shows that, in general, certain environments can transform volumes of particular sizes in more ways than others. This indicates a preferred relation between the scales of environment and volume. The exceptional rules show that it is possible for environments to exhaust their transformational capacity for nontrivial

volume sizes of close to half the environment size (environment size is double the environment thickness). Note that the exceptional rules all show local maxima/preferred scales as well. On the other hand, it is compatible with our results that there is a minimal volume size (increasing with environment thickness) after which a given environment exhausts its transformational capacity (e.g., Figure 8, which also shows a repetitive pattern). The fact that only 3 rules are exceptional is itself interesting. These rules more than others allow the environments to transform volumes in many ways.

We do not however reach a conclusive explanation for the number of functions in dependence on environment thickness and volume sizes presented in Results Section.

The preferred relation between scales of environment and volume is itself an interesting effect, which may bear significance on the nature of complexity growth in the study of living systems. Under certain conditions, environments may rapidly exhaust their transformational capacity over volumes they enclose, in turn limiting the realm of possibilities to implement functions connected to the living state. In later studies, this approach may need to be extended to study how different volume shapes and contact surfaces between environments and volumes can affect the number of induced functions.

Note that in case we made the choice to limit the number of functions by not counting functions which do not allow an additional input-output pair, i.e., pair of volume cells to output cells configuration, to be realized, the number of functions would come to capture a measure of controllability. In that case, the drop of induced functions for the exceptional rules would signify a loss of control from the environment, in spite of the device's volume increasing in size. This relates to the trade-off between stability and controllability that Janzing [5] calls lower bound of entropy influx. This means that the ability of environment cells to control degrees of freedom of a given volume conflicts with the ability to isolate the target control region. In future work, we would like to pursue this way further to tackle questions of control, controllability, and thermodynamics.

Data Availability

The data used to support the findings of this study are available from Martin Biehl (martin@araya.org) upon request. The authors have not used any third-party data, and the data exclusively consist in Mathematica software code. Any other relevant materials, books, or papers that were referred to in the manuscript are duly cited and listed in the reference section of the manuscript.

Disclosure

The opinions expressed in this publication are those of the authors and do not necessarily reflect the views of Templeton World Charity Foundation, Inc.

Conflicts of Interest

The authors declare that they have no conflicts of interest.

Acknowledgments

The work by MB on this publication was made possible through the support of a grant from Templeton World Charity Foundation, Inc.

References

- [1] C. Langton, *Artificial Life: Proceedings of an Interdisciplinary Workshop on the Synthesis and Simulation of Living Systems*, Addison-Wesley Longman Publishing Co. Inc., New York, NY, USA, 1989.
- [2] J. Von Neumann and A. W. Burks, "Theory of self-reproducing automata," *IEEE Transactions on Neural Networks*, vol. 5, no. 1, pp. 3–14, 1966.
- [3] R. D. Beer, "The cognitive domain of a glider in the game of life," *Artificial Life*, vol. 20, no. 2, pp. 183–206, 2014.
- [4] A. Adams, A. Berner, P. Davies, and S. Walker, "Physical universality state-dependent dynamical laws and open-ended novelty," *Entropy*, vol. 19, no. 9, p. 461, 2017.
- [5] D. Janzing, "Is there a physically universal cellular automaton or Hamiltonian?," 2010, <https://arxiv.org/abs/1009.1720>.
- [6] D. Deutsch, "Constructor theory," *Synthese*, vol. 190, no. 18, pp. 4331–4359, 2013.
- [7] D. Janzing, "Simple negative result for physically universal controllers with macroscopic interface," 2018, <https://arxiv.org/pdf/1804.05954.pdf>.
- [8] M. Biehl and D. Polani, "Action and perception for spatio-temporal patterns," *Artificial Life Conference Proceedings*, vol. 14, pp. 68–75, 2017.
- [9] D. Balduzzi, "Detecting emergent processes in cellular automata with excess information," 2011, <https://arxiv.org/abs/1105.0158>.
- [10] G. J. Martinez, "A note on elementary cellular automata classification," *Journal of Cellular Automata*, vol. 8, no. 3–4, pp. 233–259, 2013.
- [11] S. Wolfram, *A New Kind of Science*, Wolfram Media, Champaign, IL, USA, 2002.

Research Article

Role of Recovery in Evolving Protection against Systemic Risk: A Mechanical Perspective in Network-Agent Dynamics

Chulwook Park ^{1,2}

¹International Institute for Applied Systems Analysis (IIASA), Laxenburg A-2361, Austria

²Department of Physical Science, Seoul National University, Seoul 08826, Republic of Korea

Correspondence should be addressed to Chulwook Park; pcw8531@gmail.com

Received 19 March 2020; Revised 22 August 2020; Accepted 25 September 2020; Published 28 April 2021

Academic Editor: Tomas Veloz

Copyright © 2021 Chulwook Park. This is an open access article distributed under the Creative Commons Attribution License, which permits unrestricted use, distribution, and reproduction in any medium, provided the original work is properly cited.

We propose a model of evolving protection against systemic risk related to recovery. Using the failure potential in network-agent dynamics, we present a process-based simulation that provides insights into alternative interventions and their mechanical uniqueness. The fundamental operating principle of this model is that computation allows greater emphasis on optimizing the recovery within the general regularity of random network dynamics. The rules and processes that are used here could be regarded as useful techniques in systemic risk measurement relative to numerical failure reduction analyses.

1. Introduction

1.1. Background. Various contemporary studies have argued that systemic risk and abrupt failure events are related to the highly interconnected systems and networked structures created by agents [1]. Based on a simple set of properties, observations derived from several models indicate that the proportion of protection between nodes in the network can be described as a probability. This is related to how systemic risk should be coped with rather than simply predicting it based on the probability of failure (e.g., a failed bank in a financial system, asymptomatic transmission of a disease, and cognitive bias in decision-making). The risk of propagation is higher than that of independent failure events, extending to interdependent ones, which we refer to as cascading failures among system components [2]. Many scenarios that arise in simulations should be regarded not as indicating uncertainty or mistakes but rather as the consequences of inappropriate settings and interactions. In particular, proper protection against systemic risk with system components can be evolved heuristically through strategy dynamics (social learning and exploration) as a potential means of limiting failure. The present model expands this concept to investigate nonlinear randomness effects due to delayed responses, which may result in

sensitivity to small changes that are difficult to prepare or manage [3]. To assess the profound implications that this approach may have for our understanding of dynamic behavior, including protection processes, this study investigates the influence of the necessary heuristics through which a proper response could mediate risk diffusion before a system completely fails [4], as discussed below.

1.2. Literature Review. By investigating how the complexity of networked structures underpins real-world systemic phenomena, various simulation studies have identified implications for individual robustness, the propagation of systemic risk, protection flow, and collective behavior across networks [5]. A distinguishing feature of such phenomena is that they emerge from the complex interactions among individual elements in a system or from their associations with each other [3]. The effect of context-varying mechanical flux on a system's risk is highly complex. The possibility of quantifying such a risk needs to be evaluated in consideration of the distortions and patterns of such effects [4]. The investigations involve a variety of information, e.g., social contacts that are favored as the infection and spreading route, which in turn can be used to infer the characteristics of the underlying networks [6]. As demonstrated by the

existence history (e.g., the financial crisis in 2008, the outbreak of COVID-19 in 2019), a reproduction (i.e., failure, bias, or virus) varies greatly from individual to individual, which is generally believed to affect the spreading dynamics significantly [7]. Whether such individual inhomogeneity aggravates the outbreak is a challenging question, and the answer depends on the specific model [8, 9]. In particular, the connectivity patterns of individuals are key to understanding [10] how networks are structured and communicated with each other [11]. Other network properties that have been investigated include the concept of evolutionary dynamics, which helps characterize and understand the architecture of artificial systems in relation to the network properties [12]. As most tools for laying out networks are variants of an algorithm, it is difficult to use them to explore how the conditions of a network affect the network's dynamics [13]. The assessment process can be used to make macroscale observations for input performance, while approaches for microscale evaluations to simultaneously obtain more detailed insights must be treated within the structure of the network itself [14]. Several studies have reported such structures in terms of both microscale (e.g., individual incentives and relative gain versus effort) and macroscale (e.g., institutional competition and central intervention) behavior. For example, evolutionary explanations of systemic risk demonstrate how optimal decision makers are constrained when creating biased estimates of their capability and show how individuals alter their strategies in response to perceptions of resource value [15]. Standard evolutionary models in complex environments show that potentially different biases in decision-making expose different experimental groups at different transition probabilities [16]. A recent study found that by employing strong mitigation (i.e., social distancing and isolation of confirmed cases as guided by risk diffusion testing) related to the different response strategies, an outbreak can be suppressed to levels below the normal critical care capacity [10]. Although a triggered cascade can evolve over a certain time scale (i.e., days), it can be mitigated with intervention by the central system [17]. Evidence from many nowcasting and forecasting estimates indicates that in the absence of prevention and control measures other than simply isolating the risk cases, the probability of continued transmission with the projected trajectory remains high (exponential growth of the number of infections) [7, 8]. Thus, there is an urgent need to reduce propagation rates and control the growth of this risk to reduce not only the peak demand on the system but also the total number of eventually affected individuals [18].

1.3. Gap Statement. The computational modeling technique shows no bridge between the dynamics of agent nodes (with the vertex as a fundamental element) and the emergent properties of failure in recovery [19] (note that “recovery” in the context of financial systemic risk often refers to the fraction of a loan that is recovered after the default of the counterparty; here, it refers to a different quantity called “recovery time delay” similar to the concept of intervention). Most tools for laying out networks are variants of an

algorithm and hence cannot easily be used to explore how the conditions affect the dynamics of the network [20] owing to the following factors: (1) Many of them take the form of a theoretical explanatory insight constructed in response to a hypothetical assumption. (2) The type and number of individuals are arbitrary or left undefined. (3) Validation with respect to stylized mechanical parameters cannot explain their potential over-parameterization. (4) There is an extended transient or burn-in phase that is discarded before analysis [21]. (5) Most importantly, the time units for many of these models may have no clear interpretation. To address these issues, we extend the model to fit an estimation of macro-/microscale variables, such as protections and interventions. The assessment process can be used to make macro- or microscale observations of input performance, while approaches for improving the recovery delay and obtaining more detailed insights should be investigated in the structure of the network itself [22]. This requires the combination of large repositories to construct representations of trajectories that can be analyzed at different scales and from different perspectives [23]. Indeed, the mechanisms and serial algorithms that underpin our understanding of systemic risk in networked agents must be evaluated through various means. Accordingly, we can establish a common ground for the integration of knowledge and methodologies with consistent definitions and reconcile the approaches for studying networks from various fields, which will intuitively enable us to face all the difficulties and pitfalls that are inherent in interdisciplinary work.

1.4. Purpose. This study develops a modeling framework that can account for quantitative measurement in agented networks, allowing us to explore how the recovery time delay affects the risk potential in both macro- and microscale cases. To regard agent dynamics as a random network, this model follows the standard approach in agent-network modeling, where by default, a small event (agent n is hit by a shock at time t) can trigger the initial passage in a risk diffusion process. The mechanism tests the clear implications for different values of the interaction, including interruption, and how protection may be related to a set of interconnectedness with mitigation entities against failure potential, rather than solely focusing on cascading events.

1.5. Value. With the objectives of better risk assessment and effective risk reduction, this model will enable us to not only directly observe the spread of failure in agented network industries but also better understand how protection can be accomplished through intervention. This work is related to the mainstream of research that contributes to the discussion of systemic robustness.

2. Model (Process-Based Methodology)

The concept of network generation in this study is based on random processes, such as those described in graph theory [24]. Although an arbitrary construction cannot fully capture the local characteristics of individuals observed in real-

world networks, everyone in the world is connected to everyone else through a chain of mutual acquaintances or even stronger relationships [25]. To examine the systemic risks that may result from failures originating and cascading on such contact networks, together with how the networked agents may be expected to protect themselves against failure cascades, we consider an agent-based systematic-risk model with evolving protection strategies that had been developed by Ulf Dieckmann at the International Institute for Applied Systems Analysis (IIASA). This model enables agent-based simulations [26], beginning with the simple assumption that pairs of nodes can be randomly connected by an edge with a given connection probability (Table 1). Using a parameter to evaluate the impact of risk on the networked agents, we can estimate the influence of primary risk along the structure as a general failure property [27]. Through scaling for the different evolutionary (Table 2) and nonevolutionary components (Table 3), each step computes a new entity and generates a new proportion in relation to the intervention [3] (Table 4).

2.1. Operating Principles. First, each agent is characterized by two values: capital and strategy. An agent that has lost all of its capital is regarded as failed. Initially, only one agent is given as failed. Each agent is assigned to a node of the network, which is given with a number n of nodes, a connection probability p_d , and a resultant adjacency matrix A . Second, at each time step, units of payoff (c) are added to each agent's capital, of which fractions f_m and f_p are spent on maintenance and protection. The updated capital is expressed as $1 + (1 - f_m - f_p)c$. Third, a failure potential can originate at each node with probability p_n and can propagate through each link with probability p_l . The system may reach one of the two states after the appearance of a random probability (initially failed node of p_n through the link of p_l) and before the second probability occurs. Each failed node with a failure potential becomes a failed node with probability p_r according to the equation below. A failed node losses its capital and remains in a failed state for one time step $p_p = p_{p,\max}/(1 + c_{p,1/2}/(f_p c))$. We can measure capital in units of $c_{p,1/2}$ to obtain $p_p = p_{p,\max}/(1 + 1/(f_p c))$. Fourth, each agent's strategy values, namely, f_{p0} and f_{p1} , are updated through social learning and exploration. Social learning represents the process of choosing a random role model with probability p and imitating the role model's strategy. The probability of imitation is $p_i = 1/(1 + \exp(-s\Delta c))$, where Δc is the difference between the role model's capital and the focal agent's capital and s is the selection intensity. Then, exploration is performed by altering a randomly chosen strategy with probability p_e with a random value chosen from a normal distribution with mean 0 and standard deviation $\sigma_e [f(x|\mu, \sigma^2)]$. The protection level for each agent is determined according to the heuristics $f_p = f_{p0} + f_{p1}C$, where C is the eigenvector centrality of the graph, which is a measure of the influence of a node in a network. If A denotes the adjacency matrix of the graph, the eigenvector centrality or x must satisfy the equation $Ax = \lambda x$, where the vector is normalized to 1. We can normalize this vector to a maximum

TABLE 1: Network property (two parameters).

| | | |
|----------------------------------|--------|-------------------|
| Number of individuals (nodes) | n | $\in (1, \infty)$ |
| Connection probability (degrees) | $d(p)$ | $\in (0, 1)$ |

TABLE 2: Evolutionary part (four parameters).

| | | |
|--------------------------------|----------|--------------|
| Imitation probability | p_r | $\in (0, 1)$ |
| Selection intensity | s | $\in (0, 1)$ |
| Exploration probability | p_e | $\in (0, 1)$ |
| Normally distributed increment | σ | $\in (0, 1)$ |

TABLE 3: Nonevolutionary part (five parameters).

| | | |
|---|--------------|--------------|
| Maintenance | f_m | $\in (0, 1)$ |
| Propagation probability for each node | p_n | $\in (0, 1)$ |
| Propagation probability through each link | p_l | $\in (0, 1)$ |
| Protection maximum | $p_{p,\max}$ | $\in (0, 1)$ |
| Reference point | $c_{p,1/2}$ | $\in (0, 1)$ |

TABLE 4: Time-dependent part (four parameters).

| | | |
|---------------------|----------|-----------------|
| Time periods | t | $1 \sim \infty$ |
| Recovery rate | r_{-t} | 1 |
| Recovery time delay | t_{-r} | $1 \sim 10$ |
| Realization | tt | $1 \sim 100$ |

value, which brings the vector components closer to 1; here, f_{p1} is important for the measurement of f_p (note that we did not explicitly demonstrate this because it has been shown in a previous study [1]). The value for f_p must be truncated to the interval $(0, 1 - f_m)$. Finally, the failure potential, which lasts for only one time step ($r_{-t} = 1$), is controlled by another variable, which we refer to as the recovery time delay ($t_{-r} \in [0, \infty]$). The details of these process-based mechanisms are presented below.

2.2. Process 1. Basic Properties of Created Networks. Individuals in this model are considered as vertices (nodes), and sets of two elements are drawn as a line (edge) connecting two vertices. Data are stored in the nodes, and the edges represent the connections between them, although they can also store data. The edges between the nodes can describe any connection (adjacency) between them (Figure 1(a)). The nodes can contain any amount of data that is assigned to them, and the edges include the data of the strength of the connection they represent.

Connectivity is another essential property of this structure. A disconnected network has some vertices that cannot be reached by the edges from any other vertex (Figure 1(b)).

A disconnected network might have one vertex connected to no edges at all, or it might have two connected networks that have no connection between them. Similarly, a connected network has no disconnected vertices; thus, a metric called connectivity is used to describe a network as a whole, and it depends on the information being presented, usually identified by $(n, d[p])$. Networks also have additional properties, i.e., edges can have a direction, such that a relationship

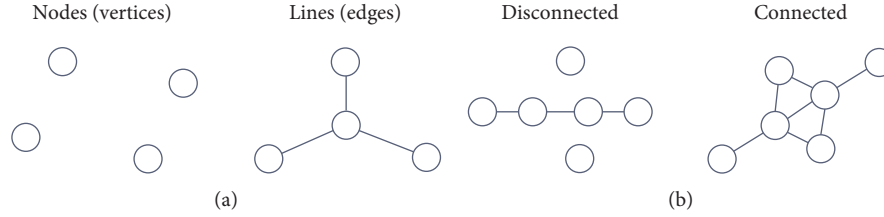


FIGURE 1: Schematic representation of nodes and lines (a) and connectivity (b).

between two nodes is only one-way and not reciprocal. However, in the present model, we used an undirected network, the edges of which have no direction, because in our case, edges are drawn between two individual nodes who have met; hence, all relationships being represented are reciprocal. Thus, the relationship created (network) is undirected and begins with edges randomly drawn between one pair of nodes at a time. For example, four nodes may have edges between them, as shown in Figure 2.

By contrast, if we take an adjacency matrix, we may consider the rows and columns of the matrix to be labeled by the vertices (nodes), giving us one, two, three, or four vertices here. We may use any actual labeling; here, we denote our adjacency matrix by A . The definition of our matrix is that an entry in row m and column n is equal to 1 if there is an edge between m and n , and 0 otherwise:

$$A_{m \times n} = \begin{matrix} & \begin{matrix} 1 & 2 & 3 & 4 \end{matrix} \\ \begin{matrix} 1 \\ 2 \\ 3 \\ 4 \end{matrix} & \begin{bmatrix} & & & \\ & & & \\ & & & \\ & & & \end{bmatrix} \end{matrix}, A = \begin{cases} 1, & \text{if } mn \in \text{edge,} \\ 0, & \text{otherwise.} \end{cases} \quad (1)$$

Note that the adjacency matrix of a network contains all the information contained in that network. Similarly, note that the presented network is given a random appearance because of the way the computer generates the visuals. If the program was to run a second time, a different picture would be generated; however, regardless of how it is run, the same relationship holds between the vertices (nodes) and the edges (line), resulting in the same degrees:

$$A = \begin{matrix} & \begin{matrix} 1 & 2 & 3 & 4 \end{matrix} \\ \begin{matrix} 1 \\ 2 \\ 3 \\ 4 \end{matrix} & \begin{bmatrix} 0 & 1 & 0 & 0 \\ 1 & 0 & 1 & 1 \\ 0 & 1 & 0 & 1 \\ 0 & 1 & 1 & 0 \end{bmatrix} \end{matrix}, \deg(v_{2m}) = 3, \deg(v_{2n}) = 3, A = \begin{bmatrix} a_{11} & a_{12} & \dots & a_{1n} \\ a_{21} & a_{22} & 1 & a_{2n} \\ \dots & \dots & \dots & \dots \\ a_{m1} & a_{m2} & \dots & a_{mn} \end{bmatrix}. \quad (2)$$

The resulting $m \times n$ matrix is obtained as $[A = G(n, p[d])]$, and any node (n) can be randomly linked to any other node. Because the collection of nodes influences the connection probability $[p[d] \in (0, 1)]$, the model investigates the distribution of the connection in the network (probability of degree) (Figure 3).

Figure 4 is based on the standard representation in network theory. Note that the vertices have *degree* d $[A = G(n, d)]$. This d -regular network has degree d for all vertices, and the resulting matrix can be compared to another well-known random network called the Erdős–Rényi network [28], obtained from $[A = G(n, p)]$, shown in Figure 5, where any node (n) can be randomly exposed to any other nodes, creating random connections.

Technically, with respect to the collection of nodes influenced by the connection probability $[p \in (0, 1)]$, it can be observed that both cases with a higher degree (on the right-hand side of the plots) show a higher probability of being connected to an agent. However, for simplicity, the model presents a random regular structure owing to the connection degree $[d \in (0, n - 1)]$ because the network has

all vertices of a certain degree (the same connection probability). In general, various network types (e.g., institutions, firms, banks, food distributors, and supply chains) have ambiguous effects in relation to individual ties because they allow for different ways of diversifying risk; this is particularly true as they influence each other in the same procedure of originating strategies and distributing security [18]. This is considered in the literature to provide strong empirical evidence for a technical approach for comparison with another network (note the lattice and calculation of eigenvector centrality (Table 5)) to obtain a simple numerical solution (Figure 6).

In the following section, analyses are conducted for the case of a random regular network such that agents within the strategy have the same level of diversification [17].

2.3. Process 2. Primary Risk Influence. Next, to observe the propagation process, the model uses an array (vector) to represent the probability of failure $[p \in (0, 1)]$ with given initially influenced nodes $(1 \leq j \leq N)$ denoted merely by

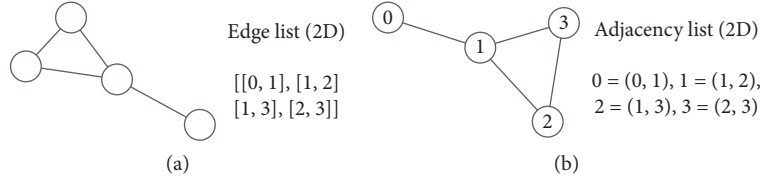


FIGURE 2: Schematic representation of the edge list (a) and the adjacency list (b).

```

=====
# CODE BOOK: Generating the graph
=====
dim = 10 # linear dimension of the network
n = dim * dim # number of nodes
edge = [] # edges of the network

# Here, we use a simple lattice as aspects of the graph.

for node in range(n):
    row = int(node / dim)
    col = int(node % dim)

    adj = [ [ (row + 1) % dim, col],
            [ row, (col + 1) % dim],
            ]

    for i in [0,1]:
        neighbour = adj[i][0] * dim + adj[i][1]
        edge.append ([node, neighbour])

G = nx.Graph()

G.add_nodes_from(range(n))
G.add_edges_from(edge)

=====
# CODE BOOK: Generating a Random Regular d-Graph
=====
G = nx.random_regular_graph(d = 9, n = n, seed = None) # n = nodes, d = connection degree [p ∈ (0,1)]
edge = np.array(G.edges()) # create random graph

A = np.array(nx.adjacency_matrix(G).todense()) # resultant adjacency matrix
=====

```

FIGURE 3: Code book: generating the graph and a random regular d-graph.

(p_j). Each node can be in one of the two states: not failed or failed. All nodes are initially without failure.

Extending the above output, given the failure dynamics, the following is obtained:

$$A = \begin{bmatrix} a_{11} & a_{12} & \cdots & a_{1n} \\ a_{21} & a_{22} & \cdots & a_{2n} \\ \cdots & \cdots & \cdots & \cdots \\ a_{m1} & a_{m2} & \cdots & a_{mn} \end{bmatrix} \begin{bmatrix} \vec{a}_1 \\ \vec{a}_2 \\ \cdots \\ \vec{a}_n \end{bmatrix} = \begin{bmatrix} a_{11}\vec{a}_1 + a_{12}\vec{a}_2 + \cdots + a_{1n}\vec{a}_n \\ a_{21}\vec{a}_1 + a_{22}\vec{a}_2 + \cdots + a_{2n}\vec{a}_n \\ \cdots \\ a_{m1}\vec{a}_1 + a_{m2}\vec{a}_2 + \cdots + a_{mn}\vec{a}_n \end{bmatrix} = B\vec{a} = \begin{bmatrix} B\vec{a}_1 \\ B\vec{a}_2 \\ \cdots \\ B\vec{a}_n \end{bmatrix}. \quad (3)$$

That is, the states matrix:

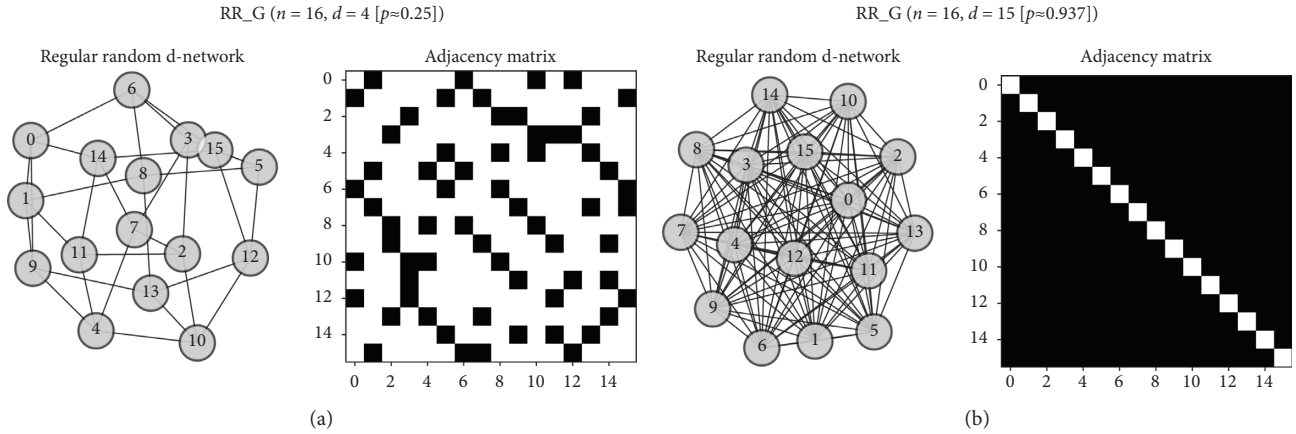


FIGURE 4: Prototype of a random regular network with its properties. The number of nodes $n = 4 * 4$; connection degree (probability) $d = 15$ (b) and $d = 4$ (a). For each section, the plots of the left-hand side show the random (regular) network that was created. The circles represent nodes with an arbitrarily assigned label from 0 to 15, and each line represents a link. The plot on the right-hand side of each section shows the adjacency matrix with entries in row m and column n (either 1 (black) or 0 (white)).

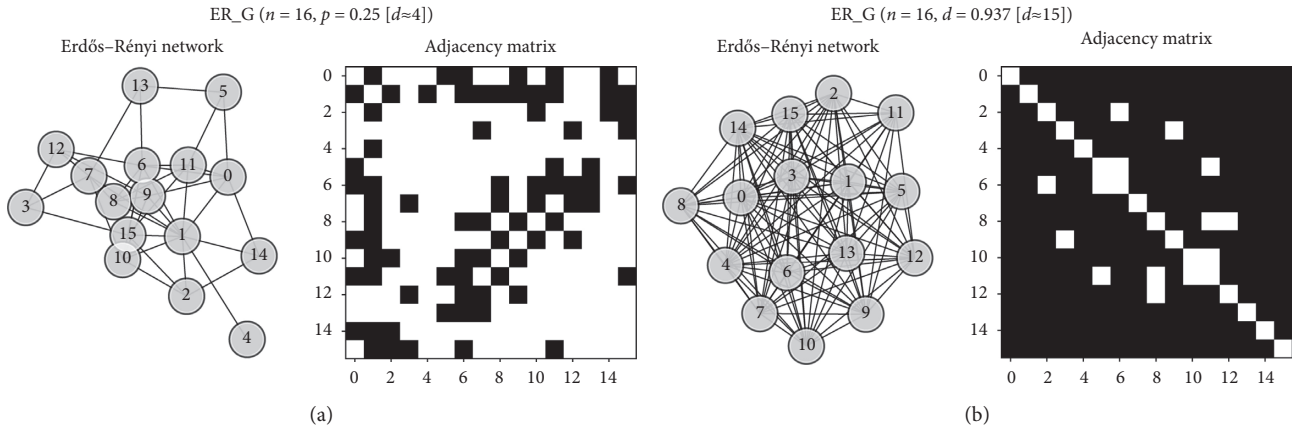


FIGURE 5: Prototype of a random network with its properties. The number of nodes $n = 16$; connection probability $p = 0.937$ (b) and $p = 0.25$ (a). The plot on the left-hand side of each half of the figure shows the random (Erdős-Rényi) network that was created. Each node is represented by a circle, with an arbitrarily assigned label from 0 to 15, and each line represents a link. The plot on the right-hand side of each section shows the adjacency matrix with entries in row m and column n (either 1 (black) or 0 (white)).

TABLE 5: Numerical result for eigenvector centrality [$Ax = \lambda x$].

| Node (i) | 0 | 1 | 2 | 3 | 4 | 5 | 6 | 7 | 8 | 9 | 10 | 11 | 12 | 13 | 14 | 15 |
|----------------------|------|-------|-------|-------|-------|-------|-------|-------|-------|-------|-------|-------|-------|-------|-------|-------|
| $d = 4$ [$p=0.25$] | 0.25 | 0.25 | 0.25 | 0.25 | 0.25 | 0.25 | 0.25 | 0.25 | 0.25 | 0.25 | 0.25 | 0.25 | 0.25 | 0.25 | 0.25 | 0.25 |
| $p = 0.25$ [$d=4$] | 0.33 | 0.237 | 0.165 | 0.207 | 0.320 | 0.223 | 0.150 | 0.171 | 0.212 | 0.100 | 0.353 | 0.227 | 0.382 | 0.231 | 0.110 | 0.339 |

d = random regular property obtained from Figure 4(a); p = random property obtained from Figure 5(a).

i.e., States Matrix

$$\begin{aligned}
 & [[1, 1, 1, 1, 0, 0, 1, 1, 1, 1,], \\
 & [0, 0, 0, 1, 1, 1, 1, 1, 1, 1,], \\
 & [0, 0, 0, 0, 0, 0, 0, 0, 0, 0,], \\
 & [0, 0, 0, 0, 1, 1, 1, 1, 1, 0,], \\
 & [0, 0, 0, 0, 1, 1, 1, 1, 1, 1,], \\
 & [0, 0, 0, 1, 1, 1, 1, 1, 1, 0,], \\
 & [0, 0, 0, 0, 0, 0, 0, 0, 0, 0,], \\
 & [0, 0, 1, 1, 1, 1, 1, 1, 1, 1,], \\
 & [0, 0, 0, 0, 0, 0, 0, 0, 0, 1,], \\
 & [0, 0, 0, 0, 0, 0, 1, 1, 1, 1,]
 \end{aligned} \tag{4}$$

```

=====
# CODE BOOK: Create centrality
=====
dim = 10                                # linear dimension of the network
n = dim * dim                            # number of nodes
edge = []                                 # edges of the network

# Here, we use a simple lattice as aspects of the graph.

for node in range(n):
    row = int(node / dim)
    col = int(node % dim)

    adj = [ [ (row + 1) % dim, col],
             [ row, (col + 1) % dim],
             ]

    for i in [0, 1]:
        neighbour = adj[i][0] * dim + adj[i][1]
        edge.append([node, neighbour])

G = nx.random_regular_graph(d=9, n=n, seed=None) # n = nodes, d = connection degree [p ∈ (0,1)]
edge = np.array(G.edges())                    # create random graph

C = nx.eigenvector_centrality(G)              # calculate eigenvector_centrality normalized [C ∈ (0,1)]
=====

```

FIGURE 6: Code book: create centrality.

```

=====
# CODE BOOK: Risk influence
=====
# for risk dynamics
pn = 0.1                                  # with this, a failure potential can originate at each node
pl = 0.3                                  # with this, a failure potential can propagate along each link

""" Failure potential can originate at each node with (pn) and can produce a failure with (1-pp). The failure potential
propagates along each link with (pl) from a failed node. """

R = (np.random.random(n) ≤ pn)             # randomly choose a certain percentage with a conditional
failure_potential[R] = 1                   # conditional if this occurs
for i in range(n):                         # loop for every individual within the loop with conditional
    if B[i, 3] > 0:                         # if the node fails
        neighbors = nx.all_neighbors(G, i)  # apply network property
        for j in neighbors:                 # find the link for the node (neighbor linked by connection)
            R = np.random.random()         # randomly choose a certain percentage
            if R ≤ pl:                       # if it is (conditional)
                failure_potential[j] = 1    # do this (failure potential goes to)
=====

```

FIGURE 7: Code book: risk influence.

Note that the matrix is denoted by $B\vec{a}$ instead of A because it no longer represents the adjacency matrix. $B\vec{a}$ is continued to be labeled as rows and columns with values of 1 and 0; the key difference is the possibility of showing the state of each node (m : 1 = failure and 0 = absence of failure) according to the time step (n) (Figure 7).

In relation to the fundamental characteristic of the model, we stipulate that an individual (node) can fail if one of its neighbors is infected with failure through a network (Figure 8). An elementary level of risk (or cascades of failure)

depends on the co-occurrence of i and j of the nodes. This implies that individuals are more biased against other individuals that are highly linked in their network.

Next, the probability of failure can be determined by the number of links from the node of the specification scaled by R/S . If we retain the individual characteristics as constant (K), R/S is equal to the risk (failure probability: $p \in (0, 1)$) as a function of the connectivity created by the connections (λx), and R is set to K/S . Nodes at lower (higher) links can be expected to have a lower (higher) connectivity to their risk.

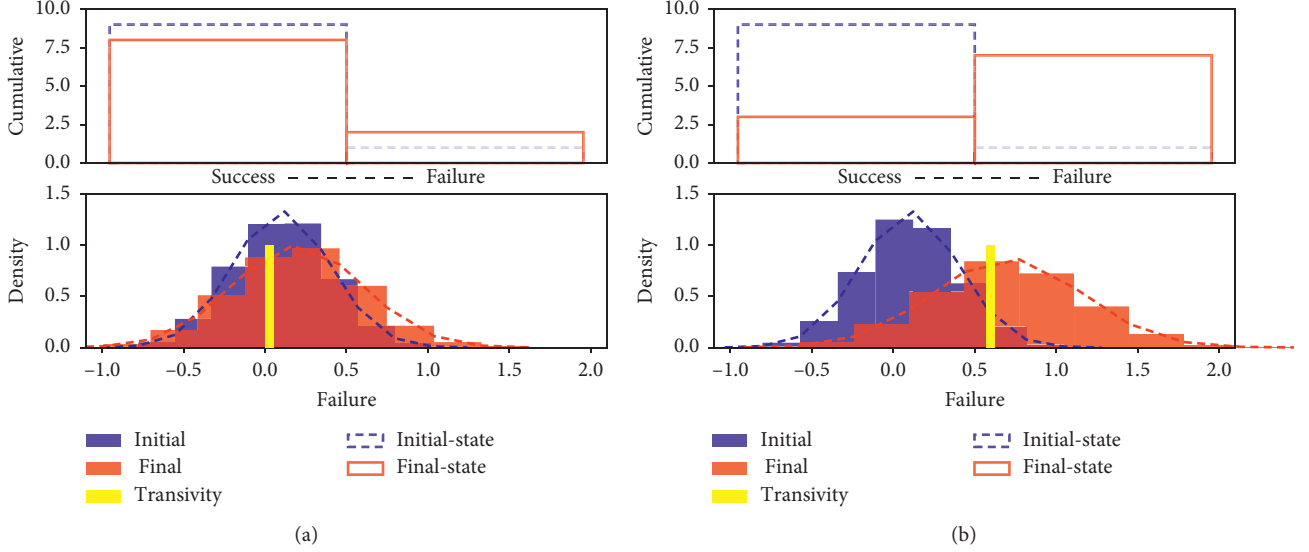


FIGURE 8: Schematic description of failure with distribution. (a) The upper left-hand side plot represents the cumulative number of absences of failure (success) nodes from the initial (blue bar) and final (red bar) cases, and (b) the upper right-hand side plot represents the increasing number of failure nodes from the initial and final cases. The lower plots represent the probability distribution between the initial failure (blue) and the final failure (red), with the likelihood as the transitivity (yellow bar). Note that the influences of these failures are computed as the frequencies of the failure nodes in their initial and final states, i.e., as relative frequencies $[f_j = h_j/N, h_j = \sum_{k=1, \dots, N; X^{(k)}=j} 1]$, where h_j is the frequency of the failure state (j), and the proportion (percentage) of occurrences of failure in the statistical ensemble corresponds to the relative frequency.

In other words, if we remove nodes from the network, the bias is reduced where the links are lower, even if they retain their individual characteristics throughout the process.

2.4. Process 3. Impose Protection against Systemic Risk. Along with the basic intuitions mentioned above, protection dynamics is also implemented. First, we divide the program into the subdynamics (*payoff*, *failure*, and *strategy*). Then, the result of each subdynamics is saved. These subdynamics are trivial problems that add complexity to the dynamics. To implement each of these, we use simple equations. These equations combine the previously computed variables with the newly added or computed variables, for example, $a \rightarrow$ store in the table, $b \rightarrow$ compute c , $d \rightarrow$ store in the table, $a + b = c \rightarrow$ lookup a , $b \rightarrow$ compute c , $d \rightarrow$ store in the

table, $a + d = e \rightarrow$ lookup a , and $d \rightarrow$ compute e . In the example given in Figure 9, we use the values already stored in the table to compute new variables. This technique is often referred to as memorization (Figure 9).

2.4.1. Payoff Dynamics. An agent is associated with each node and is characterized by its capital and strategy as follows: for each time step, each agent receives one unit of payoff, which is added to that agent's capital c , of which fractions f_m and f_p are spent on maintenance and protection, respectively; thus, the capital value is updated as $1 + (1 - f_m - f_p)c$. We used an elementwise computation with arrays for vectorization (\vec{v}) instead of a loop:

$$f_p = \vec{v}_i = \begin{bmatrix} \vec{v}_{i1} \\ \vec{v}_{i2} \\ \dots \\ \vec{v}_{in} \end{bmatrix}, f_m = \vec{v}_{ii} = \begin{bmatrix} \vec{v}_{ii1} \\ \vec{v}_{ii2} \\ \dots \\ \vec{v}_{iin} \end{bmatrix}, \vec{v}_{ii} + (-)\vec{v}_i = \begin{bmatrix} \vec{v}_{ii1} + (-\vec{v}_{i1}) \\ \vec{v}_{ii2} + (-\vec{v}_{i2}) \\ \dots \\ \vec{v}_{iin} + (-\vec{v}_{in}) \end{bmatrix} = \begin{bmatrix} \vec{v}_{iii1} \\ \vec{v}_{iii2} \\ \dots \\ \vec{v}_{iiiin} \end{bmatrix}, c = \begin{bmatrix} \vec{v}_{iii1} \\ \vec{v}_{iii2} \\ \dots \\ \vec{v}_{iiiin} \end{bmatrix} = \begin{bmatrix} c\vec{v}_{iii1} \\ c\vec{v}_{iii2} \\ \dots \\ c\vec{v}_{iiiin} \end{bmatrix} = \begin{bmatrix} \vec{v}_1 \\ \vec{v}_2 \\ \dots \\ \vec{v}_n \end{bmatrix}. \quad (5)$$

The previous initial random network property is as follows:


```

=====
# CODE BOOK: Initial parameters
=====
# Formemorization

B = np.zeros((n, 4))           # create matrix to store parameters
failure_potential = np.zeros(n) # create another matrix to store influence
protection_potential = np.zeros(n) # create another matrix to store protection potential
fp = np.zeros(n)             # create another matrix to store protection level
capital = 1                   # initial capital

# For strategies
fp0 = np.random.normal(0.4, 0.01, size = [n]) # strategy of the one (mean, SD, size = n)
fp1 = np.random.normal(0.5, 0.01, size = [n]) # strategy of the other (mean, SD, size = n)
=====

```

FIGURE 9: Code book: initial parameters.

$$A \begin{bmatrix} a_{11} & a_{12} & \dots & a_{1n} \\ a_{21} & a_{22} & \dots & a_{2n} \\ \dots & \dots & \dots & \dots \\ a_{m1} & a_{m2} & \dots & a_{mn} \end{bmatrix} + kA \begin{bmatrix} ka_{11} & ka_{12} & \dots & ka_{1n} \\ ka_{21} & ka_{22} & \dots & ka_{2n} \\ \dots & \dots & \dots & \dots \\ ka_{m1} & ka_{m2} & \dots & ka_{mn} \end{bmatrix} = B, k \in [0, 1]. \quad (6)$$

Thus, the applied output given the payoff dynamics becomes

$$B = \begin{bmatrix} b_{11} & b_{12} & \dots & b_{1n} \\ b_{21} & b_{22} & \dots & b_{2n} \\ \dots & \dots & \dots & \dots \\ b_{m1} & b_{m2} & \dots & b_{mn} \end{bmatrix} \begin{bmatrix} \vec{v}_1 \\ \vec{v}_2 \\ \dots \\ \vec{v}_n \end{bmatrix} = \begin{bmatrix} b_{11}\vec{v}_1 + b_{12}\vec{v}_2 + \dots + b_{1n}\vec{v}_n \\ b_{21}\vec{v}_1 + b_{22}\vec{v}_2 + \dots + b_{2n}\vec{v}_n \\ \dots \\ b_{m1}\vec{v}_1 + b_{m2}\vec{v}_2 + \dots + b_{mn}\vec{v}_n \end{bmatrix} = B\vec{v} = \begin{bmatrix} B\vec{v}_1 \\ B\vec{v}_2 \\ \dots \\ B\vec{v}_n \end{bmatrix}, \quad (7)$$

where the vector (\vec{v} = payoff_dynamics) components are equal to matrix B . This product is equal to $B\vec{v}$ (Figure 10).

2.4.2. Failure Dynamics. The failure potential can originate at each node with probability $p_n \in [0, 1]$, and it also propagates along each link with probability $p_l \in [0, 1]$ at each time step. The failure potential turns into failure with probability $1 - p_p$ depending on the agent's investment in protection: a possible choice is $[p_p = p_{p,\max}/(1 + c_{p,1/2}/(f_p c))]$, where protection (p_p) is equal to the applied (saturation) function. Here, $p_{p,\max}$ is a designated protection maximum, $c_{p,1/2}$ denotes an allocated reference point, and

$f_p c$ represents an evolutionary protection level multiplied by the updated capital:

$$p_p = \vec{u}_i = \begin{bmatrix} \vec{u}_{i1} \\ \vec{u}_{i2} \\ \dots \\ \vec{u}_{in} \end{bmatrix}, f_p = \vec{v}_i = \begin{bmatrix} \vec{v}_{i1} \\ \vec{v}_{i2} \\ \dots \\ \vec{v}_{in} \end{bmatrix}, f_p c = c \begin{bmatrix} c\vec{v}_{i1} \\ c\vec{v}_{i2} \\ \dots \\ c\vec{v}_{in} \end{bmatrix}. \quad (8)$$

The applied output given the failure dynamics is as follows:

$$B = \begin{bmatrix} b_{11} & b_{12} & \dots & b_{1n} \\ b_{21} & b_{22} & \dots & b_{2n} \\ \dots & \dots & \dots & \dots \\ b_{m1} & b_{m2} & \dots & b_{mn} \end{bmatrix} \begin{bmatrix} \vec{u}_1 \\ \vec{u}_2 \\ \dots \\ \vec{u}_n \end{bmatrix} = \begin{bmatrix} b_{11}\vec{u}_1 + b_{12}\vec{u}_2 + \dots + b_{1n}\vec{u}_n \\ b_{21}\vec{u}_1 + b_{22}\vec{u}_2 + \dots + b_{2n}\vec{u}_n \\ \dots \\ b_{m1}\vec{u}_1 + b_{m2}\vec{u}_2 + \dots + b_{mn}\vec{u}_n \end{bmatrix} = B\vec{u} = \begin{bmatrix} B\vec{u}_1 \\ B\vec{u}_2 \\ \dots \\ B\vec{u}_n \end{bmatrix}, \quad (9)$$

```

#=====
# CODE BOOK: Payoff dynamics
#=====
"""Each agent chooses its protection level according to the heuristics  $f_p = f_{p0} + f_{p1} * C$ , truncated to the interval
(0,1- $f_m$ ), where  $C$  is a measure of the centrality of the agent's node normalized to the interval (0,1)."""

 $f_p = B[:,1] + B[:,2] * \text{Centrality}$  # for heuristics of the protection level
 $f_p[f_p < 0] = 0$  # for truncation of the interval (0)
 $f_p[f_p > (1-f_m)] = 1-f_m$  # for truncation of the interval (0, 1- $f_m$ )

"""Each agent receives one unit of payoff, which is added to its capital  $c$ , of which fractions  $f_m$  and  $f_p$  are spent on
maintenance and protection, respectively, resulting in the updated capital  $1 + (1-f_m-f_p) * c$ ."""

 $B[:,0] = 1 + (1-f_m-f_p) * B[:,0]$  # resulting in the updated capital
#=====

```

FIGURE 10: Code book: payoff dynamics.

```

#=====
# CODE BOOK: Protection potential
#=====
# For protection
 $\text{Centrality} = np.array(\text{list}(C.values()))$  # copying C's values to make an array from a dictionary
 $f_p = B[:,1] + B[:,2] * \text{Centrality}$  # for protection level
 $f_m = 0.1$  # for maintenance

# For saturation function
 $p_{\text{max}} = 1$  # for protection maximum
 $cp = 1$  # for reference point (=cp, 1/2)

""" Failure potential turns into a failure with probability  $1-pp$ , depending on an agent's investment into protection  $pp = pp_{\text{max}} / ((1 + cp, 1/2) / (f_p c))$ ."""

 $B[:,3] = 0$  # node failed
 $\text{protection\_potential} = np.zeros(n)$  # conditional
 $\text{index} = (\text{failure\_potential} > 0)$  # return as true or false for all individuals
 $\text{protection\_potential}[\text{index}] = (p_{\text{max}} / (1 + cp / (f_p[\text{index}] * B[\text{index},0])))$  # index true goes to
 $\text{protection\_potential}[ np.isnan(\text{protection\_potential} ) ] = p_{\text{max}}$  # conditional
 $R = ((np.random.random(n) \leq 1-\text{protection\_potential}) \& \text{index})$  # randomly choose a certain % with conditional

 $B[R, 3] = 1$  # individuals with index true becomes 1
 $B[R, 0] = 0$  # individuals with index true becomes 0
#=====

```

FIGURE 11: Code book: protection potential.

where the vector (\vec{u} = failure_dynamics) components are equal to matrix B . This product is equal to $B\vec{u}$. In this section, a prewritten function (regular) is used to create a short iterate $1=D$ array for vectorization (\vec{u}) instead of using the adjacency matrix directly. This substitution shortens the loop. The failure lasts for one time step (default) and results in the loss of an agent's capital (Figure 11).

2.4.3. *Strategy Dynamics.* Each agent chooses its protection level according to the heuristics $f_p = f_{p0} + f_{p1}C$ truncated to the interval $(0, 1 - f_m)$:

$$\vec{v} \longrightarrow \vec{f} \longrightarrow f(\vec{v}),$$

$$f(\vec{v}) = \begin{cases} 0 < f(\vec{v}) < 0.9, & f_m = 0.9, \\ 0 < f(\vec{v}) < 0.1, & f_m = 0.1, \end{cases} \quad \vec{v}|_{f_p=f_{p0}+f_{p1}C}$$
(10)

For initialization of the strategy values, two arrays are added for vectorization ($(f_{p0} = w_i)$, $(f_{p1}C = Cw_i)$):

$$f_{p0} = \vec{w} = \begin{bmatrix} \vec{w}_1 \\ \vec{w}_2 \\ \dots \\ \vec{w}_n \end{bmatrix}, f_{p1}C = C\vec{w} = \begin{bmatrix} C\vec{w}_1 \\ C\vec{w}_2 \\ \dots \\ C\vec{w}_n \end{bmatrix}, \quad C \in [0, 1], \quad (11)$$

$$f_{p0} = \vec{w}_i = \begin{bmatrix} \vec{w}_{i1} \\ \vec{w}_{i2} \\ \dots \\ \vec{w}_{in} \end{bmatrix}, f_{p1}C = C\vec{w}_i = \begin{bmatrix} C\vec{w}_{i1} \\ C\vec{w}_{i2} \\ \dots \\ C\vec{w}_{in} \end{bmatrix}, \vec{w}_i + C\vec{w}_i = \begin{bmatrix} \vec{w}_{i1} + C\vec{w}_{i1} \\ \vec{w}_{i2} + C\vec{w}_{i2} \\ \dots \\ \vec{w}_{in} + C\vec{w}_{in} \end{bmatrix} = f_p = \begin{bmatrix} \vec{v}_{i1} \\ \vec{v}_{i2} \\ \dots \\ \vec{v}_{in} \end{bmatrix}. \quad (12)$$

The eigenvector centrality for node I is $Ax = \lambda x$, where A is the matrix of the network with eigenvalue λ . The strategy values f_{p0} and f_{p1} evolve through social learning and strategy exploration as follows: at each time step, each agent randomly chooses another agent as a role model with probability $p_r \in [0, 1]$ and imitates that agent's strategy values with the following probability:

$$p_i = [1 + e^{-\omega\Delta\pi}]^{-1}, \pi_r - \pi_f = \Delta\pi|_{\pi_r = \text{role model}}, \quad (13)$$

where p_i is the probability of acceptance of the role model for imitation, π_f is the capital of the focal individual, π_r is the capital of the role individual, e denotes the exponential, and ω is the intensity of the selection ($\omega < 1$ = weak selection; $\omega \infty$ = strong selection). The focal individual imitates the strategy of the nearby role individual, comparing its new capital (large $\Delta\pi$ = large capital difference; small $\Delta\pi$ = small capital difference); then, the focal individual chooses to imitate the strategy of the role individual. In relation to this imitation, a temporary matrix is employed to avoid changing and using one matrix in the loop (Figure 12).

Finally, at each time step, each agent with probability $p_e \in [0, 1]$ randomly chooses one of its two strategy values and alters it with a normally distributed increment with mean 0 and the following standard deviation (Figure 13):

$$f(x|\mu, \sigma^2) = \frac{1}{\sqrt{2\pi\sigma^2}} \exp^{-(x-\mu)^2/2\sigma^2} |x = \text{individual capital},$$

$$\mu \in R = \text{mean (location)}, \sigma^2 > 0 = \text{variance (squared scale)}. \quad (14)$$

2.5. Process 4. Reset Failure (and/or Protection) Potential. A failure lasts for one time step and results in the loss of an agent's capital, according to the reset failure potential and/or failure, as follows:

where \vec{w}_{i1} is a vectorization as the designated strategy of f_{p0} and \vec{w}_{ii} is a vectorization as the designated strategy of f_{p1} , multiplied by the eigenvector centrality from the random graph (C), which is a measure of the centrality of the agent's node, normalized to the interval $(0, 1)$:

$$\text{random}(n) < r_t = 1 \longrightarrow 1 - p_p = 0, \quad (15)$$

where $\text{random}(n) < \text{rec} = 1$ denotes randomly chosen individuals with a certain probability [$\text{random}(n)$], and the failure potential of any individual is $(1 - p_p)$, which is chosen according to a certain probability that approaches 0:

$$t_r < 1 = \text{strong intervention}, \quad (16)$$

$$t_r \longrightarrow \infty = \text{weak intervention}, \quad t_r \in [0, \infty],$$

By default, this recovery rate is implemented by resetting the failure potential after every $r_t = 1$ time step. At the same time, to control this intervention, we allowed the number of time steps to be controlled by another parameter ($t_r \in [0, \infty]$), which represents the recovery time delay (Figure 14).

2.6. Mechanical Insight of the Programming. The broader objective of this step-by-step procedure is to show the computerized process underlying the fundamental mechanisms that are used. The Tables 1–5 and matrix mentioned above account for the details of the rules and procedures (see Appendix 6 for details on the coding). In relation to the technical insights of the implementation, we present the details in Figure 15 that may interest program developers (Figure 15).

The versions on the left- and right-hand sides in Figure 15 represent vectorization using a loop and an array, respectively. Both versions are used in the development of our programming, as can be seen in the code book, which presents simple calculations. Specifically, following the step-by-step procedures of the operation, the version on the left-hand side can be recommended in general; however, it requires more time to simulate many individuals across time steps (see Output in Figure 15). Thus, in some dynamics implementations of models, we used the version on the right-hand side owing to its efficiency.

```

=====
# CODE BOOK: Imitation
=====
# For imitation dynamics
s = 1                                # selection intensity
pr = 0.9                              # imitation probability

"""Each agent randomly chooses another agent as a role model with probability pr and imitates that agent's strategy
values with probability pi."""

R = np.random.random()                # randomly choose a certain percentage only once
if R <= pr:                            # conditional
ff = i                                # focal model (each node i)
while True:                             # it is true
rr = np.random.choice(n)               # randomly choose role model
if ff != rr:                            # until focal choose a different role model
break                                  # exit out of the loop
pi = 1 / (1 + (np.exp(-s * (B[rr, 0] - B[ff, 0]))) # calculate (fermi) function
R = np.random.random()                # randomly choose a certain percentage only once
if R <= pi:                            # conditional
temp[ff, 1:3] = B[rr, 1:3]             # imitate the role model
B[:, 1:3] = temp[:, 1:3]               # update strategy values
=====

```

FIGURE 12: Code book: imitation.

```

=====
CODE BOOK: Exploration
=====
# For exploration dynamics
pe = 0.1                              # exploration probability
mu = 0.0                              # mean for normal increment
sigma = 0.1                            # standard deviation for normal increment

"""Each agent with probability pe randomly chooses one of its two strategy values and alters it by a normally
distributed increment with mean (0) and SD (sigma)."""

temp = B[:, 1:3]                       # a temporary variable to save strategies
R = np.random.random(size = [n, 2]) <= (0.5 * pe) # randomly choose a certain % with conditional
temp[R] += np.random.normal(mu, sigma, size = [n, 2])[R] # normal distributed increment
B[:, 1:3] = temp
=====

```

FIGURE 13: Code book: exploration.

3. Performance (Results)

Given the set of features in relation to the dynamics presented according to the model description, the results of the simulation show the fundamental characteristics of risk diffusion in a randomly networked system and present a framework that enables us to examine the assumptions efficiently while imposing realistic protections against failure. In particular, the simulation characterizes the role of the recovery time delay from the observations of applied dynamics over time to indicate how failure spreads.

First, individuals in the model are considered as vertices, and a set of two elements is drawn as edges connecting two vertices in relation to the information given in the graph. This representation involves two parameters: the number of nodes (n) and the probability that an edge is present (d). In network analysis, indicators of centrality identify the most important vertices within a graph, and their applications

include the identification of the most influential node(s) in a network. The eigenvector centrality of a node is defined as $Ax = \lambda x$, where A represents the adjacency matrix of the network with eigenvalue λ . The principal has an entry for each of the n vertices. The larger the entry for each vertex, the higher it's the ranking with respect to the eigenvector centrality (Figure 16).

Figure 16(a) represents the influences of failures, computed as the frequency of failure nodes in relation to their initial and final states, with the computed relative frequencies $f_j = h_j/N$, $h_j = \sum_{k=1, \dots, N; X^{(k)}=j} 1$, where h_j is the frequency of the failure state (j) and the percentage of occurrences of that failure outcome in the statistical ensemble corresponds to the relative frequency f_j . Figure 16(b) is created to be run in a number of such simulations according to the time step, as one could spread the failure through the network $P(X \in [a, b]; t) = 1/N \sum_{k=1, \dots, N; X^{(k)}(t) \in [a, b]} 1$, with a time series of the number of

```

=====
CODE BOOK: Recovery delay
=====
# for recovery rate
rec1 = 1.0 # always reset (failure potential)
rec2 = 1.0 # never reset (failure)

# fore recovery time delay
failtime = 1 # determines the number of timesteps
failtimear = np.zeros(n) # during which a node is failed
failidx = [] # index of failed nodes

""""A failure lasts for one time step and causes the loss of an agent's capital: reset failure potential and/or failure.""""

R = np.random.random(n) # randomly choose individuals with a certain(%)
index = R7 < rec1 # indexing with conditional
failure_potential[index] = 0 # individuals with index true, becomes 0 (reset the value)

failtimear[B[:, 3] == 0] += 1 # count the failed steps
failidx = ((failtimear % failtime) == 0)
=====

```

FIGURE 14: Code book: recovery delay.

| With for_loop | With vector_array |
|--|--|
| <pre> # for initial parameters B = np.zeros((n,4)) pe = 0.5 mu = 0.0 sigma = 0.01 for i in range(n): R = np.random.random() if R ≤ pe: choose = np.random.randint(1,3) norInc = np.random.normal(mu, sigma, size = None) B[i, choose] = B[i, choose] + norInc </pre> | <pre> # for initial parameters B = np.zeros((n,4)) pe = 0.5 mu = 0.0 sigma = 0.01 temp =B[:,1:3] R = np.random.random(size = [n, 2]) ≤ (0.5 * pe) temp[R] += np.random.normal(mu, sigma, size = [n,2])[R] B[:,1:3] = temp </pre> |
| ↓ | ↓ |
| <pre> R is: 0.15185496744882165 choose is: 2 0.0104693604787 R is: 0.7683043808698666 R is: 0.13780958929673937 choose is: 1 -0.0147493833134 R is: 0.3237906283769204 choose is: 2 -0.00149137311491 R is: 0.47586950300136266 choose is: 2 -0.00348010349487 R is: 0.3097678759688134 choose is: 2 -0.000587484956137 R is: 0.0728771142245623 choose is: 2 -0.00493456667833 R is: 0.12517600508302607 choose is: 1 -0.00438073778316 R is: 0.04830857294798152 choose is: 1 -0.00497596487175 R is: 0.5264128287834354 [[0. 0. 0.01046936 0.] [0. 0. 0. 0.] [0. -0.01474938 0. 0.] [0. 0. -0.00149137 0.] [0. 0. -0.0034801 0.] [0. 0. -0.00058748 0.] [0. 0. -0.00493457 0.] [0. -0.00438074 0. 0.] [0. -0.00497596 0. 0.] [0. 0. 0. 0.]] </pre> | <pre> [[True True] [True False] [True True] [False False] [True False] [False False] [False False] [False True] [False False] [False False]] [[0.00938266 -0.00177942] [-0.01086615 0.00553024] [0.01279481 -0.00112887] [0.00011118 -0.00223817] [0.00566594 0.00394121] [-0.00104304 0.01093303] [-0.00413213 0.00267854] [0.00614522 -0.00477365] [-0.00086985 -0.00050924] [-0.01461356 0.01471215]] [[0. 0.00938266 -0.00177942 0.] [0. -0.01086615 0. 0.] [0. 0.01279481 -0.00112887 0.] [0. 0. 0. 0.] [0. 0.00566594 0. 0.] [0. 0. 0. 0.] [0. 0. 0. 0.] [0. 0. -0.00477365 0.] [0. 0. 0. 0.] [0. 0. 0. 0.]] </pre> |

FIGURE 15: Numerical results using a loop (left side) and an array (right side).

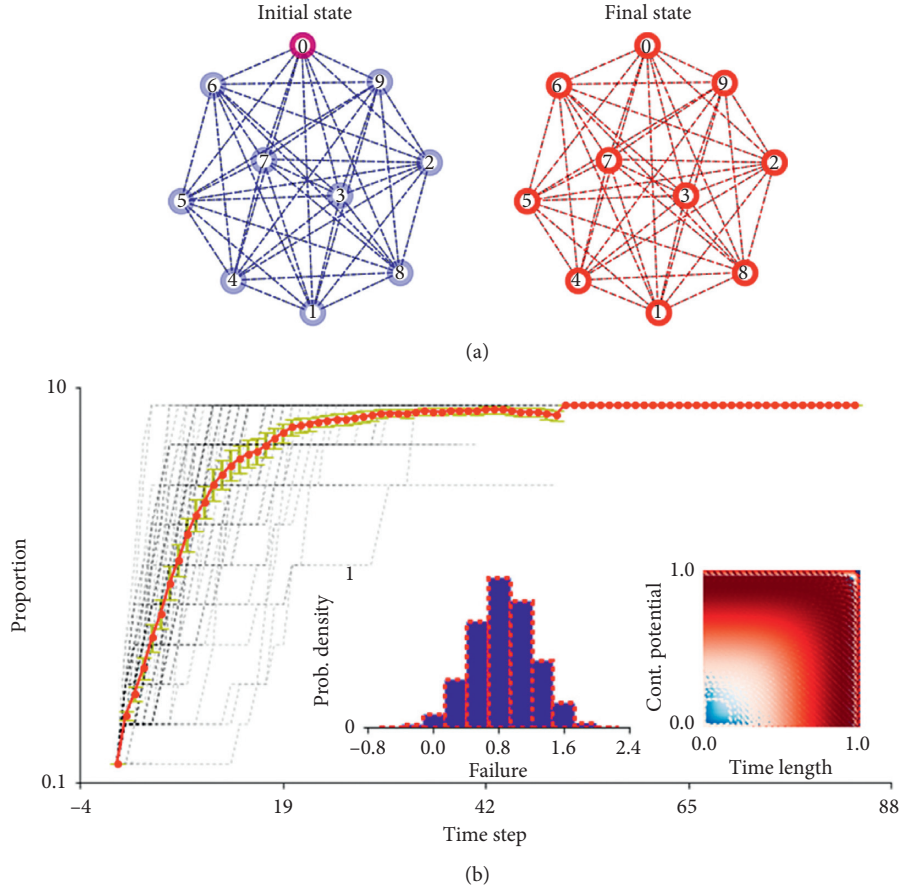


FIGURE 16: Visualization of the propagation of failure over time. (a) The individuals' state from the absence of failure (—blue) to failure (—red). (b) The time series of the number of failures for 100 realizations (black lines) until the number of failed nodes is stabilized. The horizontal axis represents the time step, and the vertical axis represents the proportion of failed nodes (the red dots denote the averages, and the yellow error bars denote the standard deviations). The histogram in the inset on the left-hand side shows the numerical distributions (failure probabilities), and the plot in the inset on the right-hand side shows the potential of failure corresponding to the time length.

failures for 100 realizations (black lines) until the number of failed nodes is stabilized. This implies that the greater the propagation from a higher rank (with respect to degree or centrality), the greater the area drawn between the failed nodes (red) and the nonfailed nodes (blue). This result intuitively implies that, primarily, higher-degree agents have greater exposure to cascading failure risk than lower-degree agents; this increases the potential for cascading failure [29].

3.1. Protection against Failure (Imposing Realistic Dynamics).

In line with our proposition, protection dynamics was applied in reference to the risk of failure. This model allows an agent to make a large investment in protection. Note that we assume that the failure potential from the dynamics becomes failure with probability $1 - p_p$ depending on the agent's investment in protection; $p_p = p_{p,\max}/(1 + c_{p,1/2}/(f_p c))$ when a failure lasts for one time step (Figure 17). The probabilities of these scenarios can be proven as follows.

First, scenario A's failure potential $1 - p_p$ is 0.527 because the investment in protection p_p is 0.473, based on the

possible choice p_p : $p_{p,\max}/(1 + c_{p,1/2}/(f_p c)) = 1/(1 + 1/(0.9*1))$, for certain parameter values ($p_{p,\max} = 1$, $c_{p,1/2} = 1$, $p_r, p_e = 0.9$, $C = 1$). Second, scenario B's failure potential $1 - p_p$ becomes 0.953 because the investment in protection p_p is 0.047 based on the possible choice p_p : $p_{p,\max}/(1 + c_{p,1/2}/(f_p c)) = 0.1/(1 + 1/(0.9*1))$, for certain parameter values ($p_{p,\max} = 0.1$, $c_{p,1/2} = 1$, $p_r, p_e = 0.9$, $C = 1$). As can be seen from the set on the left-hand side of the plot, this scenario has a better result than the set on the right-hand side, corresponding to the coexistence of failure and the absence of the 20 eulist with time. The results imply that contagion and systemic risk are likely to be intensified by the parameter setting (i.e., $p_{p,\max}$, $c_{p,1/2}$, and f_p), resulting in a significant failure cost [30]. Note that the failure potential $1 - p_p$ also changes in relation to the choice of strategy values f_{p0} and f_{p1} based on social learning ($p_r \in [0, 1]$) and exploration ($p_e \in [0, 1]$) because these probabilities can lead to different levels of protection in f_p [1].

3.2. Role of Recovery (Imposing Recovery Time Delay).

Here, we present a specific characterization to determine whether an alternative intervention could affect the failure

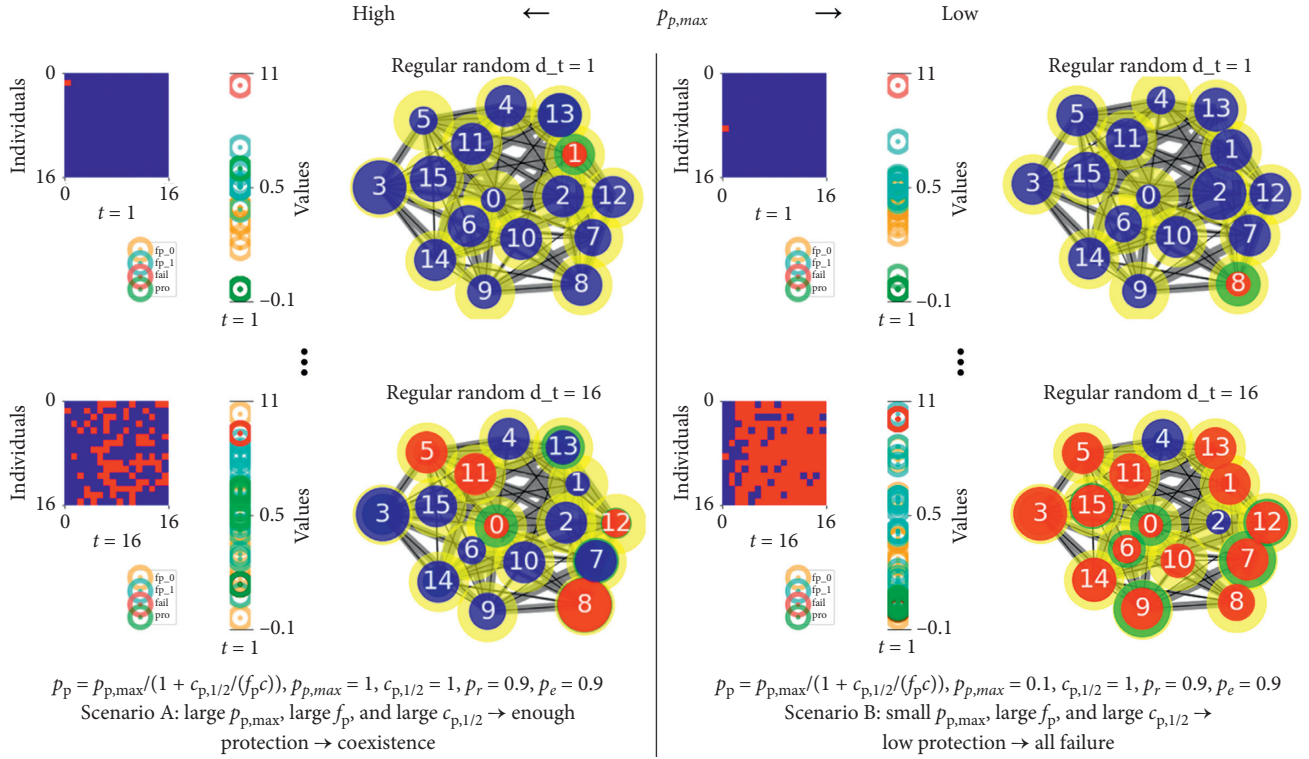


FIGURE 17: Protection dynamics against systemic risk. In each section, the plot on the left-hand side shows a matrix (horizontal axis = time step from 1 to 16; vertical axis = individuals [16]; color of the matrix = failure state: failure [red] and absence of failure [blue]). The plot in the middle shows each individual's parameter values at a given time step ($t = 16$: orange: fp_0 = strategy [1]; cyan: fp_1 = strategy [2]; red: fail = failure; green: pro = protection potential [p_p]). The plot on the right-hand side represents individuals' dynamics within a random network; node number = random label for each node, line width = eigenvector centrality, and node color = states (failure [red] ← → [blue] absence of failure; green = protection potential; yellow = initial structure of the state without failure and protection). The initialized parameters of the simulations are as follows: nodes $n = 10$, connection $d = 0.9$ (% = 5.5), $p_{p,max} = 1$, $f_{p0} = 0.4$, $f_{p1} = 0.5$, $f_m = 0.1$, $s = 1$, $\mu = 0.0$, $\sigma = 0.1$, $p_n = 0.1$, $p_l = 0.3$, and $t = 10$ (see Appendixes 1 and 2 for the results of the entire simulation).

trends observed in coexistence scenario A ($p_{p,max} = 1$, $c_{p,1/2} = 1$, $p_r, p_e = 0.9$, $C = 1$). The model shown in Figure 18 implies that contagion and systemic risk are also likely to be intensified with the recovery time delay, resulting in a significant failure cost. We observe that immediate or delayed intervention is associated with microscale propagation criteria for each node (Figure 18).

In Figure 18, the individuals can be distinguished clearly. Obviously, nodes that have immediate recovery (plots on the left-hand side) appear to have the potential to protect against the propagation of failure; on the contrary, nodes with a malfunction (plots on the right-hand side) do not have such potential. The simulation consisted of repeated trials, and each trial had two possible outcomes: failure (= red) and absence of failure (= blue). The probability of failure is the same for every trial, as in flipping a coin n times, based on the binomial variable that we defined in the model's basic structure. The probability of failure in each trial is given by $P(X) = n! / (r!(n-r)!) p^r (1-p)^{n-r} = C(n, r) p^r (1-p)^{n-r}$, where n is the total number of trials, r is the total number of failure events, and p is the probability of failure in a single trial.

In the plots on the left-hand side in Figure 18, the probability of absence of failure is approximately 0.6, and the probability of failure is 0.4 (the case probability for Scenario

A is calculated by the number of failures from the time steps: $f_j = h_j / N$, $h_j = \sum_{k=1, \dots, N; X^{(k)}=j} 1$). We assume a random variable X , which is equal to the number of failures after a certain number of time steps. One of the first conditions of this result is that it consists of a finite number of independent trials. This means that the probability of obtaining failure or absence of failure in each trial is independent of whether we obtained failure in a previous trial. Thus, in the case of the plots on the left-hand side with recovery at every time step (immediate intervention), the results of the simulation show independent trials. Another condition is that each trial clearly has one of the two discrete outcomes in which the variable X should be clearly classified as showing either failure or absence of failure with a given fixed number of trials. Then, the final condition of the probability of failure and absence of failure for each trial is constant, as we have already obtained measurements for each trial from the cases of Scenarios A and B.

Proof of the role of the recovery rate. We now examine the frequency of failed agents observed on the left-hand side in Figure 18. Suppose that at a given time, there are failed nodes (N_f) and nonfailed nodes ($N - N_f$). The number of failed nodes at $t + 1$ is given by

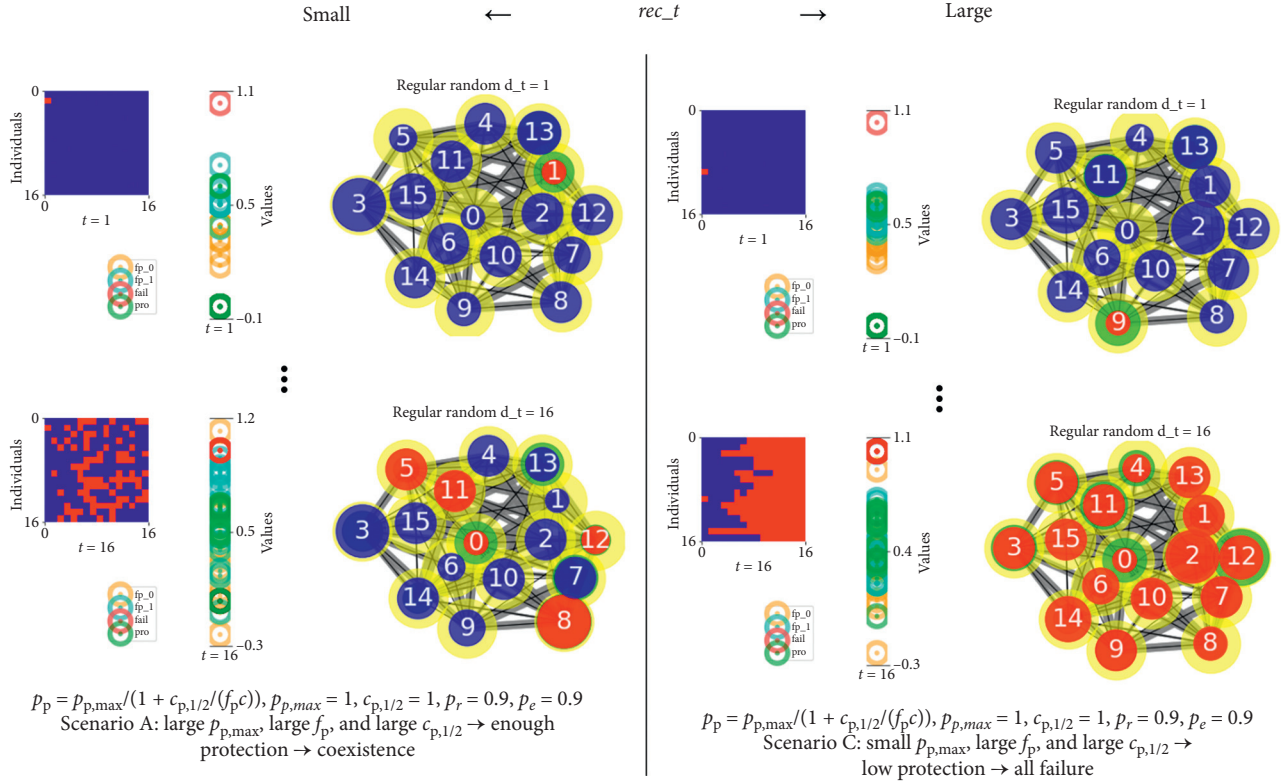


FIGURE 18: Dynamics of protection against systemic risk with recovery time delay. Using the same initial parameter values ($p_{p,max} = 1, c_{p,1/2} = 1, p_r = 0.1, p_e = 0.1, C = 1$), this set of the plots represents the time delay case (left-hand side: $r_t = 1$; right-hand side: $r_t = 5$). In each section, the plot on the left-hand side shows the matrix (horizontal axis = time step from 1 to 16; vertical axis = individuals from 1 to 16; color of the matrix = failure state: failure [red] and absence of failure [blue]) corresponding to each individual's parameter values at the given time step ($t = 16$: orange: fp_0 = strategy [1]; cyan: fp_1 = strategy [2]; red: fail = failure; green: pro = protection potential [p_p]). The graph on the right-hand side represents the dynamics in a random regular network, such that the node number = random label for each node and the node color = state (failure = red, absence of failure = blue) (see Appendix 3 for the results of the entire simulation).

$$\begin{aligned} p_A(n) &= N_f = 0.731 = N_f + p_p(N - N_f) \\ &= 0.731 + 0.5(1 - 0.731) = 0.865 = N_{NoF}, \end{aligned} \quad (17)$$

where p_p denotes the protection probability (arbitrarily designated as 0.5 only for this numerical calculation); conversely, the number of failed nodes is

$$(1 - p_p)(N - N_f) = (1 - 0.5)(1 - 0.731) = 0.135 = N_f. \quad (18)$$

Failure is propagated through an existing link with probability p_i ; at the same time, a link exists with a certain probability through the created network (p_{RR} , RR = random regular graph). Therefore, if we impose the condition that the failure potential can propagate through each link, and the propagation probability p_l is less than 1 (when the original probability p_n = constant), this equation can be modified simply by replacing p_p with

$$p'_p = 1 - (1 - p_p)(1 - (1 - p_l p_{RR}))^{N_f}. \quad (19)$$

For example, when we arbitrarily consider the protection $p_p = 0.5$ and failure propagation (p_l) through a random

network (p_{RR}) to be sufficiently high ($p_l p_{RR} = 0.9$), the protection influenced by the failure propagation p'_p becomes small because $1 - (1 - 0.5)(1 - (1 - 0.9))^{N_f} = 0.09$. On the contrary, if a weak failure propagation occurs, such as $p_l p_{RR} = 0.1$, the protection influenced by the failure propagation p'_p increases because

$$1 - (1 - 0.5)(1 - (1 - 0.1))^{N_f} = 0.95. \quad (20)$$

However, in the plots on the right-hand side in Figure 18, the probability is no longer the same but changes from trial to trial. We have the variable $X(p_l)$, which is equal to the number of failures from a designated population. It seems to represent the same operation because, with it, each trial can be classified as either a failure or an absence of failure over a fixed number of trials ($t = 16$). At the same time, there is the probability that the variable $p_l p_{RR}$ is not constant for each trial owing to the recovery time delay, which does not consist of independent trials. The probability of failure or absence of failure in the first trial would be equal to the total number of individuals between the two simulation cases:

$$p_l p_{RR}(k \text{ on } 1^{\text{st}} \text{ trial}) = 0.1. \quad (21)$$

However, the probability of the second trial (and the following trial) would not be the same because the simulation of the right-hand side case depends on what happened in the first (previous) trial:

$$p_l p_{RR}(k \text{ on } 2^{\text{nd}} \text{ trial}) \neq \text{constant}. \quad (22)$$

In other words, each trial is carried out without replacement, which results in an exponentially large difference between the two cases. Thus, this result does not meet the independent condition: the probability present in the following trial depends on what happened in the previous one. Because replacement does not take place, the probability of failure for each trail is also not constant, unlike the simulation on the left-hand side, where the probability of failure is constant:

$$p_l p_{RR}(k \text{ on } 2^{\text{nd}} \text{ trial}) = \text{constant}. \quad (23)$$

Inspired by the plausible scenarios included in the recovery delay for cases A and C in Figure 18, we focus on the comparison of the parameter $p_{p,\max}$ (when recovery delay constant = 1) with more time steps ($t=100$). This is because of the applied function $p_p [= p_{p,\max}/(1 + c_{p,1/2}/(f_p c))]$ for this application, which will primarily be decided by $p_{p,\max}$ when we consider $c_{p,1/2}/(f_p c)$ and the recovery time as constants (Figure 19). This refers to the individual for control by interventions to be protected against the risk of failure when the failure propagation mechanism influences agents' decisions as they are generated.

Figure 19 shows a scatter plot constructed using $p_{p,\max}$ (Figure 19(a)) with a clear negative correlation between failure and capital. Although it is constructed by the recovery time delay (Figure 19(b)), strong power law relationships are still obeyed in cascading failure, even if the capital values remain strong (see the averaged values for the failure and capital in the lower part of Figure 10). In the following results, this trend (failure and capital) is determined by two parameters ($p_{p,\max}$, rec_t); however, their influences do not have the same weight. Here, we should note that intervention applied to recovery can persist for a short period of time, which we could cite as a bias or rationality.

3.3. Generalize with Stationarity. Let us assume that the system has evolved and reaches stationarity, which implies that all variables have nearly constant fluctuation around their mean values. In stationarity, the state of the system can be considered independently of the initial conditions. It is useful to obtain a relationship among the variables in stationarity. First, we denote the number and fraction of failed agents by N_f and f , respectively. For stationarity, the average number of failed agents remains constant. Consider the two successive steps t and $t + 1$. Suppose that at time t , there are N_f and $N - N_f$ failed and nonfailed nodes, respectively. Therefore, the number of nonfailed nodes at $t + 1$ is $N_f + p_p(N - N_f)$, and the number of failed nodes is $(1 - p_p)(N - N_f)$. Stationarity means that the number of failed (or nonfailed) nodes remain constant (on average), i.e.,

$$N_f = (1 - p_p)(N - N_f), N_f = \begin{cases} p_p \approx 0.9, & N_f = \downarrow, \\ p_p \approx 0.1, & N_f = \uparrow, \end{cases} \quad (24)$$

$$f = \frac{1 - p_p}{2 - p_p} = \frac{(1 - p_{p,\max})f_p c + 1}{(2 - p_{p,\max})f_p c + 2}, f = \begin{cases} (2 - p_{p,\max}) \approx \uparrow, & f = \downarrow, \\ (2 - p_{p,\max}) \approx \downarrow, & f = \uparrow. \end{cases}$$

Let us define $q_p = 1 - p_p$. The above formula for f can be written as $f = q_p/(1 + q_p)$, which is simple. Here, p_p is the average probability of protection among the nonfailed nodes. Note that the protection probability for the failed nodes is zero because they have no capital. In other words, $p_p = \sum p_p(i)/N - N_f$, where $p_p(i)$ represents the protection probability for node i . In the second equality, f_p and c are defined similarly.

This relationship shows that the stationary value for f is bounded in the interval $[0, 1]$ and is a decreasing function of p_p . The limiting values seem promising. For $p_p = 1$, i.e., full protection, there is no failed agent. For $p_p = 0$, i.e., no protection, there is a failed agent. Note that at the end of each time step, all the failed agents recover (as an initial setting). If the propagation probability $p_l p_{RR}$ is less than 1, this equation should be modified by replacing p_p as follows:

$$p'_p = 1 - (1 - p_p)(1 - (1 - p_l p_{RR})^{N_f}),$$

$$p'_p = \begin{cases} p_l p_{RR} \approx 0.9, p'_p = \downarrow, \\ p_l p_{RR} \approx 0.1, p'_p = \uparrow. \end{cases} \quad (25)$$

Again, by defining $q'_p = 1 - p'_p$, we implicitly obtain f . To check the validity of these formulae with a simulation, we increase the total simulation time ($t=1,000$); for smaller $p_l p_{RR} < 1$, a longer time is required to reach stationarity (Figure 20).

Proof of the stationary state. we calculate the average value of the capital in the stationary state to prove the long-term role of the recovery time delay. First, consider the case $p_l p_{RR} = 1$. It can be easily seen that the average value of

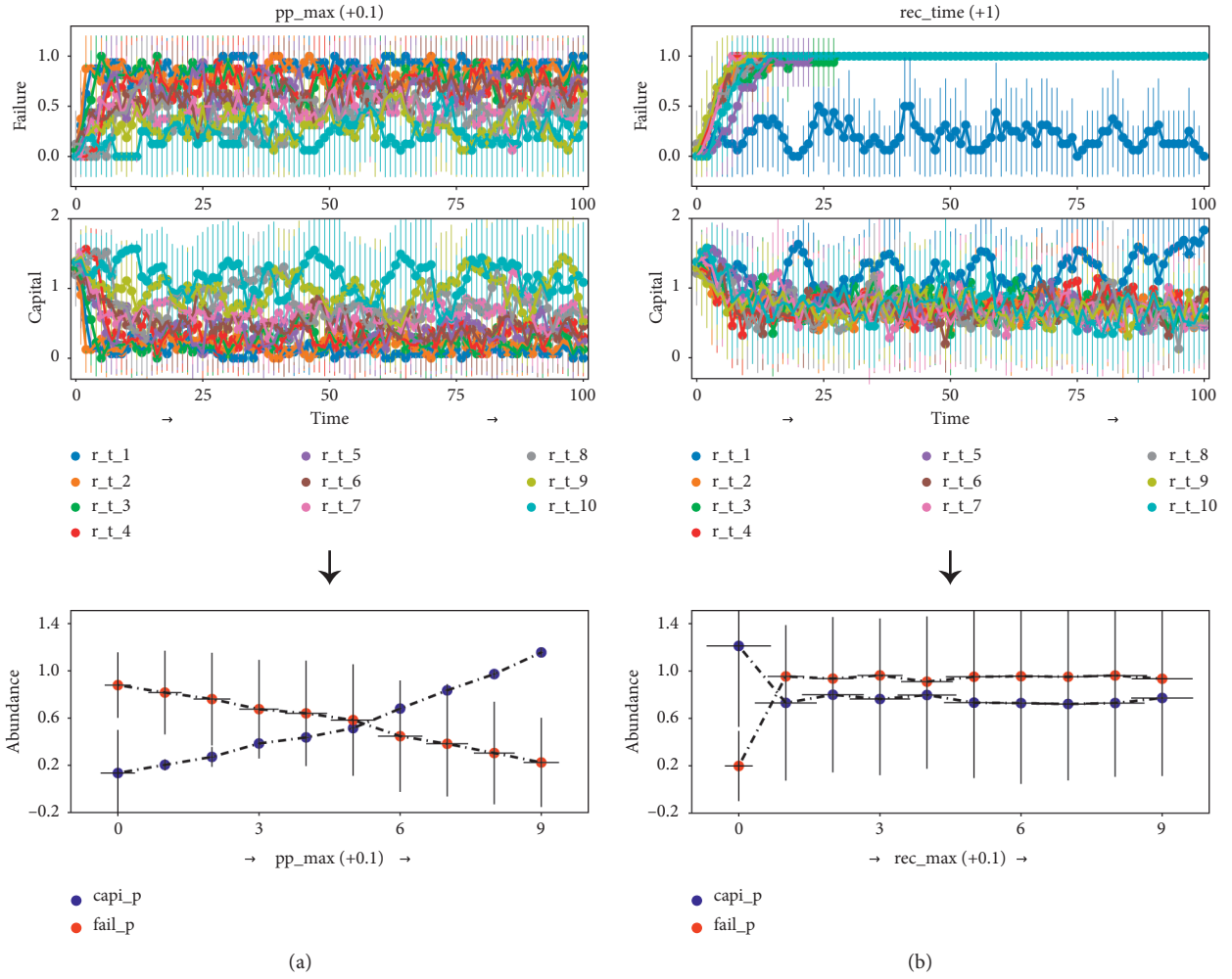


FIGURE 19: Representation of the outcomes according to the recovery time delay (b) and protection maximum (a). Using the same initialized parameter values (no delay [$r_t = 1$]), the plots represent the time delay ($r_t = 1 \sim r_t = 10$) case. The upper plot shows failure (vertical axis = value of the failure corresponding to the time step (horizontal axis)). The middle plot shows the capital (vertical axis = value of the capital corresponding to the time step [horizontal axis]). The lower plot shows the averaged outcome values (vertical axis) for capital and failure according to the recovery time delay ($\text{rec_time}[\text{+}1]$) and the protection maximum ($\text{pp_max}[\text{+}0.1]$) (see legend). All the dashed lines denote variability.

the capital in the stationary state satisfies the following equation:

$$c_{in} + p_p(1 - f_p - f_m)c = c,$$

$$c = \begin{cases} p_p \approx 0.9, & c = \uparrow, \\ p_p \approx 0.1, & c = \downarrow, \end{cases} \quad (26)$$

$$c = \begin{cases} f_p \approx \uparrow, & c = \downarrow, \\ f_p \approx \downarrow, & c = \uparrow, \end{cases}$$

where c is the average value of the capital among nonfailed individuals. Combining the above equations, we can obtain c and f_p as a function of f in the stationary state. However, it is easier to obtain c as a function of p_p , such that the protection probability should be replaced by $p'_p = 1 - (1 - p_{lPRR})(1 - (1 - p_{lPRR})^{N_f})$ when $p_{lPRR} < 1$. Therefore, we

obtain the following (note that in the simulation, we use a truncation of f_p to constrain it to the interval $[0, 1 - f_m]$ [see code book]):

$$c = \frac{p_p p'_p - c_{in}(p_{p,\max} - p_p)}{(p_{p,\max} - p_p)(p'_p(1 - f_m) - 1)}, \quad (27)$$

$$f_p = \frac{p_p(p'_p(1 - f_m) - 1)}{p_p p'_p - c_{in}(p_{p,\max} - p_p)}$$

According to the trajectories (upper part of Figure 20), the outcomes such as failure (or capital) reach a stationary state even if the trajectories from the strategies continue to evolve and exhibit different behaviors (see the inset of the upper plots). Therefore, the presence of the detailed dynamic features of the system (capital and failure) indicates

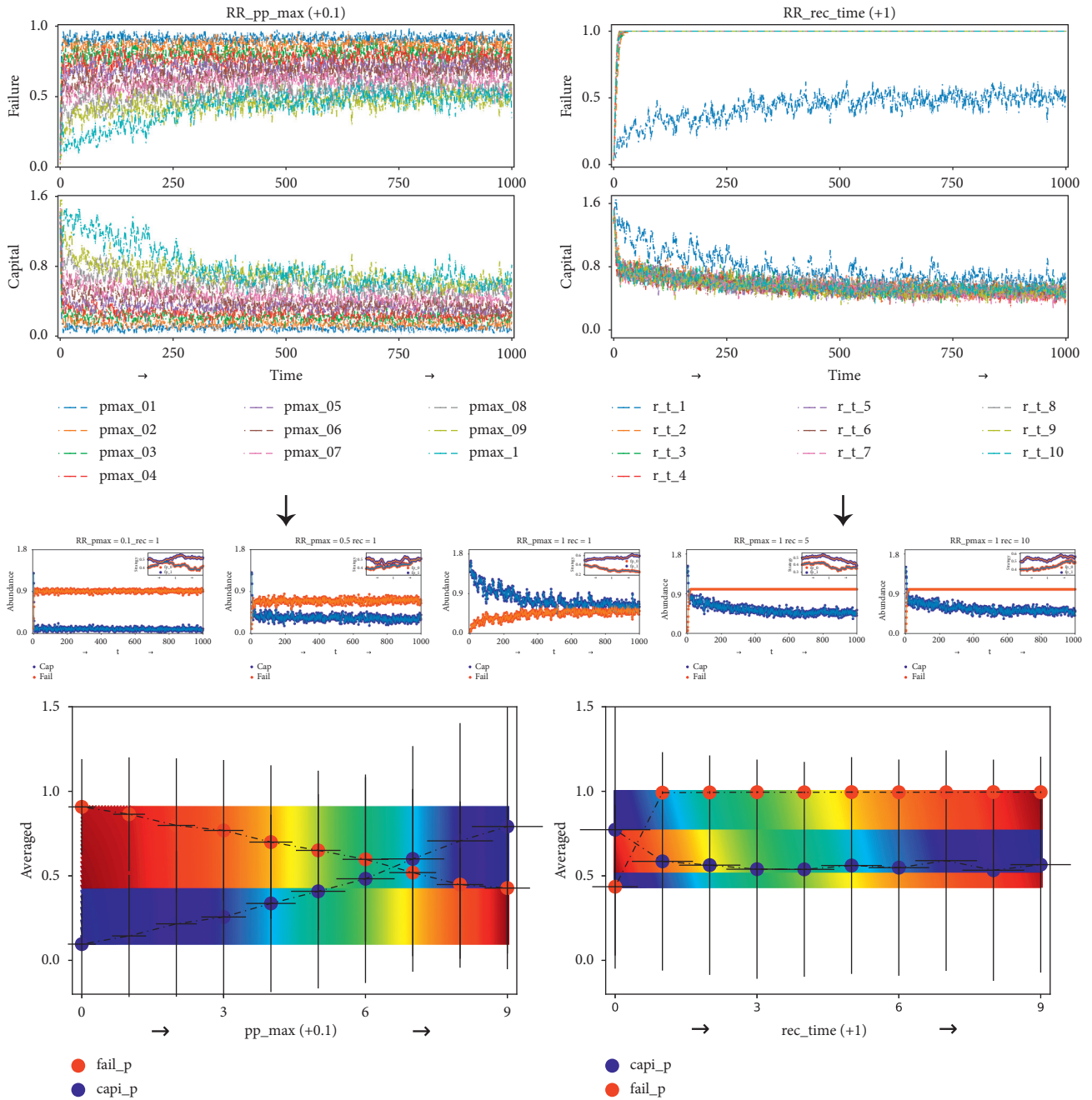


FIGURE 20: Stationarity in time series with the random regular graph (nodes = $10 * 10$, connection $d=9$, time steps = 1,000). The set on the left-hand side shows the results controlled by the protection maximum, and the set on the right-hand side shows the results with a recovery time delay (dots = averaged values; dashed lines = variation). The upper plot shows the failure and capital combined (vertical axis = value corresponding to the time step [horizontal axis]). The plot in the middle shows failure (red) and capital (blue) (vertical axis = value corresponding to the time step [horizontal axis]). The inset plot shows the trend of the two strategies (f_{p0} = red; f_{p1} = blue)] (see Appendixes 4 and 5 for the results of the entire simulation). The lower plot shows the averaged outcomes (vertical axis) for capital (blues) and failure (reds), according to the recovery time delay ($rec_time[+1]$) and protection maximum [$pp_max(+0.1)$] (see legend). The background contour shows the dominance between the outcomes, and all the dashed lines denote the variability.

the possibility of stationarity in the coevolutionary process. This observation can enable us to gain a sense of the qualitatively different nature of propagation (compared to $p_{p,max}$) within systems, such that failure is not limited to protection or strategy but is due to regulation over time. In other words, there is another rate that continues to

increase the bias as the length of the delay causes the cascading failure, even where the individuals still have potential (Figure 21).

As indicated by the protection (Figure 21; bottom, marker of green, nodes that are controlled by $p_{p,max} = 0.1$ (left-hand side) seem to lose their ability to protect, owing

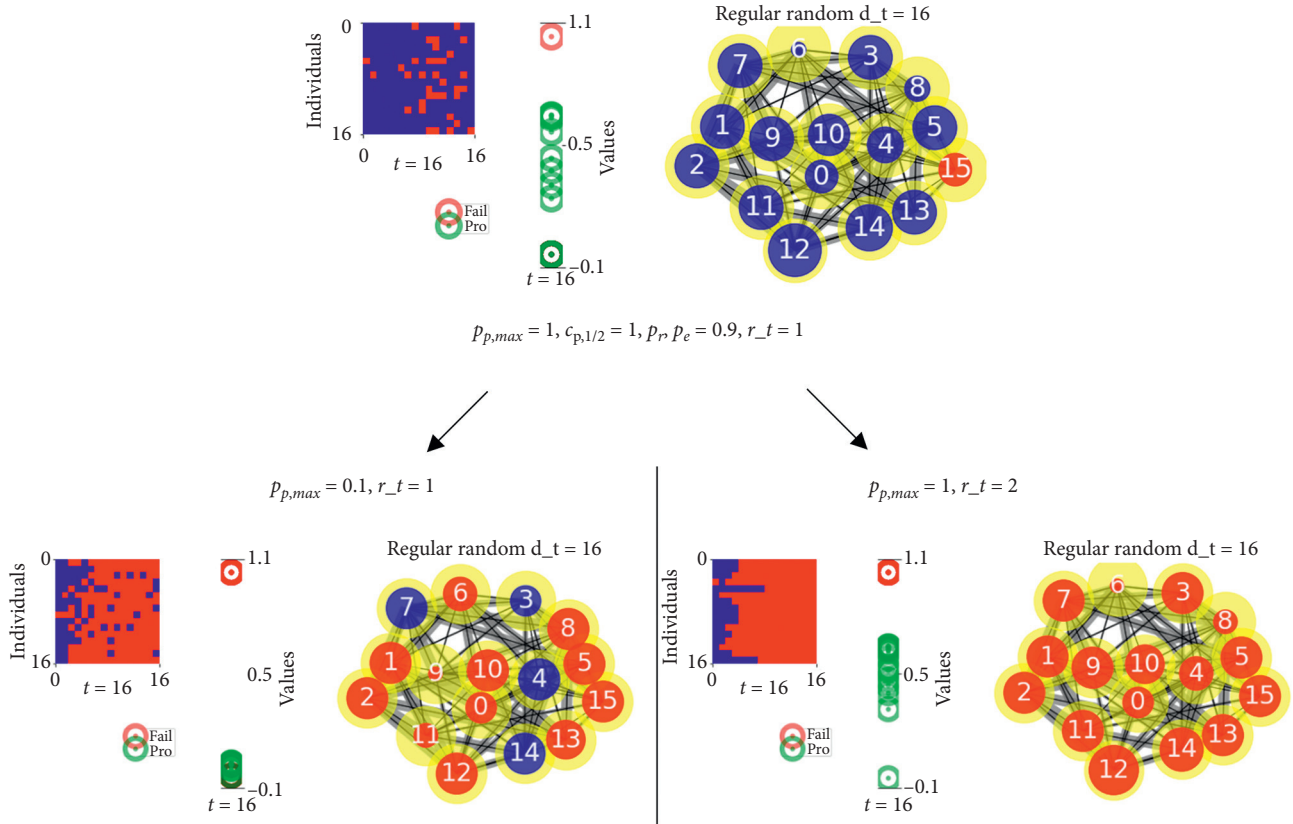


FIGURE 21: Representation of protection potential constructed by $p_{p,max}$ (lower set) and t_r (lower right-hand side). With the same initialized parameter values (upper plots: $p_{p,max} = 1$, $c_{p,1/2} = 1$, $p_r = 0.9$, $p_e = 0.9$, $C = 1$), the set of plots represents the time delay (left-hand side: $r_t = 1$; right-hand side: $r_t = 2$) case. In each section, the plot on the left-hand side shows a matrix (horizontal axis = time step from 1 to 16; vertical axis = individuals from 1 to 16; color of the matrix = failure state: failure [red] and absence of failure [blue]) corresponding to the parameter values of each individual at the given time step ($t = 16$: red: fail = failure; green: pro = protection potential). The graph on the right-hand side represents their dynamics in a random regular network; node number = random label of each node marked with a yellow background; lines = connections embedded by eigenvector centrality as the thickness; node color = states (failure = red; absence of failure = blue).

to the propagation of failure. On the contrary, nodes that are controlled by $t_r = 2$ (right-hand plots) seem to maintain their potential, even if they all feature cascading failure. We noted that the different levels of potential (between the two parameters [$p_{p,max}$, t_r]) came from their capital, as marked in blue in Figure 20 (see bottom plots of the figure).

Thus, to reduce the potential ramifications (p_p') of such additional losses to others, an immediate recovery intervention may not only be preferred to the potential damage ($1 - p_p'$) from individual failures but also guarantee that it is strategically possible for even large insolvent individuals to recover losses to uninsured connectors. Before the potential for failure can advance the propagation value, it must be identified, and the recovery value of the individual protection potential (i.e., capital) must be estimated.

4. Discussion

We presented a simple general model to quantify the protection for mitigating systemic risk, with the recovery time delay as the result. Using a simple set of properties, the

observations from this model indicate how probability describes the proportion of protection that can be characterized by how systemic risk should be coped with rather than being predicted by the probability of failure [31].

4.1. Summary of the Model. We proposed the following process-based steps (1–4) to create a model. First, *network-agent properties* were established: when the basic data structure was constructed, the functionalities of the mechanism began with a specific undirected relationship between agents through agent-based simulations, in a coexisting macroscale structure with individuals interconnected at the microscale level in the network. Next, *the primary risk influence* was established using a parameter to evaluate the impact of risk on the networked agents; the influence of primary risk was estimated along the structure as a general failure property. Then, it was necessary to implement *protection against systemic risk* by embedding protection dynamics that emphasizes the roles of payoff, failure, and strategy dynamics. Finally, *recovery* was considered through scaling for the different evolutionary and nonevolutionary components; this is crucial to the way this system functions, where each step computes a new entity and

generates a new proportion in relation to the intervention. The implications of this model are as follows.

4.2. Theoretical Implications. A suite of plausible dynamics and decentralized bottom-up mechanisms was constructed by establishing appropriate rules for the interaction, within which the system components can self-organize, including mechanisms for ensuring rule compliance (vectorized microscale implementation). This evolutionary heuristic promotes balance with respect to the interactions [32]. For example, when investment in protection is weak (low investment), a pattern of strong systemic risk emerges in the form of agent failure in networked conditions. By contrast, when investment in protection is strong (high investment), a pattern of protection emerges, with little diversification against all challenges (Figure 17). The simulation also reflected a clear correlation between a set of parameter values (between those for capital and failure and between those for the strategies of f_{p0} and f_{p1}). Thus, the strategy of social learning could be another crucial factor in resource provision that violates expectations and leads to novel trends with high impact. These results shed light on the propagation modes. The observed contagion and persistence patterns can be regarded not as a direct causal link but in relation to an accumulated rational driven by interconnectedness [33].

More importantly, in this study, the failure potential also reflects the time delay after the official failure of an individual [34]. Newly damaged individuals may affect others or may recover from the next time step onwards (recovery occurs with the rate t_r). The potential needed for recovery is related to the number of healthy individuals $n(t)$, and if individuals recover at time $t_r = 1$, the protection potential changes as follows:

$$c(t+1) = c(t) + n(t) - [1 - pp(t)]. \quad (28)$$

Once the capital is exhausted, the systemic risk increases rapidly. This is based on suitable real-time intervention related to short-term anticipation of risk flows [35]. However, because regulation occurs over time, another rate itself increases the failure potential even if the capital is still exhausted (note that the recovery rate mainly influences failure and does not have the same weight for capital). From our observations, we assume that the protection (or robustness) of an agent π_i decreases (or increases) by an amount proportional to the relative exposure of risk sharing η_{ij} . Consistent with the network of dynamics described above, the dynamics, including the recovery time delay (in time series), can be formalized as follows:

$$\begin{aligned} \pi_i &= \pi_i(0) - \frac{a}{k} \sum_j \eta_{ij} \chi_j(\tau), \\ \pi_i &= \begin{cases} \tau \approx \uparrow, & \pi_i = \downarrow, \\ \tau \approx \downarrow, & \pi_i = \uparrow. \end{cases} \end{aligned} \quad (29)$$

For convenience, with respect to the results, k substitutes the protection potential, defined by $c(t+1) = c(t) + n(t) - [1 - pp(t)]$, such that the function a determines the extent of the loss caused by the default $\chi_j(\tau)$ when we fix risk sharing η_{ij} . This indicates that the agent has defaulted at a previous time, denoted by the time variable τ . In the simulations, there was no delay during the development of the cascade ($\tau \approx 0, \tau = t_2 - t_1$). However, this dynamic differs across the default of the recovery [36]. If the system delays the intervention, the cascade tends to be much larger (following the power law) because the defaults of the neighbors of a given agent are statistically dependent on j , such that their default is more likely to cause the default of others:

$$f'(x) = \left(\frac{k}{x}\right) + c, \quad x = r_{t(t+1)}, c = 1. \quad (30)$$

In Table 6, such a range $[f'(x)]$ will be determined by failure propagation through each link in the random regular network ($p_I p_{RR}$), which was determined by the recovery time delay. We simply proved that this numerical trend of the protection probability defined by $p'_p = 1 - (1 - p_p)(1 - (1 - p_I p_{ER})^{N_f})$ could not be the same as that of $p_{p-\max}$ [when $p_I p_{ER} = \text{constant}$ (Figure 20)]. Thus, the failure influences in these simulations are not identical, as $p_{p-\max}$ changes according to these parameters, including where increases or decreases occur following a nonlinear curvature [37].

4.3. Practical Implications. We propose a modified version of the protection model against systemic risk in terms of its failure recovery mechanics, as demonstrated above. The mechanisms here are based on a few simple basic rules: a node fails at a time with a probability of failure if its failure potential is greater than or equal to that of its nearest neighbors [1], and it fails owing to the interconnected potential, although it spontaneously recovers at an external recovery or according to an intervention probability [3]. The consequences of the damage are crucial for systemic risk and controllability; however, they have not been explored systematically thus far [38]. We show how the process of embedding and the related recovery times impact the dynamics of failure processes in a network (see the section on the proof of the role of the recovery time delay). Therefore, we propose that the extent of the intervention regime in the system can be a source of evolutionary (in)stability, wherein the immediate recovery of components can mitigate damage and propagate failure in dynamic networks [17]. These decentralized management principles could be applied to logistical and production systems, or even to administrative processes and governance [18].

Governments are often reluctant to resolve insolvency in institutions [e.g., banks, firms, supply chains, and infected virus individual (i.e., Ebola, SARS, and COVID-19)], and they permit them to continue operating despite their negative effects. The length of the attendant delay causes a cascading failure, regardless of each individual's capital (i.e., immunity), which then leads to reductions in network welfare. These delays may propagate the damage to many

TABLE 6: Numerical result of the function $[f'(x)]$.

| Domain ($x = r_t$) | 1 | 2 | 3 | 4 | 5 | 6 | 7 | 8 | 9 | 10 |
|----------------------|-------|-------|-------|-------|-------|-------|--------|-------|-------|-------|
| Numerical $f'(x)$ | 2 | 1.333 | 1.2 | 1.142 | 1.111 | 1.09 | 0.1076 | 1.066 | 1.058 | 1.050 |
| Fixed mean (capital) | 0.772 | 0.585 | 0.563 | 0.539 | 0.538 | 0.561 | 0.548 | 0.589 | 0.533 | 0.566 |

other individuals in the network, increasing their fragility and probability of failure [39]. Evidence from governing systems suggests that if individuals' troubles are estimated before their capital becomes negative, institutions could, based on their risk potential, weed out the inefficient or unfortunate individuals to avoid more serious adverse effects [40]. This indicates the importance of resolving challenges to individuals as quickly as possible and developing more rapid responses to certify protected individuals by providing immediate intervention. On the contrary, prompt corrective action can increase the willingness to supply protection to reduce the chances of systemic risk [41]. Given the evolutionary mechanisms shown in this simulation model, we observed that the evolutionary response often obtains a critical value for a plausible protection potential. We demonstrated that, although structures have high potential for individual protection and a strategy to maintain their capital, the function of the interconnected recovery delay makes them weak amplifiers, where unprofitable intervention shows a high bias.

5. Concluding Remarks

Cascading failure was used to assess how rules and processes can collectively add up to a series of interconnected unsuitable outcomes. In the simulations, although every object was considered to be doing well individually, systemic risks could emerge, as the whole was vast. In other words, even if every single object is considered to be highly fitted and behaving properly (i.e., capital), there is no standard solution for proper management for everyone's benefit. Therefore, the elimination of resources needed for recovery requires a strong effort to halt cascades as they begin, when the damage is still small, and the problem may not yet be perceived as threatening. These issues can and must be treated with a proper (re)design of the system and adoption of management principles, as shown by the simulation results [42].

Many disasters in the real-world result from incorrect thinking and inappropriate system design. To address such risks more completely, a better understanding of proper intervention and resilience is crucial. However, there remains a lack of an effective method for calculating networked risk. The proposed model can facilitate realistic calculation of the interdependence and propagation of risks in a network and how they can be absorbed, and it can mediate such that both the system components and the plausible systemic intervention and outcomes will work well.

We derived a unifying framework for the interplay of observations that embed realistic dynamics such as payoff, failure, strategy, and recovery in a random regular network. The mechanics showed that the complexity should be

described by the essential features of the model's processes that capture evolutionary damage spread owing to the co-existence of crucial hypotheses in the system. Thus, it may be possible to create an account where protection and failure are not static quantities, and propagation is likely to be understood in terms of how frequently the system is in a condition that leads to a large diffusion. This availability of mechanisms raises additional expectations that predictability and controllability are a simple matter of proper system design and operation [43]. More intuitively, this study can provide a better understanding of recovery, where real-time management can overcome instabilities caused by delays in feedback or lack of information.

Data Availability

The data used to support this study can be obtained from the corresponding author upon request.

Ethical Approval

This study was approved by the local ethics committee (SNUIRB No.1509/002-002) and conformed to the ethical standards of the 1964 Declaration of Helsinki (Collaborative Institutional Training Initiative Program, report ID 20481572).

Conflicts of Interest

The author declares that there are no conflicts of interest regarding the publication of this article.

Acknowledgments

This research was supported by Basic Science Research Program through the National Research Foundation of Korea (NRF) funded by the Ministry of Education (Grant Number: 2020R111A1A01056967, PI: Chulwook Park).

Supplementary Materials


Appendix 1: the results of the entire simulation for protection dynamics against systemic risk (left-hand side of Figure 17). Appendix 2: the results of the entire simulation for protection dynamics against systemic risk (right-hand side of Figure 17). Appendix 3: the results of the entire simulation for protection dynamics against systemic risk (right-hand side of Figure 18). Appendix 4: stationarity controlled by pp,max: (nodes = $10 * 10$, connection $d = 9$, time step = 1,000). Appendix 5: stationarity controlled by rec_t: (nodes = $10 * 10$, connection $d = 9$, time steps = 1,000). Appendix 6: code book. (*Supplementary Materials*)

References

- [1] C. Park, "Network and agent dynamics with evolving protection against systemic risk," *Complexity*, vol. 2020, Article ID 2989242, 16 pages, 2020.
- [2] S. V. Buldyrev, R. Parshani, G. Paul, H. E. Stanley, and S. Havlin, "Catastrophic cascade of failures in interdependent networks," *Nature*, vol. 464, no. 7291, pp. 1025–1028, 2010.
- [3] D. Helbing, "Globally networked risks and how to respond," *Nature*, vol. 497, no. 51, p. 7447, 2013.
- [4] P. C. Trimmer, A. I. Houston, J. A. R. Marshall, M. T. Mendl, E. S. Paul, and J. M. McNamara, "Decision-making under uncertainty: "biases and Bayesians," *Animal Cognition*, vol. 14, no. 4, pp. 465–476, 2011.
- [5] R. Pastor-Satorras, C. Castellano, P. Van Mieghem, and A. Vespignani, "Epidemic processes in complex networks," *Reviews of Modern Physics*, vol. 87, no. 3, pp. 925–979, 2015.
- [6] Å. Brännström, H. Sjödin, and J. Rocklöv, "A Method for Estimating the True Number of Infections from the Reported Number of Deaths with Application to COVID-19. Submitted to Eurosurveillance," 2020.
- [7] K. Sneppen and L. Simonsen, "Impact of Superspreaders on dissemination and mitigation of COVID-19," 2020.
- [8] J. Lloyd-Smith, S. Schreiber, P. Kopp, and W. Getz, "Superspreading and the effect of individual variation on disease emergence," *Nature*, vol. 438, pp. 355–359, 2020.
- [9] T. Britton, "The Disease-Induced Herd Immunity Level for Covid-19 Is Substantially Lower than the Classical Herd Immunity Level," 2020.
- [10] H. Sjödin, A. Johansson, Å. Brännström et al., "COVID-19 healthcare demand and mortality in Sweden in response to non-pharmaceutical (NPIs) mitigation and suppression scenarios," *Tentatively Accepted for Publication by International Journal of Epidemiology. medRxiv*, vol. 2020, 2020.
- [11] A.-L. Barabási and R. Albert, "Emergence of scaling in random networks," *Science*, vol. 286, no. 5439, pp. 509–512, 1999.
- [12] O. Sporns, D. Chialvo, M. Kaiser, and C. Hilgetag, "Organization, development and function of complex brain networks," *Trends in Cognitive Sciences*, vol. 8, no. 9, pp. 418–425, 2004.
- [13] M. E. J. Newman, "The structure and function of complex networks," *SIAM Review*, vol. 45, no. 2, pp. 167–256, 2003.
- [14] S. Fortunato, "Community detection in graphs," *Physics Reports*, vol. 486, no. 3–5, pp. 75–174, 2010.
- [15] J. A. R. Marshall, P. C. Trimmer, A. I. Houston, and J. M. McNamara, "On evolutionary explanations of cognitive biases," *Trends in Ecology & Evolution*, vol. 28, no. 8, pp. 469–473, 2013.
- [16] T. W. Fawcett, B. Fallenstein, A. D. Higginson et al., "The evolution of decision rules in complex environments," *Trends in Cognitive Sciences*, vol. 18, no. 3, pp. 153–161, 2014.
- [17] S. Battiston, D. Delli Gatti, M. Gallegati, B. Greenwald, and J. E. Stiglitz, "Liaisons dangereuses: increasing connectivity, risk sharing, and systemic risk," *Journal of Economic Dynamics and Control*, vol. 36, no. 8, pp. 1121–1141, 2012.
- [18] N. Ferguson, D. Laydon, G. Nedjati Gilani et al., "Report 9: Impact of Non-pharmaceutical Interventions (NPIs) to Reduce COVID19 Mortality and Healthcare Demand," 2020.
- [19] L. Böttcher, M. Luković, J. Nagler, S. Havlin, and H. J. Herrmann, "Failure and recovery in dynamical networks," *Scientific Reports*, vol. 7, 2017.
- [20] N. Dehmamy, S. Milanlouei, and A.-L. Barabási, "A structural transition in physical networks," *Nature*, vol. 563, no. 7733, pp. 676–680, 2018.
- [21] S. Poledna, M. G. Miess, and C. H. Hommes, "Economic forecasting with an agent-based model," 2019.
- [22] X. Guardiola, R. Guimera, A. Arenas, A. Diaz-Guilera, D. Streib, and L. A. N. Amaral, "Macro-and Micro-structure of Trust Networks," 2002.
- [23] M. A. Di Muro, C. E. La Rocca, H. E. Stanley, S. Havlin, and L. A. Braunstein, "Recovery of interdependent networks," *Scientific Reports*, vol. 6, no. 1, 2016.
- [24] N. C. Wormald, "Models of Random Regular Graphs. London Mathematical Society Lecture Note Series," 1999.
- [25] A. Vespignani, "Twenty years of network science," *Nature*, vol. 558, no. 10, pp. 528–529, 2018.
- [26] E. Bonabeau, "Agent-based modeling: methods and techniques for simulating human systems," *Proceedings of the National Academy of Sciences*, vol. 99, no. 3, pp. 7280–7287, 2002.
- [27] J. M. Pacheco, A. Traulsen, and M. A. Nowak, "Coevolution of strategy and structure in complex networks with dynamical linking," *Physical Review Letters*, vol. 97, no. 25, p. 258103, 2006.
- [28] P. Erdos and A. Rényi, "On Cantor's series with convergent," *Physical Review Letters*, vol. 2, pp. 93–109, 1959.
- [29] M. O. Jackson, B. W. Rogers, and Y. Zenou, "The economic consequences of social-network structure," *Journal of Economic Literature*, vol. 55, no. 1, pp. 49–95, 2017.
- [30] S. L. Schwarcz, "Systemic Risk," 2008.
- [31] K. N. Laland, "Social learning strategies," *Animal Learning & Behavior*, vol. 32, no. 1, pp. 4–14, 2004.
- [32] M. Barthélémy and L. A. N. Amaral, "Small-world networks: evidence for a crossover picture," *Physical Review Letters*, vol. 82, no. 15, pp. 3180–3183, 1999.
- [33] D. Kahneman, "A perspective on judgment and choice: mapping bounded rationality," *American Psychologist*, vol. 58, no. 9, pp. 697–720, 2003.
- [34] J. Dermine, "Comment," *Swiss Journal of Economics and Statistics*, vol. 58, 1996.
- [35] S. Lämmer and D. Helbing, "Self-control of traffic lights and vehicle flows in urban road networks," *Journal of Statistical Mechanics: Theory and Experiment*, vol. 2008, no. 4, 2008.
- [36] P. Gai and S. Kapadia, "Contagion in financial networks," *Proceedings of the Royal Society A: Mathematical, Physical and Engineering Sciences*, vol. 466, no. 2120, pp. 2401–2423, 2010.
- [37] M. Bardoscia, F. Caccioli, J. I. Perotti, G. Vivaldo, and G. Caldarelli, "Distress propagation in complex networks: the case of non-linear DebtRank," *PLoS one*, vol. 11, no. 10, pp. 1–12, 2016.
- [38] J. Lorenz, S. Battiston, and F. Schweitzer, "Systemic risk in a unifying framework for cascading processes on networks," *The European Physical Journal B*, vol. 71, no. 4, pp. 441–460, 2009.
- [39] E. J. Kane, "Principal-agent problems in S&L salvage," *The Journal of Finance*, vol. 45, no. 3, pp. 755–764, 1990.
- [40] A. Gupta and L. Misra, "Failure and Failure Resolution in the US Thrift and Banking Industries," 1999.
- [41] G. G. Kaufman and S. A. Seelig, "Post-resolution treatment of depositors at failed banks: implications for the severity of banking crises, systemic risk, and too-big-to-fail," 2006.
- [42] Coronavirus, "Three things all governments and their science advisers must do now," *Nature*, vol. 579, 2020.
- [43] D. Helbing and A. Johansson, "Cooperation, norms, and revolutions: a unified game-theoretical approach," *PLoS One*, vol. 5, no. 10, 2010.

Research Article

Complex Service Process Optimization Based on Service Touchpoint Association and the Design Structure Matrix

Zhonghang Bai,^{1,2} Chang Liu,^{1,2} Huihui Sun,^{1,2} and Man Ding¹ 

¹College of Architecture and Art Design, Hebei University of Technology, Tianjin 300130, China

²National Technological Innovation Method and Tool Engineering, Hebei University of Technology, Tianjin 300130, China

Correspondence should be addressed to Man Ding; dingman@hebut.edu.cn

Received 18 June 2020; Revised 20 October 2020; Accepted 12 February 2021; Published 27 February 2021

Academic Editor: Tomas Veloz

Copyright © 2021 Zhonghang Bai et al. This is an open access article distributed under the Creative Commons Attribution License, which permits unrestricted use, distribution, and reproduction in any medium, provided the original work is properly cited.

Service process optimization is conducive to the innovation of enterprise services, but the poor logic design of multiple touchpoints can easily lead to problems in the service process, such as scattered layouts and repeated paths. Aiming at the promotion of service innovation and user experience, this paper takes the optimization of a single service touchpoint as the prerequisite and proposes a service process optimization method based on service touchpoint association and the design structure matrix (DSM). The association of service touchpoints is categorized into two types, namely, noncoupled and coupled association. The DSM is used to describe the two types of association between service touchpoints, and the matrix operation is used for modular identification and layering of the two kinds of association. Finally, through the above steps, the problematic service process was replanned. By using the service process optimization of a new retail convenience store as an example, the service process is divided into 6 relatively independent modules, and the order of module execution is arranged. Moreover, the optimal service process of the convenience store system is determined, and the method is verified to be feasible. Through optimization both from single service touchpoint and service process modularization, the study provides a reference for process optimization of the complex service system.

1. Introduction

In today's business environment, service companies must constantly update their processes and products to remain competitive [1]. Academic research also reflects the growing focus on service innovation [2, 3]. Service design plays a key role in service innovation and focuses on improving existing services or creating new services to introduce new service concepts into people's lives [4, 5]. With the advent of the information age, the focus of service design has shifted from tangible products to intangible services [6]. As a system, the internal service touchpoints of service design are not static and isolated, but dynamic and interactive. The service process dynamically and flexibly connects various service touchpoints, and the process focuses more on user behavior and directly affects service experience; therefore, service process optimization is an entry point for service innovation [7] and is conducive to the improvement of user experience.

Service touchpoints are the main points of the service process [8]; thus, the optimization of the service process can be considered as the optimization process of a series of touchpoints with different associations.

In the experience economy, the "physical logic" that emphasizes the rational allocation of the physical properties of objects can no longer meet people's needs; however, the "behavioral logic" that emphasizes reasonable organizational behavior has increasingly attracted more attention [9]. Determining how to analyze problems with domain logic, understanding the nature of problems, and developing breakthrough solutions to improve and measure quality remain the key challenges in service design [10]. New online channels have led to a proliferation of touchpoints [11], and poor logic design between multiple touchpoints may cause problems such as scattered layouts, repeated paths [12], and the irregularity of sequences [13], which may cause poor service experiences.

Therefore, the analysis of the association between different service touchpoints to rationally organize their logical order is crucial in service design. Most academic research on touchpoints focuses only on one type of touchpoint, namely, a specific combination of similar touchpoints [14]. The basic methods of service design such as customer journey map, service blueprint, and SERVQUAL all emphasize the expression of a single service touchpoint, but there are limitations in studying the association of touchpoints and service innovation. For example, a customer journey map is a graphical representation of touchpoints between customers and the organization. Although this visualization technology may help management understand the customer experience, it is basically useless in helping to promote innovation within the service system [15]. As the service design has become a hot spot, some scholars have tried to combine engineering or other fields to carry out service innovation. Lee et al. [16] proposed a novel knowledge-centric innovative service design (KISD) model by integrating memory-oriented-method CBR and nonmemory-oriented-method theory of TRIZ. Lee et al. [17] applies TRIZ to the intelligent parking service system. Wang et al. [18] integrated the existing fields of the TRIZ service design knowledge system and the emerging fields of the non-TRIZ service design knowledge system, and proposed a new system and a collaborative intelligence method-DSIT for creating and evaluating complex service systems using multi-criteria data analytics. Lee et al. [19] established a customer-centric approach to service conceptualization. This method combines abductive logic concepts—the EDGE approach—and the computer-aided system SCO explorer to solve the ambiguity, uncertainty, and unstructuredness of customer demand knowledge in the conceptualization of innovative data mining-based systems, and establishes a customer-centric service conceptualization method. It can be seen that these methods perform service innovation from different perspectives and have achieved good results, but they often neglect to consider the problem from the important perspective of touchpoints. In service innovation from the perspective of service touchpoints, the goal is not necessarily to create touchpoints, but to reorder or coordinate touchpoints. Touchpoints orchestration is generally considered the key to service success [20]. The purpose of this paper is to optimize the service process from the perspective of service touchpoint association. Because many service design methods are not suitable for studying service touchpoint association, methods outside the service design field are also considered for use to study the service touchpoint association. A design structure matrix (DSM) [21] can clearly describe the method of information transmission between various elements in a system, the information required by each element during the execution process, and the corresponding elements provided by the generated information [22]. Because the DSM has a unique role in information flow analysis, it is widely used in process optimization and other fields. Aiming at the problem of the reasonable organization of service touchpoint logic in service process optimization, this paper proposes a method for the optimization of the service process from the perspective of the service

touchpoint association based on a DSM and a matrix operation. Service process optimization is inseparable from service modularization [23], and DSM is a common module division method. Applying DSM to the service design can describe the information dependence relationship between the touchpoints in the complex service system in the form of a matrix, and modularize and layer the touchpoints throughout the entire service process to finally achieve the optimization of the service process.

In order to fully improve user experience and make up for the shortcomings of single touchpoint optimization in service process optimization, this article optimizes the service process in two aspects: single service touchpoint and service touchpoint association. First, use the service touchpoint optimization method proposed by Bai et al. [24]. This method optimizes the problem of service touchpoint that affects the user experience in the service process from the micro perspective of the elements of touchpoint based on TRIZ and analogy design. Then, aiming at the problem of how to rationally organize the logic of service touchpoints in service process optimization, based on the DSM and the matrix operation, a method for optimizing service process from the macro perspective of service touchpoint association is proposed. And, the above methods were used to re-plan the service process of a convenience store in Tianjin.

The remainder of this paper is organized as follows. Section 2 presents a literature review of service touchpoint research and DSM methods. In Section 3, a method for the identification and layering of associated service touchpoints based on the DSM is proposed. Section 4 describes the overall flow of service process optimization based on service touchpoint association and DSM. Section 5 takes the optimization of the service process of an unmanned convenience store as an example, and uses this method. Section 6 describes the results of the case and verifies the feasibility and potential of the method. Finally, Section 7 presents the conclusion and the future outlook.

2. Literature Review

2.1. Service Touchpoints. Service touchpoints are derived from the service encounter theory [25] and are the “critical moment” of service encounters [8]. In 1985, Shostack [26] officially proposed the concept of service encounters when studying the problem of enterprise service quality management. He pointed out that service encounters between customers and service systems are a key factor that affects customer satisfaction. After decades of development, Larivière et al. [27] proposed the concept of “service encounters 2.0” based on the rapid development of technology, which include “any customer-company interaction that results from a service system consisting of interconnected technologies (owned by the company or customer), people (employees and customers), physical/digital environment, and company/customer processes.” Although scholars have different understandings of the service encounter, they can be roughly divided into two categories: (1) the connotation of the narrow sense of binary contact service encounters [28] and (2) the connotation of broad, multi-interaction service

encounters [26]. At present, scholars generally adopt the broad connotation of service encounters when conducting empirical research, i.e., all touchpoints of customers when they receive services are service contacts, and include technical touchpoints, physical entity touchpoints, interpersonal touchpoints, invisible touchpoints, etc. [29]. Service touchpoints run through every link of the entire service process and refer to the interaction points between users and service personnel, products, services, brands, etc., during service. The many and complicated touchpoints and the intangible experience involved present a major design challenge; however, each service touch point that occurs throughout the customer journey must be carefully designed and managed, and service innovation occurs at every touchpoint on this journey [8].

2.2. Service Process. Volpi and Paulino [30] emphasized that service is a process and proposed a service triangle consisting of three elements: service provider, customer, and media. The three interact with each other to complete service behaviors. By experiencing different touchpoints, customers can feel the value of the entire service process [31]. Therefore, some scholars have optimized the service process from the perspective of service touchpoints. Wang et al. [32] discerned customer touchpoints during user-product interaction by observing user behavior, proposed a customer touchpoint association model, and established a new service system. Kim et al. [33] explained the difference between automatic taxis and manned taxis via customer journey maps and touchpoints. In addition, via the design of touchpoints, he determined the issues that should be considered for the transformation of autonomous taxis. In the industry 4.0 environment, more emphasis is placed on effective communication between customers and manufacturers [34], which makes the service systems highly complex. The rapid growth of complex service systems has introduced new changes to the service design [35]. Customers begin to interact with service providers in a multi-channel environment, and they use multiple channels in parallel and often switch between them, which increases the possibility of unsmooth service flow. A complex service system usually contains multiple service touchpoints, and the interactions between customers and service providers constitute service touchpoints. Therefore, it is necessary to research the association between service touchpoints to ensure that the service process is reasonable. Although some scholars have considered and explored the association between touchpoints in service design, the research method for this aspect is imperfect: Clatworthy [20] coordinated multiple touchpoints in the service process via integrated marketing, customer relationship management, and collaborative design research, which presented the first step in the establishment of a touchpoint knowledge system for service design. Roto et al. [36] proposed a multi-touchpoint experience design that combines service design (through multiple touchpoints), experience design (through the utilization of user needs), and omni-channel design (through the utilization of brand identity) to define company goals of customer satisfaction. The above research only stays at the stage of theoretical research, does not

describe specific methods, and has not been applied in practice. In order to verify the necessity of the research on the association of service touchpoints, Li [37] considered the characteristics of children's medical institutions and enhanced the connection between touchpoints by considering the use of a unified theme design, making it easier for users to find corresponding clinics and play a guiding role. Cheng [38] proposed the principle of museum touchpoint construction: maintaining the association of the touchpoints and maintaining the consistency of the touchpoints, thereby bringing users a better user experience in the service process. These studies have confirmed the value of studying the association of touchpoints through some specific cases but have not formed a general method to optimize the service process from the perspective of service touchpoint association.

Service process modularization can not only improve service productivity but also improve customer satisfaction. Carlborg and Kindström [39] divide the service into 4 different types and propose the modularization strategy of service process, respectively. Luo et al. [40] realized the division of the service module by using the fuzzy tree graph on the basis of identifying and quantifying the correlation between the process activities of the service-oriented manufacturing system, so as to achieve the purpose of process improvement. Service process modularization is to analyze the whole service process and subdivide it into a series of activity elements, and then aggregate the activity elements with the same function into the same subprocess module according to dependencies between activities. Therefore, service touchpoints with high association can be divided into a module to guide service process optimization.

In view of the above research on service process optimization methods, this paper mainly studies the method of modularizing the service process from the perspective of service touchpoint association, after optimizing a single touchpoint.

2.3. DSM. A DSM maps the information dependency between tasks to a Boolean matrix, which is called Binary DSM. As shown in Figure 1, it is a design process consisting of n subtasks. The relationship between the subtasks is mapped to a matrix, the rows and columns of which correspond to the n subtasks. When the subtask ai requires the output information of the subtask aj , the matrix element $aij = 1$; otherwise, $aij = 0$. Nonzero values below the main diagonal of the DSM represent feed-forward information; nonzero values above the main diagonal represent feedback information, indicating that there is an iteration in the design process.

A DSM is derived from a directed graph, which can express the association between the corresponding activities of each node in the process through the arcs or edges between the nodes [41]. There is a one-to-one correspondence between the DSM and the directed graph, i.e., a unique directed graph can be drawn from a DSM; conversely, a unique DSM can be constructed based on a directed graph.

To establish a dynamic matrix model that reflects the essential connection of the design process, Daniel and Whitney [42] summarized the interaction between design

| | | | | | | |
|---------------------------|---|------------------------|---|---|---|---|
| | | ← Feedback information | | | | |
| ↓ Feedforward information | | a | b | c | d | e |
| | a | a | 1 | | | 1 |
| | b | 1 | b | | 1 | |
| | c | | 1 | c | | |
| | d | | 1 | | d | 1 |
| e | 1 | | | 1 | e | |

FIGURE 1: DSM.

activities (or tasks) into three forms, namely, serial dependence, parallel independence, and interactive coupling, as exhibited in Table 1.

- (1) Serial dependence relationship: there is only one acting path between two design activities; the dynamic characteristics are expressed as a series of A and B activities
- (2) Parallel independence relationship: there is no information interaction between two design activities, and there exists a completely independent mode of action; the dynamic characteristics are expressed as A and B activities that can be performed simultaneously
- (3) Interactive coupling relationship: there is information interaction between the two design activities, and the information connection between A and B is two-way, i.e., activity A requires the information of activity B, and vice versa; the dynamic characteristics are expressed by A and B, and only multiple iterations of the information between B characteristics can complete the design task

A DSM is a modeling tool that identifies the relationship between tasks by displaying the information flow more efficiently [43]. Sari et al. [44] applied a DSM to the production process of dust filters and sorted their production process relevance to solve the problem of disorder in the production process. Marjanović et al. [45] proposed an enhanced DSM sorting algorithm based on gradient optimization. This method considers the driving factors of the product architecture and provides effective suggestions for the planning process. Zhang et al. [46] conducted a modular analysis of the medical process based on a DSM and genetic algorithm (GA), which reduced the complexity of the service process and increased the flexibility between the modules. Based on the analysis of the service processes, Yang and Shan [47] defined the association between service elements with a DSM and proposed a new business module identification method. It can be seen that DSM achieves process optimization by analyzing the relationship between elements and dividing modules. Most engineering design methods are proposed for smart products rather than smart services [48]. At present, most scholars' research on

DSM-based process optimization has also been aimed at product design processes, and the research on the application of service processes is scarce. In spite of there being a few applications in service design, they are only for specific areas, and there remains a lack of a set of methods that can be applied to most service process optimization scenarios. Although DSM was originally applied in the field of product design, the tasks in the product design process and the service touchpoints in the service process play similar roles, and both are the main elements of the process. Therefore, DSM can be used to analyze the relationship between different touchpoints, so that the service process can be modularized and layered. This paper introduces service touchpoints to the DSM, and aims to construct a process optimization method that can be applied to complex service systems with multiple service touchpoints, so as to solve the problems that affect user experience in the service process.

3. DSM-Based Service Touchpoint Association Identification and Layering Method

The purpose of the DSM-based service process optimization is to modularize and sort all service touchpoints with different associations to ensure both the rationality of the service process sequence and the location of touchpoints. By considering the service process as a design process, the service touchpoint is a subtask, and the interaction between the service touchpoints can be expressed by a DSM. First, a DSM of service touchpoints in the service system is constructed with the help of the graph theory.

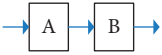
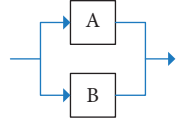
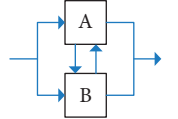
A directed graph is an ordered pair $\langle V, E \rangle$, denoted as $G = \langle V, E \rangle$, where $V = \{v_1, v_2, \dots, v_n\}$ is a finite set of nonempty nodes, E is a set of finite edges, and each edge e in E corresponds to the node pair (v_i, v_j) .

Assuming that the nodes already have the order from v_1 to v_n , then the n -order square matrix $A = (aij)n \times n$ is the adjacency matrix of G ($i, j = 1, 2, \dots, n$), where

$$aij = \begin{cases} 1, & \text{if } (v_i, v_j) \in E \text{ or } (v_j, v_i) \in E; \\ 0, & \text{otherwise.} \end{cases} \quad (1)$$

If the touchpoint in the service process is regarded as the node V in the directed graph G , and if the association between the touchpoints is regarded as the finite edge E , then the adjacency matrix of G is actually the DSM of the action association between the service touchpoints. According to the functional association between the design activities proposed by Daniel et al. (see Table 1), service touchpoints are categorized into two types, namely, touchpoints with coupled or uncoupled association, respectively. Coupled-associated touchpoints include all touchpoints that have a two-way interaction with other touchpoints, while uncoupled-associated touchpoints include independent touchpoints that are parallel to all touchpoints and have the same unidirectional dependency association with some touchpoints. In the DSM, the two types of touchpoints are modularized and layered separately.

TABLE 1: DSM and directed graphs describing the system characteristics. Associated description of three activities in the system.

| Association | Serial dependency | Parallel independent | Interactive coupling | | | | | | | | | | | | | | | | | | | | | | | | | | | |
|--------------------|--|--|---|---|---|--|---|---|---|--|--|--|---|---|---|--|---|---|---|--|--|--|---|---|---|--|---|---|---|--|
| Association form |  |  |  | | | | | | | | | | | | | | | | | | | | | | | | | | | |
| DSM representation | <table border="1" style="display: inline-table; vertical-align: middle;"> <tr><td style="background-color: black;"></td><td>A</td><td>B</td></tr> <tr><td>A</td><td style="background-color: black;"></td><td>0</td></tr> <tr><td>B</td><td>1</td><td style="background-color: black;"></td></tr> </table> | | A | B | A | | 0 | B | 1 | | <table border="1" style="display: inline-table; vertical-align: middle;"> <tr><td style="background-color: black;"></td><td>A</td><td>B</td></tr> <tr><td>A</td><td style="background-color: black;"></td><td>0</td></tr> <tr><td>B</td><td>0</td><td style="background-color: black;"></td></tr> </table> | | A | B | A | | 0 | B | 0 | | <table border="1" style="display: inline-table; vertical-align: middle;"> <tr><td style="background-color: black;"></td><td>A</td><td>B</td></tr> <tr><td>A</td><td style="background-color: black;"></td><td>1</td></tr> <tr><td>B</td><td>1</td><td style="background-color: black;"></td></tr> </table> | | A | B | A | | 1 | B | 1 | |
| | A | B | | | | | | | | | | | | | | | | | | | | | | | | | | | | |
| A | | 0 | | | | | | | | | | | | | | | | | | | | | | | | | | | | |
| B | 1 | | | | | | | | | | | | | | | | | | | | | | | | | | | | | |
| | A | B | | | | | | | | | | | | | | | | | | | | | | | | | | | | |
| A | | 0 | | | | | | | | | | | | | | | | | | | | | | | | | | | | |
| B | 0 | | | | | | | | | | | | | | | | | | | | | | | | | | | | | |
| | A | B | | | | | | | | | | | | | | | | | | | | | | | | | | | | |
| A | | 1 | | | | | | | | | | | | | | | | | | | | | | | | | | | | |
| B | 1 | | | | | | | | | | | | | | | | | | | | | | | | | | | | | |

3.1. Identification and Layering of Uncoupled-Associated Touchpoints. In the initial DSM, touchpoints that only have the same one-way dependency with some touchpoints appear as zero row sums or zero column sums. (1) If the cells of a row element in the DSM are all empty, it means that the execution of the element does not require the input of information from other activities. This type of touchpoint is then placed at the front of the row (priority). (2) If the cells of a column element in the DSM are all empty, it means that the element has not output information to other activities after completion. The touchpoint is then arranged at the end of the column to be executed later. (3) The touchpoints that are independent of all touchpoints in parallel appear as zero row sum and zero column sum. Because this type of touchpoint will not be associated with other touchpoints, it can be executed in parallel with other activities without considering the order of such touchpoints. The uncoupled-associated touchpoints can be eliminated from the initial DSM to obtain the incidence matrix, A , of the initial DSM.

3.2. Identification and Layering of Coupled-Associated Touchpoints. In the service system, the coupled association between service touchpoints is the main reason for the complicated service process. In this case, a variety of matrix operations (division, splitting, joining, clustering) can be used to optimize the matrix based on the maximization of the identification of coupling activities. The relevant knowledge of the graph theory is used to modularize and layer the coupled-associated touchpoints in the DSM to reduce service process iteration and improve service efficiency.

According to the relevant knowledge of the graph theory, the problem of identifying coupled-associated touchpoints can be transformed into a problem of strongly connected components of the graph.

Definition 1. Let u and v be the two nodes in the directed graph $G = \langle V, E \rangle$. If there is a pathway from node u to node v , it is said that node u is reachable to node v . If any two nodes are mutually reachable, then G is called a strongly connected graph [49].

Definition 2. Let $G = \langle V, E \rangle$ be a directed graph, where $V = \{v_1, v_2, \dots, v_n\}$, and it is assumed that the nodes already

have an order from v_1 to v_n . An n -order square matrix $P = (p_{ij})_{n \times n}$ ($i, j = 1, 2, \dots, n$) is defined, where

$$p_{ij} = \begin{cases} 1, & \text{there is at least one non-zero length path from } v_i \text{ to } v_j; \\ 0, & \text{otherwise.} \end{cases} \quad (2)$$

The matrix P is called the reachability matrix of the graph, and can be obtained from the correlation matrix A (A is a Boolean matrix, and its calculation rules follow those of Boolean algebra) via the following algorithm:

$$P = (A + I)r = (A + I)r - 1 \neq (A + I)r - 2 \neq \dots \neq A + I, \quad r \leq n - 1, I \text{ is the identity matrix.} \quad (3)$$

Definition 3. Let P be the reachability matrix of A and P^t be the transposed matrix of P ; then, G 's strongly connected matrix $Q = P \cap P^t$.

$$Q = P \cap P^t = \begin{bmatrix} P_{11} & P_{12} & \dots & P_{1n} \\ P_{21} & P_{22} & \dots & P_{2n} \\ \vdots & \vdots & \ddots & \vdots \\ P_{n1} & P_{n2} & \dots & P_{nn} \end{bmatrix} \cap \begin{bmatrix} P_{11} & P_{21} & \dots & P_{n1} \\ P_{12} & P_{22} & \dots & P_{n2} \\ \vdots & \vdots & \ddots & \vdots \\ P_{1n} & P_{2n} & \dots & P_{nn} \end{bmatrix} \\ = \begin{bmatrix} P_{11}^2 & P_{12}P_{21} & \dots & P_{1n}P_{n1} \\ P_{21}P_{12} & P_{22}^2 & \dots & P_{2n}P_{n2} \\ \vdots & \vdots & \ddots & \vdots \\ P_{n1}P_{1n} & P_{n2}P_{2n} & \dots & P_{nn}^2 \end{bmatrix}. \quad (4)$$

Therefore, nodes v_i and v_j are mutually reachable if and only if $p_{ij} \cdot p_{ji} = 1$. Thus, if the nonzero element of the i -th row of the matrix Q is in the j_1, j_2, \dots, j_k -th columns, then the nodes $v_i, v_{j_1}, v_{j_2}, \dots, v_{j_k}$ are in the same strongly connected component. The subgraph derived from $\{v_i, v_{j_1}, v_{j_2}, \dots, v_{j_k}\}$ is then a strongly connected component of G [49]. It can be determined from the graph theory that service touchpoints in the same strongly connected component have the largest coupled association, so they can be clustered into one module.

Definition 4. The service touchpoints in the same strongly connected component are at the same level. Therefore, one of the service touchpoints can be selected to represent a strongly connected component. The reduced matrix P' can be obtained by reducing the reachability matrix P .

Definition 5. For each node v_i , the set of its reachable nodes is defined as v_i 's reachable set $R(V_i)$. R is composed of the nodes corresponding to the columns where all elements in the row in the DSM in which V_i is are "1." Similarly, the set of nodes that reach v_i is defined as the predecessor set $A(V_i)$, which is composed of nodes corresponding to rows where all elements in the column in the DSM in which V_i is are "1" [50]. The reachable set $R(V_i)$ and the predecessor set $A(V_i)$ of the matrix A are determined according to the reachability matrix P' . The element $\sum V_n$ of $R(V_i) \cap A(V_i) = R(V_i)$ is determined. The strongly connected component represented by the touchpoint V_n is then at the highest level in the strongly connected subset L1. By removing the highest level, the L2 and L3 layers can be obtained in turn.

4. Service Process Optimization Flow Based on Service Touchpoint Association and the DSM

Service process optimization based on service touchpoint association and DSM is a process of using DSM to describe service touchpoint association on the premise of single service touchpoint optimization, and then identifying and ordering the touchpoint with matrix operation. The optimization flow is presented in Figure 2, and it includes four components: (1) optimization of single service touchpoint; (2) construction of a service touchpoint DSM; (3) identification of coupled and uncoupled service touchpoints; and (4) level analysis of service touchpoints.

4.1. Optimization of Single Service Touchpoint. Single service touchpoint optimization adopts the method proposed by BAI Zhong-hang. According to the model of analogy problem-solving, the interaction relationship between the components of the service touchpoint that affect the user experience is analogized with the substance-field model, so as to construct the service touchpoint model. Then, with the guidance of standard solutions, the problems existing between service touchpoint components are solved.

4.1.1. Identification of Problem Service Touchpoints. Obtain all service touchpoints of the service system according to field observation and other research methods. Combining the results of the survey, set up offline survey questionnaires to quantify customer satisfaction with the convenience store shopping experience, obtain problem service touchpoints, and tap new user needs.

4.1.2. Problem Service Touchpoint Model Construction. First, analyze the problem touchpoints to be optimized to find out the customer components, service provider components, and media components of the touchpoint, and then

analyze the relationship between each component (lack/harmful/insufficient) to determine the role of the service touchpoint components' types of relationships. Finally, the problem touchpoint model is constructed.

4.1.3. Optimization of Problem Service Touchpoints. Combining the analysis of the function relationship of the service touchpoint model, query and apply the type 1, 2, 3, and 5 standard solutions to solve the problem, specifically:

Step 1. Combining the function relationship of the service touch point model, query and apply the type 1 or type 2 standard solution to solve the problem. Among them, when the model interaction type is lacking, the type 1.1 standard solution is queried and applied; when the model interaction type is harmful, the type 1.2 standard solution is queried and applied; when the model interaction type is insufficient, the type 1.1 or type 2 standard solution is queried and applied. In the process of standard solution query, system resource analysis and design constraint analysis can be combined to select sublevel standard solutions.

Step 2. Query and apply the type 3 standard solution to further improve the above optimized system.

Step 3. Evaluate the optimization plan for service touchpoints. Design the survey questionnaire again to investigate the user's satisfaction with the optimized service touchpoint, and compare it with the user satisfaction before the optimization. Determine whether the service touchpoint model optimization plan is sufficient. If not, return to step 1; if the optimization plan is sufficient but you want a better plan, query and apply the type 5 standard solution.

Step 4. Query and apply type 5 standard solutions to further optimize service touchpoints.

4.2. Construction of Service Touchpoint DSM. A DSM can express the service touchpoints and their interaction in the form of a matrix. According to the directed graph of service touchpoints, a matrix of different associations of service touchpoints in the service process can be constructed. This includes the following two steps:

- (1) Draw a directed graph of the service system. First, determine the set of service touchpoints after the optimized service system for a single touchpoint and then analyze the interactions between them. Finally, determine the directed edge according to the action association between the service touchpoints and Definition 1, thereby creating a directed graph.
- (2) Build a service touchpoint DSM. Determine the initial DSM corresponding to the directed graph in step 1 and Definition 2.

4.3. Identification of Coupled and Uncoupled Service Touchpoints. Service touchpoint identification is the division of the touchpoints into two categories and their separate

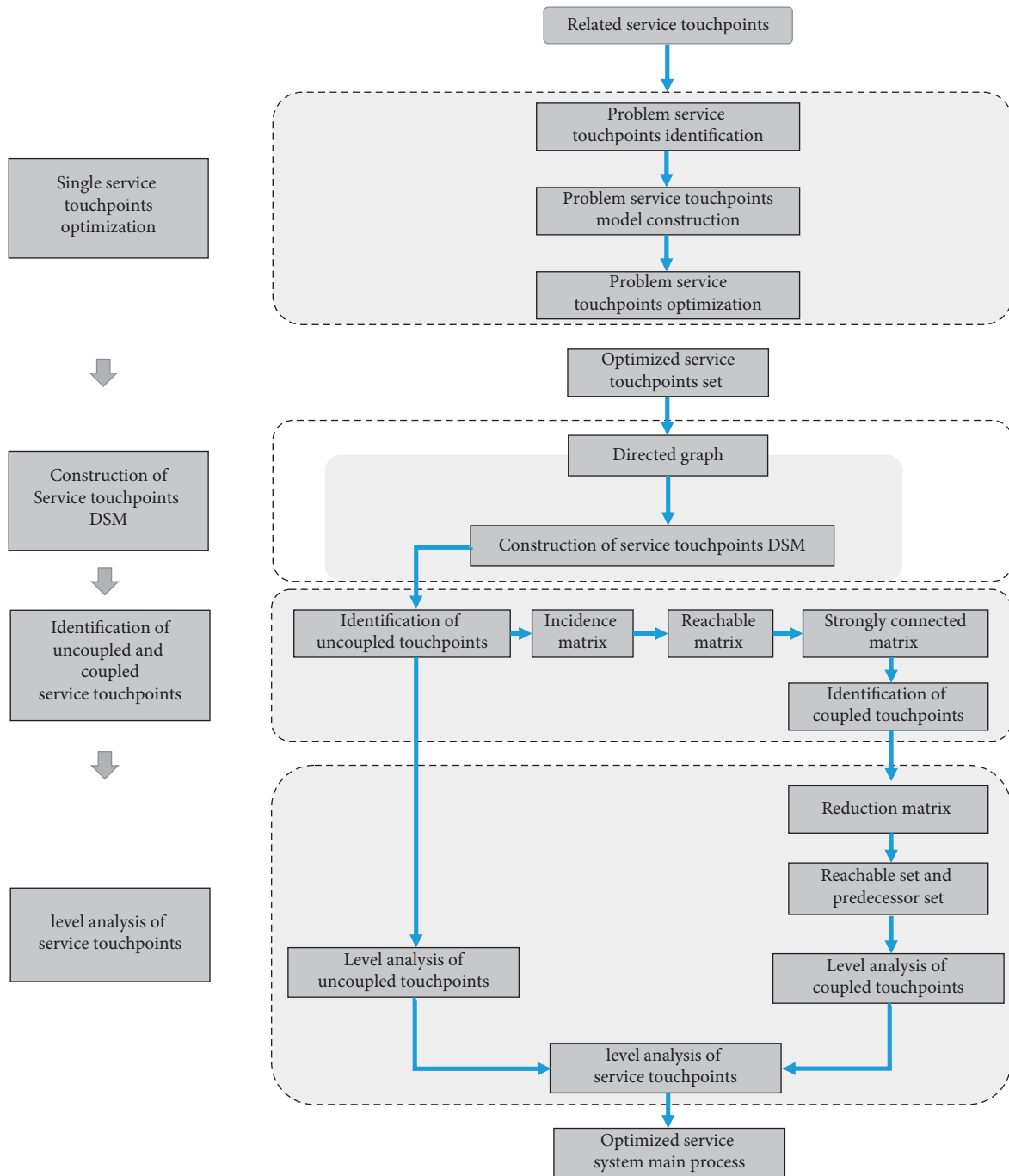


FIGURE 2: Service process optimization flow based on service touchpoints' association and DSM.

identification. This process is divided into two steps, namely, the identification of uncoupled touchpoints and the identification of coupled touchpoints.

- (1) Identification of uncoupled touchpoints. According to the initial DSM, the elements corresponding to the zero row and the zero column can be obtained; the touchpoints corresponding to these elements are uncoupled touchpoints.
- (2) Identification of coupled touchpoints. The purpose of the identification of coupled touchpoints is to

modularize touchpoints with high degrees of association via the matrix operation, which is divided into the following steps. (a) Eliminate uncoupled touchpoints to obtain the incidence matrix A . (b) Derive the reachable matrix P according to Definition 2. (c) According to Definition 3, derive the strongly connected matrix Q and the strongly connected components. (d) The service touchpoints in the strongly connected component are strongly related, so they are coupled touchpoints. The coupled touchpoints constitute a coupling module.

4.4. Level Analysis of Service Touchpoints. The establishment of a service system reachability matrix can clarify the levels of activities and structural details. The purpose of the DSM level division is to divide the coupling modules into different levels according to the priority order. The steps to find the hierarchical relationship of service touchpoints based on the reachability matrix are as follows:

- (1) Level analysis of coupled-associated touchpoints. According to the content of uncoupled-associated touchpoints identified in Sections 4.3 (1) and 3.1, the uncoupled-associated touchpoints are given either priority or endmost execution.
- (2) Level analysis of uncoupled-associated touchpoints. (a) According to Definition 4, the reduction matrix P' of the reachable matrix is obtained by reduction transformation. (b) The highest layer L1 of the coupling module is determined based on the reduction matrix P' and Definition 5. (c) The highest-level element of the coupling module is removed, and the previous step (b) is then performed. The coupling module levels L2, L3, etc., can be determined in turn.
- (3) According to the execution order of uncoupled and coupled touchpoints, the overall relationship of each touchpoint module in the service process can be obtained.

5. Convenience Store Service Process Optimization Based on Service Touchpoint Association and DSM

In the era of “new retail,” convenience stores, as one of the foremost scenarios of community consumption, have become an important entry point of user traffic. For consumers, the convenience store mainly carries emergency needs and small-scale fragmented shopping needs, and therefore provides great convenience. The development of domestic convenience stores is mainly concentrated in Beijing, Shanghai, and domestic capital cities. The new retail model of convenience stores has broad prospects in the country. However, due to their late start, various institutional facilities remain imperfect and are prone to problems such as cumbersome service processes and poor user experience.

Based on the principle of “user-centered” in service design, this paper takes the convenience store on Wu'ai Road in Tianjin as an example, to optimize the offline experience of customers in the convenience store. Specifically, it is the process of optimizing the convenience store service process from the customer's point of view, taking the optimization of a single service touchpoint as the premise, using DSM to integrate and sort all touchpoints in the customer's shopping behavior. Experience the entire service process through the method of service travel to discover the bad experiences in the process, as shown in Figure 3. By experiencing the service process, the service touchpoints of the convenience store can be obtained accordingly, as shown in Table 2.

Based on the previous survey results, a customer journey map was drawn, as shown in Figure 4. It can be clearly seen

that there are repetitions and twists in the customer shopping process.

5.1. Optimization of Single Service Touchpoint

5.1.1. Identification of Problem Service Touchpoints. A questionnaire was designed based on the service touchpoints obtained from the above survey. A Likert five-level scale was used to score the satisfaction of convenience store service touchpoints and randomly sent to the surrounding users who had experienced the convenience store. The results of the questionnaire show that customers have the lowest satisfaction in the analysis stage of the commodity competition. Exploring the specific reasons for the low satisfaction at this stage through user interviews, it is found that customers are mainly dissatisfied with the price discounts and promotional activities of the commodity, which leads to the lack of satisfactory commodity in the analysis of commodity competition. After consulting the data, it is found that the high cost of convenience stores has forced them to maintain normal operations by increasing the gross profit margin of the commodity, and the excessively high gross profit margin will affect the price of the commodity and thus affect customer satisfaction. The survey results of the “2019 China Convenience Store Prosperity Index Report” show that turnover, total monthly cost (distribution of losses, water and electricity property costs, tax company management and other miscellaneous expenses, labor costs, etc.), and monthly rent affect the cost of convenience stores. Among them, the development pressure of convenience stores mainly comes from rent cost and labor cost. This article focuses on solving the problem of labor service cost that causes low satisfaction with the touchpoint of commodity competition analysis.

5.1.2. Construction of Service Touchpoint Model of Commodity Competition Analysis. In the convenience store service system, in order to improve the user shopping experience and increase satisfaction, the convenience store staff provides customers with many manual services such as loading, replenishment, consulting, and cashier. However, the increase in labor costs has increased the selling price of the commodity and affected the satisfaction of users in the analysis of competing commodity. Analyze the touchpoint of this process: the process provides the corresponding service demand information, achieves the established design purpose, and belongs to the integrity of the model, but the interaction between the components produces harmful effects (increased cost, affecting user experience). Establish the corresponding touchpoint model, as shown in Figure 5. The customer component C is the consumer, the service provider component P is the convenience store (employee), and the media component M is the information.

5.1.3. Optimization of Problem Service Touchpoints

Step 1. Query the standard solution based on the analysis of the service touchpoint model in Figure 5.

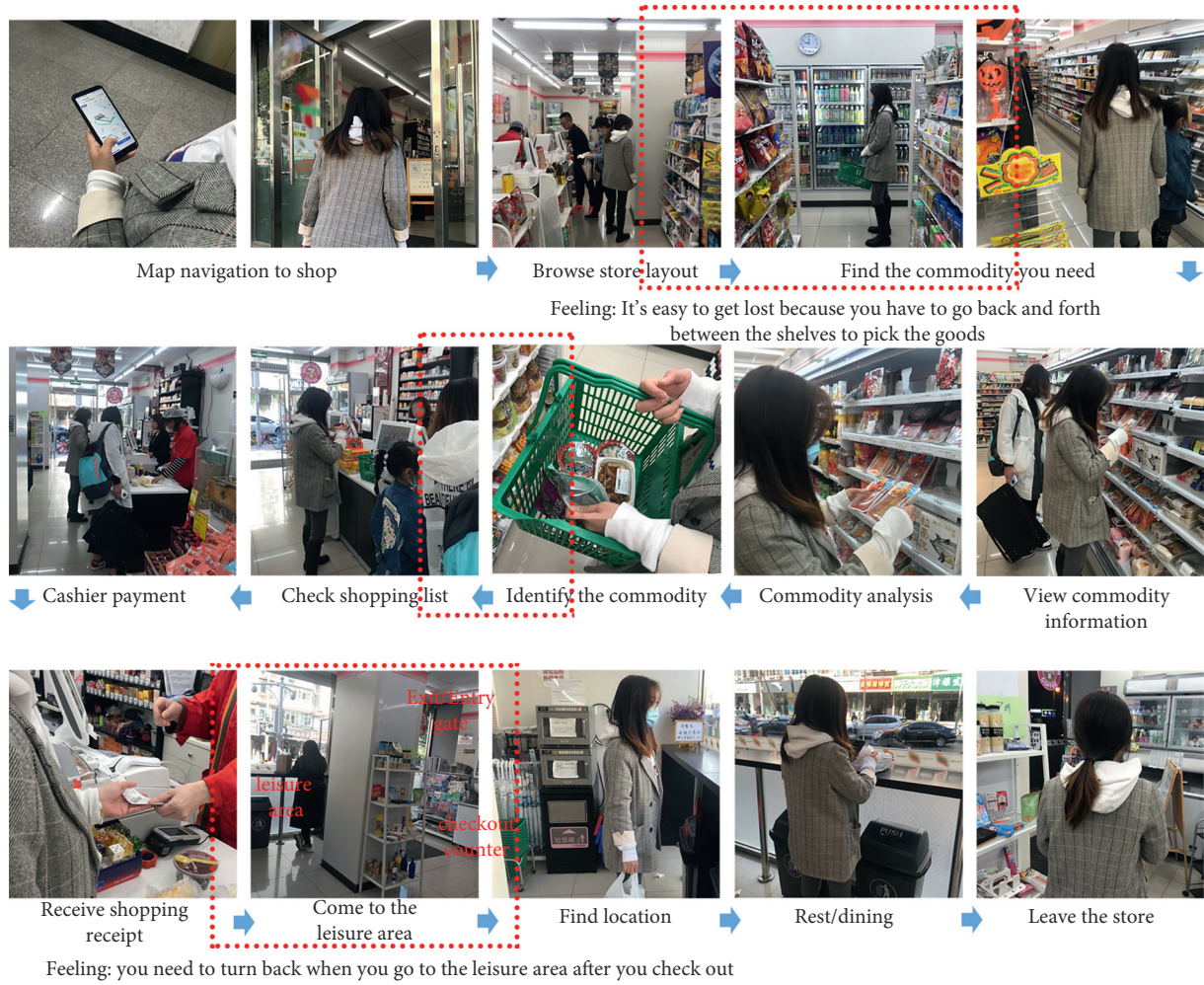


FIGURE 3: Convenience store service process experience.

TABLE 2: Summary of service touchpoints of convenience store system.

| Shopping phase | Service touchpoints |
|------------------------------|--|
| Before shopping | (a) Generate shopping demand |
| | (b) Map navigation to the store |
| Shopping | (c) Browse store layout |
| | (d) Find the commodity you need |
| | (e) View commodity information |
| | (f) Commodity analysis |
| | (g) Identify the commodity (end of shopping) |
| | (h) Check shopping list |
| | (i) Cashier payment |
| (j) Receive shopping receipt | |
| After shopping | (k) Come to the leisure area |
| | (l) Find a seat |
| | (m) Rest/dining |
| | (n) Evaluation feedback |
| | (o) Leave the store |
| | (p) After-sales service |

First, according to the standard solution classification in TRIZ, the type 1.2 (No. 9–No. 13) standard solution is initially selected for solving the problem.

Secondly, analyze the system resources and design constraints, and select the appropriate sublevel standard solution. Combined with the analysis of the internal and external resources of the touchpoint system and related design constraints, as shown in Table 3, the selection of standard solution No. 9 has both useful and harmful effects in a system. S1 and S2 do not need to be in direct contact. S3 is introduced to eliminate harmful effects to guide the specific scheme generation.

Finally, use system resources to establish specific solutions. As traditional retail companies face the dilemma of high cost and low growth, using new technologies such as the Internet to achieve “open source and reduce expenditure” and reduce corporate costs is an effective way to enhance corporate competitiveness. In response to this problem, part of the work of the convenience store is undertaken through the application of new technologies, which can reduce the number of employees employed by the convenience store and reduce or even eliminate the harmful effects caused by labor costs. Through the application of new technologies such as artificial intelligence, EPC system network, and big data, a reasonable division

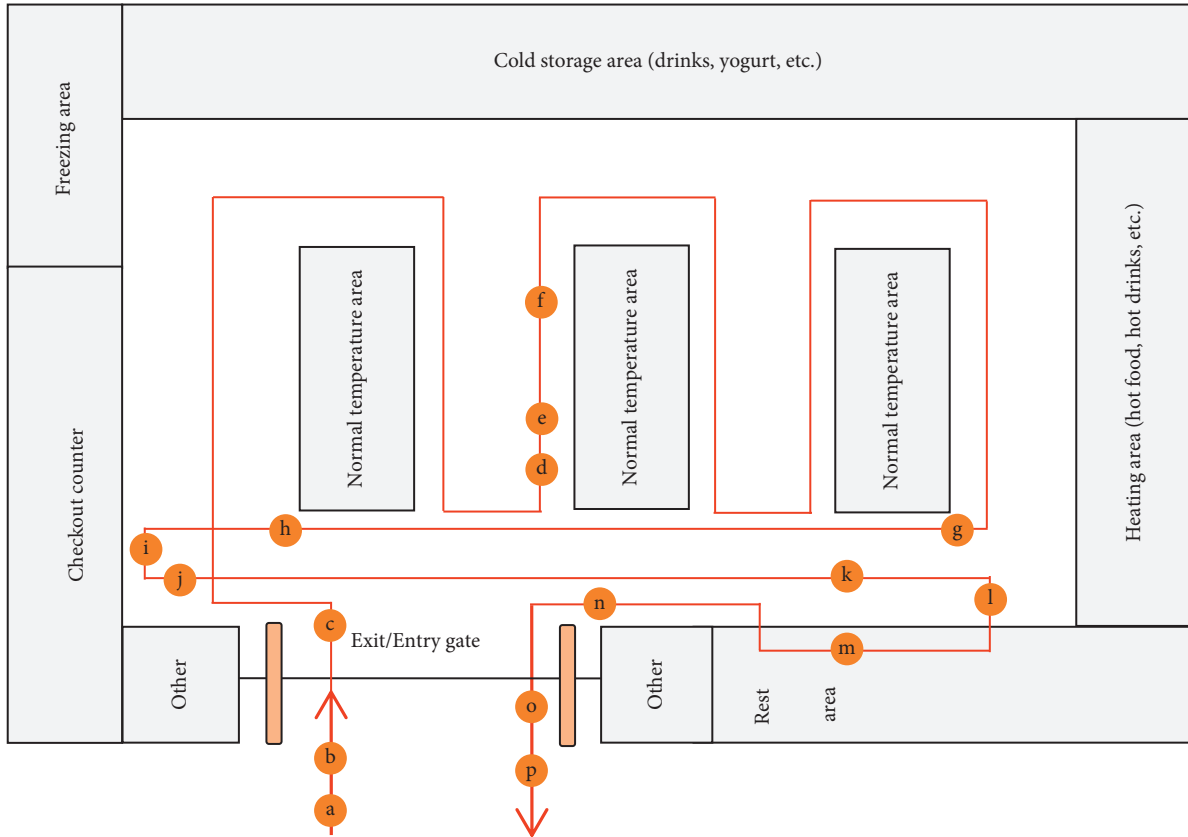


FIGURE 4: Customer journey map.

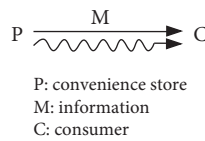


FIGURE 5: Model analysis of touchpoint of commodity competition analysis.

TABLE 3: Summary of service touchpoints of convenience store system.

| Method | Specific analysis |
|----------------------------|---|
| System resource analysis | The price of commodity in convenience stores is mainly determined by factors such as store personnel costs, rental costs, and commodity costs. The internal resources of the labor cost system at the touchpoint of commodity competition analysis mainly include new technologies, such as big data in the system, EPC system network, artificial intelligence, data resources, logistics resources, etc. System external resources mainly include brand vendors, suppliers, data resources outside the system, and the environmental field resources. |
| Design constraint analysis | First, the selected sublevel standard solution can solve the problem of labor cost; secondly, the selected sublevel standard solution should not increase or increase the cost of the merchant as much as possible; finally, the selected sublevel standard solution is technically feasible. |

of labor between humans and machines is carried out to reduce personnel input. Allocate human resources to assist and supervise the application of new technologies,

and let the machine (technology) take on mechanized and repetitive tasks, such as cashiers, customer service, and replenishment.

Such a convenience store only needs a manager, a number of self-service equipment (to perform tasks such as loading commodity, cashiers, etc.), and a background monitoring system platform, which realizes the reconstruction of the convenience store's people-goods-field. It not only reduces labor costs but also improves customer experience. The reconstructed service touchpoint model is shown in Figure 6.

Step 2. Query the type 3 standard solution to further improve the commodity competition analysis touchpoint system. The purpose is to optimize the system obtained by applying the type 1.2 standard solution to make the system composition more reasonable. In step 1, the standard solution (No. 9) was used to construct an effective and complete touchpoint model, allowing the new technology to take on manual work and thereby solve the problem of high labor costs in convenience stores. According to the guidance of type 3 standard solution, further improvements are made to the system. According to the analysis of system resources and design constraints in Table 3, standard solution No. 37 (to produce dual systems or multiple systems) is selected to continue optimizing the existing systems and transferring them to dual systems or multiple systems. In this way, a store manager, a number of self-service equipment, and a background monitoring system platform can be responsible for operating several convenience stores at the same time, so that the system can further reduce labor costs.

Step 3. After redesigning the questionnaire to analyze the optimized service touchpoints, it is found that the above concept is acceptable. At present, convenience stores have reduced labor costs by introducing new equipment, but they also need to improve the shopping experience of customers. Therefore, it is necessary to apply type 5 standard solution for further improvement.

Step 4. The type 5 standard solution is to simplify or improve the solution obtained from the standard solution operations of type 1 to type 3 (introduction of substances/utilization of existing fields in the system/state transfer/application of natural phenomena) to simplify the final problem solution. Through analysis, select No. 65 (using the existing field in the environment) in the type 5 standard solution to provide users with a leisure experience and enhance customers' shopping experience. On the basis of the existing food and beverage area, it provides convenient services such as self-service charging, self-service umbrella, self-service express delivery, downloading and printing, dating and entertainment, etc., to increase user satisfaction with shopping by increasing excitement demand.

Through the above analysis, the convenience store service system has been optimized in two aspects, and the user experience has been initially improved: the first is to change to the store manager system unmanned

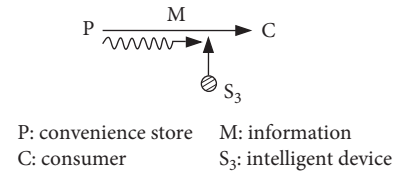


FIGURE 6: Optimized model of touchpoint of commodity competition analysis.

convenience store retail model. The payment method is changed to face ID payment, and then the cash register and cashier will be cancelled. This reduces the cost of convenience stores, while providing customers with more favorable and lower-profit commodity. It eliminates the bad experience of customers due to the high price of the commodity during the analysis of commodity competition, and also reduces the waiting time for queuing to pay. The second is to increase convenience services in the leisure area to provide customers with additional quality service experience. The touchpoints of the optimized convenience store service system are shown in Table 4:

5.2. Construction of Service Touchpoint DSM in a Convenience Store System

5.2.1. Draw a Directed Graph of the Convenience Store System. First, a directed graph of the convenience store system was drawn according to the relevant service touchpoints in the system optimized in 5.1 and their interactions, as presented in Figure 7.

5.2.2. Build the Initial DSM of Service Touchpoints of the Convenience Store System. There is a one-to-one correspondence between the directed graph and the DSM. According to the directed graph presented in Figure 7, the initial DSM of the convenience store system was determined, as exhibited in Table 5.

5.3. Identification of Uncoupled and Coupled Service Touchpoints in the Convenience Store System

5.3.1. Identification of Uncoupled-Associated Touchpoints of the Convenience Store System. The uncoupled-associated touchpoints of the initial DSM were identified and are presented in Table 5, where touchpoint A belongs to the zero row sum but no touchpoint belongs to the zero column sum. Therefore, only the touchpoint A in the convenience store system is an uncoupled-associated touchpoint.

5.3.2. Identification of Coupled-Associated Touchpoints of the Convenience Store System

- (a) The touchpoint A was eliminated from the initial DSM to obtain the incidence matrix A of the initial DSM.

TABLE 5: Initial DSM of the convenience store system.

| | a | b | c | d | e | f | g | h | i | j | k | l | m | n | o | p | q | r | s | t |
|---|---|---|---|---|---|---|---|---|---|---|---|---|---|---|---|---|---|---|---|---|
| a | | | | | | | | | | | | | | | | | | | | |
| b | 1 | | | | | | | | | | | | | | | | | | | |
| c | | 1 | | | | | | | | | | | | | | 1 | | | | |
| d | | 1 | 1 | | | | | | | | | | | | 1 | | | | | |
| e | | | | 1 | | | | | | | | | | | | | | | | |
| f | | | | 1 | 1 | | 1 | 1 | 1 | | 1 | | | | | | | | | |
| g | | | | | | 1 | | | | | | | | | | | | | | |
| h | | | | | | | 1 | | | | | | | | | | | | | |
| i | | | | | | | 1 | 1 | | | | | | | | | | | | |
| j | | | | | | | | | 1 | | | | | | | | | | | |
| k | | | | | | | | | | 1 | | | | | | | | | | |
| l | | | | | | | | | | | 1 | | | | | | | | | |
| m | | | | | | | | | | 1 | | 1 | | | | | | | | |
| n | | | | | | | | | | | | | 1 | | | | | | | |
| o | | 1 | 1 | | | | | | | | | | | | 1 | | | | | |
| p | | | | | | | | | | | | | | | | | 1 | | | |
| q | | | | | | | | | | | | | | | | 1 | 1 | | | |
| r | | | | | | | | | | | | | | | | | | 1 | | 1 |
| s | | | | | | | | | | | | | | | | | | | 1 | 1 |
| t | | | | | | | | | | | | | | | | | | | | 1 |

(c) The strongly connected matrix Q and the strongly connected component of the incidence matrix A were determined.

$$Q = \begin{pmatrix}
 1 & 0 \\
 0 & 1 & 1 & 1 & 1 & 1 & 1 & 1 & 1 & 1 & 1 & 1 & 1 & 1 & 1 & 0 & 0 & 0 & 0 & 0 & 0 \\
 0 & 1 & 1 & 1 & 1 & 1 & 1 & 1 & 1 & 1 & 1 & 1 & 1 & 1 & 1 & 0 & 0 & 0 & 0 & 0 & 0 \\
 0 & 1 & 1 & 1 & 1 & 1 & 1 & 1 & 1 & 1 & 1 & 1 & 1 & 1 & 1 & 0 & 0 & 0 & 0 & 0 & 0 \\
 0 & 1 & 1 & 1 & 1 & 1 & 1 & 1 & 1 & 1 & 1 & 1 & 1 & 1 & 1 & 0 & 0 & 0 & 0 & 0 & 0 \\
 0 & 1 & 1 & 1 & 1 & 1 & 1 & 1 & 1 & 1 & 1 & 1 & 1 & 1 & 1 & 0 & 0 & 0 & 0 & 0 & 0 \\
 0 & 1 & 1 & 1 & 1 & 1 & 1 & 1 & 1 & 1 & 1 & 1 & 1 & 1 & 1 & 0 & 0 & 0 & 0 & 0 & 0 \\
 0 & 1 & 1 & 1 & 1 & 1 & 1 & 1 & 1 & 1 & 1 & 1 & 1 & 1 & 1 & 0 & 0 & 0 & 0 & 0 & 0 \\
 0 & 1 & 1 & 1 & 1 & 1 & 1 & 1 & 1 & 1 & 1 & 1 & 1 & 1 & 1 & 0 & 0 & 0 & 0 & 0 & 0 \\
 0 & 1 & 1 & 1 & 1 & 1 & 1 & 1 & 1 & 1 & 1 & 1 & 1 & 1 & 1 & 0 & 0 & 0 & 0 & 0 & 0 \\
 0 & 0 & 0 & 0 & 0 & 0 & 0 & 0 & 0 & 0 & 0 & 0 & 0 & 0 & 0 & 1 & 0 & 0 & 0 & 0 & 0 \\
 0 & 0 & 0 & 0 & 0 & 0 & 0 & 0 & 0 & 0 & 0 & 0 & 0 & 0 & 0 & 1 & 0 & 0 & 0 & 0 & 0 \\
 0 & 0 & 0 & 0 & 0 & 0 & 0 & 0 & 0 & 0 & 0 & 0 & 0 & 0 & 0 & 0 & 1 & 1 & 1 & 1 & 1 \\
 0 & 0 & 0 & 0 & 0 & 0 & 0 & 0 & 0 & 0 & 0 & 0 & 0 & 0 & 0 & 0 & 1 & 1 & 1 & 1 & 1 \\
 0 & 0 & 0 & 0 & 0 & 0 & 0 & 0 & 0 & 0 & 0 & 0 & 0 & 0 & 0 & 0 & 1 & 1 & 1 & 1 & 1
 \end{pmatrix}. \tag{7}$$

According to the strongly connected matrix, there are five strongly connected components in the incidence matrix A : $\{b\}$, $\{c, d, e, f, g, h, i, j, k, l, m, n, o\}$, $\{p\}$, $\{q\}$, and $\{r, s, t\}$. After excluding the coupled touchpoints, the convenience store service process was divided into five modules.

5.4. Level Analysis of Convenience Store Service Touchpoints.

(1)

Level analysis of uncoupled-associated convenience store service touchpoints. Touchpoint A belongs to the zero line sum, so arranging the touchpoint at the front of the line takes precedence.

(2) Level analysis of coupled-associated convenience store service touchpoints.

$$p1 = \begin{matrix} 1 & 0 & 0 & 0 & 0 \\ 1 & 1 & 0 & 0 & 0 \\ 1 & 1 & 1 & 0 & 0. \\ 1 & 1 & 1 & 1 & 0 \\ 1 & 1 & 1 & 1 & 1 \end{matrix} \quad (8)$$

(a) Touchpoint c was selected to represent the strongly connected components $\{c, d, e, f, g, h, i, j, k, l, m, n, o\}$. Touchpoint r was selected to represent the strongly connected components $\{r, s, t\}$. The corresponding rows and columns of $\{j, k, l, m, n, o\}$ with $\{s, t\}$ in the convenience store reachable matrix were deleted, and a 5×5 reduced matrix P' was obtained.

(b) The reachable set $R(V_i)$ and the predecessor set $A(V_i)$ of the incidence matrix A were determined according to the reduction matrix P' , and the intersection $R(V_i) \cap A(V_i)$ was determined from the predecessor set and the reachable set, as shown in Table 6. The element of $R(V_i) \cap A(V_i) = R(V_i)$ was found to be b , and b is then the highest layer L1 in the strongly connected subset.

(c) The highest level of the coupling set was removed, and step (b) was repeated. In turn, the level relationship of the coupling set was determined.

(3) According to the order of coupled- and uncoupled-associated touchpoints, the overall level relationship of each touchpoint module was obtained. As shown in Table 7, the convenience store service process was divided into 6 levels in total.

By combining the touchpoint level relationship table and the service system directed graph established in Section 5.2, a modularized and layered directed graph of the convenience store system was obtained, as presented in Figure 8.

6. Results and Discussion

By comparing the directed graph after optimization with that before optimization, it is evident that the directed graph before optimization is chaotic and unorganized; the number of modules is 0; and it is not clear which touchpoints have

strong associations. It is possible to arrange the strongly associated touchpoints in different positions or with no association, and the process is unclear. It needs to go back and find to complete the entire process, which would affect the service experience.

The directed graph after clustering identification and level division is divided into 6 simpler modules for information transmission. The service touchpoints in each module maintain strong association relationships, while each module maintains a weak association relationship. The level relationship is clear at a glance, and the order of execution is clearly visible. The optimized directed graph provides effective guidance for the logical design of the orientation, layout, location, and distance between each service touchpoint, thereby improving the service experience. Even if the existing conditions cannot be changed, some eye-catching related information can be added at specific locations according to the flowchart to visually associate the touchpoints, thereby improving the service experience.

According to the optimized directed graph, the main flow chart of the convenience store service system was redesigned, including the layout of the touchpoints. The execution order of the touchpoints should correspond to the level in Figure 8. For example, touchpoint p (find seat) belongs to level 4, and touchpoint q (entertainment/friends/convenience service) belongs to level 5, so p must be executed before q ; The touchpoints in any level should not be set too far away, it is better to set a guide flag. For example, touchpoint l (determine payment) and o (come to leisure area)) belong to the same level, so the location should be as close as possible when designing the process. Before optimization, the two touchpoints were too far apart, causing customers to experience repeated routes; change the arrangement of shelves from side-by-side to surrounding. The aim is to prevent customers having to repeat the route multiple times between touchpoint e (browse the store layout) and touchpoint i (end of shopping). The customer shopping process mainly includes the following stages. As presented in Figure 9. (1) The face/code-scanning entry stage: the customer enters the store by scanning his or her face or scanning a code from an app (first-time entry requires registration). The entry gate can communicate customer information to the store manager cloud server. (2) The product selection stage: when a customer picks up goods from a shelf, the intelligent shelf can automatically record the customer's shopping list based on the customer's information in the cloud, and can monitor the quantity and type of commodity. (3) The face/code-scanning payment stage: when the customer arrives at the exit gate that is connected to the cloud service to scan his or her face or code, the gate screen displays the customer's shopping information. The exit gate then opens and the customer walks out of the store to complete his or her shopping. Within 15 minutes, customers can receive an electronic shopping list. (4) The entertainment stage: customers can choose to dine in the entertainment area, download and print documents, rent and lend media, collect packages, and other activities.

TABLE 6: Reachable set, predecessor set, and their intersection.

| Node | Reachable set $R(V_i)$ | Predecessor set $\underline{A}(V_i)$ | $R(V_i) \cap \underline{A}(V_i)$ |
|----------|------------------------------|--------------------------------------|----------------------------------|
| b | b | b, $\sum c$, p, q, $\sum r$ | b |
| $\sum c$ | b, $\sum c$ | $\sum c$, p, q, $\sum r$ | $\sum c$ |
| p | b, $\sum c$, p | p, q, $\sum r$ | p |
| q | b, $\sum c$, p, q | q, $\sum r$ | q |
| $\sum r$ | b, $\sum c$, p, q, $\sum r$ | $\sum r$ | $\sum r$ |

TABLE 7: Overall level relationship table of the convenience store touchpoints.

| Level | Touchpoints |
|-------|---------------------------------------|
| L1 | a |
| L2 | b |
| L3 | c, d, e, f, g, h, i, j, k, l, m, n, o |
| L4 | p |
| L5 | q |
| L6 | r, s, t |

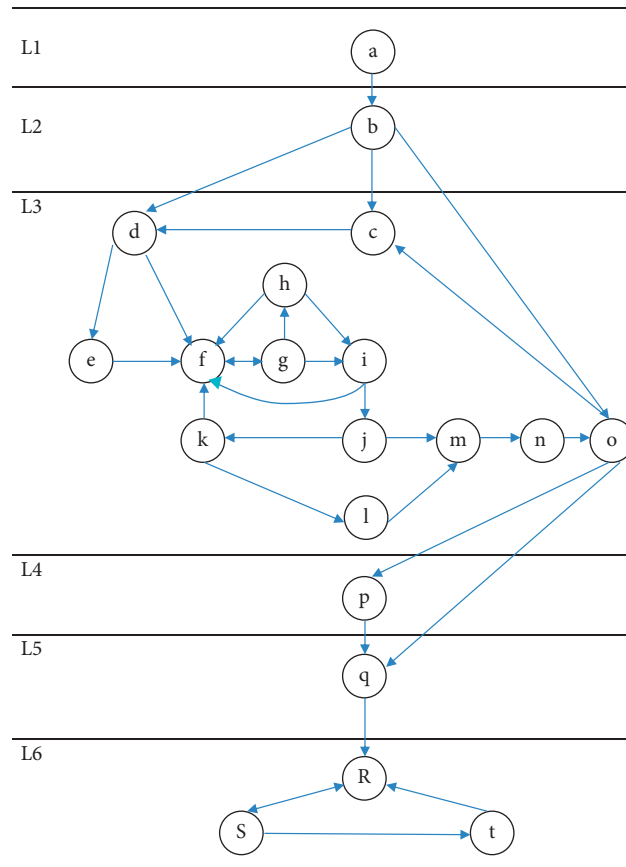


FIGURE 8: The directed graph of the optimized convenience store system.

Compared with the customer journey map before optimization, the optimized flowchart does not have repeated tortuous routes, and it relies on new technologies such as big data, cloud platforms, and EPC system network to provide users with a brand new and smoother offline retail shopping experience. In a convenience store, users can not only obtain high-quality and low-cost commodity efficiently but also

enjoy convenient services such as downloading and printing, renting and lending, and picking up and collecting express delivery. At the same time, it also empowers users to successfully complete their shopping without the interruption of staff, which enhances the user's sense of pleasure in the shopping process and the sense of accomplishment of successful shopping.

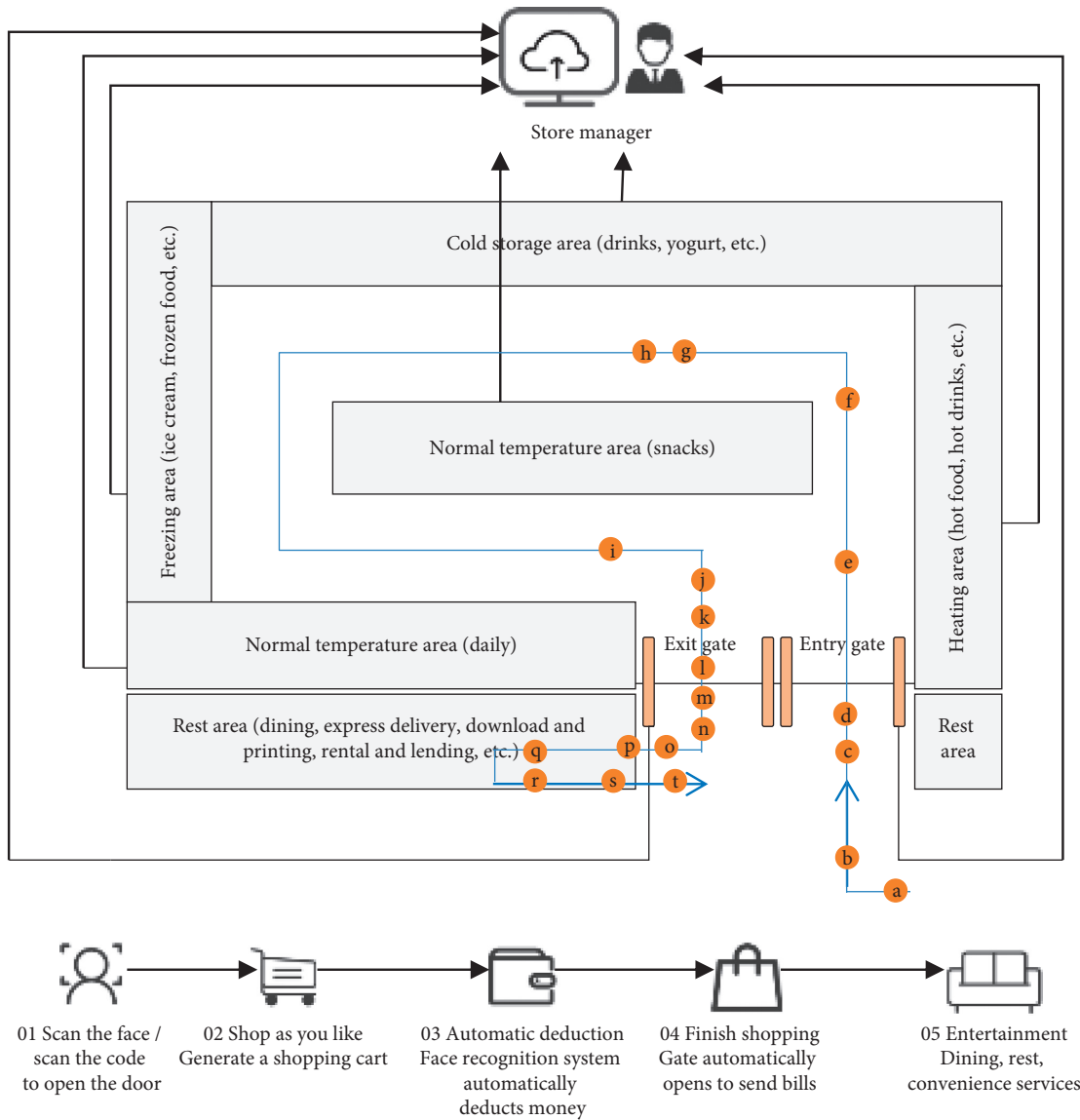


FIGURE 9: The main flowchart of the convenience store service system.

Carrying out modularization and layering on the service process and decomposing the complex service process into modules composed of different service touchpoints has the following beneficial effects on the operation of convenience stores: (1) The optimization of the service process enables customers to enjoy a better experience, enhances the reputation of merchants, and correspondingly brings better benefits to convenience stores. (2) Able to achieve modular management of services to give full play to the expertise of each department, and effectively control the generation and removal of service problems. For example, level 3 is managed by the business department, while level 6 is managed by the after-sales department. (3) It is conducive to the derivation of service organizations and the realization of outsourcing agents to obtain economies of scale. Service outsourcing can be implemented by the map navigation included in Level 2 and convenient services included in Level 5. The purpose is to use the advantages of external resources to obtain more benefits.

7. Conclusion

This paper expands the application scope of the DSM to the optimization of service design from the perspective of the association of service touchpoints. This paper systematically introduces a service process optimization flow based on the DSM on the premise of single touchpoint optimization, including the construction of a service touchpoint DSM, the identification of service touchpoints, and the level analysis of service touchpoints. Case studies have demonstrated that a DSM can achieve the optimization of complex service processes by fully taking into account the association of touchpoints. It avoids the one-sidedness caused by the traditional optimization method, which only considers a single touchpoint and cannot reasonably organize the logical association between the touchpoints.

The goal of this work was to improve the service experience and provide a reference for complex service process

optimization; however, there remained certain limitations to this study. In the model proposed in this paper, the touchpoints with high association are modularized and layered; however, the order of the touchpoints within the module after modularization is not considered. In addition, customer needs should be taken into account when optimizing service processes. Therefore, the proposed method of complex service process optimization from the perspective of service touchpoints requires further study.

Data Availability

The relevant data in this article were obtained by the author's personal investigation and research and can be made available upon request.

Conflicts of Interest

The authors declare that there are no conflicts of interest regarding the publication of this paper.

References

- [1] R. Thakur and D. Hale, "Service innovation: a comparative study of U.S. and Indian service firms," *Journal of Business Research*, vol. 66, no. 8, pp. 1108–1123, 2013.
- [2] J. Vink, B. Edvardsson, K. Wetter-Edman, and B. Tronvoll, "Reshaping mental models—enabling innovation through service design," *Journal of Service Management*, vol. 30, no. 1, pp. 75–104, 2019.
- [3] K. Wetter-Edman, J. Vink, and J. Blomkvist, "Staging aesthetic disruption through design methods for service innovation," *Design Studies*, vol. 55, pp. 5–26, 2018.
- [4] A. L. Ostrom, M. J. Bitner, S. W. Brown et al., "Moving forward and making a difference: research priorities for the science of service," *Journal of Service Research*, vol. 13, no. 1, pp. 4–36, 2010.
- [5] M. P. Joly, J. G. Teixeira, L. Patrício, and D. Sangiorgi, "Leveraging service design as a multidisciplinary approach to service innovation," *Journal of Service Management*, vol. 30, pp. 681–715, 2019.
- [6] Y.-H. Wang, C.-H. Lee, and A. J. C. Trappey, "Service design blueprint approach incorporating TRIZ and service QFD for a meal ordering system: a case study," *Computers & Industrial Engineering*, vol. 107, pp. 388–400, 2017.
- [7] Q. Luo, "User-oriented service design and innovation," in *Proceedings of the 2011 International Conference of Information Technology, Computer Engineering and Management Sciences*, Nanjing, China, 2011.
- [8] C. Deng, "Touch the service touchpoints," *Zhuangshi*, vol. 6, pp. 13–17, 2010.
- [9] X. Xiangyang, "Interaction design: from logic of things to logic of behaviors," *Zhuangshi*, vol. 1, pp. 58–62, 2015.
- [10] C.-H. Lee, X. Zhao, and Y.-C. Lee, "Service quality driven approach for innovative retail service system design and evaluation: a case study," *Computers & Industrial Engineering*, vol. 135, pp. 275–285, 2019.
- [11] E. Pantano and M. Viassone, "Engaging consumers on new integrated multichannel retail settings: challenges for retailers," *Journal of Retailing and Consumer Services*, vol. 25, pp. 106–114, 2015.
- [12] C. Meyer and A. Schwager, "Understanding customer experience," *Harvard Business Review*, vol. 85, no. 2, pp. 116–157, 2007.
- [13] R. Halvorsrud, K. Kvale, and A. Følstad, "Improving service quality through customer journey analysis," *Journal of Service Theory and Practice*, vol. 26, pp. 840–867, 2007.
- [14] S. Baxendale, E. K. Macdonald, and H. N. Wilson, "The impact of different touchpoints on brand consideration," *Journal of Retailing*, vol. 91, no. 2, pp. 235–253, 2015.
- [15] M. S. Rosenbaum, M. L. Otolara, and G. C. Ramirez, "How to create a realistic customer journey map," *Business Horizons*, vol. 60, no. 1, pp. 143–150, 2017.
- [16] C.-H. Lee, C.-H. Chen, F. Li, and A.-J. Shie, "Customized and knowledge-centric service design model integrating case-based reasoning and TRIZ," *Expert Systems with Applications*, vol. 143, Article ID 113062, 2020.
- [17] C.-H. Lee, Y.-H. Wang, and A. J. C. Trappey, "Service design for intelligent parking based on theory of inventive problem solving and service blueprint," *Advanced Engineering Informatics*, vol. 29, no. 3, pp. 295–306, 2015.
- [18] Y.-H. Wang, C.-H. Lee, and A. J. C. Trappey, "Modularized design-oriented systematic inventive thinking approach supporting collaborative service innovations," *Advanced Engineering Informatics*, vol. 33, pp. 300–313, 2017.
- [19] C.-H. Lee, C.-H. Chen, and Y.-C. Lee, "Customer requirement-driven design method and computer-aided design system for supporting service innovation conceptualization handling," *Advanced Engineering Informatics*, vol. 45, Article ID 101117, 2020.
- [20] S. Clatworthy, "Service innovation through touch-points: development of an innovation toolkit for the first stages of new service development," *International Journal of Design*, vol. 5, pp. 15–28, 2011.
- [21] D. V. Steward, "The design structure system: a method for managing the design of complex systems," *IEEE Transactions on Engineering Management*, vol. 28, no. 3, pp. 71–74, 1981.
- [22] T. R. Browning, "Applying the design structure matrix to system decomposition and integration problems: a review and new directions," *IEEE Transactions on Engineering Management*, vol. 48, no. 3, pp. 292–306, 2001.
- [23] P. Ben-hong and L. Qian, "Optimization to service modular: based on PCN," *Technology Economics*, vol. 34, pp. 14–20, 2015.
- [24] Z. Bai, H. Sun, and J.-l. Zhang, "Service contact point optimization based on TRIZ and analog design," *Packaging Engineering*, vol. 41, no. 16, pp. 91–97, 2020.
- [25] L. A. Mohr and M. J. Bitner, "The role of employee effort in satisfaction with service transactions," *Journal of Business Research*, vol. 32, no. 3, pp. 239–252, 1995.
- [26] G. L. Shostack, *Planning the Service Encounter*, Lexington Books, Lexington, MA, USA, 1985.
- [27] B. Larivière, D. Bowen, T. W. Andreassen et al., "'Service encounter 2.0': an investigation into the roles of technology, employees and customers," *Journal of Business Research*, vol. 79, pp. 238–246, 2017.
- [28] M. R. Solomon, C. Surprenant, J. A. Czepiel, and E. G. Gutman, "A role theory perspective on dyadic interactions: the service encounter," *Journal of Marketing*, vol. 49, no. 1, p. 99, 1985.
- [29] M. Zhu, X. Yan, and Q. Yuan, "Service encounter theory and its application and prospect in information system," *Journal of Modern Information*, vol. 39, pp. 149–159, 2019.
- [30] Y. D. Volpi and S. R. Paulino, "The sustainability of services: considerations on the materiality of accommodation services

- from the concept of life cycle thinking,” *Journal of Cleaner Production*, vol. 194, pp. 327–334, 2018.
- [31] M. E. Pullman and M. A. Gross, “Ability of experience design elements to elicit emotions and loyalty behaviors,” *Decision Sciences*, vol. 35, no. 3, pp. 551–578, 2004.
- [32] W. Wang, T. Wei, Y. Zhang, and Y. Wang, “A method of intelligent product design cue construction based on customer touchpoint correlation analysis and positive creativity theory,” *Advances in Mechanical Engineering*, vol. 11, pp. 1–11, 2019.
- [33] S. Kim, J. J. E. Chang, H. H. Park et al., “Autonomous taxi service design and user experience,” *International Journal of Human-Computer Interaction*, vol. 36, no. 5, pp. 429–448, 2019.
- [34] C. H. Lee, C. H. Chen, C. Lin, F. Li, and X. Zhao, “Developing a quick response product configuration system under industry 4.0 based on customer requirement modelling and optimization method,” *Applied Sciences*, vol. 9, no. 23, p. 5004, 2019.
- [35] L. Patrício, R. P. Fisk, J. Falcão e Cunha, and L. Constantine, “Multilevel service design: from customer value constellation to service experience blueprinting,” *Journal of Service Research*, vol. 14, no. 2, pp. 180–200, 2011.
- [36] V. Roto, H. Väättäjä, E. Law, and R. Powers, “Experience design for multiple customer touchpoints,” in *Proceedings of the 9th Nordic Conference on Human-Computer Interaction (NordiCHI)*, New York, NY, USA, 2016.
- [37] X. Li, “Research on the service design of pediatric medical institution,” *Zhuangshi*, vol. 2, pp. 106–109, 2018.
- [38] J. Cheng, *Research on the construction of the touch point of museum display from the perspective of service design*, Ph.D. thesis, Central China Normal University, Wuhan, China, 2017.
- [39] P. Carlborg and D. Kindström, “Service process modularization and modular strategies,” *Journal of Business & Industrial Marketing*, vol. 29, no. 4, pp. 313–323, 2014.
- [40] J. Luo, Y. Zhang, and Y. Peng, “Research on service-oriented manufacturing system process improvements based on service blueprint,” *China Mechanical Engineering*, vol. 29, pp. 2250–2258, 2018.
- [41] A. Tripathy and S. D. Eppinger, “Structuring work distribution for global product development organizations,” *Production and Operations Management*, vol. 22, no. 6, pp. 1557–1575, 2013.
- [42] E. Danie and Whitney, “Designing the design process,” *Research in Engineering Design*, vol. 2, pp. 3–13, 1990.
- [43] M. S. Park, G. Y. Cho, H. S. Lee, and S. K. Kwon, “BIM design management process using the dependency structure matrix at the introduction phase,” *Journal of the Architectural Institute of Korea Planning & Design*, vol. 28, pp. 37–45, 2012.
- [44] R. M. Sari, A. R. Matondang, and K. Syahputri, “Sequencing of dust filter production process using design structure matrix (DSM),” *IOP Conference Series: Materials Science and Engineering*, vol. 288, pp. 1–6, 2018.
- [45] D. Marjanović, M. Štorga, S. Škec, N. Bojčetić, and N. Pavković, “Augmented DSM sequencing to support product development planning,” in *Proceedings of the 2018 International Design Conference*, New Orleans, LA, USA, 2018.
- [46] X. Zhang, S. Ma, and S. Chen, “Healthcare process modularization using design structure matrix,” *Advanced Engineering Informatics*, vol. 39, pp. 320–330, 2019.
- [47] L. Yang and M. Y. Shan, “Service module identification for mass customization,” in *Proceedings of the 2008 International Conference of Production and Operation Management*, Xiamen, China, 2008.
- [48] J.-c. Cong, C.-H. Chen, P. Zheng, X. Li, and Z. Wang, “A holistic relook at engineering design methodologies for smart product-service systems development,” *Journal of Cleaner Production*, vol. 272, Article ID 122737, 2020.
- [49] Y. Fu and X. Gu, *Discrete Mathematics and Its Applications*, Electronic Industry Press, Beijing, China, 1997.
- [50] Y. Lin, *Research on approaches of business process modeling and reengineering based on design structure matrix (DSM)*, Ph.D. thesis, Northeastern University, Shenyang, China, 2011.

Research Article

Understanding Ecosystem Complexity via Application of a Process-Based State Space rather than a Potential Surface

C. Gaucherel ¹, F. Pommereau,² and C. Hély³

¹AMAP-INRAE, CIRAD, CNRS, IRD, Université de Montpellier, Montpellier, France

²IBISC, Université d'Evry, Evry, France

³Institut des Sciences de l'Évolution de Montpellier (ISEM), EPHE, PSL University, Université de Montpellier, CNRS, IRD, Montpellier, France

Correspondence should be addressed to C. Gaucherel; gaucherel@cirad.fr

Received 19 June 2020; Accepted 18 September 2020; Published 6 October 2020

Academic Editor: Tomas Veloz

Copyright © 2020 C. Gaucherel et al. This is an open access article distributed under the Creative Commons Attribution License, which permits unrestricted use, distribution, and reproduction in any medium, provided the original work is properly cited.

Ecosystems are complex objects, simultaneously combining biotic, abiotic, and human components and processes. Ecologists still struggle to understand ecosystems, and one main method for achieving an understanding consists in computing potential surfaces based on physical dynamical systems. We argue in this conceptual paper that the foundations of this analogy between physical and ecological systems are inappropriate and aim to propose a new method that better reflects the properties of ecosystems, especially complex, historical nonergodic systems, to which physical concepts are not well suited. As an alternative proposition, we have developed rigorous possibilistic, process-based models inspired by the discrete-event systems found in computer science and produced a panel of outputs and tools to analyze the system dynamics under examination. The state space computed by these kinds of discrete ecosystem models provides a relevant concept for a holistic understanding of the dynamics of an ecosystem and its abovementioned properties. Taking as a specific example an ecosystem simplified to its process interaction network, we show here how to proceed and why a state space is more appropriate than a corresponding potential surface.

1. Introduction

Most ecologists would admit that ecosystems are complex, although some might appear simple. Ecosystems appear to form emergent structures (e.g., [1, 2]), exhibit nonlinear properties (e.g., [3, 4]), and be clearly out of equilibrium (e.g., [5, 6]). Moreover, the fact that most ecosystems today strongly interact with society and contain several human groups heightens this feeling of complexity [7, 8]. Yet, most studies focus on just some components of the ecosystem, either biotic (e.g., species community), abiotic (e.g., climate, element cycles), or anthropic (ecosystem services), and a definitive demonstration of integrated ecosystem complexity is still lacking. In addition, most analyses focus on complexity at a specific time, often concentrating on patterns rather than on long-term dynamics [1, 9]. In this conceptual paper, we propose a detailed methodology for the long-term study of ecosystem dynamics and for qualifying their complexity using process-based models.

Ecosystem complexity is derived first and foremost from the combination of biotic, abiotic, and human components which also form a tangled web of continuous interactions [10–12]. Some socioecological systems seem quite simple, with few components and few processes, but these cases remain scarce. Theoretical ecologists with a true interest in the whole (socio)ecosystem, not just some parts of it, have spent decades debating ecosystem dynamics and their stability or resilience [3, 13]. Whether a potential function or a resilience surface [14–17], synthetic and conceptual models should be able to fit any specific trajectory observed in the ecosystem under study. The recent nature of ecology as a discipline and mostly partial and short-term observations provide us with a limited view of ecosystems. As a result, such models often focus on short-term dynamics and mainly on pattern analyses [9, 18, 19]. Models of complexity in ecology thus remain phenomenological. For this reason, even partially validated process-based models of ecosystems offer a promising opportunity to produce understandable,

robust long-term dynamics. Here, we intend to review the mainstream models of ecosystem dynamics, to demonstrate some of their limitations, and finally, to provide a process-based methodology that will hopefully bypass such limitations.

When studying or managing an ecosystem, be it temperate or tropical, terrestrial or aquatic, natural or anthropic, a suggested preliminary step is an exhaustive understanding of its overall dynamics. Practically speaking, ecologists today investigate whether or not a specific ecosystem studied is stable [3, 4], resilient [2, 20], and moreover how far from any tipping points or catastrophic shifts it lies [21–23]. Physics has long provided powerful tools for these objectives with regard to physical systems. For example, physical models often provide ordinary differential equation (ODE) systems and summarize the most probable dynamics (and sharp changes) into phase spaces and potential functions [24, 25]. Such syntheses then enable confident predictions of future system states, to prevent unwanted states and advise on expected states.

Despite recent attempts, such synthetic models for ecosystems are still lacking. Some theoretical models have been proposed [26–29], but they rarely fit and accurately calibrate observations, or if so, rarely study more than one state variable (e.g., biomass and/or annual rainfall). In addition, such models are probabilistic in essence, whereas possibilistic models would afford exhaustive exploration of complex (eco)system dynamics. Here, our first and most important objective is to provide ecologists with a new conceptual framework for achieving this goal of exhaustive computation of any ecosystem dynamics [30, 31], and to simultaneously illustrate the approach in a complex case study. Moreover, the mainstream models used today in ecosystem ecology still suffer from several limitations [32]. Our second objective is to list and debate these chief limitations.

For this purpose, we recently developed an original type of models [18, 30], based on the *discrete event and qualitative systems* commonly used in theoretical computer sciences [33–35]. Here, we will illustrate the approach with a qualitative Petri net in the case of an insect (termite) colony [36], which is presumed to mimic an ecosystem undergoing abrupt qualitative change, and potentially experiencing strong long-term disturbances. We will show how the qualitative *state space* (sometimes called the reachability or labeled transition space) of the modeled insect colony provides a relevant synthesis of this ecosystem’s dynamics. Finally, we will analyze this state space to verify that it is not subject to the same limitations as identified in other ecological models, and to suggest future directions.

2. State Space of a Qualitative Ecosystem

Here, we propose an original model intended to represent the overall dynamics of any complex (socio) ecosystem. The proposition states that it is possible to exhaustively capture overall ecosystem behavior on the basis of a qualitative, discrete, and integrated description of its interactions [18]. The interactions within a given ecosystem are all the relevant

processes involved in the system dynamics, hence the process-based model. This kind of discrete model has already proved useful, and interested readers may refer to papers describing the mathematical details of the method and some applications [30, 37, 38]. In the present study, we illustrate such an approach with the specific case of a simplified theoretical insect colony. This termite colony is assumed to mimic a typical ecosystem comprising biotic, abiotic, and anthropogenic-like (the farming termites) components [36], as well as all their associated (i.e., bioecological, physico-chemical, and socioeconomic) interactions. The output from the model consists in a discrete qualitative *state space* of the ecosystem, grouping all the states that the ecosystem may potentially reach from an initial state and thus all its trajectories.

We chose to model eusocial insect colonies for the reasons that they experience drastic change (*tipping points*, TPs) over time, but any other ecosystem-like models may be used (Figure 1(a)). We chose to work on Macrotermitinae termites [36] which, like some ant species, construct large colonies (up to millions of inhabitants), [39] sometimes considered as super-organisms with complex functioning. These termites cultivate fungi in special chambers, build aerial structures (called *mounds*) to improve air circulation, and divide their nests into a royal chamber, fungus chambers, and egg rooms (Figure 1(a)). Given the ability of this eusocial species to develop food production, termites might also be considered as mimicking humans (farmers) in agrosystems.

One way of conceptualizing the ecosystem under investigation is to represent it as a graph (i.e., network) of components connected by processes, the interaction network, whatever the interactions (Figure 1(b)). The model is fully qualitative (Boolean) and allows components to be present or absent only. The resulting *ecosystem graph* is then manipulated using a rigorous model based on a discrete Petri net to formalize any change in the topology of this graph (i.e., the neighboring relationships between present components). Developed in computer science [31, 35], Petri nets are commonly used in biology (e.g., [40, 41]) and are powerful tools for rigorous formalization of changes in network topologies occurring during system dynamics. Such Petri nets are radically different from traditional ecological models based on ODE equations (e.g., [2, 4]) in that they deal with topological changes in interactions during the simulation rather than dynamics carried by a fixed topology. Our approach might be closer in spirit to other attempts, such as Richard Levins’ “loop analysis” dedicated to linear systems and its most recent versions of qualitative models [42].

Discrete-event models provide *state space* outputs that can be readily analyzed to highlight relatively stable (or resilient) dynamics, tipping points, and any other specific trajectories. Such state spaces show similarities with the state-and-transition models that have proved useful in modeling ecological succession [43], except that our state spaces are deduced from predefined processes instead of being directly drawn from observations. Hence, such models are possibilistic models as they exhaustively explore the

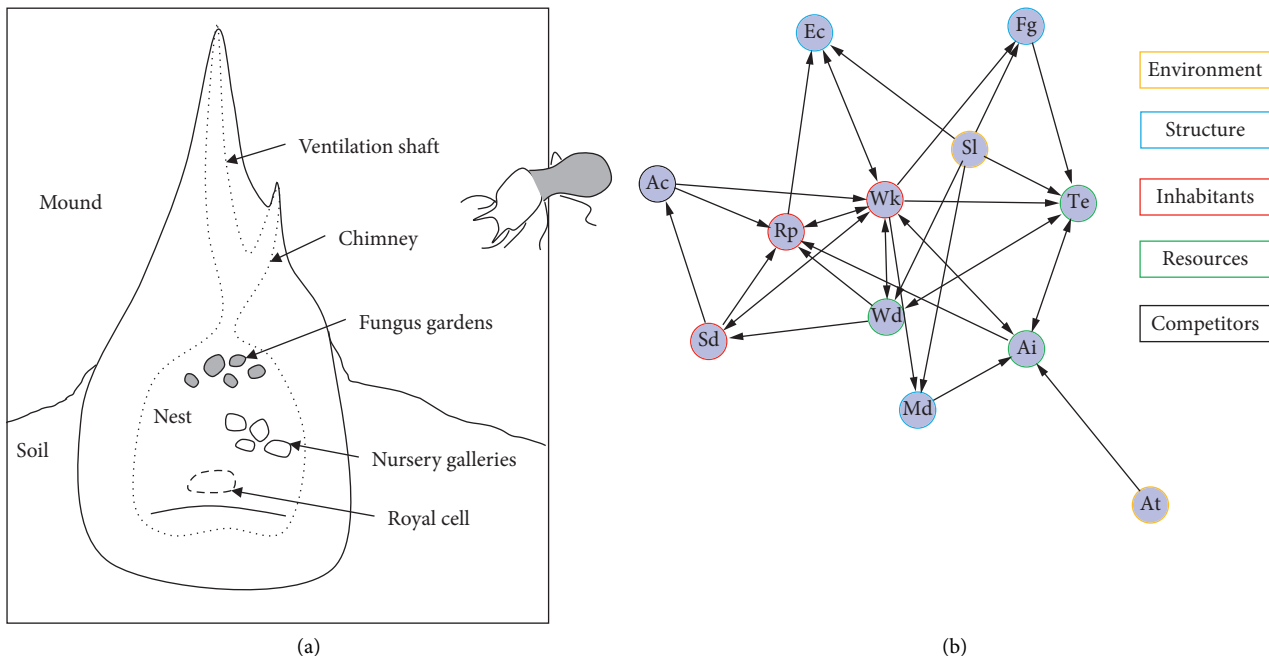


FIGURE 1: Graphic of a termite colony (a) and its simplified interaction network (b). Termites modify their environment and build a mound with various chambers to host the colony (a). The original ecosystem graph is composed of 12 nodes (Table 1) with five colors representing their different natures (b, left). Their 15 associated interactions (i.e., processes, Table 2) are shown directionally (b) from component conditions to realizations.

possible dynamics of the (eco) system, and differ strongly from traditional probabilistic models in ecology [17, 44]. It appears crucial to identify all possible trajectories to understand the overall ecosystem dynamics, rather than focusing on the most probable trajectories.

In this kind of framework, any ecosystem can be represented as a graph, in which every material component of the ecosystem (e.g., a termite population stage, fungi, air, and water) is represented by a *node*, with two Boolean states: “present” (the component is functionally present in the system and it may impact other components, also denoted as “+” or On) or “absent” (functionally absent from the system or “-” or Off). So, any *state of the system* is defined by the set of “+” and “-” nodes (Figure 1(b)). Any physicochemical, bioecological, and/or possibly socioeconomic process is translated into a Petri net *rule*, which describes the *condition* to be fulfilled, and the *realization* to be executed in such a case. Since the rules modify node states, the entire system shifts from one state to another through the discrete successive application of rules [30]. Rules progressively produce the *state space*, which provides the set of all system states reachable from the initial state and by the defined rules (Figure 2). This is easily translated and computed by any Petri net engine [35, 45].

The Petri net of the termite colony provides a highly instructive state space [30]. The termite modeling reaches only 109 states (of 2^{12} possible states, approx. 2%), so we can draw the exhaustive state space to visualize it (Figure 2). For larger systems, analysis can be performed automatically and without drawing the state space [37]. The state space graph displayed here is composed of several (colored) structures,

which we will further describe and interpret in ecological terms: the initial state (numbered 0, and represented by a hexagon, Figure 2-A), two topological structures usually called strongly connected components (SCCs, defined as a set of system states in which every state may be reached from any other state of the SCC, Figure 2-B and B’), and a number of decisive paths (e.g., irreversible ecosystem trajectories and tipping points, Figure 2-C), ultimately leading upward to basins and their associated deadlocks (states from which no other state is reachable, Figure 2-D and D’, squares). Hence, the state space provides a convenient, precise summary of the system’s behavior, its dynamic features, and all its possible qualitative trajectories.

From this state space, it is possible to compute a *merged state space* automatically aggregating all the states of the topological structures mentioned previously (Figure 3(a)). In this merged space, the SCC properties conveniently capture the ecosystem’s structural stabilities, that is, the number of states and the trajectories that qualitatively connect them (e.g., Figure 2-B). Tipping points are also visible as the successive rules (Figure 2-C and 3(a)-C) shifting the system from structural stabilities (e.g., B or B’) to deadlocks (e.g., D or D’), here meticulously identified and listed [30]. Other possible features (e.g., basins connecting the previous features) and ecosystem collapses (deadlocks) may also be computed and displayed on the same state space. Such topological analysis is usually accomplished on state spaces with as many as millions of states, in more complex and/or realistic ecosystem models [37, 38].

From this merged state space, we can then compute a potential-like surface (Figure 3(b)), referred to hereinafter as

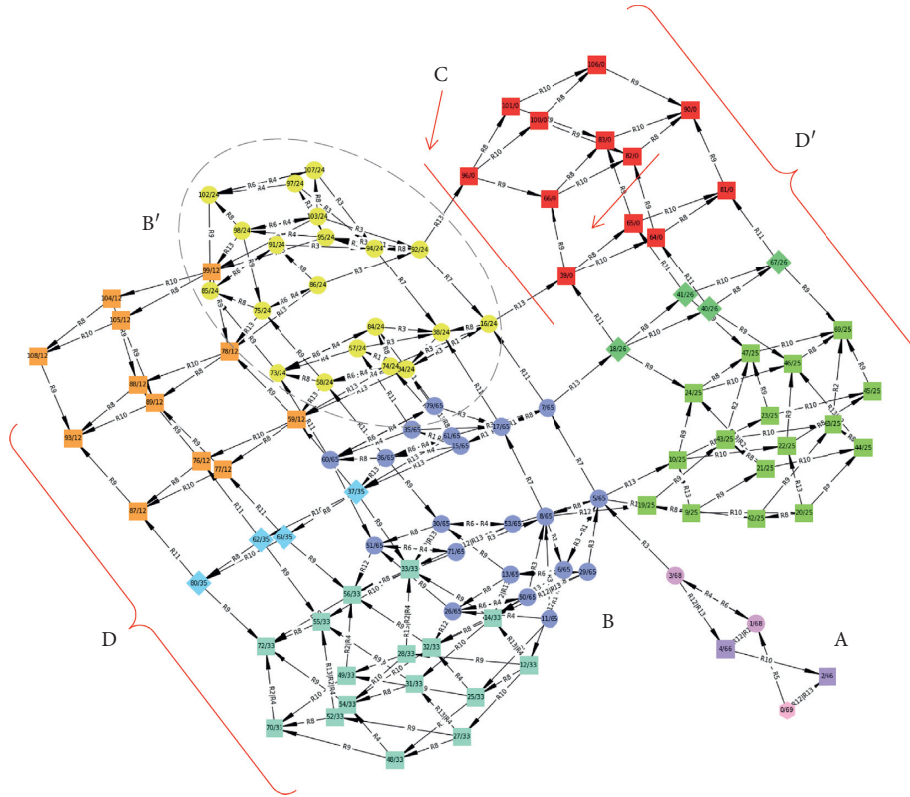


FIGURE 2: The full state space (or marking graph) of the termite colony model. The state space comprises 109 states labeled with a pair n/s where n is an identifying number for the marking and s is the number of strongly connected components (SCCs) for the basin or deadlock it belongs to. The initial state is displayed as a hexagon (A), deadlocks (states leading to a terminal state with no successor) are displayed as squares (five in total, of which two are in zones D and D', and one (A) is close to the initial state), an example of two tipping points is displayed as a red segment (C), while other states are displayed as circles. Each SCC or basin is highlighted using a separate color (e.g., SCCs B and B' are drawn in orange and green). The edges are directed and labeled with the number of the rule that was applied to perform the transition (defined in Table 2).

the *computed potential surface* to distinguish it from other *traditional surfaces* used in ecology and elsewhere [14, 17, 25]. While stabilities may be represented by wells (e.g., Figure 3(b)-B), tipping points are represented by ridges connecting these wells (e.g., Figure 3(b)-C), and deadlock states or sets of states are represented by assigning them a virtually infinite depth on the *computed potential surface* (e.g., Figure 3(b)-D), so that the system can no longer escape from them. For this purpose, we linked the width, depth, and location of each topological feature with the number of states, the number of trajectory steps, and the path connections of each feature. This representation is intended to consider different components of resilience, namely, latitude, resistance, and precariousness [17]. For example, structural stability B' involves 20 states, with a maximum of three steps required to leave it, and is irreversibly connected to B (Figure 4(a)). In this way, we built a surface that appears comparable to the traditional potential-like surfaces: yet, we highlight in the next section how different it is, once interpreted on the basis of the concepts supporting the qualitative discrete-event models used for this computation.

The state space concept provides an easy way to identify structural stabilities, tipping points, and hysteresis. We stress that such topological features do not correspond perfectly to

the so-called dynamics (i.e., with these names) in ODE models, as the system here shifts sharply from one set of discrete qualitative states to other discrete qualitative states and could theoretically stay indefinitely in each of them. When the system remains stuck in a specific structural stability (e.g., B and B' in Figure 2), all the states of such a stability are by definition connected through specific paths. The modeled ecosystem shifts from one state to the others through differentiated trajectories and then potentially comes back to the same state (Figure 4(a), blue and green arrows). These trajectories are numerous, with highly distinctive paths in terms of ecosystem composition (the present components) or other properties. For example, it is possible to plot such hysteresis as a function relating the number of ecosystem components present to the number of steps required to reach the states (Figures 4(b) and 4(c)).

Many other properties are available and often quantifiable in the state space. It is relevant to use these trajectories to characterize the structural stability (e.g., B' in Figure 4(a)), for example, by assigning it a “depth” defined by the maximum number of discrete steps required to reach the stability boundary and ultimately leave it (state colors) and representing the resistance [17]. The state space gathers as much information on transitions as on states, as it is possible

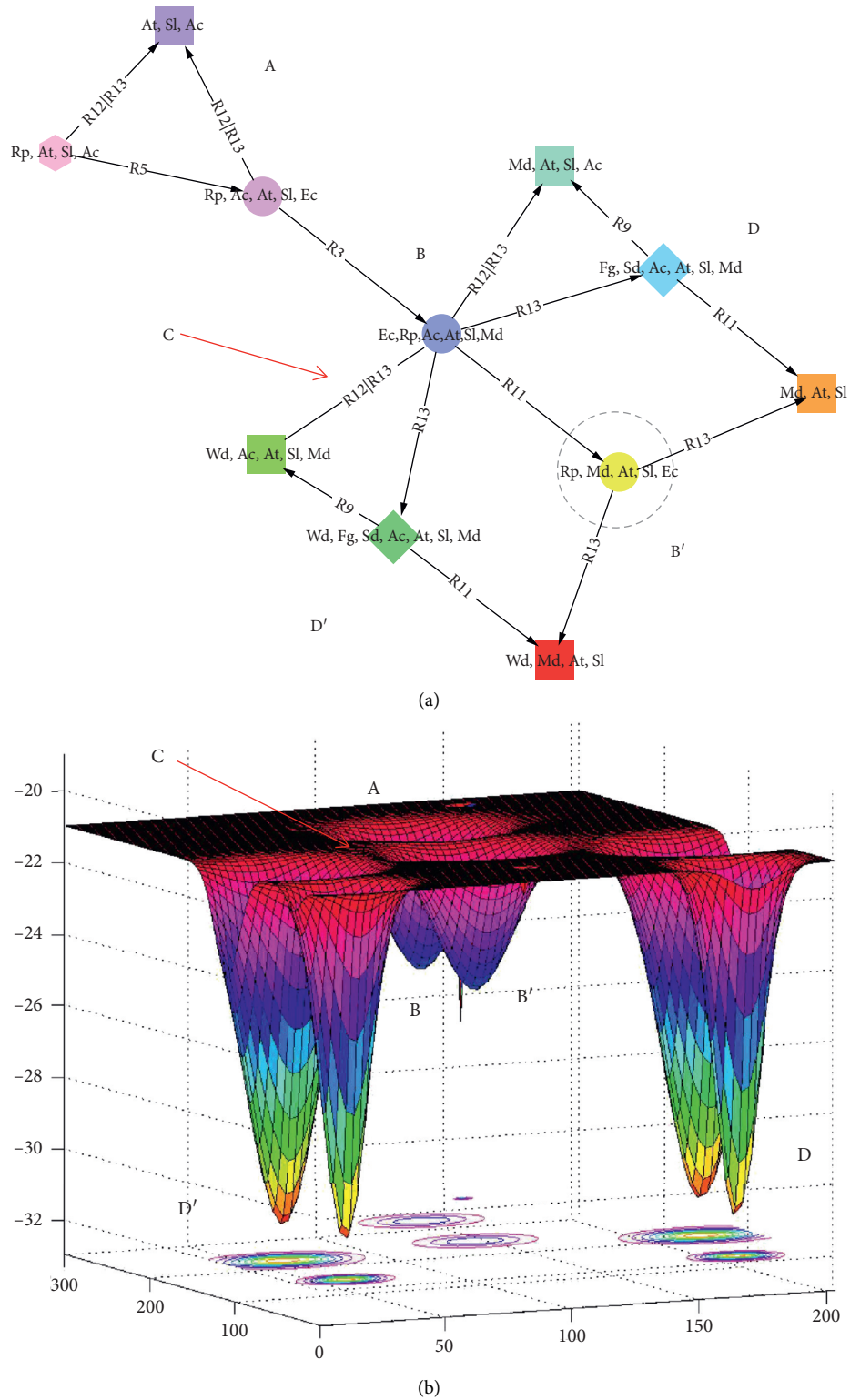


FIGURE 3: From the merged state space (a), it is possible to draw a tentative potential-like surface (b). In the merged version (a) of the full termite state space (Figure 2), each SCC and basin has been reduced to a single node and redundant paths have been removed. Nodes representing SCCs or basins (i.e., aggregate states) are noted (s) (circles) and labeled with the components present in all their states. From this reduction of the state space, specific paths leading to the main ecosystem collapses (squares), and highlighting the sharp transitions between them, can be more easily identified. For the potential surface (b), each structural stability (SCC, e.g., B and B') has been represented as a well with a width corresponding to its number of states and a depth corresponding to the maximum number of steps for escaping it. The deadlocks (e.g., D and D') are bottomless wells and are connected to other topological features with a continuous surface and sometimes through tipping points (C) (red arrow). We explain in the main text why such a representation is fallacious, though.

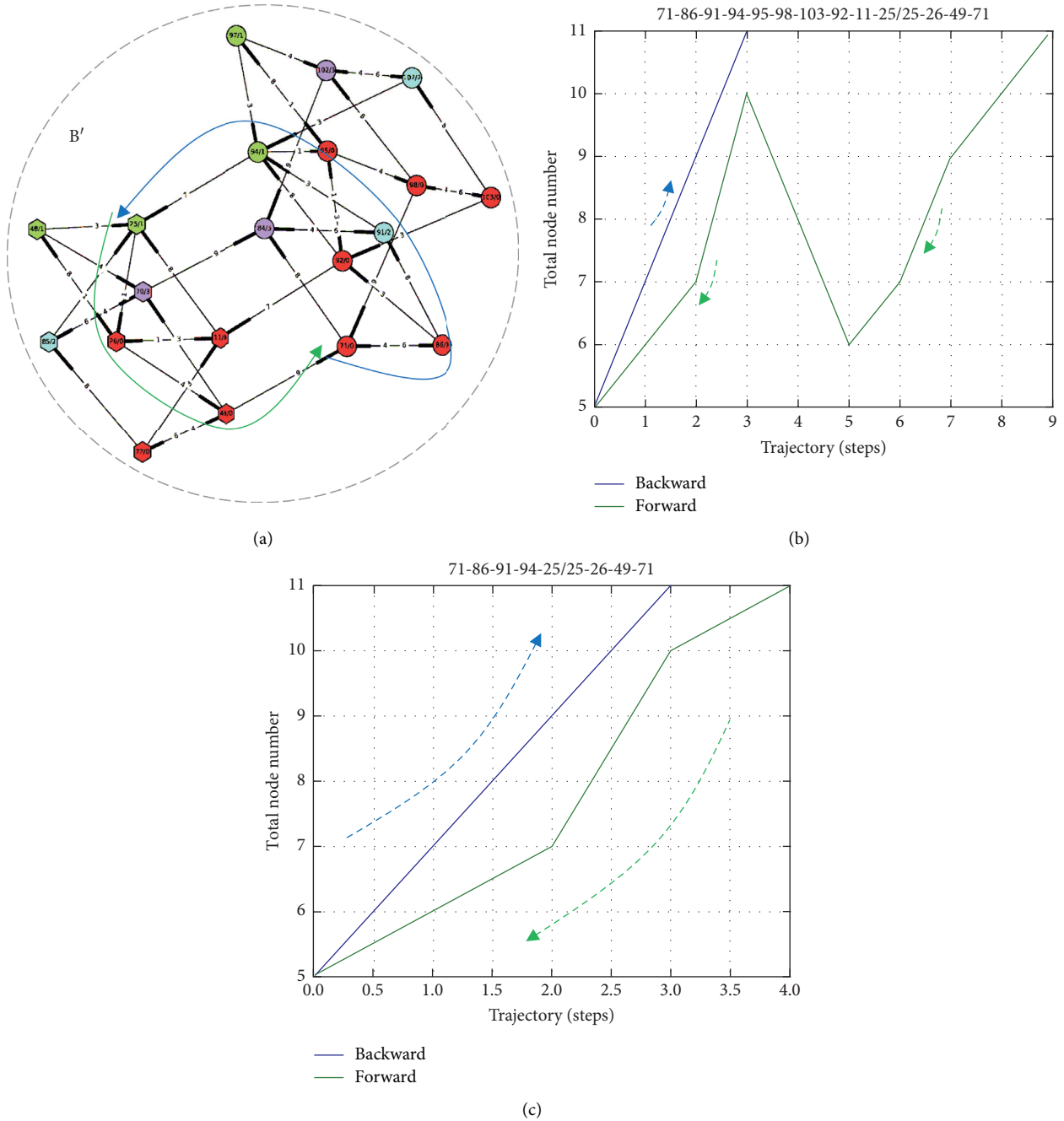


FIGURE 4: Illustration of the hysteresis found in the termite ecosystem state space (a), highlighting two specific trajectories (b). The structural stability displayed is B' (Figures 2 and 3), composed of 20 states (a) labeled with a pair n/s where n is an identifying number and s is the number of discrete steps needed to exit the B' stability (from 0 for states defining the boundary to 3 for the maximum number of steps to reach the boundary). The edges are directed and labeled with the number of the rule that was applied to perform the transition (Table 2). One specific cycling trajectory has been chosen in the B' stability (a) (blue and green arrows), and this hysteresis is highlighted in the plane (number of present components versus discrete steps, b left). A second trajectory is displayed in the same plane (b right) to highlight the fact that many trajectories in the state space may exhibit hysteresis.

to analyze which process (interaction) is responsible for which transition between states or sets of states. For example, the ecosystem shifts drastically from stability B' toward deadlock D' through a TP (Figure 3(a)-C, red arrow). It is possible to compute a similarity index between all pairs of states or topological features to estimate the TP magnitude. For example, a Jaccard index based on the present and

absent components would quantify the similarity between successive states. As an illustration, we computed this similarity index in a more complex wetland socioecosystem modeled in the same way (Figure 5(a)) [38] and automatically identified TPs such as the transitions entering deadlocks n/s 0 and 3 that were highly different from those seen previously (Figure 5(b), the two first columns of the matrix).

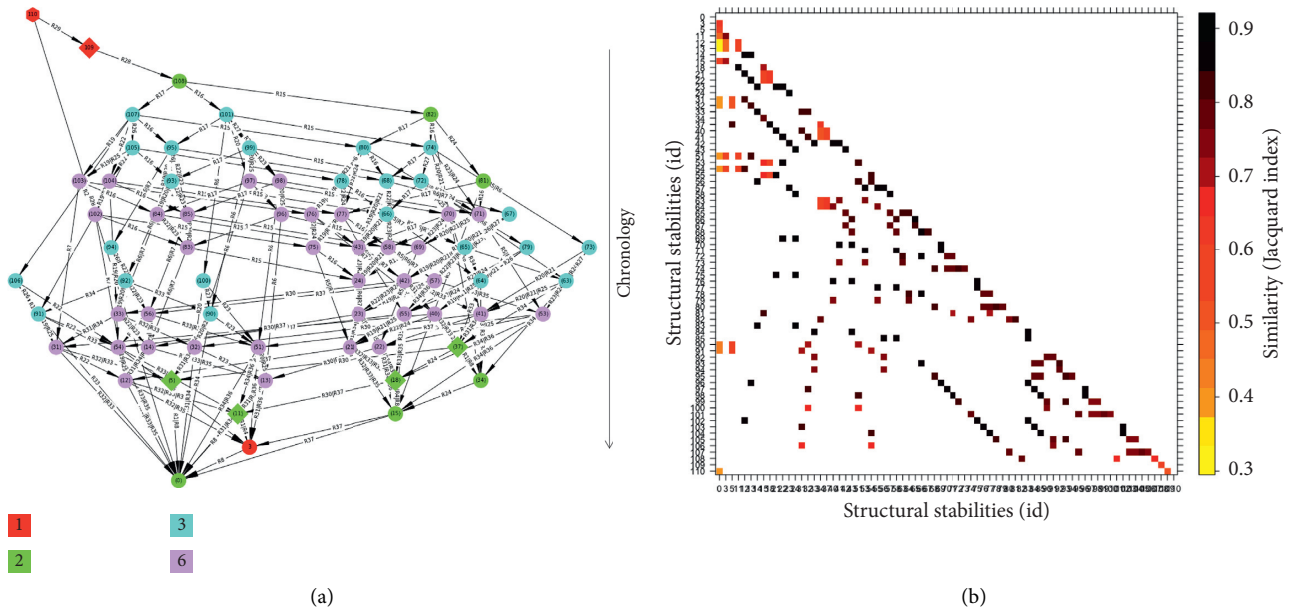


FIGURE 5: Example of a more realistic socioecosystem analyzed using a discrete qualitative model, viewed by its merged state space (a) and its tipping points (b). The state space of this wetland socioecosystem (a), a temporary marsh with pastoralism [38], should be read downward, from the initial state (pink hexagonal node on top) to the terminal structural stability (red bottom node). Different stabilities (colors and identifiers) are connected through processes (i.e., edges as directional arrows) mimicking qualitative transitions between distinct states of the socioecosystem being modeled. The similarity between these successive states (in terms of present components) may be quantified using a Jaccard index (b) (hot colors) and plotted in a connectivity matrix grouping together all the structural stabilities reached by the ecosystem. Transitions exhibiting the lowest Jaccard index values between highly different states clearly identify the ecosystem’s tipping points (b) (left column).

3. Comparison of the State Space with the Potential Surface

A process-based model such as the present model of a termite ecosystem may provide some insights in ecology. In recent years, a growing body of studies in ecology has promoted the conceptual view of (socio)ecosystem functioning that we refer to here as the *potential surface* (Figure 4(a)). Although it has sometimes been called by other names, the principle remains the same: this metaphor suggests considering any ecosystem as a ball rolling down onto a hypothetical landscape made up of a surface in a higher dimension space [15, 17]. This (hyper)surface concept is borrowed from physics, where many systems have been shown to change according to a potential parameterized by intrinsic (e.g., state variables) and extrinsic variables (e.g., environmental conditions) [24, 25]. There is no doubt that this concept is a convenient one for use in ecology too [44, 46]. This conceptual model is phenomenological, in that it potentially describes patterns in observation and is not based on knowledge of the underlying mechanisms. Metaphors are often slippery and it remains to be demonstrated that the potential as a concept is appropriate to ecosystem dynamics and to environmental processes (e.g., climatology [21, 22, 47]) in general. This section lists five possible criticisms of the potential metaphor.

3.1. Vertical Force. One critical assumption of the potential analogy concerns the *gravitational force* that constrains movements on the surface. For the system to be located

above a certain elevation assumes the energy is higher than below that elevation due to the scalar field in which the system is immersed. Does such a force exist in ecosystems? And if yes, what is the nature of this force? Indeed, if the potential surface is such an easy-to-handle metaphor, it is undoubtedly due to the restoring torque that drives the ball along to the potential surface [15]. In physical systems, any potential is the origination of a force and is directly linked to energy [11, 48]. This force is often gravity but may also be associated with electrical or chemical potentials. In ecological systems, to our knowledge, no *force* or energy has been identified or analyzed, even when living systems tend to maintain their activity, for example, by homeostasis [49]. It is even harder to imagine what the nature of this force or these processes might be, considering that ecosystems are simultaneously physical *and* biological (*and* anthropogenic) objects.

A simple thought experiment might help in understanding what is at play in this force, if anything. Take a simplified ecosystem such as vegetation in arid areas. In the absence of rainfall (the environmental conditions, say rainfall R), there is no vegetation (the state variable, biomass B) present, even on fertile soil. The absence of such variables $(B, R) = (0, 0)$ may be, and usually is, considered a stable state [28], even with a system showing stochastic noise. In other words, the potential surface concept would plot the ecosystem as a ball that has “fallen deep into” a well [44]. Now, let us push the system toward slightly wetter conditions and the emergence of vegetation. How would ecologists think the

ecosystem would behave? Would the system stay in this (putative stable) state with very little vegetation and rainfall? Will it gradually increase the biomass, form vegetation patterns, and start storing as much water as possible? Or will it simply revert to the previous state, with no vegetation and no more water?

The potential surface provides one (the?) answer. Due to the metaphoric gravitational force in the landscape, it is assumed that the ball representing the ecosystem will inevitably fall down to the stable state $(B, R) = (0, 0)$. This assumption that the vertical dimension plays a critical role (and that such a force does exist) remains to be demonstrated in ecology. This is a necessity, even if most ecologists today feel that this is the behavior at play. Some studies have already examined ecosystems in semiarid conditions or in controlled, poor environments [50]. So far, though, to our knowledge, there has been no definitive demonstration of attracting or repulsing behavior in the vicinity of stable states. The truth is that probably no ecologist knows the answer. The state space, as illustrated in the termite ecosystem (Figures 1 and 2), indicates whether the system can shift from one state to another, according to the set of processes driving the system. In our opinion, there is no driving force for the ecosystem other than these identified processes.

3.2. Reversible Isotropic Surface. Similarly, we may wonder about the inner nature of the other (horizontal) dimensions of the potential. In particular, are the ecosystem variables or the environmental conditions isotropic? Focusing on the state variable (often plotted along the x -axis), is it as easy to leave a stable state (i.e., a well, with central symmetry) leftward as it is to leave it rightward? This question is linked to the previous limitation and challenges and the possible attraction and repulsion of distinct potential zones, an area of critical study in physical systems (e.g., climatology [21, 47]). For example, let us assume that desert, savanna, and forest are alternative stable states (still a matter of debate); when leaving the savanna states, likely located between the other two, will it be “easier” for the system to reach the desert states than the forest states? Theoretically, the potential assumes perfect symmetry between both directions [17, 44], which our process-based model does not [30].

In other words, the potential surface assumes there are isotropic directions and reversible movements on it. More generally, the reversibility of each trajectory of the ecosystem can be questioned. This observation remains valid whatever the shape of the potential, possibly allowing for the hysteresis already observed in ecology [16, 32]. More radically, we may wonder whether movement *on* the potential surface is possible everywhere. In the case of simplified ecosystems with only one state variable, it may be assumed that the system can gain or lose biomass equally as easily. In the case of more realistic ecosystems, though, precisely those we are endeavoring to understand, it may be that regaining biomass is no longer possible, whatever the predator- or climate-related causes. In brief, the reversibility of the potential

surface needs to be demonstrated too. Here again, the state space of the termite ecosystem, the assumed model definition, demonstrates whether the system may reach a deadlock or exhibit irreversible dynamics (e.g., between B and B' , Figure 2).

3.3. Surface Stability over Time. It is worthy of note that biologists in the past used the concept of potential surface too. The best known example is probably the *epigenetic* (or fitness) *landscape* proposed by Waddington (Figure 6(b)) [51]. This landscape suggests that the phenotypic traits of an organism are the result of a combination of genes. The metaphor was powerful and has been widely used up until now. Yet, a growing body of biologists today believes there is a major flaw with this potential surface: it is changing (i.e., not frozen). Even when genes are responsible for the traits examined, it has been observed that this landscape is highly variable, changing over time in successive experiments [52–54]. In brief, the potential surface cannot be plotted once and for all.

We recall a critical assumption behind the potential concept used in physics: a physical system modeled as a dynamic system should be (is) ergodic. The ergodicity of a system states that it exhibits the same statistical behavior when averaged over time, in space or in any other system dimensions (i.e., in its phase space, e.g., [55]). In other words, a system that evolves over a long period tends to “forget” its initial state, statistically speaking. Some ecologists have serious doubts that ecosystems are ergodic [10, 56, 57]. Conversely, most ecologists think that ecosystems have history that strongly constrains their fate [18, 58–61]. Here again, the ecosystems we talk about are not simplified as prey-predator systems as they are sometimes discussed. Real ecosystems are thermodynamically open and have many components that are subject to evolution. To our knowledge, this ergodic property has never been demonstrated in ecology. The state space approach presented here does not assume ecosystem ergodicity in the dynamics studied (Figure 2), but it is possible to adapt the model for evolutionary and ever-changing dynamics, a perspective our team is already exploring.

3.4. The Punctual Ball and the Thin Surface. As a fruitful metaphor, the potential surface and its related concepts simplify reality so as to improve our understanding. It becomes embarrassing, however, when such simplifications provide an incorrect idea of reality. Can an ecosystem really be conceptualized as a punctual ball? An ecosystem is such a complex object comprising a large number of components and processes that it is easy to imagine that some parts of it would indeed follow a potential—its physical part, say—while another part would not [11, 57]. The reason that the whole system should exhibit a punctual location in the state space has to be explored; and why not several locations simultaneously? In addition, the system would likely exhibit stochastic behavior, rather than showing the system as a ball moving into a cloud of uncertain locations in this space (Figure 6(c)).

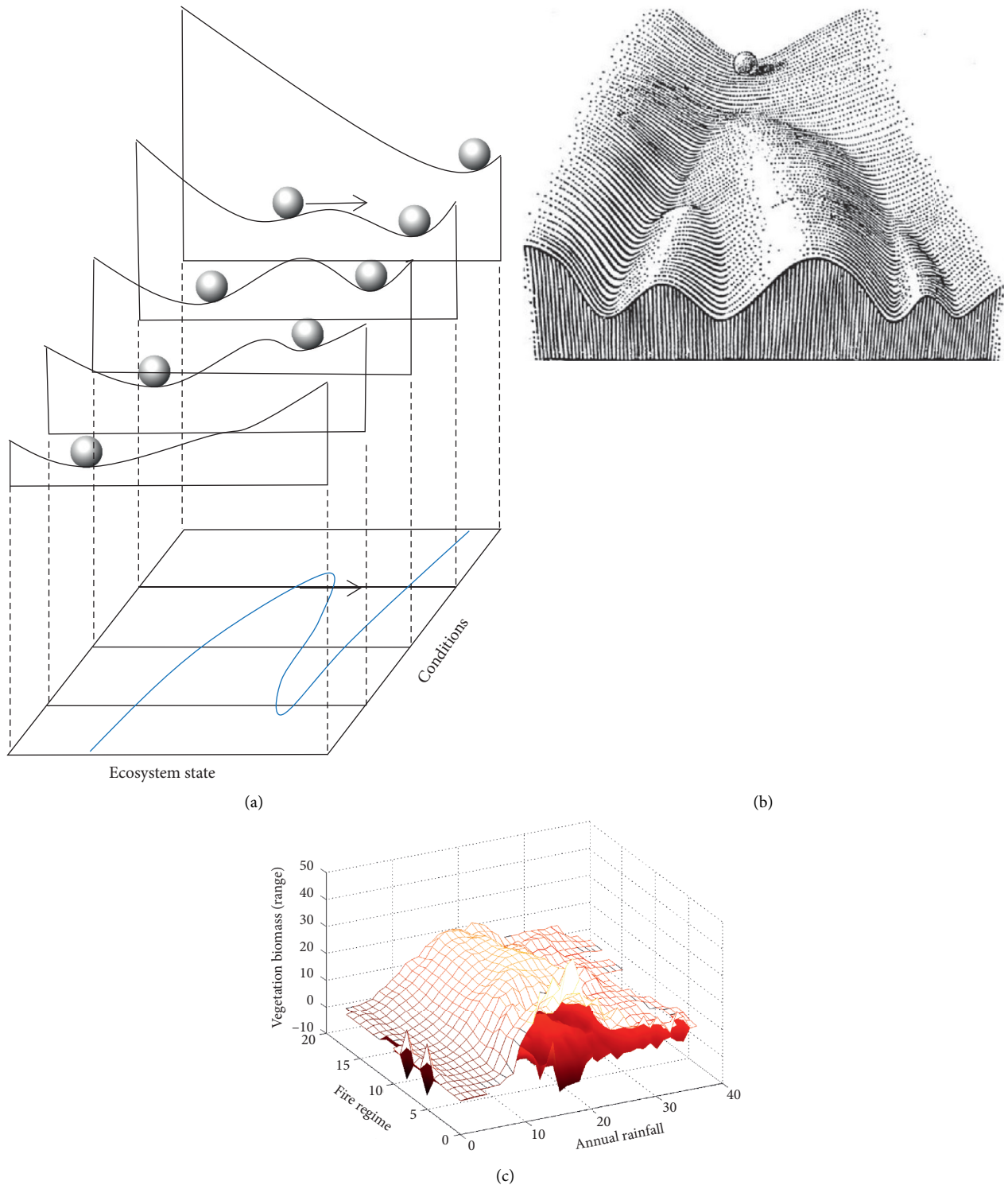


FIGURE 6: Examples of various synthetic representations of system dynamics, including a potential-like surface (a) [16], the epigenetic surface (b) [51], and the drape concept (c) inspired from [32]. Although these representations of dynamic systems appear comparable, they differ substantially in respect of their assumptions and conception of the (eco)system under investigation.

Additionally, this observation questions whether or not the (hyper)surface of the potential should have a thickness (a hypervolume) (Figure 6(c)). In physics, the system must exactly follow the potential in a mean-field approximation, even if noise often blurs the measures and the plot [48]. In

ecology, we may reasonably question whether processes follow mean field behavior, and this is often justified by the huge number of components involved in the system. As in biology (Figure 6(b)), ecological processes exhibit a high variance which makes systems more unpredictable and may

mean they show no average behavior (or that they explore rare trajectories too). The state space proposes that the ecosystem indeed follows some trajectories, but the ever-changing state compositions in this space deny the uniform and constant image of the ball (Figures 6(a) and 6(b)). The system inevitably follows the state space, however, as it contains all possible states and, according to the processes involved, it should not leave this computed shape (Figure 6(c)).

3.5. Surface Definition and Disturbances. The definition of the potential surface itself challenges ecologists. How should it be built? Which variables should be used? Ecosystem complexity suggests that many state variables should be used, whereas most ecological surfaces built so far use a single (one-dimensional) variable (e.g., [29, 44]). Yet, deserts, savannas, and forests are often assumed to belong to the same potential surface. This simplification is questionable, considering that even savannas and forests have radically different species compositions and climatic and soil conditions (e.g., [11, 12, 62]). To what extent should we merge different biomes (broad types of ecosystems) into the same potential? It is predictable that boreal forests would not belong to “the same” potential surface as tropical forests, as they are controlled by radically different conditions, essentially by temperatures and rainfall, respectively [63, 64]. There is a clear need to define potential functions with more (state) variables.

One example may illustrate this fallacy. Empirical studies of the potential surface assume that the system spends more time in stable states, and less time in unstable ones. For example, some ecologists estimate the potential surface based on this central assumption to identify the multimodal stabilities of vegetation [20, 44]. There are many examples of systems in which this assumption is revealed to be wrong. One such example is the simplistic pendulum system. In a pendulum oscillation, the stable state is at the bottom (the lowest elevation), while this is also the location at which the system has the greatest speed and, thus, at which it spends the shortest resident time. In brief, it is in no way recommended that the stable and unstable states of any system be identified on the basis of the time it spends in various states.

Furthermore, environmental conditions supposedly controlling some dimensions of the potential are not systematically external to the ecosystem. This issue has long been debated in ecology and is basically linked to the organismic conception of ecosystems [36, 65]. Tansley initially proposed the word “ecosystem” to replace the word “community,” and the debate lasted long about the inner coherency of this object. When a ball falls from the tower of Pisa, gravity is considered external to the ball being studied. In the case of many ecosystems, what does excluding disturbance from the system allow? With climate forcing, the disturbance appears to be quite obviously external, spatially and temporally, but in the case of a forest fire, an invasive species, or an intrinsic human pressure, this assumption is much less obvious [21, 32]. Can we be sure no feedback can settle between disturbances and the ecosystems studied, as is usually assumed [14, 16]? The resulting surface would likely

differ strongly depending on the status of the disturbance. Construction of the discrete, qualitative ecosystem model presented here suggests including all the processes at play in the ecosystem (Tables 1 and 2, Figure 1), be they internal or external, and computing the resulting dynamics. Hence, there is no need to confer a specific status on external disturbances.

4. Discussion and Recommendations

We can now compare the *traditional potential* from physics commonly and empirically used in ecology (Figure 6(a)) with this *potential surface* computed on the basis of the state space of a process-based model of a complex ecosystem (Figure 3(b)). Keeping in mind the limitations listed previously, the comparison reveals some striking observations:

- (a) On our computed potential surface, there is no gravitational force pushing the system downward. Only the (modeled) processes at play are capable of moving the system from one state to the next, in the state space. In particular, climbing up the surface appears as easy as falling down (Figure 3(b)). This metaphoric vertical force now appears inappropriate.
- (b) The potential surface is not isotropic and shows strongly irreversible paths as interpreted from the merged state space. When the system shifts from one structural stability, that is, from one stable area (e.g., well B, Figure 3(a)) to the neighboring stability (well B'), any return is forbidden. It is even possible to plot trajectories and hysteresis within each structural stability (Figure 4).
- (c) The computed potential surface has no reason to be stable over time. Indeed, the state space is provided here for a specific ecosystem (termite colony) composition (Figure 1(b)), but any new arrival in or departure from the system components, and its associated processes, would strongly modify the resulting state space (Figure 2).
- (d) The potential surface has been computed here on the basis of discrete events, then transformed with an assumption of continuity between states, and displayed in an arbitrary space (Figure 2). Many other representations and coordinates for each state could have been used, however, and consequently would have strongly modified the potential surface representation (Figure 3(b)). In particular, consideration of the thick surface would have disqualified this potential surface [32], instead of the discrete qualitative state space (Figure 3(a)).
- (e) A large number of variables of various natures have been used to constrain this state space and its associated potential surface (Figure 1(b)). In addition, perturbations and even disturbances are internal to the system and contribute strongly to the surface definition. This is not the case for traditional potentials [17, 44].

TABLE 1: Node categories, names, abbreviations, and descriptions of the termite colony ecosystem modeled using the discrete qualitative model (see Figure 1, adapted from [30]).

| Name | Initially | Family | Description | Comment |
|------|-----------|-------------|-----------------|--|
| Rp | Present | Inhabitants | Reproductives | The queen, the king, the eggs, and the nymphs |
| Wk | Absent | Inhabitants | Workers | All termites able to work: the larvae, workers, and pseudo-workers |
| Sd | Absent | Inhabitants | Soldiers | The termite soldiers |
| Te | Absent | Inhabitants | Termitomyces | The fungus cultivated by the termites |
| Ec | Absent | Structures | Egg chambers | All egg chambers plus the royal chamber |
| Fg | Absent | Structures | Fungal gardens | All the gardens in which the fungus is grown |
| Md | Absent | Structures | Mound | The upper structure of the colony |
| Wd | Absent | Resources | Wood | The wood stored inside the colony |
| Ai | Absent | Resources | Air of the nest | The air inside the colony |
| Sl | Present | Environment | Soil | The soil around the termite nest |
| At | Present | Environment | Atmosphere | The air around the termite nest |
| Ac | Present | Competitors | Ant competitors | All the ant species in competition with the termites |

TABLE 2: List of the rules for modeling termite ecosystem functioning and development.

| Rule | Comment |
|---|---|
| (1) $Wk^+, Te^+ \rightarrow Wd^-, ai^-$ | The workers and the fungi are consuming wood and air |
| (2) $Fg^- \rightarrow Te^-$ | The fungi need the fungal gardens in order to survive |
| (3) $Wk^+, Sl^+ \rightarrow Wd^+, Te^+, Fg^+, Ec^+, Md^+$ | The workers are foraging in the soil for wood and fungus; from the soil, the workers are building the fungal gardens, the egg chambers, and the mound |
| (4) $Wd^- \rightarrow Wk^-, Te^-$ | The workers and the fungus need to eat wood to survive |
| (5) $Rp^+, Sl^+ \rightarrow Ec^+$ | For the soil, the queen and the king can also build egg rooms |
| (6) $Rp^+, Ec^+ \rightarrow Wk^+$ | In the egg chambers, the queen and the king are producing eggs that are becoming workers |
| (7) $Wk^+, Wd^+ \rightarrow Sd^+, Rp^+$ | Eating wood, the larvae are metamorphosing into soldiers and/or nymphaea |
| (8) $Md^+, At^+ \rightarrow Ai^+$ | The air of the nest is being refreshed by passing through the mound and exchanging with the atmosphere |
| (9) $Wk^- \rightarrow Fg^-, Sd^-$ | The soldiers cannot survive without the workers to feed them, and the fungal gardens need maintenance by the workers |
| (10) $Wk^-, Rp^- \rightarrow Ec^-$ | The egg chambers need maintenance by the workers or the reproductives; otherwise they collapse |
| (11) $Sd^+ \rightarrow Ac^-$ | The soldiers are killing ant competitors intruding into the colony |
| (12) $Ac^+, Sd^- \rightarrow Wk^-, Rp^-$ | Without the soldiers, the ant competitors are invading the colony and killing the workers and the reproductives |
| (13) $Ai^- \rightarrow Rp^-, Wk^-, Te^-$ | The reproductives, the workers, and the fungus need to breathe the air of the nest to survive |

The conditions of application, realizations, and detailed explanations are given for each rule. The rule arrows indicate the transformation (rewriting) of the network at the next step [30]. Discrete systems are used to exhaustively characterize the dynamics of an integrated ecosystem (Methods in Ecology and Evolution, 00: 1–13 [30]).

For all these reasons, we think that empirical potentials appear to be inaccurate approximations of process-based ecosystem state spaces. Conversely, the state space seems to be a convenient substitute for the traditional potential [18, 30]. It has still to be tested in contrasted case studies to evaluate its interpreting power [37, 38]. The *discrete event* model family used in computer science and in biology [31, 41] appears to provide an interesting avenue for understanding ecosystem dynamics. These process-based models were developed to understand systems made up of discrete components in interaction. Some of them were initially dedicated to resource allocation or signaling networks [35, 40] and others to linguistic or landscape modeling [33, 66, 67] and plant growth [34, 68]. Such models may be combined with networks representing the constitutive entities (the nodes) and their processes (the edges), for example, to model rural landscapes [67] or ecosystems [18]. Another central advantage they offer is that they allow for rigorous formalization of the dynamics studied, as well as an understanding of system behavior in all its dimensions. They

are also intuitive, highly adaptable (e.g., with quantitative and multivalued versions), and easy to manipulate using existing software [45]. In addition, such state spaces appear conceptually similar to state-and-transition models developed to manage rangelands, well known for exhibiting multiple states and successional dynamics [43]. Ultimately, they provide interpretations of (socio)ecological entities which, when rigorously formalized, are no longer metaphorical [37, 38, 56].

There can be no doubt that ecosystems are complex, despite a few of them remaining simple. Ecosystem processes are notoriously noisy and difficult to measure, while the biological components of ecosystems often add a strong variance to the overall behavior. Despite this challenge, ecologists need to continue collecting data on ecosystems to improve the understanding of such systems and, ultimately, their management. But where does ecological complexity reside? Is it in the ecosystem state or in the ecosystem dynamics? Ecologists are commonly inclined to scrutinize a snapshot of the ecosystem (the pattern) instead of its long-

term (process) dynamics. For example, it is inappropriate to study traditional ecosystem potential on the basis of isolated states (Figure 6) rather than the trajectories connecting them (Figure 4). Ecosystems are historical objects experiencing abrupt changes with probable nonergodic behaviors [18, 55, 56]. Most ecosystem studies have been performed over relatively short timescales, typically over one or two human generations. We still know very little about the long-term behavior of ecosystems, i.e., over several generations of the slowest component, despite increasing efforts in historical ecology and paleoecology (e.g., [69, 70]). The usual variables under long-term study often concern vegetation and climate, but rarely fauna, soils, and/or human components. An understanding of long-term ecosystem behaviors is now becoming an imperative, with realistic modeling as a corollary.

At this stage, a decisive recommendation is not to neglect the process of fitting the model to observations. To date, it has been rare for traditional potentials to fit observed ecosystems [27, 44] and has mainly involved pattern and fragmented datasets. To our knowledge, it has not once been the case with process and ecosystem dynamics [32]. Most of the time, the model is displayed to interpret a posteriori observations, and not strictly fitted to them. This critical preliminary step should be performed with more variables, on longer trends and with finer models, a comment which is true for discrete event models too. Data collection in ecology is particularly challenging, considering the cost of surveying a complete ecosystem (i.e., most components) and considering the number of components, but substitutes can be found to start this program of work. Some chemostat and controlled experiments may allow for high resolution and long-term measurements [71], while some large scale ecosystems have begun to have rich databases too [27]. There appears to us to be an urgent need to start calibrating potential-like and discrete-event models on such complex data and to test their related hypotheses. To generalize the potential concept to various contrasting ecosystems, it will be necessary to confirm its power and usefulness.

These recommendations may all be summarized as a triangle of improvements that feed into the three main components of any research theme of complexity, namely, data, model, and concept research. In between, there are fits, ideas, and tools that enable continuous testing of emerging concepts such as state spaces and potential surfaces. At present, some sides of this triangle appear to be missing, with further studies being required to produce a satisfying theory of ecosystem. As shown above, potential-like surfaces may not be the most appropriate concepts for describing and understanding complex ecosystem behaviors and dynamics. Even in cases where the potential concept proved appropriate, it would be fruitful and heuristic to search for some additional views [32]. For example, we recently proposed also looking for linguistic principles in living systems and ecosystems [72].

Simultaneously seeking new mathematical tools is also an imperative; such models include these underused *qualitative discrete event models* [30]. Other tools have been

proposed in the past, and it would be a shame to ignore them or fail to fully acknowledge them. For example, Thom's work shows rich but unwieldy algebra specifically for potentials in any field [25]. Economic and ethological studies have already tried, unsuccessfully, to use these tools. In addition, we believe it is crucial to develop possibilistic models for exhaustive characterization of ecosystem trajectories, instead of probabilistic models focusing on a few dominant trajectories only.

In conclusion, we would like to warn the ecologist community of the hazards of drawing an analogy between physical and ecological systems. The history of ecology has already shown how this analogy once sent the community down potentially erroneous and/or useless pathways [11]. It is often fruitful to borrow concepts from other scientific fields, but they need to be tailored to the questions under examination at best and, at worst, they could send us off down a slippery, dangerous slope.

Data Availability

No data were used to support this study.

Conflicts of Interest

The authors declare that they have no conflicts of interest.

References

- [1] I. A. Hatton, K. S. McCann, J. M. Fryxell et al., "The predator-prey power law: biomass scaling across terrestrial and aquatic biomes," *Science*, vol. 349, no. 6252, 2015.
- [2] S. Kéfi, V. Miele, E. Wieters, S. Navarrete, and E. Berlow, "How structured is the entangled bank? The surprisingly simple organization of multiplex ecological networks leads to increased persistence and resilience," *PLoS Biology*, vol. 14, no. 8, Article ID e1002527, 2016.
- [3] R. M. May, *Stability and Complexity of Model Ecosystems*, Princeton University Press, Princeton, NY, USA, 1974.
- [4] E. Thébault and C. Fontaine, "Stability of ecological communities and the architecture of mutualistic and trophic networks," *Science*, vol. 329, no. 5993, pp. 853–856, 2010.
- [5] R. C. Dewar, C. H. Lineweaver, R. K. Niven, and K. Regenauer-Lieb, "Beyond the second law," *Entropy Production and Non-Equilibrium Systems*, Springer, Berlin, Germany, 2011.
- [6] B. C. Patten, "Network integration of ecological extremal principles: exergy, emergy, power, ascendancy, and indirect effects," *Ecological Modelling*, vol. 79, no. 1–3, pp. 75–84, 1995.
- [7] E. Ostrom, "A general framework for analyzing sustainability of social-ecological systems," *Science*, vol. 325, no. 5939, pp. 419–422, 2009.
- [8] I. Steffan-Dewenter, M. Kessler, J. Barkmann et al., "Tradeoffs between income, biodiversity, and ecosystem functioning during tropical rainforest conversion and agroforestry intensification," *Proceedings of the National Academy of Sciences*, vol. 104, no. 12, pp. 4973–4978, 2007.
- [9] C. Gaucherel, "Ecosystem complexity through the lens of logical depth: capturing ecosystem individuality," *Biological Theory*, vol. 9, no. 4, pp. 440–451, 2014.

- [10] S. P.-V. Frontier, D. A. Lepêtre, D. Davoult, and C. Luczak, *Ecosystèmes. Structure, Fonctionnement, Evolution*, Dunod, Paris, France, 4th edition, 2008.
- [11] C. Gaucherel, “Physical concepts and ecosystem ecology: a revival?” *Journal of Ecosystem and Ecography*, vol. 8, 2018.
- [12] R. E. Ricklefs and G. L. Miller, *Ecology*, Freeman, New York, NY, USA, 4th edition, 2000.
- [13] R. H. Mac Arthur and E. O. Wilson, *The Theory of Insular Zoogeography*, Princeton University Press, Princeton, NY, USA, 1963.
- [14] C. S. Holling, “Resilience and stability of ecological systems,” *Annual Review of Ecology and Systematics*, vol. 4, no. 1, pp. 1–23, 1973.
- [15] M. Scheffer, *Critical Transitions in Nature and Society*, Princeton University Press, Princeton, NJ, USA, 2009.
- [16] M. Scheffer, S. Carpenter, J. A. Foley, C. Folke, and B. Walker, “Catastrophic shifts in ecosystems,” *Nature*, vol. 413, no. 6856, pp. 591–596, 2001.
- [17] B. Walker, C. S. Holling, S. R. Carpenter, and A. Kinzig, “Resilience, adaptability and transformability in social-ecological systems,” *Ecology and Society*, vol. 9, no. 2, 2004.
- [18] C. Gaucherel, H. Théro, A. Puiseux, and V. Bonhomme, “Understand ecosystem regime shifts by modelling ecosystem development using boolean networks,” *Ecological Complexity*, vol. 31, pp. 104–114, 2017.
- [19] R. V. Solé and J. Bascompte, *Self-Organization in Complex Ecosystems*, Princeton University Press, Princeton, NJ, USA, 2006.
- [20] M. Hirota, M. Holmgren, E. H. Van Nes, and M. Scheffer, “Global resilience of tropical forest and savanna to critical transitions,” *Science*, vol. 334, no. 6053, pp. 232–235, 2011.
- [21] B. W. Brook, E. C. Ellis, M. P. Perring, A. W. Mackay, and L. Blomqvist, “Does the terrestrial biosphere have planetary tipping points?” *Trends in Ecology & Evolution*, vol. 28, no. 7, pp. 396–401, 2013.
- [22] C. Gaucherel and V. Moron, “Potential stabilizing points to mitigate tipping point interactions in earth’s climate,” *International Journal of Climatology*, vol. 37, no. 1, pp. 399–408, 2016.
- [23] E. H. van Nes, M. Hirota, M. Holmgren, and M. Scheffer, “Tipping points in tropical tree cover: linking theory to data,” *Global Change Biology*, vol. 20, no. 3, pp. 1016–1021, 2014.
- [24] R. Badii and A. Politi, *Complexity, Hierarchical Structures and Scaling in Physics*, Cambridge University Press, Cambridge, UK, 1997.
- [25] R. Thom, *Structural Stability and Morphogenesis*, Benjamin, Reading, MA, USA, 1975.
- [26] F. Accatino, C. De Michele, R. Vezzoli, D. Donzelli, and R. J. Scholes, “Tree-grass co-existence in savanna: interactions of rain and fire,” *Journal of Theoretical Biology*, vol. 267, no. 2, pp. 235–242, 2010.
- [27] M. Scheffer, S. H. Hosper, M.-L. Meijer, B. Moss, and E. Jeppesen, “Alternative equilibria in shallow lakes,” *Trends in Ecology & Evolution*, vol. 8, no. 8, pp. 275–279, 1993.
- [28] A. C. Staver, S. Archibald, and S. Levin, “Tree cover in sub-Saharan Africa: rainfall and fire constrain forest and savanna as alternative stable states,” *Ecology*, vol. 92, no. 5, pp. 1063–1072, 2011.
- [29] E. H. Van Nes and M. Scheffer, “Slow recovery from perturbations as a generic indicator of a nearby catastrophic shift,” *The American Naturalist*, vol. 169, no. 6, pp. 738–747, 2007.
- [30] C. Gaucherel and F. Pommereau, “Using discrete systems to exhaustively characterize the dynamics of an integrated ecosystem,” *Methods in Ecology and Evolution*, vol. 10, no. 9, pp. 1–13, 2019.
- [31] F. Pommereau, *Algebras of Coloured Petri Nets*, Lambert Academic Publishing (LAP), Riga, Latvia, 2010.
- [32] C. Hély, H. H. Shuggart, B. Swap, and C. Gaucherel, “The drape concept to understand ecosystem dynamics and its tipping points,” 2020.
- [33] H. Ehrig, M. Pfender, and H. J. Schneider, “Graph-grammars: an algebraic approach,” in *Proceedings of the 14th Annual Symposium on Switching and Automata Theory (Swat 1973)*, pp. 167–180, IEEE Transactions on Cybernetics, Iowa City, IA, USA, October 1973.
- [34] J.-L. Giavitto and O. Michel, “Modeling the topological organization of cellular processes,” *Biosystems*, vol. 70, no. 2, pp. 149–163, 2003.
- [35] W. Reisig, *Understanding Petri Nets*, Springer Berlin Heidelberg, Berlin, Germany, 2013.
- [36] J. S. Turner, *The Extended Organism: The Physiology of Animal-Built Structures*, Harvard University Press, Cambridge, MA, USA, 2009.
- [37] M. Cosme, C. Hély, F. Pommereau et al., “East-African rangeland dynamics: from a knowledge-based model to the possible futures of an integrated social-ecological system. In review,” 2020.
- [38] C. Gaucherel, C. Carpentier, I. R. Geijzendorffer, C. Noués, and P. F., “Long term development of a realistic and integrated ecosystem,” 2020.
- [39] H. G. Fowler, V. Pereira da-Silva, L. C. Forti, and N. B. Saes, “Population dynamics of leaf cutting ants: a brief review,” *Fire Ants and Leaf-Cutting Ants*, pp. 123–145, Westview Press, Boulder, CO, USA, 1986.
- [40] M. A. Blätke, M. Heiner, and W. Marwan, “Tutorial,” in *Petri Nets in Systems Biology*, Otto-von-Guericke University Magdeburg, Magdeburg, Germany, 2011.
- [41] J.-L. Giavitto, H. Klaudel, and F. Pommereau, “Integrated regulatory networks (IRNs): spatially organized biochemical modules,” *Theoretical Computer Science*, vol. 431, pp. 219–234, 2012.
- [42] J. M. Dambacher, H. K. Luh, H. W. Li, and P. A. Rossignol, “Qualitative stability and ambiguity in model ecosystems,” *The American Naturalist*, vol. 161, no. 6, pp. 876–888, 2003.
- [43] B. T. Bestelmeyer, A. Ash, J. R. Brown et al., “State and transition models: theory, applications, and challenges,” *Rangeland Systems*, pp. 303–345, Springer, Berlin, Germany, 2017.
- [44] M. Scheffer, S. R. Carpenter, V. Dakos, and E. H. van Nes, “Generic indicators of ecological resilience: inferring the chance of a critical transition,” *Annual Review of Ecology, Evolution, and Systematics*, vol. 46, no. 1, pp. 145–167, 2015.
- [45] B. Berthomieu, P.-O. Ribet, and F. Vernadat, “The tool TINA—construction of abstract state spaces for petri nets and time petri nets,” *International Journal of Production Research*, vol. 42, 2004.
- [46] V. N. Livina, F. Kwasniok, and T. M. Lenton, “Potential analysis reveals changing number of climate states during the last 60 kyr,” *Climate of the Past*, vol. 6, no. 1, pp. 77–82, 2010.
- [47] T. M. Lenton, V. N. Livina, V. Dakos, and M. Scheffer, “Climate bifurcation during the last deglaciation?” *Climate of the Past*, vol. 8, no. 4, pp. 1127–1139, 2012.
- [48] S. H. Strogatz, *Nonlinear Dynamics and Chaos: With Applications to Physics, Biology and Chemistry*, Perseus Publishing, New York, NY, USA, 2001.
- [49] J. Lovelock, *The Ages of Gaia: A Biography of Our Living Earth*, Oxford University Press, Oxford, UK, 2000.

- [50] O. Lejeune, M. Tlidi, and P. Couteron, "Localized vegetation patches: a self-organized response to resource scarcity," *Physical Review E*, vol. 66, no. 1, 2002.
- [51] C. H. Waddington, "The epigenotype," *Endeavour*, vol. 1, pp. 18–20, 1942.
- [52] S. Gavrillets, "Highdimensional fitness landscapes and speciation," in *Evolution—The Extended Synthesis*, M. Pigliucci and G. B. Müller, Eds., pp. 45–79, MIT Press Scholarship Online, Cambridge, MA, USA, 2010.
- [53] H. Ledford, "Language: disputed definitions," *Nature*, vol. 455, no. 7216, pp. 1023–1028, 2008.
- [54] V. V. Ogryzko, "Erwin schroedinger, francis crick and epigenetic stability," *Biology Direct*, vol. 3, no. 1, p. 15, 2008.
- [55] J. Vollmer, "Chaos, spatial extension, transport, and non-equilibrium thermodynamics," *Physics Reports*, vol. 372, no. 2, pp. 131–267, 2002.
- [56] C. Gaucherel, P. H. Gouyon, and J. L. Dessalles, *Information, the Hidden Side of Life*, ISTE, Wiley, London, UK, 2019.
- [57] E. P. Odum, "Energy flow in ecosystems: a historical review," *American Zoologist*, vol. 8, no. 1, pp. 11–18, 1968.
- [58] F. Bouchard, "How ecosystem evolution strengthens the case for functional pluralism," *Functions: Selection and Mechanisms*, pp. 83–95, Springer Netherlands, Dordrecht, Netherlands, 2013.
- [59] S. J. Gould, *Wonderful Life: The Burgess Shale and the Nature of History*, W. W. Norton & Company, New York, NY, USA, 1989.
- [60] C. Hély, P. Braconnot, J. Watrin, and W. Zheng, "Climate and vegetation: simulating the African humid period," *Comptes Rendus Geoscience*, vol. 341, no. 8-9, pp. 671–688, 2009.
- [61] K. Sterelny, "Contingency and history," *Philosophy of Science*, vol. 83, pp. 1–18, 2015.
- [62] J. Ratnam, W. J. Bond, R. J. Fensham et al., "When is a "forest" a savanna, and why does it matter?" *Global Ecology and Biogeography*, vol. 20, no. 5, pp. 653–660, 2011.
- [63] Y. Bergeron and A. Leduc, "Relationships between change in fire frequency and mortality due to spruce budworm outbreak in the southeastern Canadian boreal forest," *Journal of Vegetation Science*, vol. 9, pp. 493–500, 1998.
- [64] B. J. Stocks, M. A. Fosberg, T. J. Lynham et al., "Climate change and forest fire potential in Russian and Canadian boreal forests," *Climatic Change*, vol. 38, no. 1, pp. 1–13, 1998.
- [65] A. G. Tansley, "The use and abuse of vegetational concepts and terms," *Ecology*, vol. 16, no. 3, pp. 284–307, 1935.
- [66] N. Chomsky, *Studies on Semantics in Generative Grammar*, Mouton & Co., NV Publishers, La Haye, Netherlands, 1972.
- [67] C. Gaucherel, F. Boudon, T. Houet, M. Castets, and C. Godin, "Understanding patchy landscape dynamics: towards a landscape language," *PLoS One*, vol. 7, no. 9, Article ID e46064, 2012.
- [68] C. Godin, "Representing and encoding plant architecture: a review," *Annals of Forest Science*, vol. 57, no. 5, pp. 413–438, 2000.
- [69] C. L. Crumley, "Historical ecology: a multidimensionalecological orientation," in *Historical Ecology: Cultural Knowledge and Changing Landscapes*, C. L. Crumley, Ed., pp. 1–16, School of American Research Press, Santa Fe, NM, USA, 1994.
- [70] C. Hély, L. Bremond, S. Alleaume, B. Smith, M. T. Sykes, and J. Guiot, "Sensitivity of African biomes to changes in the precipitation regime," *Global Ecology and Biogeography*, vol. 15, no. 3, pp. 258–270, 2006.
- [71] M. J. Wade, J. Harmand, B. Benyahia et al., "Perspectives in mathematical modelling for microbial ecology," *Ecological Modelling*, vol. 321, pp. 64–74, 2016.
- [72] C. Gaucherel, *The Languages of Nature. When Nature Writes to Itself*, Lulu editions, Paris, France, 2019.

Research Article

Simulation of Nonradiative Energy Transfer in Photosynthetic Systems Using a Quantum Computer

José Diogo Guimarães,^{1,2} Carlos Tavares ,^{1,3} Luís Soares Barbosa,^{1,3,4}
and Mikhail I. Vasilevskiy^{2,4,5}

¹Department of Informatics, University of Minho, Campus of Gualtar, Braga, Portugal

²Department of Physics, University of Minho, Campus of Gualtar, Braga, Portugal

³High-Assurance Software Laboratory, INESC TEC, Department of Informatics, University of Minho, Campus of Gualtar, Braga, Portugal

⁴International Iberian Nanotechnology Laboratory, Braga, Portugal

⁵Centro de Física, Universidade do Minho, Campus de Gualtar, Braga, Portugal

Correspondence should be addressed to Carlos Tavares; ctavares@inesctec.pt

Received 3 April 2020; Revised 14 July 2020; Accepted 2 September 2020; Published 16 September 2020

Academic Editor: Tomas Veloz

Copyright © 2020 José Diogo Guimarães et al. This is an open access article distributed under the Creative Commons Attribution License, which permits unrestricted use, distribution, and reproduction in any medium, provided the original work is properly cited.

Photosynthesis is an important and complex physical process in nature, whose comprehensive understanding would have many relevant industrial applications, for instance, in the field of energy production. In this paper, we propose a quantum algorithm for the simulation of the excitonic transport of energy, occurring in the first stage of the process of photosynthesis. The algorithm takes in account the quantum and environmental effects (pure dephasing), influencing the quantum transport. We performed quantum simulations of such phenomena, for a proof of concept scenario, in an actual quantum computer, IBM Q, of 5 qubits. We validate the results with the Haken-Ströbl model and discuss the influence of environmental parameters on the efficiency of the energy transport.

1. Introduction

Photosynthesis is a vital and pervasive complex physical process in nature, where the radiation of the sun is captured by certain living beings, such as plants and bacteria, and transformed into the necessary carbohydrates needed for their survival [1, 2]. From the physics and chemistry perspective, it is a complex process occurring through several stages with several kinds of physical phenomena involved, namely, the light absorption, energy transport, charge separation, photophosphorylation, and carbon dioxide fixation [3]. The understanding of such phenomena has greatly progressed in the past 40 years with the physical characterization of the structure of many photosynthetic complexes [4–6]. The comprehension of such processes would allow for many potential huge-impact industrial breakthroughs in the field of energy, from the great efficiency improvement in energy

capture of solar panels [7] to the construction of artificial light-harvesting devices and solar fuels [8–11].

The photosynthesis begins by the absorption of a photon. It occurs via excitation of a pigment molecule, which acts as a light-harvesting antenna connected to the rest of the photosynthetic apparatus by protein molecules. Photosynthetic pigment-protein complexes transfer the absorbed sunlight energy, in the form of molecular electronic excitation, to the reaction center, where charge separation initiates a series of biochemical processes [2]. This work is focused on the first stage of photosynthesis, more precisely on the transport of the absorbed radiation energy from the antenna to the reaction center, which proceeds in the form of the so-called Excitonic Energy Transfer (EET), as schematically shown in Figure 1.

This transport is known to be very efficient in photosynthesis, as is the whole process, with the overall quantum

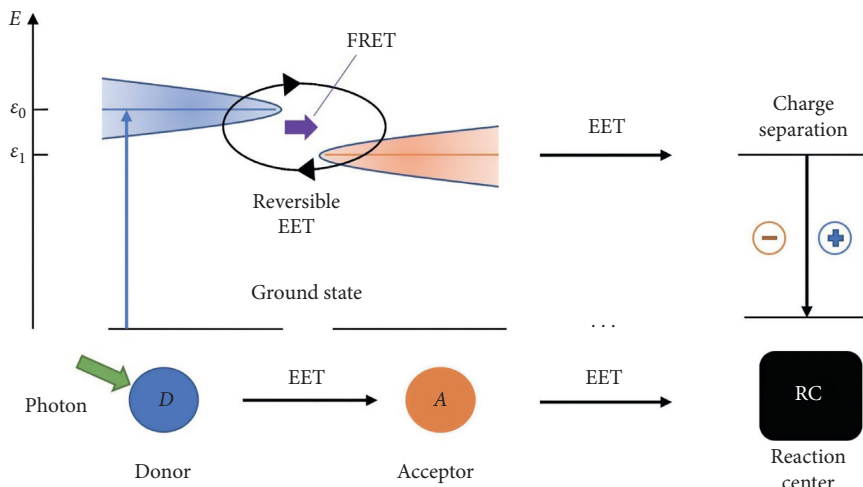
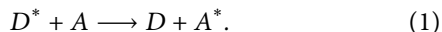


FIGURE 1: Schematics of the energy transfer process from light-harvesting antenna (the donor) through a chain of acceptor molecules to the reaction center. The excited states of the participating molecules, denoted as ϵ_m , are broadened and they allow for resonance energy transfer via irreversible Förster-type resonant process of exciton transfer from donor to acceptor even if $\epsilon_m \neq \epsilon_{m+1}$, which is denoted by the thick arrow labelled FRET. However, if the coupling between the donor and the acceptor molecules is strong enough, the process becomes reversible and the exciton can go to and through many times before it is transferred; this situation is labelled by “reversible EET” and it does not require matching of the energy levels ϵ_m and ϵ_{m+1} .

efficiency of initiation of charge separation per absorbed photon up to 95% [2]. The absorbed photon creates an exciton on the antenna molecule, which can eventually transfer it to other molecules. In this context, it is called donor, while the others are called acceptors and the EET process can be described by the following reaction equation:



The physics of the mechanisms behind equation (1) will be discussed in the following section. Here we just notice that EET is a complex process that can be irreversible (i.e., unidirectional) or reversible, that is, coherent over some period of time, as evidenced by experimental observations of long-lived oscillatory features in the dynamical response of several photosynthetic systems [12–14]. Moreover, it is strongly influenced by the environment. The donor-acceptor pair is not isolated from the rest of the world and is an example of so-called open systems [15]. It must be treated as a subsystem of a larger system including a thermal bath. The properties of the latter are crucial because it introduces relaxation and dephasing into the system directly involved in the EET and, therefore, influences the efficiency of the energy transport.

Open quantum systems cannot be described by a wave function because one does not have enough information to specify it; only a (less detailed) description in terms of a density matrix is possible, which represents a statistical mixture of states or a mixed state (see Supplementary Information A.1). The dynamics of such a system can be determined by solving an equation of motion for the density matrix. Such equations of motion are called quantum master equations. Finding exact solutions to the master equations is extremely difficult but there is a wide range of theoretical approaches and techniques available to make their

mathematical simplification and numerical simulations. These approaches can be divided into several groups according to the regime under study, characterized by the coupling strength between the bath and the system and the existence of memory effects in the bath (i.e., whether the system can be considered as Markovian or not). Broadly speaking, for the weak-coupling Markovian regimes, perturbative approaches are applicable, such as the Bloch-Redfield and Lindblad master equations [2, 16], which can be extended to medium coupling strengths and non-Markovian regimes by including higher-order system-bath interaction terms [17, 18]. For the latter regime, there are also non-perturbative techniques based on the use of path integrals to dissipative systems [19], which can be used to create sets of solvable systems of hierarchical equations, the so-called hierarchical equations of motion (HEOM) [20–22]. Open quantum systems that do not have the Markovian property, for example, because of a too small size of the bath effectively coupled to the system, which keeps memory of the past, are much more difficult for theoretical description because the dynamics equation is nonlocal in time.

However, even within the Markov approximation, the calculations quickly become computationally intractable for realistic photosynthetic systems and environment models. The computational cost of simulating a photosynthetic complex consisting of N molecules with a theoretical tool such as the HEOM grows exponentially with N . A possible computational solution that has been arising to bypass this type of problems is the use of quantum simulation, where it is expected to obtain large performance increases in terms of space, as the number of qubits’ growth is just polynomial, and in terms of time, where an exponential gain is expected.

The use of quantum mechanics to make calculations about quantum mechanics, promising great computational

advantages, was firstly proposed by Feynman [23, 24]. The field of quantum simulation is under a fast-paced and intense development, finding already application across all fields of physics and using many different physical implementations [25]. Closer to the present work, there are works on quantum transport [26, 27] and on the quantum simulation of dissipative systems [28]. Particularly on the quantum simulation of photosynthesis, we would like to highlight the papers in [29–31], using superconducting qubits and [32] employing a Nuclear Magnetic Resonance (NMR) simulator [33]. The latter is of particular relevance to the work carried out here as it was dedicated to the quantum simulation of the energy transport with environmental actions, where the environment effect is simulated naturally by an appropriate filtering of environmental noise [34], within the NMR system. In this case, the implementation is specific for the EET (i.e., nonuniversal), and the model Hamiltonian was extracted from spectroscopic data for a photosynthetic system [35]. We are simulating the same Hamiltonian as in [32] and starting from the same assumptions, however, the simulation algorithm is completely different, since we conceived a digital quantum simulation designed to run in a universal quantum computer, the commercially available IBM Q of 5 qubits [36]. Our implementation contains a quantum part, aimed at simulating the unitary part of the system’s evolution, and a classical part that simulates the stochastic interaction with the environment, the latter only being able to mimic pure dephasing environmental effects.

2. Physics of the Energy Transport in Photosynthesis

2.1. Förster and Redfield Approaches. The molecules of the light-harvesting complexes usually are not electronically coupled to each other and charge transfer via electron tunneling is improbable. Hence, energy transfer can occur between them through electromagnetic interaction, without net charge transport, because the whole (neutral) exciton is transferred. Such processes are known to take place between molecules [37] or artificial nanostructures such as quantum dots [38] if appropriate conditions are met, which were first formulated by Förster [39]:

- (i) The distance between the donor and acceptor molecules must be sufficiently small because the transfer probability decreases quickly with the distance between them (R), usually as R^{-6}
- (ii) There must be a resonance between the excited states of the donor and acceptor molecules (“Resonance” here means that the energy spectra of the two molecules, broadened because of a number of natural reasons, overlap-see Figure 1)
- (iii) An increase of the refractive index of the surrounding medium decreases the transfer rate

Förster’s approach is based on the second-order perturbation theory (the so-called “Fermi’s Golden Rule”), where the perturbation operator is the electromagnetic

interaction between two transient dipoles corresponding to allowed optical transitions in the donor and acceptor molecules, respectively. It originated the term “Förster resonance energy transfer” (FRET), which applies to an irreversible hopping of an exciton from the donor to the acceptor. The FRET rate (transition probability per unit time) can be expressed by the following relation [2]:

$$k_F = \frac{J^2}{2\pi\hbar^2} \int_{-\infty}^{+\infty} d\omega L_D(\omega) I_A(\omega), \quad (2)$$

where J is the coupling constant, ω is the angular frequency of the electromagnetic field, and $L_D(\omega)$ and $I_A(\omega)$ denote dimensionless lineshape functions of the donor and acceptor molecules, directly related to the energy spectrum of each molecule. The integral is called the spectral overlap between the molecules. The coupling constant, in the dipole-dipole approximation, is given by [37]

$$J = \left\langle \frac{1}{\eta^2 R^3} [((d_A \cdot n) \cdot d_D) - 3(d_A \cdot n)(d_D \cdot n)] \right\rangle, \quad (3)$$

where η is the refractive index of the medium, d_D (d_A) is the transient dipole moment of the donor (acceptor) molecule, $n = (R/R)$, R is the radius vector between the two molecules, and the angular brackets stand for angular average over different orientations of the dipoles.

Even though equation (2) (and the approach itself) is too simplistic to describe all possible situations in EET, defining this characteristic transfer rate allows for the formulation of the following conditions for FRET to occur:

- (i) If the difference between the energies of the excited state energy of the donor (ε_0) and acceptor (ε_1) molecules is small, $|\varepsilon_0 - \varepsilon_1| \ll J$, and these states are in resonance, the energy transfer between the molecules can occur with a high probability
- (ii) If $|\varepsilon_0 - \varepsilon_1| \gg J$ (off-resonance), the exciton is trapped in the donor molecule because it has a very low probability of being transferred; in this case, it either stays in the molecule and later the donor molecule will decay to the ground state, dissipating the energy, or transfers the energy to a different acceptor nearby

As pointed out above, the initial idea of Förster was that an exciton is irreversibly transferred from a donor to an acceptor. More recently, it has been shown experimentally that quantum coherent transport, where energy is transported in the form of wave-packets, has a significant role in many important physical effects, including the photosynthesis [40–42]. The Förster theory does not apply in this regime, as it simply ignores coherence. Later, in 1957, Redfield [43] proposed a transport theory, which applies to the opposite regime of strong coupling between the donor and acceptor [2, 40, 44] (although originally it appeared in the context of NMR spectroscopy). Within this concept, the exciton forms a coherent state based on the whole donor-acceptor pair and oscillates between the two molecules. This system can be described by the following Hamiltonian:

$$\hat{H}_S = \sum_{m=0}^1 \varepsilon_m |m\rangle \langle m| + J(|0\rangle \langle 1| + |1\rangle \langle 0|), \quad (4)$$

where $|m\rangle$ denotes the exciton on the molecule m . The eigenstates of (4) are linear combinations of $|0\rangle$ and $|1\rangle$. Coherent dynamics correspond to the presence of nonzero off-diagonal elements in the density matrix describing the evolution of the quantum system. Their oscillation (or quantum beating) is indicative of coherence [2]. For the system with Hamiltonian (4), the description in terms of state vectors is perfectly possible but it will not be the case if interactions with environment are taken into account. Therefore, we may introduce the density matrix description at this point. The evolution of the off-diagonal elements of the system's density matrix, written in the energy basis (where the Hamiltonian is diagonal) and denoted as ρ_{ij} , is given by

$$\rho_{ij}(t) = e^{(-it\sqrt{(\varepsilon_0 - \varepsilon_1)^2 + 4J^2/\hbar})} \rho_{ij}(0), \quad i \neq j, \quad (5)$$

(see Supplementary Information A.2 for the derivation). These states are perturbed by interactions with the environment (the bath), which destroys their coherence. Mathematically, it is expressed in the form of a master equation, which is known as the Bloch-Redfield equation; its general form can be found, for example, in [16]. This consideration is extendable to a chain of molecules and can be seen as (partially) coherent transport [40]. The presence of the latter, observable through coherent oscillations of the energy levels of molecules across different sites (the quantum beating), was first conjectured in the 30s [45] and theoretically predicted in more recent works [44, 46]. It became possible to observe them more recently, thanks to the advances of optical spectroscopy techniques [12–14, 47], and it was achieved even at room temperature [42]. In these experiments, it was possible to confirm the substantial impact of such coherent effects on the excitation energy transfer in photosynthetic systems [2]. Moreover, the importance of environmental noise in the quantum transport involving coherence was also discussed more recently [15, 48] and it is not fully understood yet.

2.2. Decoherence. Processes caused by the molecules' environment may destroy coherence and thus influence this type of energy transport [2, 15, 49]; moreover, they can foster it. Indeed, completely coherent oscillations (called Rabi floppings in atomic physics) between different molecular sites do not correspond to an energy flux. Breaking the oscillatory evolution at some moment may help in transferring the exciton along the molecular chain.

If interactions exist between a system and its environment, they affect the (pure) states of the system, introducing "errors" and making these states mixed. It means the so-called phenomenon of decoherence, which, by the way, has been the main obstacle to the success of quantum computation. Decoherence processes can be divided into three categories: (i) amplitude damping, (ii) dephasing, and (iii) depolarization, which are briefly described below [50].

2.2.1. Amplitude Damping. Environment interactions with the system may cause a loss of the amplitude of one or more system's states. The spontaneous emission of a photon from the system (i.e., from one of the molecules) to the environment is an example of this kind of process, so that the system returns to its ground state (without exciton) [51]. For a two-level system (e.g., a qubit), this type of decoherence contracts the Bloch sphere along the z -axis (see Supplementary Information A.1).

2.2.2. Phase Damping or Dephasing. Such interactions conserve the energy of the system, contrary to the amplitude damping. A phase damping channel removes the superposition of the system state; that is, the off-diagonal terms of the system's density matrix decay over time down to zero. It is a process of removing the coherence of the system, causing a classical probability distribution of states and, therefore, imposing some classical behaviour in a quantum system. A simple way to look at this type of decoherence is also to think of the system interacting with the environment, where the relative phases of the system's states become randomized by the environment. This randomness comes from a distribution of energy eigenvalues of the environment. As a result, the evolution of the quantum system's Rabi cycle ceases but the time-average populations of the states may not change and this is the case of the pure dephasing. For a two-level system with a pure dephasing interaction, the Bloch sphere contracts in the $x - y$ plane.

2.2.3. Depolarization. This type of decoherence changes system's state, which initially is pure, to a mixed state, with a probability P of another pure state and the probability $(1 - P)$ of the initial state of the system. It is equivalent to saying that, for a single qubit, an initial pure state represented on the Bloch sphere has suffered a contraction over all dimensions of the sphere (with the contraction degree that depends on the probability P). It can be thought of as a combination of the other two types of decoherence.

The amplitude damping is certainly detrimental for EET, since the energy is simply dissipated into the environment. The action of dephasing processes progressively eliminates the coherence (off-diagonal) elements in the system's density matrix, causing the oscillation amplitude to decay (beating suppression). It eventually turns the diagonal matrix elements (populations) into (non-correlated) classical probabilities, a process known as thermal relaxation, for which the existence of coherence in a system is time-limited. On the other hand, it has also been shown that dephasing processes can have a positive role in the coherent transport of energy [2]. First, it yields random fluctuations in the energy spectrum of each molecule, which can bridge the energy gap between the molecules, momentarily turning a nonresonant system into a resonant one. Second, dephasing can also help in avoiding the existence of the so-called coherence traps in a molecular chain, a kind of deadlocks in energy transport where the exciton can be confined [2]. Thus, the result of action of a decoherence source on an EET system is not obvious a

priori. Below we shall consider a simple model of pure dephasing consisting in a telegraph-type classical noise affecting the donor-acceptor pair.

3. Materials and Methods

We aim at exploring the energy transport underlying the photosynthesis, throughout time, under two regimes: (i) in an isolated system and (ii) under an action of the environment causing decoherence. In the “no-decoherence” case (i), one can study the evolution of system’s state vector, which obeys the following equation:

$$|\Psi_{t_f}\rangle = e^{(-i\hat{H}(t_f-t_i)/\hbar)}|\Psi_{t_i}\rangle \equiv \hat{U}|\Psi_{t_i}\rangle, \quad (6)$$

for a time-independent Hamiltonian. Here t_f and t_i are the upper and lower limits of the time interval to study. In order to be able to do the calculation of the system’s evolution on a quantum computer, it is necessary to provide a suitable qubit encoding for the possible states and an approximation for the Hamiltonian evolution operator, \hat{U} , in terms of quantum gates and circuits (computational Hamiltonian). The time, a continuous entity in equation (6), has to be discretized onto a set of intervals, Δt , where the Hamiltonian of interest can be approximated as constant. The actual computational process is given by the repeated application of the evolution operator on the prepared state $|\Psi_i\rangle$, for s times, of the computational Hamiltonian, such that $t_i + s \cdot \Delta t = t_f$. The process is finished by the observation of the desired properties, that is, a set of measurements, in the appropriate basis, on the end state.

Concerning the particular qubit encoding chosen, a chain of $N = 2^q$ molecules is encoded by a set of q qubits, where $|m\rangle$ corresponds to the excitation (exciton) on the m -th molecule; for example, for a two-molecule chain, state $|0\rangle$ represents the exciton on the first molecule and $|1\rangle$ represents the excitation on the second one, and a possible successful transport of energy would correspond to the transition of the state $|0\rangle$ to the state $|1\rangle$. We denote this as the site basis. The computational Hamiltonians under this encoding for the cases under study are discussed in the following sections. From now on, we shall set $\hbar = 1$. Also, it is convenient to measure the energies/frequencies in cm^{-1} , as this is common in spectroscopy.

3.1. No-Decoherence Hamiltonian. Considering a small chain of N molecules, the system’s Hamiltonian in the site basis reads as follows:

$$\hat{H}_S = \sum_{m=0}^{N-1} \varepsilon_m |m\rangle \left\langle m \right| + \sum_{m \neq n} J_{mn} |m\rangle \left\langle n \right|, \quad (7)$$

where ε_m is the first excited state energy of the molecule m and J_{nm} is the electronic coupling between the molecules n and m . The Hamiltonian (7) for just two molecules (1 qubit), identical to equation (4), in the 2×2 matrix form, reads

$$\hat{H}_S = \begin{pmatrix} \varepsilon_0 & J \\ J & \varepsilon_1 \end{pmatrix}. \quad (8)$$

Its evolution operator is given by

$$|\Psi(t)\rangle = e^{-i\hat{H}_S t} |\Psi(0)\rangle \equiv \hat{U}(t) |\Psi(0)\rangle. \quad (9)$$

Although the Hamiltonian (8) possesses nondiagonal elements, finding a good approximation in terms of quantum circuits is relatively straightforward. A possible strategy for this is by finding a diagonalizing transformation, T , of the Hamiltonian, such that

$$\hat{H}_S = T^\dagger \hat{H}_{S\text{-diag}} T. \quad (10)$$

where $\hat{H}_{S\text{-diag}}$ is the diagonal Hamiltonian. Therefore, the evolution operator can be rewritten as follows:

$$\hat{U}(t) = e^{-i\hat{H}_S t} = T^\dagger e^{-i\hat{H}_{S\text{-diag}} t} T. \quad (11)$$

The problem now reduces to the approximation of the T operator (and its adjoint) and the Hamiltonian $\hat{H}_{S\text{-diag}}$, which can all be efficiently approximated in quantum circuits. The latter operator is diagonal in the site basis; thus the unitary evolution operator can be expressed as

$$\hat{U}(t) = e^{-i\hat{H}_S t} = T^\dagger \left[\prod_{m=0}^{N-1} e^{-iE_m t} \right] T = T^\dagger \left[\prod_{m=0}^1 e^{-iE_m t} \right] T. \quad (12)$$

The T and T^\dagger matrices can be implemented by simple rotations, $R_y(\theta)$ and $R_y(-\theta)$, for a two-molecule system. However, for a higher number of molecules, a rotational decomposition algorithm together with the Gray code [51], which decomposes a matrix in the multiplication of a single qubit and CNOT gates, has to be used. Using this particular algorithm, the gate complexity for N molecules is $\mathcal{O}(N^2 \log^2[N])$ [51]. On the other hand, the diagonalized evolution operator,

$$\hat{U}(t) = \begin{pmatrix} e^{-iE_0 t} & 0 \\ 0 & e^{-iE_1 t} \end{pmatrix}, \quad (13)$$

translates into trivial phase rotations over each of the energy eigenstates $|E_i\rangle$ of the system with the respective energy eigenvalues E_i . This operator can be constructed as a sequence of $CR_Z(\phi_i)$ gates applied to an ancilla qubit (initialized at $|1\rangle$), where the angle is given by $\phi_i = -2E_i t$, $i = 1, 2$. The X gates are used to “select” the eigenvector to which the controlled rotation is to be applied. The circuit implementation of the operator defined in (13) is illustrated in Figure 2. The gate complexity of this operator, in terms of single qubit and CNOT gates for N molecules, is $\mathcal{O}(N \log[N])$.

For the whole circuit, resulting from the sequencing of $T^\dagger \hat{H}_{S\text{-diag}} T$, the number of qubits required to simulate a molecular chain of N elements is $2 \log_2 N$ and the gate count scales with $\mathcal{O}(N^2 \log^2 N)$ single qubit and CNOT gates. The transformations T and T^\dagger , in the general case, possess a

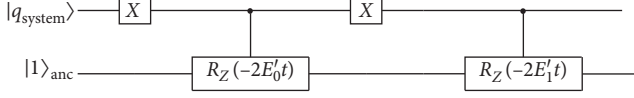


FIGURE 2: Implementation of the system's evolution operator. $|q_{\text{system}}\rangle$ is the state vector of the system's qubit in the energy eigenbasis.

high circuit depth, which makes the system hard to simulate accurately, with low error rate, in the current available quantum computers.

3.2. Introducing Decoherence into the System. We shall implement artificial decoherence as pure dephasing by adding Markovian fluctuations to the Hamiltonian. This approach is considered a good approximation in the high-temperature regime for the bath [15, 44, 50]. The actual algorithm to be used is the one of [52], which is used to simulate open quantum systems, with pure dephasing, modeling the action of the decoherence as classical random fluctuations (a telegraph-type classical noise affecting the system). The actual Hamiltonian for this system reads

$$\hat{H} = \hat{H}_S + \hat{H}_F, \quad (14)$$

and it consists of the system Hamiltonian, \hat{H}_S , of the previous section and the perturbation of a bistable fluctuator environment, \hat{H}_F . The latter simply shifts the energy by a constant value for each molecule, ($\pm g_m/2$), as illustrated in Figure 3. Explicitly,

$$\hat{H}_F = \sum_{m=0}^1 \chi_m(t) \hat{A}_m, \quad (15)$$

where $\hat{A}_m |m\rangle \langle m|$ is the projection operator and, considering one fluctuator interacting with each molecule m ,

$$\chi_m(t) = g_m \xi_m(t). \quad (16)$$

The function $\xi_m(t)$ switches the fluctuator between the positive and negative values (appearing randomly) at a given fixed rate γ and g_m is the fluctuation strength (or the coupling strength to a molecule m). Physically, the action of the fluctuations is typically stronger for the excited states [44, 53] and g can be larger than the donor-acceptor coupling J .

The implementation of such random bivalued function $\xi_m(t)$ can be done in a straightforward way by a classical pseudorandom numbers generator with a probability of 50% of the values $(-1/2)$ and $(1/2)$. For circuit generation purposes, the values resulting from the random sampling have to be provided in advance of the quantum simulation.

The fluctuator interaction Hamiltonian and the system Hamiltonian do not commute, so, in order to generate an appropriate quantum circuit, one needs to apply an

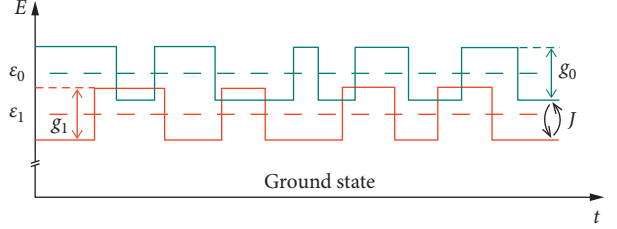


FIGURE 3: Uncorrelated random fluctuations applied to donor and acceptor's excited state energies, ϵ_0 and ϵ_1 . Each molecule is affected by one fluctuator, which generates a telegraph-type classical noise. The fluctuators switch randomly between the positive and negative values at a given fixed rate, so that the periods of time when the molecule energy is constant, $\epsilon_m + (g_m/2)$ or $\epsilon_m - (g_m/2)$, are random. J is the coupling strength between the molecules that can be seen as the rate of hoppings between these fluctuating energy levels.

approximation technique such as the Trotter product formula [54]. Under this approximation, the unitary evolution operator of the Hamiltonian, for a time $t = N_i \Delta t$, where N_i is the number of iterations and Δt is the iteration time-step, becomes

$$\begin{aligned} U(N_i \Delta t) &= \left(e^{-i\hat{H}\Delta t} \right)^{N_i} = \left(e^{-i\hat{H}_F \Delta t} T^\dagger e^{-i\hat{H}_S \Delta t} T \right)^{N_i} \\ &= \left(\left[\prod_{m=0}^1 e^{\pm i(g_m/2)\Delta t} \right] T^\dagger \left[\prod_{m=0}^1 e^{-iE_m \Delta t} \right] T \right)^{N_i}, \end{aligned} \quad (17)$$

where E_m denote the eigenvalues of the system Hamiltonian.

Note that the projection operator \hat{A}_m is not present in the evolution operator (17) because the latter is used in its eigenbasis, that is, the site basis. The fluctuator interaction evolution operator $e^{\pm i(g_m/2)\Delta t}$ is a selective rotational gate over a molecule m $|m\rangle$, which can be implemented by a set of X gates and a controlled gate $\text{CR}_Z(\phi_m)$ with angle $\phi_m = \pm g_m \Delta t$, applied over an ancilla qubit initialized at $|1\rangle$. The whole circuit is presented in Figure 4 for one iteration. The fluctuator waiting time (interval of time between switches), that is, $(1/\gamma)$, can only be equal to or higher than the iteration time-step, Δt . The switching in the fluctuator-molecule coupling strength is performed at every $(1/\gamma \Delta t)$ iteration, where $a \Delta t = (1/\gamma)$, $a \in \mathbb{N}$.

Usually in the study of open quantum systems with a dilated system's Hilbert space (as is the case here), different measurement techniques are required [51, 52]; however, in this case, the open system is simulated in a closed form so, similar to the no-decoherence case, the measurement over the site basis suffices. The full algorithm (random values generator plus the actual simulation) must be performed several times, so that the results of all runs are averaged.

Let us consider the simulation for a time t , using an iteration time-step Δt , and assuming that the environment can have more than one fluctuator interacting with each

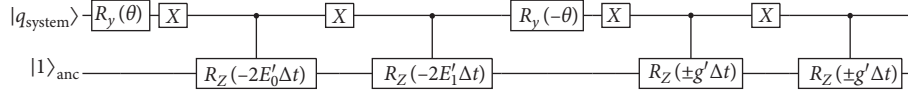


FIGURE 4: Implementation of one iteration of the system with decoherence algorithm. Here $|q_{\text{system}}\rangle$ represents the system's qubit state vector in the site basis.

molecule as well as the chain can have more than just two elements. Then the fluctuator interaction evolution operator requires the following gate resource complexity for a single run: $\mathcal{O}((t/\Delta t)[N(\log_2 N + F)])$ single qubit and CNOT gates, where N is the number of molecules and F is the number of fluctuators interacting with each one.

In the implementation of the system with decoherence, the algorithm gate resources complexity is $\mathcal{O}((t/\Delta t)[N^2 \times \log_2^2 N + NF])$ for a single run. This simulation, yet again, possesses a very high circuit depth, which makes its application unfeasible in quantum computers. The number of necessary qubits is the same as that in the no-decoherence simulation ($2 \log_2 N$).

It also requires $\mathcal{O}(NR \sum_{j=0}^F t\gamma_j)$ random numbers to be classically generated, where R is the number of runs of the algorithm and γ_j is the switching rate of the fluctuator j interacting with the molecule. The number of required simulation runs to average the results and obtain an error $\epsilon > 0$ is predicted to scale as $\mathcal{O}([F(t/\Delta t)]^2/\epsilon^2)$. This complexity is calculated based on the possible nondegenerate energy state outcomes of the entire chain in the simulation for a time t . These outcomes are caused by the bistable random fluctuations; therefore, the possible nondegenerate energy state outcomes for each molecule obey a discrete Gaussian probability distribution.

4. Results

We conducted simulation experiments for the quantum transport in a molecular chain using the algorithm described in the previous section. We executed the simulation for the coherent system on a real quantum computer, IBM Q of 5 qubits, while the pure dephasing scenario was simulated on the QASM quantum simulator in both the near-resonant and nonresonant regimes. For the validation purposes, we compared the results for the coherent system with the theoretical predictions obtained by solving the Schrödinger equation (see Supplementary Information A.2).

As for the decoherent regime, we used a classical computation of the stochastic Haken-Ströbl model [15, 55]. The simulations and circuits involved, encoded in the Qiskit platform [36], can be performed in the following url: <https://github.com/jakumin/Photosynthesis-quantum-simulation>.

4.1. Coherent Regime. The scenario for this regime was simulated with a simple chain of two molecules. As discussed in Materials and Methods and using the parameters proposed in [32], we define the system's Hamiltonian as follows:

Near-resonant regime:

$$H_S = \begin{pmatrix} 13000 & 126 \\ 126 & 12900 \end{pmatrix} \text{cm}^{-1}. \quad (18)$$

Nonresonant regime:

$$H_S = \begin{pmatrix} 12900 & 132 \\ 132 & 12300 \end{pmatrix} \text{cm}^{-1}. \quad (19)$$

The results for both regimes were obtained using an actual quantum device (IBMQ London of 5 qubits) and can be seen in Figures 5 and 6, respectively. Due to the stochastic nature of quantum computers, the experiments were conducted with 2048 shots for each time value. The specific optimized quantum circuits used in this experiment are presented in Supplementary Information A.3. In the following results, the probability of the donor and acceptor molecules being excited is denoted by $P(0) = \langle 0|\rho_S(t)|0\rangle$ and $P(1) = \langle 1|\rho_S(t)|1\rangle$, respectively. Taking the fluctuator's switching rate to be $\gamma = 0$ or the fluctuator-molecule coupling strength to be $g = 0$, one has the coherent regime. These simulations show the limiting case of the Redfield regime, that is, the very weak system-environment coupling, $g \ll J$. The quantum beatings, observed in the simulation results, can be thought of as a reversible transfer of energy between the molecules, where the excitation goes back and forth across the molecules [56].

In the performed simulations, the near-resonant and nonresonant regimes have a maximum probability of $\sim 90\%$ and $\sim 20\%$, respectively, of the energy being transferred to the acceptor molecule. Using the quantum Liouville equation [2] (see Supplementary Information A.2), the period of the quantum beating is $T_{\text{near-res}} \approx 123$ fs for the near-resonant regime and $T_{\text{non-res}} \approx 51$ fs for the nonresonant regime. These periods are in the femtosecond timescale of the experimentally observable quantum beatings [12, 41, 42]. The simulation results show a similar behaviour to that of those predicted by the Schrödinger and quantum Liouville equations, where the off-curve points are predominantly originated by errors in the quantum hardware.

4.2. Decoherent Regime. The scenario for the regime with decoherence introduced is, in some respect, similar to the one presented for the coherent regime for a chain of two molecules. No further changes are made to the Hamiltonian discussed in the Introduction of decoherence in the system. The quantum simulation results are compared with a theoretical evolution based on the stochastic Haken-Ströbl model in the form of the Lindblad master equation [15, 55]. The Lindblad equations were solved in a classical computer using QuTiP [57], a quantum open-systems software framework. The set of Lindblad equations, correspondent to the model in this setting, had one free

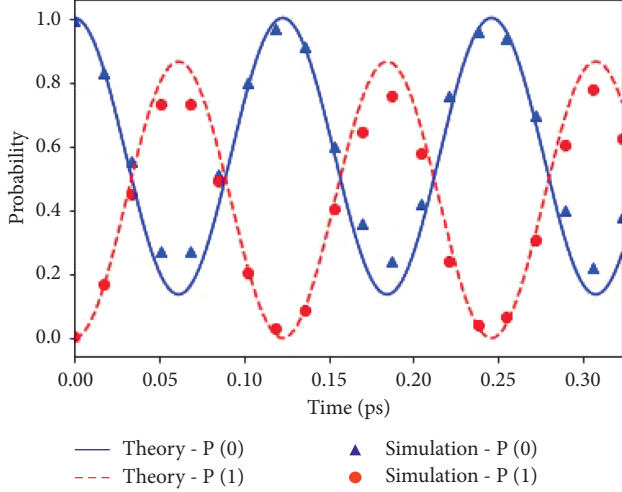


FIGURE 5: Evolution dynamics of the isolated system obtained by employing the quantum algorithm for the near-resonant system: simulation results (points) and theory (lines).

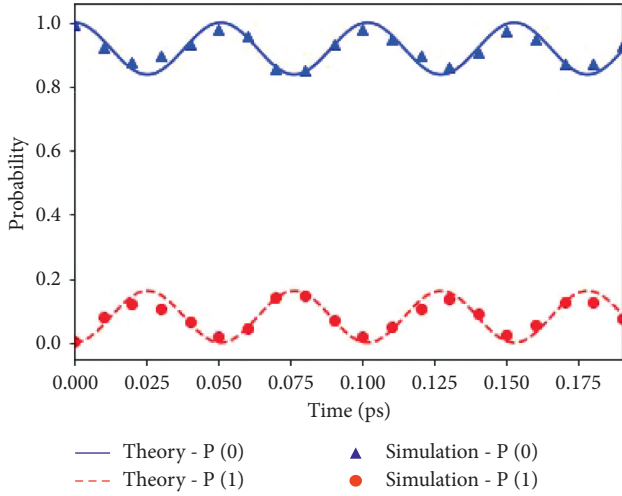


FIGURE 6: Evolution dynamics of the isolated system obtained by employing the quantum algorithm for the nonresonant system: simulation results (points) and theory (lines).

parameter regarding the environment, the dephasing rate, γ_{deph} . The Lindblad equation in the Haken-Ströbl model reads

$$\frac{d\rho}{dt} = \mathcal{L}[\rho] = -i[H_S, \rho] + \gamma_{\text{deph}} \sum_m \left(L_m \rho(t) L_m^\dagger - \frac{1}{2} \rho(t) L_m^\dagger L_m - \frac{1}{2} L_m^\dagger L_m \rho(t) \right), \quad (20)$$

where $L_m = |m\rangle\langle m|$ are the Lindblad operators, responsible for the system-environment interaction. The system Hamiltonian, H_S , is given by the matrix in (18) for the near-resonant system and the matrix in (19) for the nonresonant system.

For each quantum simulation performed, a fitting process has been employed by adjusting the dephasing rate

of the Haken-Ströbl model, so that the system's evolutions in both classical and quantum algorithms have similar behaviours. This enables one to perform a direct comparison between both theories and to find the actual dephasing rate of the modeled environment over the various regimes considered in this work.

The environment contains only one fluctuator interacting with each molecule with switching rate $\gamma = 125$ THz. As mentioned above, the dephasing rate, γ_{deph} , for the Lindblad equation is adjusted to the behaviour of the system under the action of a fluctuation strength g . For the fluctuation strength in the algorithm varying within the interval $[100, 1000] \text{ cm}^{-1}$, and the corresponding dephasing rate of the Haken-Ströbl model lies in the $\sim [2.3, 70]$ THz range. Due to the existence of random fluctuations, a large number of samples had to be generated. The algorithm was implemented with 250 runs, where 5000 shots were performed for each time t . Figures 7 and 8 present the simulation results for different values of the fluctuation strength, along with the theoretical evolution dynamics, for the near-resonant and nonresonant systems, respectively.

It is seen in Figures 7 and 8 that oscillation amplitudes decay over time, as expected, due to the loss of relative phase coherence between the excited states of the two molecules, evidenced by the disappearance of the quantum beatings. This is associated with the irreversible evolution when the system loses its capacity of performing coherent transport. Additionally, it is clear that the system is led to a classical distribution of the populations in the site eigenbasis.

In the regime under the study, where the environment is assumed to be at thermal equilibrium, the final probability distribution is calculated in the limit of the classical Boltzmann distribution $\langle m | \rho_S(t \rightarrow \infty) | m \rangle = \text{const} \times e^{-(\epsilon_m/k_B T)}$. Here k_B is the Boltzmann constant, T is the temperature of the bath, and const is a normalization constant [50]. Taking the limit of very high temperatures, the population terms approach the Boltzmann distribution $\langle 0 | \rho_S(t \rightarrow \infty) | 0 \rangle \approx \langle 1 | \rho_S(t \rightarrow \infty) | 1 \rangle \approx (1/2)$, which is compatible with the results obtained. The relaxation cannot be fully observed in Figures 7(a), 8(a), and 8(b) because a very large number of iterations would be required for this.

The switching rate must be high enough to observe the dephasing effects. Here we used a value ≈ 33 times larger than the transfer rate, J (i.e., the fluctuator waiting time must be shorter than J^{-1}). As observed in the simulations, it is a suitable value for observing the relevant effects of random fluctuations in the system. At very low rates, it leads the system's evolution to a behaviour similar to the previously observed in the no-decoherence regime (Figures 5 and 6).

The time that coherence lasts in the system is essentially defined by the fluctuation strength, g : in Figures 7(a), 7(b), 8(a), and 8(b) (lower g) the coherence is maintained for some time, while in Figures 7(c), 7(d), 8(c), and 8(d) (higher g) it is quickly suppressed. In the latter regime, an approximated diffusive motion drives the system's evolution, where quantum beating is practically absent. The time that the quantum beating lasts in these simulations (until it reaches an approximate nonoscillating behaviour) is about

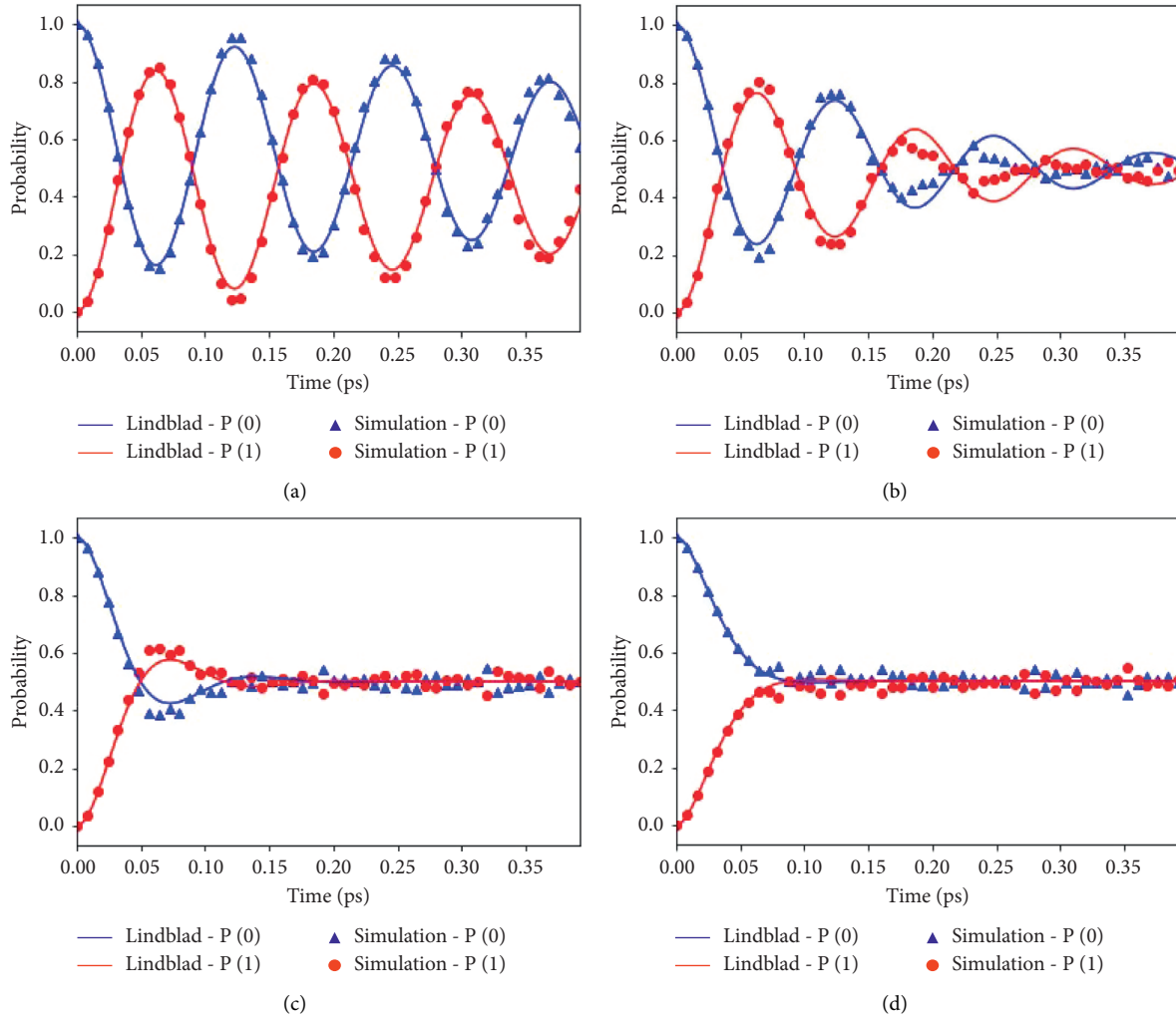


FIGURE 7: Evolution dynamics of the system with decoherence obtained by employing the quantum algorithm for the near-resonant system: simulation results (points) and theory (lines). (a) $g = 1000 \text{ cm}^{-1}$; $\gamma_{\text{deph}} = 2.3 \text{ THz}$. (b) $g = 300 \text{ cm}^{-1}$; $\gamma_{\text{deph}} = 10 \text{ THz}$. (c) $g = 700 \text{ cm}^{-1}$; $\gamma_{\text{deph}} = 41 \text{ THz}$. (d) $g = 1000 \text{ cm}^{-1}$; $\gamma_{\text{deph}} = 70 \text{ THz}$.

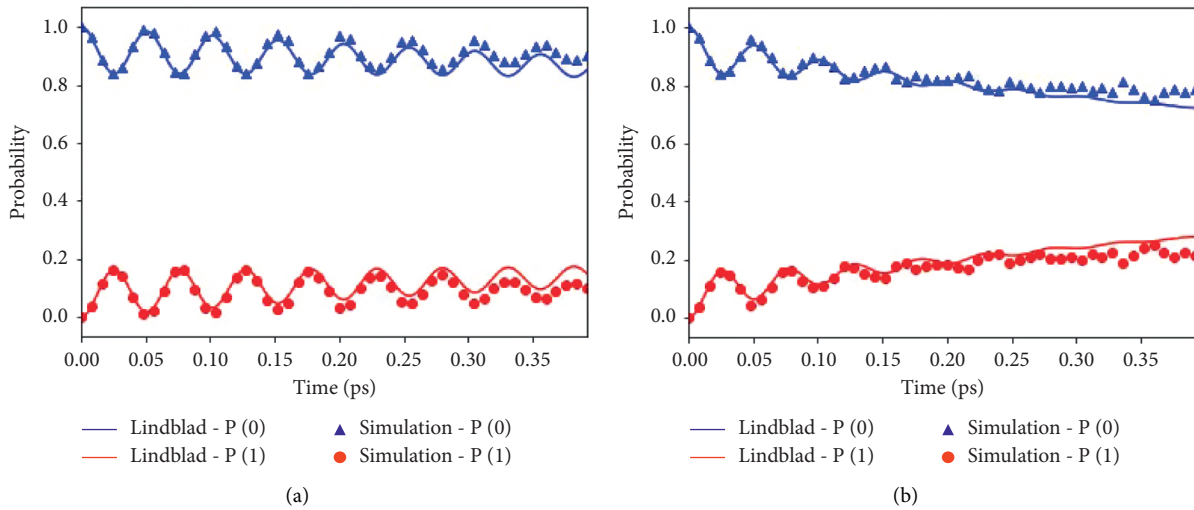


FIGURE 8: Continued.

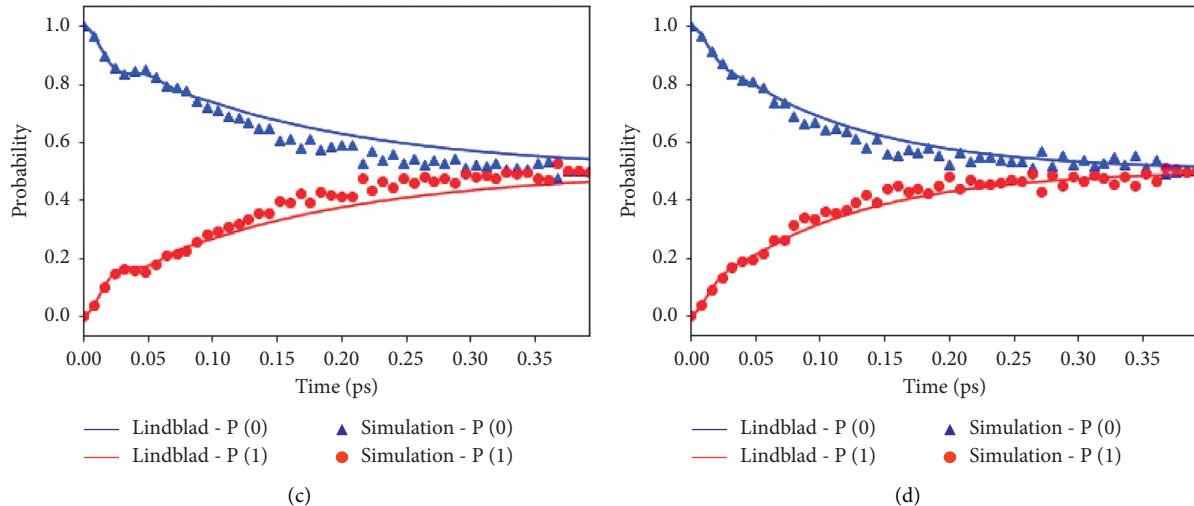


FIGURE 8: Evolution dynamics of the system with decoherence obtained by employing the quantum algorithm for the nonresonant system: simulation results (points) and theory (lines). (a) $g = 1000 \text{ cm}^{-1}$; $\gamma_{\text{deph}} = 2.3 \text{ THz}$. (b) $g = 300 \text{ cm}^{-1}$; $\gamma_{\text{deph}} = 10 \text{ THz}$. (c) $g = 700 \text{ cm}^{-1}$; $\gamma_{\text{deph}} = 41 \text{ THz}$. (d) $g = 1000 \text{ cm}^{-1}$; $\gamma_{\text{deph}} = 70 \text{ THz}$.

350 fs in Figure 7(b) (near-resonant system) and 200 fs in Figure 8(b) (nonresonant system), with a fluctuation strength $g = 300 \text{ cm}^{-1}$. At a longer time, it has been experimentally observed to persist ($t > 660 \text{ fs}$ [42]), a timescale which could be modeled in the present simulation by changing the environment parameters, that is, lowering the fluctuation strength g , as can be observed in Figures 7(a) and 8(a).

5. Discussion and Conclusions

Two main conclusions can be drawn from the presented results:

- (i) There is a very good agreement between the solution of the Schrödinger equation and the coherent quantum algorithm results in the reproduction of the purely oscillatory evolution of the isolated quantum system.
- (ii) There also is a good agreement between the results obtained by the Haken-Ströbl model and the quantum algorithm. The increase of the dephasing rate implies an increase in the fluctuation strengths; thus, a faster suppression of the quantum beatings can be observed, as predicted theoretically [15].

Therefore, the correctness of the results obtained in the quantum simulations is verified.

The results obtained in the present work were not directly compared with [32] due to the different timescales used. The major difference lies in the physical implementation, NMR versus universal quantum computer, where there might be an advantage for the former from the viewpoint of the scalability and reliability, at the current state of quantum technology. However, there is a clear advantage of the quantum computer, from the viewpoint of easiness of implementation, as it is also possible to implement circuits of arbitrary precision, harder to do with the NMR simulator, which is dependent on a

Hamiltonian mapping process. The computational advantage verified for the NMR simulator still holds after the present work, as the number of executions for the algorithm of this work is polynomial on the precision required, although the circuit generation may be problematic, as a matrix diagonalization operation is necessary (complexity estimated in $O(N^3)$).

To conclude, we proposed a quantum algorithm to simulate the energy transfer phenomenon present in general photosynthesis, under the presence of quantum coherence between the molecules and the decoherence effects caused by environmental interference. Using this algorithm, we also performed simulations in the commercially available quantum computer of IBM, IBM Q of 5 qubits, for the coherent scenario, and in the quantum simulator (QASM) for the decoherent scenario. For validation purposes, we also computed the evolution of analogous systems using well-established (classical) methods in literature, obtaining quite similar results between the methods. The results obtained were also in agreement with the predictions that can be found in literature, for the role of the quantum coherent and dephasing effects in the energy transport of photosynthesis: for the high-temperature environment defined here, it was clear that dephasing, modeled as energy fluctuations in the site energies, limited the time quantum coherence lasts in light-harvesting antenna. Moreover, it was also verified that the fluctuation strength and the switching rate of the Markovian fluctuator environment are directly related to the energy transfer efficiency, allowing the simulation of different transport regimes by setting them appropriately.

Similar to [32], this setting revealed itself as an interesting platform for the study of the quantum and environmental effects in a small photosynthetic system, and therefore we consider that the use of quantum simulations may be a feasible alternative in systems with medium-strong coupling and non-Markovian systems in the future. However, the algorithm obtained, due to the high requirements of

gates and qubits, is not scalable to real-world photosynthetic systems, with the current state of quantum technology. Hence, this simulation should be seen as a proof of concept, since a realistic quantum simulation of a photosynthetic system would have to involve hundreds of light-harvesting molecules, which is beyond the current quantum technology. Furthermore, the algorithm only effectively simulates pure dephasing baths. For future work, we aim at extending it to new types of bath, that is, those allowing for higher exciton recombination rates and non-Markovian effects, as well as to new geometries of photosynthetic systems, in particular to the Fenna-Matthews-Olson complex [2].

Data Availability

The data, codes, and other tools used in this work are available upon request.

Conflicts of Interest

The authors declare that there are no conflicts of interest.

Acknowledgments

Carlos Tavares was funded by Fundação para a Ciência e a Tecnologia (FCT) under Grant no. SFRH/BD/116367/2016, funded under the POCH programme and MCTES national funds. This work was financed by the European Regional Development Fund (ERDF) through the Operational Programme for Competitiveness and Internationalisation (COMPETE 2020 Programme) and by national funds through the Portuguese funding agency, Fundação para a Ciência e a Tecnologia (FCT), within project KLEE (POCI-01-0145-FEDER-030947) and the Strategic Funding UIDB/04650/2020 of the Centre of Physics.

Supplementary Materials

A.1: brief introduction to quantum systems. A.2: solution of the Schrödinger and Liouville equations for the two-molecule system. A.3: circuits for the coherent regime. (*Supplementary Materials*)

References

- [1] N. Lambert, Y.-N. Chen, Y.-C. Cheng, C.-M. Li, G.-Y. Chen, and F. Nori, "Quantum biology," *Nature Physics*, vol. 9, no. 1, pp. 10–18, 2013.
- [2] M. Mohseni, Y. Omar, G. S. Engel, and M. B. Plenio, *Quantum Effects in Biology*, Cambridge University Press, Cambridge, England, 2014.
- [3] G. R. Fleming and R. v. Grondelle, "The primary steps of photosynthesis," *Physics Today*, vol. 47, no. 2, pp. 48–55, 1994.
- [4] Y. C. Cheng and R. J. Silbey, "Coherence in the b800 ring of purple bacteria lh2," *Physical Review Letters*, vol. 96, no. 2, Article ID 028103, 2006.
- [5] J. Deisenhofer and H. Michel, "The photosynthetic reaction center from the purple bacterium rhodospseudomonas viridis," *Science*, vol. 245, no. 4925, pp. 1463–1473, 1989.
- [6] S. Wolf-Dieter, O. Klukas, N. Krauß, W. Saenger, P. Fromme, and H. Tobias Witt, "Photosystem i of synechococcus elongatus at 4 Å resolution: comprehensive structure analysis," *Journal of Molecular Biology*, vol. 272, no. 5, pp. 741–769, 1997.
- [7] N. S. Lewis, "Research opportunities to advance solar energy utilization," *Science*, vol. 351, no. 6271, 2016.
- [8] D. Gust, T. A. Moore, and A. L. Moore, "Mimicking photosynthetic solar energy transduction," *Accounts of Chemical Research*, vol. 34, no. 1, pp. 40–48, 2001.
- [9] D. Gust, T. A. Moore, and A. L. Moore, "Solar fuels via artificial photosynthesis," *Accounts of Chemical Research*, vol. 42, no. 12, pp. 1890–1898, 2009.
- [10] E. Romero, V. I. Novoderezhkin, and R. van Grondelle, "Quantum design of photosynthesis for bio-inspired solar-energy conversion," *Nature*, vol. 543, no. 7645, pp. 355–365, 2017.
- [11] L. Xu, Z. R. Gong, M.-J. Tao, Ai Qing et al., "Artificial light harvesting by dimerized möbius ring," *Physical Review E*, vol. 97, no. 4, Article ID 042124, 2018.
- [12] G. S. Engel, T. R. Calhoun, E. L. Read et al., "Evidence for wavelike energy transfer through quantum coherence in photosynthetic systems," *Nature*, vol. 446, no. 7137, pp. 782–786, 2007.
- [13] R. Hildner, D. Brinks, J. B. Nieder, R. J. Cogdell, and N. F. van Hulst, "Quantum coherent energy transfer over varying pathways in single light-harvesting complexes," *Science*, vol. 340, no. 6139, pp. 1448–1451, 2013.
- [14] H. Lee, Y.-C. Cheng, and G. R. Fleming, "Coherence dynamics in photosynthesis: protein protection of excitonic coherence," *Science*, vol. 316, no. 5830, pp. 1462–1465, 2007.
- [15] P. Rebentrost, M. Mohseni, I. Kassal, S. Lloyd, and Alán Aspuru-Guzik, "Environment-assisted quantum transport," *New Journal of Physics*, vol. 11, no. 3, Article ID 033003, 2009.
- [16] J. Jan, J. I. David, M. B. Plenio, S. F. Huelga, and J. H. Cole, "Bloch-redfield equations for modeling light-harvesting complexes," *The Journal of Chemical Physics*, vol. 142, no. 6, Article ID 064104, 2015.
- [17] S. Jang, J. Cao, and R. J. Silbey, "Fourth-order quantum master equation and its markovian bath limit," *The Journal of Chemical Physics*, vol. 116, no. 7, pp. 2705–2717, 2002.
- [18] D. R. Reichman and R. J. Silbey, "On the relaxation of a two-level system: beyond the weak-coupling approximation," *The Journal of Chemical Physics*, vol. 104, no. 4, pp. 1506–1518, 1996.
- [19] R. P. Feynman and F. L. Vernon Jr, "The theory of a general quantum system interacting with a linear dissipative system," *Annals of Physics*, vol. 24, pp. 118–173, 1963.
- [20] A. Ishizaki and Y. Tanimura, "Nonperturbative non-markovian quantum master equation: validity and limitation to calculate nonlinear response functions," *Chemical Physics*, vol. 347, no. 1-3, pp. 185–193, 2008.
- [21] Y. Tanimura, "Stochastic liouville, Langevin, fokker-planck, and master equation approaches to quantum dissipative systems," *Journal of the Physical Society of Japan*, vol. 75, no. 8, Article ID 082001, 2006.
- [22] Y. Tanimura and R. Kubo, "Time evolution of a quantum system in contact with a nearly Gaussian-markoffian noise bath," *Journal of the Physical Society of Japan*, vol. 58, no. 1, pp. 101–114, 1989.
- [23] R. P. Feynman, "Simulating physics with computers," *International Journal of Theoretical Physics*, vol. 21, no. 6/7, 1982.
- [24] S. Lloyd, "Universal quantum simulators," *Science*, vol. 273, pp. 1073–1078, 1996.
- [25] M. G. Julia, S. Ashhab, and F. Nori, "Quantum simulation," *Reviews of Modern Physics*, vol. 86, no. 1, p. 153, 2014.

- [26] C. Maier, T. Brydges, P. Jurcevic et al., “Environment-assisted quantum transport in a 10-qubit network,” *Physical Review Letters*, vol. 122, no. 5, Article ID 050501, 2019.
- [27] D. W. Schönleber, A. Eisfeld, M. Genkin, S. Whitlock, and S. Wüster, “Quantum simulation of energy transport with embedded rydberg aggregates,” *Physical Review Letters*, vol. 114, no. 12, p. 123005, 2015.
- [28] R. Di Candia, S. P. Julen, A. Del Campo, E. Solano, and J. Casanova, “Quantum simulation of dissipative processes without reservoir engineering,” *Scientific Reports*, vol. 5, no. 1, pp. 1–7, 2015.
- [29] S. Mostame, P. Reberntrost, A. Eisfeld et al., “Quantum simulator of an open quantum system using superconducting qubits: exciton transport in photosynthetic complexes,” *New Journal of Physics*, vol. 14, no. 10, p. 105013, 2012.
- [30] P. Anton, A. Bargerbos, F. A. Y. N. Schröder et al., “Studying light-harvesting models with superconducting circuits,” *Nature Communications*, vol. 9, no. 1, pp. 1–7, 2018.
- [31] M.-J. Tao, H. Ming, Ai Qing, and Fu-G. Deng, “Quantum simulation of clustered photosynthetic light harvesting in a superconducting quantum circuit,” 2018, <http://arxiv.org/abs/1810.05825>.
- [32] Bi-X. Wang, M.-J. Tao, Ai Qing et al., “Efficient quantum simulation of photosynthetic light harvesting,” *NPJ Quantum Information*, vol. 4, no. 1, pp. 1–6, 2018.
- [33] X.-L. Zhen, F.-H. Zhang, G. Feng, H. Li, and G.-Lu Long, “Optimal experimental dynamical decoupling of both longitudinal and transverse relaxations,” *Physical Review A*, vol. 93, no. 2, Article ID 022304, 2016.
- [34] A. Soare, H. Ball, D. Hayes et al., “Experimental noise filtering by quantum control,” *Nature Physics*, vol. 10, no. 11, pp. 825–829, 2014.
- [35] Q. Ai, T.-C. Yen, B.-Y. Jin, and Y.-C. Cheng, “Clustered geometries exploiting quantum coherence effects for efficient energy transfer in light harvesting,” *The Journal of Physical Chemistry Letters*, vol. 4, no. 15, pp. 2577–2584, 2013.
- [36] A. Cross, “The ibm q experience and qiskit open-source quantum computing software,” *Bulletin of the American Physical Society*, vol. 63, no. 2018.
- [37] D. L. Andrews and B. S. Sherborne, “Resonant excitation transfer: a quantum electrodynamic study,” *The Journal of Chemical Physics*, vol. 86, no. 7, pp. 4011–4017, 1987.
- [38] J. R. Santos, M. I. Vasilevskiy, and S. A. Filonovich, “Cascade upconversion of photoluminescence in quantum dot ensembles,” *Physical Review B*, vol. 78, p. 245422, 2008.
- [39] T. Förster, *Delocalized Excitation and Excitation Transfer*, Florida State University, Tallahassee, FL, USA, 1965.
- [40] A. Chenu and G. D. Scholes, “Coherence in energy transfer and photosynthesis,” *Annual Review of Physical Chemistry*, vol. 66, no. 1, pp. 69–96, 2015.
- [41] E. Collini, C. Y. Wang, K. E. Wilk, P. M. G. Curmi, B. Paul, and G. D. Scholes, “Coherently wired light-harvesting in photosynthetic marine algae at ambient temperature,” *Nature*, vol. 463, no. 7281, pp. 644–647, 2010.
- [42] G. Panitchayangkoon, D. Hayes, K. A. Fransted et al., “Long-lived quantum coherence in photosynthetic complexes at physiological temperature,” *Proceedings of the National Academy of Sciences*, vol. 107, no. 29, pp. 12766–12770, 2010.
- [43] A. G. Redfield, “On the theory of relaxation processes,” *IBM Journal of Research and Development*, vol. 1, no. 1, pp. 19–31, 1957.
- [44] J. A. Leegwater, “Coherent versus incoherent energy transfer and trapping in photosynthetic antenna complexes,” *The Journal of Physical Chemistry*, vol. 100, no. 34, pp. 14403–14409, 1996.
- [45] F. Perrin, “Théorie quantique des transferts d’activation entre molécules de même espèce. cas des solutions fluorescentes,” *Annales de Physique*, vol. 10, pp. 283–314, 1932.
- [46] R. S. Knox, “Electronic excitation transfer in the photosynthetic unit: reflections on work of william arnold,” *Photosynthesis Research*, vol. 48, no. 1-2, pp. 35–39, 1996.
- [47] R. van Grondelle and V. I. Novoderezhkin, “Energy transfer in photosynthesis: experimental insights and quantitative models,” *Physical Chemistry Chemical Physics*, vol. 8, no. 7, pp. 793–807, 2006.
- [48] J. Cao and R. J. Silbey, “Optimization of exciton trapping in energy transfer processes,” *The Journal of Physical Chemistry A*, vol. 113, no. 50, pp. 13825–13838, 2009.
- [49] M. Mohseni, P. Reberntrost, S. Lloyd, and Alan Aspuru-Guzik, “Environment-assisted quantum walks in photosynthetic energy transfer,” *The Journal of Chemical Physics*, vol. 129, no. 17, p. 11B603, 2008.
- [50] H.-P. BreuerF. Petruccione et al., *The Theory of Open Quantum Systems*, Oxford University Press on Demand, Oxford, UK, 2002.
- [51] M. A. Nielsen and I. Chuang, *Quantum Computation and Quantum Information*, Cambridge University Press, Cambridge, England, 2010.
- [52] H. Wang, S. Ashhab, and F. Nori, “Quantum algorithm for simulating the dynamics of an open quantum system,” *Physical Review A*, vol. 83, no. 6, Article ID 062317, 2011.
- [53] J. Adolphs and T. Renger, “How proteins trigger excitation energy transfer in the fmo complex of green sulfur bacteria,” *Biophysical Journal*, vol. 91, no. 8, pp. 2778–2797, 2006.
- [54] W. Nathan, D. Berry, P. Høyer, and B. C. Sanders, “Higher order decompositions of ordered operator exponentials,” *Journal of Physics A: Mathematical and Theoretical*, vol. 43, no. 6, Article ID 065203, 2010.
- [55] H. Haken and G. Strobl, “An exactly solvable model for coherent and incoherent exciton motion,” *Zeitschrift für Physik A Hadrons and nuclei*, vol. 262, no. 2, pp. 135–148, 1973.
- [56] Y.-C. Cheng, G. S. Engel, and G. R. Fleming, “Elucidation of population and coherence dynamics using cross-peaks in two-dimensional electronic spectroscopy,” *Chemical Physics*, vol. 341, no. 1-3, pp. 285–295, 2007.
- [57] J. R. Johansson, P. D. Nation, and F. Nori, “Qutip: an open-source python framework for the dynamics of open quantum systems,” *Computer Physics Communications*, vol. 183, no. 8, pp. 1760–1772, 2012.

Research Article

Study of the Complexity Game of Supply Chain Green Innovation Introduction under EPR Policy and Government Subsidies

Xueli Zhan ^{1,2} Yi Tian ¹ Chengjin Liu ¹ Aili Hou ¹ and Junhai Ma ¹

¹College of Management and Economics, Tianjin University, Tianjin 300072, China

²School of Economics, Beijing Wuzi University, Beijing 101149, China

Correspondence should be addressed to Yi Tian; yit20160831@126.com and Chengjin Liu; liuchengjin@tju.edu.cn

Received 10 March 2020; Revised 23 June 2020; Accepted 13 July 2020; Published 9 September 2020

Guest Editor: Tomas Veloz

Copyright © 2020 Xueli Zhan et al. This is an open access article distributed under the Creative Commons Attribution License, which permits unrestricted use, distribution, and reproduction in any medium, provided the original work is properly cited.

Nowadays, with global scientific and technological levels rapidly improving, innovation has been a great need for enterprises to solve the dilemma. Combined with EPR (Extended Producer Responsibility) and the topic of remanufacturer, adopting green innovation has been an effective way when green supply chain management is applied. In this paper, we focus on the activity of green innovation and build a model where the manufacturer will invest in green innovation to improve the product availability rate of recycled products and save the cost in the process of remanufacturing. Besides, we take three stages in a cycle into consideration, that is, production/sale, recycling used production, and remanufacture/sale, and meanwhile, the government gives a subsidy to enterprises to encourage the activity of recycling. In the process of model solving, we take a dynamic decision-making way into consideration. We find that the decision adjustment speed of players has a significant effect on the stability, and in a long dynamic repeated game process, with the speed of decision adjustment increasing, the system enters into chaos at the end of the process. It is interesting that when the speed of decision adjustment exceeds the critical point of the bifurcation diagram, the profit of the manufacturer decreases and then enters a chaotic state. Besides, with the level of subsidies increasing, the area of stable region decreases gradually. Certain investment has a positive effect on product selling and recycling as well as the profit, and the government subsidy undoubtedly raises the profit of manufacturers and encourages the activity of recycling. In the end, we make chaos control by adjusting the decision method.

1. Introduction

Due to the increasing environmental preoccupation, the potential economic benefits, and the legislation pressure, supply chain management has changed to focus on environmental impacts of production and Earth resources' preservation [1]. More and more emphases have been put on a closed-loop supply chain because of its benefit of recycling processes which are the possibility of economic viability and environmental sustainability [2]. As we all know, closed-loop supply chain contains two parts, the forward supply chain and the reverse supply chain, in which the new product development, product design and engineering, procurement and production, marketing, sales, distribution, and after-sale service are realized in the forward supply chain, and then, the reverse supply chain refers to used products' collection,

testing, sorting, refurbishing, recovery, recycling, remarketing, reselling, and so on [3, 4]. The closed-loop supply chain expands the connotation of the traditional supply chain and realizes protecting the environment because it increases the utilization ratio of raw materials and reduces the emission levels. Based on that, the closed-loop supply chain has become a new trend in logistics and supply chain management. In China, the EPR pilot work carried out by the Ministry of Industry and Information Technology, Ministry of Finance, Ministry of Commerce, and Ministry of Science and Technology continues to progress, and the EPR recycling has also achieved periodic results.

Remanufacturing is an important part of the closed-loop supply chain which makes resource sustainable possibly. Remanufacturing is the process in which a used product transforms into a "new" product or into a product satisfying

quality level that meets the recently approved American National Standards Institute definition for remanufacturing [5]. Remanufacturing expands the concept of “product life cycle” which usually refers to product manufacturing, use, and disposal. After the birth of the remanufacturing industry, besides the three phases we said, product maintenance and using advanced remanufacturing technology to repair and reconstruction are also needed to be considered in the product design. The USA is the largest remanufacturer in the world, and the output rose 15 percent to at least \$43 billion, supporting 180,000 full-time US jobs by remanufacturing between 2009 and 2012. So, remanufacture benefits not only the environment but also the development of economic. In 2008, the Chinese National Development and Reform Commission launched a pilot program of auto part remanufacturing, and 14 firms were selected and supported to start up remanufacturing, seven of which are auto manufacturers (or their subsidiaries) and the others even are part suppliers [6].

Nowadays, with global scientific and technological levels rapidly improving and to reply to the pressures from customers, competitors, and regulators, innovation has been a great need for enterprises [7, 8]. So, combined with the topic of remanufacturing, adopting green innovation is becoming so important when green supply chain management is applied. Based on what we refer to, the questions we try to answer can be shown as follows. First of all, considering the government’s financial intervention and the competition in the market, does a manufacturer need to invest in green innovation to improve the product availability rate of recycled products? Then, how about taking a dynamic decision-making way into consideration? How will product prices evolve in repeated games? What will happen to the stable domain? Besides, what can we do to control chaos?

So, innovation in this paper can be concluded as follows. In our model, we take recycling and remanufacturing into consideration, and there are three stages in a cycle, that is, production/sale, recycling used production, and remanufacture/sale. Then, combined with the recycling of used products, we take manufacturer and supplier into consideration and answer the question of whether a manufacturer needs to invest in green innovation to improve the product availability rate of recycled products. Besides, based on the complex system theory, we take a dynamic decision-making way into consideration instead of limitations into a single period static decision. In the end, the way of controlling chaos is discussed.

The rest of this paper is organized as follows. In Section 2, we review the relevant literature. In Section 3, we describe the problem and show the symbols and assumptions of our model. In Section 4, we build and solve the model and get equilibrium points. Results are also analyzed. In Section 5, through the numerical simulation, we get the bifurcation diagram and stability domain diagram to express chaos. In Section 6, chaos control is made. In the end, we provide the conclusions in Section 7.

2. Literature Review

Innovation pushes society and economics toward development, and under the background of environmental

protection and sustainability, green innovation is becoming more and more essential. A lot of literature has researched green innovation investment in recent years. Xie et al. [9] built a dynamic model using data of 28 industries in 10 years and studied green process innovation from the perspective of the financial performance of the manufacturing industry. Ley et al. [10] researched the relationship between energy prices and green innovation activities from an industry level. Olson [11] took the green innovation value chain (GIVC) as the tool to analyze the financial feasibility of green products from the perspective of multiple stakeholders. What has been expressed in many studies is that pressure from regulators has a positive effect on green product innovation [12]. Sheu and Chen [13] also verified that governmental financial intervention has a positive effect on the green profit of the enterprise. Then, Ashkan [14] further expressed the benefit of governmental financial intervention. Generally speaking, there are three kinds of governmental financial interventions which are subsidy, taxes, and insurance [13, 15, 16]. Under a three-stage game framework, Subrata [17] established centralized and decentralized conservation models to gain a fair understanding of the advantages of government subsidies to consumers and manufacturers. By comparing the profit, greening level, consumer surplus, and environmental improvement of each member under two different incentive policies, Nielsen et al. [18] came up with a decision support framework for the selection and successful implementation of environmentally friendly products is obtained. At the same time, Izabela Ewa [18] also compared three kinds of government policies to study issues such as government subsidy policy with optimal pricing in the closed-loop supply chain, investment decision to improve product quality, and product recycling under the goal of social welfare optimization. Huang et al. [19] established a series of game models to study the impact of green loans and government subsidies on enterprises’ green innovation activities. Inspired by the above studies, we build a closed-loop supply chain and research the investment of green innovation considering governmental financial intervention.

The closed-loop supply chain has raised much attention from more and more scholars. Remanufacturing is an important process of the closed-loop supply chain that has been put more and more emphasis on. In the study of remanufacturing and closed-loop supply chain management, competition between new and remanufactured products, inventory management, quality, pricing, and who carries out recycling and remanufacturing activities are the five main issues [3, 20–22]. Maiti and Giri [22] built a closed-loop supply chain in which a manufacturer produces new products and sells them to the retailer; besides, he also produces remanufactured products and sells them to the secondary market. They analyzed the model under four different decision structures and got the optimal decision. Turki et al. [1] considering manufacture, remanufacture, transportation, and warehouse built a closed-loop supply chain model and used simulation to obtain the optimal values of decision variables. Hong et al. [2] verified the effect

of technology licensing on supply chain members' decision. And they built a two-period closed-loop supply chain in which, as for the patent holder, the manufacturer produces new and remanufactured products and, as for the licensee, a remanufacturer collects used products and produces remanufactured products at the same time. Giovanni and Zaccour [3] built a two-period closed-loop supply chain and analyzed whether the remanufacturer should outsource the collection of the used products to the retailer. Hosoda and Disney [23] researched the dynamics of a closed-loop supply chain and got the optimal decision to minimize inventory costs of the manufacturer. Li et al. [20] analyzed the relationship between product quality improvement and remanufacturing making by a monopolist manufacturer. However, there are a lot of studies we can access to discuss remanufacturing, but few scholars researched that supplier is responsible for remanufacturing. Then, we take inspiration from [6] who researched the question about whether the supplier or manufacturer remanufactures in a closed-loop supply chain and built a closed-loop supply chain to discuss who would invest in green innovation and remanufacture on the component level. Tang et al. [24] conducted a Stackelberg game to examine pricing and warranty decisions under two warranty models, which consist of a manufacturer and a retailer. Li et al. [25] have a study about the investigations of product design and its impact on the operations of a two-echelon closed-loop supply chain. Wang et al. [26] examined the benefit of the reward-penalty mechanism in a two-period closed-loop supply chain and analyzed by game models.

By analyzing the above literature, we can find that most scholars assume that the manufacturers are entirely rational. However, in a long time, supply chain members' decision stage is a dynamic process. They have imperfect information about the market and are bounded rational. So, we introduce nonlinear dynamics theory as a solution. Nonlinear dynamics theory is an effective tool theory and has been widely researched. Bao and Ma [27] studied the quantity decision by considering the product quality in parallel supply chains where two manufacturers produce substitute products and then sell them to their downstream retailers separately; the alternatives are analyzed. Ma and Guo [28] applied nonlinear dynamic theory with different adjustment mechanisms and expectations in a supply chain and analyzed the impacts of key parameters on the stability of the positive Nash equilibrium point. Ma et al. [29] built a closed-loop supply chain model with dual-channel recycling composed of one manufacturer and one-third-party, made a number of simulations [7, 30], analyzed macroeconomic models with Hopf bifurcation theory, and found some phenomenon in these nonlinear dynamic models. Ma and Xie [31] aimed at the color TV recycling market, built the model, and researched related parameters' effect on the system's stability; in the end, they made chaos control. Dai et al. [32] constructed a continuous dual-channel closed-loop supply chain model with the delayed decision under government intervention. They analyzed the related parameters' influence and used delay feedback control method to control the chaos.

3. Model Construction

In this work, we focus on the activity that the manufacturer will invest in green innovation to realize remanufacturing considering government financial intervention. As we all know, extended producer responsibility system, which refers to the responsibility that the producer needs to take not only in the production process but also in the entire life cycle, especially the recycling and disposal, has been recognized by many countries. So based on this, we build a model containing two manufacturers, one of which invests in green innovation, and we take recycling and remanufacturing into consideration. In the first stage, manufacturers produce new products and sell them to consumers; in the second stage, manufacturers, respectively, collect used products they produced from consumers; in the third stage, manufacturers will remanufacture. The whole stages constitute a cycle of production activities in the supply chain. Meanwhile, one of the manufacturers invests in green innovation to improve the product availability rate of recycled products which means that, as for a product, the proportion of its reusable component increases and the manufacturer saves cost during remanufacturing.

The timeline of decision-making is as follows: the activities of a whole cycle can be expressed as three stages and the two manufacturers move simultaneously. In stage 1, manufacturers produce new products, set prices, and then sell them to the market. Manufacturer 1 decides the green innovation level and invests in this stage. In stage 2, manufacturers recycle used products, respectively. In stage 3, manufacturers remanufacture recycled products and sell them to customers again. The timeline of the decision-making process can be described in Figure 1.

In our model, two manufacturers produce two kinds of homogeneous products and the price of new products produced by two manufacturers in the period t ($t = 1, 2, 3, \dots$) is $p_1(t)$ and $p_2(t)$. They compete in the market and we use θ which belongs to $(0, 1)$ for the degree of substitution between two kinds of similar products; these assumptions are similar to some existing papers (such as Xie and Ma, Ma et al. [33], and Ma et al. [29]). In this market, we assume that customers prefer purchasing products having a low price, and the sensitivity to price can be captured by b . So, the demand function of each kind of product in the period t is shown as follows:

$$\begin{cases} q_1(t) = \alpha_1 - b(p_1(t) - \theta p_2(t)), \\ q_2(t) = \alpha_2 - b(p_2(t) - \theta p_1(t)), \end{cases} \quad (1)$$

where α_i ($\alpha_i > 0$) means the market capacity.

In the second and third stages, manufacturers collect used products from customers and remanufacture them. $p'_1(t)$ and $p'_2(t)$ are used to represent the price of used products in the period t given by the manufacturer. We assume that based on the producer's responsibility extension system, the manufacturer only collects used products produced by himself, and meanwhile, all used products collected by the manufacturer will be remanufactured. In the process of recycling, customers also have price sensitivity which is captured by f . The recycling market capacity in the period t

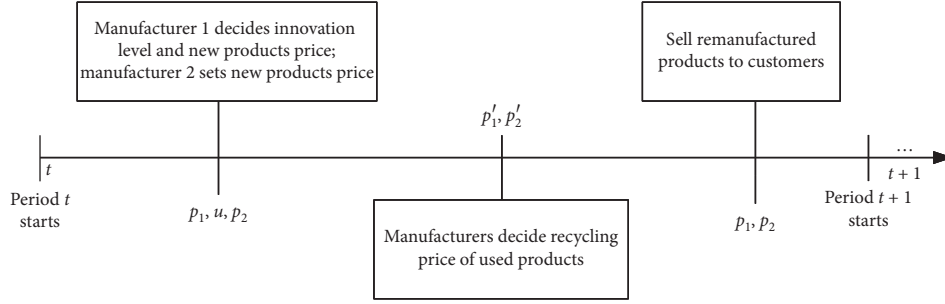


FIGURE 1: The timeline of decision-making.

is represented by $\lambda_1 q_1(t)$ and $\lambda_2 q_2(t)$, where λ_i is the collection rate of used products and bounded by 0 and 1. Then, the amount of recycled used products by each manufacturer in the period t which is represented by $q'_1(t)$ and $q'_2(t)$ can be shown as follows:

$$\begin{cases} q'_1(t) = \lambda_1 q_1(t) + f p'_1(t), & f p'_1(t) < q_1(t-1), \\ q'_2(t) = \lambda_2 q_2(t) + f p'_2(t), & f p'_2(t) < q_2(t-1), \end{cases} \quad (2)$$

With environmental issues getting more and more serious, the government tries to figure out the dilemma of global warming and overexploitation of resources by inducing the manufacturers to produce green products. So, governmental subsidies, a kind of government financial intervention, are adopted when enterprises achieve the governmental goal [13]. In our model, the government encourages enterprises to carry on the activity of recycling. So, it gives a subsidy to enterprises according to the value of recycled used products, which is

$$\begin{cases} \pi_1(t) = (p_1(t) - c_1)(q_1(t) - q'_1(t)) + (p_1(t) - (1-u)c'_1 - p'_1(t))q'_1(t) - \beta u^2 + \gamma p'_1(t)q'_1(t), \\ \pi_2(t) = (p_2(t) - c_2)(q_2(t) - q'_2(t)) + (p_2(t) - c'_2 - p'_2(t))q'_2(t) + \gamma p'_2(t)q'_2(t), \end{cases} \quad (3)$$

where c_1 is the unit cost of production when new products are produced and c'_1 represents the unit cost of production when remanufactured products are produced. There are some constraints: (1) $q'_i < q_i$, $i = 1, 2$: the number of recycled products cannot be larger than the number of new products manufactured in stage one. (2) $q'_i, q_i \geq 0$, $i = 1, 2$: the output is nonnegative.

Besides the assumptions we mentioned above, there are some other assumptions needed to be clarified. First of all, we ignore the costs of inventory holding, inventory shortage, transportation, and so on to simplify the model. Then, we assume that new products and remanufactured products have the same quality. Recycled products of the same quality can be sold again for the same price. For example, the gold ornament is recycled through channels and can be reprocessed into an ornament for sale. As long

as the quality of the gold is the same, the price will be the same. Besides, we assume that the manufacturers in our model are bounded rational.

$\gamma p'_2(t)q'_2(t)$. γ is the government subsidy rate for remanufactured products and is nonnegative. Responding to government requirements and improving competitiveness, the manufacturers take the responsibility of recycling and remanufacturing, and one of them invests in related greener technology to improve the product availability rate of recycled products, which can be expressed by u , and the manufacturer also saves some cost in the process of remanufacturing. The amount of investment can be expressed by $I = \beta u^2$, where the parameter β is the investment efficiency; the bigger the investment efficiency is, the more cost the manufacturer will put into the investment. $I = \beta u^2$ can also be expressed by $u = \sqrt{I/\beta}$ which is consistent with the marginal diminishing effect. With the product availability rate of recycled products increasing, the manufacturer can save the cost uc'_1 . Then, the profits of manufacturers can be expressed as follows:

as the quality of the gold is the same, the price will be the same. Besides, we assume that the manufacturers in our model are bounded rational.

4. Model Solving

According to what we stated, there are three stages in our model where manufacturers produce new products and sell them to customers, and then, they collect the used products and remanufacture them. We divide the process into two pricing stages in which the new products are priced first and the used products can be priced then. So, we use the classic backward induction to solve this game model. Manufacturers decide their price of used products in the period t to maximize their profit first; then based on imperfect information, manufacturers are bounded

rational and decide their price of used products in the period $t + 1$.

Substituting equations (1) and (2) into equation (3) and taking the partial derivative of $p_1'(t)$ and $p_2'(t)$, then we get the following:

$$\begin{cases} \frac{\partial \pi_1(t)}{\partial p_1'(t)} = c_1 f + c_1' f (-1 + u) + (-1 + \gamma)(2f p_1'(t) + (\alpha_1 - b p_1(t) + b \theta p_2(t)) \lambda_1), \\ \frac{\partial \pi_2(t)}{\partial p_2'(t)} = c_2 f - c_2' f + (-1 + \gamma)(2f p_2'(t) + (\alpha_2 - b p_2(t) + b \theta p_1(t)) \lambda_2). \end{cases} \quad (4)$$

We make $(\partial \pi_1(t)/\partial p_1'(t)) = 0$ and $(\partial \pi_2(t)/\partial p_2'(t)) = 0$; then, the result can be shown as follows:

$$\begin{cases} p_1'(t)^* = \frac{f(c_1 - c_1'(1 - u)) + \lambda_1(\gamma - 1)(\alpha_1 - b(p_1(t) - \theta p_2(t)))}{2f(1 - \gamma)}, \\ p_2'(t)^* = \frac{f(c_2 - c_2') + \lambda_2(\gamma - 1)(\alpha_2 - b(p_2(t) - \theta p_1(t)))}{2f(1 - \gamma)}. \end{cases} \quad (5)$$

Substituting equation (5) into equation (3), then the profit functions can be rewritten as follows:

$$\begin{cases} \pi_1 = \left(p_1 + \frac{1}{2}c_1(2 - \lambda_1)\right)(-b p_1 + b \theta p_2 + \alpha_1) - u^2 \beta + \frac{f c_1^2 - 2f(1 - u)c_1 c_1'}{4(1 - \gamma)} + \frac{(f(-1 + u)c_1' + (-1 + \gamma)(b p_1 - b \theta p_2 - \alpha_1)\lambda_1)^2}{4f(1 - \gamma)}, \\ \pi_2 = (b \theta p_1 - b p_2 + \alpha_2) \left(\frac{1}{2}\lambda_2(c_2 - c_2') - (p_2 - c_2)\right) + \frac{f(c_2 - c_2')^2}{4(1 - \gamma)} + \frac{(1 - \gamma)\lambda_2^2}{4f}(b \theta p_1 - b p_2 + \alpha_2)^2. \end{cases} \quad (6)$$

The marginal return of manufacturers is

$$\begin{cases} \frac{\partial \pi_1}{\partial u} = \frac{f c_1'(c_1 + (-1 + u)c_1')}{2(1 - \gamma)} - \frac{\lambda_1 c_1'}{2}(b p_1 - b \theta p_2 - \alpha_1) - 2u \beta, \\ \frac{\partial \pi_1}{\partial p_1} = b(c_1 - 2p_1 + \theta p_2) + \alpha_1 - \frac{1}{2}b(c_1 + (-1 + u)c_1')\lambda_1 - \frac{b(-1 + \gamma)(b p_1 - b \theta p_2 - \alpha_1)\lambda_1^2}{2f}, \\ \frac{\partial \pi_2}{\partial p_2} = b(c_2 + \theta p_1 - 2p_2) + \alpha_2 + \frac{1}{2}b(-c_2 + c_2')\lambda_2 + \frac{b(-1 + \gamma)(b \theta p_1 - b p_2 + \alpha_2)\lambda_2^2}{2f}. \end{cases} \quad (7)$$

In reality, limited to obtaining information, the enterprise cannot learn about the exact innovation output decisions that its rival makes and the decisions are not made by maximizing the profits [7]. Besides, in the long term, the decision process of the manufacturers is dynamic, and

manufacturers will adjust their decisions every stage. According to the assumptions we made earlier, manufacturers in our model are bounded rational. So, they make decisions in the period $t + 1$ based on price and the marginal profit in the period t . The decision variable adjustment

coefficient is introduced and the results of the repeated game in a long time can be shown as follows:

$$\begin{cases} u(t+1) = u(t) + wu(t) \frac{\partial \pi_1(t)}{\partial u(t)}, \\ p_1(t+1) = p_1(t) + v_1 p_1(t) \frac{\partial \pi_1(t)}{\partial p_1(t)}, \\ p_2(t+1) = p_2(t) + v_2 p_2(t) \frac{\partial \pi_2(t)}{\partial p_2(t)}. \end{cases} \quad (8)$$

During the process of a repeated game, manufacturers adjust their pricing strategy on the basis of the marginal profit and pricing decision in the period t . When the marginal profit of a manufacturer in the period t is positive,

the same strategy would be adopted by the manufacturer in the next period $t+1$; on the other hand, when the marginal profit in the period t is negative, the manufacturer would adjust his pricing strategy and recycled product availability rate decision. When a manufacturer adjusts pricing and investment decision in the period $t+1$, the whole system stability will be affected.

To get the equilibrium, we make $u(t+1) = u(t)$, $p_1(t+1) = p_1(t)$, and $p_2(t+1) = p_2(t)$. Then, we obtain eight points. But in our model, we just consider two manufacturers both carried on the competition. So, $u^* = 0$, $p_1^* = 0$, and $p_2^* = 0$ are not taken into consideration. In the end, the equilibrium can be obtained as

$$(u^*, p_1^*, p_2^*), \quad (9)$$

where

$$\begin{aligned} u^* &= (fc_1'(fc_1'(2f(-4+\theta^2) + b(-1+\gamma)(-2+\theta^2)\lambda_2^2) - (-1+\gamma)\lambda_1(2f(b\theta c_2 + 2\alpha_1 + \theta\alpha_2) + bf\theta(-c_2 + c_2')\lambda_2 \\ &\quad + b(-1+\gamma)(\alpha_1 + \theta\alpha_2)\lambda_2^2) + c_1(-2f^2(-4+\theta^2) + b(-1+\gamma)(-2f(-2+\theta^2)\lambda_1 + (-f(-2+\theta^2) - b(-1+\gamma)(-1+\theta^2)\lambda_1)\lambda_2^2)) \\ &\quad \cdot (f^2c_1'^2(2f(-4+\theta^2) + b(-1+\gamma)(-2+\theta^2)\lambda_2^2) + 2\beta(-1+\gamma)(4f^2(-4+\theta^2) + b(-1+\gamma)(2f(-2+\theta^2)\lambda_2^2 \\ &\quad + \lambda_1^2(2f(-2+\theta^2) + b(-1+\gamma)(-1+\theta^2)\lambda_2^2)))^{-1}, \\ p_1^* &= -\left(\left(2f\left(f\left(4\beta(-1+\gamma) + fc_1'^2\right)(2\alpha_1 + \theta\alpha_2) + 4bf\beta(-1+\gamma)c_1'\lambda_1 + 2b\beta(-1+\gamma)^2(2\alpha_1 + \theta\alpha_2)\lambda_1^2\right) \right. \right. \\ &\quad - bf\theta c_2\left(f^2c_1'^2 + 2\beta(-1+\gamma)(2f + b(-1+\gamma)\lambda_1^2)\right)\left(-2 + \lambda_2\right) + bf\theta c_2'\left(f^2c_1'^2 + 2\beta(-1+\gamma)(2f + b(-1+\gamma)\lambda_1^2)\right)\lambda_2 \\ &\quad + b(-1+\gamma)(-2 + \lambda_2) + bf\theta c_2'\left(f^2c_1'^2 + 2\beta(-1+\gamma)(2f + b(-1+\gamma)\lambda_1^2)\right)\lambda_2 + b(-1+\gamma)\left(f\left(4\beta(-1+\gamma) + fc_1'^2\right)(\alpha_1 + \theta\alpha_2) \right. \\ &\quad + 2bf\beta(-1+\gamma)c_1'\lambda_1 + 2b\beta(-1+\gamma)^2(\alpha_1 + \theta\alpha_2)\lambda_1^2) + bfc_1\left(fc_1'^2 - 2\beta(-1+\gamma)(-2 + \lambda_1)\right)(4f + b(-1+\gamma)\lambda_2^2) \\ &\quad \cdot \left(b\left(2f\left(f(-4+\theta^2)\left(4\beta(-1+\gamma) + fc_1'^2\right) + 2b\beta(-1+\gamma)^2(-2+\theta^2)\lambda_1^2\right) \right. \right. \\ &\quad \left. \left. + b(-1+\gamma)\left(f(-2+\theta^2)\left(4\beta(-1+\gamma) + fc_1'^2\right) + 2b\beta(-1+\gamma)^2(-1+\theta^2)\lambda_1^2)\lambda_2^2\right)\right)\right)^{-1}, \\ p_2^* &= -\left(\left(2f\left(f\left(4\beta(-1+\gamma) + fc_1'^2\right)(\theta\alpha_1 + 2\alpha_2) + 2bf\beta(-1+\gamma)\theta c_1'\lambda_1 + 2b\beta(-1+\gamma)^2(\theta\alpha_1 + \alpha_2)\lambda_1^2\right) \right. \right. \\ &\quad - 2bf c_2\left(f^2c_1'^2 + \beta(-1+\gamma)(4f + b(-1+\gamma)\lambda_1^2)\right)\left(-2 + \lambda_2\right) + 2bf c_2'\left(f^2c_1'^2 + \beta(-1+\gamma)(4f + b(-1+\gamma)\lambda_1^2)\right)\lambda_2 \\ &\quad + b(-1+\gamma)\left(f\left(4\beta(-1+\gamma) + fc_1'^2\right)(\theta\alpha_1 + 2\alpha_2) + 2bf\beta(-1+\gamma)\theta c_1'\lambda_1 + 2b\beta(-1+\gamma)^2(\theta\alpha_1 + \alpha_2)\lambda_1^2\right)\lambda_2^2 \\ &\quad + bf\theta c_1\left(fc_1'^2 - 2\beta(-1+\gamma)(-2 + \lambda_1)\right)(2f + b(-1+\gamma)\lambda_2^2) \\ &\quad \cdot \left(b\left(2f\left(f(-4+\theta^2)\left(4\beta(-1+\gamma) + fc_1'^2\right) + 2b\beta(-1+\gamma)^2(-2+\theta^2)\lambda_1^2\right) \right. \right. \\ &\quad \left. \left. + b(-1+\gamma)\left(f(-2+\theta^2)\left(4\beta(-1+\gamma) + fc_1'^2\right) + 2b\beta(-1+\gamma)^2(-1+\theta^2)\lambda_1^2)\lambda_2^2\right)\right)\right)^{-1}. \end{aligned} \quad (10)$$

Based on the result, we can obtain the Jacobian matrix of this model as follows:

$$J = \begin{pmatrix} j_{11} & -\frac{1}{2}buwc'_1\lambda_1 & \frac{1}{2}buw\theta c'_1\lambda_1 \\ -\frac{1}{2}bc'_1p_1v_1\lambda_1 & j_{22} & \frac{b\theta p_1v_1(2f+b(-1+\gamma)\lambda_1^2)}{2f} \\ 0 & \frac{b\theta p_2v_2(2f+b(-1+\gamma)\lambda_2^2)}{2f} & j_{33} \end{pmatrix}, \quad (11)$$

$$j_{11} = 1 - 4uw\beta + \frac{wc'_1(-fc_1 + (f - 2fu)c'_1 - (-1 + \gamma)(bp_1 - b\theta p_2 - \alpha_1)\lambda_1)}{2(-1 + \gamma)},$$

$$j_{22} = 1 + \frac{1}{2}v_1(2(b(c_1 - 4p_1 + \theta p_2) + \alpha_1) - b(c_1 + (-1 + u)c'_1)\lambda_1) - \frac{bv_1\lambda_1^2}{2f}(1 - \gamma)(2bp_1 - b\theta p_2 - \alpha_1),$$

$$j_{33} = 1 + v_2(b(c_2 + \theta p_1 - 4p_2) + \alpha_2) - \frac{b\lambda_2v_2}{2}(c_2 - c'_2) - \frac{v_2}{2f}(b(1 - \gamma)(b\theta p_1 - 2bp_2 + \alpha_2)\lambda_2^2).$$

From the Jacobian matrix of equation (9), we can find the characteristic equation of the matrix. So, we can obtain the characteristic equation of J as follows:

$$f(\lambda) = \lambda^3 + z_2\lambda^2 + z_1\lambda + z_0,$$

$$z_2 = -(j_{11} + j_{22} + j_{33}),$$

$$z_1 = \frac{b^2p_1v_1(-f^2uwc'_1\lambda_1^2 + \theta^2p_2v_2(2f+b(-1+\gamma)\lambda_1^2)(-2f-b(-1+\gamma)\lambda_2^2))}{4f^2} + j_{22}j_{33} + j_{11}(j_{22} + j_{33}), \quad (12)$$

$$z_0 = -j_{11}j_{22}j_{33} + \frac{j_{11}}{4f^2}(b^2\theta^2p_1p_2v_1v_2(2f-b(1-\gamma)\lambda_1^2)(2f-b(1-\gamma)\lambda_2^2))$$

$$+ \frac{1}{8f^2}(b^2fuwc'_1p_1v_1\lambda_1^2(2fj_{33} + b\theta^2p_2v_2(2f-b(1-\gamma)\lambda_2^2))).$$

The stability conditions can be shown as follows, based on the Jury stability criterion [34] and equation (10):

$$\begin{cases} f(1) = 1 + z_2 + z_1 + z_0 > 0, \\ f(-1) = -1 + z_2 - z_1 + z_0 < 0, \\ |z_0| < 1, \\ |z_0^2 - 1| > |z_0z_1 - z_2|. \end{cases} \quad (13)$$

5. Numerical Simulation

In Sections 2 and 3, we build and figure out the model. Considering the reality, we assume that manufacturers are

bound rational because of limited information and they make decisions on the basis of the marginal profit and pricing decision in the period t . They carry on repeated games in a long time. In every stage, the manufacturer constantly adjusts the pricing strategy to get closer to the optimal price of profit maximization. As the results shown in Figure 1, when the speed of price adjustment is too high, the system will become unstable and enter the chaotic state. To understand the process of dynamic change accurately, we do numerical simulations, in which we set $\alpha_1 = 10$, $\alpha_2 = 8$, $b = 1$, $\theta = 0.6$, $\lambda_1 = 0.7$, $\lambda_2 = 0.6$, $f = 2$, $c_1 = 2$, $c_2 = 1.5$, $c'_1 = 0.4$, $c'_2 = 0.4$, $\beta = 10$, $\gamma = 0.5$, $w = 1$, $v_1 = 0.1$, and $v_2 = 0.1$. And then, we can get the equilibrium point $(u^*, p_1^*, p_2^*) = (0.11, 7.53, 6.71)$.

5.1. Stability Analysis. There are lots of parameters in the equilibrium of our model and it is difficult to analyze the model directly. So, we verify the stability of this model by doing numerical simulation according to the actual situation. The discrete triangle in Figure 2 is also part of the stability region. Then, the stable region about w , v_1 , and v_2 is shown in Figure 2:

5.2. Influence of the Speed of Adjustment on the Stability of the System. In Figures 3–5, the bifurcation diagrams and largest Lyapunov exponent describe the change of u , p_1 , and p_2 with their adjustment parameters. As shown in Figures 3–5, with v_1 increasing, the status of the system keeps stable at the beginning; then, it becomes bifurcation and ended in chaos. In a stable status, p_1 from manufacturer 1 is higher than p_2 from manufacturer 2. When the value of w , v_1 , and v_2 exceeds the critical points of bifurcation diagram, u , p_1 , and p_2 bifurcate and then enter a chaotic state.

The largest Lyapunov exponent presents the system's state. When the largest Lyapunov exponent is smaller than zero, the manufacturers' decision system is stable. When the largest Lyapunov exponent is equal to zero, bifurcation happens. When the largest Lyapunov exponent is bigger than zero, the manufacturers' decision system enters chaos. When the values of w , v_1 , and v_2 are small, the largest Lyapunov exponent is smaller than zero, which means that the system is stable. When the largest Lyapunov exponent is equal to zero first, bifurcation happens in the system. With w , v_1 , and v_2 increasing continuously, there are some dots above the X -axis; that is, the largest Lyapunov exponent is bigger than zero.

As w , v_1 , and v_2 change, the profits of the two manufacturers will also fluctuate. In Figures 6–8, we further explore the impact of w , v_1 , and v_2 on profits.

From Figures 6–8, we can draw a conclusion that the profits of both manufacturers fluctuate with the expansion of the three parameters. This result also shows that excessive adjustment will lead to vicious competition in the market and result in instability. Among them, w has the least impact on profits, while v_1 has the greatest impact on profits.

5.3. Influence of the Investment and the Government Subsidy on the Stability of the System. We further analyze the effect of the manufacturer's investment on the stable region of the system. In our work, one of the manufacturers invests in green innovation to improve the product availability rate of recycled products, which is captured by u . We range u from 0 to 1 and obtain the 3D stable region with a change of v_1 , v_2 , and u which is shown in Figure 9. By observing Figure 9, we can find that whatever u is, the stable region stays the same all the time. That is, the product availability rate of recycled products has no effect on the stable region of the system.

Then, we analyze the effect of the government subsidy on the stability of the system. In our model, the government gives a subsidy to the enterprise on the basis of the value of recycled used products and the amount of subsidy is $\gamma p_2'(t)q_2'(t)$. We change γ from 0 to 1 and get a stable region with a change of v_1 , v_2 , and γ . By observing Figure 10, we can

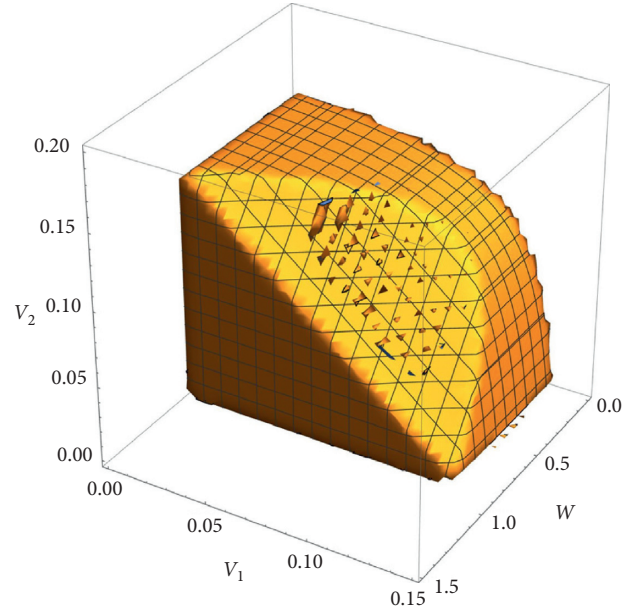


FIGURE 2: The stable region with a change of w , v_1 , and v_2 .

draw the conclusion that with γ increasing, the area of stable region decreases gradually. To make the result clear, we set $\gamma = 0$, $\gamma = 0.3$, $\gamma = 0.5$, $\gamma = 0.7$, and $\gamma = 0.9$ and get the stable region with a change of v_1 and v_2 which can be seen in Figure 10.

In Figure 11, the red-border area, the blue-border area, the green-border area, the purple-border area, and the black-border area are obtained when we set $\gamma = 0$, $\gamma = 0.3$, $\gamma = 0.5$, $\gamma = 0.7$, and $\gamma = 0.9$, respectively. It is clear that the bigger the γ is, the smaller the area of the stable region is, which is consistent with the result we get from Figure 11. Based on this result, it can also be concluded that the government needs to set an appropriate level of subsidies to keep the stability of the system.

5.4. Effect of Parameters on the Nonlinear Dynamic Game System. First of all, we focus on the impact of the investment and the government subsidy on the system. We set $\alpha_1 = 10$, $\alpha_2 = 8$, $b = 1$, $\theta = 0.6$, $\lambda_1 = 0.7$, $\lambda_2 = 0.6$, $f = 2$, $c_1 = 2$, $c_2 = 1.5$, $c_1' = 0.4$, $c_2' = 0.4$, and $\beta = 10$ and illustrate how the price, demand, recycling price, recycling quantity, and profit go with the investment and government subsidy on the equilibrium point. The price p_1 with a change of u is shown in Figure 12.

Figures 13–16 reveal the impact of the investment and government subsidy on manufacturer 1. We find that the effect of the investment on manufacturer 1 is linear. With the increase of the investment, the price of product 1 drops slightly. By contrast, the demand, recycling price, and recycling quantity increase in this process. And the profit increases first but then decreases after reaching the maximum value. Based on those facts, we can draw the conclusion that certain investment has a positive force for product selling and recycling and the profit. However, too much investment will harm the profit of the manufacturer.

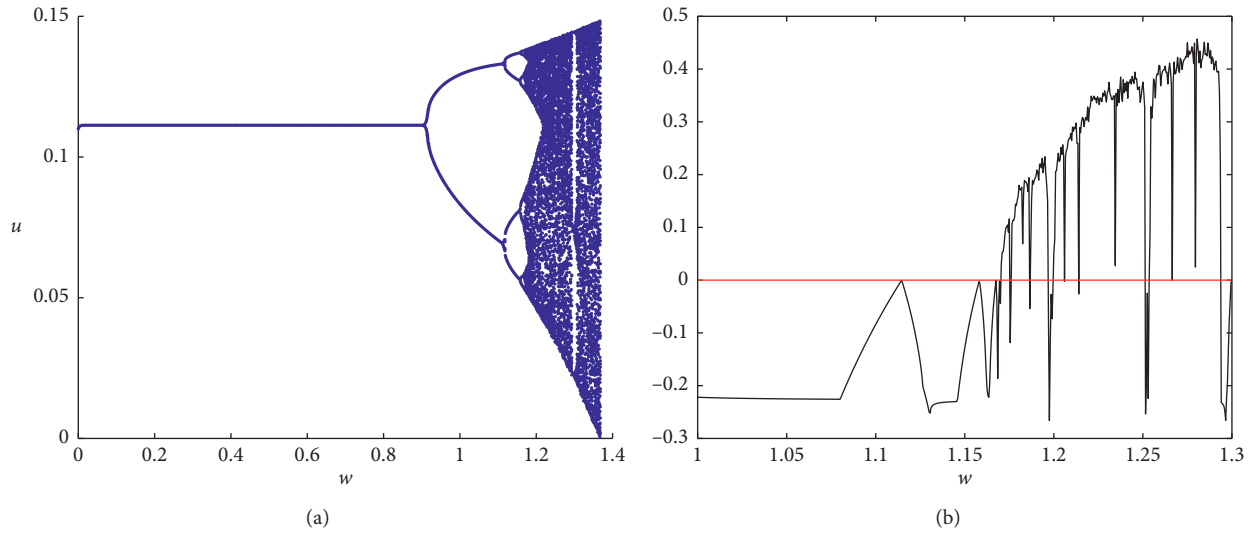


FIGURE 3: Bifurcation diagram and largest Lyapunov exponent of u w.r.t. w .

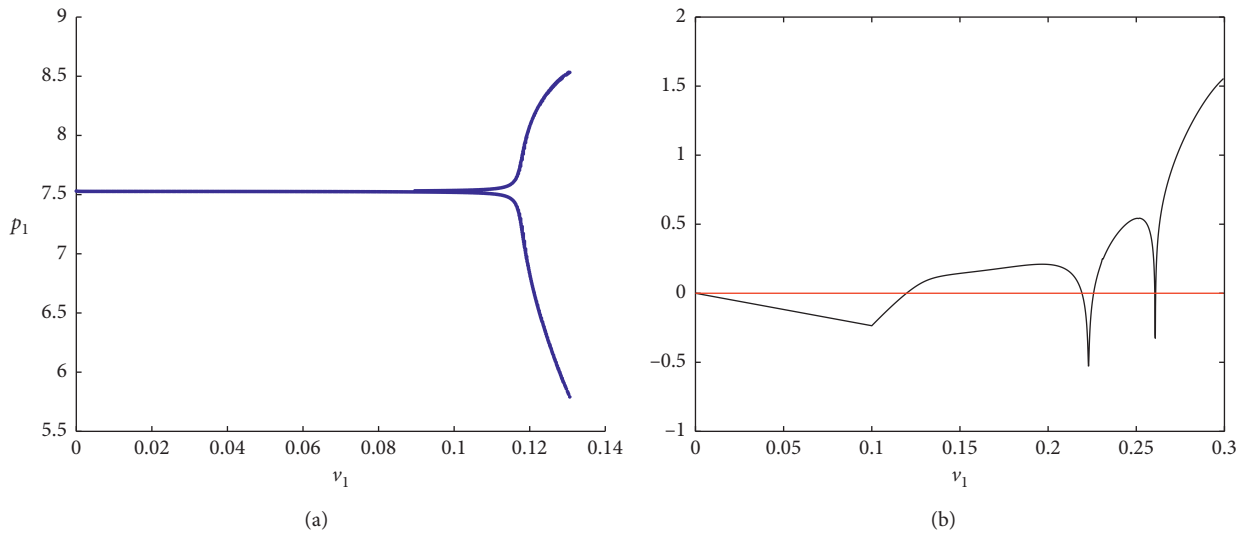


FIGURE 4: Bifurcation diagram and the largest Lyapunov exponent of p_1 w.r.t. v_1 .

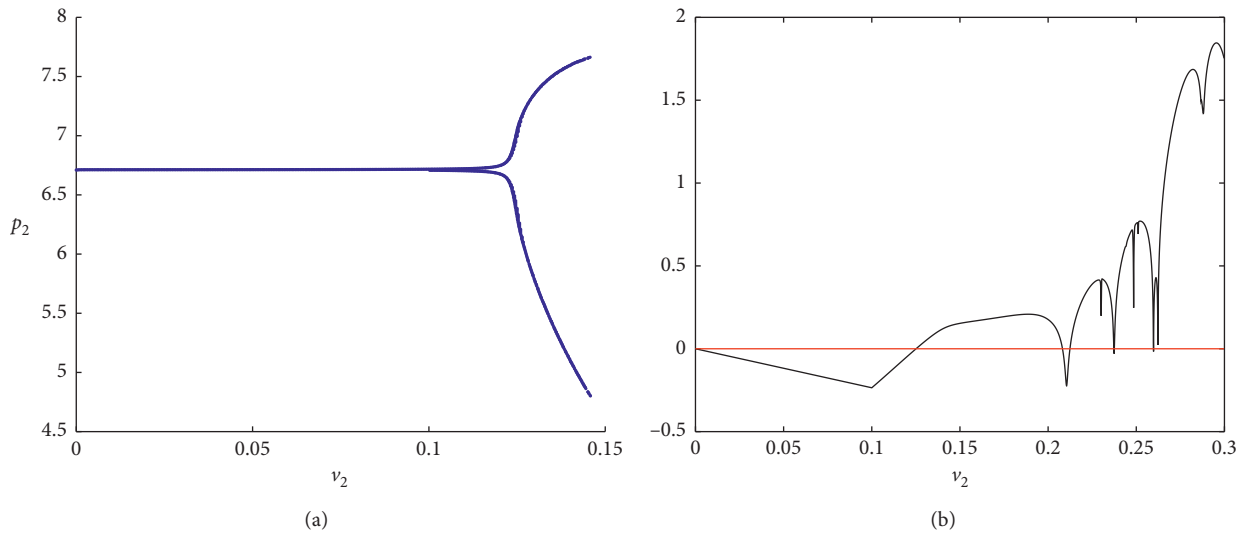


FIGURE 5: Bifurcation diagram and the largest Lyapunov exponent of p_2 w.r.t. v_2 .

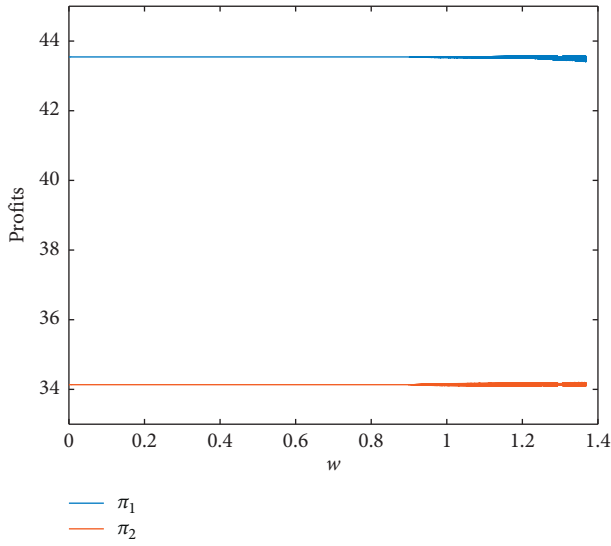


FIGURE 6: The profits of the two manufacturers with a change of w .

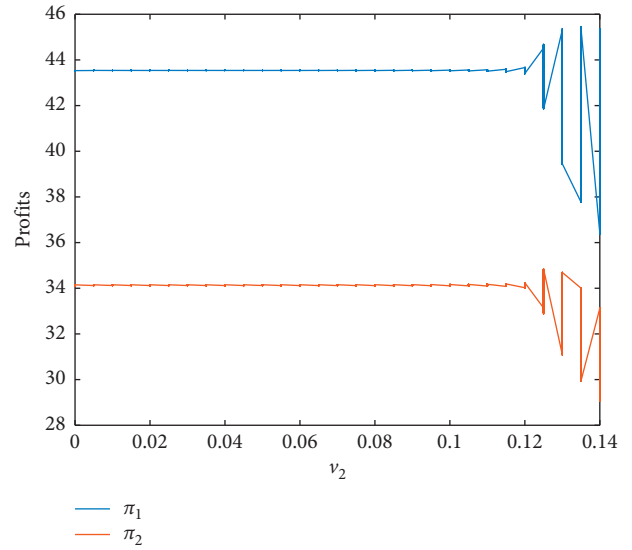


FIGURE 8: The profits of the two manufacturers with a change of v_2 .

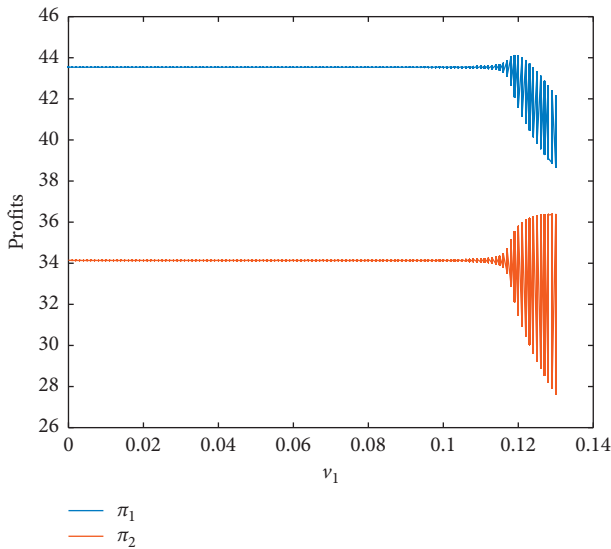


FIGURE 7: The profits of the two manufacturers with a change of v_1 .

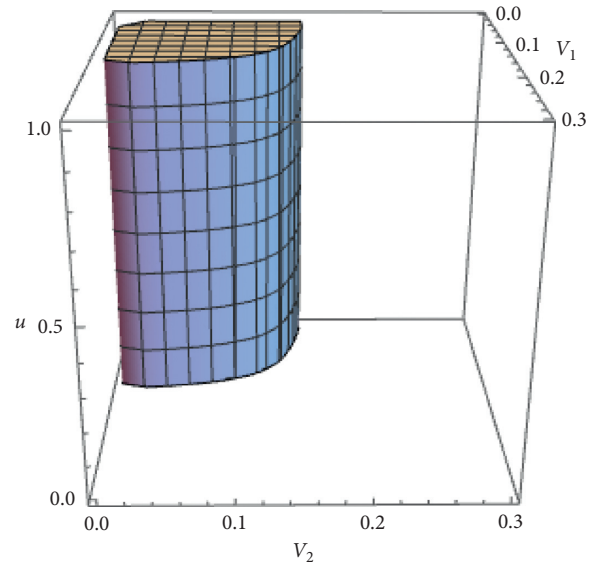


FIGURE 9: The 3D stable region with a change of v_1 , v_2 , and u .

Compared to the investment, the government subsidy has a contrary impact on the price and the demand. But the government subsidy promotes the recycling price and recycling quantity similar to the way the investment does, but it is not linear. And the government subsidy undoubtedly raises the profit of manufacturer 1.

We further analyze the effect of investment of manufacturer 1 and governmental subsidy on the pricing decision and profit of manufacturer 2. The result can be seen in Figures 17–21. With the product availability rate of recycled products increasing, the price, the demand, and the profit of manufacturer 2 decrease slightly. In our model, manufacturer 1 invests in green innovation to improve the product availability rate of recycled products which leads manufacturer 1 to have an advantage when competing with manufacturer 2. Accordingly, manufacturer 2 is at a disadvantage in the competition. However, with the increase of

the investment, both the price and the amount of recycling used products remain unchanged. There is no competition between manufacturers in the recycling market, since we assume that the manufacturer only collects used products produced by himself. Compared to the investment, the government subsidy has a positive impact on the price and has a negative impact on demand. But the government subsidy promotes the recycling price and recycling quantity similar to the result we get earlier. And the government subsidy undoubtedly raises the profit of manufacturer 2.

Next, we will explore the impact of the collection rate on the profits of both manufacturers.

From Figure 22, we can see that when the value of λ_2 is lower and the value of λ_1 is higher, the profit of manufacturer 1 is higher. Conversely, when λ_2 is higher and λ_1 is lower, manufacturer 2's profit is higher. This shows that a

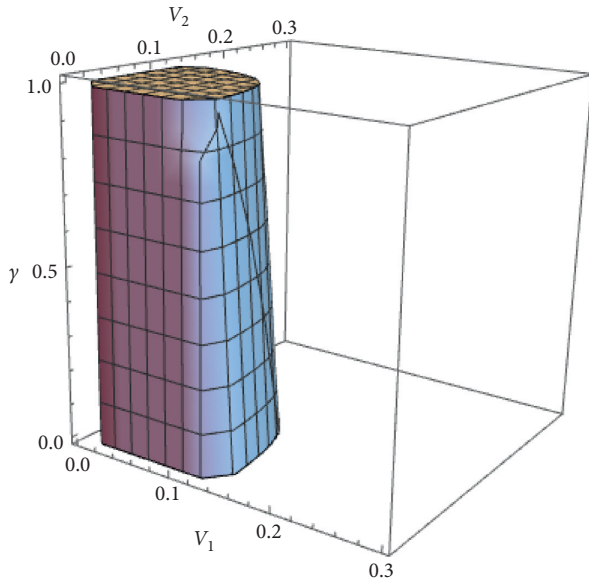


FIGURE 10: The 3D stable region with a change of v_1 , v_2 , and γ .

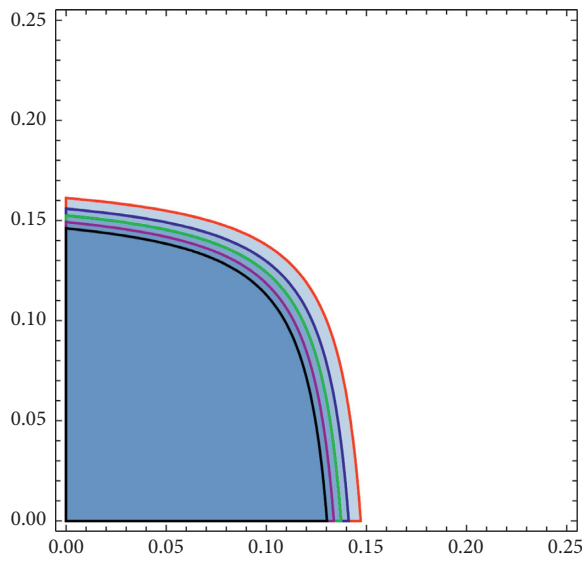


FIGURE 11: The stable region with a change of v_1 and v_2 .

high collection rate is connected with high profits. This is also in line with reality.

In the end, we focus on the impact of the investment, the price sensitivity, and the degree of substitution between two kinds of similar products on the system.

From Figures 23 and 24, we can draw the following conclusions. Among the three decision-making factors, the product substitution rate has the most significant impact on the manufacturer's profit, followed by the price sensitivity, and the impact of investment is the smallest. Therefore, manufacturers should first pay attention to product innovation and change the substitution rate of products. In addition, manufacturers should set reasonable selling prices to meet consumers' demand, and finally, manufacturers should invest more in products if they can.

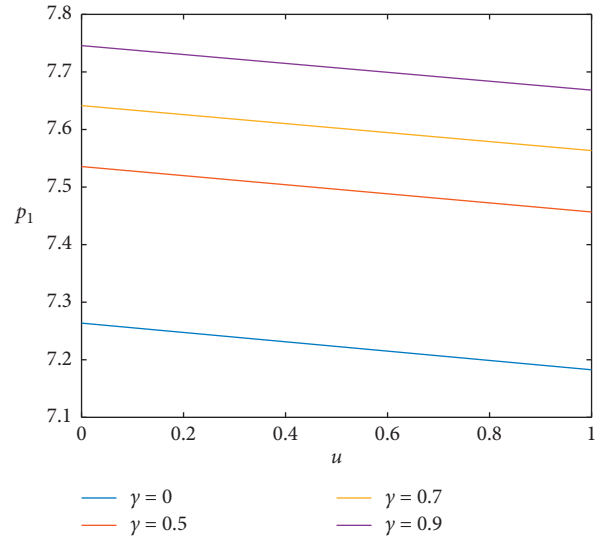


FIGURE 12: The price p_1 with a change of u .

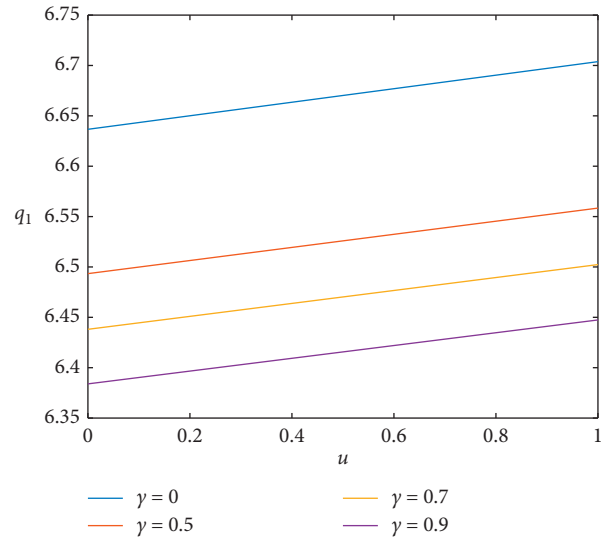


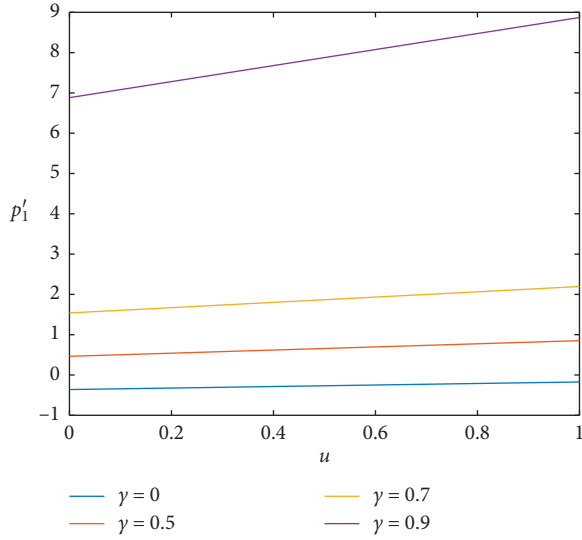
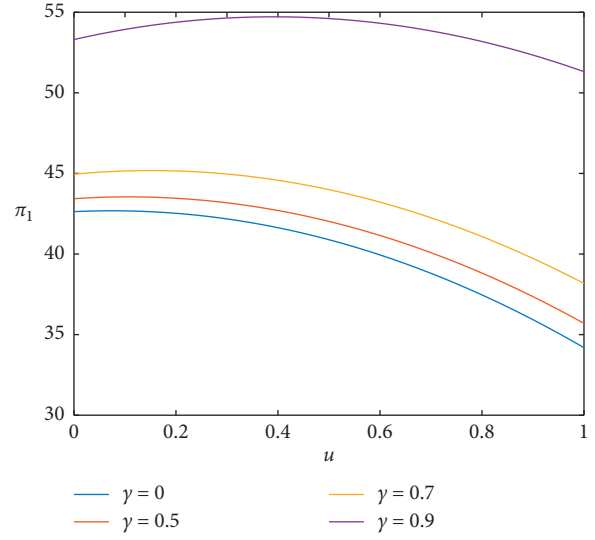
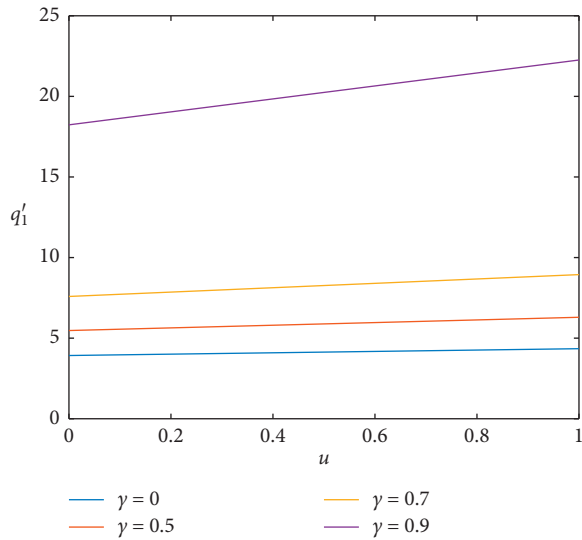
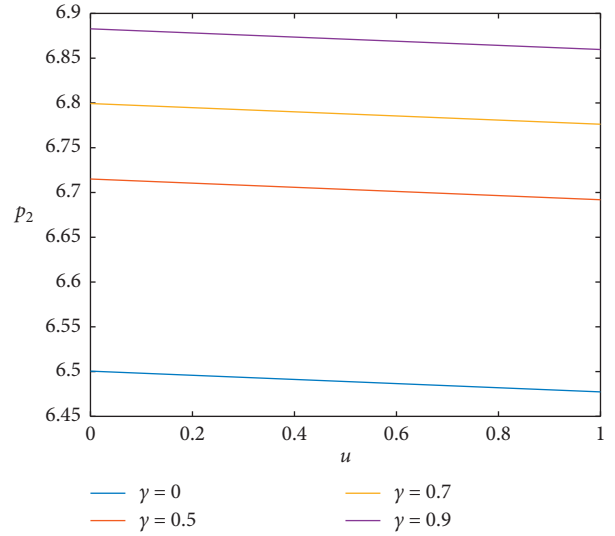
FIGURE 13: The demand q_1 with a change of u .

5.5. Change of Pareto Solutions on the Dynamic Game System. In this section, we focus on the effect of the adjustment rates of the two manufacturers on the Pareto solutions.

From Figure 25, we can see that as the period increases, the range of Pareto solutions gradually expands. When the dynamic game reaches a certain period, the range of Pareto solution tends to be stable. When $v_1 < 0.18$ and $v_2 < 0.2$, there are inferior solutions to the system. Therefore, with the development of the dynamic game, the two manufacturers should increase their adjustment rate to avoid the generation of the inferior solution, so as to realize the Pareto optimization of the whole system.

6. Chaos Control

As the result has shown earlier, once the speed of adjustment of the participants in the market exceeds a reasonable

FIGURE 14: The recycling price p'_1 with a change of u .FIGURE 16: The profit π_1 with a change of u .FIGURE 15: The recycling quantity q'_1 with a change of u .FIGURE 17: The price p_2 with a change of u .

threshold, the market would fall into a state of complex chaos, which will cause disordered fluctuations in the price decision and the amount of recycling used products. As a result, manufacturers are unable to make the optimal response in the current period; thus, their profits will also have violent fluctuations. Considering this result from the chaos, it is necessary to control chaos effectively to ensure the stability of market competition and benefit the whole system. In this section, based on the characteristics of the whole decision-making process, we introduce the method by adjusting the decision method to control the chaos. Thus, the delay control method and the parameter adjustment control method are considered.

Firstly, control analysis is carried out through parameter adjustment control. Managers can control chaotic behavior

by introducing a control parameter g . Wang [35] realized a chaos control by setting the control parameter as g . Under parameter adjustment control, the simultaneous decision system can be expressed as

$$\begin{cases} p_1(t+1) = (1-g) \left(p_1(t) + v_1 p_1(t) \frac{\partial \Pi_1(t)}{\partial p_1(t)} \right) + g p_1(t), \\ p_2(t+1) = (1-g) \left(p_2(t) + v_2 p_2(t) \frac{\partial \Pi_2(t)}{\partial p_2(t)} \right) + g p_2(t). \end{cases} \quad (14)$$

Then, we use the delay control method to control chaos. The core idea of the delay control method is to use feedback to the system after a time delay (2016). That is, we take part of the information that is the output signal of the system into consideration. When making a decision next period, we

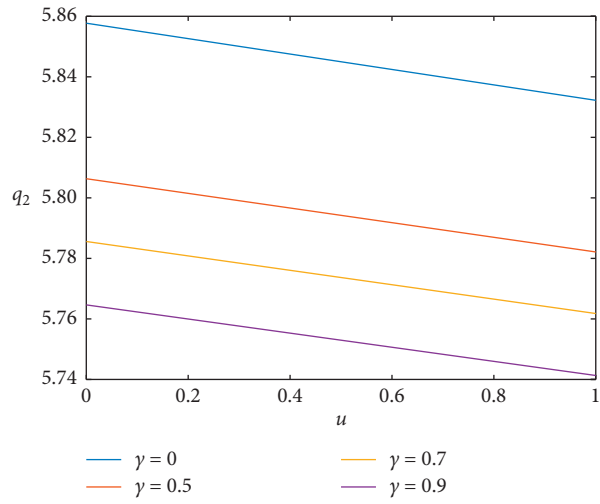


FIGURE 18: The demand q_2 with a change of u .

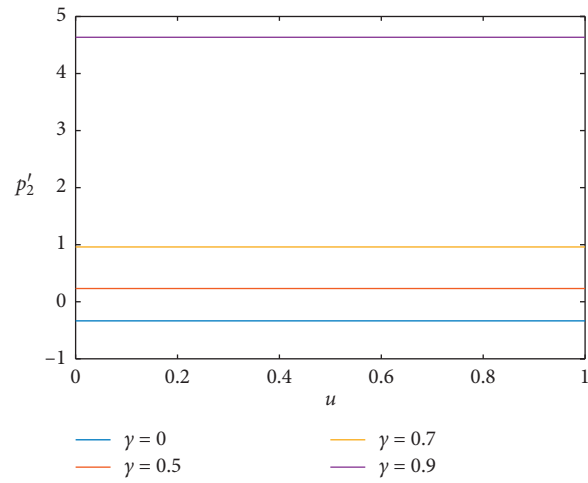


FIGURE 19: The recycling price p_2' with a change of u .

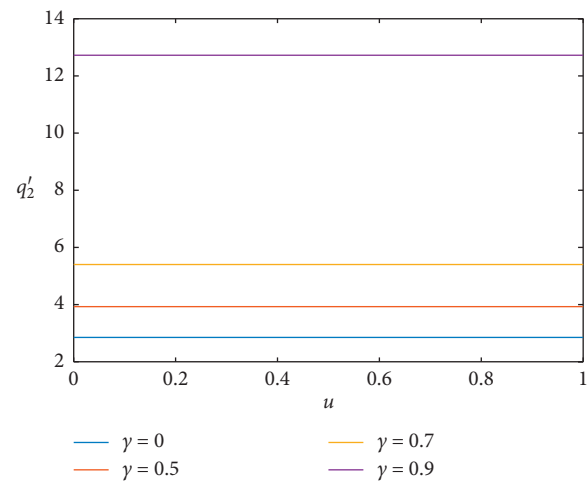


FIGURE 20: The recycling quantity q_2' with a change of u .

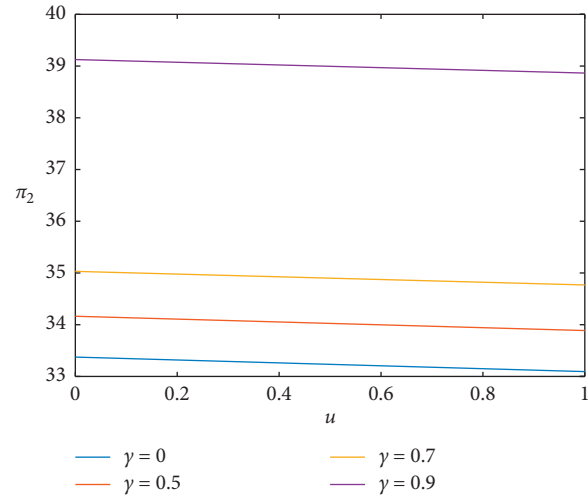


FIGURE 21: The profit π_2 with a change of u .

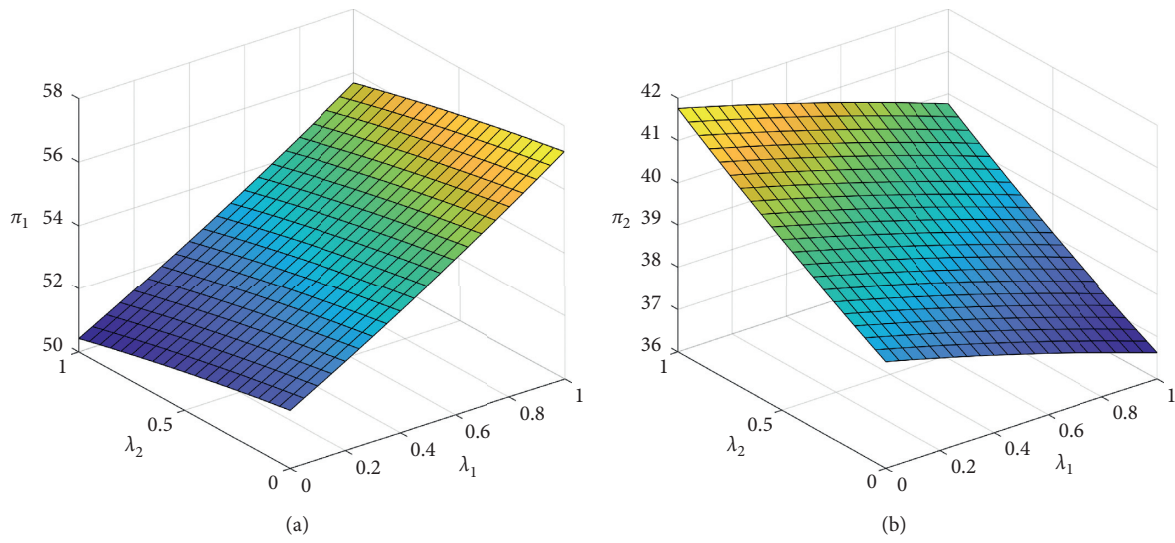


FIGURE 22: The profits with a change of λ_1 and λ_2 .

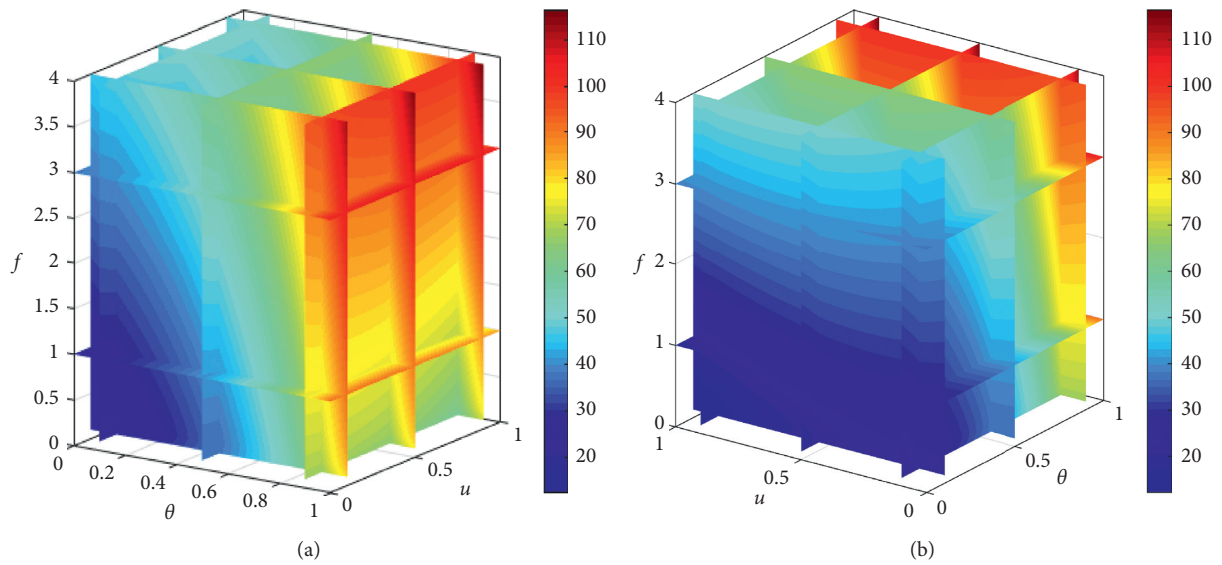


FIGURE 23: The effect of u , θ , and f on the profit of manufacturer 1. (a) Back. (b) Front.

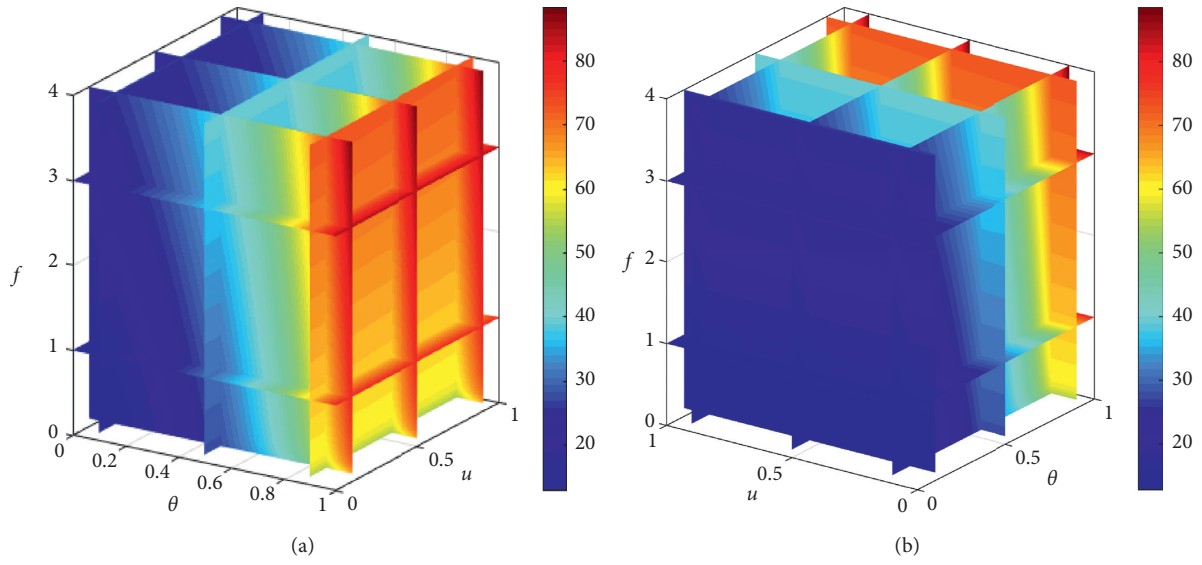


FIGURE 24: The effect of u , θ , and f on the profit of manufacturer 2. (a) Back. (b) Front.

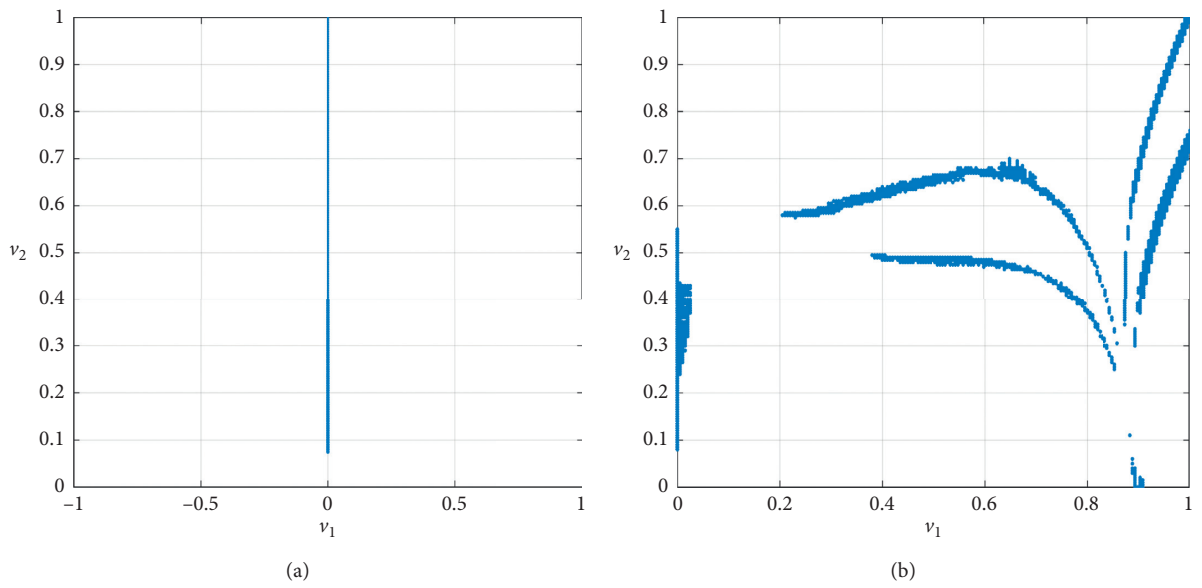


FIGURE 25: Continued.

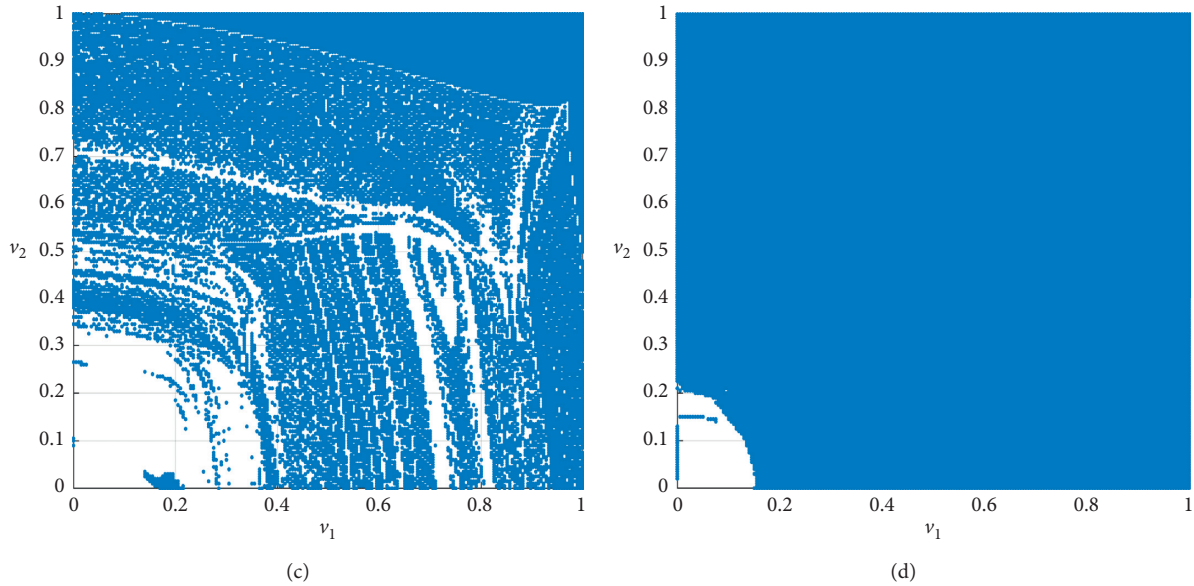


FIGURE 25: Pareto solutions with a change of v_1 and v_2 in different periods. (a) Period 1. (b) Period 5. (c) Period 10. (d) Period 100.

consider the decision in the period, t , and decision in the period, $t + 1$. Thus, the dynamic adjustment model can be shown as follows:

$$\begin{cases} p_1(t+1) = p_1(t) + v_1 p_1(t) \frac{\partial \Pi_1(t)}{\partial p_1(t)} + v(p_1(t+1) - p_1(t)), \\ p_2(t+1) = p_2(t) + v_2 p_2(t) \frac{\partial \Pi_2(t)}{\partial p_2(t)} + v(p_2(t+1) - p_2(t)). \end{cases} \quad (15)$$

We set the same parameters where $\alpha_1 = 10, \alpha_2 = 8, b = 1, \theta = 0.6, \lambda_1 = 0.7, \lambda_2 = 0.6, f = 2, c_1 = 2, c_2 = 1.5, c_1 = 0.4, c_2 = 0.4, \beta = 10, u = 0.3,$ and $\gamma = 0.5$ and set $v_1 = 0.5, v_2 = 0.5$. Under this condition, the original system is in a chaotic state. Firstly, we introduce the parameter g to control the system. Through numerical simulation, we draw the bifurcation diagram with the parameter g increasing as follows.

From Figure 26, we can see that with the increase of parameter g , the price decision of the two manufacturers gradually gets out of chaos. And when $g = 0.78$, the whole system enters a stable state, and the two manufacturers can have a stable price decision.

Then, we introduce the control parameter v and add delayed feedback into the decision signal. Through numerical simulation, we draw the bifurcation diagram with the control parameter v increasing as follows.

As is shown in Figure 27, the instability of the system is effectively eliminated after adding delayed feedback into the pricing decision. When v is small, the state of the system is chaos. With the control parameter v increasing, the state of the system is going into bifurcation and stable gradually. In the end, the system keeps stable when $v > 0.34$, where the manufacturers can make effective decisions. We can draw the conclusion that delay control is a good way to control the

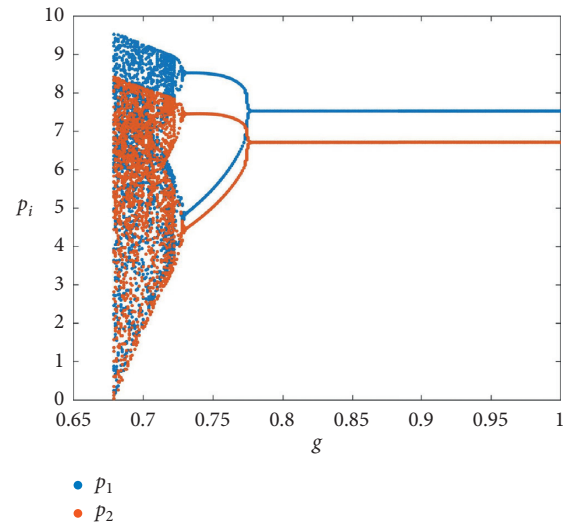


FIGURE 26: Bifurcation diagram with g increasing.

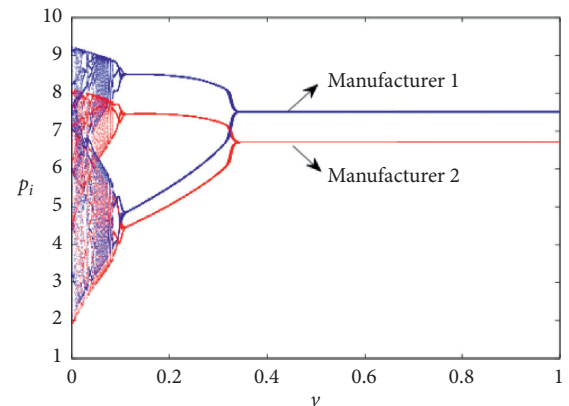


FIGURE 27: Bifurcation diagram with v increasing.

system based on the response of the manufacturers. Li and Yu [36] also prove that delay control can effectively solve the chaotic imagination that may arise in the development of the system. So, manufacturers can consider this method to solve the chaos phenomenon in the multiperiod system.

7. Conclusion

Considering the increasing environmental preoccupation, the potential economic benefits, and the legislation pressure, great attention has been paid to green innovation. In this paper, we focus on the activity of green innovation and build a model where the manufacturer will invest in green innovation to improve the product availability rate of recycled products and save the cost in the process of remanufacturing and the other manufacturers do not invest in green innovation. Besides, we take three stages in a cycle into consideration, that is, production/sale, recycling used production, and remanufacture/sale, and meanwhile, the government encourages enterprises to carry on the activity of recycling and gives a subsidy to enterprises according to the value of recycled used products. In the process of model solving, considering repeated games between two manufacturers in this system, a dynamic decision-making way is used. Then, we analyze the influence of the speed of adjustment on the stability of the system, the influence of the investment, and the government subsidy on the stability of the system and the effect of the investment and the government subsidy on the system. At the end of this research, we make chaos control. The conclusions we made are shown as follows [10, 35, 37–42]:

- (1) The decision adjustment speed of players has a significant effect on stability, and in a long dynamic repeated game process, with the speed of decision adjustment increasing, the system enters into chaos at last. Besides, when the speed of decision adjustment exceeds the critical point of the bifurcation diagram, the profit of the manufacturer decreases and then enters a chaotic state. So, an appropriate adjustment speed should be adopted.
- (2) The investment of the product availability rate of recycled products has no effect on the stable region of the system; with the level of subsidies increasing, the area of stable region decreases gradually, so the government needs to set an appropriate level of subsidies to maintain the stability of the system.
- (3) Certain investment has a positive force for the product selling and recycling and the profit, and the government subsidy undoubtedly raises the profits of manufacturers and encourages the activity of recycling used products.
- (4) We make chaos control through adjusting the decision method and the result shows that this method really has good control of the chaos of the system.

However, there are still some limitations. For example, the classic linear demand function is adopted in the model; however, there is a certain gap between this linear demand

function and the reality; we do not take model structure into consideration. We leave this for the future.

Data Availability

The data used to support the findings of this study are available from the corresponding author upon request. The questionnaire data were acquired mainly through e-mail and filling out paper.

Conflicts of Interest

The authors declare no conflicts of interest.

Acknowledgments

This research was supported by the National Natural Science Foundation of China (No. 71571131).

References

- [1] S. Turki, S. Didukh, C. Sauvey, and N. Rezg, "Optimization and analysis of a manufacturing-remanufacturing-transport-warehousing system within a closed-loop supply chain," *Sustainability*, vol. 9, no. 4, p. 561, 2017.
- [2] X. Hong, K. Govindan, L. Xu, and P. Du, "Quantity and collection decisions in a closed-loop supply chain with technology licensing," *European Journal of Operational Research*, vol. 256, no. 3, pp. 820–829, 2017.
- [3] P. D. Giovanni and G. Zaccour, "A two-period game of a closed-loop supply chain," *European Journal of Operational Research*, vol. 232, pp. 22–40, 2014.
- [4] H. Krikke, I. I. Blanc, and S. van de Velde, "modularity and the design of closed-loop supply chains," *California Management Review*, vol. 46, no. 2, pp. 23–39, 2004.
- [5] J. D. Abbey and V. D. R. Guide, "A typology of remanufacturing in closed-loop supply chains," *International Journal of Production Research*, vol. 56, no. 1-2, pp. 374–384, 2018.
- [6] Y. Xiong, Q. Zhao, and Y. Zhou, "Manufacturer-remanufacturing vs supplier-remanufacturing in a closed-loop supply chain," *International Journal of Production Economics*, vol. 176, pp. 21–28, 2016.
- [7] J. Ma and W. Ren, "Complexity and Hopf bifurcation analysis on a kind of fractional-order IS-LM macroeconomic system," *International Journal of Bifurcation and Chaos*, vol. 26, no. 11, Article ID 1650181, 2016.
- [8] M. E. Porter and V. D. Linde, "Green and competitive," *Harvard Business Review*, vol. 73, no. 5, pp. 120–134, 1995.
- [9] X. Xie, J. Huo, G. Qi, and K. X. Zhu, "Green process innovation and financial performance in emerging economies: moderating effects of absorptive capacity and green subsidies," *IEEE Transactions on Engineering Management*, vol. 63, no. 1, pp. 101–112, 2016.
- [10] M. Ley, T. Stucki, and M. Woerter, "The impact of energy prices on green innovation," *The Energy Journal*, vol. 37, no. 1, pp. 41–75, 2016.
- [11] E. L. Olson, "Perspective: the green innovation value chain: a tool for evaluating the diffusion prospects of green products," *Journal of Product Innovation Management*, vol. 30, no. 4, pp. 782–793, 2013.
- [12] H. K. Chan, R. W. Y. Yee, J. Dai, and M. K. Lim, "The moderating effect of environmental dynamism on green

- product innovation and performance,” *International Journal of Production Economics*, vol. 181, pp. 384–391, 2016.
- [13] J.-B. Sheu and Y. J. Chen, “Impact of government financial intervention on competition among green supply chains,” *International Journal of Production Economics*, vol. 138, no. 1, pp. 201–213, 2012.
- [14] H. Ashkan, “Competition of two green and regular supply chains under environmental protection and revenue seeking policies of government,” *Computers & Industrial Engineering*, vol. 82, pp. 103–114, 2015.
- [15] H. Peng, “Optimal subsidy policy for accelerating the diffusion of green products,” *Journal of Industrial Engineering & Management*, vol. 6, no. 2, pp. 673–679, 2013.
- [16] C. Wang, P.-y. Nie, D.-h. Peng, and Z.-h. Li, “Green insurance subsidy for promoting clean production innovation,” *Journal of Cleaner Production*, vol. 148, pp. 111–117, 2017.
- [17] S. Subrata, S. Majumder, and I. E. Nielsen, “Is it a strategic move to subsidized consumers instead of the manufacturer?” *IEEE Access*, vol. 7, pp. 169807–169824, 2019.
- [18] I. E. Nielsen, S. Majumder, S. S. Sana, and S. Saha, “Comparative analysis of government incentives and game structures on single and two-period green supply chain,” *Journal of Cleaner Production*, vol. 235, pp. 1371–1398, 2019.
- [19] Z. Huang, G. Liao, and Z. Li, “Loaning scale and government subsidy for promoting green innovation,” *Technological Forecasting and Social Change*, vol. 144, pp. 148–156, 2019.
- [20] G. Li, M. Reimann, and W. Zhang, “When remanufacturing meets product quality improvement: the impact of production cost,” *European Journal of Operational Research*, vol. 271, no. 3, pp. 913–925, 2018.
- [21] J. P. Gayon, S. Vercraene, and S. D. P. Flapper, “Optimal control of a production-inventory system with product returns and two disposal options,” *European Journal of Operational Research*, vol. 262, no. 2, pp. 499–508, 2017.
- [22] T. Maiti and B. C. Giri, “Two-way product recovery in a closed-loop supply chain with variable markup under price and quality dependent demand,” *International Journal of Production Economics*, vol. 183, pp. 259–272, 2016.
- [23] T. Hosoda and S. M. Disney, “A unified theory of the dynamics of closed-loop supply chains,” *European Journal of Operational Research*, vol. 269, no. 1, pp. 313–326, 2017.
- [24] J. Tang, B.-Yi Li, K. W. Li, Z. Liu, and J. Huang, “Pricing and warranty decisions in a two-period closed-loop supply chain,” *International Journal of Production Research*, vol. 58, no. 6, pp. 1688–1704, 2020.
- [25] Z. Liu, K. W. Li, B.-Y. Li, J. Huang, and J. Tang, “Impact of product-design strategies on the operations of a closed-loop supply chain,” *Transportation Research Part E: Logistics and Transportation Review*, vol. 124, p. 7591, 2019.
- [26] W. Wang, J. Ding, and H. Sun, “Reward-penalty mechanism for a two-period closed-loop supply chain,” *Journal of Cleaner Production*, vol. 203, pp. 898–917, 2018.
- [27] B. Bao and J. Ma, “Dynamic game behavior of retailers considering the quality of substitute products based on delay decision,” *International Journal of Bifurcation and Chaos*, vol. 27, no. 13, Article ID 1750206, 2017.
- [28] J. Ma and Z. Guo, “The parameter basin and complex of dynamic game with estimation and two-stage consideration,” *Applied Mathematics and Computation*, vol. 248, pp. 131–142, 2014.
- [29] J. Ma, W. Lou, and Y. Tian, “Bullwhip effect and complexity analysis in a multi-channel supply chain considering price game with discount sensitivity,” *International Journal of Production Research*, vol. 57, no. 17, pp. 5432–5452, 2019.
- [30] J. Ma and H. Tu, “Analysis of the stability and Hopf bifurcation of money supply delay in complex macroeconomic models,” *Nonlinear Dynamics*, vol. 76, no. 1, pp. 497–508, 2014.
- [31] J. Ma and L. Xie, “The comparison and complex analysis on dual-channel supply chain under different channel power structures and uncertain demand,” *Nonlinear Dynamics*, vol. 83, no. 3, pp. 1379–1393, 2016.
- [32] D. Dai, F. Si, and J. Wang, “Stability and complexity analysis of a dual-channel closed-loop supply chain with delayed decision under government intervention,” *Entropy*, vol. 19, no. 11, p. 577, 2017.
- [33] W. Lou and J. Ma, “Complexity of sales effort and carbon emission reduction effort in a two-parallel household appliance supply chain model,” *Applied Mathematical Modelling*, vol. 64, pp. 398–425, 2018.
- [34] Y. Choo and D. Kim, “Simple proof of jury test for complex polynomials,” *IEICE Transactions on Fundamentals of Electronics, Communications and Computer Sciences*, vol. E93-A, no. 2, pp. 550–552, 2010.
- [35] A. Y. Wang, “Adaptive parameter adjustment of dynamical systems for chaos,” in *Proceedings of the International Conference on Informatics, Cybernetics, and Computer Engineering Melbourne*, 2011.
- [36] L. Li and F. Yu, “New results on delay-dependent stability for time-delay chaotic systems via time-delay feedback control,” in *Proceedings of the 2009 Chinese Control and Decision Conference*, Guilin, China, June 2009.
- [37] I. E. Sana, S. Majumder, and S. Saha, “Game-theoretic analysis to examine how government subsidy policies affect a closed-loop supply chain decision,” *Applied Sciences-Basel*, vol. 10, pp. 1–23, 2019.
- [38] J. Ma and H. Wang, “Complexity analysis of dynamic non-cooperative game models for closed-loop supply chain with product recovery,” *Applied Mathematical Modelling*, vol. 38, no. 23, pp. 5562–5572, 2014.
- [39] L. Xie, J. Ma, and H. Han, “Implications of stochastic demand and manufacturers’ operational mode on retailer’s mixed bundling strategy and its complexity analysis,” *Applied Mathematical Modelling*, vol. 55, pp. 484–501, 2018.
- [40] L. Xie, J. Ma, and M. Goh, “Supply chain coordination in the presence of uncertain yield and demand,” *International Journal of Production Research*, pp. 1–17, 2020.
- [41] J. Ma, Y. Hou, W. Yang, and Y. Tian, “A time-based pricing game in a competitive vehicle market regarding the intervention of carbon emission reduction,” *Energy Policy*, vol. 142, p. 111440, 2020.
- [42] B. Bao, J. Ma, and M. Goh, “Short- and long-term repeated game behaviours of two parallel supply chains based on government subsidy in the vehicle market,” *International Journal of Production Research*, pp. 1–24, 2020.

Research Article

Predicting Excavation-Induced Tunnel Response by Process-Based Modelling

Linlong Mu ^{1,2}, Jianhong Lin,^{1,2} Zhenhao Shi ^{1,2} and Xingyu Kang^{1,2}

¹Department of Geotechnical Engineering, Tongji University, Shanghai 200092, China

²Key Laboratory of Geotechnical and Underground Engineering of Ministry of Education, Tongji University, Shanghai 200092, China

Correspondence should be addressed to Zhenhao Shi; 1018tjzhenhao@tongji.edu.cn

Received 17 December 2019; Revised 19 March 2020; Accepted 3 April 2020; Published 28 April 2020

Guest Editor: Tomas Veloz

Copyright © 2020 Linlong Mu et al. This is an open access article distributed under the Creative Commons Attribution License, which permits unrestricted use, distribution, and reproduction in any medium, provided the original work is properly cited.

Potential damages to existing tunnels represent a major concern for constructing deep excavations in urban areas. The uncertainty of subsurface conditions and the nonlinear interactions between multiple agents (e.g., soils, excavation support structures, and tunnel structures) make the prediction of the response of tunnel induced by adjacent excavations a rather difficult and complex task. This paper proposes an initiative to solve this problem by using process-based modelling, where information generated from the interaction processes between soils, structures, and excavation activities is utilized to gradually reduce uncertainty related to soil properties and to learn the interaction patterns through machine learning techniques. To illustrate such a concept, this paper presents a simple process-based model consisting of artificial neural network (ANN) module, inverse modelling module, and mechanistic module. The ANN module is trained to learn and recognize the patterns of the complex interactions between excavation deformations, its geometries and support structures, and soil properties. The inverse modelling module enables a gradual reduction of uncertainty associated with soil characterizations by accumulating field observations during the construction processes. Based on the inputs provided by the former two modules, the mechanistic module computes the response of tunnel. The effectiveness of the proposed process-based model is evaluated against high-fidelity numerical simulations and field measurements. These evaluations suggest that the strategy of combining artificial intelligence techniques with information generated during interaction processes can represent a promising approach to solve complex engineering problems in conventional industries.

1. Introduction

With the rapid development of cities, it becomes frequent that deep excavations constructed for the foundation of high-rise buildings and/or underground space are next to existing subway or sewage tunnels [1–4]. As illustrated in Figure 1, the stress releases caused by excavations inevitably result in ground movements that can subsequently cause the deformations of tunnels and structural damages such as lining cracks and joint dislocations [5]. These problems can impair the operation of subways/sewage systems and even cause civilian casualties. Therefore, it is critical for engineers to accurately predict the response of tunnels subjected to adjacent deep excavations.

Uncertainty is the distinct feature of geotechnical engineering in that soils and rocks created by natural processes are variable in their composition, behaviour, and distributions. Such variability of the subsurface conditions, combined with the nonlinear interactions between multiple agents (e.g., soils, excavation support structures, construction activities, and tunnel structures), make the prediction of excavation-induced tunnel response a rather complex and difficult task. The latter is currently solved normally by involving numerical modelling techniques associated with advanced soil constitutive models [1, 6, 7]. Nevertheless, constructing a numerical model that can generate reasonable outcomes requires considerable expertise in numerical modelling and a systematic material characterization

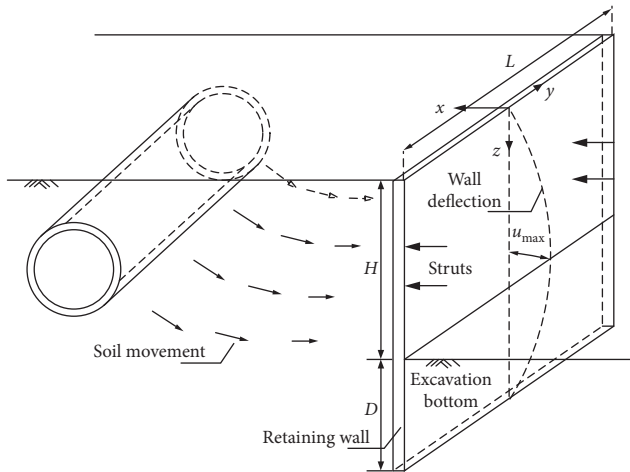


FIGURE 1: Schematics showing the influence of deep excavations on adjacent tunnels.

program to calibrate soil models. These prerequisites, quite possibly, are unrealistic for many civil engineers. There is another reason why an alternative strategy is needed to analyse the problem. In the last decade, building information modelling (BIM) has shown its potential in transforming the construction industry by facilitating the digitalization and automation of the full-lifecycle operations (i.e., design, construction, and maintenance) of buildings and infrastructures [8, 9]. Accordingly, a large amount of data pertaining to different stages of structures is collected by BIM platforms. To exploit such big data and enable dynamic and automated managements of excavation construction, analysis models that are capable of self-learning and computationally efficient are necessary.

This work proposes an initiative to devise an adaptive and efficient solution to the engineering problem discussed above, by harnessing the power generated by process-based modelling, where information generated during construction processes is used to reduce the uncertainty associated with subsurface conditions and recognize the interaction patterns between soils, structures, and excavation activities, so that the response of adjacent tunnels can be accurately predicted. To proof this concept, here we build a simple process-based model consisting artificial neural network (ANN) module, inverse modelling module, and mechanistic module. As will be described in the following, the mechanistic component is responsible for computing the response of tunnels under given deformations of excavation support structures. The latter cannot be easily obtained from conventional mechanical models, as they are influenced by a large number of variables, including excavation geometries, excavation support structures, and soil mechanical properties. Here, we exploit ANN's advantages in recognizing patterns of complex interactions involving multiple factors [10, 11] and use it to predict the deformations of excavation support structures. To further reduce the uncertainty associated with the soil properties fed into the ANN model, the module of inverse modelling [12–14] is utilized to search for an optimal set of soil parameters that can minimize the difference between measured deformations of excavation

support structures and those predicted by ANN. The advantage of collaborating the two machine learning techniques for engineering practice is reflected in that the inverse modelling will use field measurements at the early stages of construction processes to optimize soil parameters, thus consequently improving the predictions of the ANN model for later and more critical stages of the same project. The development of ANN models in the field of civil engineering normally faces the obstacle of lacking field data for model training. Aimed at constructing a platform to explore the potential of ANN models in civil engineering practices, here we train the ANN model by synthetic cases generated by numerical simulations. As will be shown in the following, such ANN model can provide useful information for real-world applications.

The rest of the paper is organized as follows. We will first present the mechanistic model used to compute the response of tunnels, followed by a description of the construction, training, and validation of the ANN model, as well as the inverse modelling module. Finally, the performance of the proposed hybrid model is evaluated against field measurements obtained from an excavation project next to the tunnels of a subway in China.

2. Mechanistic Model for Computing Response of Tunnel due to Adjacent Excavations

We formulate the mechanistic model based on the strategy of two-stage analysis [4, 15–17], where free-field soil movements or stress changes caused by excavation (i.e., the soil displacements and stress releases that would occur without the presence of tunnels) are first estimated, and the response of tunnel is subsequently evaluated by idealizing the tunnel structure as an elastic beam sitting either on nonlinear spring (i.e., the so-called Winkler subgrade reaction hypothesis) or elastic continuum [17, 18] and by imposing the displacements or stresses fields obtained from the first stage. Here, we build a displacement-controlled two-stage model (see Figure 1), as it can deliver more accurate predictions in particular for shallowly embedded tunnels where the presence of tunnels can significantly alter ground stress fields but soil displacements to a limited extent.

2.1. Free-Field Soil Movements Induced by Excavation. A crucial element in the two-stage model is to estimate the free-field soil movements caused by excavations. Numerous studies have indicated that appropriate consideration of small-strain behaviour of soils (i.e., considerably high stiffness at very small-strain levels and a nonlinear stiffness degradation with strain magnitudes) is essential for correctly predicting the soil movements associated with the construction activities of braced excavations [19–21]. Accordingly, we adopt the following closed-form expressions for the free-field soil movements proposed by Mu and Huang [22], which are obtained by fitting finite element (FE) simulations with a soil constitutive model that considers small-strain behaviour:

$$\begin{aligned}
u_s(x, y, z) &= u_{\max} \cdot a_x \cdot e^{-9((z-H)/(H+D))^2 - \pi(y/R)^2} \cdot e^{-((x/z) - b_x)/c_x)^2}, \\
w_s(x, y, z) &= \begin{cases} 0.8u_{\max} \cdot a_z \cdot \left(\frac{x}{H} + 0.5\right) \cdot e^{-\pi(y/R)^2 - ((z/x) - b_x)/c_x)^2}, & 0 \leq x \leq 0.5H, \\ 0.8u_{\max} \cdot a_z \cdot \left(-0.6\frac{x}{H} + 1.5\right) \cdot e^{-\pi(y/R)^2 - ((z/x) - b_x)/c_x)^2}, & 0.5H \leq x \leq 2H, \\ 0.8u_{\max} \cdot a_z \cdot \left(-0.05\frac{x}{H} + 0.2\right) \cdot e^{-\pi(y/R)^2 - ((z/x) - b_x)/c_x)^2}, & 2H \leq x \leq 4H, \end{cases} \quad (1)
\end{aligned}$$

where u_s and w_s denote the soil movements along the vertical direction and horizontal direction perpendicular to the retaining wall (the horizontal displacements parallel to the wall are often negligible); x , y , and z are spatial coordinates of soils (see Figure 1); and the variables L and H denote the length and depth of the excavation, respectively, D is the embeded depth of the retaining wall, while $R = L[0.069 \ln(H/L) + 1.03]/2$ is a composite geometry factor. The coefficient a_x , b_x , c_x , a_z , b_z , and c_z are functions of soil spatial coordinates and excavation geometries, and their specific expressions can be found in Mu and Huang [22]. It should be emphasized that the soil displacement field of equation (1) is a function of the maximum deflection of earth retaining wall u_{\max} defined in Figure 1. The latter quantity will be predicted by the ANN model described later.

2.2. Tunnel Response Subjected to Prescribe Soil Displacements. With the soil displacement fields described above, we further evaluate the tunnel response by idealizing it as an elastic beam that complies with Euler-Bernoulli beam theory:

$$\begin{aligned}
\frac{d^4 u}{dy^4} + \frac{k}{EI} (u - u_s) &= 0, \\
\frac{d^4 w}{dy^4} + \frac{k}{EI} (w - w_s) &= 0, \quad (2)
\end{aligned}$$

where u and w are the vertical and horizontal displacements of the tunnel, u_s and w_s are the soil displacements prescribed by equation (1), EI is the bending stiffness of tunnel, and y is the axial direction of the tunnel. The variable k in equation (2) denotes modulus of subgrade reaction (i.e., the stiffness of the springs connected to the beam, see Figure 2). To consider the influences of the burial depth and size of tunnel on soil reactions, the expression proposed by Yu et al. [23] is adopted here:

$$k = \frac{3.08}{\eta} \frac{E_s}{1 - \nu_s^2} \sqrt{\frac{E_s B}{EI}}. \quad (3)$$

In equation (3), B is the tunnel diameter, E_s and ν_s are Young's modulus and Poisson's ratio of soils, and η is a correction coefficient that depends on the burial depth of tunnel z :

$$\eta = \begin{cases} 2.18, & z/B \leq 0.5, \\ 1 + \frac{1}{1.7(z/B)}, & z/B > 0.5. \end{cases} \quad (4)$$

We use the finite difference method to solve the governing equation of equations (2) and (3). As depicted in Figure 2, the tunnel along its longitudinal axis is equally divided into small beam elements with their lengths given by $h = S/n$, where n is the number of elements and S is the length of the tunnel. As equation (2) involves fourth-order derivatives, two virtual joints are added to both ends of the tunnel so that equation (2) can be approximated by the central difference scheme:

$$w_{i+2} - 4w_{i+1} + 6w_i - 4w_{i-1} + w_{i-2} = 4\lambda^4 h^4 (w_{si} - w_i), \quad (5)$$

where $\lambda = \sqrt[4]{k/4EI}$ is the flexibility eigenvalue of the beam equation and the assembly of the governing equation for each beam elements leads to the following discretized form of the equation of motions for the tunnel:

$$[K]\{w\} = \{F\}, \quad (6)$$

where the vector $\{w\} = [w_0, w_1, \dots, w_i, \dots, w_{n-1}, w_n]$ contains the nodal displacements of the tunnel, while $\{F\} = [kw_{s(0)}, kw_{s(1)}, \dots, kw_{s(i)}, \dots, kw_{s(n-1)}, kw_{s(n)}]$ contains the corresponding nodal force determined under the assumption that shear forces and moments acting on both ends of the tunnel are negligible (i.e., the axial dimension of the tunnel is much greater than the size of the excavation). The matrix $[K]$ in equation (6) is the generalized system stiffness expressed as

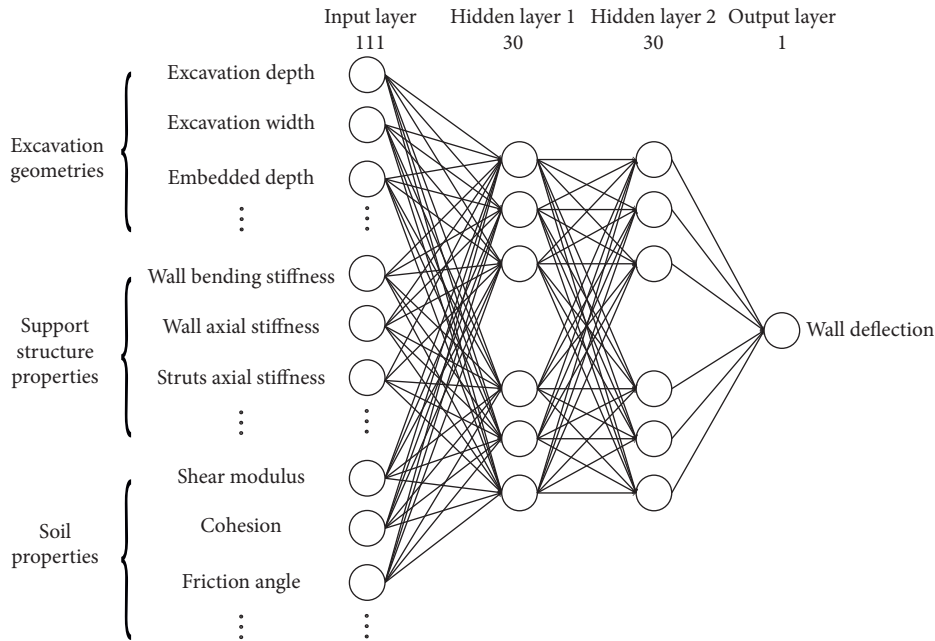


FIGURE 3: Layered structure of the proposed neural network.

TABLE 1: ANN input layer.

| Excavation geometries | Mechanical properties of support structures | Soil properties (parameterized through HSS model) |
|---|---|---|
| Excavation depth | Bending stiffness of retaining wall, EI | Shear modulus at very small strains |
| Excavation width | Axial stiffness of retaining wall, EA | Cohesion |
| Embedded depth of retaining wall | Poisson's ratio of retaining wall material | Angle of internal friction |
| Excavation depth divided by the layers of struts | Axial stiffness of struts, EA | etc. |
| Vertical distance between excavation bottom and the nearest lateral support | | |
| Averaged vertical and lateral space between struts | | |

number of reliable samples are required to train the model. Ideally, the types of data used to train the ANN model shall be the same as those involved while utilizing ANN to actually predict. Accordingly, the best training information comes from actual engineering projects where the ANN model is intended to apply, including accurate descriptions of excavation geometries, the sizes and materials of support structures, the HSS model parameters for each of soils layers encountered, and finally a reliable measurement of retaining wall deflections. Unfortunately, reported case studies that contain both information pertaining to the inputs and outputs of the ANN model is currently not enough for training the model. As a workaround, we train the ANN model through synthetic samples generated by two-dimensional finite element (FE) simulations. Training our ANN model by synthetic examples leads to two additional advantages. First, the generated datasets can cover the wide ranges of each input attribute (e.g., the ranges of excavation depth, soil strength, and structure stiffness) possibly encountered in engineering practice. Second, compared with actual field data, the datasets generated by numerical

simulations tend to be free of noises associated with factors excluded by the ANN model (like man power and the management levels), thus helping the ANN concentrate on the correlation between its inputs and outputs.

Totally, 1943 synthetic samples are generated by varying ANN input parameters randomly but within typical ranges encountered in engineering practice (e.g., the space between lateral braces varies from 3 m to 12 m and excavation length varies from 20 m to 80 m). Examples of employed training samples (note that soil parameters are excluded due to space limitations) are shown in Table 2.

We use the backpropagation algorithm coded in PyTorch module to train our ANN model, and this supervised learning process involves five epochs of forward activation towards outputs and backward errors propagation of adjusting connection weights. The activation function utilized for ANN nodes is rectified linear unit (ReLU), the optimization method is Adam, and the cost function is average sum-of-squares error (MSE). Among all synthetic samples, 70% is used to train the ANN model, while the rest is reserved as the validation set used by the learning algorithm.

TABLE 2: Examples of synthetic samples employed to train the ANN model.

| Excavation geometries | | Retaining wall properties | | | Internal brace properties | | | |
|-----------------------|-----------|--|---------------------|--------------------|---------------------------|-------------------|-------------------|----------------------|
| Depth (m) | Width (m) | EI (10^6 kN \times m ² /m) | EA (10^6 kN/m) | Embedded depth (m) | Vertical space (m) | Lateral space (m) | EA (10^6 kN) | Wall deflection (mm) |
| 4.9 | 40 | 1.507 | 18.1 | 30.1 | 4.0 | 4 | 3 | 1.33 |
| 20 | 40 | 1.507 | 18.1 | 15.0 | 2.9 | 3 | 3 | 35.54 |
| 5 | 60 | 1.667 | 20.0 | 30.0 | 3.6 | 4 | 2 | 5.39 |
| 21 | 80 | 1.667 | 20.0 | 14.0 | 4.23 | 9 | 16 | 46.20 |

2.3.3. Neural Network Validation. To assess the performance of the trained model, we compare the retaining wall deflections predicted by ANN and those computed by FE simulations for 46 different combinations of variables other than those used for synthetic samples. Figure 4 shows that the maximum wall deflection predicted by the ANN model reasonably agrees with that calculated by the high-fidelity numerical simulations, with the mean relative error of 12.2%. The ANN model is further examined against data from three actual excavation projects [27–29], where soil parameters and wall deflection measurements are all reported. As shown in Table 3, the model predictions and field measurements match reasonably. The latter fact suggests that although the ANN model is trained by synthetic samples, it is capable of predicting the deformations of excavation support structures in actual engineering practice.

2.4. Inverse Model for Reducing Uncertainty with Soil Parameters. Among all input parameters of the constructed ANN model, those related to the mechanical properties of soils have the highest degree of uncertainty attributed to natural variations of soils and the disturbance effects associated with coring, transporting, and trimming soil specimens before they are tested in laboratories. On the contrary, while soils in the field preserve the highest integrity, currently there lacks theoretical frameworks capable of estimating soil constitutive parameters by directly interpreting in situ measurements. To more accurately determine soil parameters and predict retaining wall deflections, we combine the proposed ANN model with inverse modelling, which automatically searches for accurate descriptions of soil properties by minimizing the difference between measured retaining wall deflections and those computed by the ANN model. The most important advantage of collaborating the two machine learning techniques for engineering practice is that the inverse modelling can use field measurements at early stages of construction activities to optimize soil parameters, thus improving the predictions of the ANN model for later and more critical stages of the same project.

The inverse modelling is achieved here through a nonlinear optimization algorithm based on an objective function of the least-squares form:

$$S = \sum_i^m (y_i - y'_i(b))^2 \omega_i, \quad (8)$$

where b contains the soil parameters to be determined; y and y' denote the vectors of field observations and ANN

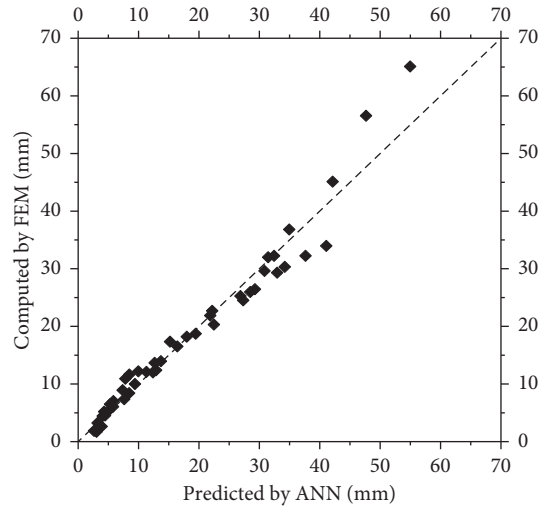


FIGURE 4: Comparison between maximum retaining wall deflections computed by finite element simulations and predicted by the ANN model.

predictions, respectively; the number of observation response is m ; the symbol ω_i denotes weight assigned to different observations based on their reliability and accuracy and here given by the inverse of the error variance that corresponds to each observation, i.e., $\omega_i = 1/\sigma_i^2$ [13]. An optimal set of soil parameters that minimizes the objective function of equation (9) is automatically searched by a modified Gauss–Newton algorithm with additional damping and Marquardt parameters [30, 31].

We use two statistic indexes related to the optimization algorithm to determine whether certain soil parameters can be accurately and uniquely determined through the inverse modelling scheme described above:

$$CSS_j = \sqrt{\frac{1}{m} \sum_{i=1}^m \left(\frac{\partial y'_i}{\partial b_j} \right)^2 \omega_i}. \quad (9)$$

CSS_j is the so-called composite scaled sensitivity used to indicate the degree of the overall influences of the j^{th} soil parameters on all observable responses ($i = 1$ to m) selected entering into the inverse model, such as retaining wall deflections. It should be emphasized that even for the same parameters, CSS can vary when different field observations are involved, and therefore, the value of CSS can effectively identify the possibility of reducing the uncertainty associated

TABLE 3: Comparison between measured maximum deflections of retaining wall in case studies and ANN predictions.

| Case number | 1 | 2 | 3 |
|----------------------|-------|-------|-------|
| Measurements (mm) | 48.30 | 20.40 | 23.52 |
| ANN predictions (mm) | 47.60 | 23.35 | 20.76 |
| Relative error (%) | 1.45 | 14.45 | 11.72 |

with particular parameters with respect to given types of field measurement. The second useful statistic index is the parameter correlation coefficient:

$$\text{PCC}_{ij} = \frac{V_{ij}}{\sqrt{V_{ii}V_{jj}}}, \quad (10)$$

which measures the degree of correlation between the i^{th} and j^{th} parameters. A pair of parameters that are highly correlated to each other, indicated by high PCC values, usually cannot be simultaneously determined through the inverse modelling scheme described above, as the uniqueness of the solution cannot be ensured. V_{ij} in equation (10) denotes the component of the variance-covariance matrix:

$$[V] = \frac{S}{m-n} \left(\left[\frac{\partial y'}{\partial b} \right]^T [\omega] \left[\frac{\partial y'}{\partial b} \right] \right)^{-1}, \quad (11)$$

where n denotes the number of parameters to be determined; S is the value of the objective function defined in equation (8); and $[\partial y'/\partial b]$ is a matrix containing the gradient of the observation with respect to soil parameters, while $[\omega]$ is a diagonal matrix with its component given by ω_i defined above.

3. Evaluation of Mechanistic-Machine Learning Hybrid Model

3.1. Determining Input Parameters for ANN Model. The excavation project located in Hangzhou, China [32], provides an unique opportunity to assess the proposed model for analyzing the response of tunnel subjected to adjacent excavation. In this case study, the deep excavation extends to the depths of 15 m to 18.55 m below ground surface and is beside the tunnels of a subway's north and south lines. The smallest distance between the excavation and the tunnels is only 7 m, while the averaged horizontal space is around 9 m. The length of the excavation parallel to the tunnels is 245 m. The depth of the tunnel crown varies from 9.3 m to 13.3 m, and the diameter of the tunnel is 6.2 m. To reduce the excavation-induced impacts on the tunnels, the part of the excavation next to the tunnels adopts a composite retaining wall of 1000 mm thick diaphragm wall and cast-in-place piles, and the embedded depth of the retaining wall is 6 m. The internal supports consist of three layers of reinforced concrete struts. According to these in situ conditions, the geometries of the excavation that are fed into the ANN model are obtained (i.e., see those depicted in Figure 5, note that the width of the excavation is 70 m and the horizontal space between struts is 6 m). The mechanical properties of excavation support structures used in the ANN model are summarized in Table 4, as reported in the case study. Here,

we increase the thickness of the diaphragm wall to 1500 mm to consider the strengthening effects due to the additional cast-in-place piles.

The subsurface at the site is composed of three strata, among which the first layer is categorized as sandy silt (SM), while the second and third layers are clayey silt (CM), as shown in Figure 5. Table 5 summaries the hardening soil small parameters for the first two layers (i.e., those within the range of the retaining wall) calibrated from laboratory measurement [32]. These soil properties are adopted in the ANN model.

3.2. Model Performance. Figure 6 compares the measured deflection profiles of retaining wall against the maximum deflections predicted by the ANN model that corresponds to two consecutive stages of the excavation (i.e., excavate to 13 m and 16 m depths). Because of the large number of variables involved in this problem, we consider the ANN prediction still acceptable, although it tends to overestimate the wall deformations. The maximum discrepancy is around 8 mm occurred for the excavation to the shallower depth, and the prediction is improved as the construction proceeds in that the difference between measured and predicted maximum wall deflection reduces to 5 mm as the excavation reaches 16 m.

Among the resources that may result in the mismatches described above, the uncertainty embedded with the characterization of soil properties is a primary contributor. The fact that the deformations of the excavation support structures predicted by the ANN model are greater than those observed suggests the possibility that soil specimens have been disturbed and consequently weakened before they are tested. To minimize the influences of the uncertainty associated with the parameters for soils, we employ the inverse modelling described in the previous section. To constrain the number of parameters to be determined and consequently enhance inverse modelling performance, for each layer we only directly optimize two parameters, the reference stiffness modulus E_{50} and the reference shear strain threshold $\gamma_{0.7}$, i.e., one controls the soil behaviour at large strains and the other for small strains. The statistic indexes associated with these two candidates show that they can noticeably affect the retaining wall deflections and are not strongly correlated with each other. The stiffness parameters G_0 , E_{oed} , and E_{ur} are indirectly optimized as we assume that they keep constant proportions to E_{50} , while other parameters are not changed as they have relatively insignificant influences on the deformations of excavation support structures. The field measurement entering into the inverse modelling is the retaining wall deflections corresponding to the excavation depth of 13 m (i.e., observation

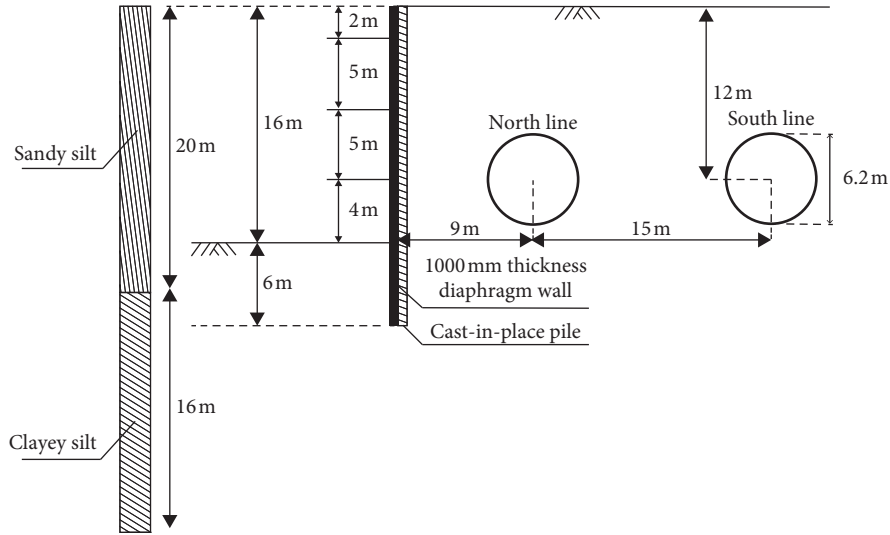


FIGURE 5: Schematics showing the excavation and tunnel geometries in the case study of Hangzhou, China.

TABLE 4: Mechanical properties of excavation support and tunnel structures in the case study of Hangzhou, China.

| Retaining wall | | Strut | | Tunnel | | | |
|--|--|-----------------|----------------------------|--------------|---------------|-----------------------|-----------------|
| EI ($10^6 \text{ kN} \times \text{m}^2/\text{m}$) | EA ($10^6 \text{ kN}/\text{m}$) | Poisson's ratio | EA (10^6 kN) | Diameter (m) | Thickness (m) | Young's modulus (GPa) | Poisson's ratio |
| 8.44 | 45 | 0.2 | 21.6 | 6.2 | 0.35 | 28 | 0.2 |

TABLE 5: Soil parameters before and after inverse analysis.

| Stratum | Original | | Optimized | |
|--|-----------------------|-----------------------|-----------------------|-----------------------|
| | Sandy silt | Clayey silt | Sandy silt | Clayey silt |
| Thickness (m) | 20 | 16 | 20 | 16 |
| Unit weight (kN/m^3) | 19.3 | 18.9 | 19.3 | 18.9 |
| E_{50}^{ref} (MPa) | 15.00 | 9.00 | 3.09 | 1.85 |
| $E_{\text{oed}}^{\text{ref}}$ (MPa) | 15.00 | 9.00 | 3.09 | 1.85 |
| $E_{\text{ur}}^{\text{ref}}$ (MPa) | 60.00 | 50.00 | 12.36 | 10.3 |
| G_0^{ref} (MPa) | 200.00 | 184.00 | 41.19 | 37.9 |
| $\gamma_{0.7}$ | 2.00×10^{-4} | 4.00×10^{-4} | 4.12×10^{-5} | 8.23×10^{-5} |
| c (kPa) | 5 | 6 | 5 | 6 |
| φ ($^\circ$) | 34 | 18.5 | 34 | 18.5 |
| M | 0.8 | 0.8 | 0.8 | 0.8 |

from the earlier stage of construction). The optimized soil parameters are listed in Table 3.

The ANN predictions based on those updated soil parameters are included in Figure 6. The results clearly show that the soil parameters optimized by solely using the observations from early construction stages also lead to a good prediction of the response at later and more critical stages of construction. Moreover, Figure 6 emphasizes that, with a reasonable set of soil parameters, the trained ANN model can reasonably represent the deformations of the earth retaining wall.

By inputting the maximum deflections of earth retaining wall into the mechanistic model, the response of the two tunnels next to the excavation can be computed. The measured vertical and horizontal displacements of the

tunnels that correspond to the excavation depth of 16 m are shown in Figure 7 (only the maximum displacements are reported), together with results obtained by using the proposed analytical model. The mechanical and geometrical properties of the tunnel structure used in the computation are listed in Table 3. Moreover, the length of the tunnels is set to 1000 m so that the shear forces and moments acting on both ends of the tunnels can be neglected. Young's modulus and Poisson's ratio for the soils surrounding the tunnels (i.e., see equation (3)) are converted from the optimized G_0 (considering the rather small soil movements around the tunnel) and γ_{ur} of the top sandy silty layer, i.e., where the tunnel is embedded.

It is seen from Figure 7 that three types of maximum retaining wall deflections are used to compute tunnel

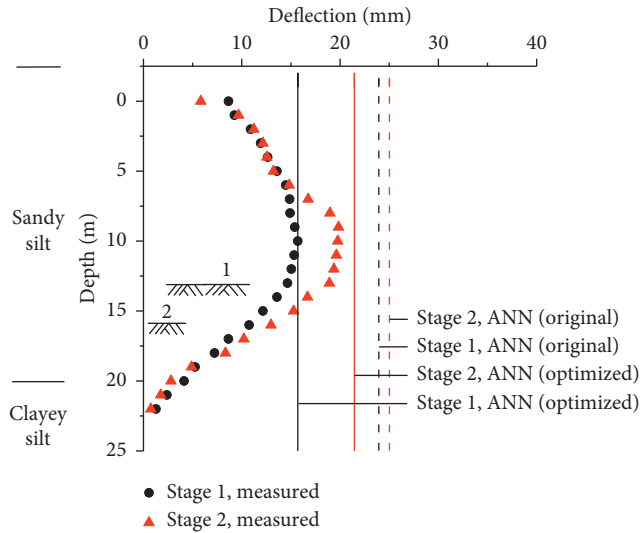


FIGURE 6: Comparison between measured retaining wall deflections in the case study of Hangzhou, China, and those predicted by the ANN model. Ground surface symbol shows the excavation depths corresponding to the two stages (i.e., stage 1: excavate to 13 m; stage 2: excavate to 16 m).

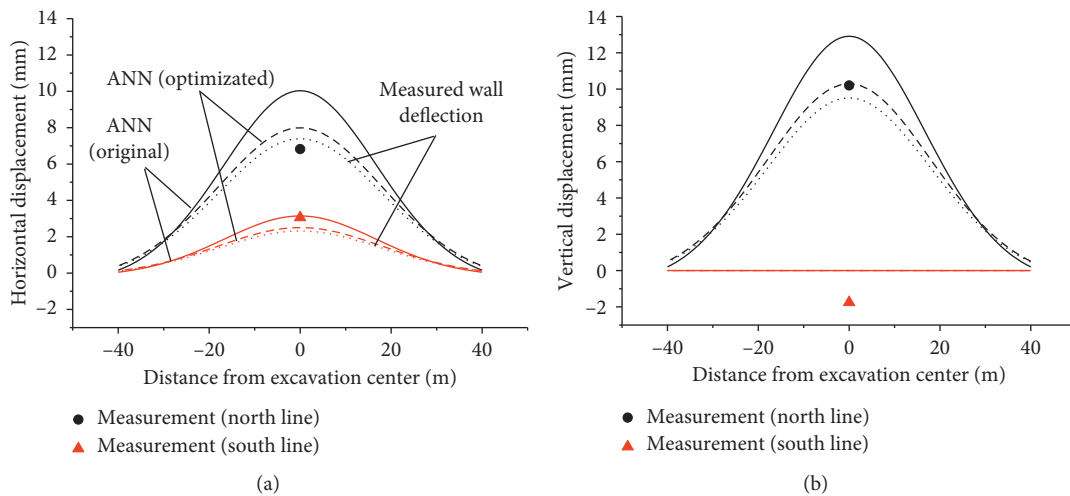


FIGURE 7: Comparison between measured and predicted tunnel displacements caused by adjacent excavation.

displacements, including the actual field measurements and ANN predictions based on the original and optimized soil parameters. The first observation from Figure 7 is that the computed results based on the measured wall deflection agree well with the measured tunnel response, thus suggesting that the mechanistic model can reasonably predict the tunnel displacements provided that the retaining wall deflection is accurately determined. By comparing the tunnel response computed by using the ANN predictions with the original and optimized soil parameters, the adaptivity and learning ability achieved by collaborating two machine learning techniques is emphasized in that by collecting observations at early stages of the excavation project, and the soil characterization updated by inverse modelling can form the basis of a new ANN prediction of the retaining wall deformations and consequently gradually improve the prediction regarding the response of adjacent tunnels.

4. Conclusion

An accurate prediction of the response of adjacent tunnels is critical for the plan, design, and construction of deep excavations in congested urban areas. The uncertainty and variability inherent to the subsurface compositions, extent, and behaviour and the nonlinear interactions between multiple agents (e.g., excavation support structures, soil strata, and tunnel structures) are the two primary resources leading to the complexity and difficulty of this task. This paper proposes an initiative to tackle this problem using process-based modelling, where information extracted from the construction processes of deep excavation is used to recognize the interaction patterns between multiple agents and to reduce the uncertainty associated with subsurface conditions, such that the response of tunnels induced by adjacent deep excavations can be accurately predicted. To

proof the concept, we propose a simple process-based model composed of mechanistic module, artificial neural network (ANN) module, and inverse modelling module. These components are specialized in addressing particular challenging aspects of the targeted engineering problem but are interrelated forming a collaborative group. Specifically, the mechanistic component is responsible for computing the response of tunnel in accordance with the deflections of earth retaining wall. To predict the latter information, the ANN model is built aimed at learning and recognizing the patterns involved in the interactions between excavation geometries, excavation support structures, and soil properties. The inverse modelling module is included to reduce the uncertainty associated with soil parameters entering into the ANN model, which enables automatic learning and update of soil properties with the accumulation of information generated during construction processes. The main conclusions that can be drawn from this work include the following:

- (1) While being trained by synthetic samples, the ANN model can reasonably predict the maximum deflections of retaining wall measured in actual engineering projects.
- (2) The mechanistic model can reasonably predict the displacements of tunnels caused by adjacent excavations provided that the deflections of earth retaining wall can be accurately estimated.
- (3) The quality of the ANN prediction highly depends on the characterization of soil parameters. Inverse modelling based on the ANN model can reduce the uncertainty associated with soil parameters and consequently improves the prediction of retaining wall deformations and tunnel displacements.

Lastly, it should be noted that the work presented here merely represents the first step towards accurately predicting the influences of deep excavations on adjacent tunnels by harnessing the power of process-based modelling. Despite the promising features exhibited by the ANN model trained by synthetic cases, the information obtained from real-world engineering projects is indispensable and the best dataset for training the model. For this purpose, next step that may be undertaken is to integrate the proposed model into BIM platforms such that (1) the ANN model can be trained by big data collected from actual deep excavation projects, (2) the uncertainty associated with site-specific soil properties can be reduced by inverse modelling with the accumulation of field observations, and (3) deep excavations can be managed dynamically and adaptively to protect nearby tunnels.

Data Availability

The data of field measurements, results generated by finite element simulations, and the proposed analytical model, which are used to support the findings of this study, are included within the article. The entire dataset of samples used for training the ANN model is available from the corresponding author upon request.

Conflicts of Interest

The authors declare that there are no conflicts of interest regarding the publication of this paper.

Acknowledgments

This study was supported by the Shanghai Science and Technology Committee Rising-Star Program (19QC1400500) and Fundamental Research Funds for the Central Universities.

References

- [1] M. Doležalová, "Tunnel complex unloaded by a deep excavation," *Computers and Geotechnics*, vol. 28, no. 6-7, pp. 469–493, 2001.
- [2] Z. Hu, Z. Yue, J. Zhou, and L. G. Tham, "Design and construction of a deep excavation in soft soils adjacent to the Shanghai metro tunnels," *Canadian Geotechnical Journal*, vol. 40, no. 5, pp. 933–948, 2003.
- [3] S. Shen, H. Wu, Y. Cui, and Z. Yin, "Long-term settlement behaviour of metro tunnels in the soft deposits of Shanghai," *Tunnelling and Underground Space Technology*, vol. 40, pp. 309–323, 2014.
- [4] J. Zhang, J. Chen, J. Wang, and Y. Zhu, "Prediction of tunnel displacement induced by adjacent excavation in soft soil," *Tunnelling and Underground Space Technology*, vol. 36, pp. 24–33, 2013.
- [5] C. Chang, C. Sun, S. Duann, and R. Hwang, "Response of a taipei rapid transit system (TRTS) tunnel to adjacent excavation," *Tunnelling and Underground Space Technology*, vol. 16, no. 3, pp. 151–158, 2001.
- [6] X. Huang, H. F. Schweiger, and H. Huang, "Influence of deep excavations on nearby existing tunnels," *International Journal of Geomechanics*, vol. 13, no. 2, pp. 170–180, 2001.
- [7] M. Li, J. Chen, J. Wang, and Y. Zhu, "Comparative study of construction methods for deep excavations above shield tunnels," *Tunnelling and Underground Space Technology*, vol. 71, pp. 329–339, 2018.
- [8] S. Azhar, "Building information modeling (BIM): trends, benefits, risks, and challenges for the AEC industry," *Leadership and Management in Engineering*, vol. 11, no. 3, pp. 241–252, 2011.
- [9] R. Volk, J. Stengel, and F. Schultmann, "Building information modeling (BIM) for existing buildings—literature review and future needs," *Automation in Construction*, vol. 38, pp. 109–127, 2014.
- [10] I. A. Basheer and M. Hajmeer, "Artificial neural networks: fundamentals, computing, design, and application," *Journal of Microbiological Methods*, vol. 43, no. 1, pp. 3–31, 2000.
- [11] A. K. Jain, J. Jianchang Mao, and K. M. Mohiuddin, "Artificial neural networks: a tutorial," *Computer*, vol. 29, no. 3, pp. 31–44, 1996.
- [12] E. P. Poeter and M. C. Hill, "Inverse models: a necessary next step in ground-water modeling," *Ground Water*, vol. 35, no. 2, pp. 250–260, 1997.
- [13] R. J. Finno and M. Calvello, "Supported excavations: observational method and inverse modeling," *Journal of Geotechnical and Geoenvironmental Engineering*, vol. 131, no. 7, pp. 826–836, 2005.
- [14] L. Mu, R. J. Finno, M. Huang, T. Kim, and K. Kern, "Defining the soil parameters for computing deformations caused by

- braced excavation,” *Maejo International Journal of Science and Technology*, vol. 9, no. 2, pp. 165–180, 2015.
- [15] K. J. Xu and H. G. Poulos, “3-D elastic analysis of vertical piles subjected to “passive” loadings,” *Computers and Geotechnics*, vol. 28, no. 5, pp. 349–375, 2001.
- [16] N. Loganathan, H. G. Poulos, and K. J. Xu, “Ground and pile-group responses due to tunnelling,” *Soils and Foundations*, vol. 41, no. 1, pp. 57–67, 2001.
- [17] L. Mu, M. Huang, and R. J. Finno, “Tunnelling effects on lateral behavior of pile rafts in layered soil,” *Tunnelling and Underground Space Technology*, vol. 28, no. 1, pp. 192–201, 2012.
- [18] A. Klar, T. E. B. Vorster, K. Soga, and R. J. Mair, “Soil-pipe interaction due to tunnelling: comparison between Winkler and elastic continuum solutions,” *Géotechnique*, vol. 55, no. 6, pp. 461–466, 2005.
- [19] R. J. Jardine, D. M. Potts, A. B. Fourie, and J. B. Burland, “Studies of the influence of non-linear stress-strain characteristics in soil-structure interaction,” *Geotechnique*, vol. 36, no. 3, pp. 377–396, 1986.
- [20] J. H. Atkinson and G. Salfors, “Experimental determination of stress-strain-time characteristics in laboratory and in situ tests,” in *Proceedings of the 10th European Conference on Soil Mechanics and Foundation Engineering*, A. A. Balkema, Rotterdam, Netherlands, pp. 915–956, May 1991.
- [21] J. H. Atkinson, “Non-linear soil stiffness in routine design,” *Géotechnique*, vol. 50, no. 5, pp. 487–508, 2000.
- [22] L. Mu and M. Huang, “Small strain based method for predicting three-dimensional soil displacements induced by braced excavation,” *Tunnelling and Underground Space Technology*, vol. 52, pp. 12–22, 2016.
- [23] J. Yu, C. Zhang, and M. Huang, “Soil-pipe interaction due to tunnelling: assessment of Winkler modulus for underground pipelines,” *Computers and Geotechnics*, vol. 50, pp. 17–28, 2013.
- [24] T. Benz, *Small-strain stiffness and its numerical consequences*, Ph.D. thesis, University of Stuttgart, Stuttgart, Germany, 2007.
- [25] S. Likitlersuang, C. Surarak, D. Wanatowski, E. Oh, and A. Balasubramaniam, “Finite element analysis of a deep excavation: a case study from the Bangkok MRT,” *Soils and Foundations*, vol. 53, no. 5, pp. 756–773, 2013.
- [26] S. Liao, S. Wei, and S. Shen, “Structural responses of existing metro stations to adjacent deep excavations in Suzhou, China,” *Journal of Performance of Constructed Facilities*, vol. 30, no. 4, Article ID 04015089, 2015.
- [27] J. Yin, “Application of hardening soil model with small strain stiffness in deep foundation pits in Shanghai,” *Chinese Journal of Geotechnical Engineering*, vol. 32, pp. 166–172, 2010, in Chinese.
- [28] Y. Shi, J. Ruan, and C. Wu, “Xiamen area typical stratum of HS-small model for small strain parameters sensitivity analysis,” *Science Technology and Engineering*, vol. 17, no. 2, pp. 105–110, 2017, in Chinese.
- [29] F. Liu, “Influence on adjacent tunnel in process of deep foundation,” Master’s thesis, Zhejiang University, Zhejiang, China, 2015, in Chinese.
- [30] K. Levenberg, “A method for the solution of certain non-linear problems in least squares,” *Quarterly of Applied Mathematics*, vol. 2, no. 2, pp. 164–168, 1944.
- [31] D. W. Marquardt, “An algorithm for least-squares estimation of nonlinear parameters,” *Journal of the Society for Industrial and Applied Mathematics*, vol. 11, no. 2, pp. 431–441, 1963.
- [32] H. Zhou, “Study on the influence of excavation to adjacent existing tunnels in sandy silt area,” Master’s thesis, Zhejiang University of Technology, Zhejiang, China, 2015, in Chinese.

Research Article

Depth Penetration and Scope Extension of Failures in the Cascading of Multilayer Networks

Wen-Jun Jiang, Run-Ran Liu , and Chun-Xiao Jia 

Research Center for Complexity Sciences, Hangzhou Normal University, Hangzhou, Zhejiang 311121, China

Correspondence should be addressed to Run-Ran Liu; runranliu@163.com

Received 16 December 2019; Revised 7 March 2020; Accepted 17 March 2020; Published 25 April 2020

Guest Editor: Tomas Veloz

Copyright © 2020 Wen-Jun Jiang et al. This is an open access article distributed under the Creative Commons Attribution License, which permits unrestricted use, distribution, and reproduction in any medium, provided the original work is properly cited.

Real-world complex systems always interact with each other, which causes these systems to collapse in an avalanche or cascading manner in the case of random failures or malicious attacks. The robustness of multilayer networks has attracted great interest, where the modeling and theoretical studies of which always rely on the concept of multilayer networks and percolation methods. A straightforward and tacit assumption is that the interdependence across network layers is strong, which means that a node will fail entirely with the removal of all links if one of its interdependent nodes in other network layers fails. However, this oversimplification cannot describe the general form of interactions across the network layers in a real-world multilayer system. In this paper, we reveal the nature of the avalanche disintegration of general multilayer networks with arbitrary interdependency strength across network layers. Specifically, we identify that the avalanche process of the whole system can essentially be decomposed into two microscopic cascading dynamics in terms of the propagation direction of the failures: depth penetration and scope extension. In the process of depth penetration, the failures propagate from layer to layer, where the greater the number of failed nodes is, the greater is the destructive power that will emerge in an interdependency group. In the process of scope extension, failures propagate with the removal of connections in each network layer. Under the synergy of the two processes, we find that the percolation transition of the system can be discontinuous or continuous with changes in the interdependency strength across network layers, which means that a sudden system-wide collapse can be avoided by controlling the interdependency strength across network layers. Our work not only reveals the microscopic mechanism of global collapse in multilayer infrastructure systems but also provides stimulating ideas on intervention programs and approaches for cascade failures.

1. Introduction

Many real-world complex systems, both natural [1] and man made [2–5], can be described as multilayer or interdependent networks given the existence of different levels of interdependence across network layers. Recent theoretical studies on networks with two or more layers show that when the nodes in each network are interdependent on the nodes in other networks, even small initial failures can propagate back and forth and lead to the abrupt collapse of the whole system [5–10]. In this sense, multilayer networks are more fragile than single-layer networks in resisting the propagation of initial failures [6]. In recent years, we have witnessed considerable progress in the study of multilayer networks with the aid of percolation theory [11–13]. It has been found that multilayer networks are not as fragile as in

theoretical studies under certain specific conditions such as those given link overlap [14, 15], geometric correlations [16, 17], correlated community structures [18], interlayer degree correlations [19, 20], intralayer degree correlations [21], asymmetry in interdependence [22], and autonomous nodes [23–25] being able to facilitate the viability of nodes and alleviate the suddenness of the collapse in an interdependent system. In addition, some features of real interdependent systems, such as spatial constraints [26–30], clustering [31, 32], and degree distribution [33, 34], also enhance the robustness and mitigate cascading failures of interdependent networks.

A key question in the modeling of multilayer networks is how to describe the interdependencies across network layers. A straightforward method employed in most previous models of cascading failures in multilayer networks is

assuming that the layer interdependence is “strong,” where a failure node can cause all of its interdependent neighbors to fail completely [6, 23, 35–40]. This assumption has already been extended extensively to the study of cascading dynamics in networks under different conditions such as interdependency groups in single-layer networks [41–43] and k -core percolation [44], weak percolation [45], and redundant percolation [46] in multilayer networks. Nevertheless, this assumption is somewhat simplistic and cannot cover the case where nodes are weakly interdependent. For instance, in a civil transportation system, the flow of passengers from city to city depends on a number of transportation modes such as coaches, trains, airplanes, and ferries. When any mode becomes unavailable, the total failure of the other three modes seems impossible, e.g., when a local train station is shut down, passenger flow into the city may be decreased: some passengers destined for this city may cancel their trips, and the transferring passengers would switch to other cities to reach their destinations. The reduction of passenger flow can cause some routes in other modes to not operate properly, and carriers experience financial or other losses; for instance, airlines may cancel flights if passenger numbers are below expectations. Specifically, the interdependence across network layers can be “weak,” and the failure of a node cannot destroy all of its dependency nodes in other network layers with certainty [47, 48]. Under these circumstances, the failure of a train station can cause one or more of its interdependent nodes in other network layers to suffer damage or even failure, e.g., the failure of a local coach station, which can further lead to failures in more modes and deteriorate the connectivity of the city. By this token, there may exist a cascading process underlying a group of interdependent nodes across network layers, which means that the microscopic mechanism of global collapse in multilayer networks could include not only the propagation of failures from node to node inside a certain network layer but also the cascading process of failures across network layers. In this paper, we regard the propagation of failures inside a network layer as “inner-layer cascading” and the propagation of failures in a dependency group across network layers as “cross-layer cascading.”

Previous networks that have considered the “strong” interdependence ignore the microscopic process of “cross-layer cascading,” as the failure of one node will destroy all its interdependent neighbors. In this paper, we aim to model the cascading dynamics in multilayer networks within a more general situation by using the assumption of “weak” interdependence [47], where the strength of interdependence can be tuned by introducing a tolerance parameter α . Using a comprehensive theoretical study and numerical simulations, we find that the cascading dynamic in multilayer networks is essentially the synergistic result of “cross-layer cascading” and “inner-layer cascading.” In particular, we find that the system can undergo different types of percolation with changing tolerance parameters α . Specifically, the system percolates as an abrupt (first-order) percolation transition for small values of α . With increasing α exceeding a critical value α_c , the system percolates in a continuous (second-order) manner. However, for scale-free

networks, the phenomenon of double phase transitions occurs for some moderate parameter values of α , where the networks in the system first percolate in a continuous (second-order) manner and then experience a first-order phase transition in an abrupt manner at another phase transition point.

2. Model

We consider a multilayer network consisting of M layers of networks, where each network layer has N nodes. We label the network layers with Latin letters A, B, C , and so on, and the nodes in each network layer are labeled with Arabic numbers $1, 2, \dots, N$. Therefore, each node in a certain network layer can be identified as a pair of coordinates (x, X) , with x denoting the node label and X denoting the layer label. The nodes across network layers with the same Arabic number are interdependent on each other, i.e., they are replica nodes. As shown in Figure 1, the nodes $(1, A)$, $(1, B)$, $(1, C)$, and $(1, D)$ are interdependent nodes in network layers A, B, C , and D , respectively. When one of these nodes fails, the other three nodes will suffer damages. Similarly, the other nodes can be also divided into several interdependent groups by their Arabic number labels. The nodes in the same network layer X are linked by a set of connectivity links, and the connectivity degree of nodes follows a degree distribution p_k^X . In this paper, we consider the case where the M network layers within the multilayer system have an identical degree distribution for simplicity.

The cascading in the multilayer networks is triggered by randomly selecting a fraction $1 - p$ of nodes and their replicas as initially failed nodes. For each network layer, all the links of failed nodes are removed simultaneously, which breaks the network layer into a number of connected components [49]. The nodes in the isolated components are treated as failed ones, and the nodes in the giant component are functional. Due to the interdependency among the replica nodes across network layers, a failed node will cause a certain level of damage to its replicas, where the damage degree is controlled by the tolerance parameter α . Specifically, when one node in a network layer fails, each connectivity link of its viable interdependency replicas in other network layers will be removed with a probability $1 - \alpha$. Along with the removal of the connectivity links, the network layers will be further fragmented and, thus, lead to more failures. After a number of iterations of link removal caused by node failures and node isolations resulting from network fragmentation, the system can reach a steady state. In this iterative process, the failures can propagate from layer to layer through the interdependencies among replica nodes, and the failures can also propagate from node to node along with the removal of connectivity links in a certain network layer simultaneously. Here, we regard the propagation of failures inside a network layer as “scope extension” and the propagation of failures in an interdependency group across network layers as “depth penetration.” Especially, it should be noticed that there is a microscopic cascading in the process of depth penetration: a failed node can lead more node failures in its replicas and, thus, lead more and more

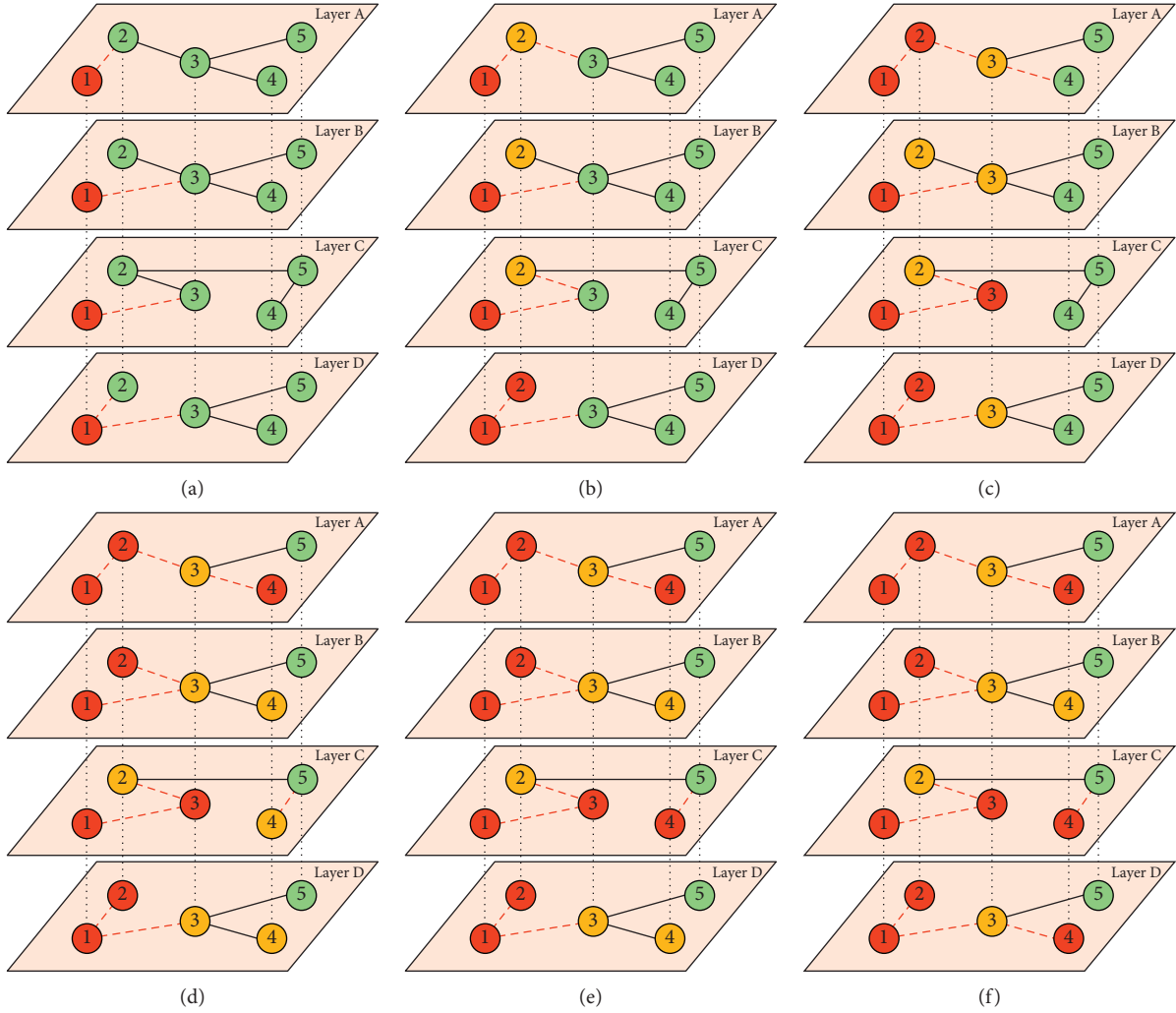


FIGURE 1: Schematic diagram of the cascading process in a four-layer network. The nodes in different layers with the same Arabic number are replica nodes, and they are connected by dotted lines. The functional links are marked in solid lines and the failed links are marked in dashed lines. The functional nodes are marked in green, the failed nodes are marked in red, and the yellow nodes are still viable after being damaged. At stage (A), the replicas with the Arabic number 1 are removed from all layers. At stage (B), the node (2, D) becomes isolated from the giant component in layer D and fails, which leads to the link removal of its replicas in layers A, B, and C. At stage (C) the node (3, C) becomes isolated from the giant component in layer C and fails, which leads to the link removal of its replicas in layers A, B, and D. Simultaneously, node (2, A) becomes isolated and fails due to the removal of link 23 in layer A, which further leads to the link removal of its replicas in layers B and C. At stage (D), the node (4, A) becomes isolated from the giant component in layer A and fails, which leads to the link removal of its replicas in layers B, C, and D. Simultaneously, node (2, A) becomes isolated and fails due to the removal of link 23 in layer B. At stage (E), the node (4, C) becomes isolated from the giant component and fails, which leads to the link removal of its replicas in layers B and D. At stage (F), the node (4, D) becomes isolated and fails, and the system reaches the final steady state. (a) Stage A. (b) Stage B. (c) Stage C. (d) Stage D. (e) Stage E. (f) Stage F.

node failures in its replicas. Schematic illustration of cascading process of a four-layer system is shown in Figure 1. In this paper, we use the relative size S^X of the giant component in each layer of network X to measure the robustness of the network.

3. Theory

We use the method of probability generation functions [50, 51] to obtain the theoretical solution of the model, and the generating function $G_0^X(x) = \sum_k p_k^X x^k$ is employed to generate the degree distribution p_k^X of layer X . Similarly, the

generating function $G_1^X(x) = \sum_k p_k^X k x^{k-1} / \langle k \rangle^X$ is used to generate the excess degree distribution of a node reached by following a random link, where $\langle k \rangle \equiv \sum_k p_k^X k$ represents the average degree of the network layer X . In particular, we define R^X as the probability that a randomly chosen link in network X leads to its giant component in the steady state of the system. For the case where the M network layers in the system have a same degree distribution, $p_k^X = p_k$. Accordingly, $G_0^X(x) \equiv G_0(x)$, $G_1^X(x) \equiv G_1(x)$, $R^X \equiv R$, and $\langle k \rangle^X \equiv \langle k \rangle$. Assuming that each network of M network layers is tree-like, we aim to obtain the probability S^X that a random node is in the giant component of layer X . Because

each layer has the same degree distribution, we have $S^A = S^B = S^C \dots \equiv S$. Following a randomly chosen link in the layer X , we arrive at a node (x, X) of degree k with t failed replicas. Therefore, each link of node (x, X) can be preserved with a probability α^t . Considering that the degree k follows the probability distribution $k p_k / \langle k \rangle$, the probability that a random link can lead to the giant component follows $\alpha^t [1 - k p_k / \langle k \rangle (1 - \alpha^t R)^{k-1}]$, which can be simplified as $\alpha^t [1 - G_1(1 - \alpha^t R)]$ in terms of the generating function $G_1(x)$. If the number t of failed replicas for a given node follows a probability distribution $f(t)$, we can obtain the self-consistent equation for R by summing over all possible t .

$$R = p \sum_{t=0}^{M-1} \alpha^t [1 - G_1(1 - \alpha^t R)] f(t) \equiv h(R). \quad (1)$$

Similarly, we can obtain the probability S that a random node is in the giant component:

$$S = p \sum_{t=0}^{M-1} [1 - G_0(1 - \alpha^t R)] f(t). \quad (2)$$

The solution process of equations (1) and (2) utilizes the probability distribution function $f(t)$, which can be obtained by using the probability R . Considering that there are t failed replicas for a random node (x, X) in the layer X at steady state, the viable probability of each replica is $1 - G_0(1 - \alpha^t R)$, and the remaining $M - t - 1$ replicas are all viable with probability $[1 - G_0(1 - \alpha^t R)]^{M-t-1}$. Because the failures can propagate from layer to layer through the interdependencies among replica nodes, we assume that there are s failed replicas caused by the link removal of other nodes in the corresponding network layers, and there are $t - s$ failed nodes induced by the s failed replicas. The probability of s failed replicas existing caused by isolation is $G_0^s(1 - R)$. After that, the probability of $t - s$ additional replicas failing is $[G_0(1 - \alpha^s R) - G_0(1 - R)]^{t-s}$. Therefore, $f(t)$ satisfies

$$f(t) = \binom{M-1}{t} [1 - G_0(1 - \alpha^t R)]^{M-t-1} \sum_{s=0}^t \binom{t}{s} G_0^s \cdot (1 - R) [G_0(1 - \alpha^s R) - G_0(1 - R)]^{t-s}. \quad (3)$$

For a given degree distribution p_k , we can obtain the final size S of the giant component in a certain layer by solving equations (1) and (2) simultaneously.

When $\alpha \rightarrow 1$, the interdependence across network layers is weakest, and the system percolates in a second-order manner as in single-layer networks [52, 53]. When $\alpha \rightarrow 0$, the interdependence across network layers is the strongest, and the system percolates in a first-order manner [10]. Therefore, the manner of percolation transitions can be determined by the value of α , and the critical value α_c is defined as the switch point of the percolation transition from a second-order to a first-order. For the second-order percolation transition, the probability R tends to zero when p is close to the second-order percolation point p_c^{II} . We can use

the Taylor expansion of equation (1) for $R \equiv \epsilon \rightarrow 0$ and $p \rightarrow p_c^{\text{II}}$:

$$h(\epsilon) = h'(0)\epsilon + \frac{1}{2}h''(0)\epsilon^2 + O(\epsilon^3) = \epsilon. \quad (4)$$

Ignoring the high-order terms of ϵ , we have $h'(0) = 1$ when $p \rightarrow p_c^{\text{II}}$. We, thus, have the condition for the second-order percolation transitions

$$p_c^{\text{II}} \alpha^{2M-2} G_1'(1) = 1, \quad (5)$$

and the second-order percolation point

$$p_c^{\text{II}} = \frac{1}{\alpha^{2M-2} G_1'(1)}. \quad (6)$$

When $\alpha = 1$ or $M = 1$, the second-order percolation transition point $p_c^{\text{II}} = 1/G_1'(1)$, which is coincident with the result for the ordinary percolation in a single-layer network [53]. In addition, we can also find the second-order percolation point p_c^{II} increases with the increase of M , which means the more network layers a system has, the more fragile it becomes.

At the first-order phase transition point p_c^{I} , the probability R jumps from R_c to zero or a nontrivial value, and the curve of $y = h(R) - R$ is tangent with the straight line $y = 0$:

$$\left. \frac{dh(R)}{dR} \right|_{R=R_c, p=p_c^{\text{I}}} = 1. \quad (7)$$

In this paper, we resort to the numerical method to solve equations (1) and (7) for the first-order percolation transition point p_c^{I} .

When $\alpha = \alpha_c$, the conditions for the first- and second-order percolation transitions are satisfied simultaneously, i.e., $p_c^{\text{I}} = p_c^{\text{II}}$ for $R_c \rightarrow 0$ at the percolation transition point. At this time, equation (4) reduces to

$$\frac{1}{2}h''(0)\epsilon^2 + O(\epsilon^3) = 0. \quad (8)$$

Therefore, we know that $h''(0) = 0$ when $p \rightarrow p_c$ and $\alpha = \alpha_c$. We can have

$$\alpha^3 G_1''(1) + 2(\alpha^2 - 1)(M-1)G_1'(1)G_0'(1) = 0. \quad (9)$$

By the solution of equation (9), we can obtain the switch point α_c of first-order and second-order percolation transitions. For multilayer random networks, the degree of nodes follows Poisson distribution, and equation (9) can be simplified as

$$\alpha_c^3 + (2M-2)\alpha_c^2 - (2M-2) = 0. \quad (10)$$

Therefore the value of α_c is only relevant to M . For scale-free networks, equation (9) can be written as

$$\frac{\alpha_c^3 \langle k(k-1)(k-2) \rangle}{\langle k \rangle \langle k(k-1) \rangle} + (2M-2)\alpha_c^2 - (2M-2) = 0, \quad (11)$$

where the brackets $\langle \cdot \rangle$ denote the average over the degree distribution. Therefore, α_c depends not only on M but also on the degree distribution p_k for multilayer scale-free networks.

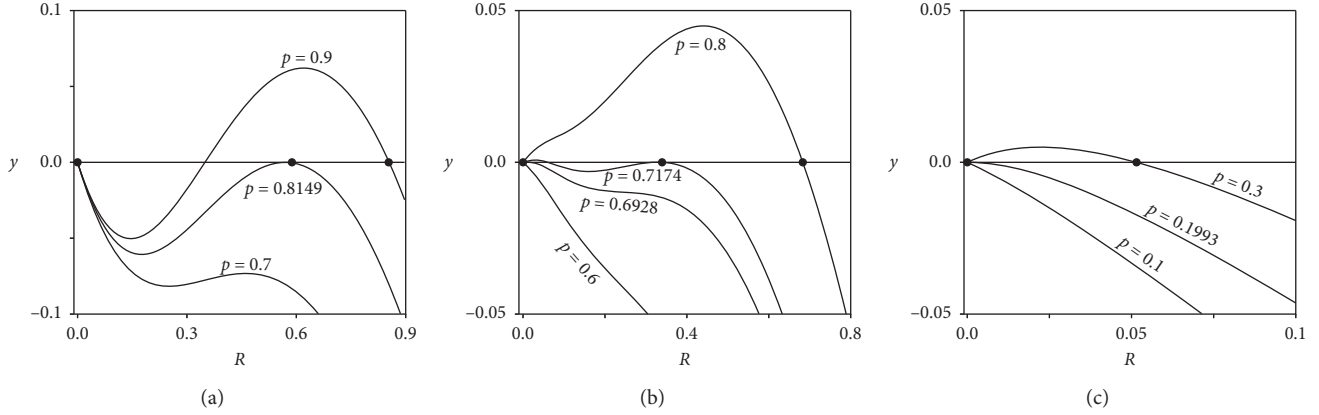


FIGURE 2: The graphical solutions of equation (1) for different values of p and α , as marked by the black dots. (a) The result for $\alpha = 0.5$, (b) the result for $\alpha = 0.65$, and (c) the result for $\alpha = 0.9$. For each panel, the degree distribution of networks follows a truncated power-law distribution $p_k \sim k^{-\gamma}$ ($k_{\min} \leq k \leq k_{\max}$), where $k_{\min} = 2$, $k_{\max} = 141$, and $\gamma = 2.3$.

Figure 2 shows the function curves $y = h(R) - R$ for different values of p , from which we can validate the existence of first- and second-order percolation transitions. Figure 2(a) shows the graphical solutions of equation (1) for $\alpha < \alpha_c$, from which we can find that the solution of R is given by the tangent point when $p = p_c^I$, indicating a discontinuous percolation transition. From Figure 2(c), we can find that the nontrivial solution of R emerges at the point $p = p_c^{II}$, at which the function curve $y = h(R) - R$ is tangent with the R axis at $R = 0$, indicating a continuous percolation transition. Interestingly, we also found that the system undergoes double phase transitions for some moderate values of α if the degree distribution p_k of the systems is scale-free, as shown in Figure 2(b). In this case, the system first percolates in a second-order manner and then experiences a first-order phase transition with increased p , and conditions (5) and (7) should be satisfied at the phase transition points p_c^{II} and p_c^I successively. If condition (5) cannot be satisfied, the double phase transition reduces to a single first-order percolation transition, and if condition (7) cannot be satisfied, the double phase transition reduces to a single second-order percolation transition. Using these conditions, we can locate the boundary between double phase transitions and single first-order phase transitions and the boundary between double phase transitions and single second-order percolation transitions.

4. Results

4.1. Synthetic Network. In this paper, we take two special multilayer networks with $M = 3$ and $M = 4$ layers as examples to illustrate the characteristics of percolation dynamics. Figures 3(a) and 3(b) show the size S of the giant component as functions of p for different values of α in three-layer random networks and four-layer random networks with $\langle k \rangle = 4$, respectively. For both three-layer and four-layer random networks, we find that the system can percolate in a discontinuous manner for $\alpha = 0.8$ or in a continuous manner for a larger value of $\alpha = 0.95$. In addition, the percolation transition point of three-layer

networks is less than that of four-layer networks, which means that three-layer networks are always more robust than four-layer networks. Simultaneously, we find that the critical point α_c separating the types of percolation transitions depends on the number of layers in the system. Similar results can also be found for three-layer random networks and four-layer random networks with $\langle k \rangle = 5$. In Figure 3, the theoretical predictions for the size S of the giant component as functions of p and percolation transition points p_c^I (p_c^{II}) are also provided, from which we can find that they agree with the simulation results very well.

The results for multilayer scale-free networks are also provided in Figure 4. For each network layer of the system, the degree of the nodes follows a truncated power-law distribution with an average $\langle k \rangle$, and the degree distribution is $p_k \sim k^{-\gamma}$ ($k_{\min} \leq k \leq k_{\max}$), where k_{\min} and k_{\max} are the minimum and maximum of the degree, respectively, and γ denotes the power law exponent. Similarly, we can also find that the system can percolate in a discontinuous manner for a small value of α or in a continuous manner for a large value of α , and the three-layer networks are more robust than four-layer networks for both $\langle k \rangle = 4$ and $\langle k \rangle = 5$. Interestingly, we can also find that the four-layer networks can undergo a double phase transition for $\alpha = 0.65$. Specifically, the system first percolates as a continuous phase transition and then undergoes a discontinuous phase transition with increasing p . With increasing α , the discontinuous phase transition disappears, and the system reduces to a single continuous phase transition. With decreasing α , the continuous phase transition disappears, and the system reduces to a single discontinuous phase transition.

Figures 5(a) and 5(b) show the percolation transition points p_c as functions of α for three- and four-layer random networks with different average degrees, respectively. For both three- and four-layer random networks, the manners of percolation transition are classified as discontinuous and continuous by a critical value of α_c , and the critical value of α_c only depends on the number of network layers M in a system, which coincides the theoretical result provided by

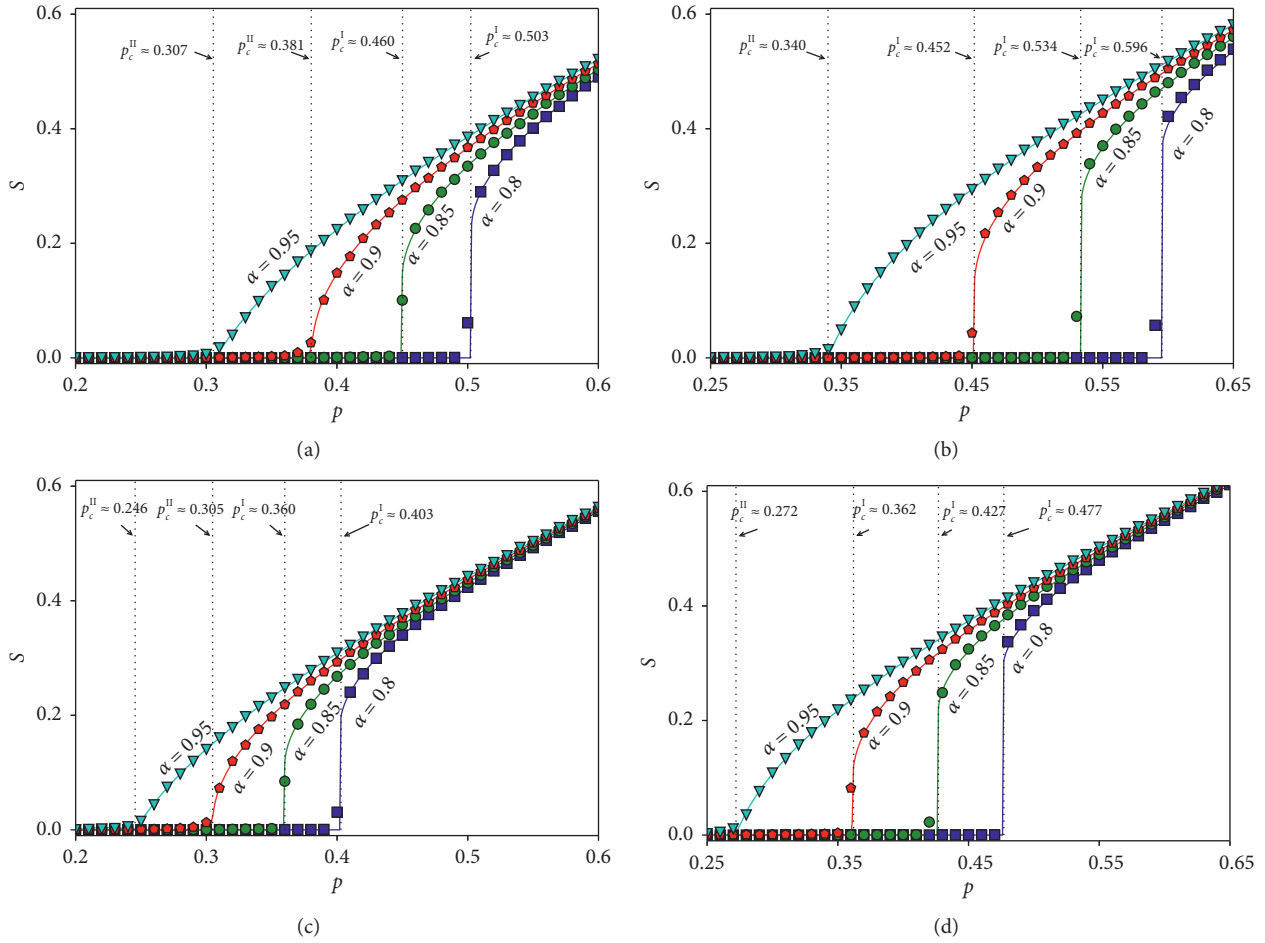


FIGURE 3: Simulation results for percolation transitions on three-layer and four-layer random networks. (a), (b) The results for three-layer and four-layer random networks with $\langle k \rangle = 4$, respectively. (c), (d) The results for three-layer random networks and four-layer random networks with $\langle k \rangle = 5$, respectively. The results were obtained by averaging over 100 independent realizations, and the network size was $N = 10^5$. The solid lines behind the symbols denote the theoretical predictions that were obtained by equations (1) and (2). The vertical dashed lines denote the first- and second-order percolation transition points predicted by equations (5) and (7), respectively.

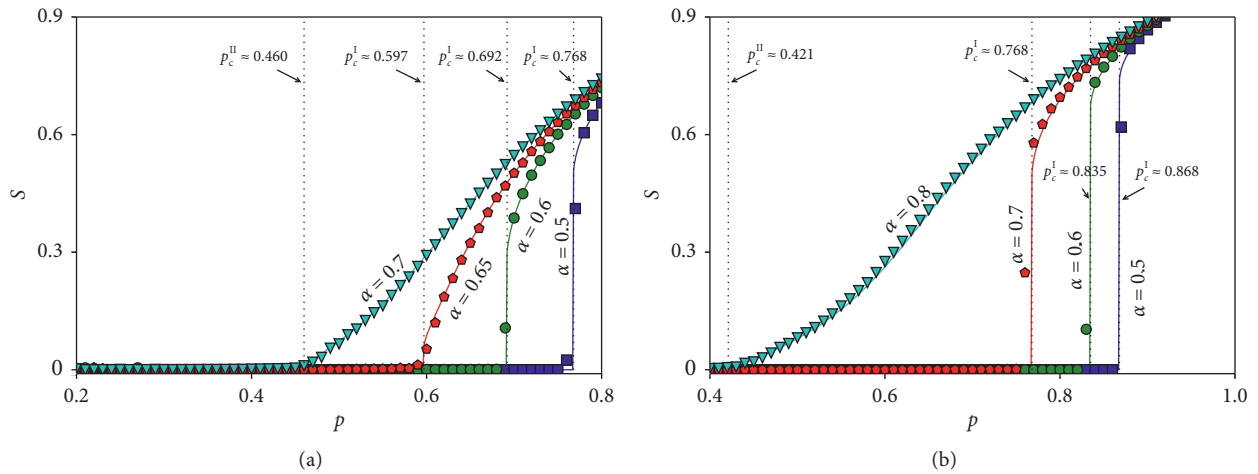


FIGURE 4: Continued.

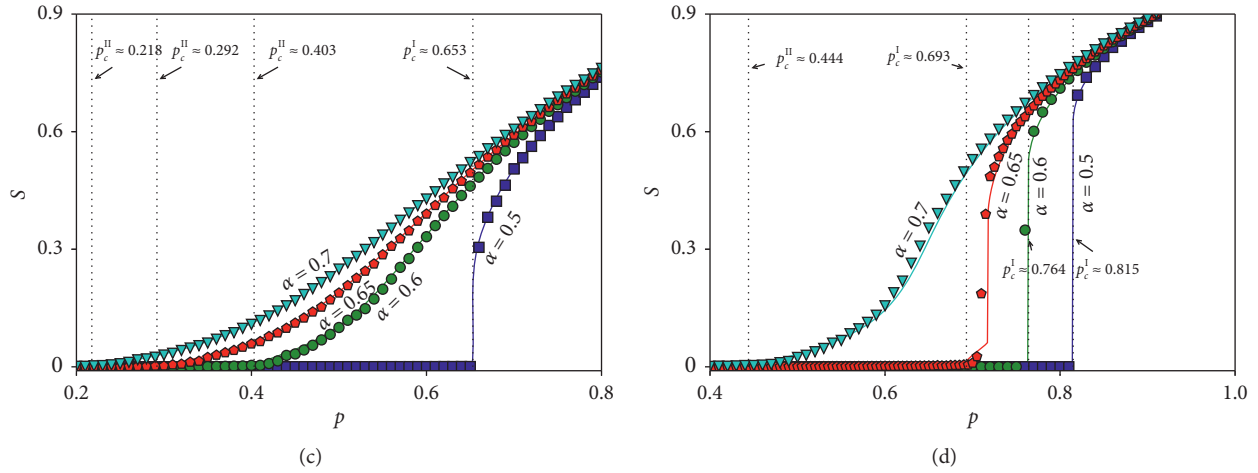


FIGURE 4: Simulation results for percolation transitions on three- and four-layer scale-free networks. (a), (b) The results for three- and four-layer scale-free networks with $\langle k \rangle = 4$, respectively. (c), (d) The results for three- and four-layer scale-free networks with $\langle k \rangle = 5$, respectively. When the average degree $\langle k \rangle = 4$, the parameter settings for the power-law distribution are $k_{\min} = 2$, $k_{\max} = 63$, and $\gamma = 2.5$. When the average degree $\langle k \rangle = 5$, the parameter settings are $k_{\min} = 2$, $k_{\max} = 141$, and $\gamma = 2.3$. The simulation results were obtained by averaging over 100 independent realizations, and the network size is $N = 10^5$. The solid lines behind the symbols denote the theoretical predictions that were obtained by equations (1) and (2). The vertical dashed lines denote the first- and second-order percolation transition points predicted by equations (5) and (7), respectively.

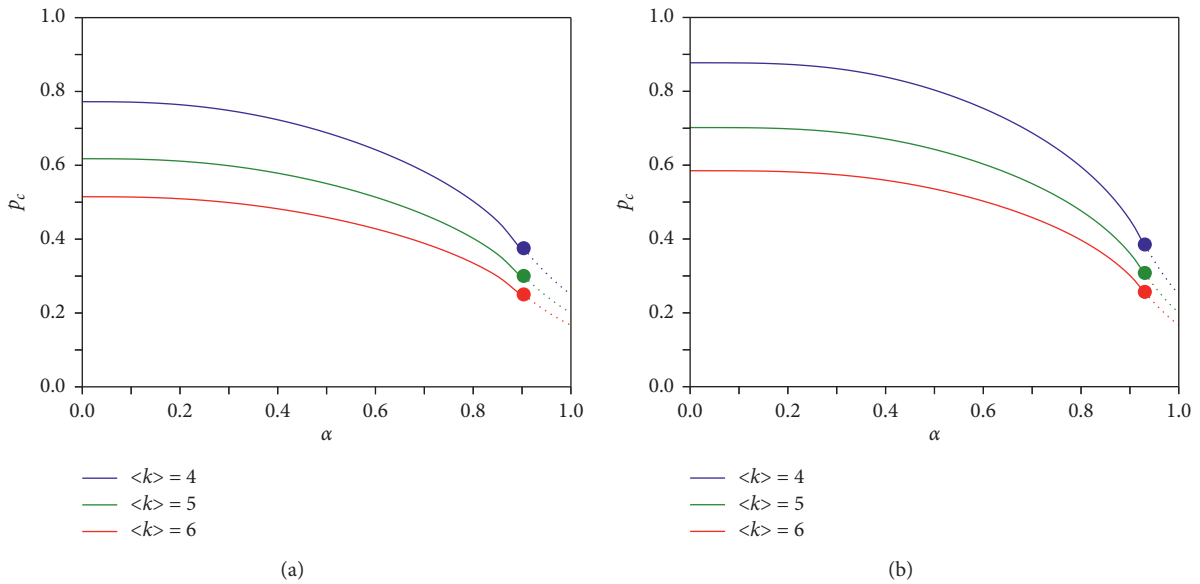


FIGURE 5: Continued.

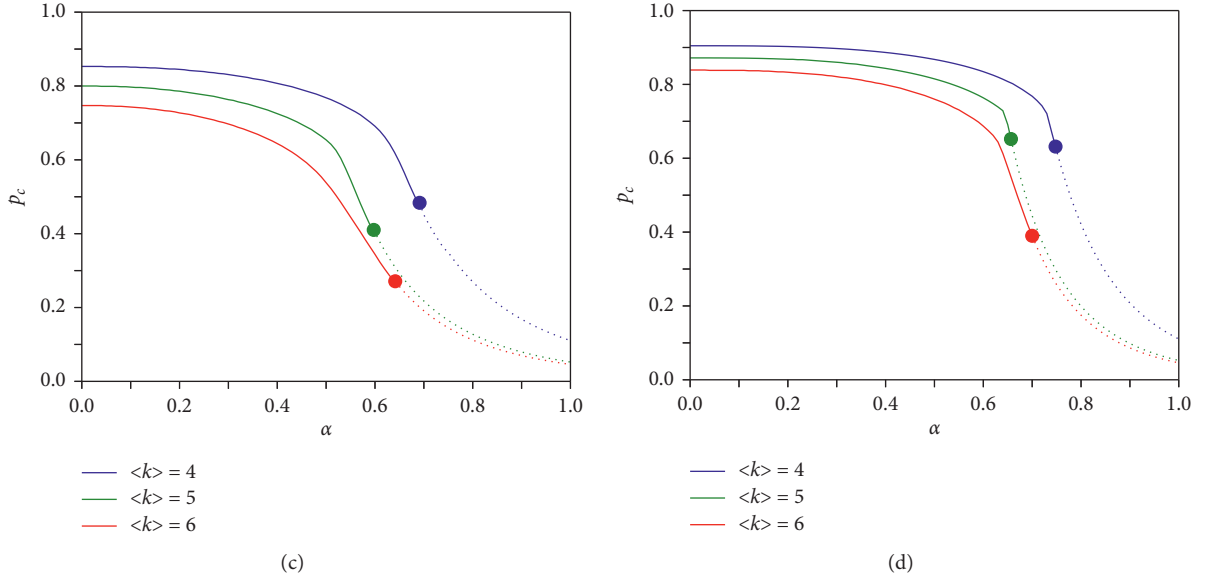


FIGURE 5: (Color online) (a) The percolation transition point p_c ((p_c^I) or (p_c^{II})) versus α for three-layer random networks, where the average degree $\langle k \rangle$ is 4, 5, and 6 from top to bottom, respectively. (b) Corresponding results for four-layer random networks. (c) The corresponding results for three-layer scale-free networks of average degree $\langle k \rangle$ 4, 5, and 6 (corresponding to a power-law exponent of degree distribution -2.6 , -2.3 , and -2.1 from top to bottom, respectively) with minimum degree 2. (d) Corresponding results for four-layer scale-free networks.

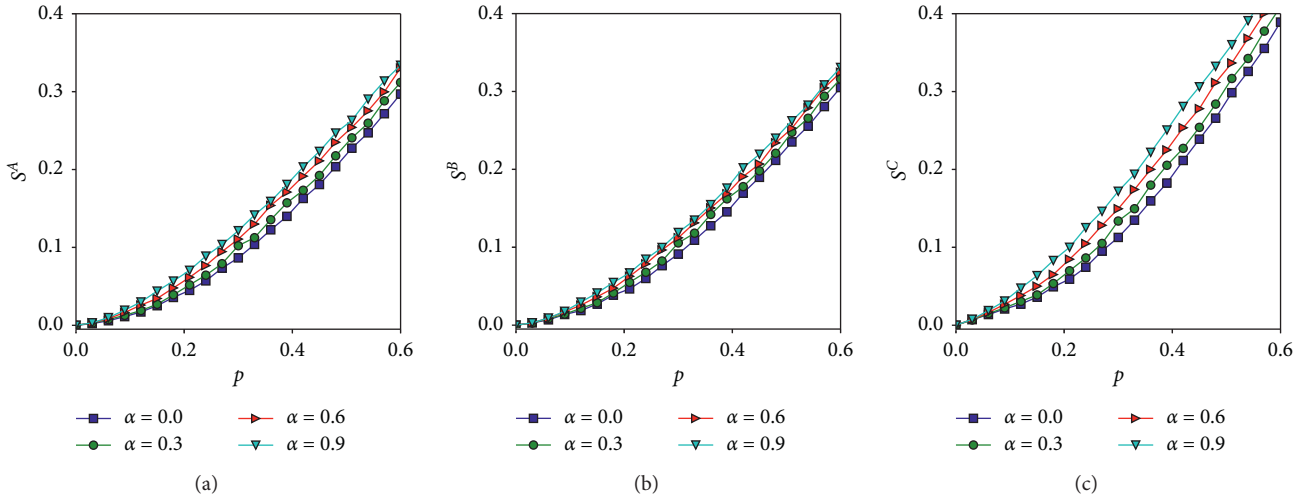


FIGURE 6: Percolation in multilayer empirical networks. The system consists of the three layers of networks A, B, and C which represent three major carriers: American Airlines (AA), Delta Air Lines (DL), and United Airlines (UA), respectively. (a–c) The sizes of the giant components of the network layers A, B, and C as functions of p for different values of α , respectively. The data points are the result of averaging over 1000 statistical realizations. (a) AA. (b) DL. (c) UA.

equation (10). Figures 5(c) and 5(d) show the percolation transition points p_c as functions of α for three- and four-layer scale-free networks with different average degrees, respectively, from which we can also find that the manners of percolation transition are classified as discontinuous and continuous by a critical value of α_c ; however, the specific value of α_c depends on the parameter settings of the degree distributions. These results imply that the robustness of a multilayer network increases with the increase of the average

degree of network layers and decreases with the increase of the number M of network layers. For multilayer random networks, the collapse manner is irrelevant to the average degree of the networks, and abrupt breakdown cannot be avoided by the increase of the average degree. For multilayer scale-free networks, the collapse manner is relevant to the number M of network layers and the parameters of degree distribution, i.g., minimum degree, maximum degree, and power law exponent.

4.2. Empirical Networks. To address the percolation process in empirical multilayer networks, we consider a three-layer system constituting the three major carriers in the United States: Delta Air Lines (DL), American Airlines (AA), and United Airlines (UA). In each layer of a network, nodes represent airports, and links between two airports are connected in the layers if there is at least one flight operated by a given carrier. We construct the multilayer system using the dataset from OpenFlights (<https://openflights.org/data.html>). For civil flights of the three major carriers, there are in total $N = 310$ nodes (functioning airports). Some of the nodes do not appear as connected in all the layers, leading to a difference in the relative sizes of the giant components. Figures 6(a)–6(c) show the sizes S of the giant component as functions of p for AA, DL, and UA, respectively. We can find that a large value of α always leads to a larger size S of the giant component for three layers, which means that the robustness of the system can be improved greatly by restricting the interdependence across network layers with increasing α .

5. Conclusions and Discussion

The interdependence of real multilayer networks is generally weak in layer-to-layer interactions, where the failure of one node usually does not result in failures of interdependent nodes across all network layers. In this paper, we have examined the percolation process and the robustness of a multilayer network when the interdependence of nodes across networks is weak. We reveal that the avalanche process of the whole system can be essentially decomposed into two microscopic cascading dynamics in terms of the propagation direction of failures: depth penetration and scope extension. Specifically, the former describes the propagation of failures across network layers and thus is regarded as “cross-layer cascading,” while the latter describes the propagation of failures inside a network layer and, thus, is regarded as “inner-layer cascading.” With the coaction of the two cascading dynamics, a multilayer network can disintegrate via first- or second-order percolation transitions in the case of initial failures, where the interdependence across network layers plays important roles in determining the percolation behaviors of the system. When the interdependence of network layers is weak, the failures of nodes can neither penetrate into deep network layers nor cause great destructiveness to their interdependent replicas, which inhibits the spread of failure and makes the system percolate via a second-order percolation transition. When the interdependence of network layers is strong, the failures of nodes can penetrate into deep network layers in a cascading manner and spread with a broad scope through various network layers, which, thus, makes the system collapse abruptly. These results prove that the process of “cross-layer cascading” dominates over the process of “inner-layer cascading” and plays a crucial role in determining the robustness of a multilayer system.

The present work essentially reveals the complexity of cascading failures, and previous works ignoring the weak interdependence may underestimate the complexity.

Specifically, the cascading dynamics that occur across network layers cannot be produced in a strong layer-to-layer interdependence of multilayer networks. Therefore, our method insights for the intervention of cascading failures in a multilayer network and evidences the idea that imposing restrictions on “cross-layer cascading” can restrain the spread of failures more effectively. Our work not only offers a new understanding of the cascading failure dynamics of multilayer networks but also implies that the strength of interdependence can be used for enhancing the robustness of multilayer structured infrastructure systems. That is to say, the penetration depth of cascading failures can be significantly reduced and thus the scale of cascading failures is also decreased by imposing restrictions on the strength of interdependence if the strength of interdependence is adjustable. For some other systems with fixed or nonadjustable interdependence across network layers, our finding is also meaningful for the robustness assessment. In this case, we can evaluate the robustness of such system by the parameters such as average degrees, number of network layers, strength of interdependence, and so on.

It has been found that overlapping links [14, 15] of real multilayer networks are able to relieve the destruction of cascading failures and improve robustness of the systems. Therefore, it is meaningful to study the percolation on multilayer networks with overlapping links in terms of tunable interdependency strength across networks in future works. Specifically, for a system with M network layer, any two networks of it may have overlapping links and the degree of overlap may change with the varying of combination of network layers. We believe that the study of this issue will yield richer results.

Data Availability

The data of empirical networks used in this paper were downloaded from the website OpenFlights (<https://openflights.org/data.html>), which contains basic data for multiple airports and flights worldwide, and we extract the data of civil flights of United States to built a three-layer network. The data of simulation used to support the findings of this study are available from the corresponding author upon request.

Conflicts of Interest

The authors declare that they have no conflicts of interest.

Acknowledgments

This work was supported by the National Natural Science Foundation of China under grant no. 61773148.

References

- [1] D. F. Klosik, A. Grimbs, S. Bornholdt, and M.-T. Htt, “The interdependent network of gene regulation and metabolism is robust where it needs to be,” *Nature Communications*, vol. 8, no. 1, p. 534, 2017.

- [2] M. Ouyang, "Review on modeling and simulation of interdependent critical infrastructure systems," *Reliability Engineering & System Safety*, vol. 121, pp. 43–60, 2014.
- [3] S. M. Rinaldi, J. P. Peerenboom, and T. K. Kelly, "Identifying, understanding, and analyzing critical infrastructure interdependencies," *IEEE Control Systems*, vol. 21, no. 6, pp. 11–25, 2001.
- [4] F. Radicchi, "Percolation in real interdependent networks," *Nature Physics*, vol. 11, no. 7, pp. 597–602, 2015.
- [5] J. Wu, J. Zhong, Z. Chen, and B. Chen, "Optimal coupling patterns in interconnected communication networks," *IEEE Transactions on Circuits and Systems II: Express Briefs*, vol. 65, no. 8, pp. 1109–1113, 2018.
- [6] S. V. Buldyrev, R. Parshani, G. Paul, H. E. Stanley, and S. Havlin, "Catastrophic cascade of failures in interdependent networks," *Nature*, vol. 464, no. 7291, pp. 1025–1028, 2010.
- [7] M. Kivela, A. Arenas, M. Barthelemy, J. P. Gleeson, Y. Moreno, and M. A. Porter, "Multilayer networks," *Journal of Complex Networks*, vol. 2, no. 3, pp. 203–271, 2014.
- [8] J. Gao, S. V. Buldyrev, S. Havlin, and H. E. Stanley, "Robustness of a network of networks," *Physical Review Letters*, vol. 107, no. 19, Article ID 195701, 2011.
- [9] J. Gao, S. V. Buldyrev, H. E. Stanley, and S. Havlin, "Networks formed from interdependent networks," *Nature Physics*, vol. 8, no. 1, pp. 40–48, 2012.
- [10] G. J. Baxter, S. N. Dorogovtsev, A. V. Goltsev, and J. F. F. Mendes, "Avalanche collapse of interdependent networks," *Physical Review Letters*, vol. 109, no. 24, Article ID 248701, 2012.
- [11] H. Kesten, *Percolation Theory for Mathematicians*, Birkhäuser Press, Boston, MA, USA, 1982.
- [12] D. Stauffer and A. Aharony, *Introduction to Percolation Theory*, Taylor & Francis Press, London, UK, 1992.
- [13] S.-W. Son, G. Bizhani, C. Christensen, P. Grassberger, and M. Paczuski, "Percolation theory on interdependent networks based on epidemic spreading," *EPL (Europhysics Letters)*, vol. 97, no. 1, p. 16006, 2012.
- [14] D. Cellai, E. López, J. Zhou, J. P. Gleeson, and G. Bianconi, "Percolation in multiplex networks with overlap," *Physical Review Letters*, vol. 88, Article ID 052811, 2013.
- [15] Y. Hu, D. Zhou, R. Zhang, Z. Han, C. Rozenblat, and S. Havlin, "Percolation of interdependent networks with intersimilarity," *Physical Review E*, vol. 88, no. 5, Article ID 052805, 2013.
- [16] K.-K. Kleineberg, M. Boguñá, M. Ángeles Serrano, and F. Papadopoulos, "Hidden geometric correlations in real multiplex networks," *Nature Physics*, vol. 12, no. 11, pp. 1076–1081, 2016.
- [17] K.-K. Kleineberg, L. Buzna, F. Papadopoulos, M. Boguñá, and M. A. Serrano, "Geometric correlations mitigate the extreme vulnerability of multiplex networks against targeted attacks," *Physical Review Letters*, vol. 118, no. 21, Article ID 218301, 2017.
- [18] A. Faqeeh, S. Osat, and F. Radicchi, "Characterizing the analogy between hyperbolic embedding and community structure of complex networks," *Physical Review Letters*, vol. 121, no. 9, Article ID 098301, 2018.
- [19] B. Min, S. D. Yi, K.-M. Lee, and K.-I. Goh, "Network robustness of multiplex networks with interlayer degree correlations," *Physical Review E*, vol. 89, no. 4, Article ID 042811, 2014.
- [20] R. Parshani, C. Rozenblat, D. Ietri, C. Ducruet, and S. Havlin, "Inter-similarity between coupled networks," *EPL (Europhysics Letters)*, vol. 92, no. 6, p. 68002, 2011.
- [21] L. D. Ducruet, P. A. Macri, H. E. Stanley, and L. A. Braunstein, "Triple point in correlated interdependent networks," *Physical Review E*, vol. 88, no. 5, Article ID 050803, 2013.
- [22] R.-R. Liu, C.-X. Jia, and Y.-C. Lai, "Asymmetry in interdependence makes a multilayer system more robust against cascading failures," *Physical Review E*, vol. 100, no. 5, Article ID 052306, 2019.
- [23] R. Parshani, S. V. Buldyrev, and S. Havlin, "Interdependent networks: reducing the coupling strength leads to a change from a first to second order percolation transition," *Physical Review Letters*, vol. 105, no. 4, Article ID 048701, 2010.
- [24] C. M. Schneider, N. Yazdani, N. A. M. Arajo, S. Havlin, and H. J. Herrmann, "Towards designing robust coupled networks," *Scientific Reports*, vol. 3, no. 1, p. 1969, 2013.
- [25] L. D. Valdez, P. A. Macri, and L. A. Braunstein, "A triple point induced by targeted autonomization on interdependent scale-free networks," *Journal of Physics A: Mathematical and Theoretical*, vol. 47, no. 5, Article ID 055002, 2014.
- [26] Y. Berezin, A. Bashan, M. M. Danziger, D. Li, and S. Havlin, "Localized attacks on spatially embedded networks with dependencies," *Scientific Reports*, vol. 5, no. 1, p. 8934, 2015.
- [27] A. Bashan, Y. Berezin, S. V. Buldyrev, and S. Havlin, "The extreme vulnerability of interdependent spatially embedded networks," *Nature Physics*, vol. 9, no. 10, pp. 667–672, 2013.
- [28] M. M. Danziger, A. Bashan, Y. Berezin, and S. Havlin, "Percolation and cascade dynamics of spatial networks with partial dependency," *Journal of Complex Networks*, vol. 2, no. 4, pp. 460–474, 2014.
- [29] L. M. Shekhtman, Y. Berezin, M. M. Danziger, and S. Havlin, "Robustness of a network formed of spatially embedded networks," *Physical Review E*, vol. 90, no. 1, Article ID 012809, 2014.
- [30] K. Gong, J.-J. Wu, Y. Liu, Q. Li, R.-R. Liu, and M. Tang, "The effective healing strategy against localized attacks on interdependent spatially embedded networks," *Complexity*, vol. 2019, Article ID 7912857, 10 pages, 2019.
- [31] S. Shao, X. Huang, H. E. Stanley, and S. Havlin, "Robustness of a partially interdependent network formed of clustered networks," *Physical Review E*, vol. 89, Article ID 032812, 2014.
- [32] X. Huang, S. Shao, H. Wang, S. V. Buldyrev, H. Eugene Stanley, and S. Havlin, "The robustness of interdependent clustered networks," *EPL (Europhysics Letters)*, vol. 101, no. 1, p. 18002, 2013.
- [33] T. Emmerich, A. Bunde, and S. Havlin, "Structural and functional properties of spatially embedded scale-free networks," *Physical Review E*, vol. 89, no. 6, Article ID 062806, 2014.
- [34] X. Yuan, S. Shao, H. E. Stanley, and S. Havlin, "How breadth of degree distribution influences network robustness: comparing localized and random attacks," *Physical Review E*, vol. 92, no. 3, Article ID 032122, 2015.
- [35] X. Yuan, Y. Hu, H. E. Stanley, and S. Havlin, "Eradicating catastrophic collapse in interdependent networks via reinforced nodes," *Proceedings of the National Academy of Sciences*, vol. 114, no. 13, pp. 3311–3315, 2017.
- [36] L. B. Shaw and I. B. Schwartz, "Enhanced vaccine control of epidemics in adaptive networks," *Physical Review E*, vol. 81, no. 4, Article ID 046120, 2010.
- [37] D. Zhao, L. Wang, S. Li, Z. Wang, L. Wang, and B. Gao, "Immunicization of epidemics in multiplex networks," *PLoS One*, vol. 9, no. 11, Article ID e112018, 2014.
- [38] J. C. Nacher and T. Akutsu, "Structurally robust control of complex networks," *Physical Review E*, vol. 91, no. 1, Article ID 012826, 2015.

- [39] Z. Wang, D. Zhou, and Y. Hu, "Group percolation in interdependent networks," *Physical Review E*, vol. 97, no. 3, Article ID 032306, 2018.
- [40] R.-R. Liu, C.-X. Jia, and Y.-C. Lai, "Remote control of cascading dynamics on complex multilayer networks," *New Journal of Physics*, vol. 21, Article ID 045002, 2019.
- [41] A. Bashan and S. Havlin, "The combined effect of connectivity and dependency links on percolation of networks," *Journal of Statistical Physics*, vol. 145, no. 3, pp. 686–695, 2011.
- [42] A. Bashan, R. Parshani, and S. Havlin, "Percolation in networks composed of connectivity and dependency links," *Physical Review E*, vol. 83, no. 5, Article ID 051127, 2011.
- [43] M. Li, R.-R. Liu, C.-X. Jia, and B.-H. Wang, "Critical effects of overlapping of connectivity and dependence links on percolation of networks," *New Journal of Physics*, vol. 15, no. 9, Article ID 093013, 2013.
- [44] N. Azimi-Tafreshi, J. Gómez-Gardeñes, and S. N. Dorogovtsev, "k-core percolation on multiplex networks," *Physical Review E*, vol. 90, no. 3, Article ID 032816, 2014.
- [45] G. J. Baxter, S. N. Dorogovtsev, J. F. F. Mendes, and D. Cellai, "Weak percolation on multiplex networks," *Physical Review E*, vol. 89, no. 4, Article ID 042801, 2014.
- [46] F. Radicchi and G. Bianconi, "Redundant interdependencies boost the robustness of multiplex networks," *Physical Review X*, vol. 7, no. 1, Article ID 011013, 2017.
- [47] R.-R. Liu, D. A. Eisenberg, T. P. Seager, and Y.-C. Lai, "The "weak" interdependence of infrastructure systems produces mixed percolation transitions in multilayer networks," *Scientific Reports*, vol. 8, no. 1, p. 2111, 2018.
- [48] R.-R. Liu, M. Li, and C.-X. Jia, "Cascading failures in coupled networks: the critical role of node-coupling strength across networks," *Scientific Reports*, vol. 6, p. 35352, 2016.
- [49] M. Molloy and B. Reed, "A critical point for random graphs with a given degree sequence," *Random Structures & Algorithms*, vol. 6, no. 2-3, pp. 161–180, 1995.
- [50] S.-W. Son, G. Bizhani, C. Christensen, P. Grassberger, and M. Paczuski, "Percolation theory on interdependent networks based on epidemic spreading," *EPL*, vol. 97, p. 16006, 2011.
- [51] L. Feng, C. P. Monterola, and Y. Hu, "The simplified self-consistent probabilities method for percolation and its application to interdependent networks," *New Journal of Physics*, vol. 17, Article ID 063025, 2015.
- [52] R. Cohen, K. Erez, D. ben-Avraham, and S. Havlin, "Resilience of the internet to random breakdowns," *Physical Review Letters*, vol. 85, no. 21, pp. 4626–4628, 2000.
- [53] D. S. Callaway, M. E. J. Newman, S. H. Strogatz, and D. J. Watts, "Network robustness and fragility: percolation on random graphs," *Physical Review Letters*, vol. 85, no. 25, pp. 5468–5471, 2000.

Research Article

Set-Based Differential Evolution Algorithm Based on Guided Local Exploration for Automated Process Discovery

Si-Yuan Jing ^{1,2}

¹School of Computer Science, Leshan Normal University, Leshan 614000, China

²Key Lab of Internet Natural Language Processing of Sichuan Provincial Education Department, Leshan Normal University, Leshan 614000, China

Correspondence should be addressed to Si-Yuan Jing; siyuan-jing@hotmail.com

Received 15 October 2019; Revised 25 December 2019; Accepted 3 February 2020; Published 12 March 2020

Guest Editor: Tomas Veloz

Copyright © 2020 Si-Yuan Jing. This is an open access article distributed under the Creative Commons Attribution License, which permits unrestricted use, distribution, and reproduction in any medium, provided the original work is properly cited.

Evolutionary algorithm is an effective way to solve process discovery problem which aims to mine process models from event logs which are consistent with the real business processes. However, current evolutionary algorithms, such as GeneticMiner, ETM, and ProDiGen, converge slowly and in difficulty because all of them employ genetic crossover and mutation which have strong randomness. This paper proposes a hybrid evolutionary algorithm for automated process discovery, which consists of a set-based differential evolution algorithm and guided local exploration. There are three major innovations in this work. First of all, a hybrid evolutionary strategy is proposed, in which a differential evolution algorithm is employed to search the solution space and rapidly approximate the optimal solution firstly, and then a specific local exploration method joins to help the algorithm skip out the local optimum. Secondly, two novel set-based differential evolution operators are proposed, which can efficiently perform differential mutation and crossover on the causal matrix. Thirdly, a fine-grained evaluation technique is designed to assign score to each node in a process model, which is employed to guide the local exploration and improve the efficiency of the algorithm. Experiments were performed on 68 different event logs, including 22 artificial event logs, 44 noisy event logs, and two real event logs. Moreover, the proposed algorithm was compared with three popular algorithms of process discovery. Experimental results show that the proposed algorithm can achieve good performance and its converge speed is fast.

1. Introduction

Process-based information system (PIS), including workflow management system (WfMS), customer relationship management (CRM), enterprise resource planning (ERP), has become the fundamental infrastructure of modern enterprises. PIS can greatly improve the operational efficiency of enterprises. Besides that, it will record the information of business processes, such as name of activities, time of activities happening, life cycle of activities, to form event logs. The XES Standard, published by IEEE in 2016, provides a unified and extensible language to standardize the content and format of event logs. Process mining technique can be used to discover a process model from a XES event log. It is hoped that the mined process model is as consistent as possible with the real business process. The obtained process model can be used to improve business processes of

enterprises, increase production efficiency, and optimize products. For example, ASML employs process discovery technique to optimize the wafer scanner during the production of lithography machines. The ERP system of SAP uses the process discovery technique to assist users design business process, analyze the bottleneck of business, and plan resource. Philips collects the event logs from their medical devices around the world to analyze customers' habits. By this way, they can optimize their medical products and shorten the time of product development.

Generally, there are three major tasks in process mining, including process discovery, conformance checking, and process enhancement [1]. Process discovery aims to obtain a process model, which is as consistent as possible with the real business process. Most studies are focused on mining binary relations of any two activities in event logs from the perspective of control flow. Beyond that, it can also discover

the knowledge contained in the event log from other perspectives, such as organization, time, resource, and so on. Conformance checking is used to measure the deviation of a mined process from a real business process by replaying the event log on the mined process model. This technique can be used for the diagnosis of the process model as well as the analysis of business bottleneck. Process enhancement focuses on changing or extending a prior process model. For example, by using time-stamp in an event log, the model can be enhanced to analyze bottleneck, estimate remaining time, and discover hierarchical process model. In this paper, I only focus on the process discovery technique from the perspective of control flow.

The α -algorithm, proposed by van der Aalst et al., is usually regarded as a milestone in the field of process mining [2]. It models the workflow by Petri net and can effectively find the causal relation, parallel relation, and choice relation between any two activities from the event log. After that, some variants of the α -algorithm were proposed, just like $\alpha+$ algorithm [3] and $\alpha++$ algorithm [4]. However, there are many shortcomings in the α -series algorithms, such as ability to resist noise, alignment-based fitness, and precision. To address these problems, some more efficient algorithms were proposed, such as ILP Miner [5] and inductive miner [6, 7]. The former was proposed recently by van Zelst et al., which is based on integer linear programming. The latter was proposed by Leemans et al. Both of them show good performance when dealt with small event logs.

Evolutionary algorithm is an effective way to solve the problem of process mining. de Medeiros et al. [8] firstly employed the genetic algorithm (GA) in process mining, named as GeneticMiner. By defining good fitness function as well as genetic operators (i.e., crossover and mutation), the GeneticMiner can find a process model, which is consistent with the real process. Cheng et al. [9, 10] indicated that the GeneticMiner cannot effectively discover parallel structures from event logs; therefore, they proposed a hybrid technique, which is based on integration of GeneticMiner, particle swarm optimization, and differential evolution to improve the result of process mining. Vázquez-Barreiros et al. [11] proposed another algorithm, named ProDiGen, which improves the GeneticMiner by introducing hierarchical fitness function to find complete, precise, and minimal structure process models. Buijs et al. [12–14] employed evolutionary tree to present process models and proposed an alignment-based technique to guide the mutation in GA. However, it is unbearable to embed alignment-based local search in mutation operation because it is too time-consuming. In general, the advantage of the genetic algorithm includes good antinoise, and it can deal with a major part of key problems in process mining by a unified framework, such as invisible tasks, non-free-choice structure, and tasks with duplicated name. However, the convergence speed of current GA-based algorithms is too slow because all of them adopt random search.

In this paper, a hybrid evolutionary algorithm for process mining is proposed, named DEMiner. The innovation of our work includes three parts:

- (1) A hybrid evolutionary strategy is proposed in this work. In our method, DEMiner firstly approximates the optimal process model by a set-based DE algorithm; when the prematurity is detected, a guided local exploration method will join in the evolution process to help the algorithm skip out the local optimum.
- (2) Two set-based DE operators, i.e., a set-based mutation operator and a set-based crossover operator, are designed for differential evolution of causal matrix.
- (3) A fine-grained evaluation method is proposed to guide the local exploration by assigning scores to all the nodes in the candidate process models. This method can not only help the population avoid prematurity but also improve the efficiency of the DEMiner.

The rest of this paper is organized as follows. Section 2 introduces some basic knowledge of process mining, such as Petri net and causal matrix, as well as the DE algorithm. Section 3 explains the proposed algorithm in detail. The experiments as well as the analysis of experimental results are given in Section 4. Finally, Section 5 gives conclusions.

2. Preliminaries

2.1. Process Mining. In the problem of process mining, a process model is generally modeled as a place/transition net (abbreviated as P/T Net), which is a variant of classic Petri net. The definition of P/T is given below.

Definition 1 (P/T Net) [2]. A P/T Net is a tuple $N = (P, T, F)$, where P is a finite set of places, T is a finite set of transitions, $P \cap T = \emptyset$, and $F = (P \times T) \cup (T \times P)$ is a finite set of directed arcs.

Let $N = (P, T, F)$ be a P/T Net. Elements of $P \cup T$ are called nodes. A node x is an input node of another node y if $\langle x, y \rangle \in F$. Similarly, a node x is an output node of another node y if $\langle y, x \rangle \in F$. Furthermore, a symbol $\bullet x$ denotes all the input nodes of node x ; that is, $\bullet x = \{y \mid \langle y, x \rangle \in F \wedge y \in P \cup T\}$. Similarly, $x \bullet$ denotes all the output nodes of x . Based on the P/T Net, a formal definition of workflow net (abbreviated as Wf-Net) is given.

Definition 2 (Wf-Net) [2]. Let $N = (P, T, F)$ be a P/T Net, and t is a fresh identifier not in $P \cup T$. N is a Wf-Net if

- (1) P contains an input place i such that $\bullet i = \emptyset$
- (2) P contains an output place o such that $o \bullet = \emptyset$
- (3) $\tilde{N} = (P, T \cup t, F \cup \{\langle t, i \rangle, \langle o, t \rangle\})$ is strongly connected

Figure 1 shows a process model, which is represented by a Wf-Net. The circles denote places, and the squares denote transitions. The transitions in Wf-Net represent the activities (also called tasks) in the real business process. The black dot in the initial place denotes a token. A transition is enabled to be fired if all of the input places contain tokens. The word “fire” means that an activity is ready to be executed. If a

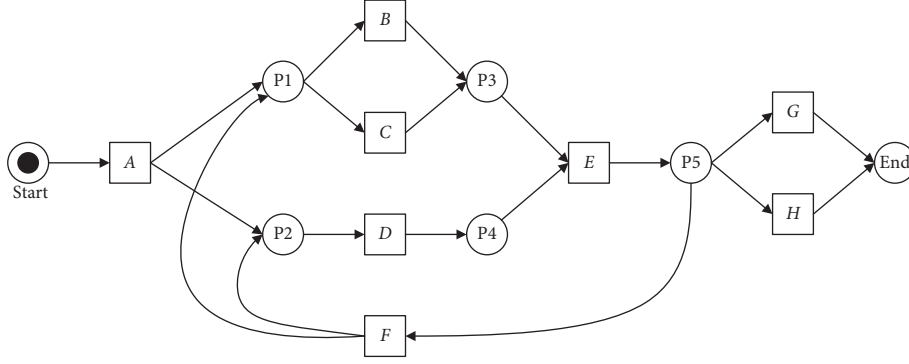


FIGURE 1: An illustrating example of process model.

transition fires, tokens in its input places are removed; meanwhile, tokens are put in its output places. For example, if the transition “A” is fired, the token in place “start” would be removed and the place “P1” and “P2” will get a token, respectively. After that, three transitions “B,” “C,” and “D” would be enabled. Note that “P1” just has one token; in other words, although two transitions (a.k.a. “B” and “C”) are enabled, only one can be fired. Thus, the possible sequences between “A” and “E” include $\{B, D\}$, $\{C, D\}$, $\{D, B\}$, and $\{D, C\}$.

Given a sound Wf-Net $N = (P, T, F)$, we say $\delta \in T^*$ is an event trace and $W \in P(T^*)$ is an event log, which consists of traces. Take the above process model as an example, and it can induce lots of event traces, just like ABDEG, ACDEH, ADBEFCDG, and so on.

The first problem required to be solved in evolution-based process mining is coding of chromosome. Unfortunately, it is hard to directly employ Petri net for evolution. de Medeiros proposed the causal matrix to represent the process model, which has been applied to many evolutionary algorithms of process mining, such as ProDiGen and GeneticMiner. The definition of the causal matrix is given below.

Definition 3 (Causal Matrix) [8]. A causal matrix is a tuple $CM = (A, C, I, O)$, where

- (1) A is a finite set of activities
- (2) $C = A \times A$ is the causality relation
- (3) $I: A \rightarrow P(P(A))$ is the input condition function
- (4) $O: A \rightarrow P(P(A))$ is the output condition function

Since we usually need to compare the process model presented by the causal matrix with other models presented by Petri net, a method of mapping the P/T Net to the causal matrix is required. Definition 4 shows a method for converting a P/T Net to a causal matrix.

Definition 4 (Mapping of a P/T Net to a Causal Matrix) [8]. Let $N = (P, T, F)$ be a P/T Net. The mapping of N is a tuple $\Pi_{N \rightarrow CM} = (A, C, I, O)$, where

- (1) $A = T$
- (2) $C = \{(t_1, t_2) \in T \times T \mid t_1 \cdot \cap \cdot t_2 \neq \emptyset\}$

- (3) $I: T \rightarrow P(P(T))$ such that $\forall_{t \in T} I_{\Pi}(t) = \{p \mid p \in \cdot t\}$
- (4) $O: T \rightarrow P(P(T))$ such that $\forall_{t \in T} O_{\Pi}(t) = \{p \mid p \in t \cdot\}$

To explain the mapping process, we convert the process model in Figure 1 to a causal matrix, which is shown in Table 1. Take activity “E” as an example, and it has two input places “P3” and “P4.” Furthermore, the input transitions of “P3” are transitions “B” and “C,” and the input transition of “P4” is transition “D,” and thus, $I_{\Pi}(E) = \{\{B, C\}, \{D\}\}$. It should be noted that those activities in the same subset of $I_{\Pi}(t)$ have an OR-join relation, and those different subsets in $I_{\Pi}(t)$ have an AND-join relation. On the contrary, activities in the same subset of $O_{\Pi}(t)$ have an OR-split relation and those different subsets have an AND-split relation. Besides, $I_{\Pi}(t) = \{\}$ demonstrates that the input of the activity is empty and $O_{\Pi}(t) = \{\}$ demonstrates the output of the activity is empty.

2.2. Differential Evolution Algorithm. Differential evolution algorithm (DE), firstly proposed by Das et al. in 1995, is a stochastic method simulating biological evolution, in which the individuals adapted to the environment are preserved through repeated iterations [15]. Compared to other evolutionary algorithms, the DE algorithm has some advantages, such as better global searching ability, fast convergence speed, and strong robustness.

The major steps of DE include mutation, crossover, evaluation, and selection, which is similar with GA. DE starts with a population, which contains N randomly generated individuals (also known as chromosomes). The individual is represented by a vector $\vec{X}_{i,G} = [x_{1,i,G}, x_{2,i,G}, \dots, x_{D,i,G}]$, where i denotes the i -th individual, G denotes current generation, and D denotes the dimension of the vector. In the step of mutation, DE generates a *donor* vector $\vec{V}_{i,G} = [v_{1,i,G}, v_{2,i,G}, \dots, v_{D,i,G}]$ for the i -th individual (called *target* vector). It firstly chooses three distinct vectors $\vec{X}_{r_{1,i,G}}$, $\vec{X}_{r_{2,i,G}}$, and $\vec{X}_{r_{3,i,G}}$ from the population. The indices $r_{1,i}$, $r_{2,i}$, and $r_{3,i}$ are mutually exclusive integers randomly chosen from the range $[1, N]$. Then, the difference of any two of these three vectors (i.e., $\vec{X}_{r_{2,i,G}}$ and $\vec{X}_{r_{3,i,G}}$) is scaled by a scalar factor F , and then the scaled difference is added to the last vector

TABLE 1: Causal matrix of the process model.

| Activity | $I(\text{Activity})$ | $O(\text{Activity})$ |
|----------|----------------------|----------------------|
| A | {} | {{B, C}, {D}} |
| B | {{A, F}} | {{E}} |
| C | {{A, F}} | {{E}} |
| D | {{A, F}} | {{E}} |
| E | {{B, C}, {D}} | {{F, G, H}} |
| F | {{E}} | {{B, C}, {D}} |
| G | {{E}} | {} |
| H | {{E}} | {} |

$\vec{X}_{r_{1,i},G}$; it finally obtains the *donor* vector. Such process can be expressed by the following formula:

$$\vec{V}_{i,G} = \vec{X}_{r_{1,i},G} + F \cdot (\vec{X}_{r_{2,i},G} - \vec{X}_{r_{3,i},G}). \quad (1)$$

To enhance the potential diversity of the population, a crossover operation comes into play after generating the donor vector. The donor vector exchanges its components with the target vector $\vec{X}_{i,G}$ under this operation to form the trial vector $\vec{U}_{i,G} = [u_{1,i,G}, u_{2,i,G}, \dots, u_{D,i,G}]$. There are two popular ways for crossover in DE, which are exponential crossover (or two-point modulo) and binomial crossover (or uniform). This paper just introduces the latter, which is given in formula (2), where Cr is the crossover rate and j_{rand} is a random number. The condition $j = j_{\text{rand}}$ guarantees that at least one element of the donor vector will be selected. The obtained trial vector will be evaluated by a predefined fitness function. If the fitness of the trial vector is higher than the fitness of the target vector, the DE algorithm would replace the target vector by the trial vector; otherwise, it keeps the target vector:

$$u_{j,i,G} = \begin{cases} v_{j,i,G}, & \text{if } (\text{rand}_{i,j}[0, 1] \leq \text{Cr} \vee j = j_{\text{rand}}), \\ x_{j,i,G}, & \text{otherwise.} \end{cases} \quad (2)$$

3. DEMiner: A Hybrid Evolutionary Algorithm for Process Discovery

3.1. Framework of DEMiner. The GA-based process mining algorithms, including GeneticMiner [8], ProDiGen [11], and ETM [12], suffer from the problem that all of them need hundreds or even thousands of generations to converge to a solution. The reason behind this problem is that the genetic operators follow a completely random way, without taking advantage of the information of the log and the errors of the mined model during the parsing of the traces. The ProDiGen solves this problem in a simple way that it selects an incorrectly parsed activities as the crossing point in the step of crossover. However, it cannot significantly improve the speed of convergence because the process of crossover is also random. The ETM employed the alignment-based technique for local exploration to accelerate the convergence. However, the total running time is also unacceptable because the alignment algorithm is too time-consuming.

In this section, I will introduce a hybrid evolutionary algorithm for automated process discovery, called DEMiner. The main steps of DEMiner are shown in Figure 2. It can be

seen from the figure that the major difference between DEMiner and the traditional evolutionary algorithm is that it needs to select a specific evolutionary strategy in the loop. Step V is a set-based DE algorithm (abbreviated as DE or DE algorithm), which is in charge of fast approximation of the optimal solution. However, the DE algorithm usually falls into local optimum. To overcome the premature convergence, I employ Step VI, which is a guided local exploration algorithm. The local exploration algorithm can take advantage of the error information during the parsing of the log and help DEMiner quickly skip out the local optimum.

The pseudocode of DEMiner is given in Algorithm 1. The algorithm skips out the loop when the number of generation is higher than a predefined threshold *maxGenerations* or the *timesNotChange* is higher than *maxNotChange*. The variable *timesNotChange* records how long the population has not been replaced. In the loop, two statistics, i.e., *meanFitness* and *devFitness*, are used to detect whether the algorithm appears premature convergence. The former is the mean fitness of the population, and the latter is the deviation of the fitness value. If *meanFitness* and *devFitness* are lower than predefined thresholds *MF* and *DF*, at the same time, I think the algorithm is premature. Besides two statistics, a random number *rand* is used in the condition. The reason behind this consideration is that the global searching ability of the local exploration algorithm is lower than the DE algorithm. Sometimes, the local exploration may make an individual move forward, but it may not cause significant changes in two statistics. Therefore, the proposed algorithm will randomly choose a strategy if it falls into local optimum. Next, I will introduce these steps in detail.

3.2. Population Initialization. The population initialization method used in DEMiner follows the heuristic method proposed in [8], which is based on the causal relation between activities. Except that, there are two changes in our method, called gene bank and taboo list, which can improve the performance of DEMiner.

Gene bank is a set of chromosomes (i.e., individuals), including the individuals that are in current population and the individuals that have been eliminated during the evolution. To reduce the cost of memory space, the individuals in gene bank will be serialized; in other words, they will be converted to a simple format. For example, $I_{\text{ind}}(E) = \{\{B, C\}, \{D\}\}$ will be converted to a string " $I(E) = [[B, C], [D]]$." If the algorithm generates an individual which has been in gene bank, the individual would be discarded without calculation of its fitness value.

Taboo list keeps a set of historical operations of local exploration. In DEMiner, an important step, called guided local exploration, is employed to search around a specified node. The local exploration requires to randomly select one of the three operations, which are adding an arc, deleting an arc, or redistributing a node. These operations that have been performed, no matter they are useful or useless, are forbidden to be selected again. Every node has a taboo list, and these lists will be initialized to empty at the beginning.

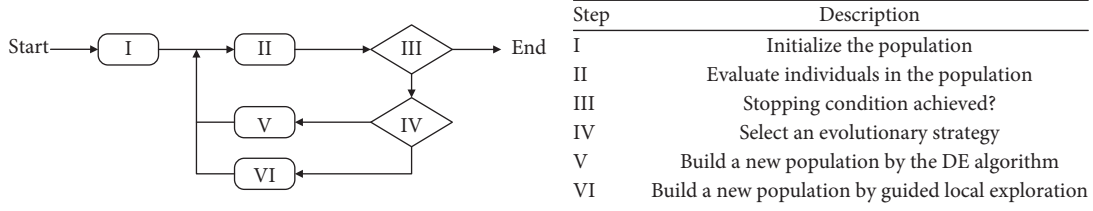


FIGURE 2: Framework of the DEMiner.

```

(1) Initialize population
(2) Evaluate population
(3) Calculate meanFitness and devFitness of the population
(4) generation ← 1, timesNotChange ← 0
(5) while generation ≤ maxGenerations && timesNotChange ≤ maxNotChange do
(6)   if meanFitness ≥ MF && devFitness ≤ DF && rand ≤ R do
(7)     Generate the trial individuals by the guided local exploration
(8)   else
(9)     Generate the trial individuals by the DE algorithm
(10)  Evaluate the trial individuals
(11)  if the fitness of the trial individuals is higher that the fitness of the target targets do
(12)    Replace population
(13)    timesNotChange ← 0
(14)  else
(15)    timesNotChange++
(16)  Update meanFitness and devFitness
(17)  generation++

```

ALGORITHM 1: Pseudocode of DEMiner.

3.3. *Fitness Function*. Generally, two metrics should be considered when evaluating a process model, which are completeness and precision [16]. The completeness quantifies the ability of a discovered process model that it can accurately parse the traces recorded in the event log. A natural way to define a completeness metric is the number of correctly parsed traces divided by the total number of traces. However, such definition is too coarse because it cannot indicate how many parts of an individual are correct when the individual does not properly parse a trace. Consider two process models: one is a totally incorrect process model, and the other just misses an arc; the above method cannot distinguish the two individuals because both of them cannot correctly parse the log. Due to this, I employ the partial completeness given in [8], which takes into account the correctly parsed activities as well as the number of tokens, which are missing or not consumed during the parse. I use the symbol “ C_f ” to denote the completeness metric.

A discovered process model may not be appropriate even if it gets completeness. For example, a flower model can parse arbitrary event logs, but it is useless. Precision is used to quantify the fraction of the behavior allowed by the model, which is not seen in the event log. However, it is hard to give a proper definition of precision because it has to detect all the extra behavior, i.e., possible path in the model but not in the log. In [4], the definition of the precision is $\text{allEnabledActivities}(L, CM)$ divided by $\text{max}(\text{allEnabledActivities}(L, CM))$, where $\text{allEnabledActivities}(L, CM)$ is

the number of enabled activities when a log L is parsed by an model CM . The denominator is a function which returns the max number of enabled activities in the population. It is easy to find that the precision of each individual depends on the rest of the population. In this work, I consider another definition of precision proposed in [11] (see formula (3)). It is easy to find that the more the activities enabled in a process model is, the lower the precision of the process model is:

$$P_f = \frac{1}{\text{all Enabled Activities}(L, CM)} \quad (3)$$

Generally, I need to assign weighted coefficients to combine the two metrics in a weighted sum [17]. However, it is difficult to combine the two metrics in an appropriate way because the used precision is not normalized. Therefore, a hierarchical method is employed to define the fitness function in this work. Because the completeness is more important than the precision when evaluating a discovered process model, I firstly compare the completeness of two process models; if their completeness is equal, then I compare their precision. By this way, when the completeness of all individuals are equal to 1, the individual that has better precision would win. It is easy to notice that the hierarchical fitness function can be easily extended by other metrics, such as structure complexity and generalization.

3.4. Differential Evolution Algorithm. The DE algorithm contains a loop which goes through all individuals in the population. For each individual (called the *target* individual), it firstly generates a *donor* individual based on three randomly selected individuals (mutation operation), and then it combines the *target* individual and the *donor* individual to get a *trial* individual (crossover operation). It must be emphasized that, due to the obtained *donor/trial* individual may be inconsistent, both of them should be repaired before going to next step. Then, the *trial* individual will be evaluated if it is not in the gene bank. If the fitness value of the *trial* individual is higher than the fitness of the *target* individual, the *target* individual would be replaced by the *trial* individual; meanwhile, the *trial* individual would be added into the gene bank. It can be seen that there are three key steps in the DE algorithm, which are mutation, crossover, and repair. Next, the details of the three steps will be explained.

3.4.1. Mutation. Current set-based evolutionary algorithms usually employ crisp sets to represent the candidate solutions (which are called individuals or chromosome in GA). For example, Chen et al. [18] proposed a set-based particle swarm optimization algorithm in which the candidate solutions are represented by a set of ordinal pairs. However, the causal matrix is a type of much more complex set. The elements in $I(\text{Activity})$ and $O(\text{Activity})$ are crisp sets, such as $I_{\text{ind}}(E) = \{\{B, C\}, \{D\}\}$. Therefore, the traditional set-based mutation operators cannot be directly used in this work. In Ou-Yang's method [9, 10], the mutation operator randomly selects ingredients from three individuals, and then use them to update the target individual to obtain a donor individual. The advantage of the method is that some good ingredients (e.g., parallel structure) can be directly transplanted to the target individual, which can improve the searching ability of the GeneticMiner. However, Ou-Yang's method cannot be directly employed in this work because the proposed algorithm is entirely based on the DE algorithm. In other words, it needs more flexible mutation operators.

This section introduces two novel operators, which allow the proposed algorithm to perform differential mutation on the causal matrix. The definitions of the two operators are given below.

Definition 5 (Minus Operator between Two Sets). Given a causal matrix $\text{CM} = (A, C, I, O)$ and two sets $S_1, S_2 \in P(P(A))$. The relative complement $S_1 - S_2$ of S_2 in S_1 is defined as

$$S_1 - S_2 = \{e \mid e \in S_1 \wedge e \notin S_2\}. \quad (4)$$

Definition 6 (Plus Operator between Two Sets). Given a causal matrix $\text{CM} = (A, C, I, O)$ and two sets $S_1, S_2 \in P(P(A))$. Then, $S_1 + S_2$ is defined as

$$S_1 + S_2 = \left\{ e \mid e \in \left\{ e' / \cup S_2 \mid e' \in S_1 \right\} \vee e \in S_2 \right\}, \quad (5)$$

where \cup denotes a generalized union operation and $e' / \cup S_2$ means that it removes the elements in $\cup S_2$ from e' . It is

easy to find that the plus operator will keep the elements in S_2 . The reason behind this consideration is that S_2 in formula (4) is, in fact, the result from formula (3) (a.k.a. the difference of two sets). By this way, it can greatly change the structure of S_1 and enhance the potential diversity of a trial individual.

Figure 3 gives an illustrating example. Given three sets which represent three distinct input sets of activity D , $S_1 = \{\{A, B, C\}\}$, $S_2 = \{\{A, B\}, \{B, C\}\}$, and $S_3 = \{\{A, C\}, \{B, C\}\}$. In terms of the definition of mutation in DE (see formula (1)), it requires to firstly calculate the difference of S_2 and S_3 and then add the difference to S_1 . Based on Definitions 5 and 6, we can get $S_2 - S_3 = \{\{A, B\}\}$ and then $\text{Donor} = S_1 + \{\{A, B\}\} = \{\{A, B\}, \{C\}\}$. Note that the scale factor F is not used in the mutation.

3.4.2. Crossover. The aim of crossover is combining a donor individual and a target individual to generate a trial individual. The trial individual would take the place of the target individual if its fitness is higher than the target individual. There are two kinds of popular crossover methods, which are the exponential and the binomial. I employ the latter in this work. The pseudocode of the binomial operator is shown below. "Cr" is called the crossover rate. The binomial crossover is performed on each of the activity node whenever a randomly generated number "rand" between 0 and 1 is less than or equal to the "Cr" (Algorithm 2). The "r" is a randomly chosen index, which ensures that the trial individual can get at least one component from the donor individual.

3.4.3. Repair. As is known to all, individuals obtained in the iterative process of evolutionary algorithms are always inconsistent. For example, it is possible to get a trial individual in which $I_{\text{ind}}(E) = \{\{B, C\}, \{D\}\}$, but $O_{\text{ind}}(D)$ does not contain activity "E." Besides that, the input of the "start" activity as well as the output of the "end" activity may be not empty. Therefore, a repair operation is required to be performed on the donor individual as well as the trial individual. In the GA-based process mining algorithms, such as GeneticMiner and ProDiGen, the repair operation is simple because the crossover as well as the mutation are performed on a designated point. The repair operation in this work is much more complex because the mutation as well as the crossover operation are performed on all nodes in a causal net. In other words, it is required to repair all nodes in a causal matrix. Before introducing the algorithm of repair, I firstly give the definition of consistence for a causal matrix.

Definition 7 (Consistence of a Causal Matrix). Let $\text{CM} = (A, C, I, O)$ be a causal matrix, and we say it is consistent if

- (1) $I(\text{start}) = \emptyset \wedge O(\text{start}) \neq \emptyset$, where "start" is the beginning activity
- (2) $O(\text{end}) = \emptyset \wedge I(\text{end}) \neq \emptyset$, where "end" is the ending activity

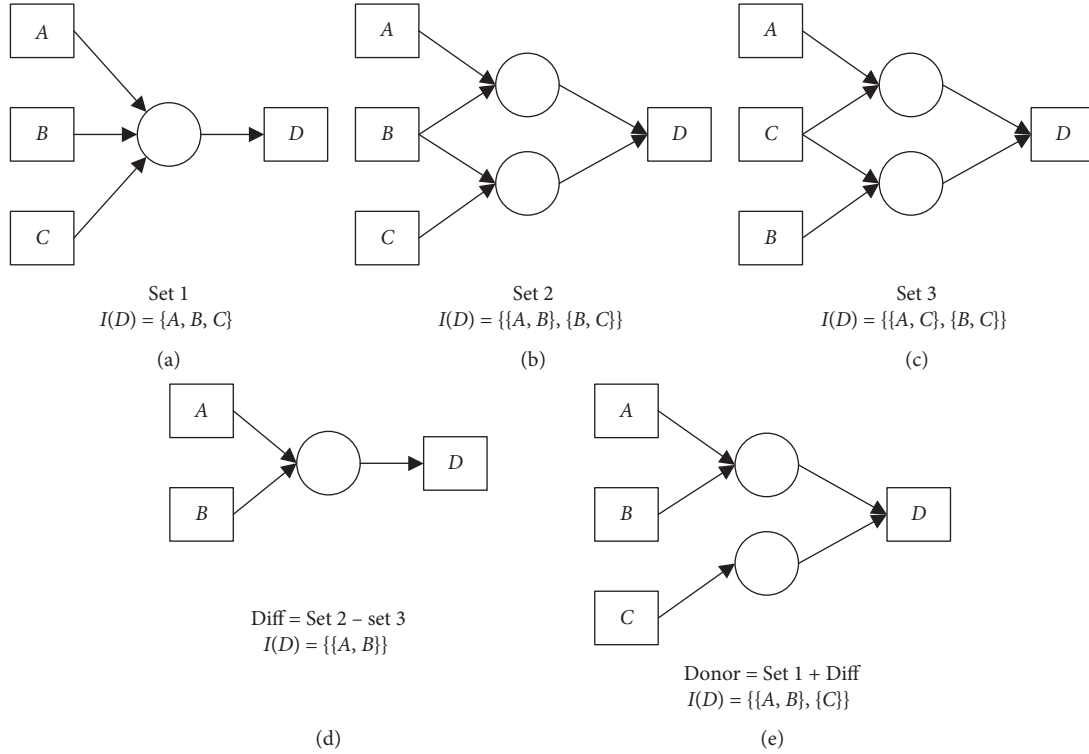


FIGURE 3: Illustrating example of the differential mutation operators.

```

(1) Add the activities A into the trial individual
(2) Generate a random number r between 1 and length(A)
(3) foreach t in A do
(4)   if rand < Cr || i = r do
(5)      $I_{\text{trial}}(t) \leftarrow I_{\text{donor}}(t)$ 
(6)      $O_{\text{trial}}(t) \leftarrow O_{\text{donor}}(t)$ 
(7)   else
(8)      $I_{\text{trial}}(t) \leftarrow I_{\text{target}}(t)$ 
(9)      $O_{\text{trial}}(t) \leftarrow O_{\text{target}}(t)$ 

```

ALGORITHM 2: Pseudocode of the binomial crossover.

- (3) For $\forall t' \in \cup I(t), t \in \cup O(t')$, where $t, t' \in A \wedge t \neq \text{start} \wedge t' \neq \text{end}$
- (4) For $\forall t' \in \cup O(t), t \in \cup I(t')$, where $t, t' \in A \wedge t \neq \text{end} \wedge t' \neq \text{start}$

The pseudocode of repair is given in Algorithm 3. Steps 1–6 are in charge of repairing the “start” node as well as the “end” node. It firstly lets the $I_{\text{ind}}(\text{start})$ and $O_{\text{ind}}(\text{end})$ be empty. Then, it would generate a new input set (output set) for $O_{\text{ind}}(\text{start})$ ($I_{\text{ind}}(\text{end})$) if they are empty. From Steps 7 to 19, the algorithm goes through all nodes in the causal matrix and repair $I_{\text{ind}}(t_1)$ and $O_{\text{ind}}(t_1)$, respectively. There are two choices in the repair operation. Take the repair of the input of t_1 for an example; if the output of t_2 does not contain t_1 , it may randomly add t_1 to $O_{\text{ind}}(t_2)$ or remove t_2 from $I_{\text{ind}}(t_1)$. By this way, we will finally obtain a consistent individual.

3.5. Guided Local Exploration. Although evolutionary algorithms, including the GA algorithm and the DE algorithm, have strong ability of global search, all of them suffer from the problem of premature convergence. In [14], van Eck et al. proposed a local exploration method based on alignment. In the method, a A^* algorithm is employed to find the optimal alignment between a process model and an event trace.

By this way, it can find out the abnormal areas in the process model. However, the alignment-based local exploration has two drawbacks. Firstly, it can only locate the abnormal area but not a node, which is too coarse to guide the exploration. Secondly, although the technique can accelerate the convergence of the GA algorithm, the execution time of the A^* algorithm is so long, which makes the total execution time unbearable.

This paper proposes an efficient and simple method to guide local exploration, which can help DEMiner skip out

```

(1)  $I_{\text{ind}}(\text{start}) \leftarrow \emptyset$ 
(2)  $O_{\text{ind}}(\text{end}) \leftarrow \emptyset$ 
(3) if  $O_{\text{ind}}(\text{start}) = \emptyset$  do
(4)   Generate an output set for  $O_{\text{ind}}(\text{start})$ 
(5) if  $I_{\text{ind}}(\text{end}) = \emptyset$  do
(6)   Generate an input set for  $I_{\text{ind}}(\text{end})$ 
(7) foreach  $t_1$  in  $A$  do
(8)   foreach  $t_2$  in  $\cup I_{\text{ind}}(t_1)$  do
(9)     if  $\cup O_{\text{ind}}(t_2)$  does not contain  $t_1$  do
(10)      if  $\text{rand} < 1/2 \parallel \text{length}(\cup I_{\text{ind}}(t_1)) \leq 1$  do
(11)        Add  $t_1$  to  $O_{\text{ind}}(t_2)$ 
(12)      else
(13)        Remove  $t_2$  from  $I_{\text{ind}}(t_1)$ 
(14)      foreach  $t_2$  in  $\cup O_{\text{ind}}(t_1)$  do
(15)        if  $\cup I_{\text{ind}}(t_2)$  does not contain  $t_1$  do
(16)          if  $\text{rand} < 1/2 \parallel \text{length}(\cup O_{\text{ind}}(t_1)) \leq 1$  do
(17)            Add  $t_1$  to  $I_{\text{ind}}(t_2)$ 
(18)          else
(19)            Remove  $t_2$  from  $O_{\text{ind}}(t_1)$ 

```

ALGORITHM 3: Pseudocode of repair of a candidate individual.

the local optimum and move forward to the global optimum. The method is based on token-based log replay, which is also employed in evaluation of the process model (a.k.a. causal matrix) in this work. The original algorithm for parsing a log on a causal matrix only records three types of information, which are “*allParsedActivities*,” “*allMissingTokens*,” and “*allExtraTokensLeftBehind*.” The *allParsedActivities* denotes the total number of activities which are correctly parsed, the *allMissingTokens* denotes the number of missing tokens in all event traces, and the *allExtraTokensLeftBehind* denotes the number of tokens that are not consumed after the parsing. In our method, besides those, it requires to record the nodes that where the parsing errors happen, including miss tokens during the parsing or left behind tokens after the parsing. By this way, it can achieve fine-grained evaluation of all nodes.

It is easy to find that the proposed method has several advantages. Firstly, it can accurately locate the abnormal nodes and improve the efficiency of the local exploration. Secondly, the time complexity of the proposed method is much lower than the alignment-based method because it does not need extracomputation. The evaluation of nodes can be finished along with the evaluation of the individual. The formulas of fine-grained evaluation are given below, in which $C_f^i(t)$ represents the score of $I_{\text{ind}}(t)$ and $C_f^o(t)$ represents the score of $O_{\text{ind}}(t)$:

$$C_f^i(t) = \frac{\text{all Missing Tokens}(L, CM, t)}{\text{all Parsed Activities}(L, CM, t)}, \quad (6)$$

$$C_f^o(t) = \frac{\text{all Extra Tokens Left Behind}(L, CM, t)}{\text{all Parsed Activities}(L, CM, t)}.$$

The pseudocode of the guided local exploration is shown in algorithm 4. Step 2 employs a roulette wheel strategy to randomly select a node for local exploration. The node with a lower score has great probability to be

selected. Step 3 randomly selects a direction for exploration, i.e., “input” or “output.” Steps 4–28 randomly choose a mutation operation, including randomly add an arc to the node, randomly delete an arc from the node, and randomly redistribute the structure of the node. An example for illustrating the redistribution operation is that given $I_{\text{ind}}(E) = \{\{B, C\}, \{D\}\}$, it may get $I_{\text{ind}}(E) = \{\{B, C, D\}\}$ or $I_{\text{ind}}(E) = \{\{B\}, \{C, D\}\}$ after the redistribution. In the algorithm, a *taboo list* is used to record the history of local exploration. Some operations which are useless (a.k.a. cannot make the individual move forward) are recorded in the *taboo list*. By this way, it can improve the efficiency of the local exploration.

4. Experiments

In this section, I give the experiments as well as the analysis. The experiments are focused on two aspects. The first is to evaluate that whether the DE algorithm and the guided local exploration are efficient to accelerate the convergence speed of the proposed algorithm. The second is to evaluate the performance of the proposed algorithm (a.k.a. the DEMiner). Next, the event logs used in the experiments will be introduced.

4.1. Event Logs. In the experiments, 66 event logs were used for evaluation of the proposed algorithm. The event logs can be classified into three groups. The first group contains 22 artificial event logs which are from [8, 19] and can be downloaded from <https://svn.win.tue.nl/repos/prom/DataSets/GeneticMinerLogs/>. The description of the event logs is shown in Table 2. The process models that generate these logs include different structures, such as sequence, choice, parallelism, loops, and invisible tasks. These process models, represented as Petri nets and heuristic nets, can be found in [19].

```

(1) foreach ind in population do
(2)   selected  $\leftarrow$  randomly select an activity from ind
(3)   mutationType  $\leftarrow$  randomly select a direction for exploration
(4)   if rand < 1/3 do // randomly add an arc
(5)     if mutationType = "input" do
(6)       precursor  $\leftarrow$  select a precursor of selected activity which is not in  $I_{ind}$ (selected)
(7)       arc  $\leftarrow$  <precursor, selected>
(8)     else
(9)       successor  $\leftarrow$  select a successor of selected activity which is not in  $O_{ind}$ (selected)
(10)      arc  $\leftarrow$  <selected, successor>
(11)     if add arc is allowed in taboo list do
(12)       Add arc into ind
(13)     else go to 5
(14)   else if rand < 2/3 do // randomly delete an arc
(15)     if mutationType = "input" do
(16)       precursor  $\leftarrow$  select an activity from  $I_{ind}$ (selected)
(17)       arc  $\leftarrow$  <precursor, selected>
(18)     else
(19)       successor  $\leftarrow$  select an activity from  $O_{ind}$ (selected)
(20)       arc  $\leftarrow$  <selected, successor>
(21)     if delete arc is allowed in taboo list do
(22)       Delete arc from ind
(23)     else go to 15
(24)   else // redistribute the node
(25)     if mutationType = "input" do
(26)       Redistribute  $I_{ind}$ (selected)
(27)     else
(28)       Redistribute  $O_{ind}$ (selected)

```

ALGORITHM 4: Pseudocode of the guided local exploration.

In the event logs, the traces with same event sequence are grouped together.

The second group, which is used to evaluate the antinoise ability of the DEMiner, contains 44 event logs. These event logs were generated based on the first group of event logs, which contain 5% and 10% noise, respectively. Three different types of operations for noise generation were used, including randomly add an event into a trace, randomly delete an event from a trace, and randomly swap two adjacent events in a trace. To incorporate noise, the traces of the original noise-free logs were randomly selected and then one of the three noise types was applied and each one with an equal probability of 1/3.

The third group includes two real event logs, both of which are downloaded from https://data.4tu.nl/repository/collection:event_logs. The first event log which was named "BPI2013cp" records the process information from the Volvo IT problem management system. It includes 1487 traces as well as 6660 events. The second event log which was named "Sepsis" records the events of sepsis cases from a hospital ERP system. It includes 1050 traces as well as 15214 events.

4.2. Convergence Speed and Running Time. This section introduces the experiments for evaluation of the efficiency of the DE algorithm as well as the guided local exploration method.

This section evaluates whether the DE algorithm and the guided local exploration are efficient to accelerate the convergence speed of the proposed algorithm. Four different strategies are considered in the experiment, which are the DE algorithm without local exploration (denoted as DE), the DE algorithm with random local exploration (denoted as DE + Random Search), the DE algorithm with guided local exploration (denoted as DE + Guided Search), and the GA. It should be explained that (1) the random search used in the second strategy is the genetic mutation in the GeneticMiner, and (2) the third strategy is the DEMiner proposed in this work, and (3) the GA algorithm follows the framework in this work but uses the genetic operators of the GeneticMiner. Three metrics are employed in the experiments, which are completeness, precision, and generation (i.e., number of iterations). To avoid the inaccuracy of the experimental results caused by randomness, each algorithm was run 10 times and the average value of each metric as well as its standard deviation is calculated.

The first group of event logs was used for the evaluation. The computer for experiments is equipped with a 2.5 GHz CPU and 8 GB memory. The parameters setting is shown in Table 3. It should be explained that the population size is the number of activities multiplied by 1~2. The parameter "MF" is set to 0.7 because the local exploration is not hoped to be involved in the search too early. The parameter "DF" is set to 0.2 which is used for detection of premature convergence. In fact, a slight change of these parameters,

TABLE 2: Description of event logs.

| Model | # tasks | # traces | # events | Sequence | Choice | Parallelism | Length one loop | Length two loop | Structured loop | Arbitrary loop | Invisible tasks |
|---------|---------|----------|----------|----------|--------|-------------|-----------------|-----------------|-----------------|----------------|-----------------|
| a5 | 7 | 300 | 2189 | ✓ | ✓ | ✓ | ✓ | | | | |
| a6nfc | 8 | 300 | 2040 | ✓ | ✓ | ✓ | | | | | ✓ |
| a7 | 9 | 300 | 2032 | ✓ | ✓ | ✓ | | | | | |
| a8 | 10 | 300 | 1803 | ✓ | ✓ | ✓ | | | | | |
| a10skip | 12 | 300 | 2665 | ✓ | ✓ | ✓ | | | | | ✓ |
| al1 | 9 | 300 | 3976 | ✓ | ✓ | ✓ | | | | ✓ | |
| al2 | 13 | 300 | 5800 | ✓ | ✓ | ✓ | | | | ✓ | |
| bn1 | 42 | 300 | 11100 | ✓ | ✓ | | | | | | |
| bn2 | 42 | 300 | 24540 | ✓ | ✓ | | | | ✓ | | ✓ |
| bn3 | 42 | 300 | 35527 | ✓ | ✓ | | | | ✓ | | ✓ |
| choice | 12 | 300 | 2400 | ✓ | ✓ | | | | | | |
| h3p4 | 12 | 300 | 5637 | ✓ | ✓ | ✓ | | | ✓ | | |
| h6p18 | 7 | 300 | 9844 | ✓ | ✓ | | ✓ | ✓ | ✓ | | ✓ |
| h6p30 | 19 | 300 | 14851 | ✓ | ✓ | | | | | | ✓ |
| h6p36 | 12 | 300 | 3000 | ✓ | ✓ | | | | | | |
| h6p41 | 16 | 300 | 3600 | ✓ | ✓ | ✓ | | | | | |
| h6p45 | 8 | 300 | 2400 | ✓ | ✓ | ✓ | | | | | |
| l1l | 6 | 300 | 1987 | ✓ | ✓ | | ✓ | | | | |
| l2l | 6 | 300 | 4932 | ✓ | ✓ | | | ✓ | | | |
| l2lOpt | 6 | 300 | 2622 | ✓ | ✓ | | | ✓ | | | |
| l2lSkip | 6 | 300 | 4554 | ✓ | ✓ | | | ✓ | | | ✓ |
| paral5 | 10 | 300 | 3000 | ✓ | | ✓ | | | | | |

TABLE 3: Parameter settings.

| Parameter | Setting |
|-----------------|---------|
| Population size | 1~2 |
| maxGenerations | 400 |
| maxNotChange | 20~40 |
| MF | 0.7 |
| DF | 0.2 |
| R | 0.5 |
| Cr | 0.6 |

e.g., the MF is set to 0.6~0.8 and the DF is set to 0.1~0.2, would not affect the performance of the algorithm, including the quality of mining results as well as the convergence speed.

The experimental results are shown in Table 4. For completeness, it can be seen that the four algorithms (from left to right in Table 3) always achieve completeness 1.00 on 1 event logs, 10 event logs, 20 event logs, and 12 event logs, respectively. The result demonstrates that the “pure” DE algorithm cannot achieve the best model; a.k.a., it always falls into local optimum. Then, for precision, the “DE” algorithm achieves the best precision on just one event log. Except that, the “DE + Random Search” and the “GA” achieve the best precision on 2 event logs, and the “DE + Guided Search” achieves the best precision on 14 event logs stably. From the two metrics, it can be seen that the “DE + Guided Search” plays much better than other three strategies. For generation, it requires to exclude the “DE” algorithm because it always suffers from premature convergence. Among the remaining algorithms, it is obvious that the “DE + Guided Search” has the fastest convergence speed and the “GA” has the slowest convergence.

To illustrate the time complexity of the DEMiner, the running time of “DE + Guided Search” is also recorded, which is shown in Figure 4. From the figure, it can be seen that the minimum running time is about 3 seconds (“a6nfc”) and the maximum running time is about 80 seconds (“bn3”). This proves the time performance of the DEMiner.

Based on the above results, some conclusions can be drawn. (1) The “DE” algorithm always falls into local optimum. (2) The “DE + Random Search” and the “GA” can discover process models with similar quality, but the former has faster convergence speed than the latter. Note that both of the two algorithms use random search (i.e., the genetic mutation). The difference is that the “DE + Random Search” employs the DE algorithm. It proves that the DE algorithm can quickly approximate the optimal solution and accelerate the convergence speed. (3) Based on the experimental results of the “DE + Random Search” and the “DE + Guided Search,” it can be seen that the latter achieves much better results than the former. This explains that the guided local exploration is efficient to help the DE algorithm skip out the local optimum and improve the searching ability of the DEMiner.

4.3. Performance on Artificial Event Logs

4.3.1. Setup. This section compares the performance of the DEMiner with three popular process mining algorithms. Through the experiments, I want to evaluate the performance as well as the antinoise ability of the DEMiner. The selected process mining algorithms for comparison include Heuristics Miner (HM) [20], ILP Miner [5], and ETM Miner [12]. Among these algorithms, HM is a popular tool of process mining, which outputs a heuristic net as a mining

TABLE 4: Comparison of different methods.

| Event logs | DE | | | DE + Random Search | | | DE + Guided Search | | | GA | | |
|------------|-------------|---------------------|--------|--------------------|---------------------|---------|--------------------|---------------------|---------|-------------|---------------------|----------|
| | Cp. | Prec. (10^{-4}) | Gen. | Cp. | Prec. (10^{-4}) | Gen. | Cp. | Prec. (10^{-4}) | Gen. | Cp. | Prec. (10^{-4}) | Gen. |
| a5 | 0.91 ± 0.02 | 1.05 ± 0.18 | 27 ± 3 | 1.00 | 2.58 ± 0.04 | 92 ± 21 | 1.00 | 2.64 | 63 ± 10 | 1.00 | 2.60 ± 0.04 | 88 ± 21 |
| a6nfc | 0.85 ± 0.04 | 1.92 ± 0.36 | 28 ± 2 | 0.99 ± 0.01 | 3.52 ± 0.08 | 51 ± 12 | 1.00 | 3.58 ± 0.02 | 25 ± 3 | 0.98 ± 0.02 | 3.49 ± 0.08 | 105 ± 36 |
| a7 | 0.82 ± 0.05 | 1.82 ± 0.19 | 31 ± 4 | 0.93 ± 0.02 | 2.42 ± 0.12 | 70 ± 22 | 0.98 ± 0.02 | 2.51 ± 0.08 | 55 ± 13 | 0.97 ± 0.03 | 2.37 ± 0.10 | 90 ± 18 |
| a8 | 0.92 ± 0.01 | 2.21 ± 0.17 | 27 ± 5 | 0.98 ± 0.02 | 3.49 ± 0.16 | 73 ± 18 | 1.00 | 3.98 | 33 ± 4 | 1.00 | 3.71 ± 0.15 | 60 ± 17 |
| a10skip | 0.90 ± 0.04 | 2.68 ± 0.09 | 30 ± 3 | 1.00 | 2.75 ± 0.04 | 32 ± 6 | 1.00 | 2.81 | 27 ± 4 | 1.00 | 2.77 ± 0.04 | 43 ± 14 |
| all | 0.76 ± 0.07 | 0.92 ± 0.12 | 35 ± 6 | 0.98 ± 0.01 | 1.28 ± 0.17 | 36 ± 10 | 1.00 | 1.57 ± 0.02 | 28 ± 6 | 0.99 ± 0.01 | 1.22 ± 0.19 | 91 ± 23 |
| al2 | 0.87 ± 0.03 | 0.48 ± 0.13 | 32 ± 5 | 1.00 | 0.52 ± 0.08 | 38 ± 9 | 1.00 | 0.63 ± 0.03 | 49 ± 17 | 1.00 | 0.45 ± 0.12 | 49 ± 9 |
| bn1 | 0.97 ± 0.02 | 0.71 ± 0.11 | 24 ± 2 | 1.00 | 0.85 | 45 ± 11 | 1.00 | 0.85 | 26 ± 5 | 1.00 | 0.83 ± 0.02 | 48 ± 12 |
| bn2 | 0.99 ± 0.01 | 0.32 ± 0.05 | 22 ± 2 | 1.00 | 0.37 ± 0.01 | 27 ± 5 | 1.00 | 0.38 | 25 ± 4 | 1.00 | 0.35 ± 0.03 | 33 ± 8 |
| bn3 | 0.91 ± 0.04 | 0.21 ± 0.03 | 24 ± 2 | 0.97 ± 0.02 | 0.23 ± 0.02 | 61 ± 14 | 1.00 | 0.25 | 44 ± 14 | 0.94 ± 0.04 | 0.21 ± 0.03 | 76 ± 17 |
| choice | 0.88 ± 0.04 | 1.09 ± 0.10 | 35 ± 5 | 0.98 ± 0.01 | 1.92 ± 0.18 | 49 ± 12 | 1.00 | 2.78 | 41 ± 11 | 1.00 | 2.33 ± 0.14 | 63 ± 10 |
| h3p4 | 0.85 ± 0.03 | 0.92 ± 0.17 | 22 ± 1 | 1.00 | 1.21 ± 0.03 | 30 ± 6 | 1.00 | 1.28 ± 0.08 | 31 ± 7 | 1.00 | 1.29 ± 0.05 | 46 ± 12 |
| h6p18 | 0.73 ± 0.09 | 0.35 ± 0.12 | 42 ± 6 | 0.93 ± 0.03 | 0.52 ± 0.06 | 85 ± 16 | 0.97 ± 0.02 | 0.58 ± 0.06 | 85 ± 32 | 0.96 ± 0.03 | 0.53 ± 0.04 | 122 ± 45 |
| h6p30 | 0.92 ± 0.03 | 0.28 ± 0.08 | 29 ± 3 | 0.97 ± 0.02 | 0.35 ± 0.04 | 42 ± 10 | 1.00 | 0.43 | 42 ± 10 | 0.99 ± 0.01 | 0.38 ± 0.04 | 44 ± 8 |
| h6p36 | 1.00 | 2.80 | 20 ± 0 | 1.00 | 2.80 | 20 ± 0 | 1.00 | 2.80 | 20 ± 0 | 1.00 | 2.80 | 20 ± 0 |
| h6p41 | 0.85 ± 0.03 | 1.12 ± 0.06 | 32 ± 4 | 1.00 | 2.12 ± 0.03 | 64 ± 12 | 1.00 | 2.15 | 34 ± 8 | 0.98 ± 0.02 | 2.20 ± 0.04 | 75 ± 21 |
| h6p45 | 0.74 ± 0.05 | 1.19 ± 0.08 | 39 ± 5 | 0.94 ± 0.03 | 2.33 ± 0.15 | 79 ± 15 | 1.00 | 2.79 ± 0.05 | 46 ± 12 | 0.98 ± 0.01 | 2.08 ± 0.18 | 109 ± 27 |
| ll1 | 0.68 ± 0.13 | 0.92 ± 0.19 | 31 ± 3 | 0.92 ± 0.04 | 1.14 ± 0.28 | 84 ± 12 | 1.00 | 2.40 | 47 ± 7 | 0.95 ± 0.03 | 1.58 ± 0.13 | 94 ± 19 |
| l2l | 0.94 ± 0.03 | 1.14 ± 0.14 | 22 ± 2 | 1.00 | 1.35 ± 0.09 | 36 ± 8 | 1.00 | 1.44 | 27 ± 5 | 1.00 | 1.42 ± 0.10 | 36 ± 5 |
| l2lOpt | 0.81 ± 0.06 | 1.38 ± 0.18 | 22 ± 1 | 1.00 | 2.71 ± 0.03 | 36 ± 11 | 1.00 | 2.75 | 25 ± 2 | 1.00 | 2.75 | 48 ± 9 |
| l2lSkip | 0.73 ± 0.11 | 1.02 ± 0.07 | 25 ± 2 | 0.99 ± 0.01 | 1.42 ± 0.07 | 48 ± 10 | 1.00 | 1.60 | 32 ± 6 | 1.00 | 1.14 ± 0.07 | 54 ± 12 |
| para15 | 0.71 ± 0.08 | 1.13 ± 0.16 | 35 ± 4 | 0.91 ± 0.04 | 1.37 ± 0.11 | 82 ± 18 | 1.00 | 1.66 ± 0.06 | 52 ± 10 | 0.93 ± 0.04 | 1.26 ± 0.17 | 102 ± 31 |

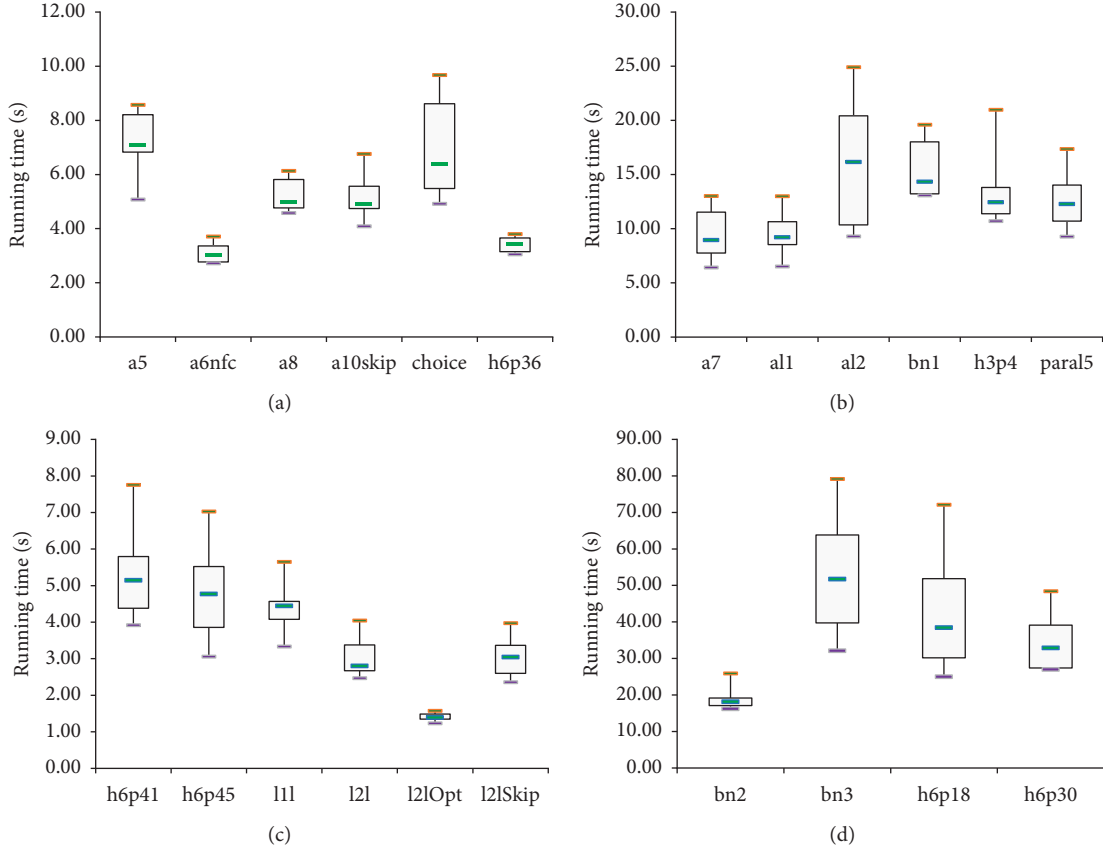


FIGURE 4: Running time of DEMiner on 22 event logs.

result, and ILP Miner as well as ETM are two state-of-the-art algorithms in the field of process mining. ProM 6.9 which is the most popular process mining platform was used in the experiments [21]. Parameters of the three algorithms were set to default. Because ILP Miner and ETM output a Petri net and a process tree as a mining result, respectively, the obtained models must be converted to causal matrices based on Definition 4. By this way, the four algorithms can be evaluated by a unified way. Specially, if the outputting model contains invisible transitions (e.g., the ETM), it would be converted to causal matrices by hand.

Four metrics defined in [8, 19] were used to evaluate the algorithms in the experiments. The metrics include behavioral precision (Bp), behavioral recall (Br), structural precision (Sp), and structural recall (Sr). The Bp and Br are based on the parsing of an event log by the mined model and the original model. The former detects how much behavior is allowed by the mined model that is not by the original model. The latter detects for the opposite. Moreover, the closer the values of Bp and Br to 1.0, the higher the similarity between the original and the mined models. The Sp and Sr metrics are based on the causality relations of the mined and original models, the former detects how many causality relations the mined model has that are not in the original model, and the latter detects for the opposite. Different from the Bp and Br, the Sp and Sr measure the similarity from the structural point of view. When the

original model has connections that do not appear in the mined model, Sr will take a value smaller than 1, and, in the same way, when the mined model has connections that do not appear in the original model, Sp will take a value lower than 1.0.

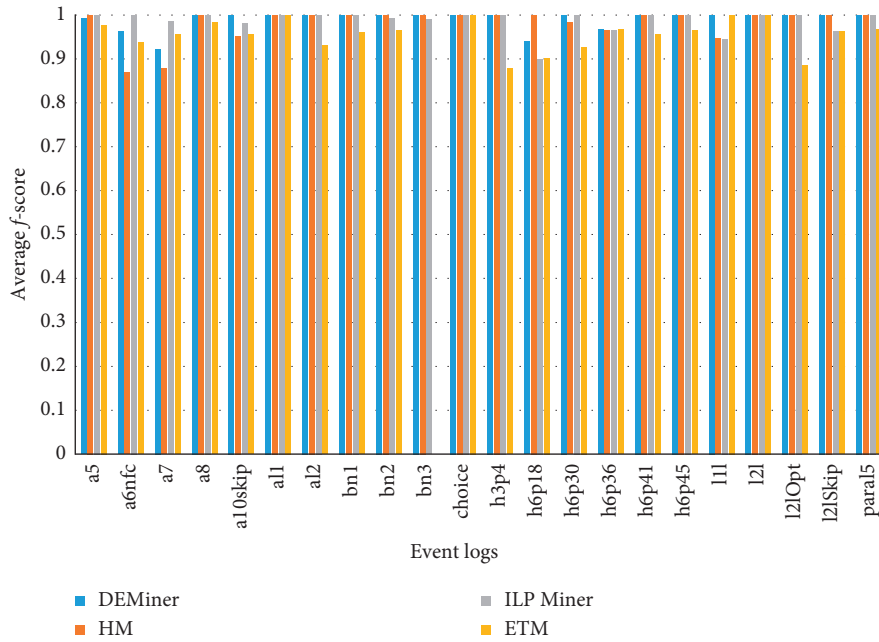
4.3.2. Noise-Free Event Logs. First of all, the experiments were performed on 22 noise-free event logs. The results are listed in Table 5, in which the best results on each log are in italics. From the results, it is easy to find that the performance of the DEMiner is slightly better than other three algorithms. The DEMiner achieves the optimal solutions (i.e., four metrics are equal to 1) on 18 event logs. The HM, ILP Miner, and ETM achieve the optimal solutions on 16 event logs, 14 event logs, and 5 event logs, respectively. To compare the four algorithms more intuitively, a combinatorial metric, called average f -score, is designed, which is shown as follows:

$$f\text{score}_{\text{ave}} = \frac{B_p \cdot B_r}{B_p + B_r} + \frac{S_p \cdot S_r}{S_p + S_r}. \quad (7)$$

The results are shown in Figure 5. From the figure, it is easy to find that the DEMiner only lost to other algorithms on four event logs, which are “a5,” “a6nfc,” “a7,” and “h6p18.” Except that, the DEMiner obtained the best results on the remaining 18 event logs. Moreover, the average f -

TABLE 5: Comparison of four algorithms’ performance on 22 event logs without noise.

| Event logs | DEMiner | | | | HM | | | | ILP Miner | | | | ETM | | | |
|------------|---------|------|------|------|------|------|------|------|-----------|------|------|------|------|------|------|------|
| | Br | Bp | Sr | Sp | Br | Bp | Sr | Sp | Br | Bp | Sr | Sp | Br | Bp | Sr | Sp |
| a5 | 1.00 | 0.98 | 1.00 | 1.00 | 1.00 | 1.00 | 1.00 | 1.00 | 1.00 | 1.00 | 1.00 | 1.00 | 1.00 | 0.91 | 1.00 | 1.00 |
| a6nfc | 1.00 | 0.94 | 0.93 | 1.00 | 0.87 | 0.68 | 0.93 | 1.00 | 1.00 | 1.00 | 1.00 | 1.00 | 0.98 | 0.91 | 0.93 | 0.93 |
| a7 | 1.00 | 0.83 | 0.98 | 0.92 | 0.86 | 0.78 | 0.95 | 0.92 | 1.00 | 0.99 | 0.95 | 1.00 | 0.96 | 0.92 | 0.97 | 0.97 |
| a8 | 1.00 | 1.00 | 1.00 | 1.00 | 1.00 | 1.00 | 1.00 | 1.00 | 1.00 | 1.00 | 1.00 | 1.00 | 0.98 | 1.00 | 0.95 | 1.00 |
| a10skip | 1.00 | 1.00 | 1.00 | 1.00 | 1.00 | 0.91 | 0.90 | 1.00 | 1.00 | 0.97 | 1.00 | 0.95 | 0.96 | 0.86 | 1.00 | 1.00 |
| al1 | 1.00 | 1.00 | 1.00 | 1.00 | 1.00 | 1.00 | 1.00 | 1.00 | 1.00 | 1.00 | 1.00 | 1.00 | 1.00 | 1.00 | 1.00 | 1.00 |
| al2 | 1.00 | 1.00 | 1.00 | 1.00 | 1.00 | 1.00 | 1.00 | 1.00 | 1.00 | 1.00 | 1.00 | 1.00 | 0.95 | 0.88 | 0.94 | 0.95 |
| bn1 | 1.00 | 1.00 | 1.00 | 1.00 | 1.00 | 1.00 | 1.00 | 1.00 | 1.00 | 1.00 | 1.00 | 1.00 | 0.97 | 0.91 | 0.98 | 0.98 |
| bn2 | 1.00 | 1.00 | 1.00 | 1.00 | 1.00 | 1.00 | 1.00 | 1.00 | 1.00 | 1.00 | 0.99 | 1.00 | 0.98 | 0.98 | 0.96 | 0.98 |
| bn3 | 1.00 | 1.00 | 1.00 | 1.00 | 1.00 | 1.00 | 1.00 | 1.00 | 1.00 | 0.98 | 1.00 | 0.98 | — | — | — | — |
| choice | 1.00 | 1.00 | 1.00 | 1.00 | 1.00 | 1.00 | 1.00 | 1.00 | 1.00 | 1.00 | 1.00 | 1.00 | 1.00 | 1.00 | 1.00 | 1.00 |
| h3p4 | 1.00 | 1.00 | 1.00 | 1.00 | 1.00 | 1.00 | 1.00 | 1.00 | 1.00 | 1.00 | 1.00 | 1.00 | 0.93 | 0.82 | 0.94 | 0.82 |
| h6p18 | 0.96 | 0.86 | 0.94 | 1.00 | 1.00 | 1.00 | 1.00 | 1.00 | 1.00 | 0.80 | 1.00 | 0.80 | 0.95 | 0.82 | 0.92 | 0.92 |
| h6p30 | 1.00 | 1.00 | 1.00 | 1.00 | 1.00 | 0.98 | 1.00 | 0.95 | 1.00 | 1.00 | 1.00 | 1.00 | 0.92 | 0.98 | 0.90 | 0.91 |
| h6p36 | 1.00 | 0.95 | 0.92 | 1.00 | 1.00 | 0.95 | 0.92 | 1.00 | 1.00 | 0.95 | 0.91 | 1.00 | 1.00 | 0.95 | 0.92 | 1.00 |
| h6p41 | 1.00 | 1.00 | 1.00 | 1.00 | 1.00 | 1.00 | 1.00 | 1.00 | 1.00 | 1.00 | 1.00 | 1.00 | 0.93 | 0.99 | 0.95 | 0.95 |
| h6p45 | 1.00 | 1.00 | 1.00 | 1.00 | 1.00 | 1.00 | 1.00 | 1.00 | 1.00 | 1.00 | 1.00 | 1.00 | 0.98 | 0.98 | 0.95 | 0.95 |
| l1l | 1.00 | 1.00 | 1.00 | 1.00 | 0.95 | 0.97 | 0.87 | 1.00 | 0.95 | 0.97 | 0.86 | 1.00 | 1.00 | 1.00 | 1.00 | 1.00 |
| l2l | 1.00 | 1.00 | 1.00 | 1.00 | 1.00 | 1.00 | 1.00 | 1.00 | 1.00 | 1.00 | 1.00 | 1.00 | 1.00 | 1.00 | 1.00 | 1.00 |
| l2lOpt | 1.00 | 1.00 | 1.00 | 1.00 | 1.00 | 1.00 | 1.00 | 1.00 | 1.00 | 1.00 | 1.00 | 1.00 | 0.91 | 0.83 | 0.90 | 0.90 |
| l2lSkip | 1.00 | 1.00 | 1.00 | 1.00 | 1.00 | 1.00 | 1.00 | 1.00 | 1.00 | 0.95 | 1.00 | 0.90 | 1.00 | 0.95 | 1.00 | 0.90 |
| para5 | 1.00 | 1.00 | 1.00 | 1.00 | 1.00 | 1.00 | 1.00 | 1.00 | 1.00 | 1.00 | 1.00 | 1.00 | 1.00 | 0.93 | 0.97 | 0.97 |

FIGURE 5: Average f -score of four algorithms on 22 event logs without noise.

score achieved by the DEMiner on the rest 4 event logs is over 0.9. It demonstrates that the DEMiner has good performance. Later, a deep analysis is given.

There are four event logs that the DEMiner could not achieve the best results, which are “a5,” “a7,” “h618,” and “h6p36.” The mining results which were repeated most often are shown in Figure 6. In the figure, the incorrect parts have been labeled by red color. Moreover, the dotted lines denote the missing arcs (a.k.a in the original model

but is not discovered by the DEMiner), and the solid line denotes the incorrect connections (a.k.a. structural errors).

In Figure 6(a), it can be seen that the mined model lacks a cycle $\langle E, E \rangle$. In the original model, there are two cycles on the node “E.” The reason behind this phenomenon is that the operators of differential mutation proposed in this work (Definitions 5 and 6) will remove such structure during the evolution. Assume $S1 = \{\{E\}, \{E\}, \{B, C\}\}$ and $S2 = \{\{E\}, \{B\}\}$,

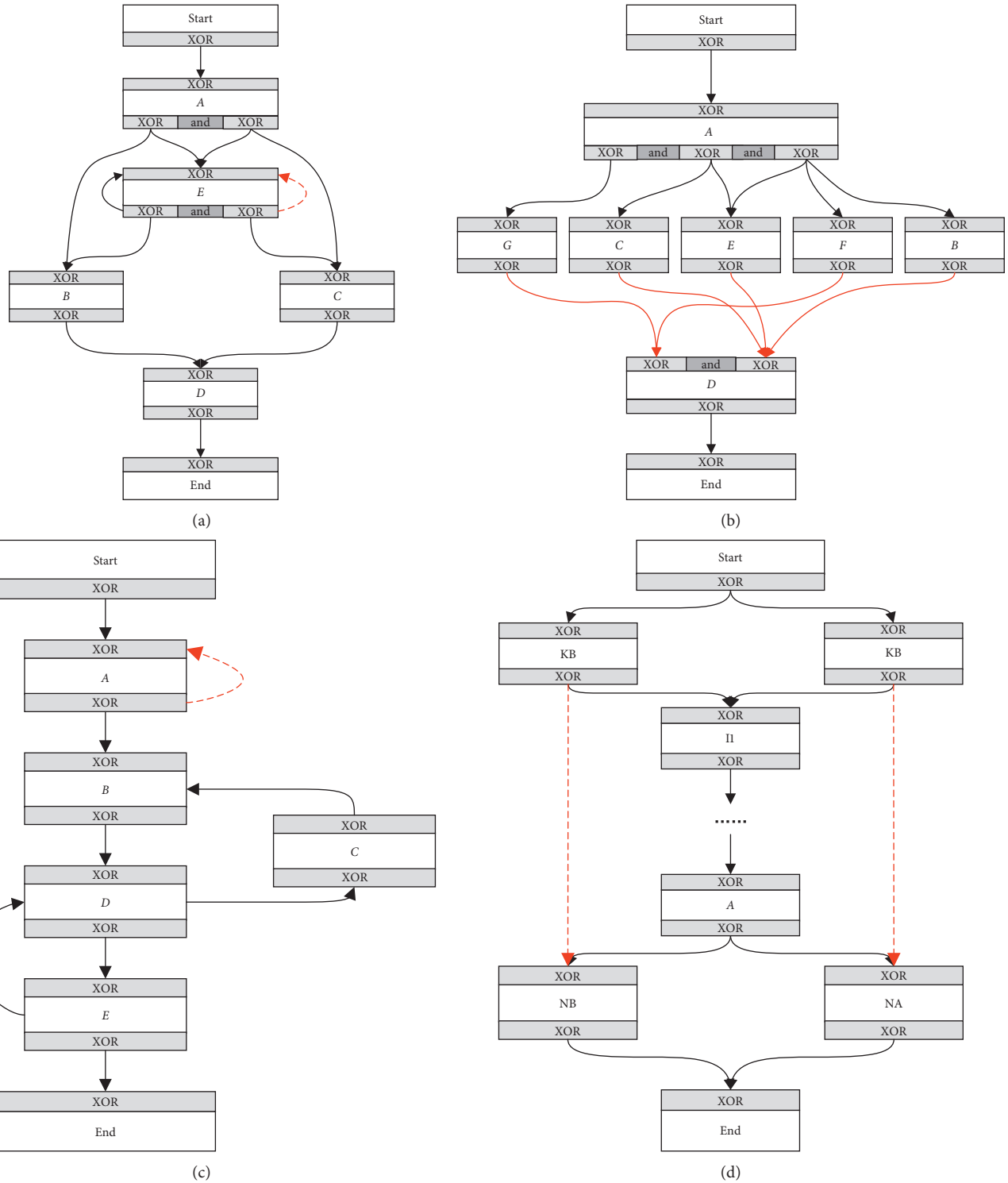


FIGURE 6: Mining results of four event logs: (a) a5; (b) a7; (c) h6p18; (d) h6p36.

then $S1-S2 = \{\{B, C\}\}$; in other words, the two subsets $\{E\}$ would be removed from $S1$ by the minus operation. Furthermore, assume $S1 = \{\{E\}, \{E\}, \{B, C\}\}$ and $S2 = \{\{E\}, \{B, C\}\}$; it is easy to find that the two sets will obtain the same completeness value, but the precision value of $S1$ is lower than that of $S2$ (the former has more enabled activities). In other words, $S1$ would be replaced by $S2$ during the

evolution. Similarly, this phenomenon also appears in the event log “h6p18.”

Next, in the mined model of “a7,” the input set of node “D” is $\{\{2, 4\}, \{3, 7, 8\}\}$, which is $\{\{2\}, \{3, 7\}, \{4, 7, 8\}\}$ in the original model. The reason behind this incorrectness is also the differential mutation operations. It is easy to find that removing the intersection part of two sets is a high

TABLE 6: Comparison of four algorithms’ performance on 22 event logs with 5% noise.

| Event logs | DEMiner | | | | HM | | | | ILP Miner | | | | ETM | | | |
|------------|---------|------|------|------|------|------|------|------|-----------|------|------|------|------|------|------|------|
| | Br | Bp | Sr | Sp | Br | Bp | Sr | Sp | Br | Bp | Sr | Sp | Br | Bp | Sr | Sp |
| a5 | 1.00 | 0.84 | 1.00 | 0.95 | 1.00 | 0.78 | 0.86 | 0.95 | 1.00 | 1.00 | 1.00 | 1.00 | 0.94 | 0.84 | 1.00 | 0.83 |
| a6nfc | 0.98 | 0.65 | 0.96 | 0.74 | 0.87 | 0.68 | 1.00 | 0.83 | 0.81 | 0.75 | 0.64 | 0.80 | 0.84 | 0.75 | 0.86 | 0.95 |
| a7 | 1.00 | 0.78 | 0.95 | 0.74 | 0.82 | 0.78 | 0.88 | 0.72 | 1.00 | 0.76 | 0.68 | 0.64 | 0.85 | 0.81 | 0.78 | 0.70 |
| a8 | 1.00 | 0.74 | 0.98 | 0.69 | 1.00 | 0.79 | 0.84 | 0.80 | 1.00 | 0.70 | 0.78 | 0.82 | 0.89 | 0.81 | 0.67 | 1.00 |
| a10skip | 1.00 | 0.83 | 0.94 | 0.72 | 0.85 | 0.62 | 0.82 | 0.71 | 1.00 | 0.81 | 0.94 | 0.75 | 0.96 | 0.66 | 0.88 | 0.75 |
| al1 | 1.00 | 0.77 | 0.96 | 0.94 | 0.92 | 0.81 | 0.82 | 0.76 | 1.00 | 0.81 | 1.00 | 0.90 | 0.91 | 0.77 | 0.84 | 0.85 |
| al2 | 0.97 | 0.74 | 0.99 | 0.80 | 0.96 | 0.67 | 0.82 | 0.59 | 1.00 | 0.82 | 0.88 | 0.73 | 0.95 | 0.82 | 0.94 | 0.75 |
| bn1 | 1.00 | 0.95 | 1.00 | 0.92 | 1.00 | 0.88 | 1.00 | 0.83 | 1.00 | 1.00 | 1.00 | 1.00 | 1.00 | 0.98 | 0.94 | 0.94 |
| bn2 | 1.00 | 0.92 | 1.00 | 0.92 | 1.00 | 0.88 | 1.00 | 0.82 | 1.00 | 0.88 | 1.00 | 0.89 | 0.92 | 0.83 | 0.95 | 0.84 |
| bn3 | 0.97 | 0.92 | 1.00 | 0.91 | 0.96 | 0.87 | 0.91 | 0.84 | 1.00 | 0.88 | 0.98 | 0.94 | — | — | — | — |
| choice | 0.98 | 0.72 | 0.96 | 0.84 | 0.89 | 0.72 | 0.77 | 0.80 | 1.00 | 0.75 | 1.00 | 0.83 | 1.00 | 0.73 | 0.92 | 0.86 |
| h3p4 | 0.96 | 0.78 | 0.98 | 0.76 | 1.00 | 0.71 | 0.94 | 0.69 | 1.00 | 0.75 | 0.95 | 0.80 | 0.96 | 0.80 | 0.87 | 0.82 |
| h6p18 | 1.00 | 0.69 | 1.00 | 0.84 | 1.00 | 0.82 | 1.00 | 0.79 | 0.93 | 0.78 | 1.00 | 0.80 | 1.00 | 0.84 | 0.86 | 0.82 |
| h6p30 | 0.98 | 0.77 | 0.98 | 0.83 | 0.89 | 0.76 | 0.81 | 0.70 | 1.00 | 0.81 | 0.85 | 0.78 | 0.94 | 0.83 | 0.80 | 0.80 |
| h6p36 | 1.00 | 0.74 | 0.90 | 0.86 | 0.94 | 0.80 | 0.83 | 0.72 | 1.00 | 0.75 | 0.94 | 0.82 | 1.00 | 0.76 | 0.87 | 0.81 |
| h6p41 | 0.99 | 0.79 | 1.00 | 0.80 | 0.94 | 0.78 | 0.95 | 0.77 | 0.92 | 0.80 | 1.00 | 0.79 | 0.85 | 0.81 | 0.78 | 0.82 |
| h6p45 | 0.97 | 0.73 | 1.00 | 0.72 | 0.93 | 0.69 | 0.86 | 0.73 | 0.92 | 0.77 | 1.00 | 0.75 | 0.90 | 0.82 | 0.81 | 0.76 |
| l1l | 1.00 | 0.80 | 0.91 | 0.82 | 0.84 | 0.81 | 0.78 | 0.83 | 1.00 | 0.78 | 1.00 | 0.85 | 0.88 | 0.81 | 0.73 | 1.00 |
| l2l | 1.00 | 0.93 | 1.00 | 0.83 | 0.97 | 0.92 | 0.86 | 0.89 | 0.94 | 0.96 | 1.00 | 0.87 | 1.00 | 0.89 | 1.00 | 0.90 |
| l2lOpt | 0.99 | 0.91 | 0.98 | 0.95 | 1.00 | 0.88 | 1.00 | 0.91 | 1.00 | 0.90 | 1.00 | 0.91 | 0.91 | 0.90 | 0.90 | 1.00 |
| l2lSkip | 1.00 | 0.90 | 1.00 | 0.83 | 0.98 | 0.93 | 0.89 | 0.90 | 1.00 | 0.94 | 0.97 | 0.85 | 0.90 | 0.87 | 0.90 | 0.80 |
| para5 | 0.98 | 0.83 | 1.00 | 0.82 | 0.87 | 0.80 | 0.78 | 0.83 | 0.99 | 0.92 | 0.86 | 0.82 | 1.00 | 1.00 | 1.00 | 1.00 |

probability event in the proposed algorithm. Assume two sets $S1 = \{3, 7\}$ and $S2 = \{4, 7, 8\}$, $S1 + S2 = \{\{3, 7\}, \{8\}\}$ in terms of Definition 6. It can be seen that the intersection of two sets is removed. From above analysis, it can be found that the proposed method could not achieve the best results in some rare cases (e.g., two circles on a same node and existing redundant structures). However, from another perspective, it shows that the proposed method prefer the model with low structural complexity.

For “h6p36,” the four algorithms discovered the same model shown in Figure 6(d). The mined model lacks two arcs $\langle KB, NB \rangle$ and $\langle KA, NA \rangle$, which exist in the original model (heuristic net) [19]. Through analysis, I find the original heuristic net is incorrect. From the CPN model of “h6p36,” it can be seen that the model just has two parallel paths starting with “KA” and “KB,” respectively. However, the giving heuristic net has two arcs, i.e., $\langle KA, NA \rangle$ and $\langle KB, NB \rangle$, which may lead to two nonexistent paths $\{\text{Start}, KA, NA, \text{End}\}$ and $\{\text{Start}, KB, NB, \text{End}\}$. Therefore, the mining results of four algorithms can perfectly fit to the event log in fact.

4.3.3. Noisy Event Logs. Next, the experiments were performed on 22 event logs with 5% noise. The experimental results are shown in Table 6. The performance of the HM degrades significantly. Noise also affects other two algorithms, but their performance degradation is smaller than the HM algorithm. Moreover, the ETM can also discover the optimal process models on “para5,” which did not achieve the best result before. Similarly, the average f -score of the

four algorithms are calculated (see Figure 7). It can be seen from the figure that the performance of DEMiner slightly degrades and it achieves the best results on 13 event logs. Moreover, the average f -score of the DEMiner is between 0.8 and 1.0.

Later, the experiments were performed on the event logs with 10% noise. The experimental results are listed in Table 7, and the average f -score of the four algorithms is shown in Figure 8. From the table, we can see that the DEMiner achieves the best results on 14 event logs, and the other three algorithms (from left to right) achieves the best models on 2, 7, and 4 event logs, respectively. We can see that the ETM discovers the optimal model on “a7” and “a8,” which contain 10% noise, but it does not find the optimal model on the same logs that with 5% noise. This is because the two logs are independent; i.e., the inserted noise may be totally different. Through careful comparison of Figures 7 and 8, it can be found that the performance of the DEMiner dose not degrade significantly, and it keeps in a stable level. Based on the experiments on two groups of event logs with noise, a conclusion can be drawn that the DEMiner has good antinoise ability. However, we should notice that the DEMiner cannot discover the optimal solutions on all event logs with noise. This phenomenon demonstrates that the DEMiner cannot yet avoid noise interference.

4.4. Performance on Real Event Logs. This section shows the performance of the DEMiner on two real event logs, i.e., “BPI2013cp” and “Sepsis.” In the experiments, a “start”

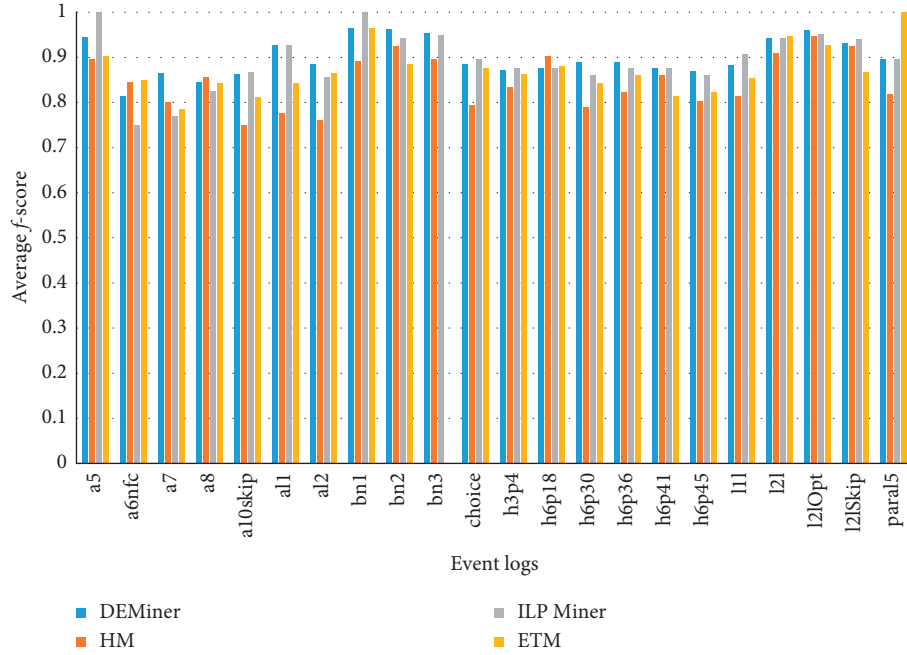
FIGURE 7: Average f -score of four algorithms on 22 event logs with 5% noise.

TABLE 7: Comparison of four algorithms' performance on 22 event logs with 10% noise.

| Eventlogs | DEMiner | | | | HM | | | | ILP Miner | | | | ETM | | | |
|-----------|---------|------|------|------|------|------|------|------|-----------|------|------|------|------|------|------|------|
| | Br | Bp | Sr | Sp | Br | Bp | Sr | Sp | Br | Bp | Sr | Sp | Br | Bp | Sr | Sp |
| a5 | 0.98 | 0.81 | 0.96 | 0.85 | 0.89 | 0.90 | 0.83 | 1.00 | 0.96 | 0.88 | 0.92 | 0.84 | 0.92 | 0.86 | 0.92 | 0.81 |
| a6nfc | 1.00 | 0.84 | 0.98 | 0.86 | 1.00 | 0.89 | 0.91 | 0.93 | 1.00 | 0.89 | 0.92 | 0.87 | 0.98 | 0.91 | 0.86 | 0.93 |
| a7 | 1.00 | 0.94 | 1.00 | 0.80 | 1.00 | 0.88 | 0.94 | 0.86 | 1.00 | 0.95 | 1.00 | 0.98 | 1.00 | 1.00 | 1.00 | 1.00 |
| a8 | 1.00 | 0.85 | 1.00 | 0.88 | 0.97 | 0.91 | 0.82 | 0.83 | 1.00 | 0.73 | 0.98 | 0.93 | 1.00 | 1.00 | 1.00 | 1.00 |
| a10skip | 0.99 | 0.76 | 0.97 | 0.69 | 0.84 | 0.73 | 0.86 | 0.70 | 0.91 | 0.79 | 0.86 | 0.73 | 0.90 | 0.74 | 0.82 | 0.62 |
| al1 | 0.97 | 0.73 | 0.91 | 0.93 | 0.91 | 0.67 | 0.75 | 0.60 | 0.95 | 0.81 | 0.85 | 0.92 | 0.92 | 0.73 | 0.84 | 0.81 |
| al2 | 0.92 | 0.80 | 1.00 | 0.75 | 0.89 | 0.73 | 0.74 | 0.79 | 0.94 | 0.79 | 0.83 | 0.84 | 0.88 | 0.62 | 0.81 | 0.80 |
| bn1 | 1.00 | 0.78 | 1.00 | 0.84 | 0.92 | 0.83 | 0.87 | 0.75 | 1.00 | 0.75 | 0.90 | 0.82 | 0.96 | 0.69 | 0.93 | 0.97 |
| bn2 | 1.00 | 0.74 | 1.00 | 0.87 | 0.98 | 0.74 | 0.93 | 0.77 | 1.00 | 0.73 | 0.99 | 0.82 | 1.00 | 0.74 | 0.95 | 0.90 |
| bn3 | 0.97 | 0.84 | 0.96 | 0.79 | 1.00 | 0.79 | 0.91 | 0.74 | 0.96 | 0.84 | 0.95 | 0.82 | — | — | — | — |
| choice | 1.00 | 0.77 | 1.00 | 0.68 | 0.95 | 0.70 | 0.80 | 0.83 | 1.00 | 0.77 | 1.00 | 0.78 | 1.00 | 0.72 | 0.94 | 0.76 |
| h3p4 | 0.98 | 0.70 | 0.96 | 0.69 | 0.95 | 0.66 | 0.89 | 0.63 | 0.93 | 0.77 | 0.92 | 0.72 | 0.96 | 0.70 | 0.85 | 0.72 |
| h6p18 | 0.92 | 0.64 | 0.90 | 0.77 | 0.96 | 0.75 | 0.95 | 0.78 | 0.92 | 0.76 | 0.92 | 0.80 | 0.93 | 0.74 | 0.92 | 0.70 |
| h6p30 | 0.96 | 0.77 | 0.97 | 0.82 | 0.96 | 0.76 | 0.95 | 0.78 | 0.95 | 0.78 | 0.96 | 0.80 | 0.92 | 0.80 | 0.86 | 0.75 |
| h6p36 | 1.00 | 0.89 | 0.80 | 0.78 | 1.00 | 0.88 | 0.84 | 0.76 | 1.00 | 0.88 | 0.81 | 0.74 | 1.00 | 0.91 | 0.85 | 0.80 |
| h6p41 | 0.96 | 0.77 | 0.98 | 0.76 | 0.91 | 0.74 | 0.92 | 0.77 | 0.93 | 0.73 | 0.95 | 0.78 | 0.87 | 0.80 | 0.88 | 0.72 |
| h6p45 | 1.00 | 0.82 | 1.00 | 0.85 | 0.94 | 0.72 | 0.88 | 0.90 | 0.96 | 0.82 | 1.00 | 0.90 | 0.90 | 0.74 | 0.83 | 0.76 |
| l1l | 1.00 | 0.75 | 1.00 | 0.84 | 0.87 | 0.75 | 0.92 | 0.80 | 1.00 | 0.78 | 0.94 | 0.85 | 0.87 | 0.75 | 0.83 | 0.82 |
| l2l | 1.00 | 0.77 | 0.99 | 0.80 | 0.98 | 0.83 | 0.91 | 0.77 | 0.99 | 0.82 | 0.95 | 0.81 | 1.00 | 0.74 | 0.98 | 0.83 |
| l2lOpt | 1.00 | 0.88 | 0.99 | 0.79 | 1.00 | 0.82 | 1.00 | 0.73 | 1.00 | 0.80 | 0.98 | 0.77 | 0.98 | 0.85 | 0.89 | 0.82 |
| l2lSkip | 0.98 | 0.75 | 0.96 | 0.73 | 0.97 | 0.80 | 0.92 | 0.74 | 0.98 | 0.77 | 0.92 | 0.80 | 0.90 | 0.75 | 0.96 | 0.76 |
| paral5 | 0.95 | 0.74 | 0.97 | 0.77 | 0.90 | 0.78 | 0.84 | 0.71 | 0.88 | 0.82 | 0.95 | 0.79 | 0.82 | 0.76 | 0.73 | 0.63 |

event as well as an “end” event was added to each trace at the running time. It ensures that each path has the same “start” node and the “end” node. To eliminate the randomness of evolution, the DEMiner was executed 10 times on each event log. The processes of evolution on two event logs are shown in Figures 9 and 10, respectively. The

ordinate denotes the completeness metric, and the abscissa denotes the number of generations, which is scaled from 1 to 100. Here, I only record the completeness value because it is monotonous. On the contrary, the precision value may fluctuate greatly along with the change in the completeness value. From the two figures, it

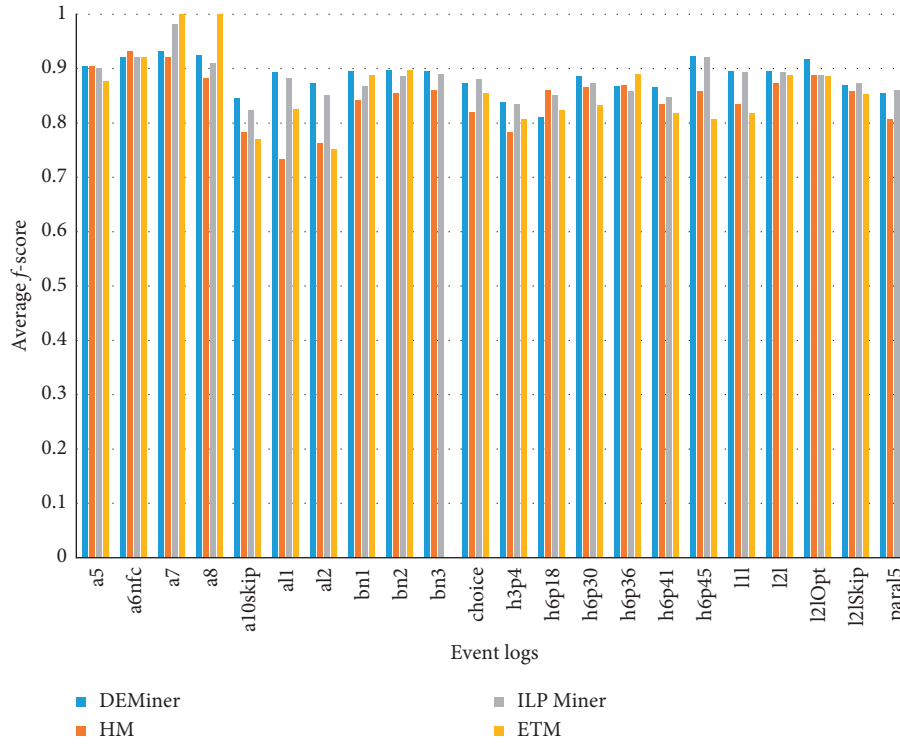


FIGURE 8: The average f -score of four algorithms on 22 event logs with 10% noise.

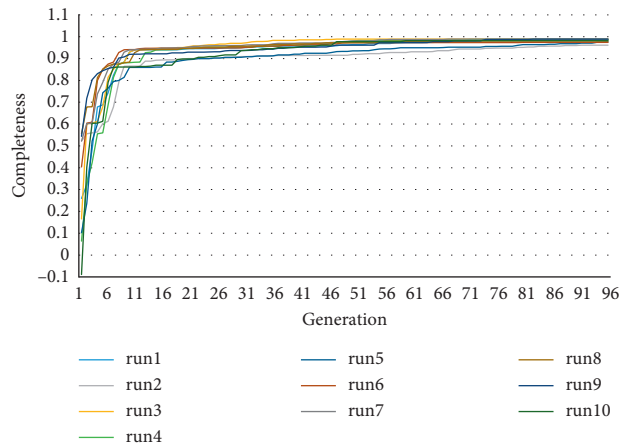


FIGURE 9: The completeness curves for 10 runs on BPI2013cp.

can be seen that the DEMiner converges fast on two event logs.

Furthermore, three metrics were employed to evaluate the efficiency of the DEMiner, which are alignment-based fitness [22], alignment-based precision [23], and the combined f -score [24]. The calculating results, including the average value and the standard deviation, are

listed in Table 8. Compared with the results given in [24], it is easy to find that the results obtained by the DEMiner is slightly lower than the result obtained by the ETM on “Sepsis,” and the results obtained by the DEMiner is better than the result obtained by the ETM on “BPI2013cp”. This proves that the DEMiner can play well on the real event logs.

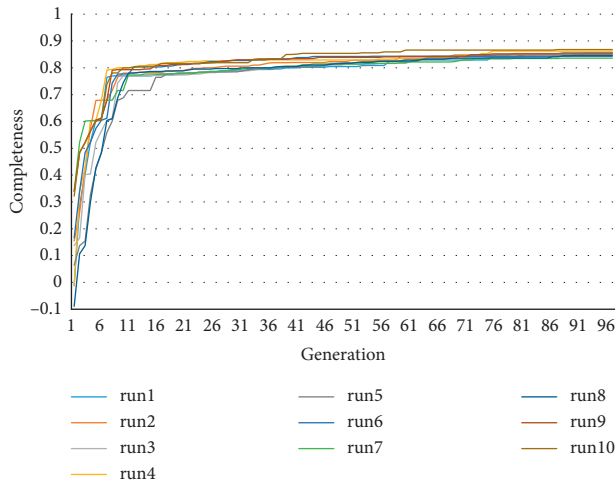


FIGURE 10: The completeness curves for 10 runs on Sepsis.

TABLE 8: The alignment-based fitness and precision of the DEMiner on two real event logs.

| Event log | Fitness | Precision | f -score |
|-----------|-----------------|-----------------|-----------------|
| BPI2013cp | 0.97 ± 0.02 | 0.82 ± 0.06 | 0.88 ± 0.04 |
| Sepsis | 0.88 ± 0.04 | 0.61 ± 0.03 | 0.72 ± 0.03 |

5. Conclusions

This paper proposes a new process mining algorithm, named DEMiner. The proposed algorithm is based on a hybrid evolutionary strategy, which consists of a set-based DE algorithm and a guided local exploration algorithm. Meanwhile, some techniques are employed to improve the efficiency of the DEMiner, such as gene bank, taboo list, and consistence repair. To evaluate the performance, 68 event logs were used in the experiments. Some conclusions can be drawn based on the experimental results:

- (1) Through comparison of the four different strategies (i.e., DE, DE + Random Search, DE + Guided Search, and GA), the “DE + Guided Search” outperforms the rest strategies and it can achieve the best quality solution as well as the fastest convergence speed. Moreover, the results prove that the DE algorithm can rapidly approximate the optimal solution, but it always suffers from premature convergence. The guided local exploration can help the DE algorithm skip out the local optimum and improve the efficiency of the proposed algorithm.
- (2) Through comparing the performance of DEMiner with three popular process mining algorithms (i.e., HM, ILP Miner, and ETM) on 22 noise-free event logs and 44 noisy event logs, it shows that the DEMiner can achieve the best result on most of the event logs. Furthermore, based on the experimental results on 2 real event logs, it can be concluded that the DEMiner can work well on real-world events logs. This proves the effectiveness and the efficiency of the proposed algorithm.

However, we can see that the DEMiner did not successfully discover an optimal process model from any one of the 44 noisy event logs. This demonstrates the drawback of the DEMiner. Besides that, it is hard for the DEMiner to discover some rare structures, such as two circles on a node. This is the future work for us.

Data Availability

The event logs used to support the findings of this study are included within the article, which can be downloaded from <https://svn.win.tue.nl/repos/prom/DataSets/GeneticMinerLogs/>. The corresponding process model can be found in [19].

Conflicts of Interest

The author declares that there are no conflicts of interest.

Acknowledgments

This work was supported by the Project of Science and Technology Bureau of Leshan (Grant no. 18JZD117), the Scientific Research Fund of Leshan Normal University (Grant no. ZZ201822), the Key Projects of Sichuan Provincial Education Department of China (Grant no. 18ZA0239), and the Project of Key Lab of Internet Natural Language Processing of Sichuan Provincial Education Department (no. INLP201903).

References

- [1] W. M. P. van der Aalst, *Process Mining: Data Science in Action*, Springer-Verlag, Berlin, Germany, 2nd edition, 2016.
- [2] W. van der Aalst, T. Weijters, and L. Maruster, “Workflow mining: discovering process models from event logs,” *IEEE Transactions on Knowledge and Data Engineering*, vol. 16, no. 9, pp. 1128–1142, 2004.
- [3] A. Medeiros, B. Dongen, W. M. P. van der Aalst et al., “Process mining for ubiquitous mobile systems: an overview and a concrete algorithm,” in *Proceedings of the Ubiquitous Mobile Information and Collaboration Systems*, pp. 156–170, Riga, Latvia, June 2004.
- [4] L. Wen, W. M. P. van der Aalst, J. Wang, and J. Sun, “Mining process models with non-free-choice constructs,” *Data Mining and Knowledge Discovery*, vol. 15, no. 2, pp. 145–180, 2007.
- [5] S. J. van Zelst, B. F. van Dongen, W. M. P. van der Aalst, and H. M. W. Verbeek, “Discovering workflow nets using integer linear programming,” *Computing*, vol. 100, no. 5, pp. 529–556, 2018.
- [6] S. J. J. Leemans, D. Fahland, and W. M. P. van der Aalst, “Discovering block-structured process models from event logs containing infrequent behaviour,” in *Proceedings of the 2013 Business Process Management Workshops*, pp. 66–78, Beijing, China, August 2013.
- [7] S. J. J. Leemans, D. Fahland, and W. M. P. van der Aalst, “Scalable process discovery and conformance checking,” *Software & Systems Modeling*, vol. 17, no. 2, pp. 599–631, 2018.
- [8] A. K. A. de Medeiros, A. J. M. M. Weijters, and W. M. P. van der Aalst, “Genetic process mining: an

- experimental evaluation,” *Data Mining and Knowledge Discovery*, vol. 14, no. 2, pp. 245–304, 2007.
- [9] H.-J. Cheng, C. Ou-Yang, and Y.-C. Juan, “A hybrid approach to extract business process models with high fitness and precision,” *Journal of Industrial and Production Engineering*, vol. 32, no. 6, pp. 351–359, 2015.
- [10] C. Ou-Yang, H.-J. Cheng, and Y.-C. Juan, “An integrated mining approach to discover business process models with parallel structures: towards fitness improvement,” *International Journal of Production Research*, vol. 53, no. 13, pp. 3888–3916, 2014.
- [11] B. Vázquez-Barreiros, M. Mucientes, and M. Lama, “Pro-DiGen: mining complete, precise and minimal structure process models with a genetic algorithm,” *Information Sciences*, vol. 294, pp. 315–333, 2015.
- [12] J. C. A. M. Buijs, B. F. van Dongen, and W. M. P. van der Aalst, “A genetic algorithm for discovering process trees,” in *Proceedings of the IEEE Congress Evolutionary Computation*, pp. 1–8, Brisbane, Australia, June 2012.
- [13] J. C. A. M. Buijs, B. F. van Dongen, W. M. P. van der Aalst et al., “On the role of fitness, precision, generalization and simplicity in process discovery,” in *Proceedings of the on the Move to Meaningful Internet Systems Conference*, pp. 305–322, Rome, Italy, September 2012.
- [14] M. L. van Eck, J. C. A. M. Buijs, and B. F. van Dongen, “Genetic process mining: alignment-based process model mutation,” in *Business Process Management Workshops*, pp. 291–303, Springer, Cham, Switzerland, 2014.
- [15] S. Das and P. N. Suganthan, “Differential evolution: a survey of the state-of-the-art,” *IEEE Transactions on Evolutionary Computation*, vol. 15, no. 1, pp. 4–31, 2011.
- [16] W. van der Aalst, A. Adriansyah, and B. van Dongen, “Replaying history on process models for conformance checking and performance analysis,” *Wiley Interdisciplinary Reviews: Data Mining and Knowledge Discovery*, vol. 2, no. 2, pp. 182–192, 2012.
- [17] B. Xu, X. Chen, X. H. Huang, and L. Tao, “A multistrategy-based multiobjective differential evolution for optimal control in chemical processes,” *Complexity*, vol. 2018, Article ID 2317860, 22 pages, 2018.
- [18] W. N. Chen, J. Zhang, H. S. H. Chung et al., “A novel set-based particle swarm optimization method for discrete optimization problems,” *IEEE Transactions on Evolutionary Computation*, vol. 14, no. 2, pp. 278–300, 2010.
- [19] A. K. Alves de Medeiros, *Genetic process mining*, Ph.D. thesis, Eindhoven Universiteit of Technology, Eindhoven, Netherlands, 2006.
- [20] A. J. M. M. Weijters and J. Ribeiro, “Flexible heuristics miner (FHM),” in *Proceedings of the IEEE Symposium on Computational Intelligence and Data Mining*, pp. 310–317, Paris, France, April 2011.
- [21] B. van Dongen, A. K. Alves de Medeiros, H. M. W. Verbeek et al., “The prom framework: a new era in process mining tool support,” in *Proceedings of the 26th International Conference on Applications and Theory of Petri Nets*, pp. 444–454, Miami, FL, USA, June 2005.
- [22] A. Adriansyah, B. van Dongen, and W. M. P. van der Aalst, “Conformance checking using cost-based fitness analysis,” in *Proceedings of the 15th IEEE International Enterprise Distributed Object Computing Conference*, pp. 55–64, Helsinki, Finland, August 2011.
- [23] A. Adriansyah, J. Munoz-Gama, J. Carmona et al., “Alignment based precision checking,” in *Proceedings of the International Workshop on Business Process Intelligence*, pp. 137–149, Tallinn, Estonia, September 2012.
- [24] A. Augusto, R. Conforti, M. Dumas et al., “Automated discovery of process models from event logs: review and benchmark,” *IEEE Transactions on Knowledge and Data Engineering*, vol. 31, no. 4, pp. 686–705, 2019.

Research Article

Freight Time and Cost Optimization in Complex Logistics Networks

Egemen Sert,^{1,2} Leila Hedayatifar ,¹ Rachel A. Rigg,¹ Amir Akhavan,¹ Olha Buchel,¹ Dominic Elias Saadi,¹ Aabir Abubaker Kar,¹ Alfredo J. Morales,¹ and Yaneer Bar-Yam¹

¹New England Complex Systems Institute, 277 Broadway, Cambridge, MA 02139, USA

²Department of Electrical and Electronics Engineering, Middle East Technical University, Ankara, Turkey

Correspondence should be addressed to Leila Hedayatifar; leila@necsi.edu

Received 12 November 2019; Accepted 3 February 2020; Published 29 February 2020

Guest Editor: Tomas Veloz

Copyright © 2020 Egemen Sert et al. This is an open access article distributed under the Creative Commons Attribution License, which permits unrestricted use, distribution, and reproduction in any medium, provided the original work is properly cited.

The complexity of providing timely and cost-effective distribution of finished goods from industrial facilities to customers makes effective operational coordination difficult, yet effectiveness is crucial for maintaining customer service levels and sustaining a business. Logistics planning becomes increasingly complex with growing numbers of customers, varied geographical locations, the uncertainty of future orders, and sometimes extreme competitive pressure to reduce inventory costs. Linear optimization methods become cumbersome or intractable due to the large number of variables and nonlinear dependencies involved. Here, we develop a complex systems approach to optimizing logistics networks based upon dimensional reduction methods and apply our approach to a case study of a manufacturing company. In order to characterize the complexity in customer behavior, we define a “customer space” in which individual customer behavior is described by only the two most relevant dimensions: the distance to production facilities over current transportation routes and the customer’s demand frequency. These dimensions provide essential insight into the domain of effective strategies for customers. We then identify the optimal delivery strategy for each customer by constructing a detailed model of costs of transportation and temporary storage in a set of specified external warehouses. In addition, using customer logistics and the k -means algorithm, we propose additional warehouse locations. For the case study, our method forecasts 10.5% savings on yearly transportation costs and an additional 4.6% savings with three new warehouses.

1. Introduction

Logistics is widely recognized as the most complex among business processes. The challenge of coordinating with multiple suppliers for raw materials and partially finished goods, and the challenge of delivering next-stage finished goods to customers, all in the correct amounts in a timely fashion and in coordination with production processes, despite uncertainty due to independent decision-making of customers, is daunting. These coordination processes are particularly challenging because of the need to optimize costs and maximize customer satisfaction. It is particularly difficult to keep transportation networks optimized when operations span thousands of miles and serve thousands of customers. Logistics is known to be a highly complex challenge that is not amenable to traditional linear optimization strategies due to

its high dimensionality and rigidity in the face of limited accuracy and variation of conditions [1–3]. Optimizing a nonlinear system is quite challenging as the output solution is not unique and simply a linear combination of the independent parts [4]. So while mathematical models should be helpful to explore the space of possible strategies and propose optimal solutions when operations become complex [5], solving such models becomes more difficult as the number of strategies and considered variables increases [6].

The issue of complexity in supply chains has been explored from a number of perspectives [7–12]. The literature on these problems, generally divided into the location-routing problem (LRP) [13–15] and the warehouse location problem (WLP) [16–18], provides a range of proposed solutions. For both the LRP and the WLP, there is an objective function to be minimized. The function may consider the

freight cost from production facilities to customers, the storage cost for storing goods in warehouses, and the cost for opening new warehouses. Each approach involves imposing constraints on the objective function to make the optimization more reliable, which makes the solution harder and more time-consuming for large complex systems. Therefore, the LRP and WLP together remain open problems in the field of supply chain management, requiring further improvements in analytical methods.

Solutions to the LRP typically are addressed with capacity constraints on warehouses and/or vehicles, called the capacitated LRP (CLRP) [13, 14, 19, 20]. Capacity can refer to the capacity of warehouses to store goods, the number of vehicles for transport, or the carrying capacity of vehicles. The objective is to find an optimum set of routes that minimizes the total transport distance so that each customer is served with a compatible vehicle and the total demand by customers per route is compatible with the capacity of vehicles on that route [21]. The time window of deliveries is another constraint that can be considered, which suggests a hybrid multiobjective algorithm [22]. The multiechelon LRP (LRP-2E) is another set of solutions to optimize freight costs and delivery time by adding a new layer to the logistic network [23–30], resulting in three layers: production facilities, external warehouses, and customers. Solutions to the WLP typically recommend optimal new warehouse locations to more efficiently serve customers [17, 31]. In most of the problems, a set of potential warehouses with known opening or storage costs is considered. Decisions are made about which warehouses (distribution centers or depots) to keep open to minimize route costs. These methods are categorized into two classes, uncapacitated and capacitated facility location problems [32–34]. For capacitated facility location problems, one more constraint is added to the objective function [35–37]. The uncapacitated facility location problem simplifies to a k -means or k -medians clustering problem [38–40] when the facility opening cost or storage cost is considered to be zero [33].

Here, we show that a simplified parameterized space can provide insight into the optimization challenge and a more detailed quantitative modeling approach that focuses on the relevant details can be successfully applied to real-world optimization with substantial financial benefits for an industrial company. We propose two models to optimize companies' logistics networks, including the route from production facilities to the customers, by using existing warehouses and also recommending additional warehouse locations. To address the LRP, we define a customer space to better clarify the complexity in the logistics of customer-warehouse routes. The space is classified with two strategies: direct and indirect shipment strategies. In the direct strategy, goods are sent to the customer directly from a production facility using box or bulk trucks. In the indirect strategy, in advance of an order by the customer, goods are shipped to an external warehouse near the customer using trains and then "last-mile" shipped by trucks when orders are placed. Our methods identify the strategy for each customer that is most cost-effective and enables delivery to the customer within a predefined time interval. The choice of strategies and

vehicles depends on the frequency of orders and amount of demand from customers. To address the WLP, in addition to optimization over existing facilities, we identified potential additional warehouse locations using the k -means algorithm weighted by the customer demand quantity. With these new warehouses, we estimate that savings can be further increased. We apply these methods to a medium-sized American manufacturing company with a particular logistics network, consisting of multiple production facilities, external warehouses, and customers along with three types of shipment methods (box truck, bulk truck, and train).

The rest of this paper is organized as follows: In Section 2, we describe our methodology, including the design of a customer space, a mathematical model to characterize customers and determine favorable strategies for each customer type, and a method to optimize warehouse locations. In Section 3, we describe our results that demonstrate effective optimization of shipment and storage costs. In Section 4, we summarize our conclusions.

2. Methodology and Framework

2.1. Customer Space. In order to develop a general understanding of the assignment of strategies to customers and the effectiveness of each strategy, we first created a descriptive model of customer characteristics named the "customer space" (see Figure 1). Each customer is characterized by two variables: the distance of the most used shipment route from the customer to the production facility and the customer demand frequency. The demand frequency is the ratio of the total quantity ordered by the customer to the customer life span using historical corporate data. The expected relationship between these two variables and the choice of strategies is as follows:

- (i) The direct strategy is most effective for (1) customers close to production facilities, regardless of demand frequency, or (2) customers who order rarely, regardless of distance, as illustrated by the blue region in Figure 1(b). For close customers, maintaining an external warehouse is unnecessary given that the proximity of customers ensures rapid delivery. For low-demand customers, the uncertainty of order arrivals makes it inefficient to plan ahead, and shipping directly is a practical solution.
- (ii) The indirect strategy becomes optimal when the customer's distance to production facilities is long and orders are frequent above a certain level, as illustrated by the green region in Figure 1(b). When both demand and distance are large enough, the certainty of ordering behavior supports the replenishment of inventory in external facilities before the customer even places the next order. Cheaper, slower transportation alternatives are possible between production facilities and external warehouses. When the customer places the next order, the goods will already be at the external warehouse and can be rapidly delivered to the customer. This indirect strategy may reduce transportation-

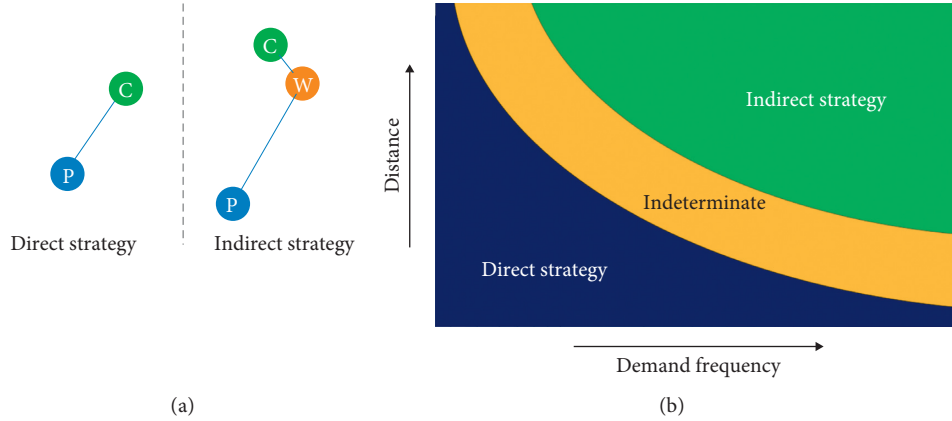


FIGURE 1: Shipping strategies. (a) The direct strategy (left) consists of shipping goods from the production facility (blue circle) to customers (green circle). The indirect strategy (right) delivers goods first to an external warehouse (orange circle), where goods are stored and subsequently shipped to customers (green circle). (b) Overview of the customer space and the associated optimal transportation strategies.

associated costs while preserving or even improving customer satisfaction.

- (iii) The best strategy for customers with intermediate distance and intermediate demand will depend upon details of the freight and storage cost information, as illustrated by the yellow region in Figure 1(b).

2.2. Optimization via Route Strategies. To solve the problem of choosing the best storage and transportation strategy for each customer, we first constructed a model of the costs of shipment and storage to decide between direct and indirect strategies. The better strategy depends on the direct delivery time and on analysis of cost of shipment and storage. We defined the direct delivery time as the time between the shipment of a good and its delivery to the customer. According to corporate policy, the maximum delivery time for finished goods is set to two days for customer satisfaction. Delivery time is calculated using truck speeds of 70 miles per hour and 8 hours of driving per day and railcar speeds of 49 miles per hour and 24 hours of travel per day. If the time of direct delivery is more than two days, adequate customer satisfaction requires using the indirect strategy as an imposed constraint.

The mathematical model evaluates the costs of the direct and indirect strategies and includes a production facility (P), external warehouse (W), and customer (C), as illustrated in Figure 2. The potential costs include c_d , the cost of shipment from P to C; c_w , the cost of shipment from P to W; c_s , the cost of storage at W; and c_o , the cost of shipment from W to C. The freight costs c_d , c_w , or c_o must also be multiplied by the number of shipments n_d , n_w , or n_o , respectively. The number of shipments depends on the demand from the customer. The customer's expected demand over a year is estimated to be the demand frequency multiplied by the days in a year. We considered the number of shipments in a year to be the ratio of total demand to the shipment carrying capacity of trucks and railcars. The cost J for a given strategy π is then

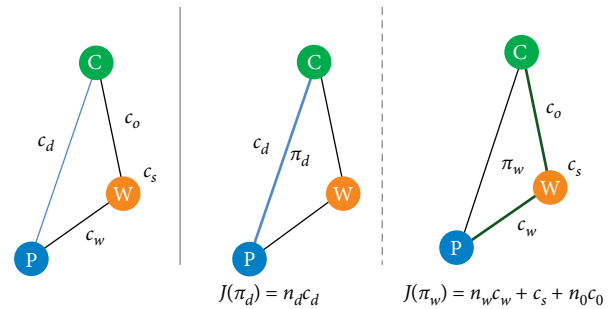


FIGURE 2: Shipping strategies of a product from a production facility (P) to a customer (C), with an option to use an external warehouse (W). Strategies are associated with freight and storage costs. Costs c_d , c_w , and c_o represent the freight costs associated with the respective labelled transportation links. The cost c_s denotes the storage cost of the material in the external warehouse (W). The number n denotes the number of times the shipment is made. Every strategy π is associated with a cost $J(\pi)$.

determined for the direct strategy as $J(\pi_d) = n_d c_d$ and the indirect strategy as $J(\pi_w) = n_w c_w + c_s + n_o c_o$.

Storage and freight costs depend on various parameters in the model. We calculated these costs directly based upon detailed descriptions of those costs that vary between shippers and warehouses. The storage cost c_s depends on (1) the storage facility type s , (2) the quantity that is stored q (inventory cost), (3) the time the quantity is stored t , and (4) loading u and unloading w events, giving $c_s = S(s, q, t, u, w)$. The freight cost $c_f \in \{c_d, c_w, c_o\}$ depends on (1) the carrier type s' , (2) the distance the goods are sent d , and (3) the quantity of the goods q' , giving the relationship $c_f = F(s', d, q')$. In order to calculate the actual cost based upon the company data, we extracted existing routes along with their associated distances from historical data and incorporated specific storage costs.

Finally, we defined savings for strategies as follows: Each customer i should have an optimal shipping cost, designated C_i , which also includes storage costs if present. Each customer has a current shipment route (designated route 0),

which has a known cost $C0_i$. We then independently calculated the lowest cost route (designated route 1), which has a cost $C1_i$. We calculated $C1_i$ by examining nearest warehouses and incorporating storage costs and transportation costs. Finally, we compared the current cost to our calculated costs, and if $C1_i < C0_i$, then the preferred cost, C_i , equals $C1_i$ or otherwise $C_i = C0_i$. From this, we calculated total percent savings (S) for all customers as a percentage: $S = 100 * (1 - (\sum_{i=1}^N C_i) / (\sum_{i=1}^N C0_i))$. Here, N is the total number of customers.

2.3. Optimization via Additional Warehouses. Aside from the existing external warehouses, we identified prospective locations for new warehouses for additional savings. In order to determine potential locations, we used the k -means algorithm [38–40] to find the optimum locations for the warehouses that best match the locations of customers to minimize the freight cost across all customers, C_f . Freight cost of transporting demands from the j -th warehouse to the i -th customer, A_{ij} , is the price of consumed fuel by the vehicles shipping the goods, but here it was defined as direct incurred shipping cost for the shipments in the database. It is weighted based on the overall amount of demands by customers shipped from a warehouse, D_{ij} , and is a function of the Euclidean distance, d_{ij} , between the i -th customer and the j -th warehouse:

$$\begin{aligned} C_f &= \sum_{i=1}^N \sum_{j=1}^M A_{ij} x_{ij} \\ \text{minimize} \quad & A_{ij} = F^P \times R \times D_{ij} \times d_{ij} \end{aligned} \quad (1)$$

$$\begin{aligned} \text{subject to} \quad & d_{ij} = \|w_j - c_i\| \\ & x_{ij} \in \{0, 1\}, \quad \forall i \in C, j \in W, \end{aligned}$$

$$\sum_{i=1}^N x_{ij} = 1, \quad \forall j \in W, \quad (2)$$

where the variable x_{ij} equals 1 if the customer i is served by the warehouse j and equals 0 if it is not and N and M are the number of customers and warehouses. We assigned customer demand weights according to $W_i = \lceil \sum_{k=0}^{n_i} Q_k / Q_0 \rceil$, where n_i is the number of orders by the customer i , Q_k is the quantity of the order k by the customer i , and Q_0 is an industry standard measure for a significant customer volume. The brackets $\lceil x \rceil = \text{ceil}(x)$ indicate the smallest integer greater than x . In fact, Q_0 corresponds to the average shipment size by standard vehicles. So, $D_{ij} = W_i$ if $x_{ij} = 1$; otherwise, it is 0. In the calculation of d_{ij} , c_i and w_j refer to the geographical location of customers and warehouses, respectively. Equation (2) indicates that each customer is only connected to one warehouse. Here, F^P refers to the fuel price and R refers to the average fuel consumption rate by vehicles. For simplicity, we considered one type of vehicle with a fixed shipment size.

We use the k -means algorithm to aggregate the customer locations into k disjoint groups or clusters and find a centroid C_k for each group to minimize the average squared

distance between the centroid and customer locations within each group. To consider the weight of customer demands, we assigned W_i points to the location of each customer i . The number of groups to be found is a parameter of the analysis. The algorithm is an iterative refinement technique that starts from random locations for centroids and updates the location of centroids in each iteration until reaching an optimum location for all the centroids. We considered the centroid to be an approximate optimum location for a warehouse assigned to the customers of a group. The freight cost from warehouses to customers inside the groups decreases as the number of centroids increases and slowly converges to zero. We determined the optimum number of centroids from the deceleration in the freight cost. We compared the location of currently active warehouses with the location of centroids, identifying the best locations for the additional warehouses to decrease the transportation costs. The k -means analysis dramatically reduces the number of candidate locations to be considered for cost optimization.

We added the new warehouse locations proposed by our analysis to the system. Since we cannot know the storage cost of a theoretical warehouse, we used three representative storage costs (high, medium, and low cost) based on existing warehouses to model storage costs for the proposed warehouses. We calculated potential savings for each proposed warehouse using the three cost levels.

3. Results

We tested our model on a dataset from a medium-sized manufacturing company with more than fifteen years of customer orders. The company and its customers are located primarily in the US. The logistics network has about 15 production facilities and more than 30 external warehouses and serves more than 2000 customers. The majority of the customers have not ordered more than 10 times, and due to the lack of data on these customers' ordering patterns, the direct shipment method is always chosen by the company (as discussed in Section 2.1). Therefore, we excluded customers with 10 or fewer orders from our analysis. Customers who have ordered more than 10 times may benefit from either the direct or the indirect strategy, so we chose these customers (≈ 300 customers) for analysis. Our goal was to find the strategy that minimizes the total cost for each customer. First, we estimated the total cost of each strategy from freight costs of each shipment and associated storage costs, where present. In addition to estimating the total cost of each strategy for existing warehouses, we proposed additional warehouse locations by performing clustering on the geographical location data of customers weighted by the total quantity ordered.

In order to estimate freight costs, we observed the freight costs of direct and indirect strategies used for each customer including the freight options and location data. The indirect strategy is associated with multiple shipments: one shipment from the production facility to the external warehouse and one or multiple subsequent shipments from the warehouse to the customer. Each shipment is made with one of the

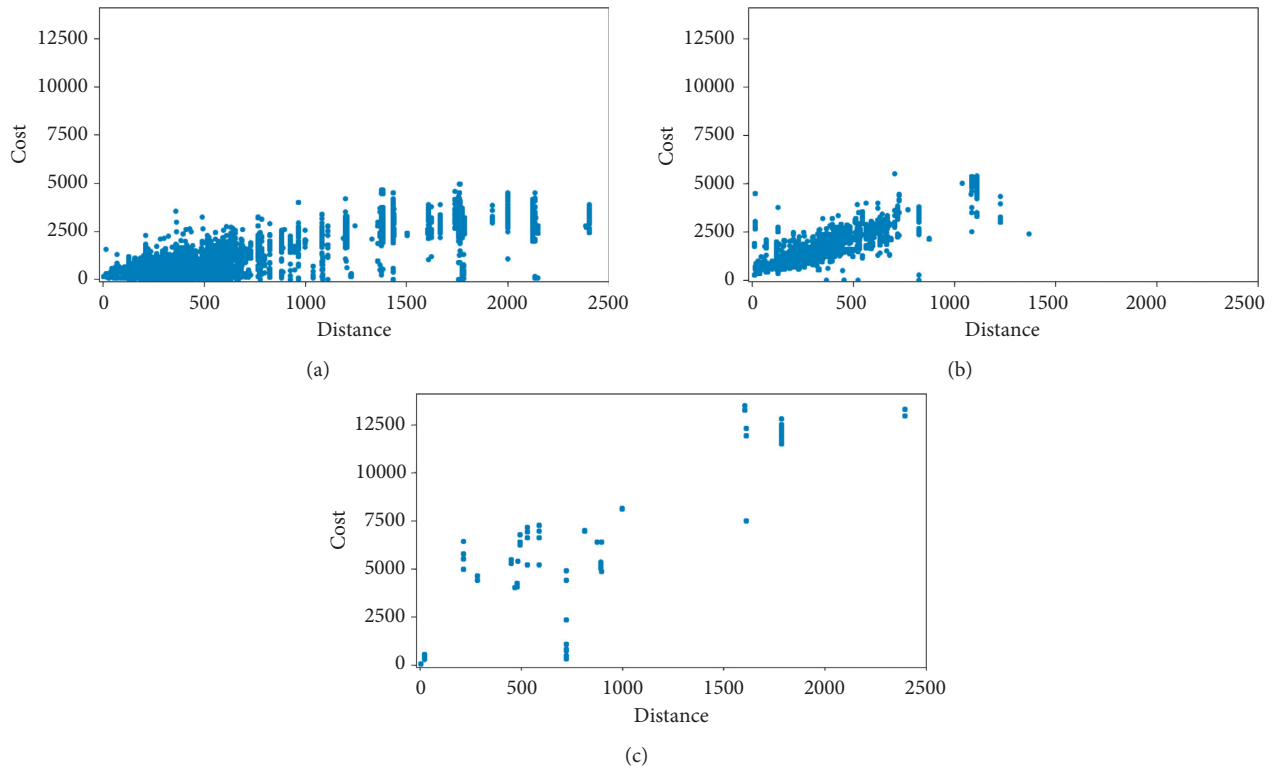


FIGURE 3: Cost versus shipping distance using actual data for three transportation options: (a) box truck; (b) bulk truck; (c) train.

following three types of vehicles: box truck, bulk truck, and train. The costs of each type are given in Figures 3(a)–3(c) for box truck, bulk truck, and train shipments, respectively. High variance in freight costs is due to different carriers having different pricing structures. Carriers may charge by distance, quantity, or both. For better classification, we obtained the freight costs of carriers by performing multiple linear regression analysis on each carrier’s historical data to extrapolate the freight costs for possible routes. We constrained the parameters of the regression model to be positive. The decomposition of the freight costs by carriers is shown in Appendix in Figures 7–9 for box truck, bulk truck, and train shipments, respectively. The plots indicate that different carriers may be specialized for different distances, different quantities, and particular customers.

In the indirect strategy, the storage cost of external warehouses is a key factor in addition to the freight cost. The benefit of using an external warehouse depends on (1) distances from the warehouse to the production facility and the customer and (2) storage costs. The shipping distance affects associated freight costs. The storage pricing is unique to each individual warehouse and is determined based upon the quantity stored, the duration of the storage, and the number of loading and unloading events that occur. Detailed cost specifications were provided by the company for each external warehouse in use. These were used for calculating the cost of the indirect strategy.

We have identified a change in strategy by the company over time in the customer space, as shown in Figure 4. Figure 4(a) shows strategy decisions for all years of the

dataset, and Figure 4(b) shows decisions for only the last two months. Green x’s denote customers for which the indirect strategy has been used at least once, while blue dots denote customers for which only the direct strategy has been used. As shown in Figure 4(a), for many customers, the indirect strategy has been used at least once regardless of demand frequency, except for demand frequency below 600 lbs/day, in which case only the direct strategy is used. For customers with large distances from production facilities, the company has used the indirect strategy for customers with high demand frequency but not for customers with low demand frequency. Meanwhile, the data for the last two months in Figure 4(b) show a change in corporate strategy, with a significant drop in the number of customers serviced by the indirect strategy. We can infer from the graph that the key variable used for strategy selection is still demand frequency, with a higher demand frequency increasing the chance of using the indirect strategy.

After fitting our model to the historical company data, we extracted optimal strategies for servicing customers. Then, we identified which strategy should optimally be used across the customer space (Figure 5). Blue dots denote customers correctly serviced with the direct strategy. Yellow triangles denote customers serviced with the direct strategy that would benefit from the indirect strategy. Green x’s denote customers correctly serviced with the indirect strategy. Magenta squares denote customers serviced with the indirect strategy that would benefit from changing external warehouses. Finally, red stars denote customers serviced with the indirect strategy that would benefit from using

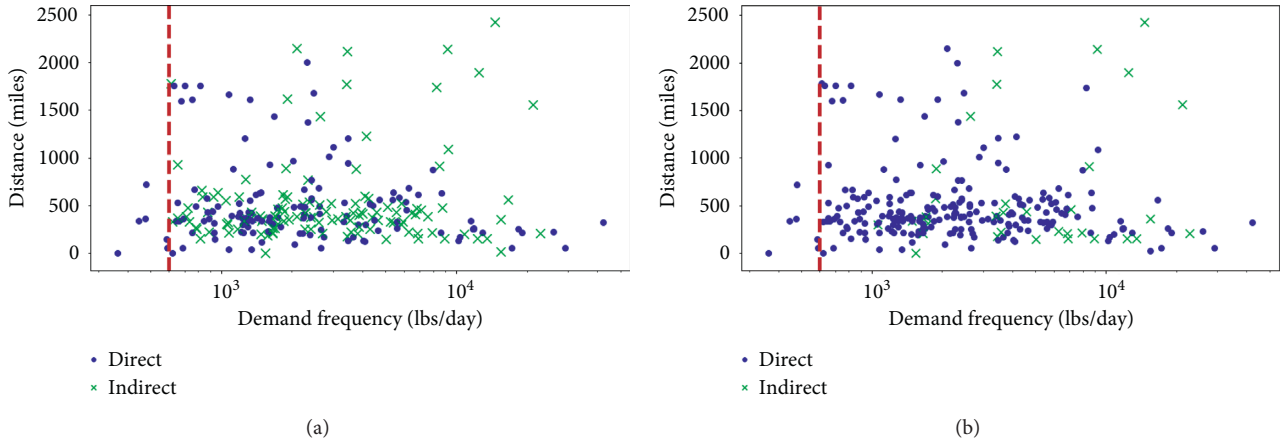


FIGURE 4: Distance versus demand frequency. Green x's denote customers that were serviced by the indirect strategy at least once, and blue dots denote customers that were only serviced by the direct strategy. Red dotted lines represent a demand frequency of 600 lbs/day; customers with a lower demand frequency only received goods by the direct strategy, per company policy. (a) All historical company data. (b) The last two months of data.

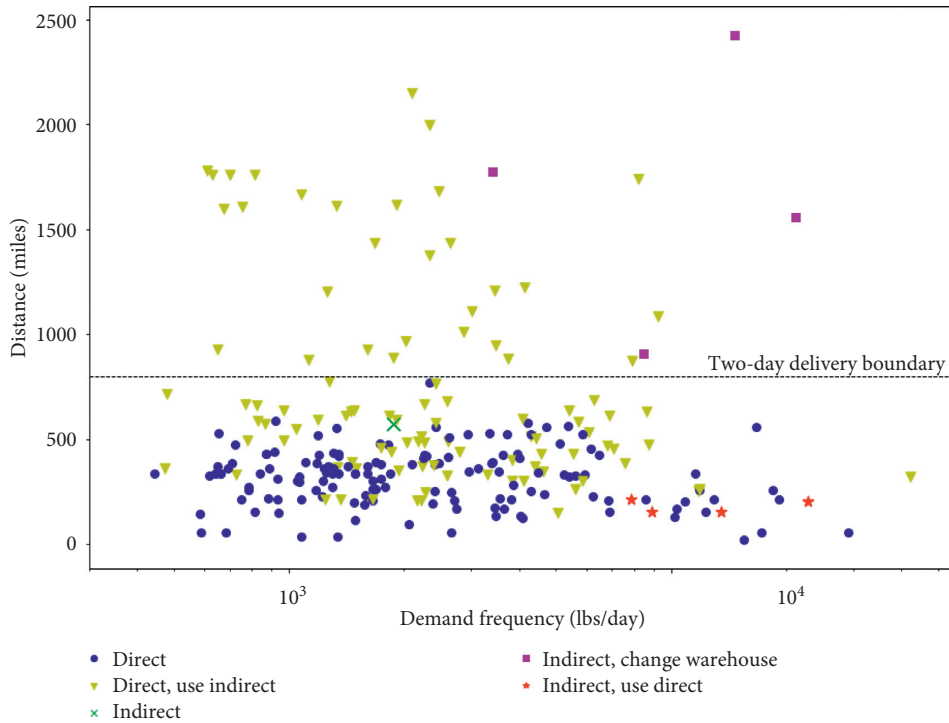


FIGURE 5: Optimal strategies for the customers shown on the customer space (distance versus demand frequency). Blue circles and green x's show customers correctly serviced by direct and indirect strategies. The rest shows the serviced strategies that must be changed to optimize the freight cost.

the direct strategy. We calculated the potential savings by comparison of the historical strategies with the proposed ones. In total, the model predicts 10.5% savings if shipments and warehouses are optimized over the current options.

In addition to the analysis of the existing warehouses, we incorporated optimum locations for extra warehouses to increase the savings. Figure 6 shows the results of warehouse optimization using the k -means algorithm. The algorithm identifies warehouse locations that minimize the freight costs, C_f , from customers to their nearest warehouse

(Figure 6(a)). The algorithm takes as the input the number of warehouses to be determined. When the number of warehouses is below 10, adding any new warehouses leads to a sharp decrease in the value of C_f , but the effect slows down for larger numbers of warehouses. The orange line shows the actual freight cost for the demands by customers which is comparable with the freight cost from a single warehouse to the customers. Note that the total number of the company's production facilities and warehouses is more than 45. In many of the shipments, the company served a customer

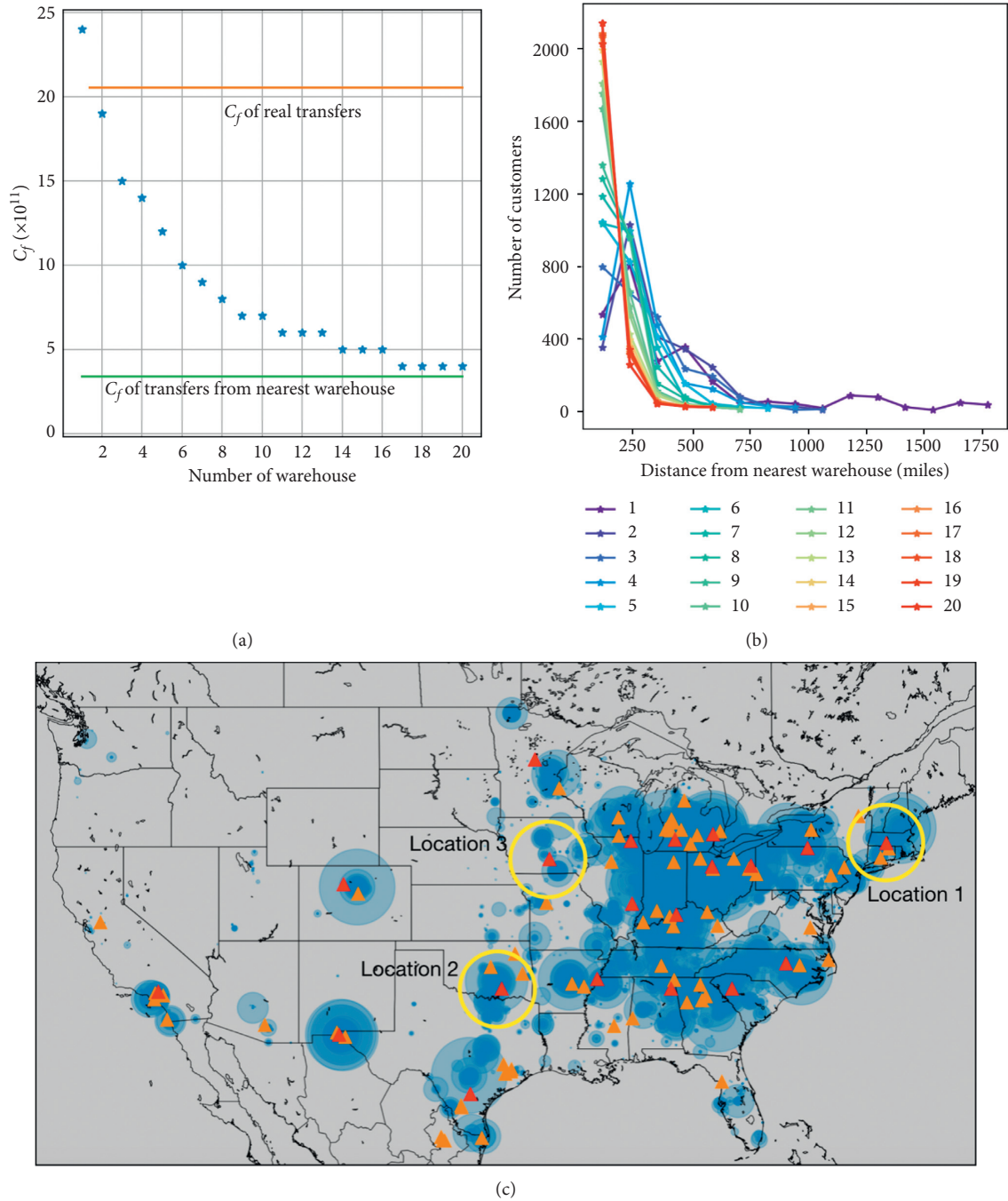


FIGURE 6: Optimal warehouse locations proposed by the k -means algorithm. (a) Freight cost decreases by increasing the number of optimized warehouses. Orange and green lines show the actual freight cost and the freight cost of transfers from the current nearest company warehouses. (b) Distribution of customers based on their distance from the nearest warehouse. (c) A network of customers (blue circles) and current (orange triangles) and optimized (red triangles) warehouse locations. Yellow circles denote geographical areas where candidate warehouses should be placed but that currently have inactive warehouses (Locations 1 and 2) or no warehouse (Location 3).

TABLE 1: Potential cost savings if additional warehouses are utilized.

| Location | Storage cost (%) | | |
|------------|------------------|--------|------|
| | High | Medium | Low |
| Location 1 | 10.5 | 10.5 | 11.0 |
| Location 2 | 10.5 | 10.5 | 10.7 |
| Location 3 | 10.7 | 11.5 | 14.4 |
| All | 10.7 | 11.5 | 15.1 |

The first three rows represent the total corporate savings of optimized delivery with the addition of one warehouse. The final line is the total savings with all three of the additional warehouses. The labels high, medium, and low denote the reference values used to calculate storage costs for the additional locations.

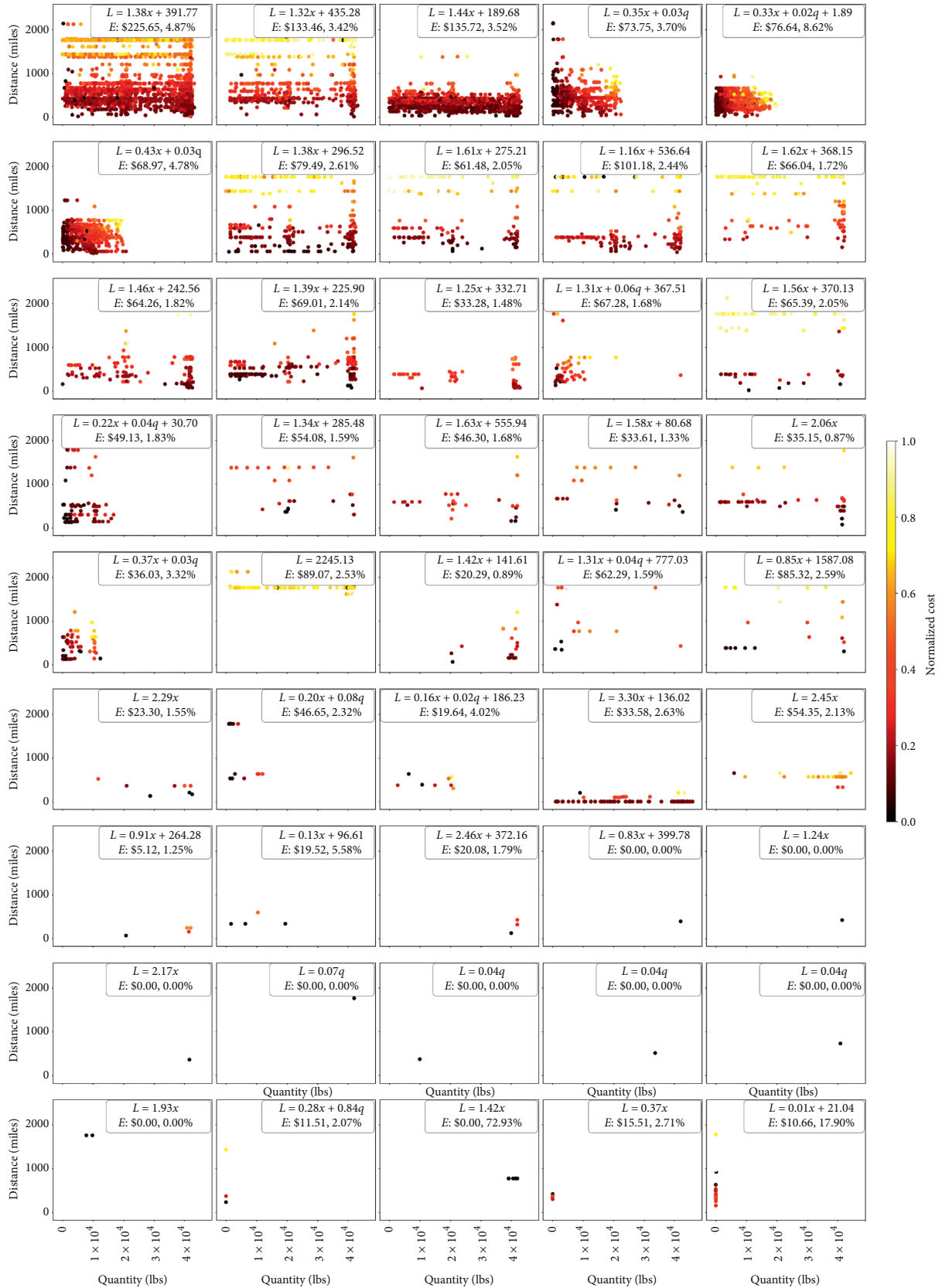


FIGURE 7: Distance versus quantity scatter plots for box truck carriers. Color indicates freight cost (key on right), normalized to $[0, 1]$ for each carrier to have a minimum cost of 0 and a maximum cost of 1. Cost equations are obtained by performing regression analysis on each carrier. Weights are constrained to have positive values. In each cost equation (inset), L indicates the cost equation of the carrier, x denotes the distance in miles, q denotes the quantity in pounds, and E denotes the absolute error of the cost regression in dollars and as a percentage. Carrier names are omitted to preserve anonymity.

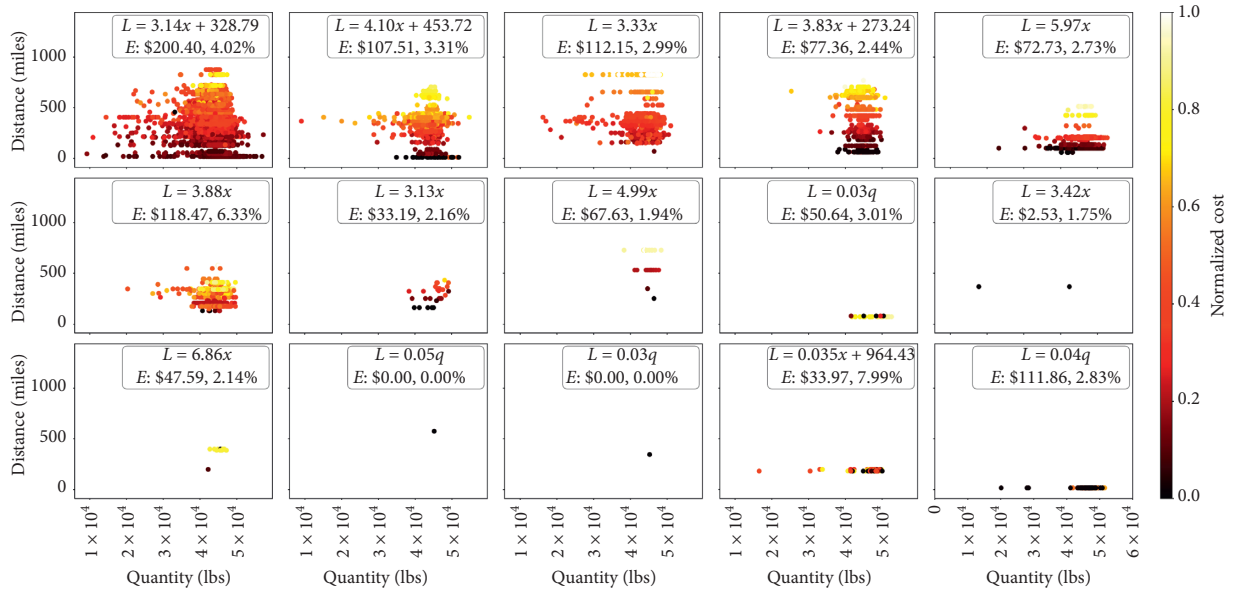


FIGURE 8: Distance versus quantity scatter plots for bulk truck carriers. Color indicates freight cost (key on right), normalized to [0, 1] for each carrier to have a minimum cost of 0 and a maximum cost of 1. Cost equations are obtained by performing regression analysis on each carrier. Weights are constrained to have positive values. In each cost equation (inset), L indicates the cost equation of the carrier, x denotes the distance in miles, q denotes the quantity in pounds, and E denotes the absolute error of the cost regression in dollars and as a percentage. Carrier names are omitted to preserve anonymity.

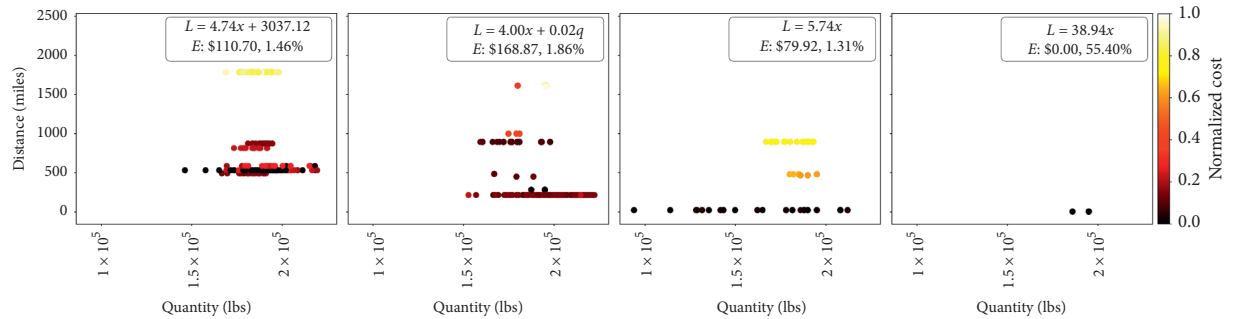


FIGURE 9: Distance versus quantity scatter plots for train carriers. Color indicates freight cost (key on right), normalized to [0, 1] for each carrier to have a minimum cost of 0 and a maximum cost of 1. Cost equations are obtained by performing regression analysis on each carrier. Weights are constrained to have positive values. In each cost equation (inset), L indicates the cost equation of the carrier, x denotes the distance in miles, q denotes the quantity in pounds, and E denotes the absolute error of the cost regression in dollars and as a percentage. Carrier names are omitted to preserve anonymity.

from a very large distance. The green line shows the freight cost if the customers have been served from their nearest warehouse which is comparable with the freight cost of shipping from 20 optimally located warehouses. In Figure 6(b), we indicate the distribution of customers based on their distance from the nearest optimized warehouse. In the presence of one optimized warehouse, most of the customers have a distance larger than 250 miles. However, adding the second and third optimized warehouses drastically reduces the distance between customers and nearest warehouses. The distances change gradually for higher numbers of warehouses.

Figure 6(c) shows the locations of all company facilities and external warehouses (orange triangles) and customers (blue circles) around the US. We randomized the location of

actual warehouses and customers for confidentiality. The size of the circles is proportional to the total order quantity by each customer, such that the more the orders a customer has placed, the larger the size of the circles. The figure shows the optimum warehouse locations (red triangles) recommended by the k -means algorithm for 20 warehouses. Some of the k -means recommended locations are not located near active warehouses, revealing significant potential cost savings.

After examining recommended warehouse locations, we identified three as particularly relevant for cost savings. The areas for the optimal warehouses are shown as yellow circles in Figure 6(c). Two of these areas (Locations 1 and 2) include previously active but currently inactive warehouses, and a third one (Locations 3) does not have either a current or a

previously active warehouse. Since we do not know the storage costs associated with the new warehouses, we used cost information of three actively used warehouses that are known to have high, medium, and low storage pricing rates for the same amount of goods being stored for the same amount of time. As a general example, storing 1,000 lbs of goods for a month would cost at a high-cost warehouse, at a medium-cost warehouse, and at a low-cost warehouse. The potential total savings including the new warehouse locations range from 10 to 15%, as shown in Table 1.

4. Conclusions

In summary, we have developed a method of characterizing the customer space and a mathematical model that provides recommendations for optimizing shipment routes of a logistics network. This is a multiscale approach to the logistics high-dimensional optimization problem. Firstly, we begin by projecting onto a low-dimensional space. We then identify a first-order boundary between strategies. Secondly, we incorporate details due to other dimensions to refine the solutions. Customer spaces also help give an aggregate view of customer behaviors and characteristics. They allow policymakers to compare customers and develop strategies based on the aggregate behavior of the system as a whole.

In particular, based on the customer space of demand frequency versus distance from the production facility, we analyzed two strategies: direct and indirect shipments. Each strategy applies to an area of the customer space with an indeterminate boundary between them. Specific company policies determine the location of the boundary generally. Moreover, detailed properties of each customer can affect the specific strategy used for that customer.

We also used the k -means algorithm to find the optimized location of warehouses based on the location of customers and their demands. The accuracy of the optimization can be improved by updating the conventional k -means algorithm to consider the capacity of warehouses and further details about customers. Still, using this optimization method, companies are able to define the locations of next potential warehouses even without details that can be determined only once they are in operation.

We have applied this analysis to a case study of a manufacturing company with particular constraints. We showed that these optimizations can provide considerable cost savings and improved service quality and customer satisfaction for the company.

Many papers have been published in location-routing problem (LRP) and warehouse location problem (WLP) fields; a few are mentioned in Introduction, but they are still open problems. It has been challenging to find solutions that are applicable to large companies with thousands of customers. While considering more constraints in the calculation of freight cost can improve the accuracy of the outputs, it would increase the complexity and make the solutions much more difficult if not impossible for large systems. Our approach has been shown to work for a company with more than 2000 customers. The future work may further improve the optimization by adding additional

constraints such as a limitation on the number of customers assigned to each facility in addition to a limitation on distance. Overall, we showed that, through a targeted approach to data analysis, we can build a heuristic understanding of the customer space and develop specific descriptive and prescriptive models to yield significant savings.

Appendix

In this section, we show company data on freight costs for a year of box truck, bulk truck, and train shipments. Figures 7–9 show freight costs of the individual shipment types decomposed by the carrier. In total, there are 45 box truck carriers, 15 bulk truck carriers, and 4 train carriers. Figure 7 shows scatter plots of individual freight events by distance and quantity. The color represents cost normalized by the maximum freight cost for that carrier (yellow denotes the maximum freight cost and black denotes the minimum freight cost). Figures 8 and 9 show similar plots for bulk truck and train carriers. The plots indicate that carriers are selected based on the quantity shipped and the freight distance. Regression results for cost functions are shown in the legend of each subplot. The symbol x denotes the distance, and q denotes the quantity.

Data Availability

Data are available at <http://www.necsi.edu/customer/data>.

Conflicts of Interest

The authors declare that they have no conflicts of interest.

Acknowledgments

We thank Irving Epstein and William Glenney for feedback and Matthew Hardcastle for proofreading the manuscript. The writing of this paper was supported by NECSI funds.

References

- [1] V. L. M. Spiegler, M. M. Naim, D. R. Towill, and J. Wikner, "A technique to develop simplified and linearised models of complex dynamic supply chain systems," *European Journal of Operational Research*, vol. 251, no. 3, pp. 888–903, 2016.
- [2] M. T. Melo, S. Nickel, and F. Saldanha-Da-Gama, "Facility location and supply chain management—a review," *European Journal of Operational Research*, vol. 196, no. 2, pp. 401–412, 2009.
- [3] Z. Zhang, Xu Wang, Q. Guo, Z. Li, and Y. Wu, "Simulation and analysis of the complex behavior of supply chain inventory system based on third-party logistics management inventory model with no accumulating of unsatisfied demand," *Complexity*, vol. 2019, Article ID 3194093, 18 pages, 2019.
- [4] D. P. Atherton and G. M. Siouris, "Nonlinear control engineering," *IEEE Transactions on Systems, Man, and Cybernetics*, vol. 7, no. 7, pp. 567–568, 1977.
- [5] Y. Bar-Yam, "Complexity rising: from human beings to human civilization, a complexity profile," in *Encyclopedia of Life Support Systems*, United Nations, Oxford, UK, 2002.

- [6] S. Zokaei, A. Jabbarzadeh, B. Fahimnia, and S. J. Sadjadi, "Robust supply chain network design: an optimization model with real world application," *Annals of Operations Research*, vol. 257, no. 1-2, pp. 15–44, 2017.
- [7] F. Isik, "Complexity in supply chains: a new approach to quantitative measurement of the supply chain complexity," in *Supply Chain Management*, P. Li, Ed., pp. 417–432, InTech, Rijeka, Croatia, 2011.
- [8] J. Aelker, T. Bauernhansl, and H. Ehm, "Managing complexity in supply chains: a discussion of current approaches on the example of the semiconductor industry," *Procedia CIRP*, vol. 7, pp. 79–84, 2013.
- [9] C.-Y. Cheng, T.-L. Chen, and Y.-Y. Chen, "An analysis of the structural complexity of supply chain networks," *Applied Mathematical Modelling*, vol. 38, no. 9-10, pp. 2328–2344, 2014.
- [10] T. Kučera and J. Chocholáč, "Outsourcing as an innovative approach to logistics services of warehousing: a case study," in *The 10th International Days of Statistics and Economics: Conference Proceedings*, Prague, Czech Republic, 2016.
- [11] T. Kucera, "Application of the activity-based costing to the logistics cost calculation for warehousing in the automotive industry," *Communications-Scientific Letters of the University of Zilina*, vol. 21, no. 4, pp. 35–42, 2019.
- [12] T. Kučera, "Logistics cost calculation of implementation warehouse management system: a case study," *MATEC Web of Conferences*, vol. 134, Article ID 00028, 2017.
- [13] G. Nagy and S. Salhi, "Location-routing: issues, models and methods," *European Journal of Operational Research*, vol. 177, no. 2, pp. 649–672, 2007.
- [14] C. Prodhon and C. Prins, "A survey of recent research on location-routing problems," *European Journal of Operational Research*, vol. 238, no. 1, pp. 1–17, 2014.
- [15] M. Schneider and M. Drexl, "A survey of the standard location-routing problem," *Annals of Operations Research*, vol. 259, no. 1-2, pp. 389–414, 2017.
- [16] Y. Abo-Elnaga, B. El-Sobky, and L. Al-Naser, "An active-set trust-region algorithm for solving warehouse location problem," *Journal of Taibah University for Science*, vol. 11, no. 2, pp. 353–358, 2017.
- [17] S. Coniglio, J. Fliege, and R. Walton, "Facility location with item storage and delivery," in *Optimization and Decision Science: Methodologies and Applications*, A. Sforza and C. Sterle, Eds., pp. 287–294, Springer International Publishing, Cham, Switzerland, 2017.
- [18] O. Vera, D. Arturo, E. Olivares-Benitez et al., "Combined use of mathematical optimization and design of experiments for the maximization of profit in a four-echelon supply chain," *Complexity*, vol. 2018, Article ID 8731027, 25 pages, 2018.
- [19] J. G. Villegas, C. Prins, C. Prodhon, A. L. Medaglia, and N. Velasco, "A grasp with evolutionary path relinking for the truck and trailer routing problem," *Computers & Operations Research*, vol. 38, no. 9, pp. 1319–1334, 2011.
- [20] S. H. H. Doulabi and S. Abbas, "Lower and upper bounds for location-arc routing problems with vehicle capacity constraints," *European Journal of Operational Research*, vol. 224, no. 1, pp. 189–208, 2013.
- [21] J. G. Villegas, C. Prins, C. Prodhon, A. L. Medaglia, and N. Velasco, "A matheuristic for the truck and trailer routing problem," *European Journal of Operational Research*, vol. 230, no. 2, pp. 231–244, 2013.
- [22] K. C. Tan, Y. H. Chew, and L. H. Lee, "A hybrid multi-objective evolutionary algorithm for solving truck and trailer vehicle routing problems," *European Journal of Operational Research*, vol. 172, no. 3, pp. 855–885, 2006.
- [23] V. R. Ghezavati, M. S. Jabal-Ameli, and A. Makui, "A new heuristic method for distribution networks considering service level constraint and coverage radius," *Expert Systems with Applications*, vol. 36, no. 3, pp. 5620–5629, 2009.
- [24] M. Eskandarpour, S. H. Zegordi, and E. Nikbakhsh, "A parallel variable neighborhood search for the multi-objective sustainable post-sales network design problem," *International Journal of Production Economics*, vol. 145, no. 1, pp. 117–131, 2013.
- [25] K. Subulan, A. S. Taşan, and A. Baykasoğlu, "Designing an environmentally conscious tire closed-loop supply chain network with multiple recovery options using interactive fuzzy goal programming," *Applied Mathematical Modelling*, vol. 39, no. 9, pp. 2661–2702, 2015.
- [26] N. Labadi, C. Prins, and M. Reghioui, "A memetic algorithm for the vehicle routing problem with time windows," *RAIRO—Operations Research*, vol. 42, no. 3, pp. 415–431, 2008.
- [27] B. N. L. Kechmane and A. Baalal, "Optimization of a two-echelon location lot-sizing routing problem with deterministic demand," *Mathematical Problems in Engineering*, vol. 2018, Article ID 2745437, 12 pages, 2018.
- [28] O. Belgin, I. Karaoglan, and F. Altıparmak, "Two-echelon vehicle routing problem with simultaneous pickup and delivery: mathematical model and heuristic approach," *Computers & Industrial Engineering*, vol. 115, pp. 1–16, 2018.
- [29] S. R. Kancharla and G. Ramadurai, "Multi-depot two-echelon fuel minimizing routing problem with heterogeneous fleets: model and heuristic," *Networks and Spatial Economics*, vol. 19, no. 3, pp. 969–1005, 2019.
- [30] R. Cuda, G. Guastaroba, and M. G. Speranza, "A survey on two-echelon routing problems," *Computers & Operations Research*, vol. 55, pp. 185–199, 2015.
- [31] C. Monthatipkul, "A non-linear program to find an approximate location of a second warehouse: a case study," *Kasetsart Journal of Social Sciences*, vol. 37, no. 3, pp. 190–201, 2016.
- [32] D. B. Shmoys, É. Tardos, and K. Aardal, "Approximation algorithms for facility location problems," in *Proceedings 29th ACM Symposium on Theory of Computing*, pp. 265–274, El Paso TX, USA, May 1997.
- [33] J. Vygen, "Approximation Algorithms for Facility Location Problems (Lecture Notes)," 2005.
- [34] Z. Drezner and H. W. Hamacher, *Facility Location: Applications and Theory*, Springer, New York, NY, USA, 2014.
- [35] E. H. L. Aarts and J. Karel Lenstra, *Local Search in Combinatorial Optimization*, Princeton University Press, Princeton, NJ, USA, 2003.
- [36] B. Manthey and M. B. Tjink, "Perturbation resilience for the facility location problem," *Operations Research Letters*, vol. 46, no. 2, pp. 215–218, 2018.
- [37] B. Korte and J. Vygen, "Facility location," in *Combinatorial Optimization*, pp. 629–665, Springer, New York, NY, USA, 2018.
- [38] S. Lloyd, "Least squares quantization in pcm," *IEEE Transactions on Information Theory*, vol. 28, no. 2, pp. 129–137, 2006.
- [39] D. Arthur and S. Vassilvitskii, "K-means++: the advantages of careful seeding," in *Proceedings of the 18th Annual ACM-SIAM Symposium on Discrete Algorithms*, New Orleans, LA, USA, 2007.
- [40] J. B. MacQueen, "Some methods for classification and analysis of multivariate observations," in *Proceedings of the Fifth Berkeley Symposium on Mathematical Statistics and Probability*, vol. 1, pp. 281–297, University of California Press, Berkeley, Calif, 1967.

Research Article

Impact of Cell Size Effect on Nutrient-Phytoplankton Dynamics

Tiancai Liao,^{1,2} Hengguo Yu ,^{2,3} Chuanjun Dai,^{2,4} and Min Zhao ^{2,4}

¹Key Laboratory of Saline-Alkali Vegetation Ecology Restoration in Oil Field, Ministry of Education, Northeast Forestry University, Harbin, Heilongjiang 150040, China

²Zhejiang Provincial Key Laboratory for Water Environment and Marine Biological Resources Protection, Wenzhou University, Wenzhou, Zhejiang 325035, China

³Department of Mathematics and Information Science, Wenzhou University, Wenzhou, Zhejiang 325035, China

⁴College of Life and Environmental Science, Wenzhou University, Wenzhou, Zhejiang 325035, China

Correspondence should be addressed to Min Zhao; zmcn@tom.com

Received 17 September 2019; Accepted 9 November 2019; Published 28 November 2019

Guest Editor: Tomas Veloz

Copyright © 2019 Tiancai Liao et al. This is an open access article distributed under the Creative Commons Attribution License, which permits unrestricted use, distribution, and reproduction in any medium, provided the original work is properly cited.

In this paper, a nutrient-phytoplankton model, which is described by a system of ordinary differential equations incorporating the effect of cell size, and its corresponding stochastic differential equation version are studied analytically and numerically. A key advantage of considering cell size effect is that it can more accurately reveal the intrinsic law of interaction between nutrient and phytoplankton. The main purpose of this paper is to research how cell size affects the nutrient-phytoplankton dynamics within the deterministic and stochastic environments. Mathematically, we show that the existence and stability of the equilibria in the deterministic model can be determined by cell size: the smaller or larger cell size can lead to the disappearance of the positive equilibrium, but the boundary equilibrium always exists and is globally asymptotically stable; the intermediate cell size is capable to drive the positive equilibrium to appear and be globally asymptotically stable, whereas the boundary equilibrium becomes unstable. In the case of the stochastic model, the stochastic dynamics including the stochastic extinction, persistence in the mean, and the existence of ergodic stationary distribution is found to be largely dependent on cell size and noise intensity. Ecologically, via numerical simulations, it is found that the smaller cell size or larger cell size can result in the extinction of phytoplankton, which is similar to the effect of larger random environmental fluctuations on the phytoplankton. More interestingly, it is discovered that the intermediate cell size is the optimal size for promoting the growth of phytoplankton, but increasing appropriately the cell size can rapidly reduce phytoplankton density and nutrient concentrations at the same time, which provides a possible strategy for biological control of algal blooms.

1. Introduction

Phytoplankton blooms, which can negatively affect the aquatic ecosystems, human health, marine fisheries, and local economy, are growing in frequency, magnitude, and duration globally in recent years [1, 2]. For example, in 2007, serious harmful algal blooms broke out in Lake Taihu, resulting in about 2 million people in Wuxi city short of drinking water for more than a week [3]. In 2011, Lake Erie experienced a record-breaking harmful algal bloom, with a peak intensity more than three times the previously observed algal blooms [4]. These have stimulated a number of scholars to study the dynamics of phytoplankton growth by many

different ways, in order to explore the possible mechanisms underlying the occurrence or termination of these blooms. Nevertheless, such a mechanism in response to the phenomena of blooms is still under investigation due to the diversity and complexity of influencing factors that can affect the growth of phytoplankton in the real aquatic ecological environments. Hence, the research in seeking for some key factors affecting the growth mechanisms of phytoplankton is currently of great interest.

However, in the real aquatic environments, the growth of phytoplankton is generally influenced by many biotic and abiotic factors, such as light [5], cell size [6], climate [7], grazer [8], carbon dioxide [9], nutrient [10], and

temperature [11], which make it difficult to determine a clear mechanism of phytoplankton blooms only through experimental studies. Actually, many ecologists, biologists, and biomathematicians increasingly realize that a mathematical model is a powerful tool for exploring biological and physical processes on the dynamic mechanisms of phytoplankton growth in relation to different factors qualitatively and quantitatively [12, 13], as the research results can help us to find out the key factors that may induce the blooms of phytoplankton but are difficult to predict in the experimental analysis, to answer that what the growth mechanism of phytoplankton is, to predict possibly when the phytoplankton blooms will occur, and to determine the optimal strategy for possible control of phytoplankton blooms [14–25]. The application of mathematical models in other research fields, such as investigating other predator-prey dynamics or infectious disease dynamics, can be found in [26–37].

In 1949, Riley et al. [38] first used the mathematical model to study the nutrient-plankton dynamics, which leads to the formulation of a growing number of mathematical models to describe the nutrient-phytoplankton dynamics or nutrient-plankton dynamics, and many dynamic mechanisms of phytoplankton growth response to various factors have been revealed [14, 15, 22, 39–47]. For example, Chen et al. [43] showed that the proper control of the ratio for nitrogen and phosphorus can more effectively control and eliminate blue-green algae blooms. Pal et al. [44] indicated that the toxin produced by phytoplankton plays a crucial role in the termination of planktonic blooms when the nutrient concentration is very high. Dai et al. [39] signified that time delay not only induces instability of a positive equilibrium but also promotes the formation of patchiness. Chatterjee et al. [41] observed that the nutrient input rate specially caused by artificial eutrophication has a great influence on controlling the planktonic blooms and maintaining stability around the coexistence equilibrium. These excellent results have made a great contribution to the research processes related to the possible mechanisms for the formation or termination of phytoplankton blooms, which in turn indicate that the modeling studies are an alternative, effective, and feasible method to investigate some important factors that may reveal the nature of the blooms of phytoplankton occurring frequently in various water bodies around the world.

Most of the existing mathematical modeling studies on the nutrient-phytoplankton dynamics or nutrient-plankton dynamics usually assume that the nutrient uptake rate, phytoplankton sinking rate, phytoplankton growth rate, and so on are independent of cell size [12, 14, 15, 22, 39–45], which have, in part, been considered to be unrealistic because the factor of cell size is capable to significantly affect the dynamic mechanisms of phytoplankton growth [48]. In fact, cell size is a master functional trait that virtually affects every aspect of phytoplankton biology at the cellular, population, and community levels [49]. Hence, the cell size of phytoplankton not only defines their metabolic activity, growth rates, and numerical abundance

but also strongly affects their contributions to biogeochemical cycles via size-dependent sinking and influences community structure and dynamics via size-dependent species interactions [50–53]. A recent remarkable experimental work, in this research direction, was carried out by Marañón et al. [6], where they further determined experimentally that the growth rate, metabolic rate, and nutrient uptake rate of phytoplankton are size-dependent by using cultures of 22 species of marine phytoplankton from five phyla, ranging from 0.1 to $10^6 \mu\text{m}^3$ in cell volume. Furthermore, by performing an in situ test of Raven's prediction that there is a reversal of the relationship between cell size and maximum achievable growth rate in unicellular algae at the low end of size classes, Bec et al. [54] found that the biomass specific production and growth rates are similar in both small and large cells but peak at intermediate cell sizes. Nevertheless, despite these facts, there is little theoretical explanation on how cell size affects the growth mechanism of phytoplankton. In recent years, a review of relevant literature shows that several plankton models taking into account the effect of cell size have been reported [55–57]. More specifically, Pu et al. [56] indicated that the coevolutionary dynamics of plankton is closely related to cell size. Zhao et al. [57] found that the cell size can significantly affect the growth and reproduction of phytoplankton. The cell size plays an important role in the dynamics of interacting phytoplankton, which has been clearly demonstrated by these recent studies.

In spite of the importance of cell size, a comprehensive understanding towards the dynamic mechanism for phytoplankton growth in relation to cell size is still lacking. Hence, naturally, some questions arise. How cell size affects the nutrient concentration and phytoplankton density? Can the cell size affect the existence and stability of the equilibria? In order to find out the answers to these questions, motivated by these works [12, 55, 56, 58], in the present study, we propose and investigate a nutrient-phytoplankton model, incorporating the effect of cell size, as follows:

$$\begin{cases} \frac{dN}{dt} = I - \frac{\mu(x)Q(x)NP}{a+N} - mN, \\ \frac{dP}{dt} = \frac{\mu(x)NP}{a+N} - s(x)P - dP, \end{cases} \quad (1)$$

subject to the initial conditions $N(0) = N_0 \geq 0$ and $P(0) = P_0 \geq 0$, where $N(t)$ and $P(t)$ are the concentration of nutrient and the density of phytoplankton at time t , respectively. Here, we assume that I is the input rate of nutrient from the environments, m is the removal rate of nutrient, and d is maximum mortality rate of phytoplankton. Let x be the cell size of phytoplankton; we suppose that $\mu(x) = (x/(a_1x^2 + a_2x + a_3))$ [55] is the maximum specific growth rate of phytoplankton as a function of cell size, and $Q(x) = \beta x^3$ [55] signifies the nutrient quota which is proportional to the cube of cell size, where a_i ($i = 1, 2, 3$) are positive empirical constants and β denotes the phytoplankton nutrient quota coefficient. The nutrient uptake rate

of phytoplankton is assumed to depend on $\mu(x)$ and $Q(x)$. That is, the term $\mu(x)Q(x)NP/(a+N)$ is taken as a Michaelis–Menten function that may provide a more realistic reflection of nutrient uptake dynamics [12], leading to a decrease in nutrient concentration, where a is the half-saturation constant of nutrient. Accordingly, the term $\mu(x)NP/(a+N)$ is the conversion efficiency of nutrient uptake by phytoplankton, which means that phytoplankton absorbs nutrient to reproduce offspring and increase the number of phytoplankton. Suppose that the sinking rate of phytoplankton is proportional to the square of cell size, i.e., $s(x) = \alpha x^2$ [55], where α is a constant whose value is affected by the density of the water and the algal cell as well as the viscosity of the water. All the parameters mentioned above are assumed to be positive. From a biological viewpoint, we need to ensure that $(dP/dt) > 0$, so it is assumed that $\mu(x) - s(x) - d > 0$ be always established by default in the whole paper.

On the other hand, in the natural world, the aquatic environment in which phytoplankton lives is always uncertain and random because of the environmental noise disturbances [59], such as unpredictable radiation, light availability, and water temperature variation. Hence, the parameters contained in deterministic models are usually assumed to be invariant constants, which have obvious limitations in modeling the natural ecological systems. Actually, most of the natural phenomena do not strictly follow deterministic laws, but rather oscillate randomly about some average behaviors. A fact further pointed out by May [60] is that the birth rate, carrying capacity, and other parameters involved the model should exhibit random fluctuation to a greater or lesser extent because of the environmental noise effects. Consequently, using stochastic differential equation models may reveal the dynamic mechanisms of phytoplankton growth more accurately compared to their deterministic counterparts. For these reasons, some authors recently introduced environmental noise fluctuations into the aquatic plankton models to study noise influences on the interplay and growth of phytoplankton [61–64]. For example, Yu et al. [61] indicated that environmental fluctuations play a key role in the termination of algal blooms. Camara et al. [63] suggested that stochastic environmental constraints have positive and negative effects on the life of *Daphnia* and algae populations. Obviously, the environmental fluctuations have a vital role in the dynamics of phytoplankton growth. In other words, stochastic environmental disturbance effects should be considered when mathematical models are used to study and model the ecological systems in nature.

Consequently, we introduce white noise perturbations into the deterministic model (1). In the existing literature, there are many different ways to incorporate the noise fluctuations into the ecological systems. In this study, by following the method in [65], we assume that stochastic environmental fluctuations mainly affect the growth of phytoplankton $\mu(x)$. In this way, $\mu(x)$ changes to a random variable $\bar{\mu}(x)$, and $\bar{\mu}(x) = \mu(x) + \delta\dot{B}(t)$, where $B(t)$ is a standard Brownian motion defined on a complete probability space $(\Omega, \mathcal{F}, (\mathcal{F}_t)_{t \geq 0}, \mathbb{P})$, $\dot{B}(t)$ indicates the white

noise, and δ represents the intensity of the white noise. Therefore, by replacing $\mu(x)$ in the deterministic model (1) with $\mu(x) + \delta\dot{B}(t)$, i.e.,

$$\begin{aligned} -\frac{\mu(x)Q(x)NP}{a+N} &\longrightarrow -\frac{\mu(x)Q(x)NP}{a+N} - \frac{\delta\mu(x)Q(x)NP}{a+N}\dot{B}(t), \\ \frac{\mu(x)NP}{a+N} &\longrightarrow \frac{\mu(x)NP}{a+N} + \frac{\delta\mu(x)NP}{a+N}\dot{B}(t), \end{aligned} \quad (2)$$

and then, model (1) becomes

$$\begin{cases} dN = \left(I - \frac{\mu(x)Q(x)NP}{a+N} - mN \right) dt - \delta \frac{\mu(x)Q(x)NP}{a+N} dB(t), \\ dP = \left(\frac{\mu(x)NP}{a+N} - s(x)P - dP \right) dt + \delta \frac{\mu(x)NP}{a+N} dB(t). \end{cases} \quad (3)$$

In the plankton ecology, the persistence and extinction of phytoplankton, which determine whether the phytoplankton is survival or not in the future, are two important topics. However, in the existing literature, the issues on how cell size affects the stochastic extinction and persistence of phytoplankton and how cell size affects the existence of ergodic stationary distribution of phytoplankton that denotes the weak stability of phytoplankton in a stochastic sense, and so on remain largely unanswered. In this paper, we did some works in this research area by studying the stochastic dynamics of model (3).

The main purpose of this paper is to investigate how cell size affects the nutrient-phytoplankton dynamics within the deterministic and stochastic environments by trying to answer the questions proposed in this paper.

In order to facilitate the mathematical analysis for model (1) and model (3) in the following paper, we define

$$X(x) = \frac{\mu(x) - s(x) - d}{d + s(x)} > 0, \quad (4)$$

and we write $X(x)$ as X for simplicity and convenience. The rest of this article is organized as follows: in Section 2, we explore the dynamics of model (1). Section 3 is devoted to studying the dynamics of model (3). In Section 4, we carry out the numerical simulations to verify the analytical results. Section 5 focuses on giving a brief discussion and the summary of the main results.

2. Dynamics of the Deterministic Model (1)

In this section, we mainly focus on investigating the positivity and boundedness of the solutions, as well as studying the existence and stability of the possible equilibria in model (1).

2.1. Positivity and Boundedness of the Solutions. Now, we first present the positivity of the solutions.

Lemma 1. *For any initial value $(N(0), P(0)) = (N_0, P_0) > 0$, all the solutions of model (1) are positive invariant.*

Proof. In model (1), we have $N(t) > 0$ and $P(t) > 0$ for any $t \in [0, B]$, where B is any positive real number. Suppose this is not true, then there exists $B_\tau \in (0, B)$ such that, for any $t \in [0, B_\tau]$, $N(t) > 0$, $P(t) > 0$, and either $N(B_\tau) = 0$ or $P(B_\tau) = 0$. Based on the nutrient and phytoplankton equations in model (1), we can obtain

$$\begin{aligned} N(t) &= N(0)\exp\left[\int_0^t\left(\frac{I}{N(s)} - \frac{\mu(x)Q(x)P(s)}{a+N(s)} - m\right)ds\right], \\ P(t) &= P(0)\exp\left[\int_0^t\left(\frac{\mu(x)N(s)}{a+N(s)} - d - s(x)\right)ds\right]. \end{aligned} \quad (5)$$

Since $(N(t), P(t))$ are defined and continuous in $[0, B_\tau]$, there exists $\varrho \geq 0$ such that for all $t \in [0, B_\tau]$,

$$\begin{aligned} N(t) &= N(0)\exp\left[\int_0^t\left(\frac{I}{N(s)} - \frac{\mu(x)Q(x)P(s)}{a+N(s)} - m\right)ds\right] \\ &\geq N(0)\exp(-B_\tau\varrho), \\ P(t) &= P(0)\exp\left[\int_0^t\left(\frac{\mu(x)N(s)}{a+N(s)} - d - s(x)\right)ds\right] \\ &\geq P(0)\exp(-B_\tau\varrho). \end{aligned} \quad (6)$$

Obviously, if $(N(0), P(0)) = (N_0, P_0) > 0$ and let $t \rightarrow B_\tau$, we have $N(B_\tau) \geq N(0)\exp(-B_\tau\varrho) > 0$ and $P(B_\tau) \geq P(0)\exp(-B_\tau\varrho) > 0$, which contradict the fact that either $N(B_\tau) = 0$ or $P(B_\tau) = 0$. Hence, for all $t \in [0, B_\tau]$, $N(t) > 0$ and $P(t) > 0$. This completes the proof.

Next, we study the boundedness of the solutions. Let $W(t) = N(t) + Q(x)P(t)$, then we have

$$\begin{aligned} \frac{dW}{dt} &= \frac{dN}{dt} + \frac{dP}{dt} \\ &= I - \frac{\mu(x)Q(x)NP}{a+N} - mN + \frac{\mu(x)Q(x)NP}{a+N} - dQ(x)P \\ &\quad - Q(x)s(x)P \\ &= I - mN - (d+s(x))Q(x)P \\ &\leq I - eW, \end{aligned} \quad (7)$$

where $e = \min\{m, (d+s(x))\}$. Thus, we have $(dW/dt) + eW \leq I$. By using the theory of differential inequality [66], for all $t \geq T \geq 0$, we have

$$0 \leq W(t) \leq \frac{I}{e} - \left(\frac{I}{e} - W(T)\right)\exp(-e(t-T)). \quad (8)$$

Hence,

$$\limsup_{t \rightarrow \infty} (N(t) + Q(x)P(t)) \leq \frac{I}{e}. \quad (9)$$

So, we can obtain the theorem as follows. \square

Theorem 1. All the solutions of model (1) that start in R_+^2 are uniformly bounded.

2.2. Existence and Stability of Equilibria. This section is devoted to investigating the existence and stability of the possible equilibria in model (1). Now, we first consider the existence of possible equilibria in model (1).

From the nutrient and phytoplankton equations in model (1), by performing a simple computation, we have that model (1) possesses two equilibria as follows:

- (a) The boundary equilibrium $E_1 = (I/m, 0)$ always exists
- (b) The positive equilibrium $E_* = (a/X, (IX - ma)/Q(x)(\mu(x) - s(x) - d))$, provided $X > (ma/I)$

Next, we deal with the stability of the equilibria in model (1). Through direct calculations, the Jacobian matrix of model (1) at equilibrium $E(N, P)$ is

$$J_E = \begin{bmatrix} \frac{\mu(x)Q(x)aP}{(a+N)^2} - m & \frac{\mu(x)Q(x)N}{a+N} \\ \frac{\mu(x)aP}{(a+N)^2} & \frac{N\mu(x) - (d+s(x))(a+N)}{a+N} \end{bmatrix}. \quad (10)$$

Obviously, the variational matrix of model (1) at the boundary equilibrium E_1 is

$$J_{E_1} = \begin{bmatrix} -m & \frac{I\mu(x)Q(x)}{I+ma} \\ 0 & \frac{(IX - ma)(d+s(x))}{ma+I} \end{bmatrix}, \quad (11)$$

and the two eigenvalues of J_{E_1} are $\lambda_1 = -m < 0$ and $\lambda_2 = (IX - ma)(d+s(x))/(ma+I)$. Hence, the stability of E_1 depends on the sign of λ_2 . That is, if $X < (ma/I)$, E_1 is locally asymptotically stable and is unstable if $X > (ma/I)$.

The variational matrix of model (1) at the positive equilibrium E_* is given by

$$J_{E_*} = \begin{bmatrix} J_{11} & J_{12} \\ J_{21} & J_{22} \end{bmatrix} = \begin{bmatrix} -\frac{X(XI - ma)}{a(X+1)} - m & -\frac{\mu(x)Q(x)}{X+1} \\ \frac{X(XI - ma)}{a(X+1)Q(x)} & 0 \end{bmatrix}, \quad (12)$$

where $J_{11} < 0$, $J_{12} < 0$, and $J_{21} > 0$. Then, it is not difficult to derive the characteristic equation of the positive equilibrium E_* which is $\lambda^2 - \text{tr}(J_{E_*})\lambda + \det(J_{E_*}) = 0$, where $\text{tr}(J_{E_*}) = J_{11} < 0$ and $\det(J_{E_*}) = -J_{21}J_{12} > 0$. Based on the Routh-Hurwitz criterion, the positive equilibrium E_* in model (1) is locally asymptotically stable when it exists.

Hence, we have the following result.

Theorem 2. For model (1), if $X < (ma/I)$, there exists the only boundary equilibrium E_1 , which is locally asymptotically stable; if $X > (ma/I)$, the positive equilibrium E_* appears and is locally asymptotically stable, but the boundary equilibrium E_1 becomes unstable.

In what follows, we provide some results concerning the global stability of the equilibria.

Theorem 3. If $X < (ma/I)$ holds, the boundary equilibrium of model (1) is globally asymptotically stable.

Proof. Letting $E_1 = (I/M, 0) = (N_1, P_1)$ and defining $f(y) = \mu(x)Q(x)y/(a+y)$ with $y \in R$, we consider the following function:

$$V_1(N, P) = \int_{N_1}^N \frac{f(s) - f(N)}{f(s)} ds + kP, \quad (13)$$

where k is a positive constant that will be determined in the paper later.

The derivative of V_1 with respect to the time t along the solutions of model (1) is

$$\begin{aligned} \frac{dV_1}{dt} &= \frac{f(N) - f(N_1)}{f(N)} \frac{dN}{dt} + k \frac{dP}{dt} \\ &= \frac{f(N) - f(N_1)}{f(N)} (-m(N - N_1) - f(N)P) \\ &\quad + \frac{k}{Q(x)} f(N)P - (s(x) + d)kP \\ &= \frac{-m(f(N) - f(N_1))(N - N_1)}{f(N)} + \left(\frac{k}{Q(x)} - 1 \right) f(N)P \\ &\quad + (f(N_1) - (d + s(x))k)P. \end{aligned} \quad (14)$$

Now, we obtain $k = Q(x) > 0$, and then, the above equation becomes

$$\begin{aligned} \frac{dV_1}{dt} &= \frac{-m(f(N) - f(N_1))(N - N_1)}{f(N)} \\ &\quad + (f(N_1) - (d + s(x))Q(x))P. \end{aligned} \quad (15)$$

Notice that $f(y) > 0$ is an increasing function for any $y > 0$, and in view of Lemma 1, if $f(N_1) - (d + s(x))Q(x) < 0$, that is, $X < (ma/I)$, one can get $(dV_1/dt) \leq 0$ and $(dV_1/dt) = 0$ if and only if $(N, P) = (N_1, P_1)$. Hence, Lyapunov–LaSalle’s invariance principle implies the global asymptotic stability of E_1 . This completes the proof. \square

Theorem 4. If $X > (ma/I)$, the positive equilibrium E_* in model (1) is globally asymptotically stable.

Proof. We consider such a function:

$$V_2(N, P) = \int_{N_*}^N \frac{f(s) - f(N_*)}{f(s)} ds + Q(x) \int_{P_*}^P \frac{s - P_*}{s} ds, \quad (16)$$

where the function $f(y)$ ($y \in R$) is the same as the definition above.

The derivative of V_2 with respect to the time t along the solutions of model (1) is

$$\begin{aligned} \frac{dV_2}{dt} &= \frac{f(N) - f(N_*)}{f(N)} \frac{dN}{dt} + Q(x) \frac{P - P_*}{P} \frac{dP}{dt} \\ &= \frac{f(N) - f(N_*)}{f(N)} [-P_*(f(N) - f(N_*)) - f(N)(P - P_*) \\ &\quad - m(N - N_*)] + (P - P_*)(f(N) - f(N_*)) \\ &= \frac{P_*(f(N) - f(N_*))^2}{f(N)} - \frac{m(N - N_*)(f(N) - f(N_*))}{f(N)}. \end{aligned} \quad (17)$$

A discussion similar to the proof of Theorem 1 shows that $(dV_2/dt) \leq 0$ and $(dV_2/dt) = 0$ if and only if $(N, P) = (N_*, P_*)$. Hence, the properties of Lyapunov functional are satisfied, which indicates that the positive equilibrium E_* is globally asymptotically stable when it exists. Considering the local asymptotic stability of the positive equilibrium, we obtain Theorem 4. This ends the proof. \square

Remark 1. Theorems 2, 3, and 4 indicate that the local stability and global stability of the E_* (or E_1) are equivalent, but the existence and stability of positive equilibrium E_* and the local or global stability of boundary equilibrium E_1 are opposite.

3. Dynamics of the Stochastic Model (3)

In this section, we study the existence and uniqueness of the solution, stochastic extinction, persistence in the mean, and a unique ergodic stationary distribution of model (3). First of all, we define a bounded set Θ as follows:

$$\Theta = \left\{ (N, P) \in R_+^2 : N + Q(x)P \leq \frac{I}{e} \right\}, \quad (18)$$

which will be used for the proofs of the following results.

3.1. Existence and Uniqueness of the Positive Solution. In model (3), the coefficients do not satisfy the linear growth condition, though they are locally Lipschitz continuous. Hence, the solution of model (3) may explore at a finite time. In this section, following the research [65], we prove that model (3) has a unique global positive solution.

Theorem 5. For any initial value $(N_0, P_0) \in \Theta$, there is a unique positive solution $(N(t), P(t))$ of model (3) on $t \geq 0$, and the solution will remain in R_+^2 with probability one.

Proof. Let $(N_0, P_0) \in \Theta$, based on the nutrient and phytoplankton equations in model (3) and by virtue of the positivity of N and P , we can get

$$\begin{aligned} \frac{d(N + Q(x)P)}{dt} &= I - mN - (s(x) + d)Q(x)P \\ &\leq I - e(N + Q(x)P), \end{aligned} \quad (19)$$

then $\lim_{n \rightarrow \infty} \sup(N + Q(x)P) \leq (I/e)$, that is,

$$\begin{aligned} \lim_{t \rightarrow \infty} \sup N(t) &\leq \frac{I}{e}, \\ \lim_{t \rightarrow \infty} \sup P(t) &\leq \frac{I}{e\beta x^3}. \end{aligned} \quad (20)$$

So, for any $c \in [0, t]$, we can obtain

$$N(c), P(c) \in \left(0, \frac{I}{e}\right) \quad \text{a.s.} \quad (21)$$

Consequently, the set Θ is a positivity invariant to model (3).

Since the coefficients of model (3) are locally Lipschitz continuous, for any given initial value (N_0, P_0) , there is a unique local solution $(N(t), P(t))$ on $t \in [0, \tau_e)$, where τ_e is the explosion time [67]. To show the solution is global, we need to show that $\tau_e = \infty$.

Let $n_0 > 0$ be sufficiently large for initial values N_0 and P_0 lying within the interval $[1/n_0, n_0]$. For each integer $n > n_0$, considering the stopping times,

$$\tau_n = \inf \left\{ t \in [0, \tau_n), N(t) \notin \left(\frac{1}{n}, n\right) \text{ or } P(t) \notin \left(\frac{1}{n}, n\right) \right\}, \quad (22)$$

and we set $\inf \Phi = \infty$ (Φ denotes the empty set). Obviously, τ_n is increasing as $n \rightarrow \infty$. Let $\tau_\infty = \lim_{n \rightarrow \infty} \tau_n$; hence, $\tau_\infty \leq \tau_e$ a.s.. Next, we only need to show $\tau_\infty = \infty$. If this is false, there is a pair of constants $T > 0$ and $\varepsilon \in (0, 1)$ such that

$$\mathbb{P}\{\tau_n \leq T\} > \varepsilon, n \geq n_1. \quad (23)$$

Define a C^2 -function $V : R_+^2 \rightarrow R_+$ by

$$V(N, P) = -\ln\left(\frac{eN}{I}\right) - \ln\left(\frac{\beta x^3 eP}{I}\right). \quad (24)$$

Using Itô's formula [68], we have

$$\begin{aligned} dV &= \left[\frac{I}{N} + \frac{\mu(x)Q(x)P}{a+N} + m + \frac{\delta^2 \mu(x)^2 Q(x)^2 P^2}{2(a+N)^2} \right. \\ &\quad \left. - \frac{\mu(x)N}{a+N} + s(x) + d + \frac{\delta^2 \mu(x)^2 N^2}{2(a+N)^2} \right] dt \\ &\quad + \frac{\delta \mu(x)(PQ(x) - N)}{a+N} dB \\ &\leq \left[\frac{\mu(x)Q(x)P}{a} + m + \frac{\delta^2 \mu(x)^2 Q(x)^2 P^2}{2a^2} + s(x) + d \right. \\ &\quad \left. + \frac{\delta^2 \mu(x)^2 N^2}{2a^2} \right] dt + \frac{\delta \mu(x)(PQ(x) - N)}{a+N} dB \\ &\leq \left[\frac{\mu(x)I}{ae} + m + s(x) + d + \frac{\delta^2 \mu(x)^2 I^2}{a^2 e^2} \right] dt \\ &\quad + \frac{\delta \mu(x)(PQ(x) - N)}{a+N} dB. \end{aligned} \quad (25)$$

Therefore,

$$dV(N(t), P(t)) \leq \varphi dt + \frac{\delta \mu(x)(PQ(x) - N)}{a+N} dB, \quad (26)$$

where $\varphi = (\mu(x)I/ae) + m + s(x) + d + (\delta^2 \mu(x)^2 I^2/a^2 e^2)$. Then,

$$\begin{aligned} \int_0^{\tau_n \wedge T} dV(N(t), P(t)) &\leq \int_0^{\tau_n \wedge T} \varphi dt \\ &\quad + \int_0^{\tau_n \wedge T} \frac{\delta \mu(x)(PQ(x) - N)}{a+N} dB, \end{aligned} \quad (27)$$

where $\tau_n \wedge T = \min\{\tau_n, T\}$. Taking the expectation of the above inequality, we get

$$\begin{aligned} EV(N(\tau_n \wedge T), P(\tau_n \wedge T)) &\leq V(N_0, P_0) + \varphi E(\tau_n \wedge T) \\ &\leq V(N_0, P_0) + \varphi T. \end{aligned} \quad (28)$$

Let $\Omega_n = \tau_n \leq T$ for $n \geq n_1$, by means of (23), then we have $\mathbb{P}(\Omega_n) \geq \varepsilon$. Note that, for every $\vartheta \in \Omega_n$, there is at least one of $N(\tau_n, \vartheta)$ and $P(\tau_n, \vartheta)$ that equals either $1/n$ or n . Therefore, $V(N(\tau_n, \vartheta), P(\tau_n, \vartheta))$ is not less than

$$\begin{aligned} \phi &= \min \left[-\ln\left(\frac{en}{I}\right) - \ln\left(\frac{\beta ex^3 n}{I}\right), -\ln\left(\frac{en}{I}\right) - \ln\left(\frac{\beta ex^3}{In}\right), \right. \\ &\quad \left. -\ln\left(\frac{e}{nI}\right) - \ln\left(\frac{\beta ex^3 n}{I}\right), -\ln\left(\frac{e}{nI}\right) - \ln\left(\frac{\beta ex^3}{nI}\right) \right]. \end{aligned} \quad (29)$$

It then follows from (28) that

$$V(N_0, P_0) + \varphi T \geq E \left[1_{\Omega_n(\vartheta)} V(N(t), P(t)) \right] \geq \varepsilon \phi, \quad (30)$$

where $1_{\Omega_n(\vartheta)}$ is the indicator function of Ω_n . Letting $n \rightarrow \infty$, we have

$$\infty > V(N_0, P_0) + \varphi T = \infty, \quad (31)$$

which is a contradiction. Hence, we have $\tau_\infty = \infty$. That is, the solution of model (3) will not explode at a finite time with probability one. This completes the proof. \square

3.2. Stochastic Persistence and Extinction of Phytoplankton.

From the proof of Theorem 5, we know that Θ is the positive invariant set of model (3). In this section, we always assume that the initial value $(N_0, P_0) \in \Theta$ and first provide the result concerning the persistence of phytoplankton. For the sake of simplicity, we define

$$\Lambda = \frac{\delta^2 \mu^2(x) I^2}{2(ea + I)^2} + s(x) + d. \quad (32)$$

Then, we have the following result.

Theorem 6. For any given initial $(N_0, P_0) \in \Theta$, if one of the following conditions holds:

$$\begin{aligned}
\text{(i)} \quad \delta^2 &< \frac{2e(I+ea)}{\text{Im}\mu(x)}, \\
X &> \frac{2m(I+ea)^2(\mu(x)-s(x)-d)}{2eI\mu(x)(I+ea)-I^2\delta^2m\mu^2(x)}, \\
\text{(ii)} \quad \delta^2 &> \frac{2e(I+ea)}{\text{Im}\mu(x)}, \\
X &< \frac{2m(I+ea)^2(\mu(x)-s(x)-d)}{2eI\mu(x)(I+ea)-I^2\delta^2\mu^2(x)m},
\end{aligned} \tag{33}$$

then the solution of model (3) obeys

$$\lim_{t \rightarrow \infty} \inf \frac{1}{t} \int_0^t P(s) ds \geq \frac{eI\mu(x) - \Lambda m(ea + I)}{eQ(x)\mu(x)(s(x) + d)} > 0 \quad \text{a.s.}, \tag{34}$$

that is, the phytoplankton in model (3) is persistent in the mean almost surely.

Proof. Based on the nutrient and phytoplankton equations in model (3), we have

$$d(N + \theta P) = (I - mN - (s(x) + d)Q(x)P)dt. \tag{35}$$

Integrating equation (35) from 0 to t on the both sides, we get

$$\begin{aligned}
(N(t) + Q(x)P(t)) - (N_0 + Q(x)P_0) &= tI - m \int_0^t N(s) ds \\
&\quad - (s(x) + d)Q(x) \\
&\quad \cdot \int_0^t P(s) ds.
\end{aligned} \tag{36}$$

Note that $N(t) + Q(x)P(t) = N_0 + Q(x)P_0$ for all $t > 0$, and therefore, we adopt

$$\frac{1}{t} \int_0^t N(s) ds = \frac{I}{m} - \frac{(s(x) + d)Q(x)}{m} \frac{1}{t} \int_0^t P(s) ds. \tag{37}$$

By Itô's formula, we have

$$\begin{aligned}
d \ln P(t) &= \left[-\frac{\delta^2 \mu^2(x)}{2} \left(\frac{N}{a+N} \right)^2 + \frac{\mu(x)N}{a+N} - s(x) - d \right] dt \\
&\quad + \frac{\delta \mu(x)N}{a+N} dB.
\end{aligned} \tag{38}$$

Let $f(N) = (N/(a+N))$, then it is easy to get $(df(N)/dN) > 0$. Hence, $f(N)$ is a strictly increasing function for any $N \in \mathbb{R}^+$. In light of $N \leq (I/e)$, we can obtain

$$\begin{aligned}
-\frac{\delta^2 \mu^2(x)}{2} \left(\frac{N}{a+N} \right)^2 + \frac{\mu(x)N}{a+N} - s(x) - d &\geq -\frac{\delta^2 \mu^2(x)I^2}{2(ea+I)^2} \\
&\quad + \frac{\mu(x)eN}{ea+I} - s(x) - d.
\end{aligned} \tag{39}$$

Integrating equation (38) from 0 to t on the both sides, we have

$$\begin{aligned}
\ln P(t) - \ln P(0) &\geq -\left[\frac{\delta^2 \mu^2(x)I^2}{2(ea+I)^2} + s(x) + d \right] t \\
&\quad + \frac{\mu(x)e}{ea+I} \int_0^t N(s) ds + \kappa(t),
\end{aligned} \tag{40}$$

where

$$\kappa(t) = \int_0^t \frac{\delta \mu(x)N(s)}{a+N(s)} dB(s). \tag{41}$$

Dividing t on both sides of equation (40) and together with equation (37), we get

$$\begin{aligned}
\frac{\ln P(t)}{t} &\geq \left(\frac{eI\mu(x)}{(ea+I)m} - \Lambda \right) - \frac{eQ(x)\mu(x)(s(x)+d)}{(ea+I)m} \frac{1}{t} \\
&\quad \int_0^t P(s) ds + \frac{\kappa(t) + \ln P(0)}{t}.
\end{aligned} \tag{42}$$

Notice that $\kappa(t)$ is a local continuous martingale with $\kappa(0) = 0$ and

$$\lim_{t \rightarrow \infty} \frac{\langle \kappa, \kappa \rangle_t}{t} \leq \left(\frac{\delta \mu(x)I}{ae+I} \right)^2 < \infty. \tag{43}$$

By the strong law of large number [69], we can achieve

$$\lim_{t \rightarrow \infty} \frac{\kappa(t) + \ln P(0)}{t} = 0 \quad \text{a.s.} \tag{44}$$

By means of Lemma 4 in [70], if $\Lambda < (eI\mu(x)/(ea+I)m)$, that is,

$$\begin{aligned}
2m(I+ea)^2(\mu(x)-s(x)-d) &< X[2eI\mu(x)(I+ea) \\
&\quad - I^2\delta^2\mu^2(x)m],
\end{aligned} \tag{45}$$

which is equivalent to

$$\begin{aligned}
X &> \frac{2m(I+ea)^2(\mu(x)-s(x)-d)}{2eI\mu(x)(I+ea)-I^2\delta^2m\mu^2(x)} \text{ provided } \delta^2 \\
&< \frac{2e(I+ea)}{\text{Im}\mu(x)},
\end{aligned} \tag{46}$$

$$\begin{aligned}
\text{or } X &< \frac{2m(I+ea)^2(\mu(x)-s(x)-d)}{2eI\mu(x)(I+ea)-I^2\delta^2\mu^2(x)m} \text{ provided } \delta^2 \\
&> \frac{2e(I+ea)}{\text{Im}\mu(x)},
\end{aligned}$$

then it follows equation (42) that

$$\lim_{t \rightarrow \infty} \inf \frac{1}{t} \int_0^t P(s) ds \geq \frac{eI\mu(x) - \Lambda m(I+ea)}{eQ(x)\mu(x)(s(x)+d)} \text{ a.s.} \tag{47}$$

This completes the proof.

Next, we study the stochastic extinction of phytoplankton in model (3). \square

Theorem 7. For any given initial $(N_0, P_0) \in \Theta$, if one of the following conditions holds:

$$\begin{aligned} \text{(i)} \quad & \delta^2 < \frac{2(I+ea)}{I\mu(x)}, \\ & X < \frac{2(I+ea)^2(\mu(x) - s(x) - d)}{2I\mu(x)(I+ea) - \delta^2\mu^2(x)I^2}, \\ \text{(ii)} \quad & \delta^2 > \frac{2(I+ea)}{I\mu(x)}, \\ & X > \frac{2(I+ea)^2(\mu(x) - s(x) - d)}{2I\mu(x)(I+ea) - \delta^2I^2\mu^2(x)}, \end{aligned} \quad (48)$$

then the solution of model (3) obeys

$$\limsup_{t \rightarrow \infty} \frac{\ln P(t)}{t} \leq \frac{I\mu(x)}{I+ea} - \Lambda < 0 \quad \text{a.s.}, \quad (49)$$

$$\text{or } \limsup_{t \rightarrow \infty} \frac{\ln P(t)}{t} \leq \frac{1}{2\delta^2} - s(x) - d < 0 \quad \text{a.s.},$$

provided $\delta^2 > \max\{(I+ea)/I\mu(x), 1/(2(s(x)+d))\}$, which implies that the phytoplankton in model (3) is stochastic extinction with probability one.

Proof. Define the following quadratic function

$$g(v) = -\frac{\delta^2\mu^2(x)}{2}v^2 + \mu(x)v - s(x) - d, \quad (50)$$

if the symmetric axis $1/\delta^2\mu(x)$ of the equation $g(v)$ is larger than $I/(ae+I)$, that is, $\delta^2 \leq ((I+ea)/\mu(x)I)$, we can find that $g(v)$ takes its maximum value g_{\max} on the interval $[0, I/(ae+I)]$ at $v = I/(ae+I)$, where

$$g_{\max} = \frac{I\mu(x)}{I+ea} - \Lambda. \quad (51)$$

Note that $f(N) = N/(a+N)$ is a strictly increasing function for $N \in [0, I/e]$ when $\delta^2 \leq ((I+ea)/I\mu(x))$; therefore, we have

$$-\frac{\delta^2\mu^2(x)}{2} \left(\frac{N}{a+N} \right)^2 + \frac{\mu(x)N}{a+N} - s(x) - d \leq g_{\max}. \quad (52)$$

Integrating equation (38) from 0 to t and dividing by t on the both sides, we get

$$\frac{\ln P(t)}{t} \leq \left(\frac{I\mu(x)}{I+ea} - \Lambda \right) t + \frac{\kappa(t) + \ln P(0)}{t}. \quad (53)$$

Taking the limit of equation (53) and considering (44), we have

$$\limsup_{t \rightarrow \infty} \frac{\ln P(t)}{t} \leq \frac{I\mu(x)}{I+ea} - \Lambda < 0 \quad \text{a.s.}, \quad (54)$$

provided $\Lambda > (I\mu(x)/(I+ea))$, i.e.,

$$2(I+ea)^2(\mu(x) - s(x) - d) > X[2I\mu(x)(I+ea) - \delta^2I^2\mu^2(x)], \quad (55)$$

which equals to

$$\begin{aligned} \delta^2 &< \frac{2(I+ea)}{I\mu(x)}, \\ X &< \frac{2(I+ea)^2(\mu(x) - s(x) - d)}{2I\mu(x)(I+ea) - \delta^2\mu^2(x)I^2}, \\ \text{or } \delta^2 &> \frac{2(I+ea)}{I\mu(x)}, \\ X &> \frac{2(I+ea)^2(\mu(x) - s(x) - d)}{2I\mu(x)(I+ea) - \delta^2I^2\mu^2(x)}. \end{aligned} \quad (56)$$

On the other hand, if the symmetric axis $1/\delta^2\mu(x)$ of the equation $g(v)$ is in the interval $[0, I/(ea+I)]$, i.e., $\delta^2 \geq ((I+ea)/I\mu(x))$, then the equation $g(v)$ reaches its maximum value $(1/2\delta^2) - s(x) - d$ at $v = 2/\delta^2\mu(x)$. By performing a similar proof processes as above, we have

$$\limsup_{t \rightarrow \infty} \frac{\ln P(t)}{t} \leq \frac{1}{2\delta^2} - s(x) - d < 0 \quad \text{a.s.}, \quad (57)$$

provided $\delta^2 > \max\{(I+ea)/I\mu(x), 1/(2(s(x)+d))\}$. This completes the proof. \square

Remark 2. Theorem 7 indicates that the phytoplankton in model (3) goes to extinction with probability one under some parameter conditions. In this case, it is natural to ask the question how will the nutrient concentration in model (3) change when the phytoplankton is extinct? In fact, when $\mathbb{P}\{\lim_{t \rightarrow \infty} P(t) = 0\} = 1$, then from the model (3), we can obtain the following equation:

$$dN(t) = (I - mN(t))dt, \quad (58)$$

by direct computation, we have $\lim_{t \rightarrow \infty} N(t) = I/m$. Hence, the nutrient concentration will be a positive constant. That is, in this situation, the noise intensity and cell size will have no impacts on the variation of nutrient, and the dynamics of $N(t)$ in model (3) will be similar to the dynamics of E_1 in the deterministic model (1).

3.3. Existence of Ergodic Stationary Distribution. In this section, we shall establish sufficient conditions for the existence and uniqueness of an ergodic stationary distribution for model (3).

Let $Z(t)$ be a regular time-homogeneous Markov process in R^d described by the stochastic differential equation:

$$dZ(t) = f(Z(t))dt + \sum_{l=1}^k g_l(Z)dB_l(t)dB(t). \quad (59)$$

The diffusion matrix of the process $Z(t)$ is defined as follows:

$$\begin{aligned} A(z) &= (a_{ij}(z)), \\ a_{ij}(z) &= \sum_{l=1}^k g_l^i(z)g_l^j(z). \end{aligned} \quad (60)$$

Lemma 2 (see [71]). *The Markov process $Z(t)$ has a unique ergodic stationary distribution $\mu(\cdot)$ if there exists a bounded open domain $D \subset R^d$ with regular boundary Γ , having the following properties:*

(B.1): there is a positive number M such that $\sum_{i,j=1}^d a_{i,j}(z)\xi_i\xi_j \geq M|\xi|^2$, $z \in D$ and $\xi \in \mathbb{R}^d$

(B.2): there exists a nonnegative C^2 -function V such that LV is negative for any $\mathbb{R}^d \setminus D$

Theorem 8. *If $X < (e^2(I + ea)^2 / (e^2(I + ea)^2 I + \delta^2 I^4))$, then for any given initial $(N_0, P_0) \in \Theta$, model (3) has a*

unique stationary distribution $\mu(\cdot)$ and it has the ergodic property.

Proof. To prove Theorem 8, we only need to validate condition (B.1) and (B.2) in Lemma 2. We first prove the condition (B.1). The diffusion matrix of model (3) is given by

$$\begin{aligned} \sum_{i,j=1}^2 a_{ij}(N, P)\xi_i\xi_j &= \left(\frac{\delta\mu(x)Q(x)NP\xi_1}{a+N} \quad \frac{\delta\mu(x)NP\xi_2}{a+N} \right) \begin{pmatrix} -\frac{\delta\mu(x)Q(x)NP\xi_1}{a+N} \\ \frac{\delta\mu(x)NP\xi_2}{a+N} \end{pmatrix} \\ &= \frac{\delta^2\mu^2(x)Q^2(x)N^2P^2}{(a+N)^2}\xi_1^2 + \frac{\delta^2\mu^2(x)N^2P^2}{(a+N)^2}\xi_2^2 \\ &\geq M_0\|\xi\|, \quad \text{for any } (N, P) \in \bar{D}_\sigma \subset \Theta, \\ \xi &= (\xi_1, \xi_2) \in \mathbb{R}_+^2, \end{aligned} \tag{61}$$

where $M_0 = \min_{(N,P) \in \bar{D}_\sigma} \left\{ \delta^2\mu^2(x)Q^2(x)N^2P^2 / (a+N)^2, \delta^2\mu^2(x)N^2P^2 / (a+N)^2 \right\}$, and then the condition (B.1) in Lemma 2 is satisfied. Next, we prove the condition (B.2).

Let

$$M = \frac{2}{\lambda} \max\{2, H\}, \tag{62}$$

where $H = \sup_{(N,P) \in \Theta} \{-2mN^2 + 2IN - 2Q(x)(s(x) + d)P^2 + (2Q(x)I + e^{-1}\delta^2 I\mu^2(x)(Q(x) + 1))P - 2(s(x) + Q(x)m + d)PN\}$ and $\lambda = (1/X) - (I + (\delta^2 I^4 / e^2(I + ea)^2)) > 0$ provided $X < (e^2(I + ea)^2 / (e^2(I + ea)^2 I + \delta^2 I^4))$. Obviously, $(M\lambda/4) \geq 1$. Then, we define a C^2 -function $V(N, P) : \Theta \rightarrow \mathbb{R}$ as follows:

$$\begin{aligned} V(N, P) &= M \left[N + P + \frac{N^2}{2\mu^2(x)} + \frac{Q^2(x)}{\mu^2(x)} \frac{P^2}{2} \right. \\ &\quad \left. + \frac{\ln P}{\mu(x) - s(x) - 1} \right] + (N + Q(x)P)^2, \end{aligned} \tag{63}$$

and it is easy to see that

$$\lim_{n \rightarrow +\infty, (N,P) \in \Theta \setminus D_n} V(N, P) = +\infty, \tag{64}$$

where $D_n = (1/n, n) \times (1/n, n)$. Furthermore, $V(N, P)$ is continuous function, and so, $V(N, P)$ must have a minimum point (N_0, P_0) in the interior of Θ . Then, we define non-negative C^2 -function $V(N, P) : \Theta \rightarrow \mathbb{R}$ in the following form:

$$\begin{aligned} V(N, P) &= M \left[N + P + \frac{N^2}{2\mu^2(x)} + \frac{Q^2(x)}{\mu^2(x)} \frac{P^2}{2} \right. \\ &\quad \left. + \frac{\ln P}{\mu(x) - s(x) - 1} \right] + (N + Q(x)P)^2 - V(N_0, P_0) \\ &:= M[V_1(N, P) + V_2(N, P) + V_3(N, P)] \\ &\quad + V_4(N, P), \end{aligned} \tag{65}$$

where $V_1(N, P) = N + P$, $V_2(N, P) = (N^2/2\mu^2(x)) + (Q^2(x)/\mu^2(x))(P^2/2)$, $V_3 = (\ln P / (\mu(x) - s(x) - 1))$, and $V_4(N, P) = (N + Q(x)P)^2 - V(N_0, P_0)$.

Making using of Itô's formula, we have

$$\begin{aligned} LV_1(N, P) &= I - \frac{\mu(x)Q(x)NP}{a+N} - mN + \frac{\mu(x)NP}{a+N} - (s(x) + d)P \\ &\leq I - mN - (s(x) + d)P + \frac{e\mu(x)NP}{I + ea} \\ &\leq I + \frac{e\mu(x)NP}{I + ea}, \end{aligned} \tag{66}$$

$$\begin{aligned}
LV_2(N, P) &= \frac{1}{\mu^2(x)} \left(IN - \frac{\mu(x)Q(x)PN^2}{a+N} - mN^2 + \frac{\delta^2\mu^2(x)Q^2(x)N^2P^2}{2(a+N)^2} \right) \\
&\quad + \left(\frac{Q(x)}{\mu(x)} \right)^2 \left(\frac{\mu(x)NP^2}{a+N} - (s(x)+d)P^2 + \frac{\delta^2\mu^2(x)N^2P^2}{2(a+N)^2} \right) \\
&\leq \frac{IN}{\mu^2(x)} - \frac{mN^2}{\mu^2(x)} + \frac{Q(x)NP}{\mu(x)(I+ea)} - \frac{(s(x)+d)Q^2(x)P^2}{\mu^2(x)} + \frac{\delta^2I^4}{e^2(I+ea)^2},
\end{aligned} \tag{67}$$

$$\begin{aligned}
LV_3(N, P) &= \frac{1}{\mu(x) - s(x) - d} \left(\frac{\mu(x)N}{a+N} - (s(x)+d) - \frac{\delta^2\mu^2(x)N^2}{2(a+N)^2} \right) \\
&\leq \frac{\mu(x)N}{a(\mu(x) - s(x) - d)} - \frac{1}{X} - \frac{\delta^2e^2N^2\mu^2(x)}{2(ea+I)^2(\mu(x) - s(x) - d)},
\end{aligned} \tag{68}$$

$$\begin{aligned}
LV_4(N, P) &= 2(NI - mN^2 - (s(x)+d)NP + Q(x)IP - Q(x)(s(x)+d)P^2) \\
&\quad + \frac{\delta^2\mu^2(x)Q(x)(Q(x)+1)N^2P^2}{(a+N)^2} \\
&\leq -2mN^2 + 2IN - 2Q(x)(s(x)+d)P^2 + (2Q(x)I + e^{-1}\delta^2I\mu^2(x)(Q(x)+1))P \\
&\quad - 2(s(x)+Q(x)m+d)PN.
\end{aligned} \tag{69}$$

Hence, we get

$$\begin{aligned}
LV(N, P) &= M(LV_1(N, P) + LV_2(N, P) + LV_3(N, P)) + V_4(N, P) \\
&\leq -M\lambda + M \left[\left(\frac{I}{\mu^2(x)} + \frac{\mu(x)}{a(\mu(x) - s(x) - d)} \right) N + \frac{(Q(x) + e\mu^2(x))NP}{\mu(x)(I+ea)} - \left(\frac{m}{\mu^2(x)} \right. \right. \\
&\quad \left. \left. + \frac{\delta^2e^2\mu^2(x)}{2(ea+I)^2(\mu(x) - s(x) - d)} \right) N^2 - \frac{(s(x)+d)Q^2(x)P^2}{\mu^2(x)} \right] \\
&\quad + [-2mN^2 + 2IN - 2Q(x)(s(x)+d)P^2 + (2Q(x)I + e^{-1}\delta^2I\mu^2(x)(Q(x)+1))P \\
&\quad - 2(s(x)+Q(x)m+d)PN].
\end{aligned} \tag{70}$$

Define a bounded closed set

$$D_\varepsilon = \left\{ (N, P) \in \Theta : \varepsilon \leq N \leq \frac{1}{\varepsilon}, \varepsilon \leq P \leq \frac{1}{\varepsilon} \right\}, \tag{71}$$

where $0 < \varepsilon < 1$ is a sufficiently small number. We choose ε sufficiently small such that

$$0 < \varepsilon < \frac{\lambda}{4((I/\mu^2(x)) + (\mu(x)/a(\mu(x) - s(x) - d)) + ((Q(x) + e\mu^2(x))/\mu(x)(I+ea)))}, \tag{72}$$

$$0 < \varepsilon < \frac{Q^2(x)(s(x)+d)(I+ea)}{\mu(x)(Q(x)+e\mu^2(x))}, \tag{73}$$

$$0 < \varepsilon < \frac{\lambda \mu(x)(I + ea)}{2(Q(x) + e\mu^2(x))}, \quad (74)$$

$$0 < \varepsilon < \frac{2m(I + ea)^2(\mu(x) - s(x) - d) + \delta^2 e^2 \mu^4(x)}{2\mu(x)(I + ea)(\mu(x) - s(x) - d)(Q(x) + e^2\mu(x))}, \quad (75)$$

$$-\frac{M\lambda}{2} + \bar{H} \leq -1, \quad (76)$$

$$-M\lambda - \left(\frac{mM}{\mu^2(x)} + \frac{M\delta^2 e^2 \mu^2(x)}{2(ea + I)^2(\mu(x) - s(x) - d)} \right) \frac{1}{\varepsilon^2} + \bar{H}_*, \quad (77)$$

$$-M\lambda - M \frac{(s(x) + d)Q^2(x)}{\mu^2(x)} \frac{1}{\varepsilon^2} + \bar{H}_*, \quad (78)$$

where

$$\begin{aligned} \bar{H} &= \sup_{(N,P) \in \Theta} \left[-2mN^2 + 2IN - 2Q(x)(s(x) + d)P^2 \right. \\ &\quad \left. + (2Q(x)I + e^{-1}\delta^2 I\mu^2(x)(Q(x) + 1))P - 2(s(x) \right. \\ &\quad \left. + Q(x)m + d)PN + M \left(\frac{I}{\mu^2(x)} \right. \right. \\ &\quad \left. \left. + \frac{\mu(x)}{a(\mu(x) - s(x) - d)} \right) N \right], \\ \bar{H}_* &= \sup_{(N,P) \in \Theta} \left[-2mN^2 + 2IN - 2Q(x)(s(x) + d)P^2 \right. \\ &\quad \left. + (2Q(x)I + e^{-1}\delta^2 I\mu^2(x)(Q(x) + 1))P - 2(s(x) \right. \\ &\quad \left. + Q(x)m + d)PN + \left(\frac{I}{\mu^2(x)} + \frac{\mu(x)}{a(\mu(x) - s(x) - d)} \right) N \right. \\ &\quad \left. + \frac{(Q(x) + e\mu^2(x))NP}{\mu(x)(I + ea)} \right]. \end{aligned} \quad (79)$$

For convenience, we divide $\Theta \setminus D_\varepsilon$ into four domains:

$$\begin{aligned} D_\varepsilon^1 &= \{(N, P) \in \Theta : 0 < N < \varepsilon\}, \\ D_\varepsilon^2 &= \{(N, P) \in \Theta : 0 < P < \varepsilon\}, \\ D_\varepsilon^3 &= \left\{ (N, P) \in \Theta : N > \frac{1}{\varepsilon} \right\}, \\ D_\varepsilon^4 &= \left\{ (N, P) \in \Theta : P > \frac{1}{\varepsilon} \right\}. \end{aligned} \quad (80)$$

Clearly, $D_\varepsilon^C = \cup_i^4 D_\varepsilon^i$. Now, we prove that $LV(N, P) \leq 1$ on D_ε^C , which is equivalent to prove it on $D_\varepsilon^1, D_\varepsilon^2, D_\varepsilon^3$, and D_ε^4 , respectively. \square

Case 1. When $(N, P) \in D_\varepsilon^1$, since $NP \leq \varepsilon P \leq \varepsilon(1 + P^2)$, we have

$$\begin{aligned} LV(N, P) &\leq -\frac{M\lambda}{4} + \left[\left(\frac{M\lambda}{\mu^2(x)} + \frac{M\mu(x)\varepsilon}{a(\mu(x) - s(x) - d)} \right. \right. \\ &\quad \left. \left. + \frac{(Q(x) + e\mu^2(x))M\varepsilon}{\mu(x)(I + ea)} \right) - \frac{M\lambda}{4} \right] \\ &\quad - \left(\frac{mM}{\mu^2(x)} + \frac{M\delta^2 e^2 \mu^2(x)}{2(ea + I)^2(\mu(x) - s(x) - d)} \right) N^2 \\ &\quad + \left[\frac{(Q(x) + e\mu^2(x))M\varepsilon}{\mu(x)(I + ea)} - \frac{M(s(x) + d)Q^2(x)}{\mu^2(x)} \right] P^2 \\ &\quad + \left[-\frac{M\lambda}{2} + H \right], \end{aligned} \quad (81)$$

which together with conditions (72) and (73), as well as the definition of M in (62), yields

$$LV(N, P) \leq -\frac{M\lambda}{4} \leq -1. \quad (82)$$

Case 2. When $(N, P) \in D_\varepsilon^2$, since $NP \leq \varepsilon N \leq \varepsilon(1 + N^2)$, we get

$$\begin{aligned} LV(N, P) &\leq \left[-\frac{M\lambda}{2} + \frac{(Q(x) + e\mu^2(x))M\varepsilon}{\mu(x)(I + ea)} \right] \\ &\quad - \frac{MQ^2(x)(s(x) + d)}{\mu^2(x)} P^2 \\ &\quad + \left[\frac{M(Q(x) + e\mu^2(x))\varepsilon}{\mu(x)(I + ea)} - M \left(\frac{m}{\mu^2(x)} \right. \right. \\ &\quad \left. \left. + \frac{\delta^2 e^2 \mu^2(x)}{2(I + ea)^2(\mu(x) - s(x) - d)} \right) \right] N^2 \\ &\quad + \left[-\frac{M\lambda}{2} + \bar{H} \right], \end{aligned} \quad (83)$$

which leads to $LV(N, P) \leq -(M\lambda/2) + \bar{H} \leq 1$ in this domain, in the view of (74)–(76).

Case 3. When $(N, P) \in D_\varepsilon^3$, we have

$$\begin{aligned}
LV(N, P) &\leq -M\lambda + M \left[-\left(\frac{m}{\mu^2(x)} \right. \right. \\
&\quad \left. \left. + \frac{\delta^2 e^2 \mu^2(x)}{2(ea + I)^2 (\mu(x) - s(x) - d)} \right) N^2 \right. \\
&\quad \left. - \frac{(s(x) + d)Q^2(x)}{\mu^2(x)} P^2 \right] + \left[-2mN^2 + 2IN \right. \\
&\quad \left. - 2Q(x)(s(x) + d)P^2 + (2Q(x)I + e^{-1}\delta^2 I \mu^2 \right. \\
&\quad \cdot (x)(Q(x) + 1))P - 2(s(x) + Q(x)m + d)PN \\
&\quad \left. + \left(\frac{I}{\mu^2(x)} + \frac{\mu(x)}{a(\mu(x) - s(x) - d)} \right) N \right. \\
&\quad \left. + \frac{(Q(x) + e\mu^2(x))NP}{\mu(x)(I + ea)} \right] \\
&\leq -M\lambda - \left(\frac{mM}{\mu^2(x)} \right. \\
&\quad \left. + \frac{M\delta^2 e^2 \mu^2(x)}{2(ea + I)^2 (\mu(x) - s(x) - d)} \right) N^2 + \bar{H}_*, \tag{84}
\end{aligned}$$

from (77), and we have $LV(N, P) \leq -1$ on $(N, P) \in D_\varepsilon^3$.

Case 4. When $(N, P) \in D_\varepsilon^4$, we have

$$\begin{aligned}
LV(N, P) &\leq -M\lambda + M \left[-\left(\frac{m}{\mu^2(x)} \right. \right. \\
&\quad \left. \left. + \frac{\delta^2 e^2 \mu^2(x)}{2(ea + I)^2 (\mu(x) - s(x) - d)} \right) N^2 \right. \\
&\quad \left. - \frac{(s(x) + d)Q^2(x)}{\mu^2(x)} P^2 \right] + \left[-2mN^2 + 2IN \right. \\
&\quad \left. - 2Q(x)(s(x) + d)P^2 + (2Q(x)I + e^{-1}\delta^2 I \mu^2 \right. \\
&\quad \cdot (x)(Q(x) + 1))P - 2(s(x) + Q(x)m + d)PN \\
&\quad \left. + \left(\frac{I}{\mu^2(x)} + \frac{\mu(x)}{a(\mu(x) - s(x) - d)} \right) N \right. \\
&\quad \left. + \frac{(Q(x) + e\mu^2(x))NP}{\mu(x)(I + ea)} \right] \\
&\leq -M\lambda - M \frac{(s(x) + d)Q^2(x)}{\mu^2(x)} P^2 + \bar{H}_*, \tag{85}
\end{aligned}$$

in view of (78), and we get $LV(N, P) \leq -1$. This ends the proof.

4. Numerical Results

In this section, we study numerically the impact of the cell size effect on the nutrient-phytoplankton dynamics in the deterministic model (1) as well as the stochastic model (3). The parameter values are taken as shown in Table 1. Unless stated otherwise, we will use them for our simulations. Additionally, in the following numerical simulation, we randomly select the initial value satisfying Θ .

4.1. Impact of Cell Size Factor in the Nutrient-Phytoplankton Dynamics of Model (1). In this section, we study the impact of the cell size effect on the concentration of nutrient and the density of phytoplankton, as well as the stability of the equilibria in model (1).

On the basis of previous theoretical analysis, let $f(x) = X - (ma/I)$, and substituting (4) and the required parameters into $f(x)$, we get $f(x) < 0$, i.e., $X < (ma/I)$ if

$$H_1 := \{x \in R \mid 0 < x < 0.07807216867 \text{ or } 2.981219088 < x\}, \tag{86}$$

and $f(x) > 0$, i.e., $X > (ma/I)$ if

$$H_2 := \{x \in R \mid 0.07807216867 < x < 2.981219088\}. \tag{87}$$

Next, we first show the impact of cell size on the nutrient concentration and phytoplankton density.

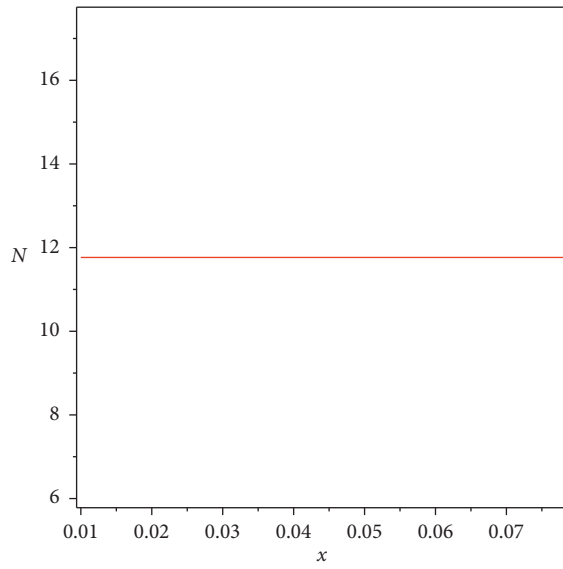
4.1.1. Impact of the Cell Size Effect on the Nutrient Concentration and Phytoplankton Density. Based on the analytical expressions for the positive equilibrium level of nutrient and phytoplankton, one can know that the nutrient concentration and phytoplankton density are closely related to cell size x . However, let $x \in H_1$; the increase of cell size x does not affect the nutrient concentration, which is clearly demonstrated in Figures 1(a) and 1(c). Furthermore, in this case, Figures 1(d) and 1(f) show that the density of phytoplankton is negative or zero. That is, the phytoplankton in model (1) cannot survive when the phytoplankton cell is smaller or larger ($x \in H_1$), which may be the main reason why the nutrient concentration does not change with the increase of cell size.

However, as the cell size increases to the domain of H_2 , the nutrient concentration is a nonmonotonic concave function with respect to cell size x (see Figure 1(b)) and phytoplankton density is a nonmonotonic convex function of cell size x (see Figure 1(e)). Nevertheless, by further analysis, we find that

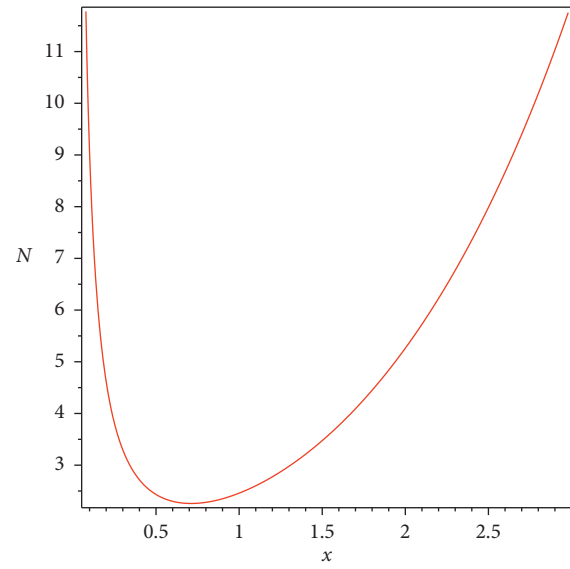
- (1) If $x \in (0.07807216867, 0.1]$, the nutrient concentration is a monotonic decreasing function with respect to cell size x (see Figure 2(a)), but phytoplankton density is a convex-line increasing function of cell size x (see Figure 2(d)), which signifies that phytoplankton can reproduce rapidly and abundantly and absorb a large amount of nutrients during its growth, resulting in a rapid increase in phytoplankton density and a corresponding rapid decrease in nutrient concentration. In fact, from

TABLE 1: Parameter values in numerical simulations for model (1) and model (3).

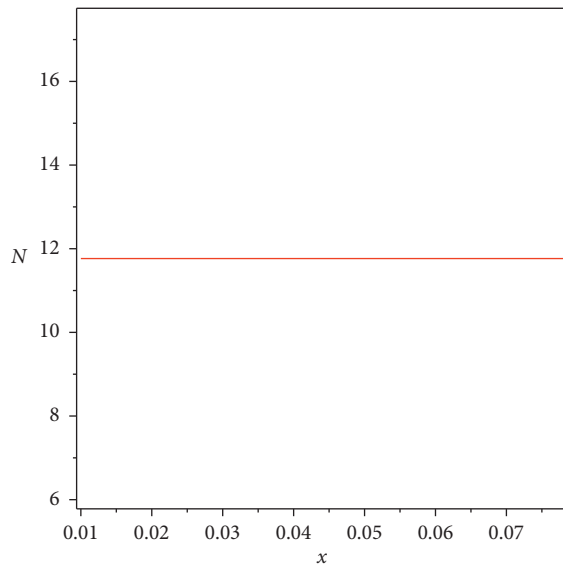
| Parameters | Unit | Values |
|--|--|-----------------|
| I : the nutrient input rate | $\mu\text{mol/Lay}$ | 10 [72] |
| α : the phytoplankton sinking rate coefficient | $1/\text{day}/\mu\text{m}^2$ | 0.1 [55] |
| β : the phytoplankton nutrient quota coefficient | $\mu\text{mol nutrient/cell}/\mu\text{m}^{-b_1}$ | 100 (estimate) |
| m : the removal rate of nutrient | $1/\text{day}$ | 0.85 (estimate) |
| d : the death rate of phytoplankton | $1/\text{day}$ | 0.1 [55] |
| a : the half-saturation constant | $\mu\text{mol/L}$ | 100 (estimate) |
| a_1 : a positive empirical constant | $1/\mu\text{m}^2$ | 0.02 [55] |
| a_2 : a positive empirical constant | $1/\mu\text{m}$ | 0.02 [55] |
| a_3 : a positive empirical constant | Unitless | 0.08 [55] |



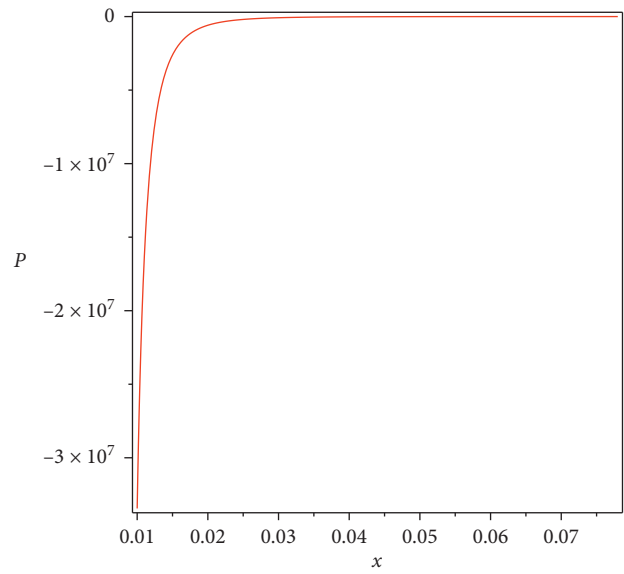
(a)



(b)



(c)



(d)

FIGURE 1: Continued.

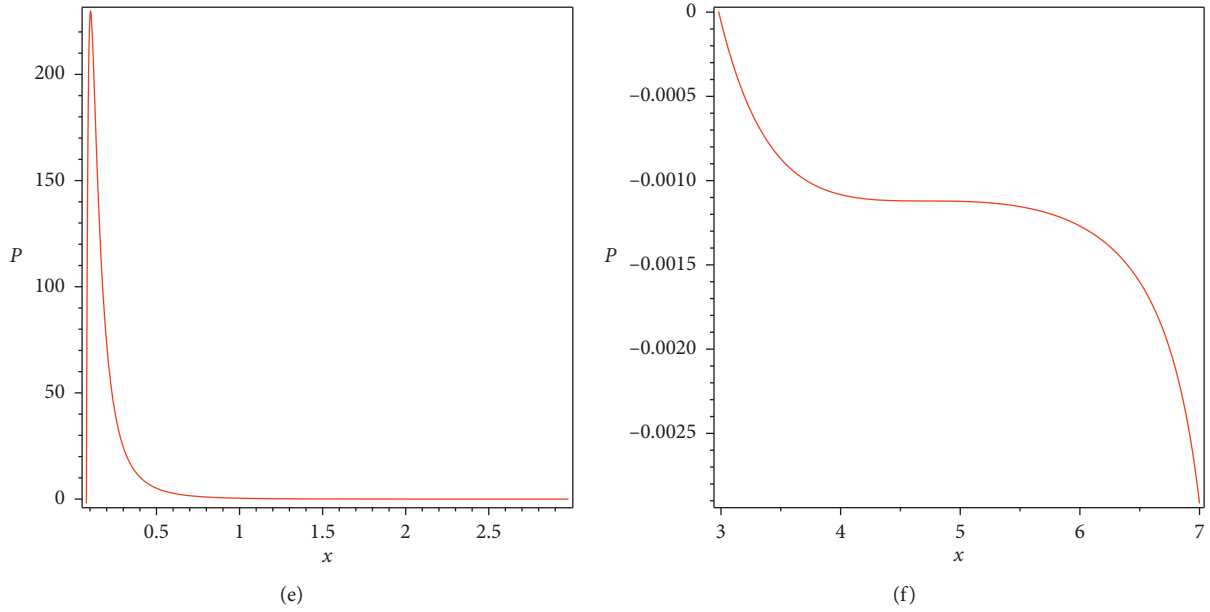


FIGURE 1: (a–c) Bifurcation diagram of nutrient in model (1) with respect to x . (d–f) Bifurcation diagram of phytoplankton in model (1) with respect to x . (a) and (d) for $x \in (0.01, 0.07807216867)$. (b) and (e) for $x \in (0.07807216867, 2.981219088)$. (c) and (f) for $x \in (2.981219088, 7)$.

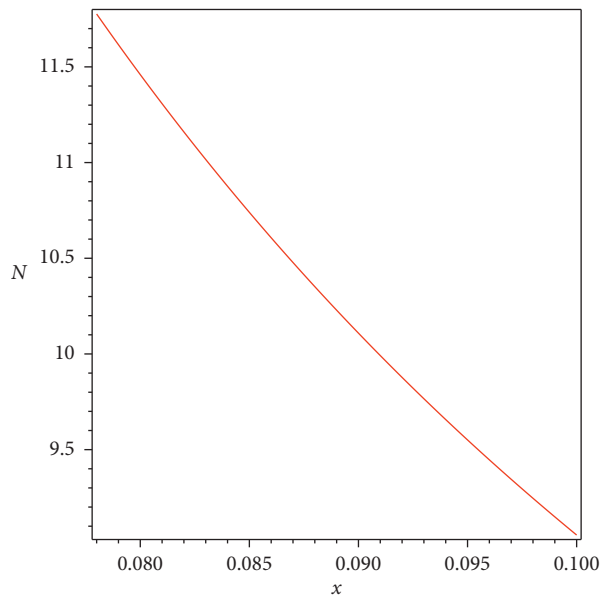
Figure 1(e) or Figures 2(d) and 2(e), we can know that the peak of phytoplankton density appears at $x = 0.1$, and so, $x = 0.1$ is the optimal size for promoting the rapid reproduction of the phytoplankton population.

- (2) If $x \in (0.1, 0.6]$, both the nutrient concentration and phytoplankton density are concave-line decreasing function of cell size x , which are shown in Figures 2(b) and 2(e), respectively. As the density of phytoplankton reaches its peak at $x = 0.1$, when the cell size of phytoplankton exceeds its optimal size, the phytoplankton density decreases with the increase of cell size, but its density is still very high, resulting in the decrease of nutrient concentration, whereas the reduction rate of the nutrient concentration is decreasing compared with that in Figure 2(a).
- (3) If $x \in (0.6, 2.981219088)$, the nutrient concentration is a concave-line increasing function with respect to x (see Figure 2(c)), but phytoplankton density is a concave-line decreasing function of cell size, as is shown in Figure 2(f). Obviously, in this case, with the increase of cell size, the density of phytoplankton decreases dramatically with the rapid increase of nutrient concentration.

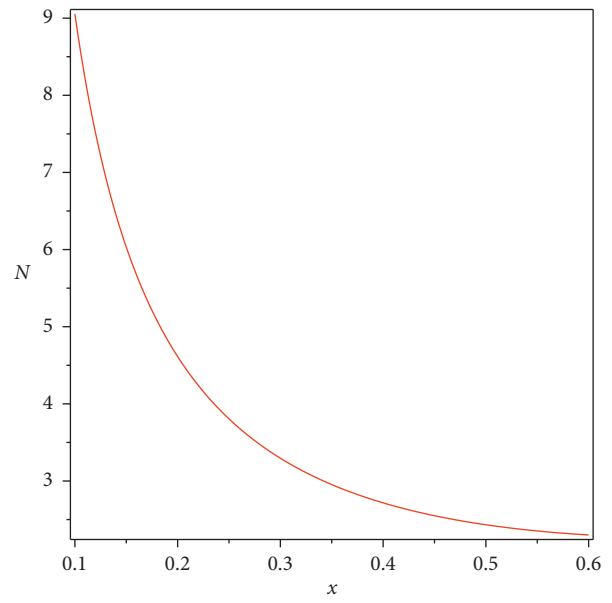
4.1.2. Impact of Cell Size Effect on the Stability of the Equilibria. The analysis indicates that the plane is divided into two regions (i) and (ii) by $I - x$ parameters, as displayed

in Figure 3(a). However, when the phytoplankton cell x is smaller or larger ($x \in H_1$), there exists a unique boundary equilibrium E_1 in the area (i), which is globally asymptotically stable (see Theorem 3). With the increase of cell size ($x \in H_2$), the positive equilibrium E_* appears in (ii) and it is globally asymptotically stable, but the E_1 becomes unstable (see Theorems 2 and 4). Then, we adopt $x = 0.05 \in H_1$ and $x = 0.51 \in H_2$; the corresponding results concerning the global stability of $E_1 = (11.76470588, 0)$ and $E_* = (2.414081849, 4.754928396)$ are shown in (i) and (ii) of Figure 3(b), respectively. It is worth noting that the only difference between (i) and (ii) in Figure 3(b) is that the cell size of phytoplankton is different. Actually, from the Figure 3(a), it is clear that the increase of cell size can lead to the stability changes at the boundary equilibrium E_1 : stable ($0 < x < 0.07807216867$) \rightarrow unstable ($0.07807216867 < x < 2.981219088$) \rightarrow stable ($x > 2.981219088$), and the existence of positive equilibrium E_* changes: nonexistence ($0 < x < 0.07807216867$) \rightarrow existence ($0.07807216867 < x < 2.981219088$) \rightarrow nonexistence ($x > 2.981219088$), which indicates that the cell size plays an important role in determining the existence and stability of the equilibria in model (1).

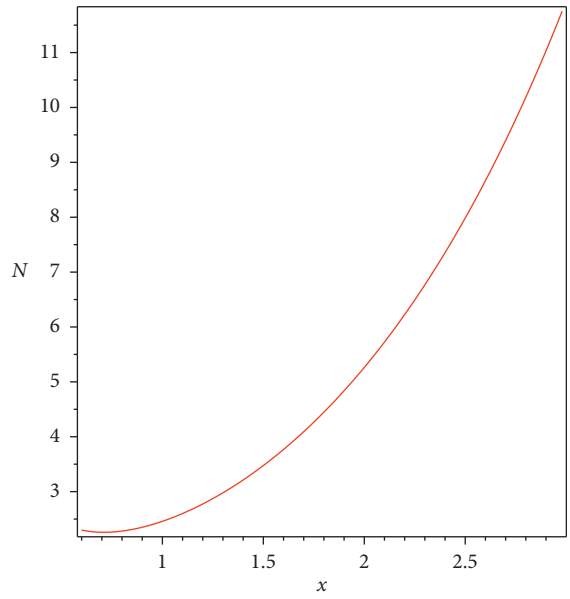
4.2. Impact of Cell Size Factor in the Nutrient-Phytoplankton Dynamics of Model (3). Now, we turn to study the impact of cell size effect on the stochastic dynamics of model (3) by using the Milstein method mentioned in Higham [73]. In this way, model (3) can be rewritten as the following discretization equation:



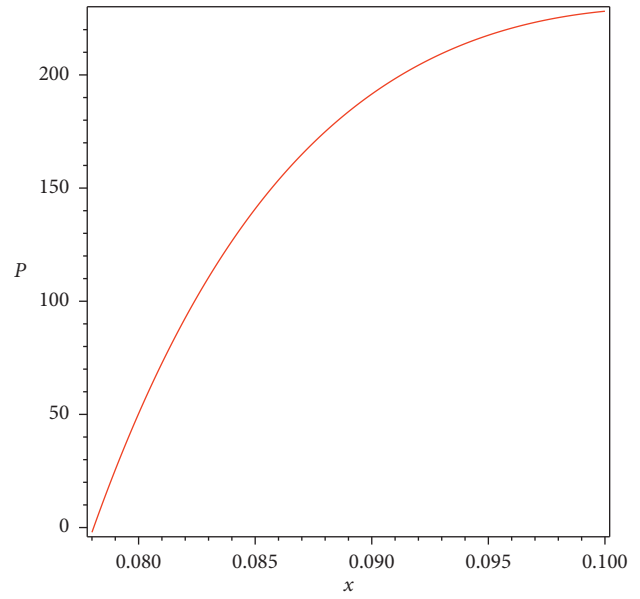
(a)



(b)



(c)



(d)

FIGURE 2: Continued.

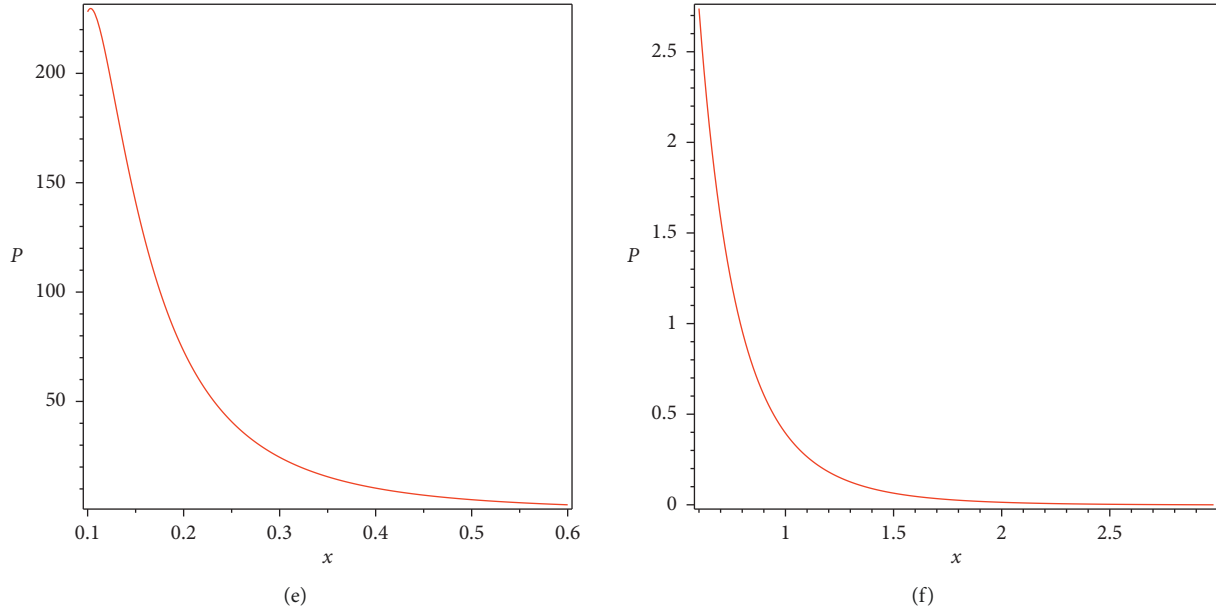


FIGURE 2: (a–c) Bifurcation diagram of nutrient in model (1) with respect to $x \in H_2$. (b–f) Bifurcation diagram of phytoplankton in model (1) with respect to $x \in H_2$. (a) and (d) for $x \in (0.07807216867, 0.1]$. (b) and (e) for $x \in (0.1, 0.6]$. (c) and (f) for $x \in (0.6, 2.981219088)$.

$$\left\{ \begin{array}{l} N_{k+1} = N_k + \left(I - \frac{\mu(x)Q(x)N_kP_k}{a + N_k} - mN_k \right) \Delta t \\ \quad - \frac{\delta\mu(x)Q(x)N_kP_k}{a + N_k} \sqrt{\Delta t} \xi_k + \frac{\delta^2}{2} \frac{\mu(x)Q(x)N_kP_k}{a + N_k} (\xi_k^2 - 1) \Delta t, \\ P_{k+1} = P_k + \left(\frac{\mu(x)N_kP_k}{a + N_k} - s(x)P_k - dP_k \right) \Delta t \\ \quad + \frac{\delta\mu(x)N_kP_k}{a + N_k} \sqrt{\Delta t} \xi_k + \frac{\delta^2}{2} \frac{\mu(x)N_kP_k}{a + N_k} (\xi_k^2 - 1) \Delta t, \end{array} \right. \quad (88)$$

where ξ_k ($k = 1, 2, \dots, n$) are independent Gaussian random variables $N(0, 1)$.

4.2.1. Impact of Cell Size and Environmental Noise Effects on the Survival of Phytoplankton. First of all, we fix $x = 0.51$ and vary $\delta = 0.1, 1.8$ to investigate how environmental noise affects the persistence of model (3).

When we take $\delta = 0.1$, by simple computations, it is not difficult to get that the condition (i) in Theorem 6 and the condition in Theorem 8 are satisfied. From Theorems 6 and 8, it can be obtained that model (3) is persistent in the mean and exists a unique stationary distribution, as is shown in Figure 4. This result signifies that the small environmental noise disturbance can make model (3) maintain some stability in the random sense and drive the solutions to be perturbed near the positive equilibrium of the deterministic model (1).

When we obtain the noise intensity $\delta = 1.8$, then the condition (ii) of Theorem 7 is satisfied. Based on Theorem 7, the phytoplankton goes to extinction with probability one, which implies that the larger environmental noise can result in the extinction of phytoplankton. Figure 5(b) clearly confirms this result. Further, in this case, the nutrient concentration is found to increase to $N = N_1 = 11.76470588 > N_* = 2.414081849$ (see Figure 5(a)), which agrees well with Remark 2.

Next, we fix $\delta = 0.1$ and change $x = 0.001, 0.15, 0.45, 0.95$ to see the effect of cell size on the survival of phytoplankton in model (3). It is clear from Figure 6 that if $x = 0.15$ or $0.45 \in H_2$, the phytoplankton is persistent and becomes extinct when $x = 0.001$ or $0.98 \in H_1$, which indicates that the smaller or larger cell size can result in the extinction of phytoplankton (see the black and pink curves) and the intermediate cell size is advantage for the persistence of phytoplankton (see the blue and green curves). Moreover, by comparing the green curve with the blue curve, it can be found that the increase of cell size can reduce the random variation of phytoplankton caused by environmental noise disturbance and decrease the density of phytoplankton.

4.2.2. Impact of Cell Size Effect on the Existence of Ergodic Stationary Distribution. In order to explore how cell size affects the existence of stationary distribution of phytoplankton and nutrient in model (3), we fix the noise intensity $\delta = 0.1$ and vary the cell size

$$x = 0.01, 0.02, 0.03, 0.04, 0.05, 0.06, \quad (89)$$

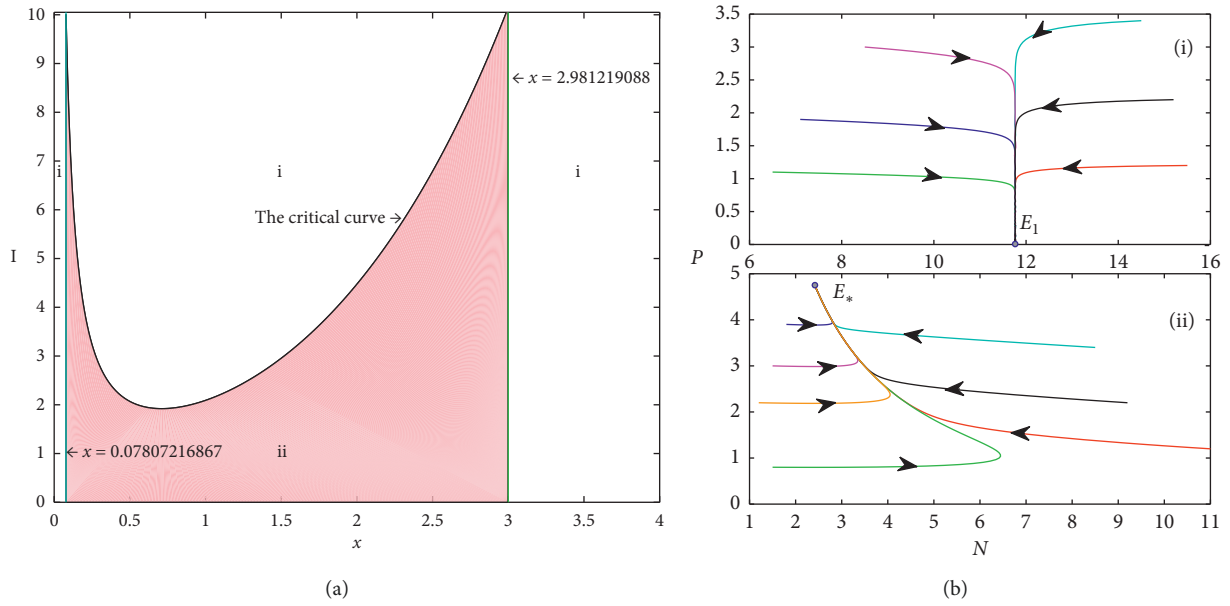


FIGURE 3: (a) Bifurcation diagram with respect to x and I , where the white area (i) indicates that there exists the only boundary equilibrium E_1 that is globally asymptotically stable, and the pink area (ii) implies that the positive equilibrium E_* is globally asymptotically stable but the boundary equilibrium E_1 is unstable. (b) The global stability of the equilibria in model (1) with different cell size x , in which (i) for the boundary equilibrium E_1 with $x = 0.05$ and (ii) for the positive equilibrium E_* with $x = 0.51$.

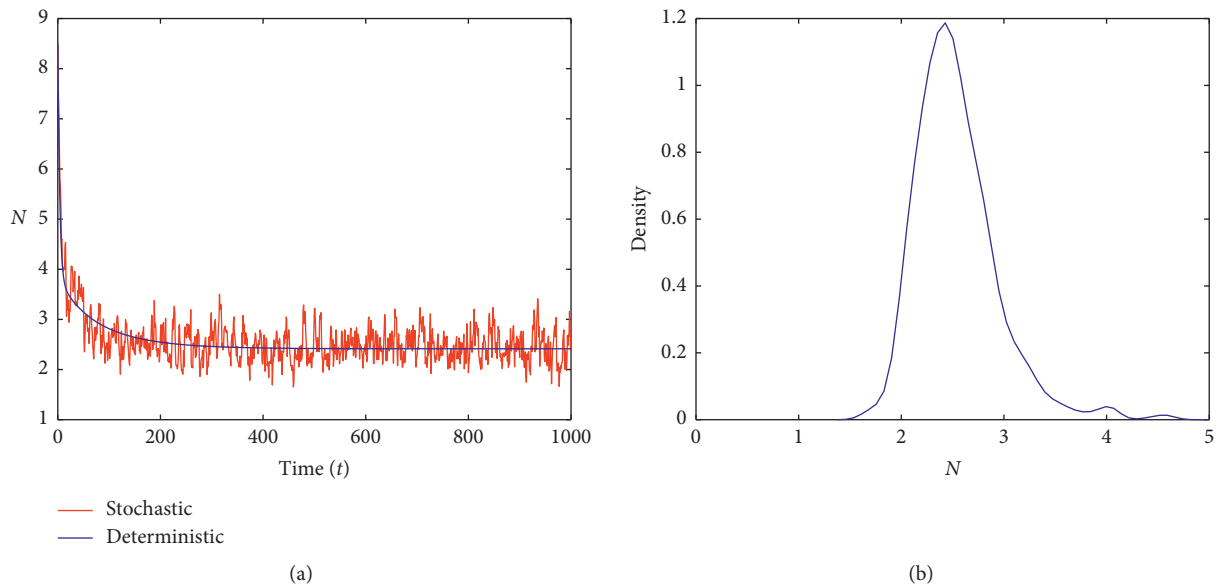


FIGURE 4: Continued.

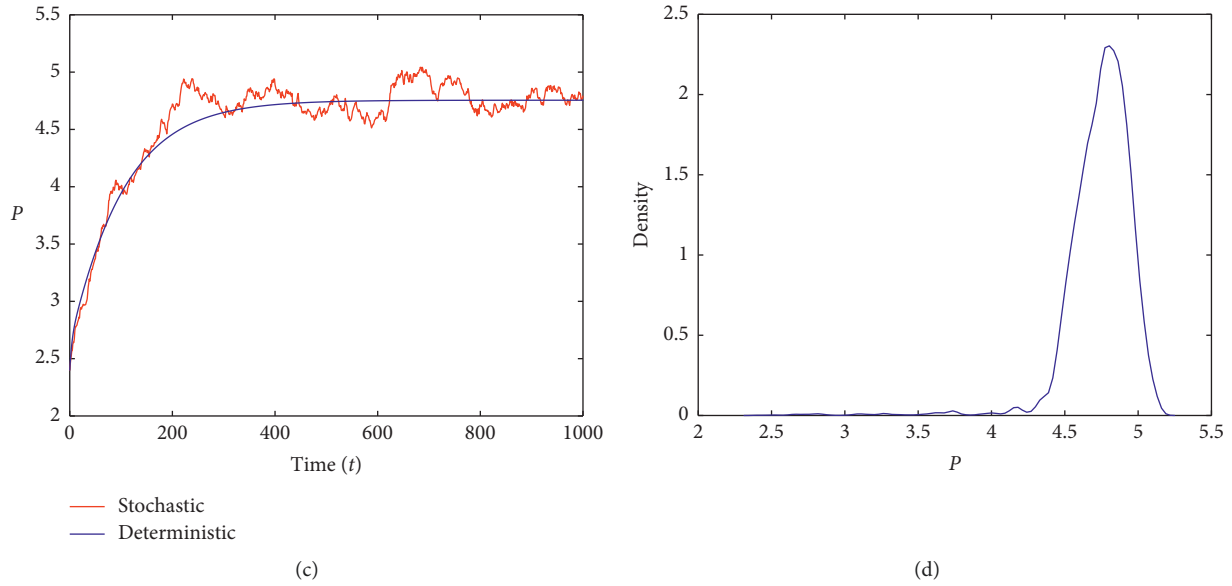


FIGURE 4: (a) and (c) are the solutions of nutrient and phytoplankton in the stochastic model (3) and its corresponding deterministic model (1) with initial value $(N_0, P_0) = (8.5, 2.4)$, respectively. (b) and (d) are the probability density function of nutrient and phytoplankton in model (3), respectively.

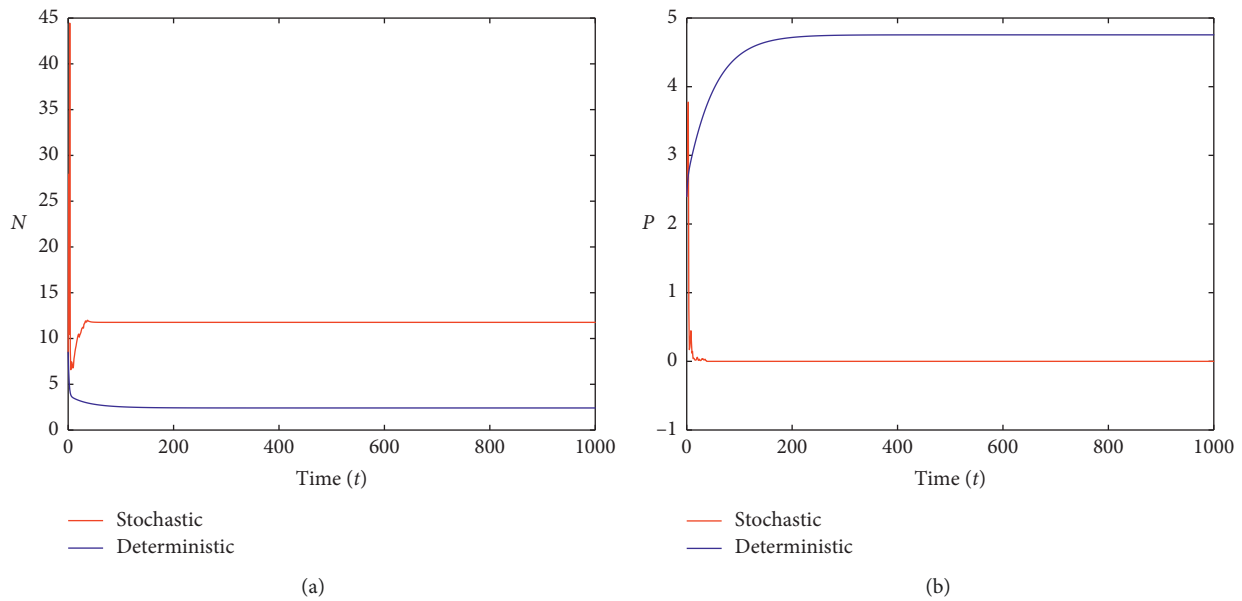


FIGURE 5: The solutions of the stochastic model (3) and its corresponding deterministic model (1) with initial value $(N_0, P_0) = (8.5, 2.4)$. (a) For the nutrient. (b) For the phytoplankton.

which satisfy the parameter condition in Theorem 8. Hence, there exists a stationary distribution of model (3), as is shown in Figure 7.

In Figure 7(a), one can find that, with the increase of cell size, the height of probability density function of phytoplankton decreases, but that of the probability density function of nutrition increases (see Figure 7(c)), which suggests that the increase of cell size is not conducive to

stabilize the nutrient-phytoplankton dynamics in a stochastic sense.

In Figure 7(b), it is shown that the maximum value of the boxplot for phytoplankton increases, while the maximum value of the boxplot for nutrient remains unchanged (see Figure 7(d)), as the cell size increases. This implies that the probability density function of phytoplankton is positively skewed (from left to right), but the probability

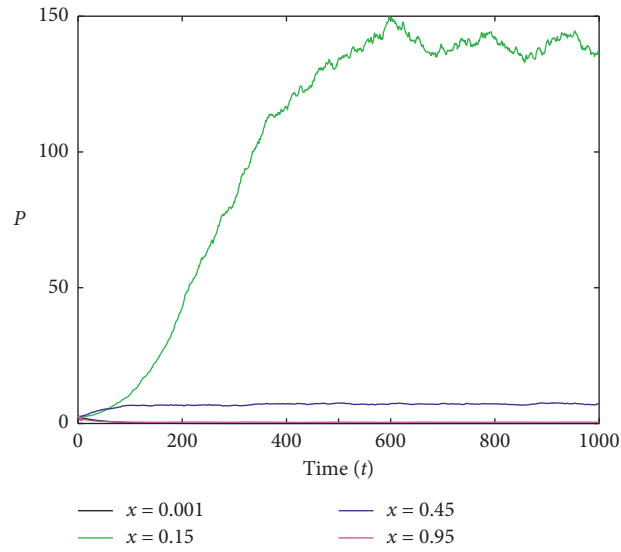


FIGURE 6: The solution of phytoplankton in model (3) with different cell size x , where the noise intensity is fixed to $\delta = 0.1$, and the black curve is for $x = 0.001$, the green curve is for $x = 0.15$, the blue curve is for $x = 0.45$, and the pink curve is for $x = 0.95$.

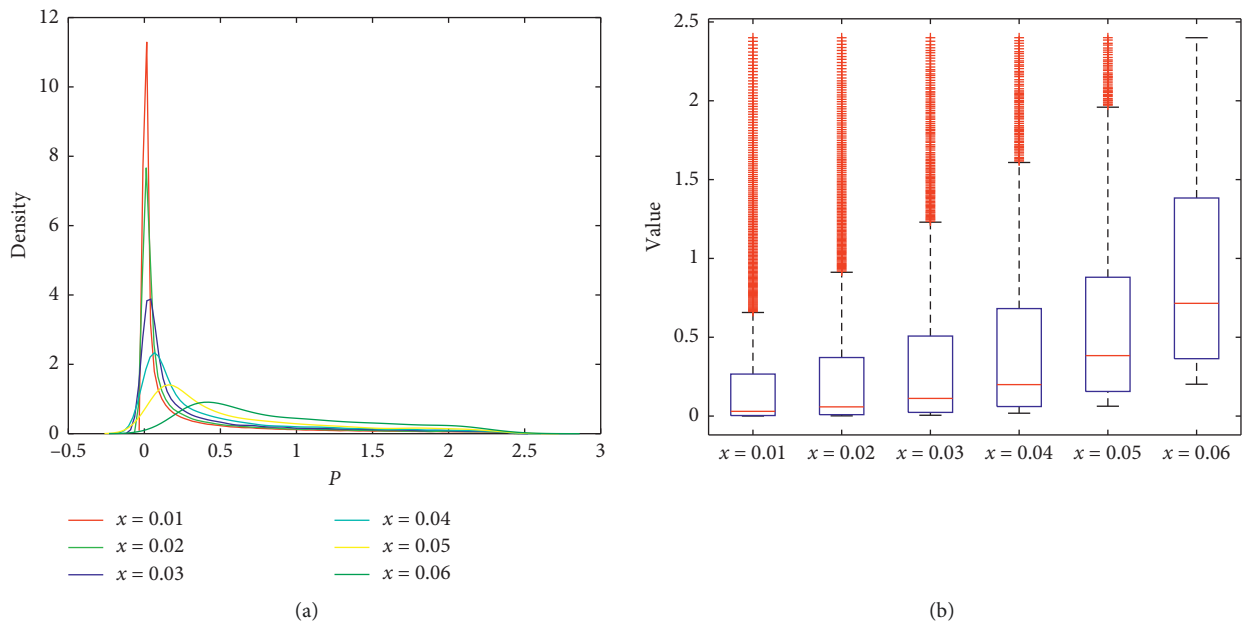


FIGURE 7: Continued.

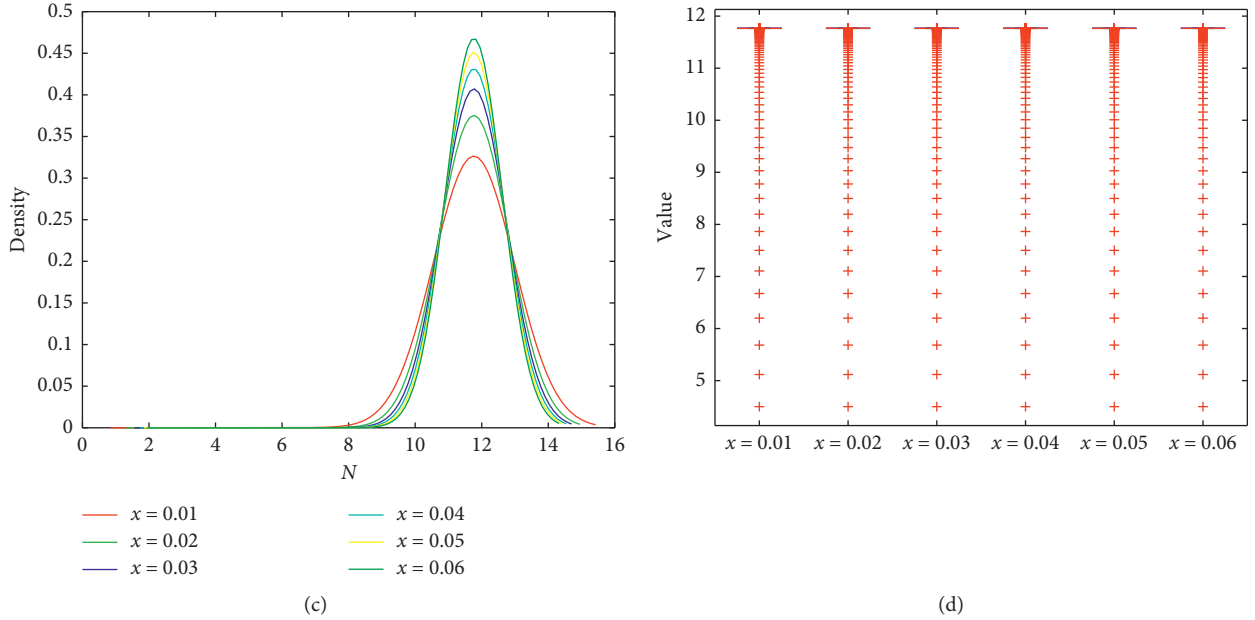


FIGURE 7: The effect of cell size on the existence of stationary distribution for model (3) with different cell size $x = 0.01, 0.02, 0.03, 0.04, 0.05, 0.06$. (a) and (c) are the probability density function of phytoplankton and nutrient in model (3), respectively. (b) and (d) are the boxplot of the solution for phytoplankton and nutrient in model (3) with the corresponding cell size, respectively.

density function of nutrition is not shifted as the cell size increases.

5. Conclusion

In recent years, many field and laboratory evidences indicated that the plankton body size, especially the cell size of phytoplankton, plays a key role in the metabolism, growth, and interaction of phytoplankton [6, 51, 54]. However, little theoretical work has been done in this field. Based on these facts, in this paper, we study analytically and numerically a deterministic nutrient-phytoplankton model taking into account the effects of cell size and its corresponding stochastic version. The consideration of the cell size effect into our proposed model, in this study, makes it different from the traditional nutrient-phytoplankton models [12, 14, 15, 22, 39–45, 61]. The main purpose of this paper is to study the cell size effects on the nutrient-phytoplankton dynamics within the deterministic and stochastic environments.

Mathematically, we show that the existence and stability of the equilibria for the deterministic model (1) can be determined by the value of X (i.e., the cell size). In other words, if $X < (ma/I)$, there exists the only boundary equilibrium that is locally and globally asymptotically stable (see Theorems 2 and 3); if $X > (ma/I)$, the positive equilibrium appears, which is locally and globally asymptotically stable, whereas the boundary equilibrium becomes unstable (see Theorems 2 and 4). For the stochastic model (3), we first prove the existence and uniqueness of the positive solution, and then, the stochastic extinction and persistence in the mean, as well as the existence of ergodic stationary distribution for model (3) are further explored. Ecologically, via

numerical simulations, we find that cell size has rich and complex impacts on the nutrient-phytoplankton dynamics in model (1) and model (3) as follow:

(i) If the cell size is smaller or larger ($0 < x < 0.07807216867$ or $x > 2.981219088$), the phytoplankton cannot survive (see Figures 1(d) and 1(f)). In these cases, the increase of cell size has no impact on the nutrient concentration (see Figures 1(a) and 1(c)). As the cell size increases to the intermediate size, that is, $0.07807216867 < x < 2.981219088$, the phytoplankton appears and its density as well as nutrient concentration begin to change significantly with cell size.

(i₁) When $0.07807216867 < x \leq 0.1$, the increase of cell size can lead to a rapid increase in phytoplankton density and result in a significant reduction in nutrient concentration (see Figures 2(a) and 2(d), respectively). However, the nutrient concentration is still high at this time and the phytoplankton density reached its peak at $x = 0.1$ (see Figures 1(e) and 2(d)), which denotes that the intermediate cell size is the optimum size for the growth of phytoplankton. This result is consistent with the experimental results obtained in [6, 54].

(i₂) When $0.1 < x \leq 0.6$, the increase of cell size is capable to decrease the density of phytoplankton and the concentration of nutrient at the same time (see Figures 2(b) and 2(e)). This suggests that this range is most advantageous for reducing the risk of phytoplankton blooms and the possibility of eutrophication of water bodies. Consequently, if the eutrophication of lakes, rivers, and other water bodies, leading to the occurrence of algal blooms, we can invest a number of

phytoplankton with cell size $x \in (0.1, 0.6]$ to possibly control these phenomena.

(i₃) When $0.6 < x < 2.981219088$, the increase of cell size can cause the significant decrease of phytoplankton and the rapid increase of nutrient concentration (see Figures 2(c) and 2(f), respectively). In this case, the density of phytoplankton is very close to zero as the cell size increases. Actually, based on Theorem 2, the phytoplankton will be extinct and the nutrient concentration will eventually increase to an invariant constant as the cell size continuously increases to greater than 2.981219088. Consequently, the increasing cell size of phytoplankton in this region can inhibit the proliferation of phytoplankton (see Figure 2(f)).

(ii) When the cell size is smaller or larger, i.e., $0 < x < 0.07807216867$ or $x > 2.981219088$, there exists the only boundary equilibrium E_1 in model (1), which is globally asymptotically stable (see (i) of Figure 3(b) and Theorem 3), but the positive equilibrium does not exist in these cases (see Theorem 2); when $0.07807216867 < x < 2.981219088$, which lies in the intermediate cell size, the positive equilibrium exists and is globally asymptotically stable, while the boundary becomes unstable (see (ii) of Figure 3(b) and Theorem 4). Hence, if we can properly control the cell size of phytoplankton to make phytoplankton and nutrient coexist stably, the phytoplankton will not grow rapidly in large quantities; thus, phytoplankton blooms may not occur, which is consistent with the conclusion in (i₂) and (i₃).

(iii) With a fixed value of cell size x , the smaller stochastic environmental fluctuations are shown to be unable to affect the persistence of model (3) (see Figure 4 and Theorem 6), but the larger stochastic environmental fluctuations can result in the extinction of phytoplankton with probability one (see Figure 5 and Theorem 7). With a fixed value of noise intensity, the smaller or larger cell size is found to be capable of causing the extinction of phytoplankton, while the intermediate cell size is in favor of the persistence of phytoplankton (see Figure 6). By comparison, the smaller random environmental disturbances and the intermediate cell size have similar positive effects on the persistence of phytoplankton, but the larger cell size, smaller cell size, and larger random environmental disturbances have similar positive effects on the extinction of phytoplankton.

(iv) For the existence of the stationary distribution for model (3), as the cell size increases, the probability density function of phytoplankton has a positive shift and its height is decreasing, but the probability density function of nutrition has hardly moved and its height is increasing (see Figure 7). This indicates that the cell size may be capable of significantly affect the distribution of phytoplankton in water bodies.

In view of the above findings, the questions raised in Section 1 have been partially well answered. Furthermore, in

comparison to the results with respect to cell size obtained in [55–57], the results of this paper are richer and more complex. Though our study cannot directly confirm that cell size is a factor inducing the phytoplankton blooms, we believe that cell size has the potential to influence the formation of this phenomena because it can affect the growth of phytoplankton and the variation of nutrient concentration in the aquatic ecosystems. Hence, the motive of this paper is not to give a feasible theoretical explanation for the size-dependent mechanisms of phytoplankton growth but to provide a new insight into understanding the intrinsic law of the nutrient-phytoplankton dynamics.

Data Availability

The data used to support the findings of this study are included within the article.

Conflicts of Interest

The authors declare that they have no conflicts of interest.

Acknowledgments

This work was supported by the National Key Research and Development Program of China (grant no. 2018YFE0103700) and the National Natural Science Foundation of China (grant nos. 61871293 and 31570364).

References

- [1] J. Huisman, G. A. Codd, H. W. Paerl, B. W. Ibelings, J. M. H. Verspagen, and P. M. Visser, “Cyanobacterial blooms,” *Nature Reviews Microbiology*, vol. 16, no. 8, pp. 471–483, 2018.
- [2] C. J. Gobler, O. M. Doherty, T. K. Hattenrath-Lehmann, A. W. Griffith, Y. Kang, and R. W. Litaker, “Ocean warming since 1982 has expanded the niche of toxic algal blooms in the North Atlantic and North Pacific oceans,” *Proceedings of the National Academy of Sciences*, vol. 114, no. 19, pp. 4975–4980, 2017.
- [3] L. Guo, “Ecology: doing battle with the green monster of Taihu lake,” *Science*, vol. 317, no. 5842, p. 1166, 2007.
- [4] A. M. Michalak, E. J. Anderson, D. Beletsky et al., “Record-setting algal bloom in lake Erie caused by agricultural and meteorological trends consistent with expected future conditions,” *Proceedings of the National Academy of Sciences*, vol. 110, no. 16, pp. 6448–6452, 2013.
- [5] A. Burson, M. Stomp, E. Greenwell, J. Grosse, and J. Huisman, “Competition for nutrients and light: testing advances in resource competition with a natural phytoplankton community,” *Ecology*, vol. 99, no. 5, pp. 1108–1118, 2018.
- [6] E. Marañoń, P. Cermeño, D. C. López-Sandoval et al., “Unimodal size scaling of phytoplankton growth and the size dependence of nutrient uptake and use,” *Ecology Letters*, vol. 16, no. 3, pp. 371–379, 2013.
- [7] H. Ullah, I. Nagelkerken, S. U. Goldenberg, and D. A. Fordham, “Climate change could drive marine food web collapse through altered trophic flows and cyanobacterial proliferation,” *PLoS Biology*, vol. 16, no. 1, Article ID e2003446, 2018.

- [8] X. Jiang, H. Gao, L. Zhang, H. Liang, and X. Zhu, "Rapid evolution of tolerance to toxic microcystis in two cladoceran grazers," *Sci. Rep.* vol. 6, p. 25319, 2016.
- [9] G. Sandrini, X. Ji, J. M. H. Verspagen et al., "Rapid adaptation of harmful cyanobacteria to rising CO₂," *Proceedings of the National Academy of Sciences*, vol. 113, no. 33, pp. 9315–9320, 2016.
- [10] D. J. Conley, H. W. Paerl, R. W. Howarth et al., "Ecology: controlling eutrophication: nitrogen and phosphorus," *Science*, vol. 323, no. 5917, pp. 1014–1015, 2009.
- [11] J. Rapala and K. Sivonen, "Assessment of environmental conditions that favor hepatotoxic and neurotoxic anabaena spp. strains cultured under light limitation and different temperatures," *Microbial Ecology*, vol. 36, no. 2, pp. 181–192, 1998.
- [12] A. Huppert, B. Blasius, and L. Stone, "A model of phytoplankton blooms," *The American Naturalist*, vol. 159, no. 2, pp. 156–171, 2002.
- [13] J. Chattopadhyay, R. R. Sarkar, and S. Mandal, "Toxin producing plankton may act as a biological control for planktonic blooms—field study and mathematical modelling," *Journal of Theoretical Biology*, vol. 215, no. 3, pp. 333–344, 2002.
- [14] Z. Qiu and H. Zhu, "Complex dynamics of a nutrient-plankton system with nonlinear phytoplankton mortality and allelopathy," *Discrete and Continuous Dynamical Systems—Series B*, vol. 21, no. 8, pp. 2703–2728, 2016.
- [15] C. J. Dai, M. Zhao, H. G. Yu, and Y. P. Wang, "Delay-induced instability in a nutrient-phytoplankton system with flow," *Physical Review E*, vol. 91, no. 3, Article ID 032929, 2015.
- [16] T. Saha and M. Bandyopadhyay, "Dynamical analysis of toxin producing phytoplankton-zooplankton interactions," *Nonlinear Analysis: Real World Applications*, vol. 10, no. 1, pp. 314–332, 2009.
- [17] R. Pal, D. Basu, and M. Banerjee, "Modelling of phytoplankton allelopathy with monod-haldane-type functional response—a mathematical study," *Biosystems*, vol. 95, no. 3, pp. 243–253, 2009.
- [18] H. Yu, M. Zhao, and R. P. Agarwal, "Stability and dynamics analysis of time delayed eutrophication ecological model based upon the zeya reservoir," *Mathematics and Computers in Simulation*, vol. 97, pp. 53–67, 2014.
- [19] B. Ghanbari and J. F. Gómez-Aguilar, "Modeling the dynamics of nutrient-phytoplankton-zooplankton system with variable-order fractional derivatives," *Chaos, Solitons & Fractals*, vol. 116, pp. 114–120, 2018.
- [20] J.-F. Zhang, S. Wang, and X. Kong, "Effects of toxin delay on the dynamics of a phytoplankton-zooplankton model," *Physica A: Statistical Mechanics and Its Applications*, vol. 505, pp. 1150–1162, 2018.
- [21] R. Han and B. Dai, "Spatiotemporal pattern formation and selection induced by nonlinear cross-diffusion in a toxic-phytoplankton-zooplankton model with Allee effect," *Nonlinear Analysis: Real World Applications*, vol. 45, pp. 822–853, 2019.
- [22] C. J. Dai, H. G. Yu, Q. Guo et al., "Dynamics induced by delay in a nutrient-phytoplankton model with multiple delays," *Complexity*, vol. 2019, Article ID 3879626, 16 pages, 2019.
- [23] H. Yu, M. Zhao, Q. Wang, and R. P. Agarwal, "A focus on long-run sustainability of an impulsive switched eutrophication controlling system based upon the zeya reservoir," *Journal of the Franklin Institute*, vol. 351, no. 1, pp. 487–499, 2014.
- [24] J. Yang and M. Zhao, "A mathematical model for the dynamics of a fish algae consumption model with impulsive control strategy," *Journal of Applied Mathematics*, vol. 2012, Article ID 452789, 17 pages, 2012.
- [25] A. Huppert, B. Blasius, R. Olinky, and L. Stone, "A model for seasonal phytoplankton blooms," *Journal of Theoretical Biology*, vol. 236, no. 3, pp. 276–290, 2005.
- [26] Y. Cai, Z. Gui, X. Zhang, H. Shi, and W. Wang, "Bifurcations and pattern formation in a predator-prey model," *International Journal of Bifurcation and Chaos*, vol. 28, no. 11, p. 1850140, 2018.
- [27] H. Zhang, Y. Cai, S. Fu, and W. Wang, "Impact of the fear effect in a prey-predator model incorporating a prey refuge," *Applied Mathematics and Computation*, vol. 356, pp. 328–337, 2019.
- [28] J. Wang, Y. L. Cai, S. M. Fu, and W. M. Wang, "The effect of the fear factor on the dynamics of a predator-prey model incorporating the prey refuge," *Chaos: An Interdisciplinary Journal of Nonlinear Science*, vol. 29, no. 8, Article ID 083109, 2019.
- [29] B. Yang, Y. Cai, K. Wang, and W. Wang, "Optimal harvesting policy of logistic population model in a randomly fluctuating environment," *Physica A: Statistical Mechanics and Its Applications*, vol. 526, Article ID 120817, , 2019.
- [30] W. Wang, X. Gao, Y. Cai, H. Shi, and S. Fu, "Turing patterns in a diffusive epidemic model with saturated infection force," *Journal of the Franklin Institute*, vol. 355, no. 15, pp. 7226–7245, 2018.
- [31] H. Liu, H. Yu, C. Dai et al., "Dynamic analysis of a reaction-diffusion impulsive hybrid system," *Nonlinear Analysis: Hybrid Systems*, vol. 33, pp. 353–370, 2019.
- [32] Y. Cai, Y. Kang, M. Banerjee, and W. Wang, "A stochastic sirs epidemic model with infectious force under intervention strategies," *Journal of Differential Equations*, vol. 259, no. 12, pp. 7463–7502, 2015.
- [33] Y. Cai, Y. Kang, and W. Wang, "A stochastic sirs epidemic model with nonlinear incidence rate," *Applied Mathematics and Computation*, vol. 305, pp. 221–240, 2017.
- [34] Y. Cai, J. Jiao, Z. Gui, Y. Liu, and W. Wang, "Environmental variability in a stochastic epidemic model," *Applied Mathematics and Computation*, vol. 329, pp. 210–226, 2018.
- [35] M. Zhao, X. Wang, H. Yu, and J. Zhu, "Dynamics of an ecological model with impulsive control strategy and distributed time delay," *Mathematics and Computers in Simulation*, vol. 82, no. 8, pp. 1432–1444, 2012.
- [36] M. Zhao, H. Yu, and J. Zhu, "Effects of a population floor on the persistence of chaos in a mutual interference host-parasitoid model," *Chaos, Solitons & Fractals*, vol. 42, no. 2, pp. 1245–1250, 2009.
- [37] C. Dai, M. Zhao, and L. Chen, "Complex dynamic behavior of three-species ecological model with impulse perturbations and seasonal disturbances," *Mathematics and Computers in Simulation*, vol. 84, pp. 83–97, 2012.
- [38] G. A. Riley, H. Stommel, and D. P. Burrpus, "Quantitative ecology of the plankton of the western North Atlantic," *Bulletin—Bingham Oceanographic Collection*, vol. 12, pp. 1–169, 1949.
- [39] C. Dai, M. Zhao, and H. Yu, "Dynamics induced by delay in a nutrient-phytoplankton model with diffusion," *Ecological Complexity*, vol. 26, pp. 29–36, 2016.
- [40] A. Sharma, A. K. Sharma, and K. Agnihotri, "The dynamic of plankton-nutrient interaction with delay," *Applied Mathematics and Computation*, vol. 231, pp. 503–515, 2014.
- [41] A. Chatterjee, S. Pal, and S. Chatterjee, "Bottom up and top down effect on toxin producing phytoplankton and its consequence on the formation of plankton bloom," *Applied*

- Mathematics and Computation*, vol. 218, no. 7, pp. 3387–3398, 2011.
- [42] S. Ruan, “Oscillations in plankton models with nutrient recycling,” *Journal of Theoretical Biology*, vol. 208, no. 1, pp. 15–26, 2001.
- [43] S. Chen, X. Chen, Y. Peng, and K. Peng, “A mathematical model of the effect of nitrogen and phosphorus on the growth of blue-green algae population,” *Applied Mathematical Modelling*, vol. 33, no. 2, pp. 1097–1106, 2009.
- [44] S. Pal, S. Chatterjee, and J. Chattopadhyay, “Role of toxin and nutrient for the occurrence and termination of plankton bloom—results drawn from field observations and a mathematical model,” *Biosystems*, vol. 90, no. 1, pp. 87–100, 2007.
- [45] S. Chakraborty, P. K. Tiwari, A. K. Misra, and J. Chattopadhyay, “Spatial dynamics of a nutrient-phytoplankton system with toxic effect on phytoplankton,” *Mathematical Biosciences*, vol. 264, pp. 94–100, 2015.
- [46] Z. Jiang, X. H. Bi, T. Zhang, and B. G. S. A. Pradeep, “Global Hopf bifurcation of a delayed phytoplankton-zooplankton system considering toxin producing effect and delay dependent coefficient,” *Mathematical Biosciences and Engineering*, vol. 16, no. 5, pp. 3807–3829, 2019.
- [47] Z. Jiang, W. Zhang, J. Zhang, and T. Zhang, “Dynamical analysis of a phytoplankton-zooplankton system with harvesting term and holling III functional response,” *International Journal of Bifurcation and Chaos*, vol. 28, no. 13, p. 1850162, 2018.
- [48] A. Verdy, F. M., and M. Follows, “Optimal phytoplankton cell size in an allometric model,” *Marine Ecology Progress Series*, vol. 379, pp. 1–12, 2009.
- [49] Z. V. Finkel, J. Beardall, K. J. Flynn, A. Quigg, T. A. V. Rees, and J. A. Raven, “Phytoplankton in a changing world: cell size and elemental stoichiometry,” *Journal of Plankton Research*, vol. 32, no. 1, pp. 119–137, 2010.
- [50] E. P. Y. Tang, “The allometry of algal growth rates,” *Journal of Plankton Research*, vol. 17, no. 6, pp. 1325–1335, 1995.
- [51] J. E. Cohen, T. Jonsson, and S. R. Carpenter, “Ecological community description using the food web, species abundance, and body size,” *Proceedings of the National Academy of Sciences (USA)*, vol. 100, no. 4, pp. 17810–1786, 2003.
- [52] K. G. Porter, “Selective grazing and differential digestion of algae by zooplankton,” *Nature*, vol. 244, no. 5412, pp. 179–180, 1973.
- [53] D. Blasco, T. T. Packard, and P. G. Coble, “Size dependence of growth rate, respiratory electron transport system activity, and chemical composition in marine diatoms in the laboratory,” *Journal of Phycology*, vol. 18, no. 1, pp. 58–63, 2004.
- [54] B. Bec, Y. Collos, A. Vaquer, D. Mouillot, and P. Souchu, “Growth rate peaks at intermediate cell size in marine photosynthetic picoeukaryotes,” *Limnology and Oceanography*, vol. 53, no. 2, pp. 863–867, 2008.
- [55] L. Jiang, O. M. E. Schofield, and P. G. Falkowski, “Adaptive evolution of phytoplankton cell size,” *The American Naturalist*, vol. 166, no. 4, pp. 496–505, 2005.
- [56] Z. Pu, M. H. Cortez, and L. Jiang, “Predator-prey coevolution drives productivity-richness relationships in planktonic systems,” *The American Naturalist*, vol. 189, no. 1, pp. 28–42, 2017.
- [57] Q. Zhao, S. Liu, and D. Tian, “Dynamic behavior analysis of phytoplankton-zooplankton system with cell size and time delay,” *Chaos, Solitons & Fractals*, vol. 113, pp. 160–168, 2018.
- [58] H. Serizawa, T. Amemiya, and K. Itoh, “Patchiness in a minimal nutrient—phytoplankton model,” *Journal of Biosciences*, vol. 33, no. 3, pp. 391–403, 2008.
- [59] T. C. Gard, “Stability for multispecies population models in random environments,” *Nonlinear Analysis: Theory, Methods & Applications*, vol. 10, no. 12, pp. 1411–1419, 1986.
- [60] R. May, *Stability and Complexity in Model Ecosystems*, Princeton University Press, New York, USA, 2001.
- [61] X. Yu, S. Yuan, and T. Zhang, “The effects of toxin-producing phytoplankton and environmental fluctuations on the planktonic blooms,” *Nonlinear Dynamics*, vol. 91, no. 3, pp. 1653–1668, 2018.
- [62] Z. Huang and G. Huang, “Mathematical analysis on deterministic and stochastic lake ecosystem models,” *Mathematical Biosciences and Engineering*, vol. 16, no. 5, pp. 4723–4740, 2019.
- [63] B. I. Camara, R. Yamapi, and H. Mokrani, “Environmental stochastic effects on phytoplankton-zooplankton dynamics,” *Nonlinear Dynamics*, vol. 96, no. 3, pp. 2013–2029, 2019.
- [64] D. Valenti, G. Denaro, B. Spagnolo et al., “Stochastic models for phytoplankton dynamics in Mediterranean sea,” *Ecological Complexity*, vol. 27, pp. 84–103, 2016.
- [65] C. Xu and S. Yuan, “An analogue of break-even concentration in a simple stochastic chemostat model,” *Applied Mathematics Letters*, vol. 48, pp. 62–68, 2015.
- [66] G. Birkhoff and G. Rota, *Ordinary Differential Equations*, John Wiley & Sons, New York, USA, 1982.
- [67] X. Mao, *Stochastic Differential Equations and Applications*, Horwood Publishing, Chichester, UK, 2nd edition, 2007.
- [68] T. Gard, *Introduction to Stochastic Differential Equations*, Marcel Dekker, New York, USA, 1988.
- [69] X. Mao, *Stochastic Differential Equations and Their Applications*, Horwood, Chichester, UK, 1997.
- [70] M. Liu, K. Wang, and Q. Wu, “Survival analysis of stochastic competitive models in a polluted environment and stochastic competitive exclusion principle,” *Bulletin of Mathematical Biology*, vol. 73, no. 9, pp. 1969–2012, 2011.
- [71] R. Z. Hasminiskii, *Stochastic Stability of Differential Equations*, Sijthoff and Noordhoff, Alphen aan den Rijn, Netherlands, 1980.
- [72] G. T. Evans and J. S. Parslow, “A model of annual plankton cycles,” *Biological Oceanography*, vol. 3, pp. 327–347, 1985.
- [73] D. J. Higham., “An algorithmic introduction to numerical simulation of stochastic differential equations,” *SIAM Review*, vol. 43, no. 3, pp. 525–546, 2001.